Protein Structure, Stability, and Interactions

Edited by

John W. Shriver

Protein Structure, Stability, and Interactions

METHODS IN MOLECULAR BIOLOGY™

John M. Walker, SERIES EDITOR

Protein Structure, Stability, and Interactions

Edited by

John W. Shriver

Departments of Chemistry University of Alabama in Huntsville, Huntsville, AL 35899 USA

Editor
John W. Shriver
Departments of Chemistry
University of Alabama in Huntsville
Huntsville, AL 35899
USA
john.shriver@uah.edu

Series Editor
John M. Walker
School of Life Sciences
University of Hertfordshire
Hatfield, Hertfordshire, AL10 9AB, UK

Printed on acid-free paper

springer.com

Preface

Characterizations of protein folding (stability) and molecular interactions (binding) are essential in many areas of biochemistry and cell biology. Neither can be viewed as an all-or-none phenomenon, and a healthy cell requires exquisite adjustment of both. Although initial descriptions of stability and interactions tend to be qualitative, an understanding of their importance requires a quantitative approach with a level of precision that matches their fine-tuning in a living cell.

Two volumes in the *Methods in Molecular Biology Series* published by Humana have been devoted to protein stability and folding. The first, *Protein Stability and Folding: Theory and Practice* (edited by Bret A. Shirley), appeared in 1995 and was primarily devoted to the basic methods utilized for studies of the thermodynamics of protein folding. The second was entitled *Protein Structure, Stability, and Folding* (edited by Kenneth "Kip" Murphy) and appeared in 2001. The goal of the second volume as stated by Kip was to serve as a companion to the first with more of an emphasis on theory, with some chapters focusing on some exciting new methods. This volume follows that path with a slight change in title to reflect the shift in emphasis: *Protein Structure, Stability, and Interactions.*

We present here an overview of some of the methods currently used to study protein stability and protein interactions, including scanning and titration calorimetry, high-field NMR and other spectroscopic methods, and analytical ultracentrifugation. Recent advances in the area of protein interactions with water, salts, and other solutes, as well as the effects of crowding have been impressive and are described in a couple of chapters. Methods for studying flexibility and intramolecular interactions in proteins, along with characterization of the unfolded state, are also included. Exciting new techniques include single-molecule methods as well as a new application of denaturants to address protein stability in vivo.

I would like to thank all of the authors, the Series Editor John M. Walker, and the publisher for their hard work and patience in putting together this volume. We hope that it proves useful to many students and workers, not only in the field of protein structural biology, but also in related fields such as cell biology where the application of physical methods will become increasingly necessary as we move toward a quantitative description of the chemistry and physics of life. Finally, I would like to thank my colleagues, and especially my family, for their understanding and support.

John W. Shriver

Contents

Contributors

JAE-HYUN CHO • *Department of Biochemistry and Molecular Biophysics, Columbia University, New York, NY, USA*

STEPHEN P. EDMONDSON • *Department of Chemistry, University of Alabama in Huntsville, Huntsville, AL, USA*

LILA GIERASCH • *Departments of Biochemistry and Molecular Biology and Chemistry, University of Massachusetts-Amherst, Amherst, MA, USA*

G. R. GRIMSLEY • *Department of Molecular and Cellular Medicine, Texas A&M Health Science Center, College Station, TX, USA*

GRISELDA HERNANDEZ • *Wadsworth Center, New York State Department of Health, and Department of Biomedical Sciences, University at Albany – SUNY, Albany, NY, USA*

ZOYA IGNATOVA • *Cellular Biochemistry, Institute of Biology and Biochemistry, University of Potsdam, Karl-Liebknecht-Str. 24–25, Haus 25, 14476 Potsdam-Golm, Germany*

ILIAN JELESAROV • *Biochemisches Institut der Universität Zürich, Zürich, Switzerland*

ANDREY KARSHIKOFF • *Karolinska Institute, Department of Biosciences and Nutrition, Stockholm, Sweden*

DAVID M. LEMASTER • *Wadsworth Center, New York State Department of Health, and Department of Biomedical Sciences, University at Albany – SUNY, Albany, NY, USA*

JAMES M. LIPCHOCK • *Department of Chemistry, Yale University, New Haven, CT, USA*

J. PATRICK LORIA • *Department of Chemistry, Yale University, New Haven, CT, USA*

GEORGE I. MAKHATADZE • *Center for Biotechnology and Interdisciplinary Studies, Rensselaer Polytechnic Institute, Troy, NY, USA*

G. ULRICH NIENHAUS • *Institute of Biophysics, University of Ulm, Ulm, Germany*

C. NICK PACE • *Department of Molecular and Cellular Medicine, Texas A&M Health Science Center, and Department of Biochemistry and Biophysics, Texas A&M University, College Station, TX, USA*

LAUREL M. PEGRAM • *Department of Chemistry, University of Wisconsin-Madison, Madison, WI, USA*

PETER L. PRIVALOV • *Department of Biology, Johns Hopkins University, Baltimore, MD, USA*

DANIEL P. RALEIGH • *Department of Chemistry, Stony Brook University, Stony Brook, NY, USA*

M. THOMAS RECORD • *Departments of Chemistry and Biochemistry, University of Wisconsin-Madison, Madison, WI, USA*

JÖRG RÖSGEN • *Department of Biochemistry and Molecular Biology, University of Texas Medical Branch, Galveston, TX, USA*

J. MARTIN SCHOLTZ • *Department of Molecular and Cellular Medicine, Texas A&M Health Science Center, and Department of Biochemistry and Biophysics, Texas A&M University, College Station, TX, USA*

KATARINA L. SCHWEIKER • *Center for Biotechnology and Interdisciplinary Studies, Rensselaer Polytechnic Institute, Troy, NY, USA*

KEVIN L. SHAW • *Department of Biology, Grove City College, Grove City, PA, USA*

JOHN W. SHRIVER • *Departments of Chemistry and Biological Sciences, University of Alabama in Huntsville, Huntsville, AL, USA*

WALTER F. STAFFORD • *Boston Biomedical Research Institute, Watertown, MA, USA*

Chapter 1

Microcalorimetry of Proteins and Their Complexes

Peter L. Privalov

Abstract

Ultrasensitive microcalorimetric techniques for measuring the heat capacities of proteins in dilute solutions over a broad temperature range (DSC) and the heats of protein reactions at fixed temperatures (ITC) are described and the methods of working with these instruments are considered. Particular attention is paid to analyzing the thermal properties of individual proteins, their stability, the energetics of their folding, and their association with specific macromolecular partners. Use of these calorimetric methods is illustrated with examples of small compact globular proteins, small proteins having loose noncompact structure, multidomain proteins, and protein complexes, particularly with DNA.

Key words: microcalorimetry, proteins, complexes, folding, stability, energetics.

1. Introduction

Ever since it was realized that the formation of the unique spatial structures of proteins and their complexes is in principle a reversible, thermodynamically driven process, investigation of their energetics has gained high priority. This has required direct measurements of the heat effects of intra- and intermacromolecular reactions of proteins in highly dilute solutions preventing their nonspecific interactions. That needed development of supersensitive calorimetric techniques, differential scanning and isothermal reaction microcalorimetry, for measuring the heats associated with change in temperature at fixed solvent conditions or with change in solvent conditions at fixed temperature, respectively *(1, 2)*. The differential scanning microcalorimeter (DSC) gained particular importance in studying the thermal properties of proteins, providing information on the stability of protein structure and its domain organization. Measurements of the heats of

reactions at fixed temperature by the isothermal titration micro-calorimeter (ITC) are required for understanding the energetics of protein interaction with various ligands. This method has gained particular importance in studying the interactions of proteins with specific macromolecular partners (e.g., other proteins and nucleic acids), the processes which represent the most basic biological functions. As will be shown below, these two methods are in fact complementary, and for a full description of the energetic basis of the structure of proteins and their specific complexes the information provided by both methods is required.

2. Microcalori-metric Techniques

2.1. Isothermal Titration Microcalorimeter

The isothermal reaction (titration) microcalorimeter (ITC) measures the heat effects of injecting small portions of one reagent into the dilute solution of another reagent (**Fig. 1.1a,b**), and thus yield the enthalpy of their association, ΔH^a (for these techniques, *see* Refs. *(2–5)*). From serial injections of the titrant one gets its binding isotherm which is expressed by the equation

$$Q = \Delta H^a \cdot V \cdot [M]_{tot} \cdot K^a \cdot [L]/\{1 + K^a \cdot [L]\}, \quad (1.1)$$
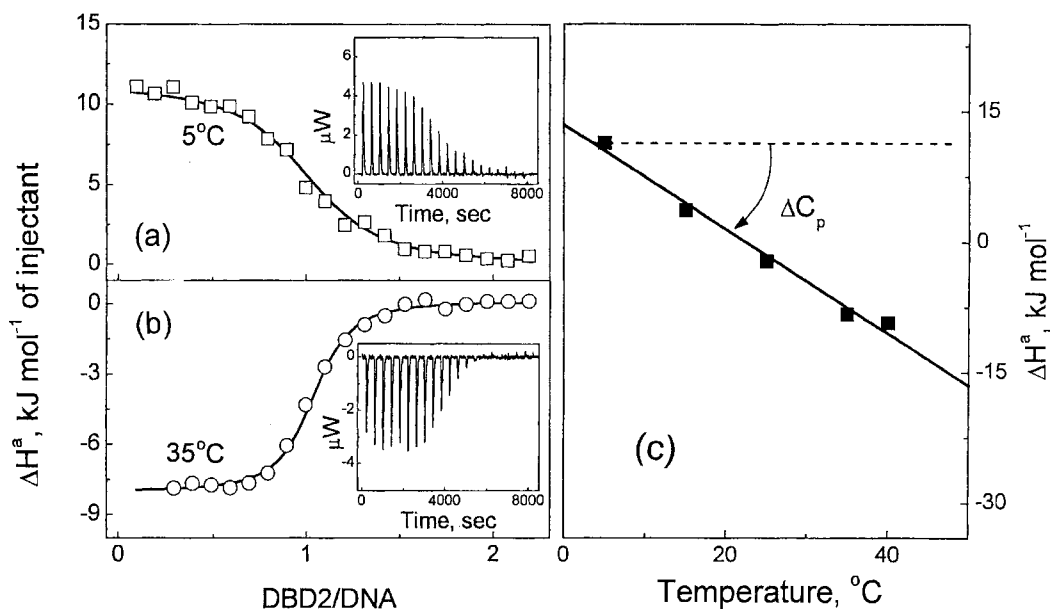
Fig. 1.1. (**a**) and (**b**) Calorimetric titration of a 16 bp DNA with the AT-hook peptide DBD2 at two different temperatures using an ITC instrument with cell volume 1.25 ml; the volume of each titrant injection was 10 μl. (**c**) The dependence of the association enthalpy on temperature that yields the heat capacity effect of association. For details, *see* Ref. *(36)*.

where K^a is the association constant, $[M]_{tot}$ is the total concentration of the protein in the calorimetric cell, and $[L]$ is the concentration of free ligand. Since $[L]$ cannot be determined directly, solution of this equation requires a rather complex fitting procedure *(4)*. Contemporary ITC instruments are equipped with an efficient program which permits automatic determination of all the binding characteristics even when the protein has several binding sites differing in binding constant and enthalpy. The K^a value thus obtained yields the Gibbs energy of association, $\Delta G^a = -RT\ln(K^a)$, and since the Gibbs energy and enthalpy are known, one can determine the entropy of association, $\Delta S^a = (\Delta H^a - \Delta G^a)/T$. Repeating the titration at various temperatures gives the temperature dependence of the enthalpy, that is, the heat capacity effect of association, $\Delta C_p^a = \partial(\Delta H^a)/\partial T$ (**Fig. 1.1c**).

It should be noted that the optimal concentration of protein to obtain a well-resolved binding isotherm is of the order of the dissociation constant, $K^d = 1/K^a$. If the association constant is too high, i.e., the dissociation constant is too low, the concentration of the solution which is titrated must also be low. Correspondingly, the heat effect of mixing with the titrant might be too small for its accurate measurement. Contemporary ITC instruments permit working with micromolar concentrations of the reagents, i.e., to study reactions with dissociation constants above micromolar. In cases for which the dissociation constant is below micromolar, it is necessary to use some other method (e.g., optical) for determination of the association constant and use the ITC only for determining the association enthalpy. This is because measurements of the enthalpy do not require determination of the full binding isotherm: the enthalpy is estimated from the heat effect of the first few injections (excluding the very first one which is usually deficient), for which all injected titrant binds to the reactant. Correspondingly, for enthalpy measurements one simply has to use concentrations of reagents that provide a large enough heat effect for its accurate determination.

One should keep in mind that the solution which is titrated and the titrant solution should differ only in the reacting components, and it is therefore essential that both solutions be dialyzed carefully in the same solvent. After dialysis both solutions should be placed under vacuum to remove dissolved gases, since bubbles, which might appear upon titration, will produce undesirable heat effects.

2.2. Differential Scanning Microcalorimeter

The DSC measures the small differences between the heat capacities of two liquids with continuous scanning over a broad temperature range (**Fig. 1.2a**). The liquids are placed in the twin cells of this differential instrument and are then heated or cooled at a fixed rate and the electric energy required to maintain the temperatures of both cells equal is recorded as a function of temperature (for techniques, *see* Refs. *(6–12)*). The important characteristics of
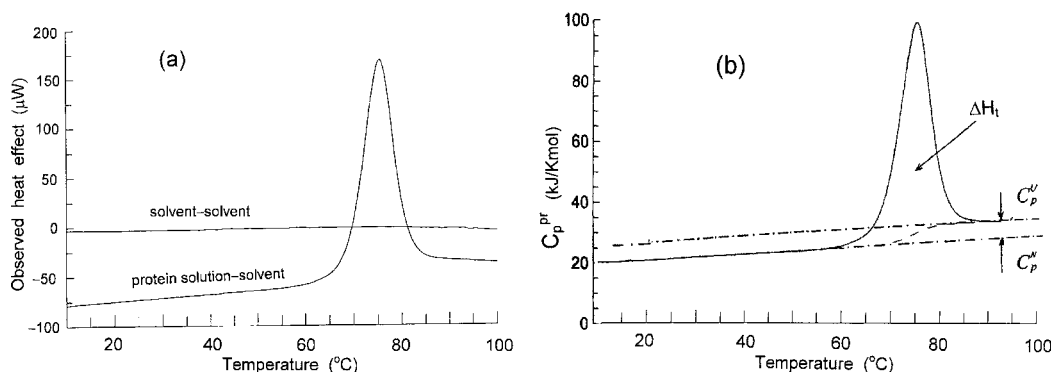
Fig. 1.2. (**a**). A DSC baseline obtained upon filling both cells with the solvent and the trace when in one of the cells the solvent is replaced by the protein solution (lysozyme in 20 mM acetate, pH 4.0, 100 mM NaCl; protein concentration 2.0 mg ml^{-1}). (**b**). The partial molar heat capacity function of lysozyme determined from the experiment shown in (**a**) which represents the apparent heat capacity difference between the protein solution and the solvent.

DSC instruments are their sensitivity, the stability of their baseline, and the ability to scan aqueous solutions with a chosen fixed rate up to $100°C$ (or higher) and down to $0°C$ (or even below). A wide operational range is important because temperature-induced changes of various proteins occur over a very broad temperature range: the temperature-induced unfolding of some thermostable proteins takes place above $100°C$, while the cold-denaturation of proteins usually occurs at temperatures below $0°C$. Thus to study these processes the aqueous solution needs to be superheated above boiling point or supercooled below freezing point.

Dust-free aqueous solution can be supercooled cautiously even down to $-15°C$, but freezing could start spontaneously any moment and damage the instrument. Therefore the instrument for such experiments must be equipped with an automatic system to rapidly heat the cells the moment freezing initiates, which is sensed by a sudden large heat evolution.

To heat an aqueous solution above $100°C$, the experiment is conducted under excess pressure: an overpressure of 2 atm permits the temperature to be raised to $120°C$. The excess pressure is also required to dissolve any possible bubbles forming in the solution upon heating. This is essential because even microscopic bubbles in the cell prevent measurement of the real difference in the heat capacities of the studied solution and the reference liquid, and thus prevent an accurate determination of the contribution of the protein to the heat capacity of the solution.

The accuracy of measuring the heat capacity differences of two liquids is determined firstly by the identity in masses of the compared liquids. In a 0.1% protein solution (i.e., 1 mg ml^{-1} concentration) the heat capacity contribution of the protein is about 0.03% of the total. To determine this with an error not exceeding 5%, the error in estimating the heat capacity of the protein

solution should be less than 0.002%. This means that the error in loading 1 ml of sample solution into the calorimetric cell should not exceed 0.01 mg, which is in practice impossible. Therefore, ultraprecise DSC instruments compare the heat capacities not of identical masses of the sample and reference solutions but of identical volumes: the operational volume of the calorimetric cells is fixed and is filled completely with the studied solutions *(8)*. This is why it is so important to load the studied liquids into the cells without bubbles, even microscopic ones. This is easier in the case of the twin capillary cell DSC instruments *(9, 10)*. The other advantages of twin capillary cells are their much smaller operational volume (0.3 ml) and that their volume does not change under excess pressure. Furthermore, they are more easily washed and reloaded with new samples without bubbles. Upon heating, the mass of liquid in a cell of fixed volume decreases because of thermal expansion. However, the thermal expansions of the dilute aqueous solution of the protein and the solvent are identical and are partly compensated by the thermal expansion of the cells. Thus the error caused by thermal expansion in the determination of the difference heat capacity is practically negligible (for details, *see* Ref. *(8)*).

In studying protein solutions, the solvent is usually used as the reference sample. By filling both calorimetric cells of a differential calorimeter with the solvent we first get the baseline (**Fig. 1.2a**). If the cells are refilled with the same solvent, there should be no change in this baseline. Such stability and reproducibility of the baseline over the whole operational temperature range is one of the most important characteristics of a scanning calorimeter and is particularly high for instruments having capillary cells. The baseline of the instrument might be not close to zero over the whole temperature range because the twin cells are not absolutely identical. Therefore, in contemporary DSC instruments the original recorded non-zero baseline is stored in the memory of the instrument and is used for automatic correction of all further recordings. The corrected recording for the solvent is very close to zero over the whole operational temperature range, as shown in **Fig. 1.2a**, and is used as a baseline in all further experiments with protein solutions in the same solvent.

On replacing the solvent in one of the cells with the protein solution the calorimetric recording shifts down on the $\Delta C_{\mathrm{p}}^{\mathrm{app}}(T)$. This shift is a consequence of the fact that the heat capacity of dissolved protein, $C_{\mathrm{p}}^{\mathrm{pr}}$, is lower than the heat capacity of the solvent which is replaced by protein. If we know the partial specific volume of the protein, $V^{\mathrm{pr}}(T)$, of the solvent, $V^{\mathrm{sol}}(T)$, and the mass of the protein in the calorimetric cell, m^{pr}, the partial specific heat capacity of protein at any temperature T can be calculated by equation *(8)*.

$$C_p(T)^{\mathrm{pr}} = C_p(T)^{\mathrm{solv}} \times V(T)^{\mathrm{pr}}/V(T)^{\mathrm{solv}} - \Delta C_{\mathrm{p}}^{\mathrm{app}}(T)/m^{\mathrm{pr}}(T). \quad (1.2)$$

The calorimetrically determined partial specific heat capacity function of the protein is the most important characteristic of its thermal properties (**Fig. 1.2b**). To obtain this function it is important to:

(a) Choose the solvent conditions appropriately (pH, ionic strength, buffer) so that the protein does not aggregate over the whole studied temperature range and the pH of the solution does not change much.

(b) Prepare protein solution of the required concentration in the chosen solvent and equilibrate it with careful dialysis against solvent. For the accurate determination of partial specific heat capacities of proteins, the error in determination of protein concentration should not exceed 3%.

(c) If the protein solution has to be supercooled below 0°C, both the solution and the solvent must be filtered using a 0.2-µm filter to remove dust particles which can initiate freezing. Before loading into the calorimetric cells both solutions should be degassed under vacuum.

(d) Fill both calorimetric cells with the solvent which will be used in the experiment, and scan the DSC up and down several times until the baseline stabilizes.

(e) Replace the solvent in one of the calorimetric cells with the protein solution. This should be done without stopping scanning, just at the moment when the instrument is scanning down in temperature and the temperature of the cells is close to room temperature. On replacing solvent with solution, the cell should not be dried but just washed with the protein solution. Drying of the cells, moreover washing them with aggressive solutions, will change the adhesive properties of their surface and re-establishing a stable baseline will require further numerous nonstop scans of the instrument with the cells filled with the solvent.

(f) All DSC experiments with solvent and then with protein solutions should be carried out under an excess pressure not lower than 2 atm.

3. The Partial Specific Heat Capacity of Proteins

The example of lysozyme (**Fig. 1.2b**) shows that compact small globular proteins do not change much upon heating up to some critical temperature, but then unfold with extensive heat

absorption resulting in a significant increase of their heat capacity, $\Delta_F^U C_p = C_p^U - C_p^F$ (for review, *see* Ref. *(12)*). The increase of heat capacity upon temperature-induced unfolding of proteins somewhat complicates the determination of the enthalpy of unfolding, i.e., the area under the heat absorption peak. This is often determined by extrapolating the initial and the final heat capacities to the mid-transition temperature, T_t, which is slightly lower than the temperature of the heat capacity peak maximum due to asymmetry of the peak *(13)*. The area of the heat absorption peak above these extrapolated lines gives the calorimetric enthalpy of unfolding, ΔH^{cal}. More justified is to use an explicit integral of the excess heat capacity to obtain a sigmoidal baseline which gradually increases from the initial to the final heat capacity values in proportion with the heat absorbed for the given temperature. A computer program, CpCalc, for estimating the excess heat capacity effect by this procedure can be obtained from TA Instruments (Linden, Utah).

The enthalpy of temperature-induced protein unfolding can also be determined from the sharpness of this process, assuming that it represents a two-state transition. If the heat capacity profile is used as an index of the reaction progress, the van't Hoff equation boils down to the following *(8, 13)*:

$$\Delta H^{vH} = RT_t^2(\partial \ln K/\partial T) = 4R \cdot T_t^2 \cdot \Delta C_p(T_t)/\Delta H^{cal}, \quad (1.3)$$

where $\Delta C_p(T_t)$ is the heat capacity peak height at the transition temperature T_t and ΔH^{cal} is the calorimetrically measured total heat absorbed in the peak. In the case of small compact globular proteins (molecular mass <20 kDa) the van't Hoff enthalpy, ΔH^{vH}, was found to be in good correspondence with the calorimetrically measured unfolding enthalpy, ΔH^{cal}. This means that unfolding of these proteins can indeed be regarded as a two-state transition; that is, their unfolding is a highly cooperative process *(12, 13)*.

In the case of a two-state transition the equilibrium constant, K_t, at the mid-transition temperature, T_t, equals 1, the Gibbs energy difference between the states at that temperature is zero, $\Delta G_t = -RT\ln(K_t) = \Delta H_t - T_t \Delta S_t = 0$, and the unfolding entropy at that temperature is $\Delta S_t = \Delta H_t/T_t$. Thus by measuring the heat effect of a temperature-induced protein transition one can determine not only the transition enthalpy but also the transition entropy at the transition temperature. If the considered transition is the temperature-induced unfolding of protein, the derived entropy represents the entropy of protein unfolding at that temperature T_t.

Thermodynamic characteristics of protein are usually calculated per gram or per mole of protein and are called the specific or molar characteristics, respectively. In many cases, however, the

specific characteristics are calculated not per gram but per gram mole of an averaged amino acid residue, which for globular proteins is about 115 g.

4. Reversibility of Protein Unfolding

Reversibility of the studied process is the prime requirement for its thermodynamic analysis. In the case of temperature-induced protein unfolding, this can be checked by scanning the studied protein both up and down. Reversibility of protein unfolding decreases dramatically upon heating above 70°C for almost all mesophilic proteins because of some degradation of their chemical structure – particularly, the oxidation of certain side chains by dissolved oxygen. Upon heating below 70°C, many small proteins show good reversibility in solutions preventing their aggregation, for example, at pHs away from the isoelectric point of the protein (**Fig. 1.3**). However, even if protein unfolding does not show perfect reversibility, it might still be analyzed thermodynamically because its temperature-induced cooperative unfolding is a much faster process than the aggregation of unfolded protein and the degradation of its exposed groups. The effect of these various factors can be reduced by decreasing protein concentration, increasing the scanning rate, and by removing dissolved oxygen.
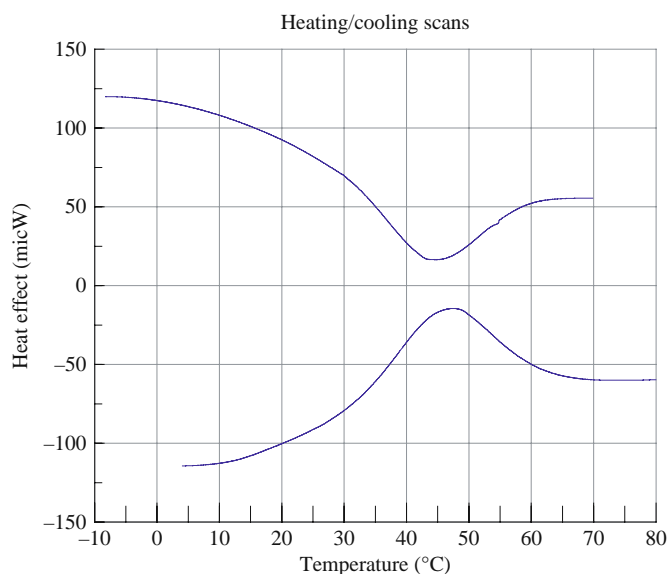
Fig. 1.3. DSC recording upon heating up to 80°C and subsequent cooling to −8°C of a solution of the HMG box from the mouse Sox-5 protein in 10 mM potassium phosphate, pH 6.0, 100 mM KCl *(16)*.

To remove oxygen, nitrogen is bubbled through the solution, which is then placed under vacuum to get rid of the remnants of both gases.

5. Heat Capacity of Folded and Unfolded Proteins

Determination of the complete heat capacity function of the unfolded protein is not straightforward because if temperature-induced protein unfolding is reversible, this state exists only above the transition temperature, while below this temperature one can have only irreversibly denatured protein. It cannot be measured either in the presence of denaturant (e.g., urea or guanidinium hydrochloride) since the later heavily solvates polypeptide chain. However, the heat capacity of the ideal unfolded protein can be modeled by summing up the heat capacities of its constituent amino acids *(14–16)*. The calorimetrically determined partial heat capacities of individual amino acid residues are listed in **Table 1.1**. As shown in **Fig. 1.4**, the calculated ideal heat capacity function of the completely unfolded polypeptide chain is in a good correspondence with the calorimetrically measured heat capacity of the unfolded protein at high temperature, and this means that if there are some residual structures in heat-denatured proteins they do not contribute much to its heat capacity. Thus, in contrast to a rather widespread opinion, the interactions between the groups of a temperature-unfolded nonaggregating protein are insignificant and can be neglected, at least to a first approximation. It is notable that since globular proteins do not differ widely in the content of various amino acid residues, the partial specific heat capacities of their unfolded states, calculated per gram or per mole of amino acid residues, are rather similar.

The situation with the native state of proteins is more complex than for the unfolded. The first calorimetric studies of a number of small compact globular proteins showed that their partial specific heat capacities are linearly increasing functions of temperature and the slopes of these functions are small and quite similar (**Fig. 1.4**). Consequently, it appeared that the difference between the heat capacities of the folded and unfolded states decreases with increasing temperature and vanishes at about 120°C. However, with an increasing number of calorimetrically studied proteins it appeared that the heat capacity of the native state of different proteins are not so similar *(17, 18–20)*: in some cases the initial slope is rather steep and its linear extrapolation crosses the heat capacity function

Table 1.1
Temperature dependence of the partial molar heat capacities of peptide units, the N- and C-terminal groups, and of side chains, R_i, of amino acid residues in J K^{-1} mol^{-1} (adapted from Ref. (*15*))

Group	Heat capacities				
	5 °C	25 °C	50 °C	75 °C	100 °C
-CO-CH-NH-	4	15	26	30	34
N+C termini	−158	−90	−21	−32	−150
R_i: side chains					
Ala	176	167	156	145	135
Arg	205	273	306	315	318
Asn	73	89	110	125	140
Asp	73	89	106	124	141
Cys	225	238	251	261	268
Gln	168	180	193	203	211
Glu	168	179	192	204	211
Gly	82	78	72	66	60
His	206	180	177	180	187
Ile	407	402	397	391	386
Leu	386	382	378	373	369
Lys	215	250	267	274	278
Met	197	176	158	150	148
Phe	396	383	370	358	348
Pro	214	178	152	143	136
Ser	76	81	86	91	97
Thr	194	184	182	186	199
Trp	471	458	446	434	424
Tyr	311	302	295	294	300
Val	325	314	305	295	286
Heme	875	1012	1155	1265	1375
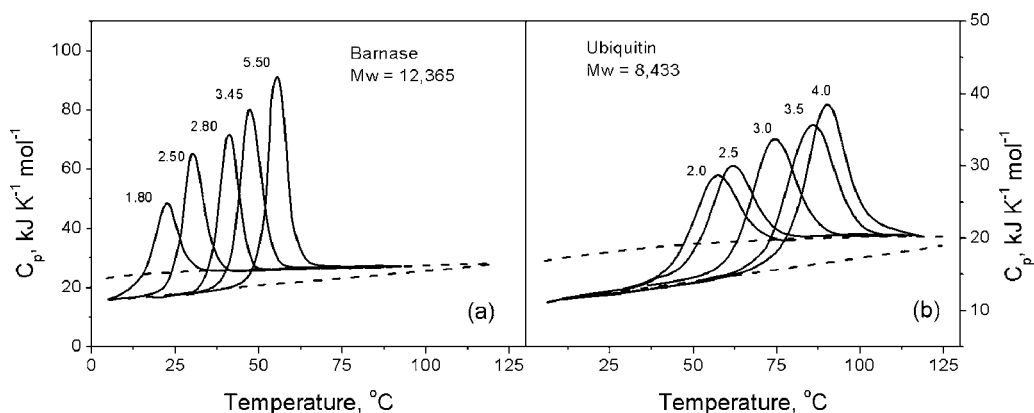
Fig. 1.4. The partial molar heat capacity functions of barnase and ubiquitin at different pHs showing the roughly linear dependence of C_p for the folded state. The heat capacity of their unfolded states is approximated by the curved functions. For details, *see* Refs. *(39, 40).*

of the unfolded state not at 120°C but at much lower temperatures (**Fig. 1.5**). Further studies showed that such a steep initial increase of the heat capacity is not an exception and the slope varies over a rather broad range (**Table 1.2**, **Fig. 1.6**). Among the studied proteins, bovine pancreatic trypsin inhibitor (BPTI) has the lowest slope: this is a compact protein with an extremely rigid structure stabilized by three S-S cross-links *(21, 15).* Dehydrated
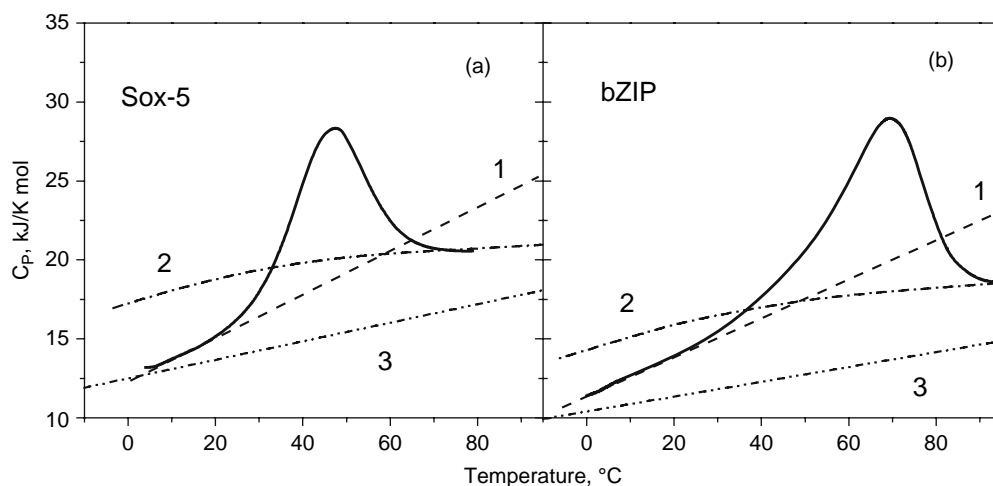
Fig. 1.5. (**a**) The partial heat capacity of the HMG box (DNA-binding domain) of mSox-5 and (**b**) the basic region/leucine zipper element of yeast GCN4. The heat capacity of the initial state in these cases increases very steeply and its linear extrapolation crosses the heat capacity of the unfolded state at temperatures much below 120°C. In both cases Line 1 is a linear extrapolation of the initial heat capacity function of the protein and Line 2 represents the calculated heat capacity function of the unfolded protein. Line 3 shows the heat capacity function of the fully folded protein BPTI, corrected to the molecular weights of Sox-5 and bZIP. This is taken as the standard partial specific heat capacity function for fully folded proteins. For details, *see* Refs. *(17, 18).*

Table 1.2

Thermodynamic characteristics of proteins calculated per mole of amino acid residue assuming a residue molecular mass of 115 Da

N	Protein (Reference)	C_p (0°C)	dC_p/dT	T_t	ΔH_t	ΔH^{tot} (120°C)
1	Anhydrous protein (22)	133	0.47			
2	BPTI (21)	141	0.65	100.5	5.3	5.7
3	Barnase (39)	140	0.70	54.3	4.8	6.7
4	Myoglobin (23)	138	0.80	70.8	3.4	7.0
5	Lysozyme (15)	140	0.82	75.3	4.3	7.3
6	Cytochrome c (15)	143	0.90	72.1	2.8	6.3
7	Ubiquitin (40)	143	0.90	90.0	4.0	6.6
8	T_4 lysozyme (42)	148	0.90	64.4	3.6	7.0
9	RNase T1 (41)	140	0.92	61.2	4.88	7.3
10	RNase A (15)	144	1.10	57.9	3.9	6.7
11	Engrailed (43)	154	1.30	48.7	2.0	7.5
12	Mat α2 (44)	163	1.43	52.2	1.7	8.0
13	Antennapedia (44)	145	1.48	55.0	3.3	6.5
14	HMGD-74 (20)	145	1.54	41.6	2.3	7.7
15	LZ-GCN4 (18)	144	1.75	62.5	0.8	9.3
16	HMG box Sox-5 (17)	148	1.88	46.1	2.23	7.2
17	Zn-finger TFIIIA (44)	153	1.73			
18	NHP6A (20)	155	2.07	38.6	1.5	7.2
19	SRY (20)	172	2.65	38.0	0.23	8.3
20	Lef-79 (20)	176	2.73	44.5	−0.3	7.3

T_t, the transition temperature; ΔH_t, the enthalpy of cooperative unfolding at the transition temperature calculated by linear extrapolation of the initial heat capacity function; ΔH_{120}, the total enthalpy of unfolding at 120°C calculated by integrating the excess heat capacity from −20°C using the heat capacity of fully folded BPTI as a baseline.

T_t in °C; C_p and ΔC_p in $kJK^{-1}mol^{-1}$, dC_p/dT in $kJK^{-2}mol^{-1}$; ΔH in $kJmol^{-1}$.
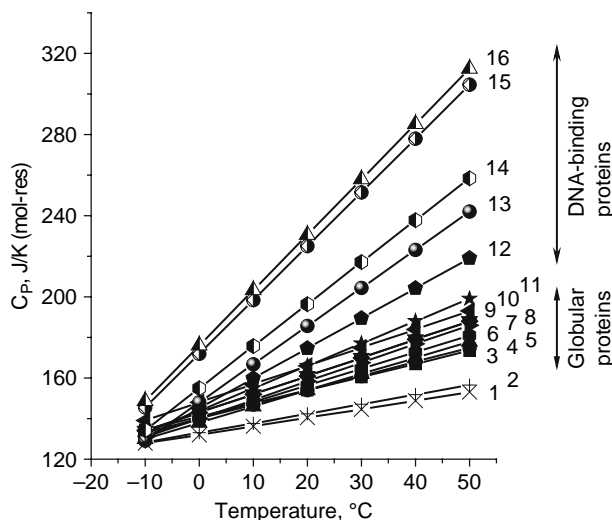
Fig. 1.6. The initial slopes of the partial specific heat capacity functions of a number of proteins. For the proteins and reference *see* **Table 1.2**; the numbers on the curves correspond to those given in the first column of this table.

proteins have an almost similar slope *(22)*. The increase of heat capacity of dehydrated proteins must be caused by intensification of their thermal motion with temperature raise. Thus the small slopes of the hydrated proteins, which are just a little bit larger than that of dehydrated proteins, can be explained by intensification of thermal vibrations of their structure and the gradual melting of the hydrating water (*see* **Section 10**). But what about proteins such as Sox-5 and bZIP having much larger slopes in the initial part of the heat capacity function?

6. Functions Specifying Protein Stability

In cases where a protein unfolds cooperatively upon heating with a sharp heat absorption, from the area of the heat absorption peak one can determine the enthalpy and entropy of protein unfolding at the transition temperature. Moreover, the resulting heat capacity increment, ΔC_p, permits estimation of the expected enthalpy and entropy of protein unfolding at other temperatures. Since according to Kirchhoff's relation $\partial(\Delta H)/\partial T = \Delta C_p$ and correspondingly $\partial(\Delta S)/\partial T = \Delta C_p/T$ integrating these relations we get the enthalpy and entropy functions of the protein:

$$\Delta H(T) = \Delta H_t + \int_{T_t}^{T} \Delta C_p \mathrm{d}T, \tag{1.4}$$

$$\Delta S(T) = \frac{\Delta H_t}{T_t} + \int_{T_t}^{T} \frac{\Delta C_p(T)}{T} \mathrm{d}T. \tag{1.5}$$

If the heat capacity difference between the unfolded and folded states of a protein does not depend on temperature (i.e., $\Delta C_p \approx$ constant), these expressions are simplified as

$$\Delta H(T) \approx \Delta H_t + \Delta C_p(T - T_t), \tag{1.6}$$

$$\Delta S(T) \approx \Delta H_t/T_t + \Delta C_p \ln(T/T_t). \tag{1.7}$$

In this approximation the enthalpy is a linear function of temperature, decreasing below T_t to zero at some temperature T_h and then changing sign (**Fig. 1.7**):

$$T_h \approx T_t - \Delta H_t/\Delta C_p \tag{1.8}$$

The entropy of unfolding also decreases with temperature below T_t, but nonlinearly, and reaches zero at a somewhat higher temperature, T_s, than does the enthalpy function:

$$T_s \approx T_t \exp(-\Delta H_t/\Delta C_p \cdot T_t). \tag{1.9}$$

Below T_s the entropy is negative.
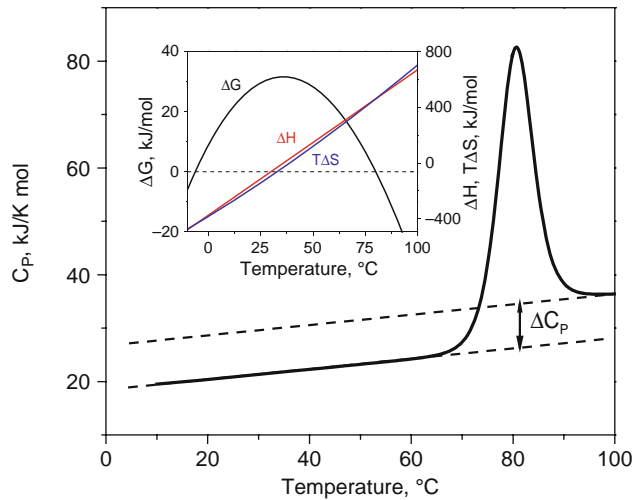
Fig. 1.7. The partial molar heat capacity function of sperm whale myoglobin. Inset: the enthalpy (ΔH), entropy factor ($T\Delta S$), and Gibbs energy (ΔG) functions of unfolding of this protein calculated by assuming that the denaturation heat capacity increment, ΔC_p, does not depend on temperature; that is, the heat capacity of the folded and unfolded states change in parallel over the whole considered temperature range *(23)*.

7. Stability of Protein

The combination of the enthalpy and entropy expressed by **Eqs. (1.4)** and **(1.5)**, or their simplified forms **(1.6)** and **(1.7)**, gives the Gibbs energy difference between the unfolded and folded states of a protein as a function of temperature:

$$\Delta G(T) = \Delta H(T) - T\Delta S(T) \approx \Delta H_t[T_t - T]/T_t$$
$$- \Delta C_p[(T_t - T) + T\ln(T/T_t)] \approx \qquad (1.10)$$
$$\approx \Delta H_t[T_t - T]/T_t - \Delta C_p([T_t - T]/4T)^2.$$

In contrast to the enthalpy and entropy functions, the Gibbs energy between the unfolded and folded states of protein is a function with an extremum (**Fig. 1.7**, inset). Its maximum is reached at the temperature T_{max}, where the temperature derivative of this function is zero:

$$\frac{\partial \Delta G}{\partial T} = \frac{\partial(\Delta H - T\Delta S)}{\partial T} = \Delta C_p - \Delta S - T\frac{\Delta C_p}{T} = -\Delta S(T_s) = 0. \quad (1.11)$$

Thus ΔG has a maximum at the temperature where the entropy of unfolding is zero, that is, $T_{max} = T_s$. At temperatures above and below T_{max} the Gibbs energy difference decreases. Since ΔG represents the work required to transfer protein from the folded to the unfolded state, it determines the stability of protein structure. It follows, therefore, that zero stability of the native state is reached at two different temperatures: at a high temperature, T_t, at which heat-denaturation of the protein takes place; and at a low temperature, $T_t{}^*$, at which one can expect cold-denaturation of the protein (for details, *see* Refs. *(23, 24)*):

$$T_T^* \approx \frac{\Delta C_p T_t^2}{2\Delta H_t + \Delta C_p T_t} = \frac{T_t^2}{3T_t - 2T_h} \qquad (1.12)$$

The distinguishing feature of cold-denaturation is that, while heat-denaturation proceeds with heat absorption and thus with an increase of enthalpy and entropy, cold-denaturation proceeds with release of heat, that is, with an enthalpy and entropy decrease. This is because at the temperature where the cold-denaturation is expected both the enthalpy and entropy of unfolding invert their sign (**Fig. 1.7**, inset).

8. Cold-Denaturation

According to the thermodynamic predictions the cold-denaturation of most globular proteins should occur at temperatures below 0°C *(23–26)*. Observation of this phenomenon is therefore
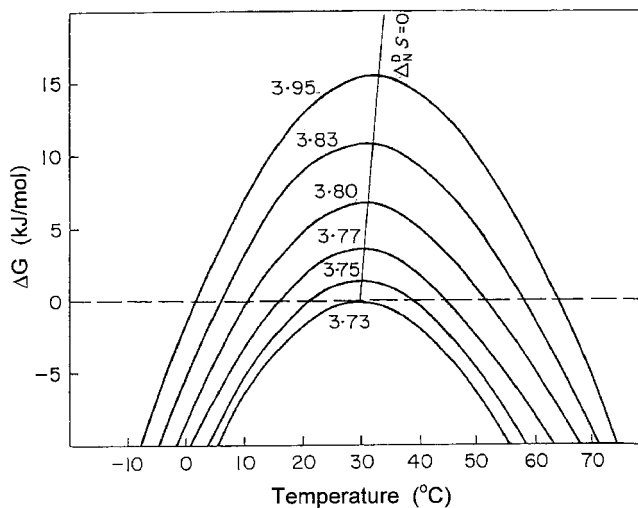
Fig. 1.8. The temperature dependence of the Gibbs energy difference of the native and denatured states of metmyoglobin in 10 mM sodium acetate solution at various pH values. For details, *see* Ref. *(23)*.

not easy since it requires supercooling of the aqueous solution. As mentioned above (*see* **Section 3**), dust-free aqueous solution can be supercooled down to at least −15°C. On the other hand, the expected temperature of cold-denaturation of a protein can be raised by the appropriate choice of the solution pH (**Fig. 1.8**) and buffer (**Fig. 1.9**). Various buffers used in studying protein
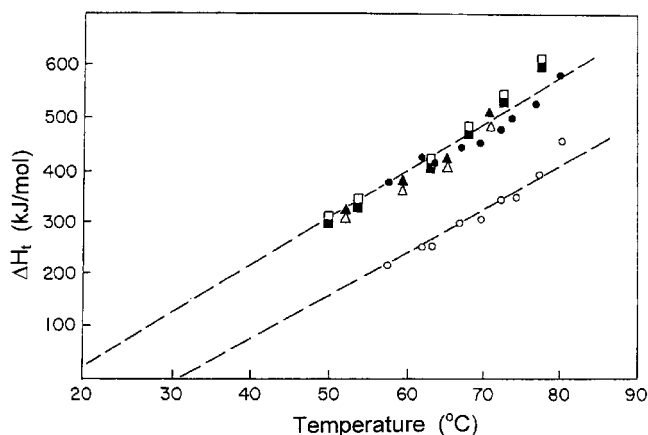
Fig. 1.9. Temperature dependence of the calorimetrically measured enthalpy of metmyoglobin denaturation at various pH values in the presence of glycine (open squares), piperazine (open triangles), and sodium acetate (open circles) buffers. The filled symbols indicate conformational transition enthalpies obtained from calorimetric data corrected for protonation/deprotonation heats of protein and buffer (*see* **Section 12**). The linear extrapolations provide the value of T_h which for the metmyoglobin in acidic solutions is highest when using sodium acetate buffer. For details, *see* Ref. *(23)*.
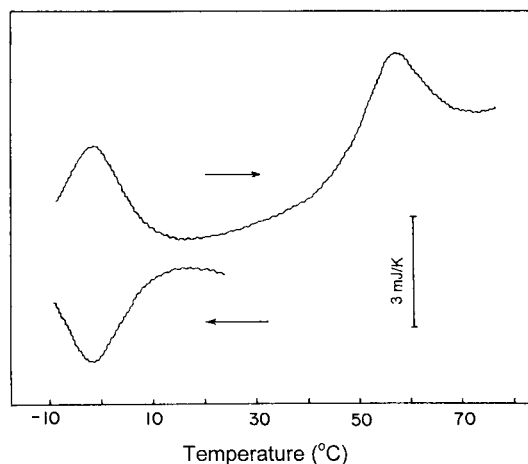
Fig. 1.10. Heat effects recorded by DSC upon cooling a apomyoglobin solution (pH 4.8, 20 mM sodium acetate) from room temperature to −10°C and subsequent heating to 80°C. The protein unfolds upon cooling below 0°C and this proceeds with heat release. On subsequent heating from −10°C, it refolds around 0°C with heat absorption and then unfolds around 60°C with the heat absorption. Thus the heat effects of the cold- and heat-denaturation differ in sign *(12)*.

solutions differ not only in their range of optimal pH but also in the enthalpy of protonation. This heat effect compensates the enthalpy of protein protonation/deprotonation upon unfolding and, correspondingly, increases the temperature T_h at which the enthalpy of protein unfolding becomes zero. According to **Eq. (1.12)**, the higher the T_h, the higher will be the cold-denaturation temperature, T_t^*. In the case of metmyoglobin, as shown in **Fig. 1.9**, sodium acetate buffer appears to be the most suitable for observing the cold-denaturation of this protein (*see* **Section 11**). **Figure 1.10** illustrates the heat effect observed by DSC upon cooling and subsequent heating of an apomyoglobin solution *(25)*. One can see that, as predicted by the thermodynamic formalism, cold-denaturation proceeds with negative enthalpy and correspondingly with an entropy decrease, in contrast to the heat-denaturation.

DSC studies of a variety of proteins led to the understanding that cold-denaturation is a very general property of globular proteins, although its observation is not always possible because it frequently occurs at too low a temperature (for a review, *see* Ref. *(24)*).

9. Heat-Denaturation

Calorimetric studies of cold-denaturation of proteins have shown that the thermodynamic formalism expressed by **Eqs. (1.4)–(1.8)** is able to predict the thermal properties of globular proteins at low

temperatures. However, an assumption that the difference between the heat capacities of the unfolded and folded states of a protein does not depend on temperature is valid only in analyzing the thermal properties of proteins at the relatively low temperatures where this difference is considerable and its decrease with temperature rise can be disregarded. However, at higher temperatures where the difference between the folded and unfolded states becomes small one cannot ignore its dependence on temperature. In the cases where the heat capacity of the unfolded and folded state cross each other at about 120°C (**Fig. 1.4**), as found for many compact globular proteins *(15)*, the enthalpy of protein unfolding would not be a linearly increasing function of temperature but a function which asymptotically approaches some constant level at this temperature (**Fig. 1.11**). However, in the cases where the heat capacities of folded and unfolded states cross each other at significantly lower temperatures (**Fig. 1.5**), at this crossing-over temperature the apparent heat capacity effect of unfolding should change sign and the enthalpy should convert from an increasing function of temperature to a decreasing function of temperature (**Fig. 1.11**, curves 3 and 4). The only explanation for such strange behavior of the enthalpy is that the apparent heat capacities of these proteins do not represent their intrinsic heat capacities.

While the small slope of the heat capacity function of a folded protein can be explained by an intensification of thermal motion of its groups and a gradual melting of the hydrated water, a large
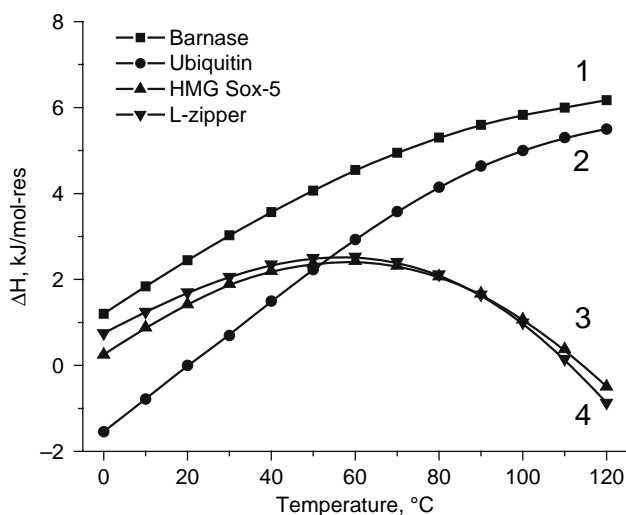
Fig. 1.11. The temperature dependencies of the enthalpy of unfolding of barnase (curve 1), ubiquitin (curve 2), the HMG box from Sox-5 (curve 3), and the leucine-zipper from GCN4 (curve 4) obtained in the assumption that the linearly extrapolated initial heat capacity function of protein represents its native folded state.

slope must mean the accumulation of much greater energy upon heating, perhaps in generating local unfolding of protein structure. It follows then that the initial slope of the heat capacity function reflects the flexibility of a protein's structure: proteins with loose, flexible structure should have steeper heat capacity slopes. If so, this excess heat effect should be taken into account when estimating the total enthalpy of protein unfolding. The question is then how to determine this excess heat? This requires the heat capacity function of a fully folded protein which could be taken as a baseline in estimating the excess heat effect.

As a standard heat capacity of a fully folded protein one can take the partial specific heat capacity function of the protein having the lowest initial heat capacity slope (**Fig. 1.6**, **Table 1.2**). Such a protein is BPTI a highly stable protein which unfolds upon heating to above 100°C *(21)*. The partial specific heat capacities of native BPTI in the temperature range from 5°C to 100°C are given in **Table 1.3** and are approximated by the equation

$$C_p(T)^{\text{BPTI}} = [1.295 + 5.926 \times 10^{-3}(T - 273.16)] \text{ JK}^{-1}\text{g}^{-1}. \quad (1.13)$$

Using the partial specific heat capacity function of BPTI as a standard of fully folded protein, C_p^F (**Fig. 1.5**, dashed-and-dotted lines), one can determine the excess heat capacity function for all other proteins, $\Delta C_p \text{exc} = [C_p^{pr} - C_p^F]]$, and by its integration determine the full enthalpy and entropy functions of protein unfolding *(11, 17, 18)*:

$$\Delta_N^U H(T) = \int_{T_o}^{T_{\max}} [C_P^{pr} - C_P^F] dT - \int_{T_{\max}}^{T} [C_P^U - C_P^F] dT \quad (1.14)$$

$$\Delta_N^U S(T) = \int_{T_o}^{T_{\max}} [(C_P^{pr} - C_P^F] d\ln T - \int_{T_{\max}}^{T} [C_P^U - C_P^F] d\ln T. \quad (1.15)$$

Here C_P^U is the molar partial heat capacity of the unfolded polypeptide chain calculated by summing up the heat capacities of the amino acid residues constituting the protein, C_P^F is the molar heat capacity of fully folded protein calculated by multiplying the specific heat capacity of BPTI on the molecular mass of the considered protein, and $T_{\max}$ is the temperature to which the protein was heated in the calorimetric experiment and at which it is assumed to be completely unfolded.

Table 1.3
Partial specific heat capacity of native BPTI (adapted from Ref. *(15)*)

T, °C	5	25	50	75	100
C_p, J K^{-1}g^{-1}	1.325	1.447	1.600	1.736	1.888

Such analysis of the heat capacity functions of calorimetrically studied globular proteins showed that in all cases their specific enthalpy and entropy of unfolding (i.e., calculated per gram or per mole of residue) are increasing functions of temperature, asymptotically approaching almost the same limit at 120°C (**Fig. 1.12**). BPTI represents an exception, since being heavily S-S crosslinked, it does not fully unfold even at 120°C.

Why then do the enthalpy and entropy, which reach definite positive values at 120°C, decrease from these values as the temperature is lowered and even change their sign? The internal interactions and conformational entropy should not decrease much on temperature reduction; moreover, they should not change sign at low temperatures. These effects can be caused only by the surrounding medium, that is, by the water (for a review, *see* Ref. *(15)*).
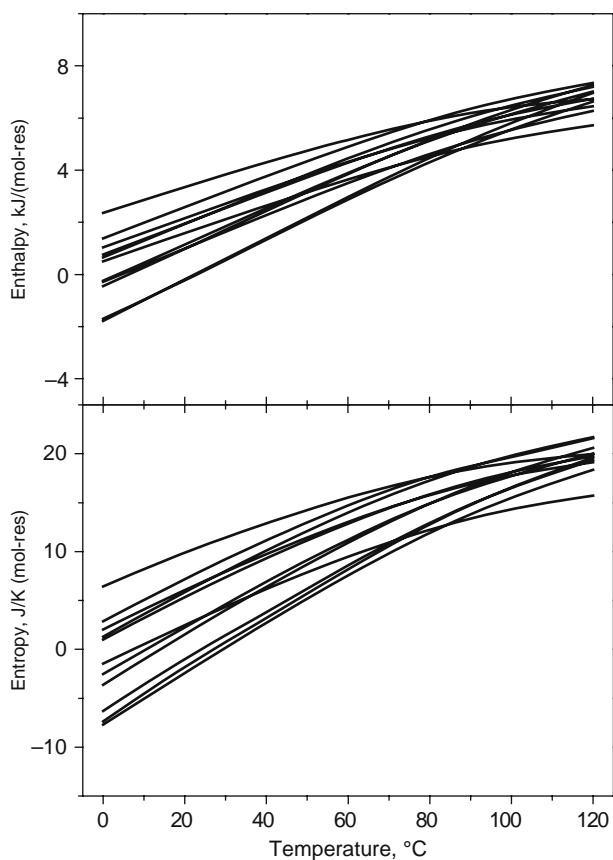
Fig. 1.12. The enthalpy and entropy functions of unfolding the several proteins listed in **Table 1.2**. These functions asymptotically approach common limits at 120°C. At this temperature the average unfolding enthalpy of all studied globular proteins appears to be (6±1) kJ per mol residue and their averaged unfolding entropy is about (15±5) J/K(mol-res). BPTI is unusual since it is not fully unfolded even at 120°C, being heavily crosslinked by S-S covalent bonds.

10. Water Contribution to the Heat Capacity of Proteins

As mentioned above, the small increase in heat capacity of some proteins with temperature rise might be associated with both an intensification of thermal vibrations of protein groups and also with the gradual melting of hydrating water. This can be checked by analyzing the possible contribution of hydration to the heat capacity of proteins. The surface-normalized heat capacity effects of hydration of all the amino acids, $\delta C_{p,i}^{\text{hyd}}(T)$, were determined calorimetrically over a broad temperature range *(15, 27, 23)* and are listed in **Table 1.4**. By knowing the water accessible surface areas of each type of protein group, ASA_i, and its surface-normalized hydration effect, one can estimate the overall hydration effect upon protein unfolding by the simple summation:

$$\Delta C_p^{\text{hyd}}(T) = \Sigma_i \delta C_{p,i}^{\text{hyd}}(T) \times \text{ASA}_i \qquad (1.16)$$

The water accessible surface area, ASA, of proteins with known structure is determined by rolling a probe of radius 1.4 Å (approximating a water molecule) over the considered surface. There are several commercial programs which can be used for this purpose.

It is notable that $\delta C_{p,i}^{\text{hyd}}$ values for all aliphatic groups are positive and similar. They are positive also for aromatic groups, but smaller in magnitude than for aliphatic groups. It is incorrect therefore to assume that aliphatic and aromatic groups are identical in their hydration properties, as is often assumed in the literature: aromatic groups are not apolar, they are in fact slightly polar. The hydration effects for charged and polar groups, in contrast to aliphatic, are negative and very different for different groups. To a first approximation, however, one can use an averaged value of the hydration heat capacity effect which takes into account the typical distribution of various polar groups in globular proteins *(15)*:

$$C_p(25°)^{\text{hyd}} = (2.14 \cdot \text{ASA}_{\text{np}} + 1.55 \cdot \text{ASA}_{\text{arom}}$$
$$-1.27 \cdot \text{ASA}_{\text{pol}})\text{JK}^{-1}\text{mol}^{-1}. \qquad (1.17)$$

It should be noted that other approximate expressions for calculating the hydration heat capacity effects have been proposed (for example, *see* Ref. *(29)*), but they do not distinguish between the hydration effects of apolar and aromatic groups.

Determination of the ASA for the unfolded protein is not as straightforward as for the folded protein because the unfolded polypeptide does not have definite structure and even the most powerful computers cannot efficiently model its rapidly changing

Table 1.4
Surface-normalized values of heat capacities, enthalpies, entropies, and Gibbs energies of hydration for various parts of amino acid residues (adapted from Ref. *(15)*)

Surface		Property	Temperature				
			5 °C	25 °C	50 °C	75 °C	100 °C
Aliphatic		δC_p^{hyd}	2.24	2.14	2.03	1.91	1.80
		δH^{hyd}	−166	−122	−70	−21	26
		δS^{hyd}	−730	−578	−409	−263	−134
Aromatic		δC_p^{hyd}	1.65	1.55	1.41	1.29	1.19
		δH^{hyd}	−180	−148	−111	−77	−46
		δS^{hyd}	−430	−319	−199	−98	−12
Polar parts of:	Arg	δC_p^{hyd}	−0.38	−0.20	−0.12	−0.04	0.01
		δH^{hyd}	−821	−827	−831	−833	−834
		δS^{hyd}	−458	−478	−492	−497	−498
	Asn	δC_p^{hyd}	−1.27	−1.01	−0.67	−0.41	−0.16
		δH^{hyd}	−871	−894	−915	−928	−936
		δS^{hyd}	−575	−654	−723	−763	−783
	As	δC_p^{hyd}	−1.72	−1.40	−1.07	−0.71	−0.40
		δH^{hyd}	−684	−715	−746	−768	−782
		δS^{hyd}	−360	−469	−569	−636	−675
	Cys	δC_p^{hyd}	1.80	2.01	2.23	2.42	2.54
		δH^{hyd}	−309	−271	−218	−160	−98
		δS^{hyd}	−535	−402	−232	−59	113
	Gln	δC_p^{hyd}	−0.38	−0.22	−0.06	0.07	0.17
		δH^{hyd}	−697	−703	−706	−706	−703
		δS^{hyd}	−571	−591	−604	−603	−594
	Glu	δC_p^{hyd}	−0.71	−0.55	−0.35	−0.17	−0.05
		δH^{hyd}	−459	−562	−573	−580	−583
		δS^{hyd}	−392	−436	−473	−492	−500

Table 1.4
(continued)

Surface		Property	Temperature 5 °C	25 °C	50 °C	75 °C	100 °C
	His	δC_p^{hyd}	−1.96	−2.43	−2.38	−2.26	−2.07
		δH^{hyd}	−1084	−1128	−1188	−1247	−1301
		δS^{hyd}	−542	−693	−888	−1060	−1211
	Lys	δC_p^{hyd}	−1.31	−1.53	−1.59	−1.36	−1.15
		δH^{hyd}	−685	−714	−753	−789	−821
		δS^{hyd}	−394	−482	−609	−716	−804
	Met	δC_p^{hyd}	−3.51	−3.83	−4.07	−4.04	−3.91
		δH^{hyd}	−399	−473	−572	−672	−774
		δS^{hyd}	−158	−412	−732	−1031	−1308
	Ser	δC_p^{hyd}	−1.62	−1.40	−1.20	−096	−072
		δH^{hyd}	−1015	−1045	−1078	−1104	−1126
		δS^{hyd}	−878	−983	−1089	−1168	−1227
	Thr	δC_p^{hyd}	−1.09	−1.29	−1.22	−0.89	−0.29
		δH^{hyd}	−1262	−1287	−1318	−1343	−1359
		δS^{hyd}	−971	−1053	−1156	−1232	−1274
	Trp	δC_p^{hyd}	1.05	0.96	1.07	1.08	1.03
		δH^{hyd}	−1181	−1161	−1135	−1110	−1084
		δS^{hyd}	−766	−693	−615	−534	−460
	Tyr	δC_p^{hyd}	−1.46	−1.48	−1.36	−1.15	−0.86
		δH^{hyd}	−824	−854	−889	−921	−946
		δS^{hyd}	−314	−415	−531	−625	−695
	CONH	δC_p^{hyd}	−2.08	−1.81	−1.56	−1.53	−1.49
		δH^{hyd}	−1662	−1702	−1745	−1785	−1823
		δS^{hyd}	−890	−1026	−1162	−1278	−1383

δC_p^{hyd} in JK^{-1}mol^{-1}Å^{-2}; δH^{hyd} in Jmol^{-1}Å^{-2}; δS^{hyd} in JK^{-1}mol^{-1}Å^{-2}.

random-coiled conformation. In earlier studies, therefore, the ASA of the unfolded protein was estimated by summing up the ASA of each amino acid as determined in an extended tripeptide, Gly-X-Gly or Ala-X-Ala. However, since Gly has no side chain and Ala has a very small one, this method gives ASA values of the side chain X without screening by the neighboring side chains. It is more justified to determine ASA by approximating the unfolded polypeptide chain in an extended conformation. In this conformation, the ASA values of groups determined by rolling the probe are smaller by about 20% than those calculated by simple summation of the surfaces of amino acid residues determined in Ala-X-Ala tripeptides, as a result of screening effects from neighboring longer side chains *(15)*.

Excluding the calculated heat capacity effect of hydration from the heat capacity of the unfolded polypeptide chain, one gets the heat capacity of the polypeptide chain without hydration effects (**Table 1.5**). It is notable that, after correction for

Table 1.5
The heat capacities of corrected for hydration effects proteins in kJK^{-1}(mol-res)$^{-1}$

State	Protein	0 ˚C	25 ˚C	50 ˚C	75 ˚C
Native	Barnase	118	139	152*	184*
	Lysozyme	126	138	153*	170*
	RNase T1	121	136	151*	168*
	Ubiquitin	124	143	164*	185*
	Averaged	122 ±3	139 ±4	±6	177* ±8
Unfolded	Barnase	117	136	150	156
	Lysozyme	136	149	165	170
	RNase T1	115	127	140	152
	Ubiquitin	130	150	162	169
	Averaged	125 ±8	140 ±9	154 ±9	162 ±8
	Anhydrous Protein*	135	147	159*	171*

* Anhydrous chymotrypsinogen *(22)*; * – linearly extrapolated values.

hydration, the heat capacities of unfolded proteins, as well as folded proteins having small initial heat capacity slopes, are very close to the heat capacities of anhydrous (dry) proteins measured in an absolute calorimeter *(22)*. This shows that the denaturational heat capacity increment of proteins in aqueous solution is mostly caused not by the increased conformational freedom of the polypeptide chain but by the change in hydration upon protein unfolding, namely of the exposed apolar groups which provide the positive heat capacity effect. Thus the heat capacity increment upon protein unfolding can be determined by analyzing the increase in the water accessible surface area of each group, 'i', of the protein, ΔASA_i:

$$\Delta C_p^{hyd}(T) = \Sigma \delta C_{p,i}^{hyd} \quad (T) \times (ASA_i^U - ASA_i^F)$$
$$= \Sigma \delta C_{p,i}^{\ hyd} \quad (T) \times \Delta ASA_i \tag{1.18}$$

It was found that the heat capacity increment calculated in this way is usually in good correspondence with the calorimetrically measured heat capacity increment of unfolding for compact globular proteins that have a small initial slope of their heat capacity function and unfold cooperatively *(15, 28)*. This correspondence is found because only for such proteins can one measure unequivocally the heat capacity increment of unfolding. For proteins having a large initial heat capacity slope this is impossible because their apparent heat capacity is not totally intrinsic but includes the heat effects associated with temperature-induced structural changes in the protein.

11. Water Contribution to the Enthalpy and Entropy of Protein Unfolding

Using the increase in the water accessible surface area, ΔASA_i, of every type of protein group, 'i', upon protein unfolding and the surface-normalized intrinsic hydration effects of these groups, δH_i^{hyd} and δS_i^{hyd}, listed in **Table 1.4**, one can estimate the enthalpy and entropy of protein hydration upon unfolding *(15)*:

$$\Delta H^{hyd} = \Sigma \delta H_i^{hyd} \times \Delta ASA_i \text{ and}$$
$$\Delta S^{hyd} = \Sigma \delta S_i^{hyd} \times \Delta ASA_i \tag{1.19}$$

The hydration entropies of polar and nonpolar groups upon unfolding of various globular proteins are shown in **Fig. 1.13**. It is striking that hydration effects of nonpolar and polar groups are
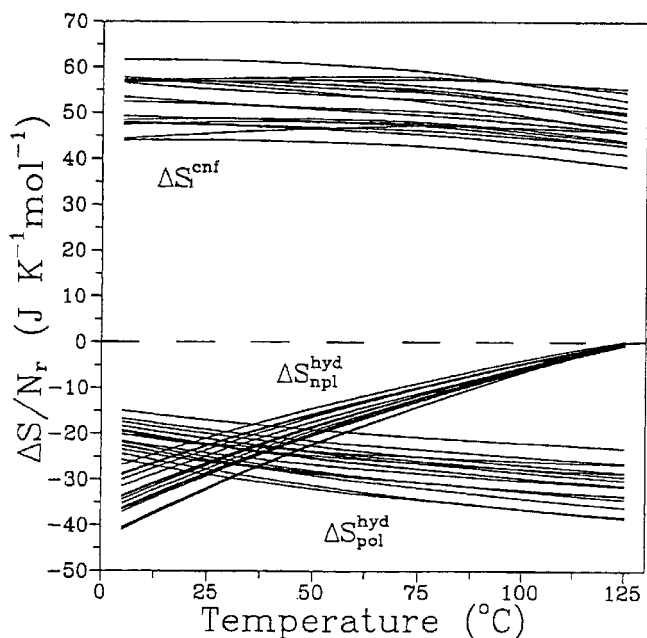
Fig. 1.13. Temperature dependence of the entropies of hydration for polar and nonpolar groups and of conformational entropies of unfolding of the globular proteins, calculated per mole of amino acid residue.

very different: the hydration entropies of nonpolar groups are negative at room temperature, decrease in magnitude with rise of temperature, and vanish at about 120°C. In contrast, the hydration entropies of polar groups are also negative at room temperature but become even more negative with temperature increase. This is because the heat capacity effects of hydrating of nonpolar and polar groups differ in sign: positive for nonpolar groups and negative for polar groups *(28, 29)*. Thus at 120°C hydration entropies of polar groups are quite considerable, varying between −25 JK^{-1} and −37 JK^{-1} per mol residue. If this hydration effect is subtracted from the calorimetrically determined entropy of protein unfolding at 120°C, one can find the conformational entropy of protein unfolding at that temperature. This appears to be about (50±10) JK^{-1} per mol residue. This value is quite close to the theoretically expected conformational entropy of protein unfolding, (40±10) JK^{-1} per mol of residue (*see* Epilogue in Ref. *(15)*).

A similar analysis of the contribution from the hydration of groups exposed upon protein denaturation showed that the enthalpy of internal interactions stabilizing protein compact structure (i.e., the contribution of hydrogen bonding and van der Waals interactions without hydration effects) is of the order of 40–50 kJ per mole of residue *(15)*.

12. Heat effect of Protein Protonation/Deprotonation

Unfolding of protein usually results in unmasking of internal titratable groups and their protonation or deprotonation depending on the pH at which the experiment is carried out. Enthalpies of deprotonation are positive and for acidic groups are rather small, while for alkaline groups are quite considerable (**Table 1.6**). Moreover, if protein unfolding is studied in a buffered solution, the protonation/deprotonation of the protein induces compensating deprotonation/protonation of the buffer. Therefore, the calorimetrically measured heat of protein unfolding also includes the heat of buffer protonation/deprotonation:

$$Pr\text{-}H + Buf \leftrightarrow Pr + Buf\text{-}H.$$

The presence of buffer can therefore change considerably the calorimetrically measured overall enthalpy of protein unfolding, as illustrated in **Fig. 1.9**. If we are interested in the net enthalpy of the conformational transition of a protein, the heat effect of protein and buffer protonation/deprotonation must be excluded from the calorimetrically measured enthalpy of protein unfolding:

$$\Delta H(p/d) = \Sigma \Delta H_i \nu_i \qquad (1.20)$$

Table 1.6
Thermodynamic characteristics of deprotonation of the titratable protein groups at 25 °C

Group	pK	$\Delta G\,kJmol^{-1}$	$\Delta H\,kJmol^{-1}$	$\Delta S\,Jmol^{-1}$
α-carboxyl (protein and glycine)	2.8	15.6	1.7	−47
Asp	3.9	21.8	4.6	−58
Glu	4.5	24.0	1.6	−75
His	6.0	33.5	28.8	−16
α-amino (protein and glycine)	9.8	54.7	43.8	−40
Tyr	10.1	56.4	25.1	−105
Lys	10.8	60.3	53.8	−22
Arg	12.5	69.8	51.8	−60

This however requires knowledge of the number of each type of group, ν_i, which protonate or deprotonate in the considered reaction.

Another possibility consists of using a buffer having heats of protonation close to that of the protein groups which are titrated. One such buffer is glycine: the enthalpies of deprotonation of its α-carboxyl and α-amino groups are rather close to that of the acidic and basic groups of proteins (**Table 1.6**). Thus the calorimetrically measured enthalpy of protein unfolding performed in the presence of this buffer can be regarded as the net enthalpy of the conformational transition. This is particularly true where the experiment is carried out at acidic pHs since the absolute enthalpies of protonation of acidic groups are small and differ little from that of the α-carboxyl group of glycine.

13. Effects of the Environment

Protein native structure can be changed and even completely disrupted not only by temperature increase but also upon changes of the environmental conditions, for example, increase or decrease of pH, increase in the concentration of denaturants, etc. The temperature-induced unfolding of protein depends on pH since it results in protonation of unmasked titratable groups which contribute to some extent to the enthalpy and entropy of unfolding (**Fig. 1.14,** *see* also **Fig. 1.4**). On the other hand, the pH-induced
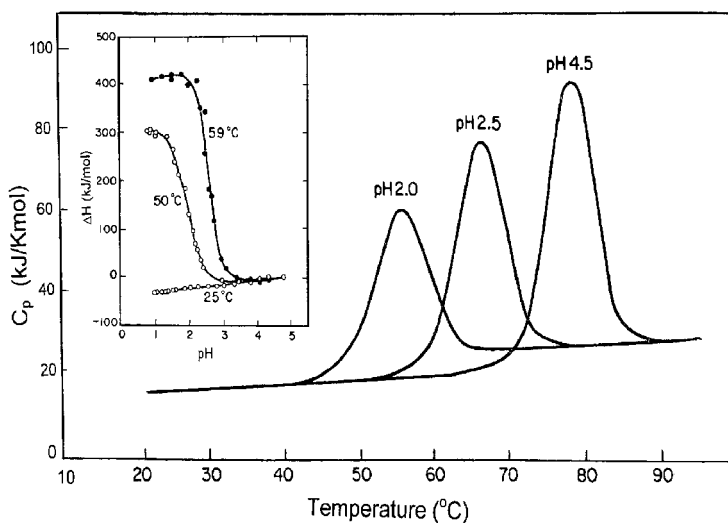
Fig. 1.14. Effect of pH on the temperature-induced heat-denaturation of lysozyme and the effect of temperature on the acid-induced denaturation of this protein (inset) studied by the DSC and ITC experiments, respectively *(30)*.

unfolding of protein depends on temperature (inset in **Fig. 1.14**). Thus the effect of temperature and pH on the stability of protein and enthalpy of its unfolding are interdependent. This interdependence of various variables can be described using standard thermodynamic functions *(30, 31)*.

Taking the state of the protein at T_o, pH_o as the standard, the enthalpy of the native and unfolded states of the protein would be described by the functions

$$H^N(T, pH)_o = \int_{T_o}^{T} C_p^N dT + H^N(pH)_{T_o}, \qquad (1.21)$$

$$H^U(T, pH) = H^N(T, pH)_o + \Delta H_t - \int_{T}^{T_t} \Delta C_p dT. \qquad (1.22)$$

Here $H^N(pH)_{T_o} = (H_{pH} - H_{pH_o})^N_{T_o}$ is the enthalpy change of the native protein on pH variation from pH_o to pH at constant temperature T_o, and ΔH_t is the enthalpy of the protein transition at T_t (for details, *see* Ref. *(30, 31)*). Combination of these two experimental datasets permits a description of the state of protein in three-dimensional coordinates by two surfaces specifying the native and unfolded states of the protein (**Fig. 1.15**). Analysis of the entropy and Gibbs energy changes on the pH-induced unfolding of protein is described in detail in *(30)*.
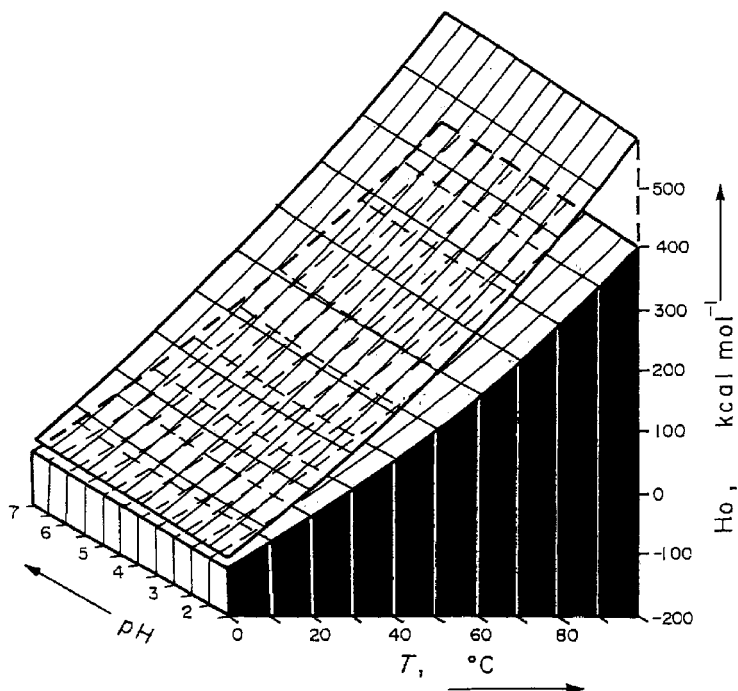
Fig. 1.15. Standard enthalpy of the native (lower surface) and unfolded lysozyme (upper surface) as a function of temperature and pH *(31)*. The enthalpy of protein unfolding at any given *T* value and pH point is determined by the difference between these surfaces at this point.

14. Analysis of the Excess Heat Capacity Function

The great advantage of a DSC experiment is that it gives the functional dependence between the enthalpy and temperature of the considered macromolecular object, that is, the two conjugate extensive and intensive fundamental characteristics of the system which includes all information on the states of this system realized over the considered temperature range *(8, 12, 33)*. This permits a detailed analysis of the process of temperature-induced changes in the protein. In practice, this analysis boils down to a computer simulation of the calorimetrically determined heat capacity function:

$$C_{\mathrm{p}}(T) = C_p^o + \frac{\partial}{\partial \mathrm{T}}[\Sigma p_i \Delta \mathrm{H}_i], \tag{1.23}$$

where $C_{\mathrm{p}}{}^{\mathrm{o}}$ is the partial molar heat capacity of the reference state. The second term accounts for any temperature-induced transitions and the possibility that the transition involves an arbitrary number of states, N. In this equation p_i represents the population of molecules in the ith state and ΔH_i its relative enthalpy. Expanding the above equation and bearing in mind that the population of each state is a function of the Gibbs free energy of that state, ΔG_i, we have

$$\begin{aligned} C_{\mathrm{p}}(T) = C_{\mathrm{p}}^{\mathrm{o}} + \{ & [\Sigma \Delta H_i^2 \exp(\Delta G_i/RT)Q] \\ & - [\Sigma \Delta H_i \exp(-\Delta G_i/RT)/Q]^2 \}/RT^2, \end{aligned} \tag{1.24}$$

where Q is the partition function and

$$\Delta G_i(T) = \Delta H_i(T) - T\Delta S_i(T), \tag{1.25}$$

$$\Delta H_i(T) = \Delta H_i(T_{\mathrm{t}}) + \int_{T_{t,i}}^{T} \Delta C_{\mathrm{p}}, i(T)\mathrm{d}T. \tag{1.26}$$

For a monomeric reaction,

$$\Delta S_i(T) = \Delta H_i(T_{\mathrm{t}})/T_{\mathrm{t}} + \int_{T_t^i}^{T} \Delta C_p^i(T)\mathrm{d}(\ln T). \tag{1.27}$$

For the multimeric reaction, $X \Leftrightarrow m_1 D_1 + m_2 D_2 + \ldots + m_k D_k$, the entropy change at the transition point, T_{t}, with half of the molecules unfolded, is

$$\Delta S_i(T_{\mathrm{t}}) = [\Delta H_i(T_{\mathrm{t}}) + RT \ln K]/T_{\mathrm{t}}, \tag{1.28}$$

where

$$K == (N/2)^{n-1} \prod_{i=1}^{k}[D_i]^{mi}. \tag{1.29}$$

Here $N = N^{\mathrm{o}}/N^{\mathrm{st}}$ is the dimensionless initial concentration of the complex relative to the standard concentration and $n = \Sigma m_i$ is the

order of reaction *(8, 32)*. A program for the deconvolution analysis of the heat capacity functions of protein is now provided with precise scanning microcalorimetric instruments; in particular, the deconvolution program CpCalc is included in the Nano-DSC manufactured by Calorimetric Sciences Corporation (Lindon, Utah).

14.1. Small Compact Globular Proteins

Small compact globular proteins are those with a small initial slope of the heat capacity function and molecular mass of the order of 10 kDa. A typical representative of this class of proteins is barnase (**Fig. 1.4a**). A deconvolution analysis of the partial molar heat capacity function of barnase shows that its temperature-induced unfolding proceeds without noticeable intermediates, that is, in a highly cooperative way (**Fig. 1.16**). Thus the structure of this class of proteins represents a single cooperative unit, the cooperative domain.
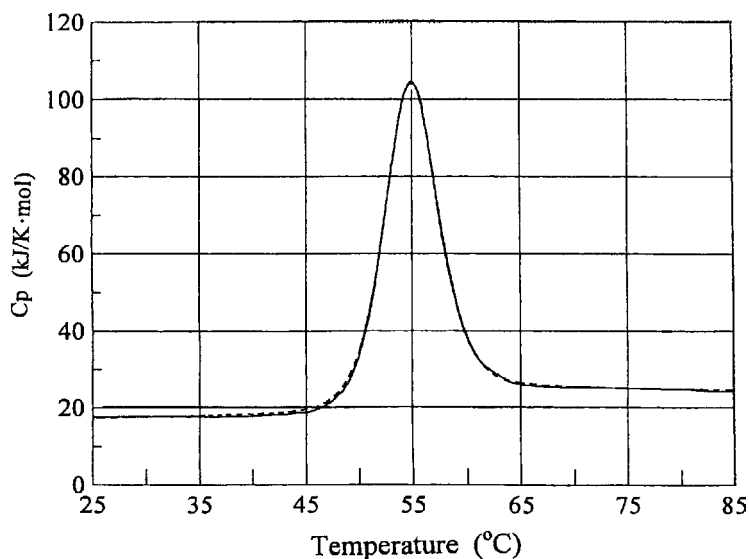
Fig. 1.16. Partial molar heat capacity function of barnase in 10 mM acetate pH 5.5, 100 mM NaCl (solid line) and its deconvolution (dashed line) showing that unfolding of barnase is perfectly approximated by a two-state transition with $T_t = 54.6°C$, $\Delta H = 541$ kJ mol^{-1}, and $\Delta C_p = 6.4$ kJ K^{-1}mol^{-1}.

14.2. Small Globular Proteins with Loose Structure

These are proteins with steep increase of the initial heat capacity which cannot be explained by intensification of thermal motion upon heating (**Fig. 1.5**). Deconvolution analysis of the heat capacity function of such proteins, namely of the DNA-binding domains of Sry and NHP6A HMG proteins, show that their structures do not represent a single cooperative domain but include two/three cooperative subdomains which unfold more or less independently upon temperature increase (**Fig. 1.17**). Since the enthalpies of unfolding of the individual subdomains are small, each of them
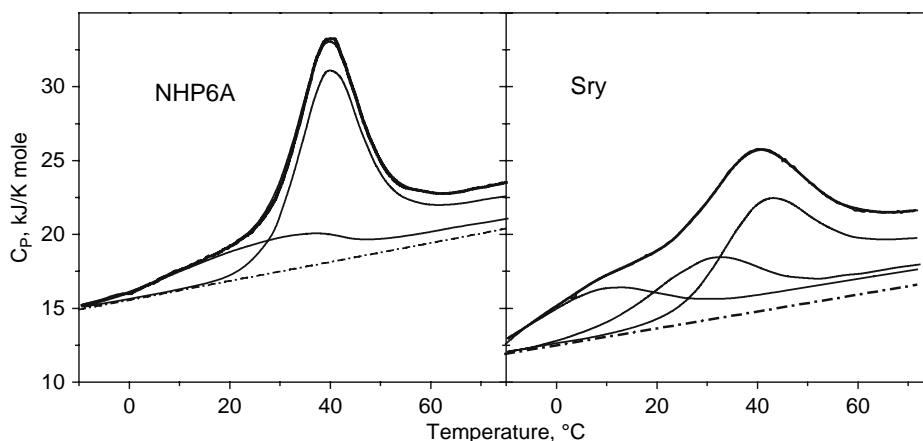
Fig. 1.17. Deconvolution analysis of the heat capacity functions of the DNA-binding domains of Sry and NHP6A HMG proteins showing that their structures do not represent a single cooperative unit but are subdivided into two (in the case of NHP6A) and three (in the case of Sry) subdomains *(20)*.

unfolds at broad temperature ranges and overlap of these heat effects results in a steep gradual increase of the apparent heat capacity function. Thus these proteins are partly unfolded at room temperature (for reviews, *see* Refs. *(11, 33)*).

14.3. Large Multidomain Proteins

The example of plasminogen (M_w = 83 kDa), is one of the most impressive illustrations of the possibility of DSC in analysis of the domain organization of large proteins (**Fig. 1.18**). Deconvolution of the excess heat capacity functions of the fragments of this protein show that its unfolding proceeds in discrete stages, each corresponding to cooperative unfolding of an individual domain *(34)*.

14.4. Dimeric Proteins

Unfolding of the dimeric proteins usually proceeds with dissociation of the unfolded polypeptides. Therefore this process represents not a mono- but a bimolecular reaction. The main difference between these reactions is that while the first one does not depend on the protein concentration, the second one does. **Figure 1.19** presents the calorimetrically studied temperature-induced unfolding of the dimeric proteins, subtilisin inhibitor from *Streptomyces* and its mutant D83C bridged by an S-S cross-link between the subunits *(35)*. Correspondingly, unfolding of this mutant, particularly the temperature of unfolding, does not depend on the concentration of protein while the unfolding of non-crosslinked wild-type protein depends on the protein concentration: with concentration increase the heat absorption peak shifts to higher temperatures. In both cases the area of the heat absorption peak represents the enthalpy of unfolding. However, while the entropy of unfolding of the monomolecular transition is determined just
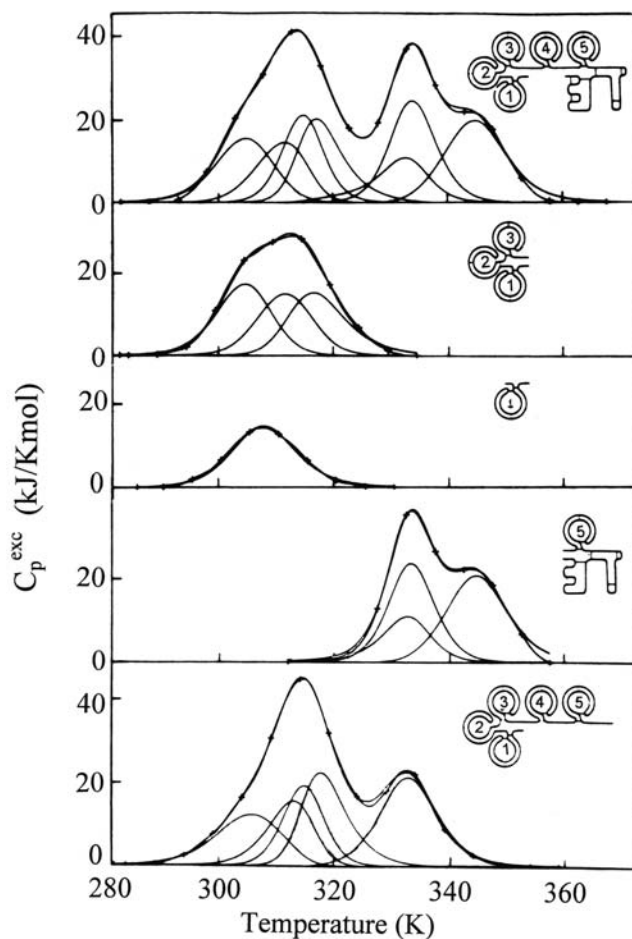
Fig. 1.18. Deconvolution of the excess heat capacity of plasminogen and its fragments, showing that this protein has seven domains, each of which unfolds as an independent structural unit. The insets show schematically the calorimetrically studied fragments of plasminogen (34).

by dividing the enthalpy of unfolding by the absolute temperature, $\Delta S_t = \Delta H_t / T_t$, for the bimolecular unfolding, according to equation (1.28), it is $\Delta S_t = \Delta H_t / T_t + R\ln(2N)$ (for details, *see* Ref. (8)). Analyzing the concentration dependence of the entropy of unfolding/dissociation of the uncrosslinked dimeric protein and comparing that with the entropy of unfolding of the crosslinked dimer permitted the first experimental determination of the entropy cost of protein association, that is, of the value of translational/rotational entropy (35).

Of particular interest is the unfolding of a dimeric protein that proceeds in several discreet steps, the last of which is the dissociation of the polypeptide chains. The example of the GCN4 leucine zipper illustrates this situation (18). The initial heat capacity function of this coiled-coil protein exhibits a rather steep slope
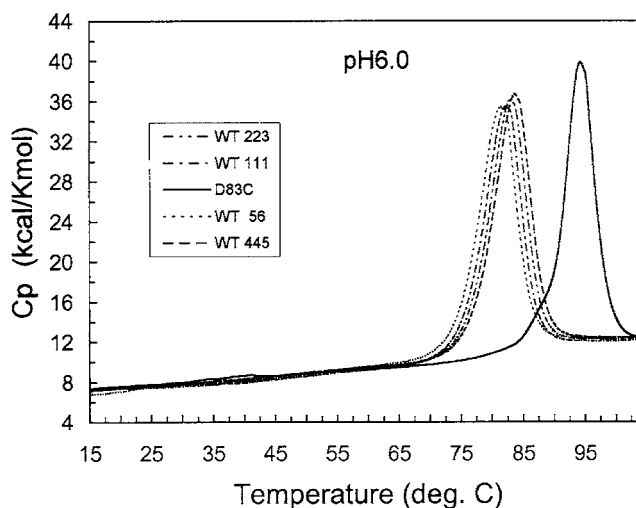
Fig. 1.19. Temperature dependencies of the partial molar heat capacities of wild-type subtilisin inhibitor from *Streptomyces* and its mutant D83C bridged by an S-S cross-linkmeasured at the different concentrations of proteins *(35)*. The used concentrations of dimers in μM are given in the inset. Note that the four heat capacity functions for the crosslinked dimer overlap perfectly but diverge for the non-crosslinked dimer.

(**Fig. 1.5b**) and according to the deconvolution analysis of the complete function it unfolds in three stages (**Fig. 1.20**). Among these stages only the last depends on concentration, that is, represents the bimolecular reaction of chain dissociation.
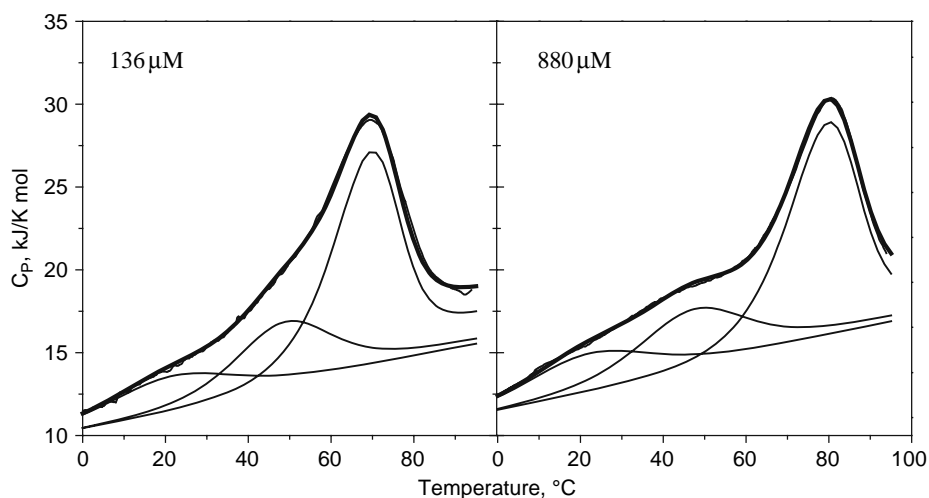
Fig. 1.20. Deconvolution of the excess heat capacity function of the GCN4 leucine zipper at the concentrations indicated in μM *(18)*. The last of the three transitions, which shows dependence on the concentration of protein, is associated with the dissociation of polypeptide chains forming this dimeric coiled-coil protein. The first transition represents unfolding of the N-terminus and the second one represents an internal repacking.

15. Formation of Protein Complexes

The energetics of the formation of protein complexes with other proteins and nucleic acids is now attracting increasing attention. It is widely accepted practice to determine the enthalpy of complex formation at different fixed temperatures using an ITC (**Fig. 1.1**). Assuming that Kirchhoff's relation ($\partial \Delta H / \partial T = \Delta C_{\mathrm{p}}$ is applicable to such cases, the dependence of the enthalpy of association on temperature is usually regarded as the heat capacity effect of complex formation, $\Delta C_{\mathrm{p}}{}^{\mathrm{a}}$.

The heat capacity effect of complex formation is a very important parameter because it is mainly caused by changes in hydration, and since hydration effects are proportional to the exposed surface areas of polar and apolar groups (*see* **Section 10**), the heat capacity change yields information on the extent and polarity of the interface formed between the components of the complex *(36, 20, 37)*. However, in using the temperature dependence of the binding enthalpy for estimating the intrinsic heat capacity effect of binding and the associated dehydration effect, it is not always appreciated that this assumes the components of this process do not change their state over the considered temperature range, that is, the heat capacities of all the components of the reaction are constant. Unfortunately, in many published papers on the thermodynamics of complex formation by proteins, the temperature dependencies of the heat capacities of the reaction components were not checked. As shown above, the heat capacity of proteins increases with temperature rather steeply, particularly in the case of DNA-binding proteins (**Fig. 1.6**), showing that their structure is partially unfolded in the temperature range at which the ITC experiments are conducted (*see* **Fig. 1.17**). As a result, the heat effect of association of such proteins is not a linear function of temperature (**Fig. 1.21a**). Since association with DNA stabilizes these proteins, i.e., they refold upon association with DNA (**Fig. 1.22**), the heat of association measured by ITC at some temperature includes the heat of protein refolding. So if we wish to determine the enthalpy of association of the fully folded protein with DNA we have to exclude the heat effect of protein refolding from the ITC-measured heat effect of association. Correction for these heat effects of temperature-induced changes in the components of the association reaction and the complex has been considered in detail in *(37)*. The corrected enthalpy of association is expressed by the following equation:

$$
\begin{aligned}
\Delta H(T)^{a}_{corr} = {} & \Delta H(T_{\mathrm{o}})^{\mathrm{a}} + \Delta C_{p}(T_{\mathrm{o}})^{\mathrm{a}}(T - T_{\mathrm{o}}) \\
& + \int_{T_{o}}^{T} [C_{p}(T) - C_{p}(T_{o})]^{\mathrm{compl}} \\
& - [C_{p}(T) - C_{p}(T_{o})]^{\mathrm{pr}} - [C_{p}(T) - C_{p}(T_{o})]^{\mathrm{DNA}} dT.
\end{aligned}
\tag{1.29}
$$
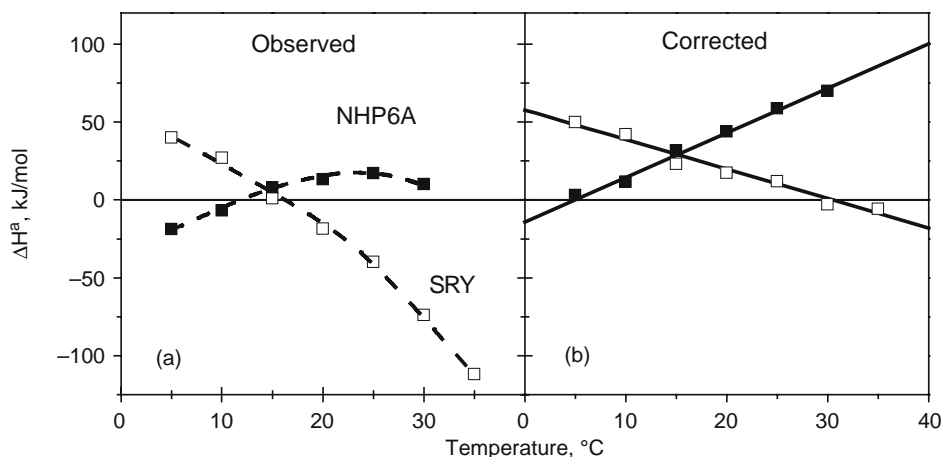
Fig. 1.21. (**a**) The ITC-measured association enthalpies of the DNA-binding domains of SRY and NHP6A HMG proteins to their target DNA duplexes. (**b**) The association enthalpies corrected for the heats of refolding the proteins upon binding. For details, *see (20)*.

The corrected enthalpies of association for the HMG boxes of SRY and NHP6a with their cognate DNA duplexes are shown in **Fig. 1.21b**. One can see that the corrections for the refolding of protein significantly alter not only the absolute values of the association enthalpies but also their dependences on temperature: they become linear. The slope of this linear function corresponds to the heat capacity effect of binding of the fully folded proteins to DNA. In the case of the sequence-specific association of the HMG box of SRY with its target DNA, while the apparent heat capacity effect is $\Delta C_p = -4.0$ kJK^{-1}mol^{-1}, the corrected value is only half this, -2.0 kJK^{-1}mol^{-1} *(20, 38)*.
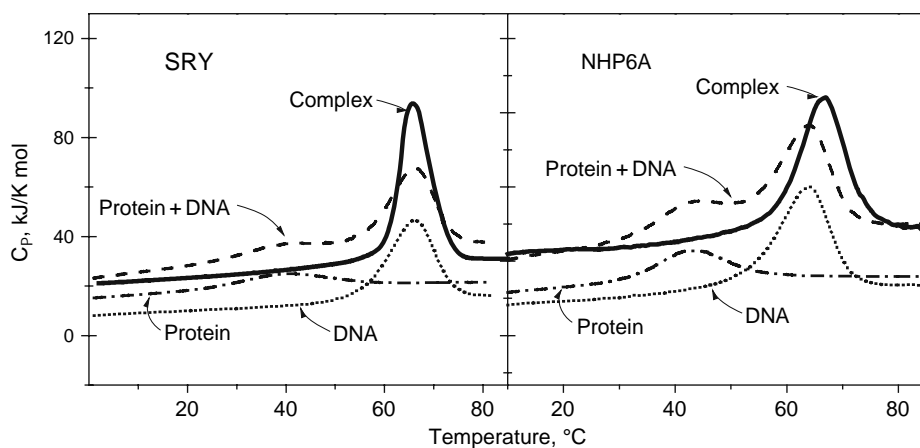
Fig. 1.22. The partial molar heat capacity functions of the free DNA-binding domains of SRY and NHP6A HMG proteins, their free cognate DNA duplexes, their complexes, and the sum of the heat capacities of the free proteins and DNA *(20)*.

Correction of the calorimetrically measured thermodynamic characteristics for refolding is especially important when making a structural analysis of the energetic basis of forming the complex. This is because in the structure of the complex determined by crystallography or NMR, the protein is folded and the interface is formed by the fully folded protein. Thus the structural parameters of forming the complex (e.g., the change in water accessible surface area (ΔASA) of the nonpolar and polar groups at the interface) would be expected to correlate with the thermodynamic characteristics of complex formation only after correcting for refolding. In the association of the HMG box DBDs with DNA considered above, binding of the sequence-specific SRY to DNA results in a negative enthalpy and negative heat capacity effect of binding, in contrast to the non-sequence-specific NHP6a for which the enthalpy and heat capacity effect of binding are positive. This shows that the sequence-specific SRY forms a much tighter interface with DNA than the non-sequence-specific NHP6a *(20)*.

It is worth noting that the Gibbs energy of binding does not require correction for refolding since the free energy of temperature-induced conformational changes of proteins at temperatures around ambient are usually small and may be neglected. Correspondingly, the binding entropy factor (calculated as the difference between the Gibbs free energy and the corrected binding enthalpy) is also corrected for protein refolding.

16. Conclusion

As follows from the above, DSC and ITC are two complementary tools which together provide the information required for the complete thermodynamic characterization of proteins and their complexes. This information is needed for understanding not only the physical mechanisms of formation and stabilization of the unique structures of proteins but also their functioning, which usually consists of recognizing and associating with specific partners, resulting in changes of both.

Acknowledgments

References

1. Privalov, P. L., Monaselidze, D. R., Mrevlishvili, G. M. et al. (1965) Heat of intramolecular fusion of macromolecules. *Soviet Physics JETP* 20 1393–1396.

2. Spokane, R. B., Gill, S. J. (1981) Titration microcalorimeter using nanomolar quantities of reactants. *Rev Sci Instrum* 52, 1728–1733.

3. Mckinnon, R., Fall, L., Parody-Morreale, A., et al. (1984) A twin titration microcalorimeter for the study of biochemical reactions. *Anal Biochem* 139, 134–139.

4. Wiseman, T., Willisten, S., Brandts, J., et al. (1989). Rapid measurement of binding constant and heats of binding using a new titration calorimeter. *Anal Biochem* 179, 131–137.

5. Bresslauer, K. J., Freire, E., Straume, M. (1992). Calorimetry: a tool for DNA and ligand–DNA studies. *Methods Enzymol.* 211, 533–567.

6. Privalov P. L., Plotnikov V. V., Filimonov, V. V. (1975). Precision scanning microcalorimeter for the study of liquids. *J Chem Thermodyn* 7, 41–47.

7. Privalov P. L. (1980). Scanning microcalorimeters for studying macromolecules. *Pure & Appl. Chem.* 52, 479–497.

8. Privalov P. L., Potekhin S.A. (1986) Scanning microcalorimetry in studying temperature-induced changes in proteins. *Methods in Enzymology,* 131, 4–51.

9. Privalov P. L., Plotnikov V. V. (1989) Three generations of scanning microcalorimeters for liquids. *Thermochim Acta* 139, 257–277.

10. Privalov, G. P., Kavina, V., Freire, E., et al. (1995) Precise scanning calorimeter for studying thermal properties of biological macromolecules in dilute solutions. *Anal Biochem* 232, 79–85.

11. Privalov G. P., Privalov, P. L. (2000) Problems and prospects in the microcalorimetry of biological macromolecules. *Methods in Enzymology,* 323, 31–62.

12. Privalov P. L. (1979) Stability of proteins. Small globular proteins. *Adv. Protein Chem* 33, 167–241

13. Privalov P. L., Khechinashvili N. N. (1974). A thermodynamic approach to the problem of stabilization of globular protein structure: a calorimetric study. *J Mol Biol* 86, 665–684.

14. Makhatadze G. I., Privalov P. L. (1990) Heat capacity of proteins. I. Partial molar heat capacity of individual amino acid residues in aqueous solutions: Hydration effect. *J Mol Biol* 213, 375–384

15. Makhatadze G. I., Privalov P. L. (1995). Energetics of protein structure. *Adv. Protein Chem.*, 47, 307–425.

16. Hackel, M., Hinz, H. J., Hedwig, G. R. (1999). A new set of peptide-based group heat capacities for use in protein stability calculations. *J Mol Biol* 291, 197–213.

17. Crane-Robinson, C., Read, C. M., Cary, P. D., et al. (1998) The energetics of HMG box interactions with DNA. Thermodynamic description of the box from mouse Sox-5. *J Mol Biol* 281, 705–717.

18. Dragan, A. I., Privalov, P. L. (2002) Unfolding of a leucine zipper is not a simple two-state transition. *J Mol Biol* 321, 891–908.

19. Dragan, A. I., Klass, J., Read, C. M., et al. (2003) DNA binding of a non-sequence-specific HMG-D protein is entropy driven with a substantial non-electrostatic contribution. *J Mol Biol* 327, 393–411.

20. Dragan, A. I., Read, C. M., Makeyeva, E. N., et al. (2004). DNA binding and bending by sequence specific HMG boxes: energetic determinants of specificity. *J Mol Biol* 343, 371–309.

21. Makhatadze, G. I., Kim, K. S., Woodward, C., et al. (1993). Thermodynamics of BPTI folding. *Protein Sci* 2, 2028–2036.

22. Hutchens, J. O., Cole, A. G., Stout, J. W. (1969). Heat capacities from 11 to 305 degrees K and entropies of hydrated and anhydrous bovine zinc insulin and bovine chymotrypsinogen A. Entropy change for formation of peptide bonds. *J Biol Chem* 244, 26–32.

23. Privalov, P. L., Griko, Yu.V., Venyaminov, S. Yu., et al. (1986) Cold denaturation of myoglobin. *J Mol Biol* 190, 487–498.

24. Privalov, P. L. (1990) Cold denaturation of proteins. *CRC Crit Rev Biochem Mol Biol* 25, 281–305.

25. Griko, Yu. V., Privalov, P. L., Venyaminov, S. Yu., et al. (1988) Thermodynamic studies of apomyoglobin structure. *Biofizika* (USSR) 33, 18–26.

26. Griko, Yu. V., Privalov P. L., Sturtevant, J. M., et al. (1988) Cold denaturation of staphylococcal nuclease. *Proc Natl Acad Sci USA* 85, 3343–3347.

27. Privalov, P. L., Makhatadze, G. I. (1992) Contribution of hydration and non-covalent interactions to the heat capacity effect on protein unfolding. *J Mol Biol* 224, 715–723.

28. Makhatadze G. I., Privalov P. L. (1993). Contribution of hydration to protein folding thermodynamics. I. The enthalpy of hydration. *J Mol Biol* 232, 639–659.

29. Spolar, R. S., Livingstone, J. R., Record, M. T. Jr. (1992). Use of liquid hydrocarbon and amide transfer data to estimate contributions to thermodynamic functions of protein folding from the removal of nonpolar and polar surface from water. *Biochemistry* 31, 3947–3955.

30. Pfeil, W., Privalov, P. L. (1976). Thermodynamic investigations of proteins. I. Standard functions for proteins with lysozyme as an example. *Biophys Chem* 4, 23–32.

31. Pfeil, W., Privalov, P. L. (1976). Thermodynamic investigations of proteins. 3. Thermodynamic description of lysozyme. *Biophys Chem* 4, 41–50.

32. Freire, E. (1994). Statistical thermodynamic analysis of differential scanning calorimetry data: structural deconvolution of heat capacity function of proteins. *Methods Enzymol* 240, 502–530.

33. Privalov, P. L. (1982). Stability of proteins: Proteins which do not present a single cooperative system. *Adv Prot Chem* 35, 1–104.

34. Novokhatny, V. V., Kudinov, S. A., Privalov, P. L. (1984). Domains in human plasminogen. *J .Mol Biol* 179, 215–232.

35. Tamura, A., Privalov, P. L. (1997). The entropy cost of protein association. *J Mol Biol* 273, 1046–1058.

36. Dragan, A. I., Liggins, J. R., Crane-Robinson, C., et al. (2003) The energetics of specific binding of AT-hooks from HMGA1 to target DNA. *J Mol Biol* 327, 393–411.

37. Privalov, P. L., Jelesarov, I., Read, C. M., et al. (1999). The energetics of HMG box interactions with DNA. Thermodynamics of the DNA bonding of the HMG box from mouse Sox-5. *J Mol Biol* 294, 997–1013.

38. Dragan, A. I., Frank, L., Liu, Y., et al. (2004). Thermodynamic signature of GCN4-bZIP binding to DNA indicates the role of water in discriminating between the AP-1 and ATF/CREB sites. *J Mol Biol* 343, 865–878.

39. Griko, Y. V., Makhatadze, G. I., Privalov, P. L., et al. (1994). Thermodynamics of barnase unfolding. *Protein Sci* 3, 669–676.

40. Wintrode, P.L., Makhatadze, G.I., Privalov, P.L. (1994). Thermodynamics of ubiquitin unfolding. *Proteins, Structure, Function and Genetics* 18, 246–253.

41. Yu, Y., Makhatadze, G. I., Pace, C. N., et al. (1994). Energetics of ribonuclease T1 structure. *Biochemistry* 33, 3312–3319.

42. Carra, J. H., Murphy, E. C., Privalov, P. L. (1996) Thermodynamic effects of mutations on the denaturation of T4 lysozyme. *Biophy J* 71, 1994–2001.

43. Dragan, A. I., Li, Z., Makeyeva, E. N., et al. (2006) Forces driving the binding of homeodomains to DNA. *Biochemistry* 45, 141–151.

44. Liggins, J. R., Privalov, P. L. (2000). Energetics of the specific binding interaction of the first three zinc fingers of the transcription factor TFIIIA with its cognate DNA sequence. *Proteins Suppl* 4, 50–62.

Chapter 2

Determining the Conformational Stability of a Protein Using Urea Denaturation Curves

Kevin L. Shaw, J. Martin Scholtz, C. Nick Pace, and Gerald R. Grimsley

Abstract

The stability of globular proteins is an important factor in determining their usefulness in basic research and medicine. A number of environmental factors contribute to the conformational stability of a protein, including pH, temperature, and ionic strength. In addition, variants of proteins may show remarkable differences in stability from their wild-type form. In this chapter, we describe the method and analysis of urea denaturation curves to determine the conformational stability of a protein. This involves relatively simple experiments that can be done in a typical biochemistry laboratory, especially when using ordinary spectroscopic techniques to follow unfolding.

Key words: conformational stability, urea denaturation, circular dichroism, fluorescence, UV absorbance spectroscopy.

1. Introduction

The stability of globular proteins is important for a number of cellular processes and is of practical concern to those who do research in medicine, drug formulation, and basic science. In this chapter, we discuss how to measure the conformational stability of the folded state, that is, how much more stable the folded conformation of a protein is relative to its unfolded states. This requires determining the equilibrium constant and free energy change, ΔG, for the reaction:

$$\text{Folded (F)} \Leftrightarrow \text{Unfolded (U)} \tag{2.1}$$

The ΔG for this reaction at 25°C in the absence of denaturant, $\Delta G(\text{H}_2\text{O})$, is known as the conformational stability of the protein. This measurement is useful for determining how stable a protein is

under physiological conditions, how the stability depends on temperature, pH, and salt, and whether an amino acid substitution changes the stability of the protein.

Aqueous urea solutions have historically been used for measuring $\Delta G(H_2O)$ *(1)* and involve relatively simple experiments. The mechanism of how urea denatures proteins has prompted much study *(2–6)*. It now appears that urea denatures proteins principally by acting as a preferred solvent for the peptide groups. As urea is added to a protein solution, the denatured or unfolded state becomes more favorable because the peptide groups are more exposed to the aqueous urea solution in this conformation than when folded. This shifts the equilibrium in **Eq. (2.1)** toward the right, producing measurable populations of folded and unfolded protein in the same solution. Thus the equilibrium constant and $\Delta G(H_2O)$ can be readily measured.

Here, we describe methods for determining and analyzing urea denaturation curves. We will not discuss denaturation by guanidinium chloride (GdmCl). Although GdmCl is a stronger denaturant and more chemically stable than urea, because it is a salt, the ionic strength of the solutions cannot be controlled with GdmCl and this may give less reliable $\Delta G(H_2O)$ values for some proteins *(7–9)*. Therefore, we recommend using urea instead of GdmCl for denaturation experiments whenever possible.

2. Materials

Urea can be purchased commercially in highly purified form; however, some lots may contain fluorescent or metallic impurities. This may only be a problem if fluorescence is used to following unfolding. A procedure for purifying urea has been described *(10)*, but this is rarely necessary. One source of urea is the Proteomics Grade Urea available from AMRESCO (Solon, OH 41139).

3. Methods

3.1. Preparing Urea Stock Solutions

1. Add approximately 60 g of urea to a tared beaker and record the mass (*See* **Note 1**). Add 0.69 g of Mops (sodium salt), 1.8 ml of 1 M HCl, and 52 ml of distilled water. Mass the mixture (113.08 g).
2. Allow the urea to dissolve and check the pH (*See* **Note 2**). Add a massed amount of 1 M HCl to adjust the pH, if necessary.

3. Prepare 30 mM Mops buffer at pH 7.0.

4. Determine the refractive index of the urea stock solution (1.4185) and the buffer solution (1.3345). Calculate ΔN by subtracting the refractive index of the buffer from the refractive index of the urea stock solution ($\Delta N = 1.4185 - 1.3345 = 0.0840$).

5. Calculate the molarity of the urea stock solution using ΔN and the equation in **Table 2.1**. Molarity, $M = 117.66 \times 0.0840 + 29.753 \times (0.0840)^2 + 185.56 \times (0.0840)^3 = 10.20$ M.

6. Calculate the molarity of the urea stock solution based on mass. The weight fraction urea (W) = 60.00/113.08 = 0.5306. The density of the urea solution relative to the density of water (d/d_o) is calculated by the equation in **Table 2.1**: $d/d_o = 1 + 0.2658 \times (0.5306) + 0.0330 \times (0.5306)^2 = 1.150$. The volume of the solution is equal to 113.08/1.150 = 98.33 ml or 0.09833 L. The molarity of the urea stock solution can then be calculated using the mass of urea, the formula weight of urea, and the volume of the solution, $M = 60.00/60.056/0.09833 = 10.16$ M.

7. Compare the molarities of the urea stock solution calculated in steps 5 and 6. If they are within 3% of each other (as is this example) the urea stock solution is suitable for use in a urea unfolding experiment (*See* **Note 3**).

Table 2.1
Useful information for the preparation of urea stock solutions

Property	Urea
Molecular weight	60.056 g/mol
Solubility (25°C)	10.49 M
d/d_o[a]	$1 + 0.2658\,W + 0.0330\,W^2$
Molarity[b] (M)	$117.66(\Delta N) + 29.753(\Delta N)^2 + 185.56\,(\Delta N)^3$
Grams of urea per gram of water to prepare:	
6 M	0.495
8 M	0.755
10 M	1.103

[a] W is the weight fraction of urea in the solution (g/g), d is the density of the solution (g/ml), and d_o is the density of water (1.0 g/ml). This equation is from **Ref.** *(35)*.
[b] ΔN is the difference in refractive index between the urea solution and water (or buffer) at the sodium D line. The equation is based on data from **Ref.** *(36)*.

3.2. Using Spectroscopic Techniques to Determine a Urea Denaturation Curve

1. Prepare a urea stock solution as described above, a concentrated protein stock solution in buffer, and a buffer solution.
2. Prepare the solutions of protein in various concentrations of urea to be used for measurements volumetrically (*See* **Note 4**). Each solution is prepared by mixing a volume of the urea stock solution, the concentrated protein solution, and the buffer solution as illustrated in **Table 2.2** (*See* **Note 5**).
3. Allow these solutions to equilibrate at the experimental temperature (*See* **Note 6** *for the best method for determining if the solution is at equilibrium*).

Table 2.2
An example showing the preparation of selected samples from the experiment illustrated in Figure 2.1

Urea Stock Solution(ml)	Protein Stock Solution (ml)	Buffer Stock (ml)	Final Urea Concentration (M)
0.000	0.075	2.925	0.000
0.067	0.075	2.858	0.225
0.135	0.075	2.790	0.450
0.202	0.075	2.723	0.675
1.213	0.075	1.712	4.050
1.280	0.075	1.645	4.275
1.347	0.075	1.575	4.500
1.415	0.075	1.510	4.725
1.482	0.075	1.443	4.950
1.549	0.075	1.376	5.175
2.695	0.075	0.230	9.000
2.769	0.075	0.156	9.250
2.844	0.075	0.081	9.500
2.919	0.075	0.060	9.750

Each sample is prepared from urea stock solution, buffer, and concentrated protein stock solution. The urea stock solution concentration in 10.02 M. The protein stock solution is 2 mg/ml and the working protein concentration is 0.05 mg/ml. The buffer stock is 10 mM potassium phosphate buffer at pH 7.0 (the urea stock solution is also buffer at this concentration and pH). The total volume of each sample is 3 ml. Only a selection of the 44 samples used to collect the data in **Fig. 2.1** are given here. They are the first four urea concentrations, five samples around the midpoint of the denauration, and the final four solutions.

4. Measure the physical parameter being used to follow unfolding for each solution (*See* **Note 7**)**.** Plot these data and determine if any additional points are needed. Both pre- and post-transition baselines should be well defined; there should be a number of points in the transition region (*See* **Note 8**)**.** If extra points are needed, prepare solutions at those urea concentrations and measure the physical parameter just as for the original solutions.

5. It can be useful to measure the pH of the solutions in the transition region, in the case of anomalous readings.

6. Example experimental results are shown in **Table 2.3**.

7. Analyze the results as described below.

3.3. Analyzing Urea Denaturation Curves

1. Plot the observed signal Y, as a function of urea concentration.

2. (*See* **Note 9** *for a detailed discussion of the theory of this step*). Fit these data using an implementation of the nonlinear least-squares method as described *(11, 12),* using typical analysis packages such as KaleidaGraph (Synergy Software, Reading, PA), SigmaPlot (Systat Software, San Jose, CA), or Origin (OriginLab Corporation, Northampton, MA), or your own

Table 2.3
Calculation of the fraction unfolded, F_U, equilibrium constant, K, and the free energy change, ΔG, for data points in the transition region of the urea denaturation curve shown in Fig. 2.2A

[Urea] (M)	Y	F_U	K	ΔG (cal/mol)
3.375	−55.97	0.103	0.115	1175
3.600	−53.55	0.152	0.180	930
3.825	−50.61	0.212	0.269	710
4.050	−46.65	0.292	0.413	480
4.275	−42.05	0.386	0.629	250
4.500	−37.08	0.487	0.950	28
4.725	−32.19	0.586	1.418	−190
4.950	−27.57	0.681	2.130	−410
5.175	−23.89	0.755	3.085	−610
5.400	−20.56	0.823	4.650	−835
5.625	−18.49	0.865	6.417	−1010

nonlinear least-squares implementation in Microsoft Excel (Microsoft Corporation, Redmond, WA).

3. Report values of C_{mid}, m, and $\Delta G(H_2O)$ obtained from Step 2.

3.4. Calculating Changes in Stability

It is often useful to know how the conformational stability of a protein changes with a perturbant, $\Delta(\Delta G)$. The perturbation may be a change in the solution conditions such as temperature, pH, salt concentration, or the addition of a cosolvent. Many researchers are interested in changes in stability produced by amino acid substitutions in the protein. In all these cases, the goal is to compare the conformational stability of proteins that differ in sequence or environment.

The calculation of $\Delta(\Delta G)$ should be based on the data that is determined most precisely by the urea denaturation experiment, which is $[urea]_{1/2}$. The error here is much smaller and less dependent on accurate determinations of the pre- and post-transition baselines compared to the m value. Furthermore, the m value can vary substantially between the wild-type protein and a variant, or between different solution conditions for the same protein, for reasons that are discussed below (13, 14). The best way to determine $\Delta(\Delta G)$ is to use a urea concentration midway between the $[urea]_{1/2}$ of the wild-type and the $[urea]_{1/2}$ of the variant, using the m value of the wild-type protein, that is,

$$\Delta(\Delta G) = \{[urea]_{1/2}(variant) - [urea]_{1/2}(Wt)\} \times m(Wt). \quad (2.2)$$

In **Eq. (2.2)** negative values of $\Delta(\Delta G)$ are obtained for variants that have $[urea]_{1/2}$ values less than that of the wild-type (i.e., the variant is less stable), and, conversely, positive values of $\Delta(\Delta G)$ indicate that the variant is more stable than the wild-type. This convention for the sign of $\Delta(\Delta G)$ is found extensively in the literature (15); however, the opposite is occasionally seen. Therefore, when reading a table of urea denaturation curve results, it is easiest to identify the sign convention by comparing $[urea]_{1/2}$ values.

3.5. Understanding the m Value

The dependence of ΔG on urea concentration, m, can be seen by the steepness of the transition region. A sharp transition over a small range of urea concentrations reflects a larger m value than a shallow, broad transition over a larger range of urea concentrations. Since the $[urea]_{1/2}$ and m values for different curves can often be visually compared by inspection, it is sometimes useful to plot multiple curves (of different proteins or variants, different solution conditions, etc.) on the same axes.

One reason the linear extrapolation method (LEM) is favored for the analysis of urea denaturation curves is that the extrapolation to determine $\Delta G(H_2O)$ depends only on a single empirical parameter, m. The m value has been shown to correlate with the

change in solvent accessible surface area (ΔASA) of the protein upon unfolding *(16)*. The realization that the *m* value is so strongly correlated with ΔASA has provided an interest in comparing *m* values and changes in *m* values with properties of the denatured or unfolded state. The denatured state of a protein is not a singular structure but a family of transiently populated structures *(17)*. A description of the structures formed in the denatured state has been challenging *(18, 19)*, yet it is clear that in the denatured state there are interactions which can influence the conformational stability of the protein *(20–22)*. A quantitative relationship between *m*, (ΔASA), and the mechanism of urea denaturation has recently been discussed by the Bolen lab *(23)*.

As discussed above, *m* values can be useful in determining how folded or compact a protein might be under certain conditions. Many proteins show larger *m* values at pH extremes *(24)*. For example, at low pH, the charged groups of amino acid side-chains are protonated, making the net charge on protein positive. Under these conditions, the denatured states might be more expanded relative to the denatured states at neutral pH due to increased charge–charge repulsion, thus increasing the value for *m*.

3.6. Using Urea Denaturation Curves to Estimate ΔC_p Without a Calorimeter

One must do thermal unfolding experiments in order to determine ΔH_m, ΔS_m, T_m, and ΔC_p, as well as $\Delta G(H_2O)$, for the unfolding reaction given in Eq. (**2.1**) (for detailed discussions of these types of experiments, *see* Refs. *(15, 25–26)*). The determination of ΔC_p, the change in heat capacity that accompanies protein unfolding, is the most difficult of these to measure, and various approaches have been discussed *(26)*.

Here we mention a useful technique that uses both urea and thermal denaturation data to determine ΔC_p. In this method, $\Delta G(H_2O)$ values from urea denaturation experiments conducted at low temperature are combined with ΔG values determined from the transition region of a thermal denaturation curve *(27, 28)*. This method is shown in **Fig. 2.1**. This stability curve can be described by the Gibbs–Helmholtz equation

$$\Delta G(T)=\Delta H_m(1-T/T_m)-\Delta C_p[(T_m-T)+T\times ln(T/T_m)], \quad (2.3)$$

and a nonlinear least-squares fit of this equation to the data in **Fig. 2.3** can be used to determine ΔC_p, as well as ΔH_m, ΔS_m, and T_m. The ΔC_p value can usually be determined in this way with an accuracy of $\approx$10%.

3.7. Concluding Remarks

Using urea denaturation curves to determine the conformational stability of a protein has a number of advantages over other methods. After learning the techniques given here, a denaturation curve can be determined and analyzed in a single day. In addition,
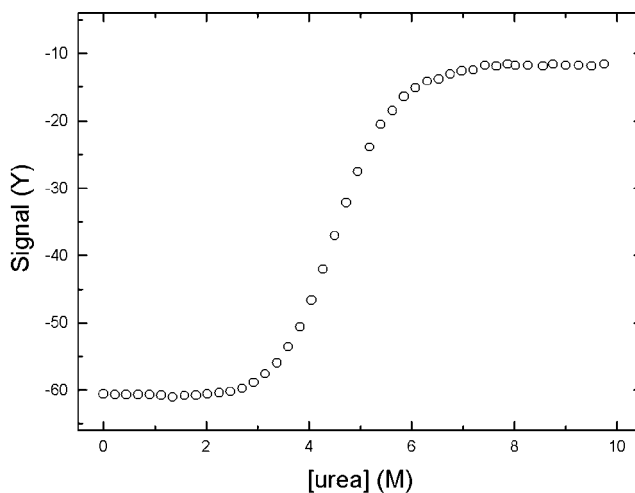
Fig. 2.1. An example urea denaturation curve determined for the *E. coli* HPr protein, using CD to follow unfolding. Note the three important parts of the curve, the pre-, post-, and transition regions.

the unfolding of a protein in the presence of urea is more likely to closely approach a two-state mechanism, and generally completely reversible. Denaturation curves of variant proteins can easily be compared to help improve our understanding of the forces that contribute to the stability of globular proteins.

4. Notes

1. **Table 2.1** gives useful information for preparing urea stock solutions. Urea stock solutions should be used within 24 h of preparation, as urea decomposes to form cyanate and ammonium ions, especially when working at high pH *(29)*. Furthermore, the cyanate ions can modify primary amines in proteins *(30)*.
2. The dissolution of urea is strongly endothermic, but it may be mildly warmed in a stirred water bath to aid the dissolution process.
3. An accurate determination of the concentration of the urea stock solution is critical. Two methods for determining the concentration of the urea stock solution are given here. If possible, these methods should be used simultaneously to determine the concentration, and hopefully both methods should provide results that agree within a few percent of each other. If one suspects the balance measurement to be unreliable, the refractive index technique in itself will suffice to accurately measure the molarity of the urea stock solution.
4. Electronic pipettes such as the Rainin EDP2 series (Rainin Instruments, Oakland, CA) are recommended for precision. New disposable test tubes are also recommended for these

solutions in order to limit the possibility of introducing contaminates.

5. The 0 M urea sample is a dilution of concentrated protein stock in buffer. The greatest urea concentration available in the experiment is a dilution of the concentrated protein stock in the stock urea solution.

6. The time required to reach equilibrium depends on the protein and the temperature at which the experiment is conducted. For example, RNase T1 will reach equilibrium in minutes at 30°C, but requires hours at 20°C. The proper equilibration time should be established for each protein and temperature. Samples that will make up the pre- and post-transition regions will equilibrate more rapidly than solutions in the transition region, where both folded and unfolded conformations must reach equilibrium. When working with an unfamiliar protein, it may be necessary to perform a pilot study to find the urea concentrations corresponding to the transition region in order to determine the time required for equilibration, and also to determine the approximate range of urea concentrations for the transition region.

7. We assume in this chapter that most readers will use common spectroscopic techniques to follow protein unfolding, such as fluorescence, circular dichroism, or UV absorption. The best technique to use is the one that shows the biggest change between the folded and unfolded forms, as shown by a comparison of their spectra in buffer and 9 M urea. Then the wavelength is chosen to follow unfolding where the properties of the folded and unfolded conformations differ most. Another consideration is the amount of protein available for experiments. If the protein has a buried tryptophan and fluorescence can be used, this will require much less protein than the other two techniques. Example spectra of folded and unfolded proteins can be seen in **Fig.** 23.1 of **Ref.** *(25)*. For the discussion below, we refer to the observed spectroscopic parameter used to follow unfolding as Υ. Regardless of which technique is used, measurement quality is improved by leaving the cuvette in place in the instrument and exchanging the samples. Samples can be removed from the cuvette by use of a Pasteur pipette, with plastic tubing on the end, connected to a manual bulb or vacuum source. Samples should be measured in sequence from the lowest to the highest urea concentration in order to minimize the error introduced by sample remaining in the cuvette.

8. A typical urea denaturation curve is shown in **Fig. 2.1**. The curve is divided into three regions. The "pre-transition region" shows how Υ for the folded protein (Υ_{F}), depends on urea concentration. Here there is little perturbation of the folded to unfolded equilibrium. The "transition region", shows how Υ
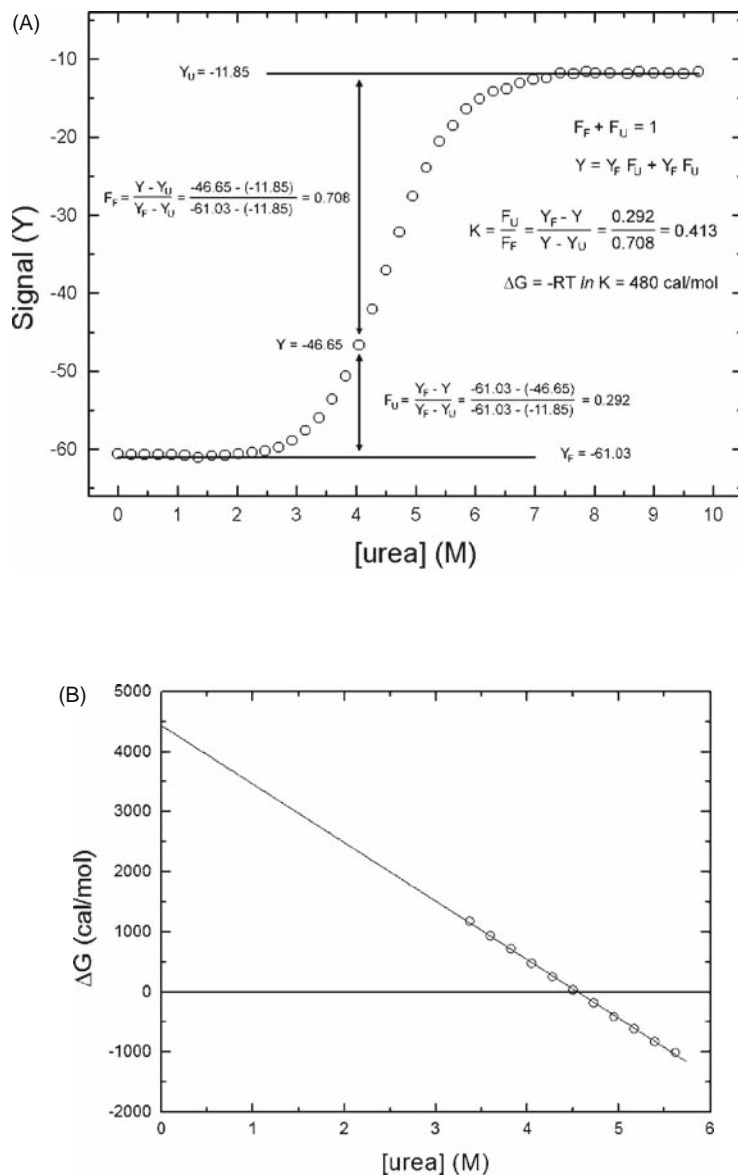
Fig. 2.2. **(A)** The urea denaturation curve of **Fig. 2.1a** showing the pre- and post-transition baselines and the calculation of K and ΔG for one point in the transition region. **(B)** The free energy change (ΔG) for each point in the transition region plotted as a function of denaturant concentration. The linear extrapolation back to 0 M urea yields the conformational stability of the protein.

varies as unfolding occurs. It is this region where the equilibrium constants for the unfolding reaction are measured. The "post-transition region" shows how Y for the unfolded protein (Y_U) depends on urea concentration. It is important to collect data in each of these regions. The data in the pre- and post-transition regions will define the signals for the folded and unfolded conformations, respectively, and the data in the transition region

will be used to measure $\Delta G(H_2O)$ of the protein. A typical unfolding curve can be obtained by preparing 20–30 samples over the entire range of urea concentration, and at a minimum, five points in each of the three regions should produce a usable curve. The data shown in **Fig. 2.1** can be obtained in several ways, depending on the protein and the available equipment. One method is to simply prepare and measure individual solutions. **Table 2.2** shows the preparation of solutions that were measured to get each data point in **Fig. 2.1**. Each solution was prepared with aliquots of the urea stock solution, a buffer solution without urea, and the protein stock solution in buffer, as detailed above. The unfolding reaction should be reversible if the thermodynamic analysis is to be valid. The best way to check this is to dilute a sample that has reached equilibrium in the post-transition region back to a urea concentration corresponding to the pre-transition region. The sample should refold and give a signal that is within $\approx 5\%$ of a sample prepared directly at that urea concentration. In general, the reversibility of protein unfolding in urea is very high, which is another reason why urea is a good denaturant for measuring protein stability.

9. The simplest analysis of the urea denaturation curve, like that illustrated in **Fig. 2.2A** and described here, assumes that only two states, the folded and unfolded forms of the protein, are present at significant concentrations. A two-state mechanism will, by definition, show only a single sigmoidal unfolding curve like that shown in **Fig. 2.2A**. If the curve shows more than a single transition, the unfolding mechanism is not two-state and the analysis of the unfolding data is more complicated *(31)*. Further information to determine whether a two-state folding mechanism is appropriate for analysis may be obtained by determining curves using multiple spectroscopic probes *(25)*. We can define the two-state model as

$$F_F + F_U = 1, \tag{2.4}$$

where F_F represents the fraction of molecules in the folded conformation and F_U represents the fraction of molecules in unfolded forms. The observed parameter Υ, at any denaturant concentration, is the sum of the signal of the folded protein multiplied by the fraction of molecules in the folded form and the signal of the unfolded forms multiplied by the signal for the unfolded protein:

$$\Upsilon = \Upsilon_F F_F + \Upsilon_U F_U. \tag{2.5}$$

Combining these equations gives

$$F_U = (\Upsilon_F - \Upsilon)/(\Upsilon_F - \Upsilon_U). \tag{2.6}$$

Now the equilibrium constant, K_{eq}, and the free energy change, ΔG, can be expressed as
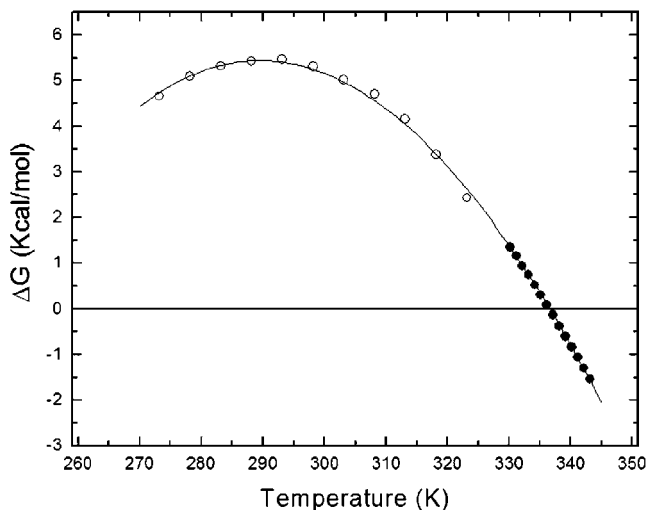
Fig. 2.3. Protein stability curve for the *E. coli* HPr protein collected in 10 mM phosphate buffer at pH 7.0. Open symbols are $\Delta G(H_2O)$ values from individual urea denaturation curve experiments at a particular temperature. Solid symbols are ΔG values from the transition region of a thermal denaturation curve, where ΔG is calculated from the equilibrium constant at that temperature as in the urea denaturation experiment. These data are from reference *(34)*. The solid line is a plot of Eq. (1.12) using the determined parameters for ΔH_m, T_m, and ΔC_p.

$$K_{eq} = F_U/F_F = F_U/(1 - F_U) = (\Upsilon_F - \Upsilon)/\Upsilon - \Upsilon_U) \qquad (2.7)$$

and

$$\Delta G = -RT \ln K_{eq} = -RT \ln [(\Upsilon_F - \Upsilon)/\Upsilon - \Upsilon_U)], \qquad (2.8)$$

where R is the universal gas constant $(1.987$ cal mol^{-1} K$^{-1})$ and T is the absolute temperature.

To use these equations as shown in **Fig. 2.2A**, the pre- and post-transition baselines must be extrapolated through the transition region so that Υ_F and Υ_U can be calculated at the same urea concentration where Υ was measured. Usually the baselines are linear as a function of the urea concentration and can be extrapolated into the transition region by least-squares analysis.

The measurement of K_{eq}, and the calculation of ΔG, is most accurate around the midpoint of the urea denaturation curve where there are significant populations of both folded and unfolded conformations. The values of K_{eq} that can be measured most accurately are in the range of 0.1–10, giving ΔG values of ± 1.5 kcal mol^{-1}. The analysis of usable points in the transition region of the urea denaturation curve shown in **Fig. 2.2A** is shown in **Table 2.3**. **Figure 2.2B** shows the dependence of ΔG as a function of urea concentration. To determine $\Delta G(H_2O)$, the measured ΔG values are extrapolated back to 0 M urea. Several methods have been proposed for making this extrapolation *(32, 33)*.

The simplest method is to assume that the linear dependence of ΔG as a function of urea concentration shown in **Fig. 2.2B** is valid to 0 M urea. This seems to be the case for a wide variety of proteins; therefore, we recommend using this LEM *(34)*. Some historic and technical details of the LEM have recently been reviewed *(20)*. Assuming that the urea dependence of ΔG is linear

$$\Delta G = \Delta G(H_2O) - m \, [\text{urea}], \tag{2.9}$$

where $\Delta G(H_2O)$ is the conformational stability of the protein in units of kcal mol^{-1} and m is denaturant dependence of the free energy change in units of kcal mol^{-1} M^{-1}. Although Eq. (2.9) can be fit to the data in **Fig. 2.2B** by a least-squares method to determine $\Delta G(H_2O)$, the entire urea denaturation curve can be described by a single equation that can be fit to the raw data using a nonlinear least-squares method *(11, 12)*. This equation assumes that the pre- and post-transition baselines are linear function of urea concentration with the Y_F, m_F, Y_U, and m_U representing the y-intercept and slope of the pre- and post-transition baselines, respectively. The equation also uses m and $\Delta G(H_2O)$ from **Eq. (2.9)**. The entire urea denaturation curve can thus be described by

$$Y = \{(Y_F + m_F[\text{urea}]) + (Y_U + m_U[\text{urea}]) \times \exp[-(\Delta G(H_2O)$$
$$-m[\text{urea}])/(RT))]\}/(1 + \exp[-(\Delta G(H_2O) - m[\text{urea}])/(RT))]) \tag{2.10}$$

This equation, with six resolvable parameters, can be fit to the experimental data by nonlinear least-squares procedures to determine $\Delta G(H_2O)$ and m. In reporting the results of denaturation curve analysis, there are several values that should always be given. $\Delta G(H_2O)$ and m should be reported for any study. Another important value, particularly for the comparison of conformational stabilities, is the urea concentration at the midpoint of the transition region [urea]$_{1/2}$. At the midpoint of the transition region, $F_U = F_N$, and the equilibrium constant, K_{eq}, is equal to 1 (**Eq. (2.7)**) and $\Delta G = 0$ (**Eq. (2.8)**). Therefore, from **Eq. (2.9)**

$$[\text{urea}]_{1/2} = \Delta G(H_2O)/m \tag{2.11}$$

and **Eq. (2.10)** can be rewritten as

$$Y = \{(Y_F + m_F[\text{urea}]) + (Y_U + m_U[\text{urea}]) \times \exp[m \times ([\text{urea}]$$
$$-[\text{urea}]_{1/2}/RT]\}/(1 + \exp[m \times ([\text{urea}] - [\text{urea}]_{1/2}/RT]), \tag{2.12}$$

which is a more useful expression for analyzing urea denaturation curves. The errors on the values determined for a protein by the urea denaturation are best estimated by repetition of the experiment, fitting each experimental curve separately and averaging the key parameters, m, [urea]$_{1/2}$, and $\Delta G(H_2O)$. The [urea]$_{1/2}$ value

can typically be determined to ±0.05 M urea, and the typical *m* value error is ≈5%. Therefore, the typical error when calculating $\Delta G(\text{H}_2\text{O})$ is ≈5%.

References

1. Tanford, C. (1964) Isothermal unfolding of globular proteins in aqueous urea solutions. J Am Chem Soc 86, 2050–2059.

2. Pace, C. N., Grimsley, G. R., Scholtz, J. M. (2005) Denaturation of proteins by urea and guanidine hydrochloride, in (Kiefhaber, T., ed.) Protein Folding Handbook, pp. 45–69. Wiley-VCH Verlag GmbH & Co. KGaA, Hamburg, Germany.

3. Goldenberg, D. P. (2003) Computational simulation of the statistical properties of unfolded proteins. J Mol Biol 326, 1615–1633.

4. Schellman, J. A.(2003) Protein stability in mixed solvents: a balance of contact interaction and excluded volume. Biophys J 85, 108–125.

5. Timasheff, S. N., Xie, G. (2003) Preferential interactions of urea with lysozyme and their linkage to protein denaturation. Biophys Chem 105, 421–448.

6. Courtenay, E. S., Capp, M. W., Saecker, R. M., et al. (2000) Thermodynamic analysis of interactions between denaturants and protein surface exposed on unfolding: interpretation of urea and guanidinium chloride *m*-values and their correlation with changes in accessible surface area (ASA) using preferential interaction coefficients and the local-bulk domain model. Proteins Suppl 4, 72–85.

7. Monera, O. D., Kay, C. M., Hodges, R. S. (1994) Protein denaturation with guanidine hydrochloride or urea provides a different estimate of stability depending on the contributions of electrostatic interactions. Protein Sci 3, 1984–1991.

8. Schellman, J. A., Gassner, N. C. (1996) The enthalpy of transfer of unfolded proteins into solutions of urea and guanidinium chloride. Biophys Chem 59, 259–275.

9. Makhatadze, G. I. (1999) Thermodynamics of protein interactions with urea and guanidinium hydrochloride. J Phys Chem B 103, 4781–4785.

10. Prakash, V., Loucheux, C., Scheufele, S., et al. (1981) Interactions of proteins with solvent components in 8 M urea. Arch Biochem Biophys 210, 455–464.

11. Santoro, M. M., Bolen, D. W. (1992) A test of linear extrapolation of unfolding free energy changes over an extended denaturant concentration range. Biochemistry 31, 4901–4907.

12. Santoro, M. M., Bolen, D. W. (1988) Unfolding free energy changes determined by the linear extrapolation method. 1. Unfolding of phenylmethanesulfonyl alpha-chymotrypsin using different denaturants. Biochemistry 27, 8063–8068.

13. Shirley, B. A., Stanssens, P., Hahn, U., et al. (1992) Contribution of hydrogen bonding to the conformational stability of ribonuclease T1. Biochemistry 31, 725–732.

14. Pace, C. N., Alston, R. W., Shaw, K. L. (2000) Charge–charge interactions influence the denatured state ensemble and contribute to protein stability. Protein Sci 9, 1395–1398.

15. Becktel, W. J., Schellman, J. A. (1987) Protein stability curves. Biopolymers 26, 1859–1877.

16. Myers, J. K., Pace, C. N., Scholtz, J. M. (1995) Denaturant *m* values and heat capacity changes: relation to changes in accessible surface areas of protein unfolding. Protein Sci 4, 2138–2148.

17. Shortle, D. (1997) Structure prediction: folding proteins by pattern recognition. Curr Biol 7, R 151–154.

18. Neri, D., Billeter, M., Wider, G., et al. (1992) NMR determination of residual structure in a urea-denatured protein, the 434-Repressor. Science 257, 1559–1563.

19. Religa, T. L., Markson, J. S., Mayor, U., et al. (2005) Solution structure of a protein denatured state and folding intermediate. Nature 437, 1053–1056.

20. Pace, C. N., Shaw, K. L. (2000) Linear extrapolation method of analyzing solvent denaturation curves. Proteins 4, 1–7.

21. Shortle, D. (1996) The denatured state (the other half of the folding equation) and its role in protein stability. FASEB J 10, 27–34.

22. Anil, B., Craig-Schapiro, R., Raleigh, D. P. (2006) Design of a hyperstable protein by

rational consideration of unfolded state interactions. J Am Chem Soc 128, 3144–3145.

23. Auton, M., Holthauzen, L. M., Bolen, D. W. (2007) Anatomy of energetic changes accompanying urea-induced protein denaturation. Proc Natl Acad Sci US A 104, 15317–15322.

24. Pace, C. N., Laurents, D. V., Thomson, J. A. (1990) pH dependence of the urea and guanidine hydrochloride denaturation of ribonuclease A and ribonuclease T1. Biochemistry 29, 2564–2572.

25. Grimsley, G. R., Huyghues-Despointes, B. M-P., Pace, C. N., et al. (2004) Measuring the conformational stability of a protein, in (Simpson, R. J., ed.), Purifying Proteins For Proteomics, pp. 535–566. Cold Spring Harbor Laboratory Press, Cold Spring Harbor, NY

26. Pace, C. N., Scholtz, J. M. (1997) Measuring the conformational stability of a protein, in (Creighton, T. E., ed.), Protein Structure: A Practical Approach. pp. 299–321. Oxford University Press, London.

27. Pace, C. N., Laurents, D. V. (1989) A new method for determining the heat capacity change for protein folding. Biochemistry 28, 2520–2525.

28. Nicholson, E. M., Scholtz, J. M. (1996) Conformational stability of the *Escherichia coli* HPr protein: test of the linear extrapolation method and a thermodynamic characterization of cold denaturation. Biochemistry 35, 1 369–11378.

29. Hagel, P., Gerding, J., Fieggen, W., et al. (1971) Cyanate formation in solutions of urea. I. Calculation of cyanate concentrations at different temperature and pH. Biochim. Biophys Acta 243, 366–373.

30. Stark, G. R. (1965) Reactions of cyanate with functional groups of proteins. 3. Reactions with amino and carboxyl groups. Biochemistry 4, 1030–1036.

31. Pace, C. N., Shirley, B. A., Thomson, J. A. (1989) Measuring the conformational stability of a protein, in (Creighton, T. E., ed.), Protein Structure: A Practical Approach, pp.311–329. IRL Press, Oxford.

32. Tanford, C. (1970) Protein denaturation. C. Theoretical models for the mechanism of denaturation. Adv Protein Chem 24, 1–95.

33. Pace, C. N. (1975) The stability of globular proteins. Crit Rev Biochem Mol 3, 1–43.

34. Greene, R. F. J., Pace, C. N. (1974) Urea and guanidine hydrochloride denaturation of ribonuclease, lysozyme, alpha-chymotrypsin, and beta-lactoglobulin. J Biol Chem 249, 5388–5393.

35. Kawahara, K., Tanford, C. (1966) Viscosity and density of aqueous solutions of urea and guanidine hydrochloride. J Biol Chem 241, 3228–3232.

36. Warren, J. R., Gordon, J. A. (1966) On the refractive indices of aqueous solutions of urea. J Phys Chem 70, 297–300.

Chapter 3

Defining the Stability of Multimeric Proteins

John W. Shriver and Stephen P. Edmondson

Abstract

The practical application of scanning calorimetry and spectroscopic methods to measure the stability of multimeric proteins is described. Oligomeric proteins are stabilized by both the intrinsic folding energy of the subunits as well as interactions between the subunits. Oligomerization results in a concentration dependence for multimer stability, which increases logarithmically with increasing concentration. Since the increase in stability does not plateau at high protein concentrations, the effect of concentration must be described quantitatively. Straightforward mathematical methods are provided for deriving the appropriate models for multimer unfolding, and methods are presented for analyzing equilibrium unfolding data and stability using the models.[†]

Key words: Differential scanning calorimetry, calorimetric enthalpy, van't Hoff enthalpy, heat capacity, fluorescence.

1. Introduction

A quantitative characterization of protein stability is best accomplished by determining the thermodynamic state functions which describe folding and unfolding *(1)*. While this is true for all proteins, it is perhaps even more true for multimers, where the stability is dependent on concentration. State functions are obtained from a characterization of the unfolding reaction equilibrium, that is, conversion of the native, N, to unfolded protein, U *(2–7)*. For monomeric proteins this is a unimolecular reaction:

$$N \underset{}{\overset{K}{\rightleftharpoons}} U \qquad \text{Scheme I}$$

For a multimeric protein unfolding leads to an increase in the number of molecular species. Multimer unfolding can occur via a two-state reaction, or it may involve multiple steps. In the simplest case, unfolding is tightly coupled to dissociation:

$$N_n \underset{}{\overset{K}{\rightleftharpoons}} nU \qquad \text{Scheme II}$$

where n is the number of subunits. Most importantly, the difference in the number of species on the left and right sides of the **Scheme II** leads to a concentration dependence of the stability. Le Chatelier's Principle indicates that increased concentration drives the reaction toward fewer species, that is, stabilization in this case. The midpoint temperature for unfolding, T_m, increases with protein concentration without reaching a plateau (*see* **Note 1**).

A complete description of multimeric protein stability requires a characterization of the effect of concentration on stability. Of particular importance is the Gibbs free energy change, ΔG°, which is an alternative expression of the equilibrium constant for folding *(8)*. A characterization of the temperature dependence of the equilibrium constant is the most convenient route to defining the thermodynamics of folding and association. Alternative approaches (e.g., chemical denaturation) are also possible, but the focus in this chapter is on using temperature to perturb the equilibrium.

We review here the basic methods for a quantitative characterization of the stability of multimeric proteins. We begin with a summary of the effect of temperature on equilibria and apply this to the unfolding of a monomer before expanding the treatment to multimeric systems. We stress that reliance on a single experimental technique is prone to errors due to potential neglect of processes that are invisible to the method selected. Further, the potential effects of linkages can only be separated from a reaction of interest by varying the concentrations of the species that may be involved in the linked reactions, including ligand concentration, pH, etc. (*see* **Chapter 6**). It is always wise to view an equilibrium from as many different perspectives as possible.

1.1. Temperature Dependence of Equilibria

The standard-state free energy, ΔG°, for a chemical reaction is related to the equilibrium constant, K, for the reaction by

$$\Delta G^\circ = -RT \ln K, \qquad (3.1)$$

where T is the temperature in kelvin, and R is the gas constant (1.99 cal/deg/mol) *(8)*. Experimentally, the standard-state free energy change is derived from an equilibrium constant. Accurate determination of thermodynamic changes for a chemical reaction (i.e., folding or binding) can only be obtained for reversible reactions under equilibrium conditions. Rearrangement yields K as a function of the free energy:

$$K = e^{\frac{-\Delta G^\circ}{RT}}. \tag{3.2}$$

The temperature dependence of the equilibrium constant (and therefore, ΔG°) is defined by the enthalpy change for a process by the van't Hoff equation *(9)*:

$$\left(\frac{\partial R \ln K}{\partial (1/T)}\right) = -\Delta H_{vh}, \tag{3.3}$$

where the subscript indicates that the enthalpy obtained from the temperature dependence of K should be distinguished from that obtained by calorimetry, that is, ΔH_{cal} (see **Section 2.1**). The enthalpy change is also temperature dependent as determined by the heat capacity change for the process at constant pressure:

$$\Delta C_p = \left(\frac{\partial \Delta H}{\partial T}\right)_p. \tag{3.4}$$

Integration of **Eq. (3.4)** provides a useful expression for the temperature dependence of the enthalpy:

$$\Delta H(T) = \Delta H(T_m) + \Delta C_p(T - T_m), \tag{3.5}$$

where the reference temperature is chosen to be T_m, the temperature at which the reaction is half-completed, and $\Delta H(T_m)$ is the enthalpy change at the T_m (*see* **Note 2**). The temperature dependence of the entropy change is *(8)*

$$\Delta S(T) = \Delta S(T_m) + \Delta C_p \ln(T/T_m). \tag{3.6}$$

Incorporating the temperature dependence of the enthalpy and entropy into the definition of free energy, $\Delta G(T) = \Delta H(T) - T\Delta S(T)$, provides a commonly used expression for the temperature dependence of the standard-state free energy of unfolding:

$$\Delta G^\circ(T) = \Delta H(T_m)\left(\frac{T_m - T}{T_m}\right) - (T_m - T)\Delta C_p + T\Delta C_p \ln\left(\frac{T_m}{T}\right). \tag{3.7}$$

Equation (3.7) demonstrates that a knowledge of the temperature dependence of ΔG° requires three parameters: T_m, $\Delta H(T_m)$, and ΔC_p. The curve defined by **Eq. (3.7)** when applied to protein folding has been referred to as the "protein stability curve" *(10)*. An example is shown in **Fig. 3.1a** (*see* **Note 3**).

The immediate goal of much of protein calorimetry is to define the protein stability curve by experimentally measuring
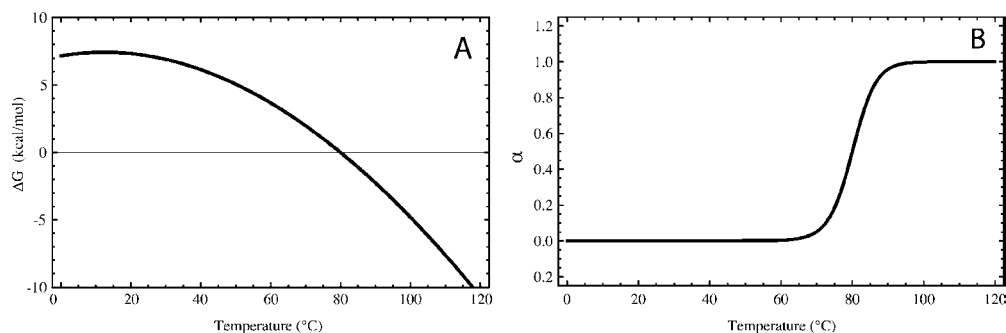
Fig. 3.1. (**A**) Simulation of a protein stability curve as defined by **Eq. (3.7)** with $\Delta H = 75$ kcal/mol, $\Delta C_p = 1000$ cal/deg/mol, and $T_m = 80°$C. (**B**) The progress curve for protein monomer unfolding showing the fractional population of the unfolded state, α_U, as a function of temperature as defined by **Eq. (3.12)** with the parameters used in **A**.

T_m, $\Delta H(T_m)$, and ΔC_p for protein unfolding *(6)*. Because ΔC_p is positive for protein unfolding, the curve is concave downwards and $\Delta G°$ is zero at two temperatures (assuming more than marginal stability). These are the heat-denaturation (T_m) and cold-denaturation midpoint temperatures *(11)*. ΔH controls the steepness of the curve at any temperature, and ΔC_p determines the degree of curvature. Defining the protein stability curve facilitates a comparison of the stabilities of different proteins at any temperature, which is more meaningful than simply measuring a T_m.

1.2. Fraction Unfolded

It is often useful to know the fraction of protein molecules unfolded under a given set of conditions, for example, at a specific temperature (*see* **Note 4**). The progress of an unfolding reaction (symbolized by α_U) is given by the fraction of the total protein converted to U:

$$\alpha_U = \frac{[U]}{[P]_{total}}. \qquad (3.8)$$

The fraction of the protein in other forms can be expressed similarly; for example, the fraction of the protein in the native form is

$$\alpha_N = \frac{[N]}{[P]_{total}}. \qquad (3.9)$$

1.3. Molecular Partition Function

The molecular partition function is a simple mathematical tool for obtaining expressions describing equilibria of any level of complexity, especially those involving multiple reactions and linkages. It is no more difficult to apply to a complex multimer unfolding reaction scheme than to a simple two-state monomer unfolding reaction. The molecular partition function is the sum of the concentrations of each species divided by the concentration of an

arbitrary reference species *(9, 12)*. For example, for the two-state unfolding of a monomer $N \Leftrightarrow U$, the partition function Q is

$$Q = \frac{[N] + [U]}{[N]} = 1 + \frac{[U]}{[N]} = 1 + K, \qquad (3.10)$$

where the reference state is chosen to be the native state. One of the advantages of Q derives from the fact that the fractional population of any state is given by the term in the partition function corresponding to that state (e.g., 1 for the N state) divided by Q. The resulting expressions for fractional occupations of each state are functions of the equilibrium constants in the entire reaction scheme. Since the temperature dependence of each K can be described using **Eqs. (3.2)** and **(3.7)**, the temperature dependence of the progress of the unfolding reactions can be obtained. The following examples should clarify these points, starting with a monomer, and then proceeding to dimer unfolding via three different mechanisms.

2. Specific Examples

2.1. Monomer Unfolding

The unfolding of a monomer (**Scheme I**) is defined by the equilibrium constant $K = [U]/[N]$. The molecular partition function Q for a monomer unfolding (with N as the reference state) is given by **Eq. (3.10)**, or simply

$$Q = 1 + K. \qquad (3.11)$$

The fractional populations of N and U, i.e. α_N and α_U, respectively, are obtained by dividing the terms in the partition function corresponding to N and U by Q:

$$
\begin{aligned}
\alpha_N &= \frac{1}{Q} = \frac{1}{1+K} \\
\alpha_U &= \frac{K}{Q} = \frac{K}{1+K}
\end{aligned}. \qquad (3.12)
$$

Equation (3.12) are the central equations which describe the temperature dependence of the fraction of folded and unfolded protein, that is, reaction progress. These are the quantities which are reflected by a spectroscopic signal that depends on the amount of folded or unfolded protein. They relate the experimentally observable signal (S_{obs}) to the thermodynamic parameters which control folding and interactions:

$$S_{obs} = \alpha_N S_N + \alpha_U S_U, \qquad (3.13)$$

where S_N and S_U are the limiting spectroscopic signal intensities for pure N and U. Because of the dependence of α_U on K, the

reaction progress is a function of T_m, $\Delta H(T_m)$, and ΔC_p. A plot of α_U as a function of temperature with typical values for T_m, $\Delta H(T_m)$, and ΔC_p shows a sigmoidal dependence of folding on temperature, with values between 0 and 1, and centered at T_m (**Fig. 3.1b**). This is the typical shape of a thermal "melting" curve often obtained with thermotropic (temperature-driven) transitions. T_m is the temperature at which the reaction is half completed, and for a monomer α_U is 0.5, and $K = 1$ at the T_m. The width of the transition is determined by the magnitude of ΔH (as defined by **Eq. (3.3)**) with larger values resulting in a narrower transition (*see* **Note 5**). A transition with a ΔH of 15 kcal/mol occurs over a temperature range of about 100°C, and therefore this represents the smallest ΔH which can be reasonably measured by these methods.

While a spectroscopic signal that reflects unfolding is directly related to α_U, a differential scanning calorimetry (DSC) signal indicates the heat necessary to drive the transition. The heat content or enthalpy of a system is a property of state and is given by the sum of the enthalpies of all the species present. The contribution of each state to the excess enthalpy relative to N is given by the fractional occupation of that state multiplied by the molar enthalpy difference relative to N. The excess enthalpy of the system (relative to N) as a function of temperature is (*see* **Fig. 3.2a**)

$$H_{excess} = \alpha_U \Delta H. \tag{3.14}$$

The heat capacity of the sample (relative to N) is given by the derivative of H_{excess} with respect to temperature:

$$C_P = \frac{dH_{excess}}{dT} = \frac{d\alpha_U}{dT}\Delta H + \alpha_U \frac{d\Delta H}{dT}. \tag{3.15}$$
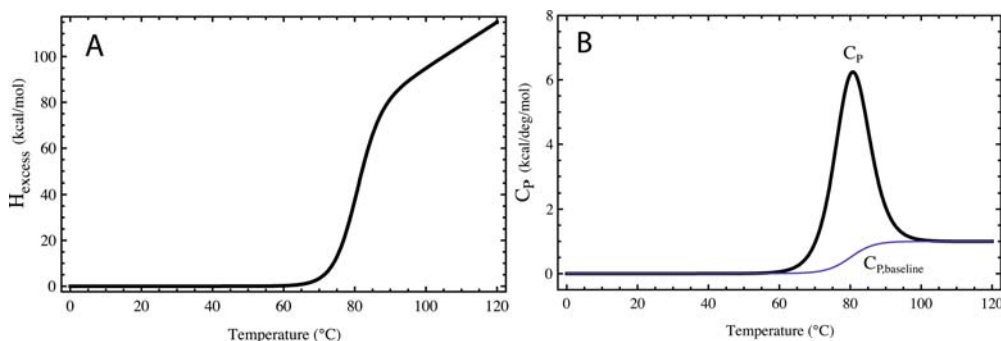
Fig. 3.2. (**A**) Simulation of the temperature dependence of the excess enthalpy as a function of temperature for the unfolding of a protein monomer as described by **Eq. (3.14)** with the thermodynamic parameters used for **Fig. 3.1**. (**B**) Simulation of a DSC endotherm for the unfolding of a monomer with parameters as in **Fig. 3.1**. The bold curve shows the observed temperature dependence of the heat capacity, C_p, for the system (*bold*), which includes the excess heat capacity plus the baseline C_p (lower curve).

The first term on the right is often referred to as an anomalous, or excess, heat capacity required to drive the unfolding reaction. It is the origin of the DSC "endotherm" caused by a thermotropic reaction such as protein unfolding (*see* **Fig. 3.2b**). We refer to it as $C_{p,\text{excess}}$, and note that at any temperature it is directly proportional to the fraction of the reaction completed. It has been referred to as the "between states" heat capacity *(13)* and arises from a change in the relative populations of N and U. Thus, unfolding of half of the protein will require that half of the total heat of unfolding be absorbed. Note that integration of the excess heat capacity from an arbitrary initial temperature T_i below the transition up to temperature T provides a measure of the progress curve as a function of temperature T:

$$\frac{\int_{T_i}^{T} C_{\text{p,excess}}\mathrm{d}T}{\Delta H} = \alpha_{\text{U}}(T), \qquad (3.16)$$

and integration over the entire endotherm provides the area under the curve, which is referred to as the calorimetric enthalpy (ΔH_{cal}) of the reaction to indicate that it is obtained directly from a calorimetric measurement:

$$\int C_{P,\text{excess}}\mathrm{d}T = \Delta H_{\text{cal}}. \qquad (3.17)$$

The calorimetric enthalpy may differ from the enthalpy which defines the temperature dependence of the equilibrium (i.e., $\Delta H(T_{\text{m}})$ in **Eq. (3.7)**), which is referred to as the van't Hoff enthalpy, ΔH_{vh}. The van't Hoff enthalpy defines the width of the transition (or DSC endotherm), while the calorimetric enthalpy defines the intensity of the endotherm. They are not necessarily the same (see **Section 3.3**). The calorimetric enthalpy is the enthalpy per molar unit defined by the investigator (e.g., per monomer), while the van't Hoff enthalpy is the enthalpy per mole of cooperative unit (which might be a multimer) and is defined by the system.

The second term on the right of **Eq. (3.15)** describes an increased weighting of the derivative of the change in enthalpy, which is the difference in heat capacity of the two states. This term represents a sigmoidal increase (defined by α_{U}) in the baseline, with the increase equal to the ΔC_{p} of the reaction. The contribution from $C_{\text{p,baseline}}$ is shown in **Fig. 3.2b**.

2.2. Dimer Unfolding Directly to Monomeric Random Coils

In the simplest case, a dimer can unfold to two random-coil monomeric chains:

$$N_2 \stackrel{K}{\rightleftharpoons} 2U \qquad \text{Scheme III}$$

The total concentration of protein, $[P]_{total}$, is expressed in terms of monomer chains (*see* **Note 6**) such that

$$[P]_{total} = [U] + 2[N], \qquad (3.18)$$

where $[U]$ and $[N]$ are the concentrations of unfolded monomer and folded dimer, respectively. The equilibrium constant for unfolding is given by

$$K = \frac{[U]^2}{[N]} = \frac{[U]^2}{0.5([P]_{total} - [U])} = \frac{2[U]^2}{[P]_{total} - [U]}. \qquad (3.19)$$

Solving for $[U]$, we obtain an expression for the concentration of unfolded monomer in terms of K and the total protein concentration *(14)*:

$$[U] = \frac{K}{4}\left(\sqrt{1 + \frac{8[P]_{total}}{K}} - 1\right). \qquad (3.20)$$

The molecular partition function is given by

$$Q = \frac{2[N_2] + [U]}{2[N_2]} = 1 + \frac{K}{2[U]} \qquad (3.21)$$

and the fractional populations of dimer and unfolded monomer are

$$\begin{aligned} \alpha_{N_2} &= \frac{1}{Q} \\ \alpha_U &= \frac{K/2[U]}{Q} \end{aligned} \qquad (3.22)$$

Substitution of **Eqs. (3.20)** and (**3.21**) into (**3.22**) provides expressions for the progress of the unfolding reaction for a dimer in terms of the total protein concentration and K. K is defined by the free energy of unfolding the dimer (**Eq. (3.2)**), which is given by

$$\Delta G^\circ(T) = \Delta H^\circ(T^\circ)\left(\frac{T^\circ - T}{T^\circ}\right) - (T^\circ - T)\Delta C_p + T\Delta C_p \ln\left(\frac{T^\circ}{T}\right), (3.23)$$

where T° is the temperature at which the free energy of unfolding of a 1.0 $\underline{M}$ protein solution is zero (the standard state is defined as 1 M total protein), $\Delta H(T^\circ)$ is the enthalpy of unfolding at T°, and ΔC_p is the change in heat capacity. T_m is the same as T° only for 1 M protein (*see* **Note 7**). The standard state is typically not accessible experimentally; it is a reference state.

The temperature dependence of α_U for a dimer is sigmoidal, but differs significantly from that for a monomer (*see* **Fig. 3.3a**). The transition for a dimer is asymmetric, with a greater increase in magnitude at temperatures below the T_m compared to that observed for a monomer. A spectroscopic signal sensitive to unfolding is defined by the fractional occupations of the N and U states (**Eq. (3.13)**), and therefore a similar asymmetry is observed.
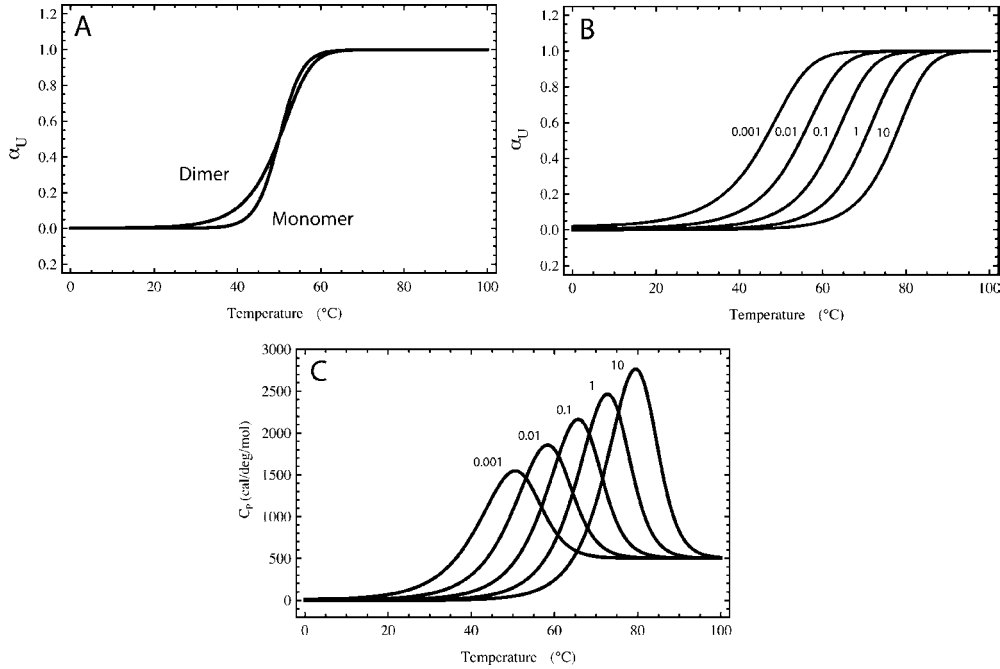
Fig. 3.3. (**A**) Comparison of the temperature dependence of monomer (**Scheme I**) and dimer (**Scheme III**) unfolding with $\Delta H = 75$ kcal/mol, $\Delta C_p = 1000$ cal/deg/mol for both. $T_m = 50°C$ for the monomer and $T° = 50°C$ for the dimer (total protein concentration = 1 M monomer chains). (**B**) The concentration dependence of the unfolding of dimer showing α_U as a function of temperature with $\Delta H = 75$ kcal/mol, $\Delta C_p = 1000$ cal/deg/mol, and $T° = 70°C$. From left to right: 0.001 M, 0.01 M, 0.1 M, 1 M, 10 M total monomer chains in the form of N_2 and U. The concentration range exceeds that accessible experimentally; it is chosen to demonstrate the lack of an upper limit at high concentration. (**C**) Temperature dependence of the DSC for unfolding a dimer according to **Scheme III** with the parameters and concentrations as in **B**.

Most importantly, the midpoint temperature of dimer unfolding depends significantly on the concentration of protein, with increasing stability promoted by increasing concentration. As seen in **Fig. 3.3b**, the stability does not reach a plateau with increasing protein concentration. Since $K = \alpha_U^2/(1 - \alpha_U)$, and $\alpha_U = [U]/(2[N] + [U])$, we can write *(14)*

$$K = \frac{2\alpha_U^2[P]_{\text{total}}}{1 - \alpha_U}.$$
(3.24)

By definition, the T_m is the temperature where $\alpha(T)$ is equal to 0.5, and therefore at this temperature $K = [P]_{\text{total}}$. Therefore, the standard-state free energy of unfolding at the T_m is

$$\Delta G° = -RT_m \ln[P]_{\text{total}} \quad \text{(at the} T_m\text{)}.$$
(3.25)

This is only zero when $[P]_{\text{total}} = 1$ M. Since $\Delta G° = -RT \ln K$, **Eq. (3.24)** demonstrates that the free energy of unfolding depends logarithmically on concentration, and therefore so does T_m. Both increase without limit (*see* **Note 8**) with increasing protein concentration (*see* **Fig. 3.4**). For a dimer it can be shown *(15)* that
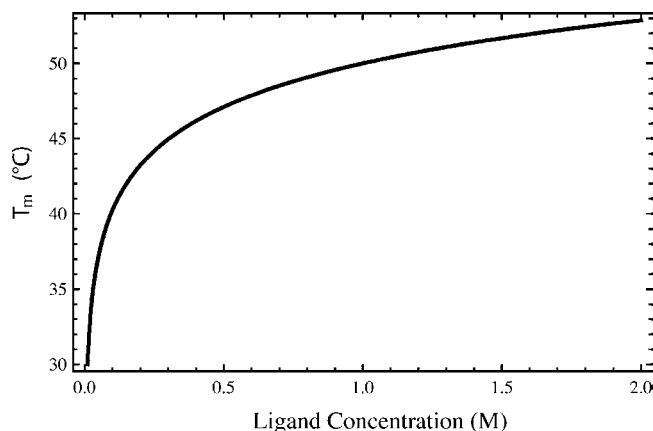
Fig. 3.4. Concentration dependence of the T_m for unfolding a dimer according to **Scheme III** with $\Delta H = 75$ kcal/mol, $\Delta C_p = 1000$ cal/deg/mol, and $T° = 50°$C.

$$\frac{1}{T_m} = \frac{R}{\Delta H_{vh}} \ln[P]_{total} + \frac{\Delta S}{\Delta H_{vh}}. \quad (3.26)$$

Because of the concentration dependence of stability and T_m, thermodynamic parameters for different oligomers (or different site-specific mutations) are typically compared at 1 M protein, the extrapolated reference state.

The excess enthalpy for the system is given by **Eq. (3.14)** (with the fractional population of U defined by **Eqs. (3.22)**). Since the concentration of protein is expressed in terms of total monomer chains, and the ΔH in **Eq. (3.14)** is defined in terms of the cooperative unit (i.e., it is ΔH_{vh}), it needs to be scaled by the size of the cooperative unit. This is accomplished by multiplying by $\Delta H_{cal}/\Delta H_{vh}$, symbolized by β, so that

$$H_{excess} = \alpha_U \Delta H \beta. \quad (3.27)$$

The derivative of H_{excess} with respect to temperature provides the excess heat capacity observed by DSC for proteins unfolding according to **Scheme II**. The endotherm is asymmetric due to the asymmetry in α_U (**Fig. 3.3c**), with a significant dependence on concentration due to shifting of the T_m coupled with the temperature dependence of ΔH.

2.3. Dimer Dissociation Linked to Unfolding

Instead of unfolding directly to two unfolded random coils, some dimers dissociate to give two folded monomers which then unfold independently to two random-coil chains:

$$N_2 \xrightleftharpoons{K_1} 2M \xrightleftharpoons{K_2} 2U$$

Scheme IV

This is best viewed as

$$
\begin{array}{c}
\text{N}_2 \overset{K_3}{\underset{}{\searrow}} \\
K_1 \updownarrow \qquad \ggtr 2\text{U} \\
2\text{M} \overset{}{\underset{K_2}{\nearrow}}
\end{array}
\qquad \text{Scheme V}
$$
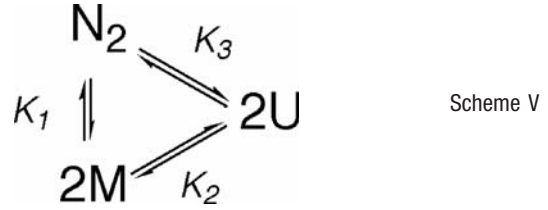
to stress the possible direct conversion of dimer to two un-folded chains (thermodynamics does not address path but only the relative populations of states). The equilibrium constants are

$$
K_1 = \frac{[\text{M}]^2}{[\text{N}_2]},
$$
$$
K_2 = \frac{[\text{U}]^2}{[\text{M}]^2}, \tag{3.28}
$$
$$
K_1 K_2 = K_3 = \frac{[\text{U}]^2}{[\text{N}_2]}.
$$

The partition function for the reaction is

$$
Q = \frac{2[\text{N}_2] + [\text{M}] + [\text{U}]}{2[\text{N}_2]} = 1 + \frac{K_1 K_2}{2[\text{U}]\sqrt{K_2}} + \frac{K_1 K_2}{2[\text{U}]} \tag{3.29}
$$

and the fractional populations of the three species are given by

$$
\alpha_{\text{N}_2} = \frac{1}{Q},
$$
$$
\alpha_{\text{M}} = \frac{K_1 K_2}{2[\text{U}]\sqrt{K_2}\,Q}, \tag{3.30}
$$
$$
\alpha_{\text{U}} = \frac{K_1 K_2}{2[\text{U}]Q}.
$$

The total concentration of protein in moles of monomeric chains is given by

$$
[\text{P}]_{\text{total}} = 2[\text{N}_2] + [\text{M}] + [\text{U}]. \tag{3.31}
$$

Rearranging **Eq. (3.31)** to obtain an expression for $[\text{N}_2]$, and substitution into the equation for $K_1 K_2$, we obtain an expression for the concentration of U in terms of K_1, K_2, and the total protein concentration:

$$
[\text{U}] = \frac{1}{4}\left(-K_1(\sqrt{K_2} + K_2) + \sqrt{K_1 K_2(K_1(1+\sqrt{K_2})^2 + 8[\text{P}]_{\text{total}})}\right). \tag{3.32}
$$

The temperature dependence of K_1 is defined by **Eq. (3.23)**, while that for K_2 is defined by **Eq. (3.7)**.
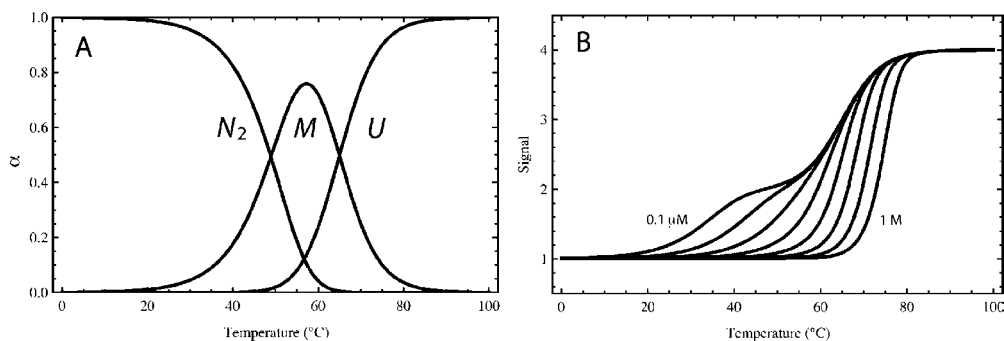
Fig. 3.5. (**A**) Temperature dependence of the factional occupations of N_2, M, and U states in **Scheme V** for unfolding a dimer with dissociation to folded monomer occurring along with unfolding to random-coil monomer chains. Reaction 1: $\Delta H = 50$ kcal/mol, $\Delta C_p = 400$ cal/deg/mol, and the dissociation constant for the dimer at 25°C was 10^{-8} M; Reaction 2: $\Delta H = 100$ kcal/mol, $\Delta C_p = 500$ cal/deg/mol, and $T_m = 65$°C for unfolding of the 10 μM protein (total monomer concentration). (**B**) Simulated temperature dependence of a spectroscopic signal sensitive to dimer dissociation and unfolding with the same parameters as in **A**, and the total protein concentration was (*left to right*): 0.1 μM, 1 μM, 10 μM, 0.1 mM, 1 mM, 10 mM, 0.1 M, and 1 M. The wide range exceeds that experimentally accessible, but demonstrates the absence of an upper limit for the stability. The signal intensities for N_2, M, and U were 1, 2, and 4, respectively.

The progress of the reactions in **Scheme V** is determined by the magnitudes of both α_M and α_U as defined in **Eq. (3.30)**(*see* **Fig. 3.5A**). The temperature dependence of spectroscopic signals depends on the signals associated with each of the species and the fractional occupations of the species (see **Section 3.1**).

$$S_{obs} = \alpha_N S_N + \alpha_M S_M + \alpha_U S_U. \qquad (3.33)$$

Simulations of a spectroscopic signal dependent on the unfolding of dimer which can dissociate to folded monomers are shown in **Fig. 3.5b**.

The temperature dependence of the excess enthalpy of the system relative to N_2 is given by

$$H_{excess} = \alpha_M \Delta H_1 \beta + \alpha_U (\Delta H_1 \beta + \Delta H_2) = \alpha_M \Delta H_1 + \alpha_U \Delta H_3 \quad (3.34)$$

(*see* **Fig. 3.6A**) and the temperature dependence of the heat capacity is given by the derivative of **Eq. (3.34)**with respect to temperature (*see* **Eq. (3.15)**). Simulations of DSC curves for a dimer unfolding according to **Scheme V** are shown in **Fig. 3.6B**.

2.4. Dimer Rearrangement Linked to Unfolding

A dimer may undergo a structural rearrangement which is linked to unfolding to two random coils:

$$N_2 \underset{}{\overset{K_1}{\rightleftharpoons}} I_2 \underset{}{\overset{K_2}{\rightleftharpoons}} 2U \qquad \text{Scheme VI}$$

Fig. 3.6. (**A**) Temperature dependence of the excess enthalpy of a dimer unfolding according to **Scheme V** with thermodynamic parameters as in Fig. **3.5B** and 0.1 mM total protein concentration (as monomer chains). (**B**) Concentration dependence of the DSC endotherm for unfolding a dimer according to **Scheme V** with parameters as in **Fig. 3.5B**. Note that with increasing concentration, the T_m for the dimer exceeds that for unfolding the dissociated monomers because the folded monomers do not occur.

which should be viewed as

Scheme VII
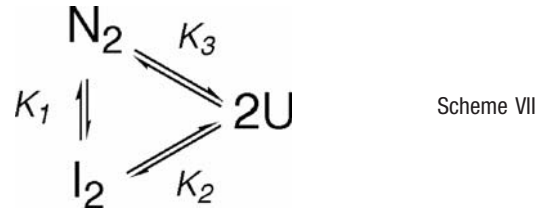
The equilibrium constants are defined as

$$K_1 = \frac{[I_2]}{[N_2]},$$

$$K_2 = \frac{[U]^2}{[I_2]}, \qquad (3.35)$$

$$K_1 K_2 = K_3 = \frac{[U]^2}{[N_2]}.$$

The partition function for the system is

$$Q = 1 + K_1 + \frac{K_1 K_2}{2[U]} \qquad (3.36)$$

and the fractional populations of the three species are given by

$$\alpha_{N_2} = \frac{1}{Q},$$

$$\alpha_{I_2} = \frac{K_1}{Q}, \qquad (3.37)$$

$$\alpha_U = \frac{K_1 K_2}{2[U]Q}.$$

The total protein concentration in monomeric chains is given by

$$[P_{total}] = 2[N_2] + 2[I_2] + [U] \qquad (3.38)$$

and the concentration of U in terms of K_1, K_2, and the total protein concentration is

$$[U] = \frac{-K_1 K_2 + \sqrt{K_1 K_2 (8[P_{total}] + K_1(K_2 + 8[P_{total}]))}}{4(1 + K_1)}. \quad (3.39)$$

The temperature dependence of a spectroscopic signal which is sensitive to dissociation and unfolding will be a function of the magnitudes of the signals associated with each of the species and the fractional occupations of each state (**Fig. 3.7**) (*see* **Section 3.1**):

$$S_{obs} = \alpha_{N_2} S_{N_2} + \alpha_{I_2} S_{I_2} + \alpha_U S_U. \quad (3.40)$$

Similarly, the temperature dependence of the excess heat of the system is given by

$$\begin{aligned} H_{excess} &= \alpha_{I_2} \Delta H_1 \beta + \alpha_U (\Delta H_1 \beta + \Delta H_2 \beta) \\ &= \alpha_{I_2} \Delta H_1 \beta + \alpha_U \Delta H_3 \beta \end{aligned} \quad (3.41)$$

and the DSC curve is obtained by taking the first derivative of **Eq. (3.41)** with respect to temperature (*see* **Eq. (3.15)**). Simulations showing the concentration dependence of H and C_p are shown in **Fig. 3.8**.

2.5. Higher-Order Multimer Unfolding

The expressions provided here for the homodimer can be extended to multimers containing more than two subunits. An expression for the concentration of U in terms of K and the total protein concentration, similar to that in **Eqs. (3.32)** and **(3.39)**, is required. This is then substituted into expressions for α (similar to
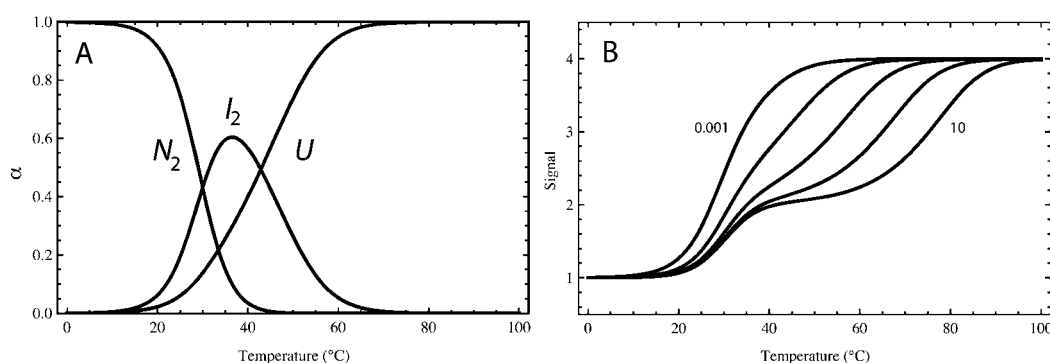
Fig. 3.7. (**A**) Temperature dependence of the factional occupations of N_2, I_2, and U states in **Scheme VII** for unfolding a dimer with structural rearrangement occurring along with unfolding to random-coil monomer chains. Reaction 1: $\Delta H = 50$ kcal/mol, $\Delta C_p = 500$ cal/deg/mol, and $T_m = 30^\circ$C for dimer rearrangement; Reaction 2: $\Delta H = 50$ kcal/mol, $\Delta C_p = 500$ cal/deg/mol, and $T^\circ = 65^\circ$C for unfolding of the dimer. Total protein concentration $= 10$ mM (monomer chains). (**B**) Simulated temperature dependence of a spectroscopic signal sensitive to dimer dissociation and unfolding with parameters as in A. Total protein concentration (*left to right*): 0.001 M, 0.01 M, 0.1 M, 1 M, and 10 M (demonstrating the lack of an upper limit). Signal intensities for N_2, M, and U were 1, 2, and 4, respectively.
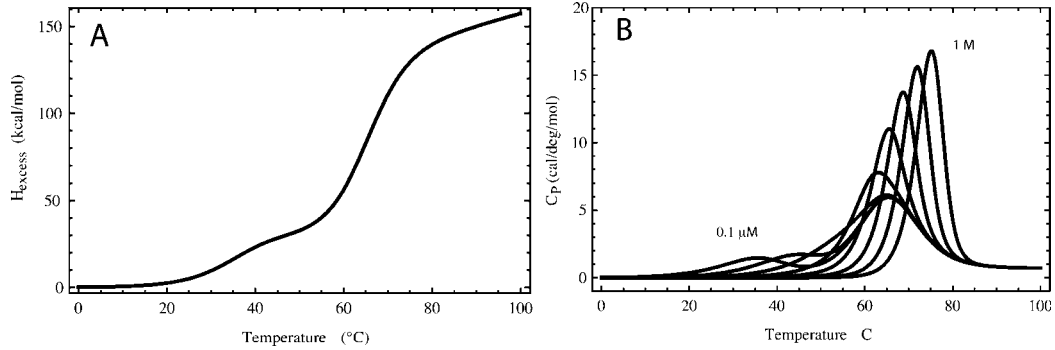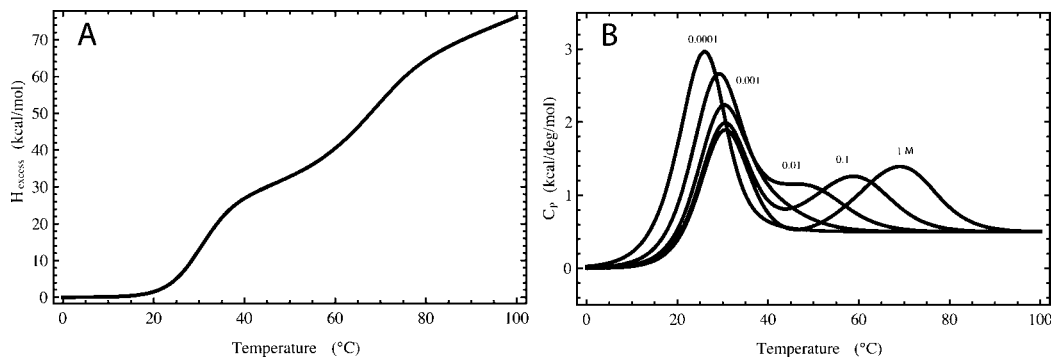
Fig. 3.8. (**A**) Temperature dependence of the excess enthalpy of a dimer unfolding according to **Scheme VII** with thermodynamic parameters as in **Fig. 3.7A** and 1 M total protein concentration (monomer chains). (**B**) Concentration dependence of DSC for unfolding a dimer according to **Scheme VII** with parameters as in **Fig. 3.7A** and the total protein concentration (*left to right*): 0.0001 M, 0.001 M, 0.01 M, 0.1 M, and 1 M (demonstrating the lack of an upper limit).

Eqs. (3.30) and **(3.37)**) for each species to obtain the temperature and concentration dependence of the reaction progress.

The equation for the equilibrium constant in terms of the progress (similar to **Eq. (3.24)**) is given by *(15)*

$$K = \frac{n\alpha_U^n [P]_{total}^{n-1}}{1 - \alpha_U}$$ (3.42)

and the dependence of T_m on protein concentration is given by

$$\frac{1}{T_m} = \frac{(n-1)R}{\Delta H_{vh}} \ln[P]_{total} + \frac{\Delta S - (n-1)R \ln 2 + r\ln(n)}{\Delta H_{vh}}.$$ (3.43)

3. Experimental Observables Reflecting Temperature-Dependent Folding and Association

3.1. Spectroscopic Signals Dependent on Folding and Association

A spectroscopic signal, S_{obs}, reflecting an equilibrium that is temperature dependent is a weighted sum of the signals from the species involved, for example, native, S_N, and unfolded species, S_U *(4, 16)*. The weights are provided by the factional occupations (α) of the species or states (similar to **Eqs. (3.13), (3.33)**, and **(3.40)**):

$$S_{obs} = \sum_i \alpha_i(T) S_i.$$ (3.44)

3.2. Heat Capacity Dependent on Folding and Association

DSC provides the temperature dependence of the heat capacity of all species present. The DSC data contains a baseline contribution, $C_{P,\text{baseline}}$, which is the second term on the right side of **Eq. (3.14)**. It is a weighted sum of the intrinsic heat capacities of all the species, for example, native, C_P^N, and unfolded, C_P^U. For a two-state reaction we obtain *(7)*

$$C_{P,\text{baseline}} = (1 - \alpha_U(T))\ C_P^N + \alpha_U(T)\ C_P^U. \qquad (3.45)$$

The baseline represents a progress curve from folded to unfolded species (**Fig. 3.1b**). For three or more states, additional terms are added to account for the contribution of each state weighted by the fractional populations of each state (similar to **Eq. (3.44)**). The baseline heat capacity is not directly observable since the observed heat capacity includes an additional contribution from the heat required to drive the reaction, that is, $C_{P,\text{excess}}$.

$$C_p = C_{p,\text{excess}} + C_{p,\text{baseline}} \qquad (3.46)$$

The excess heat capacity is an anomalous heat capacity that results from the absorption of heat needed to drive the reaction. It is the unique information obtained from DSC which distinguishes it from spectroscopic methods. The excess heat absorbed is given by the incremental change in the progress of the reaction due to a change in temperature times the molar enthalpy change for the reaction.

$$C_{p,\text{excess}} = \frac{\partial \alpha_U}{\partial T} \Delta H_{\text{cal}} \qquad (3.47)$$

This defines a peak (endotherm) with an area equal to ΔH_{cal}, the enthalpy determined by calorimetry.

3.3. van't Hoff and Calorimetric Enthalpies

The van't Hoff enthalpy defines the temperature dependence of a reaction (*see* **Eq. (3.7)**), and it is best obtained from a fitting of data reflecting the progress of the reaction as in **Eq. (3.44)** (*see* **Note 10**) or the definite integral of a DSC endotherm (*see* **Eq. (3.16)**). The van't Hoff enthalpy is obtained from an analysis of the temperature dependence of the progress of a reaction. The calorimetric enthalpy is obtained from a direct measurement of the excess heat associated with the reaction, that is, the area under a DSC endotherm given by the integral of **Eq. (3.47)**.

3.4. Cooperative Unit

Because the calorimetric enthalpy is obtained by integration of the heat capacity curve (in calories/deg/mole as a function of temperature), the molar unit for the calorimetric enthalpy is defined by the experimenter. For a multimer, the calorimetric enthalpy can be defined either as the heat change per mole of monomer, or per mole of multimer, with the stoichiometry specified by the experimenter. In contrast, the molar unit for the van't Hoff enthalpy is not arbitrary. It is by default the size of the cooperative

unit; that is, the van't Hoff enthalpy is the heat change per cooperative unit. If the cooperative unit is the multimer, the van't Hoff enthalpy will be n times the calorimetric enthalpy per mole of monomer (where n is the number of identical subunits in the multimer). The relative values of the van't Hoff and calorimetric enthalpies depend on the stoichiometry of the reaction. For a monomeric protein, the calorimetric and van't Hoff enthalpies should be equal, and $\Delta H_{cal} / \Delta H_{vh} = 1.0$ (*see* **Note 11**). For a multimer which unfolds via a two-state reaction without significantly populated intermediates, this ratio should be equal to $1/n$, where n is the number of subunits in the multimer.

4. Data Analysis

The raw data for a protein unfolding transition followed by spectroscopy is the magnitude of the spectroscopic signal as a function of temperature. The raw data in DSC is the heat flow into the sample cell per unit time (e.g., μjoules/sec or μwatts). Division of the DSC signal by the scan rate (e.g., 1 deg/min) provides the heat flow per degree change and represents the temperature dependence of the heat capacity of the solution in the sample cell.

The absolute molar heat capacity of the protein can be calculated *(3, 17)*. Routines for performing this calculation are incorporated into commercial DSC software. Division by the molecular weight provides the absolute partial specific heat capacity. Measurements of the absolute heat capacity are rarely required for the interpretation of data and will not be further discussed here.

Although commercial DSC software contains routines for extracting thermodynamic parameters from data, these are often limiting. A nonlinear least-squares fitting of the temperature dependence of calorimetric and spectroscopic signals can be obtained using a number of currently available data analysis software packages (e.g., Igor (Wavemetrics)), with mathematical models and expressions for the observables as described above.

4.1. Sloping Baselines

The spectroscopic signals for the native and unfolded protein, and also the heat capacities of the native and unfolded proteins, are generally dependent on temperature. Both the pre- and post-transition baselines can typically be described by straight lines with two parameters, for example, $A + B{*}T$. Therefore, for a two-state reaction we can write for the spectroscopic signals and excess heat capacity:

$$S_{obs} = (1 - \alpha_U(T)) \, (A + B \cdot T) + \alpha_U(T) \, (C + D \cdot T), \quad (3.48)$$

$$C_p^{\text{baseline}} = (1 - \alpha_N(T)) * (U + V \cdot T) + \alpha_N(T) * (X + \Upsilon \cdot T). \quad (3.49)$$

In **Eq. (3.49)**, if T is expressed relative to the midpoint temperature, T_m, then X is U plus the change in heat capacity (ΔC_p) at the T_m. Transitions involving three or more states can also include additional terms describing the baseline between transitions, although it is rare that sufficient data is available to define these contributions accurately and approximations are normally made to reduce the number of parameters (e.g., the parameters for the baseline of an intermediate are averages of the parameters for the pre- and post-transition baselines).

4.2. Initial Fitting: Monomer

Even when a protein is known to exist as a multimer, thermal unfolding data are usually initially fit by assuming a two-state, monomer unfolding reaction (**Scheme I**) to determine if more complicated models are justified by the data. For DSC data, it is assumed that $\Delta H_{cal}/\Delta H_{vh} = 1$, and ΔC_p is assumed to be non-zero. If the resulting fit is not satisfactory, the ΔC_p (i.e., $C_{p,\text{baseline}}$) is removed from the data as described below and the data is fit by allowing ΔH_{cal} and ΔH_{vh} to float independently.

4.2.1. Spectroscopic Data Assuming a Monomer

Thermal denaturation curves followed by CD or fluorescence can be fit by nonlinear regression using **Eq. (3.48),** along with **Eqs. (3.2), (3.7),** and **(3.12).** This is a seven-parameter fit with slope and y-intercepts for the pre- and post-transition baselines, along with T_m, $\Delta H(T_m)$, and ΔC_p for the equilibrium.

4.2.2. DSC Data with $\Delta H_{cal} = \Delta H_{vh}$ and Non-zero ΔC_p

DSC data can be fit to **Eq. (3.44)** (with three adjustable parameters (T_m, $\Delta H(T_m)$, and ΔC_p)), plus **Eq. (3.49)** (three additional parameters: U, V, and Υ, with $X = U + \Delta C_p$). For more stable proteins the post-transition baseline may not be well defined by the data. In such cases only U, V, $\Delta H(T_m)$, T_m can be fit (ΔC_p and Υ must be fixed to user-defined values). The data can be further simplified by removing the contribution of the pre-transition baseline (fit a well-defined linear section of the pre-transition baseline and subtract the derived straight line from the data).

4.2.3. DSC Data with $\Delta H_{cal} > \Delta H_{vh}$

If the DSC data cannot be fit satisfactorily with the assumption that $\Delta H_{cal} = \Delta H_{vh}$, then ΔH_{cal} and ΔH_{vh} can be fit independently. This might occur if there were simultaneous unfolding of multiple independent domains with similar midpoint temperatures, such that only one endotherm is observed and the observed ΔH_{cal} would be greater than ΔH_{vh}. A simple example might be the overlapping of two two-state transitions with identical ΔH_{cal}; and as a result, the area of the endotherm (i.e., the total observed ΔH_{cal}) would be twice that expected from the width of the transition. If

$$\beta = \frac{\Delta H_{\text{cal}}}{\Delta H_{\text{vh}}} \qquad (3.50)$$

then

$$C_{\text{p,excess}} = \beta \, \Delta H(T) \, \frac{\mathrm{d}\alpha(T)}{\mathrm{d}T}. \qquad (3.51)$$

The magnitudes of the ΔC_{p} for each transition cannot be defined by the data. It is not possible to use the complete expression for ΔG (**Eq. (3.7)**) in fitting the data. Therefore, the ΔC_{p}, or more specifically $C_{\text{p,baseline}}$, must be removed prior to nonlinear regression as described in the next section.

4.2.4. Progress Curves from DSC Data

The progress curve for an unfolding reaction can be obtained directly from DSC data by calculating the explicit integral of the heat capacity, that is, the extent of the area under the endotherm covered as a function of temperature. A progress function, $I(T)$, is obtained by taking the ratio of the integral of C_{p} from any arbitrary temperature, T_i, below the transition to temperature T, divided by the total integral of the transition. Integration is performed numerically so that

$$I(T) = \frac{\sum\limits_{t=T_i}^{T} C_{\text{p}}(T)}{\sum\limits_{t=T_i}^{T_i} C_{\text{p}}(T)}. \qquad (3.52)$$

The ratio is linear below and above the transition, and a sigmoidal transition from one linear section to the other occurs in the temperature range of the reaction. The result can be treated as if it were a spectroscopic signal representing the progress curve with sloping pre- and post-transition baselines, and an equilibrium constant as a function of T is given by

$$K = \frac{I(T) - (a_N + b_N * T)}{(a_U + b_U * T) - I(T)}. \qquad (3.53)$$

(A two-state reaction can be assumed for this purpose without introducing significant error.) $\alpha(T)$ is calculated using **Eq. (3.12).** $C_{\text{p,baseline}}$ is calculated at temperature T using $\alpha(T)$ and values for U, V, X, and Y obtained from fitting segments of the baseline before and after the transition in the DSC scan. In practice, $C_{\text{p,baseline}}$ occasionally contains a singularity, so $C_{\text{p}}^{\text{baseline}}$ can be smoothed by nonlinear regression. The fitted $C_{\text{p,baseline}}$ curve can be subtracted from the original data (i.e., C_{p}) to obtain $C_{\text{p,excess}}$ which is then fit to obtain ΔH_{cal}, ΔH_{vh}, and T_{m}.

4.2.5. Determination of ΔC_{p}

Determination of a reliable ΔC_{p} from DSC data can be difficult. Extrapolation from the difference in the DSC baselines at the T_{m} is normally unreliable due to contributions to the post-transition

baseline from processes other than unfolding (e.g., aggregation, chemical degradation). The most common method using DSC is to take advantage of the linkage of pH to stability, and vary the pH over a range in which the T_m varies (e.g. pH 2–4). Decreasing the T_m leads to a decrease in ΔH according to the Kirchhoff relation (**Eq. (3.4)**). A plot of the resulting ΔH vs. T_m (i.e., a Kirchhoff plot) is commonly linear and the slope provides an estimate of ΔC_p *(6)*. This approach may give erroneous results due to increased contributions from anion binding at lower pH *(18)*.

The most reliable method of determining ΔC_p relies on cold denaturation and may be accomplished with either spectroscopic or DSC data *(11, 19)*. When enhanced unfolding is observed at low temperature as well as at elevated temperature, the curvature of the protein stability curve is defined by a single thermal melt. Fitting the data over both cold- and heat-denaturation regions accurately specifies ΔC_p without making assumptions about the effect of anion binding at low pH.

4.3. Two-State Dimer Unfolding

Two observations typically indicate multimer unfolding in thermal unfolding data: dependence of T_m on concentration, and asymmetry in the progress curve both as a function of temperature and the DSC endotherm. Asymmetry can result from irreversible unfolding (see **Section 4.7**), but this explanation can be tested with repeated scans on the same sample.

4.3.1. Spectroscopic Data Assuming a Dimer (Two-State)

Thermal denaturation curves followed spectroscopically (e.g., by UV, CD, or fluorescence) can be fit by nonlinear regression using **Eq. (3.48),** along with **Eqs. (3.2)**, **(3.7)**, and **(3.23).** This is a seven-parameter fit with slope and *y*-intercepts for the pre- and post-transition baselines, along with $T°$, $\Delta H(T°)$, and ΔC_p for the equilibrium. In addition, it is wise to vary the concentration of protein and either demonstrate the validity of **Eq. (3.25)**, or better fit the data globally.

4.3.2. DSC Data Assuming a Dimer (Two-State)

As with a monomer, DSC data can be fit to **Eq. (3.48)** with three adjustable parameters (T_m, $\Delta H(T_m)$, and ΔC_p) plus **Eq. (3.49)** (three additional parameters: U, V, and X, with $\Upsilon = U + \Delta C_p$). Baselines are treated as described for the monomer (*see* **Section 4.2.4**). The dependence of stability on concentration is included by globally fitting multiple DSC curves obtained with differing concentrations of protein.

4.4. Dimer Unfolding with More Than One Transition

The unfolding of a dimer with more than one transition can be fit to the equations presented above for **Schemes V and VII** (spectroscopic data with **Eqs. (3.33)** or **(3.40)**, DSC with the temperature derivatives of **Eqs. (3.34)** and **(3.41)**). The linkage of a structural transition to folding is most likely indicated by a low-temperature transition which is concentration independent,

followed by a second transition at higher temperature which is concentration dependent (*see* **Fig. 3.7** and 3.**8**). Dissociation followed by unfolding of monomers will show a concentration-dependent transition which occurs after a lower temperature, concentration-independent transition (*see* **Figs. 3.5** and 3.**6**). Fitting of the ΔC_p for two overlapping transitions is problematic. In general there is no straightforward way to remove the baseline as described for a monomer above. Therefore, the ΔC_p must be included in the fitting. Under favorable circumstances, concentrations can be adjusted so that two separate transitions can be observed, and ΔC_p can be estimated from differences in the pre- and post-transition baselines. ΔC_p for a concentration-dependent peak can also be defined by a global fit of a series of data collected at different concentrations (i.e., taking advantage of the concentration dependence to fit the temperature dependence of ΔH). ΔC_p for the concentration-independent peak can be defined by varying pH. In the absence of this, the only alternative is to apportion the ΔC_p between the two transitions (e.g., by assuming that the magnitude of the ΔC_p is proportional to the ΔH).

4.5. Irreversible Unfolding

The irreversible unfolding of a protein might be described by a reversible unfolding process which is followed by an irreversible modification of the unfolded species *(20)*:

$$N \rightleftharpoons U \longrightarrow I$$

<div align="right">Scheme VIII</div>

For simplicity, the scheme shown here is for a monomer, but it can be easily expanded to encompass any of the unfolding reactions considered above. If the conversion of U to I is much faster than refolding, the kinetic mechanism is simplified to $N \rightarrow I$. Irreversibility may be due to a number of processes, including chemical modification of the unfolded protein and aggregation *(21)*. Most importantly, the thermal unfolding of an irreversible system reflects not only the equilibrium between native and folded forms (the first reaction in **Scheme VIII**), but also the kinetics of the succeeding reaction. The presence of the irreversible second step can significantly distort a DSC endotherm. The result is a shifting of the endotherm to lower temperature and a distortion of its shape which is not accurately described by any of the models above. The kinetically controlled irreversible step may be associated with significant heat changes. As a result, the endotherm for the intrinsic unfolding process can be perturbed, and its T_m shifted due to overlap with an endothermic or exothermic irreversible process (or processes) that occurs essentially simultaneously. There are no reliable methods which permit the unambiguous deconvolution of such transitions.

4.6. Error Analysis

One of the advantages of a quantitative analysis of stability data is that the error limits (precision) in the results can be firmly established. Error estimates for all parameters derived from nonlinear regression of DSC data are obtained using standard techniques which characterize the shape of the error surface in the vicinity of the minimum achieved by iteration *(22, 23)*. The Monte Carlo method of confidence interval estimation *(24)* is especially attractive for this analysis. Errors in thermodynamic functions such as ΔG are derived from fitted parameters using standard propagation formulas *(22)*; for example, the variance in ΔG is given by

$$\sigma^2_{\Delta G} = \sigma^2_{\Delta H}\left(\frac{\partial \Delta G_\mathrm{u}}{\partial \Delta H}\right)^2 + \sigma^2_{T_\mathrm{m}}\left(\frac{\partial \Delta G_\mathrm{u}}{\partial T_\mathrm{m}}\right)^2 + \sigma^2_{\Delta C_\mathrm{p}}\left(\frac{\partial \Delta G_\mathrm{u}}{\partial \Delta C\mathrm{p}}\right)^2, \ (3.54)$$

where the partial derivatives are calculated numerically by calculating the change in ΔG resulting from a small change in each of the parameters.

5. Data Collection

Detailed protocols for using UV, fluorescence, circular dichroism, and DSC for studies of protein stability have been presented in a previous volume of this series and elsewhere, and will not be reproduced here *(25–29)*. We provide here additional comments and key points that the user may find useful.

5.1. DSC Instrument Design and Performance

High-sensitivity DSC instruments appropriate for biological calorimetry can be obtained from MicroCal (Northampton, MA) and Calorimetry Sciences (Provo, UT). DSC cells are metal (e.g., gold, tantalum, or hastaloy) and are typically cylindrical. Capillary cells can eliminate baseline distortions associated with precipitate formation due to irreversible unfolding. These seem to reduce the heat contribution from the falling precipitate. This does not remove the problems associated with irreversibility (*see* **Section 4.5**).

Not only the short-term and long-term noise levels for DSC instruments are important, but also baseline reproducibility on repetitive scans and especially upon reloading an identical sample. Optimum performance is obtained if the instrument is powered by a line conditioner (e.g., Toshiba On-line UPS). The best data are obtained if the DSC is never idle, but rather is left continuously scanning on buffer when not in use.

5.2. Spectrophotometer Considerations

The primary concern for monitoring thermal melting curves followed by spectroscopy (other than proper care in operation of the spectrophotometer) is temperature control. It is essential that

temperature control be calibrated by measuring the temperature in the cell with a thermocouple. This can also be used to determine the minimum time necessary to ensure temperature equilibration following a change in temperature (typically 5–10 minutes). The cuvette should be lightly capped to prevent excessive evaporation at high temperature, but not so tight as to cause pressure buildup and damage to the cell.

5.3. Sample Considerations

Protein samples are prepared by dialyzing against the required buffer, with three changes to ensure equilibration. Buffers used in DSC should not interact with the protein, and have negligible change in pK with temperature; that is, heats of protonation should be small. Glycine and acetate are attractive since they compensate protonation changes due to protein unfolding *(6)*. Amines (including TRIS) should be avoided due to high heats of protonation. Although the metals used for fabrication of DSC cells are chosen to be essentially inert (especially to biological buffers), the susceptibility of DSC cells and associated gaskets to buffer components needs to be checked in manufacturer's documentation.

Sample concentrations are typically on the order of 1 mg/ml for DSC, and may be significantly lower for spectroscopic techniques, particularly fluorescence. Lower concentrations are also possible with the newer and more sensitive DSC instruments. Typically about 2 ml of sample is needed for both spectroscopic and DSC measurements to allow for cell loading and concentration measurements. In DSC both the sample and dialysis buffer are degassed by gentle stirring under vacuum for 5–10 minutes prior to cell loading. Sample concentrations are measured spectrophotometrically using accurate extinction coefficients. The accuracy of the spectrophotometer should also be checked using a standard, for example, carefully prepared K_2CrO_4 solution *(30)*.

Reversibility is indicated by the reproducibility of repetitive scans on the same sample. It is not normally necessary to scan beyond the T_m to demonstrate reversibility. The T_m can be obtained from an initial scan through the transition on a separate sample. If the relaxation time for the unfolding reaction at the T_m is less than a second, the protein unfolds and refolds more than a hundred times per minute. At a scan rate of 1 deg/min, a protein at the T_m will have unfolded and refolded more than a thousand times, and duplication of successive scans to the midpoint should be sufficient.

The behavior of protein samples at high temperature should be tested outside the calorimeter or spectrophotometer by heating to the highest temperature that will be used in a thermal melt scan (with identical solution conditions planned for the experiments). If the sample precipitates upon unfolding, consideration should be given to the utility of collecting quantitative data. It is doubtful that useful thermodynamic information can be obtained

from such samples due to irreversibility. In addition, removal of a precipitate from a DSC cell can be difficult (especially if the cells are capillaries).

5.4. Data Collection   Because DSC cells are pressurized, thermal unfolding measured by DSC can be performed routinely to significantly higher temperature than with spectroscopy. DSC scans to 130°C can be easily accomplished with moderate pressures of a few atmospheres. Thermal melts and DSC scans should cover a temperature range sufficient to define not only the transition, but also the baselines below and above the transitions. Care should be taken at lower temperatures to prevent freezing since expansion of the cell can damage the instrument. The scan rate should be fast enough to achieve an adequate signal-to-noise ratio and minimize the time at high temperature, but not so rapid to make the T_m scan rate dependent. A rate of 1 deg/min is commonly used in DSC, but various rates should be checked. Significantly slower scan rates are normally required with spectroscopic methods, making it more likely to observe irreversible modifications at higher temperature.

6. Notes

1. The dependence of T_m on concentration is a key criterion for arguing that a protein exists as a multimer in solution.
2. A parameter which is a function of temperature is shown with T in parentheses following the symbol for the parameter, for example, $\Delta H(T)$. The value of a parameter at a specific temperature is indicated by the value of that temperature in parentheses after the symbol for the parameter, for example, $\Delta H(T_m)$ which specifies the enthalpy change at the T_m. Care should be taken to not confuse these common conventions with multiplication; for example, $\Delta C_p(T–T_m)$ indicates the multiplication of ΔC_p by the temperature difference in parentheses. The difference should be obvious from the context.
3. Interactive *Mathematica* (Wolfram) Notebooks which can be used in conjunction with this text can be downloaded from http://daffy.uah.edu/thermo/. These permit simulations using all of the models presented here.
4. The fraction unfolded refers to the fraction converted to the U state. The unfolding reaction is all-or-nothing for each cooperative domain. Thus, for the unfolding of a monomer, 50% unfolded refers to 50% of the molecules being unfolded and 50% remain folded. It does not imply that an individual molecule can be half-unfolded. Of course, a protein may contain two independent cooperative domains, the unfolding of each is described by a two-state reaction, and conditions

can be obtained where one of the domains may be completely unfolded while the other remains folded.

5. See Section 1.0–1.1 of the *Mathematica* "Protein Folding Notebook – Melts and DSC" at http://daffy.uah.edu/thermo/.

6. The concentration of a protein which forms oligomers can be expressed in terms of either the maximal number of moles of multimer per liter, or the moles of total monomer chains per liter. The latter is more commonly used in the literature. It is important that the definition used be clearly stated when reporting results.

7. The specification of a T_m for the unfolding of a multimer has no meaning unless the concentration is specified. The T_m is not a fundamental thermodynamic parameter that can be used to characterize the stability of a multimer. The T° should be used instead.

8. We stress that the T_m for multimer does not reach an upper limit or plateau with increasing protein concentration.

9. The triangular presentation in **Schemes V** and **VII** stresses the fact that thermodynamics is not dependent on reaction path, and although we might be tempted to view I_2 dimer as a necessary intermediate, N_2 may also unfold directly to U.

10. Alternatively, the van't Hoff enthalpy can be obtained by differentiation of an appropriate equation for the equilibrium constant with respect to temperature using **Eq. (3.3)** *(15)*. For a monomeric protein

$$\Delta H_{vh}^{eff} = 4RT_m^2 \left(\frac{\partial \alpha_U}{\partial T} \right)_{T=T_m} = \frac{4RT_m^2 C_{p,max}}{\Delta H_{cal}}, \qquad (3.55)$$

while for a multimer of n subunits, it is given by

$$\Delta H_{vh}^{eff} = (2 + 2n) \frac{RT_m^2 C_{p,max}}{\Delta H_{cal}}. \qquad (3.56)$$

This function is dependent on the accuracy of a single data point, that is, $C_{p,max}$. It is therefore in general less reliable than a direct fit of the entire dataset.

11. The reaction is assumed to be two-state, with either completely folded or unfolded protein.

References

1. Makhatadze, G., Privalov, P. L. (1995) Energetics of protein structure. *Adv Protein Chem* 47, 308–425.

2. Lumry, R., Biltonen, R., Brandts, J. (1966) Validity of the "two-state" hypothesis for conformational transitions of proteins. *Biopolymers* 4, 917–944.

3. Privalov, P., Khechinashvili, N. (1974) A thermodynamic approach to the problem of stabilization of globular protein structure: a calorimetric study. *J Mol Biol* 86, 665–684.

4. Pace, C. N. (1975) The stability of globular proteins. *CRC Critical Rev Biochem.* 3, 1–43.

5. Freire, E., Biltonen, R. (1978) Statistical mechanical deconvolution of thermal transitions in macromolecules. I. Theory and application to homogeneous systems. *Biopolymers* 17, 463–479.

6. Privalov, P. (1979) Stability of proteins. Small globular proteins. *Adv Protein Chem* 33, 167–241.

7. Sturtevant, J. (1987) Biochemical applications of differential scanning calorimetry. Ann Rev Phys Chem 38, 463–488.

8. Lewis, G. N., Randall, M., Pitzer, K. S., Brewer, L. (1961) *Thermodynamics*, McGraw-Hill, New York.

9. Eisenberg, D., Crothers, D. (1979) *Physical Chemistry with Applications to the Life Sciences*, Benjamin/Cummings, Menlo Park, CA.

10. Becktel, W., Schellman, J. (1987) Protein stability curves. *Biopolymers* 26, 1859–1877.

11. Privalov, P., Griko, Y., Venyaminov, S., et al. (1986) Cold denaturation of myoglobin. *J Mol Biol* 190, 487–498.

12. Wyman, J., Gill, S. J. (1990) *Binding and Linkage: Functional Chemistry of Biological Macromolecules,* University Science Books, Mill Valley, CA.

13. Biltonen, R. L., Freire, E. (1978) Thermodynamic characterization of conformational states of biological macromolecules using differential scanning calorimetry. *CRC Crit Rev Biochem* 5, 85–124.

14. Steif, C., Weber, P., Hinz, H.-J., et al. (1993) Subunit interactions provide a significant contribution to the stability of the dimeric four-α-helical bundle protein ROP. *Biochemistry* 32, 3867–3876.

15. Marky, L. A., Breslauer, K. J. (1987) Calculating thermodynamic data for transitions of any molecularity from equilibrium melting curves. *Biopolymers* 26, 1601–1620.

16. Hermans, J., Jr. (1965) Methods for the study of reversible denaturation of proteins and interpretation of data. *Methods Biochem Anal* 13, 81–111.

17. Privalov, P. L., Makhatadze, G. I. (1990) Heat capacity of proteins. II. Partial molar heat capacity of the unfolded polypeptide chain of proteins: protein unfolding effects. *J Mol Biol* 213, 385–391.

18. McCrary, B. S., Bedell, J., Edmondson, S. P., et al. (1998) Linkage of protonation and anion binding to the folding of Sac7d. *J Mol Biol* 276, 203–224.

19. Scholtz, J. M. (1995) Conformational stability of HPr: The histidine-containing phosphocarrier protein from Bacilus subtilis. *Protein Sci.* 4, 35–43.

20. Lumry, R., Eyring, H. (1954) Conformation Changes of Proteins. *J. Phys.* Chem. 58, 110.

21. Ahern, T., Klibanov, A. (1985) The mechanism of irreversible enzyme inactivation at 100°C, *Science.*

22. Bevington, P. R., Robinson, D. K. (1992) *Data Reduction and Error Analysis for the Physical Sciences*, McGraw-Hill, New York, N.Y.

23. Johnson, M., Faunt, L. (1992) Parameter estimation by least squares methods. *Methods Enzymol* 210, 1–37.

24. Press, W., Flannery, B., Teukolsky, S., et al. (1989) Numerical Recipes: *The Art of Scientific Computing (Fortran Version)*, Cambridge University Press, Cambridge.

25. Mach, H., Volkin, D. B., Burke, C. J., et al. (1995) in (Shirley, B. A., ed.), *Protein Stability and Folding: Theory and Practice*, Humana Press, Inc., Totowa, N.J.

26. Royer, C. A. (1995) in (Shirley, B. A., ed.), *Protein Stability and Folding: Theory and Practice*, Humana Press, Inc., Totowa, N.J.

27. Kuwajima, K. (1995) in (Shirley, B. A., ed.), *Protein Stability and Folding: Theory and Practice*, Humana Press, Inc., Totowa, N.J.

28. Lopez, M. M., Chin, D. H., Baldwin, R. L., et al. (2002) The enthalpy of the alanine peptide helix measured by isothermal titration calorimetry using metal-binding to induce helix formation, *Proc Natl Acad Sci USA 99*, 1298–1302.

29. Makhatadze, G. (1998) in *Current Protocols in Protein Science*, John Wiley & Sons, New York.

30. Gordon, A., Ford, R. (1972) *The Chemist's Companion: A Handbook of Practical Data, Techniques, and References*, John Wiley, New York.

Chapter 4

Protein–Protein and Ligand–Protein Interactions Studied by Analytical Ultracentrifugation

Walter F. Stafford, III

Abstract

All biological processes involve molecular interactions that result in either binding, self-association, or hetero-associations of one form or another. It is important to understand that no interactions are completely all-or-none. Some approach all-or-none only when there is strong positive cooperativity. Examples will be given of typical biomolecular interactions and their expected dependence on concentration, in order to point out the relatively wide range of concentration over which these types of phenomena take place. This chapter is concerned both with the binding of low-molecular-weight ligands to macromolecules as well as interactions between macromolecules using analytical ultracentrifugation (AUC) as a tool for measuring association properties of these systems. The theory of sedimentation of both ideal and nonideal interacting and noninteracting systems is discussed. Examples are given of each type of system along with a discussion of how each type of system can be analyzed. Several methods of data analysis are discussed.

Key words: Analytical ultracentrifugation, sedimentation, cooperativity.

1. Introduction

1.1. Protein–Protein and Ligand–Protein Interactions

Interactions between a given protein and other proteins or between a protein and various smaller molecules and ions (ligands) are central to the regulation of all metabolic processes.

Protein–protein interactions are often themselves regulated by interactions with various ligands. The energetics of a particular interaction can be strongly influenced by the binding of a smaller ligand or ion to one of the protein species. Covalent modification, such as phosphorylation, of one of the species can also influence self-association or an interaction between it and another protein.

Elucidating these sorts of interactions by analytical ultracentrifugation (AUC) is the subject of this chapter. We will cover both the theoretical background required to understand and interpret the data as well as provide detailed descriptions of the laboratory procedures required to acquire reliable, high-quality data, along with the application of rigorous methods for the determination of hydrodynamic and thermodynamic parameters that characterize the system of interest.

1.2. Expression of Equilibrium Constants

Equilibrium constants can be expressed in a variety of units depending on the optical system in use and whether it is desired to express them on the mass concentration scale (grams per liter or grams per cubic centimeter) or the molar concentration scale (moles per liter).

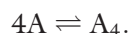### 1.2.1. Dissociation Constants versus Association Constants

When a binding interaction is written in the forward direction from reactants to complex formation, it is common to write

$$A + B \rightleftharpoons AB \qquad K_a = [AB]/[A][B],$$

where [X] denotes molar concentration of X. Furthermore, we can write that $K_d = 1/K_a$, which corresponds conveniently to the free concentration of either A or B at "half–saturation" depending on which species is considered to be the ligand and which is the receptor.

This relationship between K_a and the concentration corresponding to half-saturation becomes somewhat obscure for higher degrees of interaction when the reaction is higher-order than bimolecular.

Consider a monomer–tetramer self-association as an example of such a higher-order reaction.

$$4A \rightleftharpoons A_4.$$

The association constant for this reaction is given by

$$K_a = [A_4]/[A]^4$$

and the corresponding dissociation constant is

$$K_d = 1/K_a.$$

Note that the units of K_d are not moles per liter but are (moles/liter)^3; therefore, one must take the cube root of K_d to obtain a number with the units of concentration. Now to what fraction of saturation does this correspond and on what scale, molar or mass?

1.2.2. K_ds and the Concentration at the Half-Point

1.2.2.1. Molar Concentration Scale

Continuing with the monomer–tetramer case, we would like to know the total concentration when the monomer and tetramer are present at equimolar concentrations. For the monomer–dimer case, as just mentioned, the concentration turns out to be equal to the dissociation constant; however, for higher stoichiometries, that is no longer the case.

Consider, for example, a reversible monomer–tetramer system.

In this case we can write, as a statement of conservation of mass,

$$A_{total} = [A] + 4[A_4] = [A] + 4K_a[A]^4,$$

and solving this for $[A]$ after setting $[A] = A_{total}/2$, we have

$$A_{total,1/2} = \left(A_{total,1/2}\right)/2.0 + \left(4K_a A_{total,1/2}^4\right)/16$$

and solving for $A_{total,1/2}$, and rearranging, we have that the total concentration when half the molecules are in monomeric form, $A_{total,1/2}$:

$$A_{total,1/2} = 2K_d^{1/3}$$

1.2.2.2. Mass Concentration Scale

On the mass concentration scale, we would like to know the total concentration when half the mass of the protein is in the monomer form and the other half is in the tetrameric form. In this case we formulate the equations with mass concentrations, and we can write

$$W_{A,total} = w_A + w_{A_4} = w_A + K_a w_A^4,$$

where $K_a = (w_{A_4})/(w_A)^4$.

Now set $w_{A_4} = w_A = W_{A,total,1/2}/2$ and solve for $W_{A,total,1/2}$ in terms of $K_d = 1/K_a$ when half the mass is in tetramer form:

$$W_{A,total,1/2} = W_{A,total,1/2}/2 + K_a\left[W_{A,total,1/2}/2\right]^4.$$

We arrive at

$$W_{A,total,1/2} = 2K_d^{1/3}.$$

1.2.2.3. Conversion Between $K_{(mass)}$ and $K_{(molar)}$

The monomer–tetramer conversion of dissociation constants between molar and mass units is given by

$$K_{d,molar} = [A]^4/[A_4] = \lfloor w_A^4/w_{A_4}\rfloor\lfloor 4M_1/M_1^4\rfloor = K_{d,mass}\lfloor 4/M_1^3\rfloor.$$

Now converting from molar to mass, to get the molar concentrations when half the mass is monomer and half is tetramer we have

$$A_{\text{total},1/2} = 2 K_{\text{d,molar}}^{1/3} = \frac{2[4]^{1/3}}{M_1} K_{\text{d,mass}}^{1/3} = \frac{[4]^{1/3}}{M_1} W_{\text{A,total},1/2}.$$

For example, if the molar dissociation constant were, say, 1×10^{-15} M^3, the molar concentration of total A when half of the moles are in tetrameric form would be 2×10^{-5} M and, assuming a monomer molar mass of 30,000 g/mol (*see* the example below, **Figs. 4.7–4.9.**), the molar concentration when half the mass is in tetrameric form would be about 5.3×10^{-5} M.

2. Methods

2.1. Cells and Centerpieces

The centerpiece is the sample compartment in which sedimentation takes place. There are several types of centerpieces available for sedimentation velocity work. The double sector centerpieces are most commonly used for sedimentation velocity work and can be obtained either from BeckmanCoulter, Inc or from SpinAnalytical, Inc. There are also high-speed (SedVel60) and meniscus-matching (SedVel60-MM) versions of these centerpieces available from SpinAnalytical, Inc. The standard 12 mm centerpiece is filled with 420–450 μL of solution, while the high-speed centerpieces are typically filled with 330–360 μL of solution to put the meniscus at about 5.9 cm. Use of smaller volume results in shorter column heights resulting in lower resolution of sedimenting species.

2.2. Interference Optics

2.2.1. Alignment of the Laser

Alignment of the laser so that the beam is precisely parallel to the axis of rotation is important for at least two reasons: (1) cancellation of some of the higher-order aberrations arising from Wiener skewing will result only if the beam is exactly parallel to the axis of rotation and the camera lens is focused at the 2/3 plane of the cell (1–3); (2) it has been observed that the vertical jitter is of much lower magnitude in the solution column if the laser is aligned precisely parallel to the axis of rotation (4).

2.2.2. Alignment of Cylinder Lens

The alignment of the cylinder lens is critical to getting correct cancellation of the buffer redistribution during sedimentation. The axis of the cylinder lens must be precisely aligned perpendicularly with respect to the radius bisecting the two sectors of the centerpiece of the rotor. Proper alignment assures that the buffer

signal from corresponding radial positions in sample and reference sector as subtracted correctly. If the cylinder lens is tilted with respect to the radial axis, the signal from nonconjugate positions (i.e., from different radii) will be subtracted and a signal proportional to the radial buffer concentration gradient will be superimposed on the data. This systematic error cannot be removed by curve fitting.

Fortunately, it is fairly simple to check for misalignment of the cylinder lens. The alignment procedures have been outlined in great detail by Richards et al. in the early 1970s *(5–7)*: alignment of the cylinder lens essentially involves removing the center rib from an old double sector centerpiece and introducing a high concentration of protein (for example 60 mg/mL BSA works fine). The rotor is spun for about 30–60 minutes at 40,000 rpm until a cut-off gradient is achieved over a large portion of the solution column near both the meniscus and the base. When the cylinder lens is correctly aligned, the fringes will be straight in the regions of highest gradient on either side of the boundary and at the bottom of the cell. If the cylinder lens is misaligned, the fringes will curve either up or down on either side of the boundary and at the base.

2.2.3. Interference Window Holders

Use of interference window holders is necessary to get the highest quality data from the interference optical system of the Beckman-Coulter ProteomeLab XL-I. Instability of the timing circuitry used for firing the laser leads to variation in the TI background of the fringe patterns unless the windows are masked off with the interference window holder slits and the dwell time of the laser increased to illuminate the entire slit. A dwell time of 1.4 degrees, instead of the much shorter 0.4 degrees commonly used, will give about the same illumination when using the interference slits. The interference windows should be placed on the top of the cell.

2.2.4. Meniscus-Matching Procedure

In the meniscus-matching procedure, a special centerpiece that has a capillary channel on its surface that connects the two sectors is used. (These can be obtained from SpinAnalytical and are called SedVel60 meniscus-matching centerpieces as mentioned above). The reference sector is filled with a volume of dialysate about 20 µL more that the amount solution introduced into the sample sector. The rotor is spun at about 5000–10,000 rpm (or higher if necessary) until the sample and reference solution columns heights match. Then the rotor is stopped and the rotor gently shaken to redistribute any solute that sedimented during the matching procedure.

Meniscus matching is very important if work is being done at high dilutions. Under these conditions, correction for buffer redistribution becomes important. If the menisci are not matched, the buffer redistribution will be different in the sample and reference solutions at the same radial position and therefore will not be

correctly subtracted out of the fringe patterns. It is generally not possible with any of the currently available software packages to compensate for misalignment of the meniscus when using interference optics.

Meniscus matching is most important when using interference optics and is not commonly used with absorbance optics unless the buffer absorbs significantly at the wavelength being used such that its redistribution must be cancelled.

2.2.5. Thermal Equilibration of the Rotor

Before starting the run, the rotor should be thermally equilibrated. Typically at room temperature, about an hour will suffice. At higher or lower temperatures, longer times may be necessary.

2.2.6. Vacuum Pump

The ProteomeLab XL-A/I comes equipped with an oil diffusion pump which will cause deposition of pump oil on the optics if the instrument is run at temperatures much above room temperature. Recently we have installed a turbo-molecular pump that simply replaces the diffusion pump after fabricating a coupling that matches the existing diffusion pump flange *(4)*. This pump uses no oil and can be run for long periods of time, several days for equilibrium runs, at up to 40°C without any oil deposition allowing operation over the complete temperature range of which the instrument is capable.

2.3. Sample Preparation

2.3.1. Dialysis

Dialysis is preferred for all samples. For three or more component systems, that is, those composed of water, macromolecules, and buffer/salt, the solution must be at osmotic (i.e., dialysis) equilibrium with the solvent (water plus buffer) *(8)* in order to have proper definition of components. Osmotic equilibrium can be achieved effectively either by ordinary dialysis, by gel filtration, or with spin columns.

2.4. Analysis and Interpretation of the Data: General Considerations

2.4.1. Curve Fitting to Sedimentation Velocity and Sedimentation Equilibrium Data

2.4.1.1. Optics and the Signal

In general, an optical system gives us a signal, *S*, as a function of radius and time that evolves during the sedimentation run. We will

designate this raw signal as $S(r,t)$. It is usually a linear function of the concentration and can be represented by a relation of the following form:

$$S(r, t) = \alpha c(r, t) + B(r) + \text{noise}, \qquad (4.1)$$

where α is the proportionality constant relating concentration to the signal from a particular optical system, whether it be a refractometric, absorbance, or fluorescence signal; $c(r,t)$ is the concentration distribution as a function of radius and time; $B(r)$ is an optical background signal that is a function of radius but independent of time; and "noise" represents stochastic fluctuations of the signal.

2.4.1.1.1. Interference Optics   At each time point, the interference optics, with a correctly aligned cylinder lens, gives a signal at each radial position that is proportional to the refractive index difference between the sample sector and the reference sector at that radial position which in turn is a linear function of the concentration at that radius. In this case, α is equal to the number of fringes per mg/mL for the optical path length of the centrifuge centerpiece in use.

2.4.1.1.2. Absorbance Optics   The absorbance optics gives us data in the form of absorbance as a function of radius and time, and can be expressed by **Eq. (4.1)**, where α is the mass extinction coefficient for the optical path of the centrifuge centerpiece in use.

2.4.1.1.3. Fluorescence Optics   The fluorescence optical system gives us an arbitrary signal scaled between 0 and 2048 that is a linear function of the concentration, with α being the proportionality constant relating the magnitude of the fluorescence signal to concentration in mg/mL.

2.4.1.1.4. Pseudo-absorbance data   The Optima XL is also capable of storing data in the form of intensity as a function of radius and time, and can write that data out from both the sample and the reference sectors separately. If one takes the logarithm of the inverse of the intensity as the signal, the result will have the form of **Eq. (4.1)** and can be analyzed using appropriate methods *(9)*. This type of data is treated essentially in the same manner as interference data, that is, generally a vertical offset must be determined for the data. The alignment procedure used for interference data removes vertical jitter at the same time as it establishes the zero level.

2.4.1.2. Systematic Errors in the Data

Schuck has designated the vertical jitter observed with the interference optics of the BeckmanCoulter ProteomeLab XL-I as "radially independent, time-dependent noise" (RI noise) and the

optical background signal comprising constant systematic errors, $B(r)$, as "time-independent, radially dependent noise" (TI noise) *(10)*; we will follow that nomenclature.

There are several methods that have been developed to deal with these systematic errors inherent in AUC data. The background signal, $B(r)$, arising from inhomogeneities in the optics and dirt on the lenses (**Eq. (4.1)**), can be removed completely by taking time differences of the data and either using them as approximations to the time derivative of the signal to compute $g(s)$ *(11)* or by fitting them directly to solutions of the Lamm equation *(12–14)*. Another method whose validity depends on obtaining a good least-squares fit to the hydrodynamic portion of the data was developed by Schuck and is called systematic noise decomposition *(15)*. The background noise is highly cross-correlated with any slowly sedimenting species and success with this method depends strongly on having sedimented the slowest moving species at least half way to the bottom.

2.4.1.2.1. Precession and Vibration One type of systematic error which has not been addressed to date by any of the existing sedimentation velocity software packages is the time-dependent, radially dependent errors introduced by precession of the rotor. Although this error is relatively small in the XL-I, it can be detected with careful measurement and will degrade the quality of the signal. This often shows up as vertical stripes in the bit map residual plots provided by both SEDANAL *(12)* and SEDFIT *(16)*. Another potential source of error that we have observed can arise in machines with interference optics whose monochromator mount has become worn. As the threads on the mount wear down, the tightness of the monochromator arm becomes compromised allowing the arm to vibrate. This introduces random radial and vertical oscillations in the data patterns which cannot be removed in software.

2.4.2. Analysis of Noninteracting Systems

2.4.2.1. C(s)   The software package SEDFIT, created by Schuck *(16)*, offers an analysis method called $c(s)$, pronounced "see-of-ess", which gives the results of a least-squares fit of the data to a set of basis functions that are solutions to the Lamm equation over a range of values of sedimentation coefficient, s. It assumes a relationship between s and D at each value of s by assuming that the value of f/f_o is the same for all species. This global frictional ratio is referred to as the weight average frictional ratio. Validity of this approach relies on the assumption that all the protein components in a mixture can be represented with the same frictional ratio. It also assumes that only the processes of sedimentation and

diffusion are taking place. The effects of any reactions between species, either self-associations or hetero-associations, are not properly accounted for in the least squares modeling used by this method. Therefore, a great deal of caution should be exercised when applying $c(s)$ to interacting systems.

2.4.3. Analysis of Interacting Systems

The proper analysis of interacting systems requires the use of rigorous curve-fitting methods to obtain estimates of the parameters of interest by taking into account directly the effect of the interactions on the shape of the reaction boundary. Once the basic physical properties, like sedimentation coefficient, diffusion coefficient, and molar mass, of the individual macromolecular component species have been determined, the parameters of most interest are usually stoichiometries and free energies of association. The problem is to be able to extract these parameters and their uncertainties from complex behavior that includes several types of hydrodynamic and thermodynamic nonideality in addition to the reversible interactions taking place.

2.4.3.1. Validity of Least Squares (the L-2 norm) or Other Types of Fitting such as Least Average of the Magnitudes of the Residuals (the L-1 Norm)

The first and foremost requirement for the validity of any type of fitting is that the model chosen to represent the macromolecular system be correct. By model, we mean a set of mathematical relationships that correctly describes the macromolecular interactions in terms of stoichiometry and energetics, in addition to the other physical properties of the macromolecules involved. In many cases fitting the wrong model to the data will result in systematically varying residuals, and the incorrect choice of model will be obvious. It is also possible to fit the data to the sum of arbitrary functions such as the sum of Gaussians or, in the cylindrical coordinate system of the centrifuge, sums of arbitrary solutions to the Lamm equation. These fits can be very good with respect to magnitude and systematic variation of the residuals, but in the general case of interacting systems, the fitting parameters that give the best fit, namely s and f/f_o, have no physical meaning. To the extent that these types of fitting procedures give a good fit, they represent the original data to a degree that allows fairly accurate determination of some quantities like weight average sedimentation coefficients *(16)*.

However, even when theoretically correct procedures are applied, there can be many cases in which good fits cannot be obtained with different models because the information content of the data is insufficient to determine uniquely the "correct" association model. Other knowledge about the system must incorporated into the analysis to resolve these ambiguities, *(17, 18)*, or a wider range of intensive parameters (i.e., wider range of loading concentrations and ratios of components) must be sampled. Loading concentrations mainly, but also temperature, pH, and ionic strength, must be varied over a sufficiently wide range that all the species comprising

the system become populated to reliably detectable levels without changing the mechanism of the interactions.

2.4.3.2. Noninteracting Systems and Very Slowly Reversible, Interacting Systems

It is worthwhile considering briefly the differences in the sedimentation behavior of rapidly reversibly interacting systems compared to noninteracting systems. In a noninteracting system, under ideal conditions, each component sediments and diffuses independently of the others. Also in a noninteracting system, each macromolecular species is a separate thermodynamic component, the amount of which is given by its initial concentration. The resulting signal from a mixture of noninteracting species is the simple superposition of the signals from the individual components that would be obtained had they been present alone in the solution. One important characteristic of a noninteracting system is that the ratios of the species remain constant upon dilution and are equal to the ratios of the initial concentrations before loading into the centrifuge cell, radial dilution notwithstanding.

2.4.3.3. Rapidly Reversible, Interacting Systems

On the other hand, in an interacting system, the local concentrations of all species in the centrifuge cell are determined by the "law of mass action". We can arbitrarily divide interacting systems into self-associating and hetero-associating. In a self-associating system, which is a single thermodynamic component composed of several species, the composition of the solution at each point in the centrifuge cell is determined by the magnitude of the equilibrium constants for the reactions between the species and the total macromolecular concentration at each radial position. The simplest self-associating system would be a monomer–dimer system. The ratio of concentration of the dimer species to that of the monomer species will decrease upon dilution.

The simplest example of a hetero-associating system would be a two-component system in which two molecules, say, A and B, combine to form a product which is a noncovalent complex, AB, composed of one molecule each and A and B. It is characteristic of interacting systems that the ratios of the species comprising each component vary, according to the law of mass action, on dilution while the ratios of the components remain constant. If we add equimolar amounts of A and B to the solution, the ratio of total A to total B will remain constant upon dilution, while the ratios of species A, B, and AB to each other at each radius will depend on the total local concentration of species A, B, and AB according to the value of the equilibrium constant and the local concentration of total A and total B at each radius.

The boundaries formed by these types of reversible interacting systems are referred to as "reaction boundaries" and cannot be described as the superposition boundaries that would have been composed of independently sedimenting species A, B, and AB, or

as independently sedimenting monomer and dimer species as in the self-associating case above.

The misapplication of least-squares methods that were formulated to fit to a model comprising noninteracting species can lead to spurious results when applied to reversibly interacting systems. Often one can get surprisingly good fits of a noninteracting model to an interacting system, but the fitted parameters will have no physical meaning (i.e., it is the wrong model). The use of $c(s)$ analysis to "deconvolute" diffusion from the reaction boundaries of interacting systems has been advocated by Schuck *(19)*; as a case in point we will see below the results of $c(s)$ analysis applied to a simple reversible monomer–dimer system for which very good looking fits can be obtained (*see*, for example, **Fig. 4.4**). This system could be fit to essentially three species including only the three sedimentation coefficients and a single value of f/f_o. Therefore, all the spreading of the boundary, both from reversible reaction and from diffusion, could be represented essentially by only three diffusion coefficients. However, the particular values of the diffusion coefficients implied by the single value of f/f_o, might have a physical meaning only if the spreading due to reaction had been taken into account as well. In fact there are only two diffusion coefficients required to represent this system, that for monomer and that for the dimer, once the reaction is treated correctly. Therefore, the so-called deconvolution process has removed both types of spreading not just that from diffusion. One should exercise extreme caution when applying this nonrigorous method to reversibly interacting systems. While this method purports to deconvolute diffusion from interacting systems, it is merely approximating the boundary shape by summing up Lamm equation solutions from an arbitrary array of imaginary, nonphysical sedimenting species.

2.4.3.4. Mixed Systems

An example of a mixed system is a rapidly reversible monomer–dimer system containing some amount of cross-linked dimer. This is two-component system consisting of three species; the first component is the reversible monomer–dimer system and the second component is the cross-linked dimer. In this system, the ratio of monomer to dimer in the self-associating component would vary while the ratio of the cross-linked dimer to the monomer–dimer system would remain constant upon dilution. The cross-linked dimer would sediment independently of the reversible monomer–dimer system.

While these distinctions may seem obvious once pointed out, they are often overlooked or ignored in many analyses of macromolecular systems. Luckily, there are simple procedures that will allow one to decide which of the two possibilities or whether both exist in a particular sample. Moreover, there are

methods available to analyze these systems rigorously once they have been identified.

2.5. Theoretical Background

Before we proceed to discuss methods of analysis and interpretation of data, we will review some of the required theoretical background and give some examples of various types of systems that might be encountered in practice.

2.5.1. Law of Mass Action

Our analyses are based on the law of mass action which basically states that the rate of a chemical reaction is proportional to the effective concentrations (i.e., activities) of the reactants.

Thus for a single irreversible bimolecular reaction we can write

$$A + B \underset{k_r}{\overset{k_f}{\rightleftarrows}} C, \tag{4.2}$$

where k_f is the forward rate constant, and we have, in the ideal case, the rate of formation of the product, C, expressed by

$$\frac{\partial [C]}{\partial t} = k_f [A][B]. \tag{4.3}$$

Similarly, for a reversible bimolecular reaction we can also write for the reverse reaction that the rate of disappearance of the product, C, is expressed by

$$\frac{\partial [C]}{\partial t} = -k_r [C]. \tag{4.4}$$

The equilibrium state, for a rapidly reversible system, for which $\partial [C]/\partial t$ must be equal to zero, can be represented by equating the forward and reverse rates. Rearranging, we have

$$\frac{\partial [C]}{\partial t} = k_f [A][B] - k_r [C], \tag{4.5}$$

$$k_f [A][B] = k_r [C], \tag{4.6}$$

$$K_{eq} = \frac{k_f}{k_r} = \frac{[C]}{[A][B]}. \tag{4.7}$$

In the case of nonideal conditions, and in general, one must write that the rates are proportional to the activities of the species participating in the reaction. Activity coefficients, therefore, must be taken into account.

In this case we write

$$K_{eq} = \frac{k_f}{k_r} = \frac{a_C}{a_A a_B} = \frac{y_C}{y_A y_B} \frac{[C]}{[A][B]}, \tag{4.8}$$

where the a_i are the activities and the y_i are the molar activity coefficients.

2.5.2. Theory of Interacting Systems by Sedimentation Velocity

2.5.2.1. Ideal Systems

In general, in the ideal case, each species is characterized by four parameters, molar mass, sedimentation coefficient, partial specific volume, and loading concentration. The diffusion coefficient is related to the molar mass, the partial specific volume, and the sedimentation coefficient through the Svedberg equation:

$$\frac{s}{D} = \frac{M(1 - v\rho)}{RT}, \tag{4.9}$$

where s is the sedimentation coefficient, D is the diffusion coefficient, M is the molar mass, v is the partial specific volume, ρ is the density of the buffer, R is the gas constant, and T is the absolute temperature. Most of relationships used in this chapter have been defined in the older literature; for further information see those works and references therein *(20–24)*. The factor $(1-v\rho)$ is called the density increment, $(\partial \rho / \partial c)_{T,\mu i}$, which is an empirical quantity obtained by measuring the density of the protein solution as a function of protein concentration with the restriction that the chemical potential of all diffusible components is held constant, that is, that the solution be at osmotic (dialysis) equilibrium with respect to all diffusible components *(8)*.

The frictional coefficient is related to both the sedimentation and diffusion coefficients by the following two relationships:

$$D = \frac{RT}{N_A f} \quad \text{and} \quad s = \frac{M(1 - v\rho)}{N_A f}, \tag{4.10 A\&B}$$

where N_A is Avogadro's number.

The frictional coefficient is also related to the Stokes radius by the following relationship:

$$f = 6\pi\eta_o R_s \tag{4.11}$$

2.5.2.2. Nonideal Systems

There are two types of nonideality that must be considered, thermodynamic and hydrodynamic. Thermodynamic nonideality affects mainly diffusion and the equilibrium constants through the activity coefficients. Hydrodynamic nonideality affects both sedimentation and diffusion through the frictional coefficient.

Thermodynamic nonideality is usually treated through activity coefficients and has the form *(25)*

$$\left(1 + \frac{\partial \ln(y_i)}{\partial \ln c_i}\right). \tag{4.12}$$

Hydrodynamic nonideality is usually treated by the following empirical relation:

$$f = f_o(1 + K_s c) \tag{4.13}$$

so that

$$s = \frac{M(1 - v\rho)}{N_A f_o(1 + K_S c)} = \frac{s_o}{(1 + K_S c)}, \tag{4.14}$$

$$D = \frac{D_o}{N_A f_o(1 + K_S c)} \left(1 + \frac{\partial \ln(y)}{\partial \ln c}\right). \tag{4.15}$$

Attributing the hydrodynamic nonideality to the frictional coefficient rather than to s and D separately and the thermodynamic nonideality to the diffusion coefficient has been proposed by Harding and Johnson in 1985 *(26)* and used recently in a more approximate form by Solyovvia et al. in 2001 *(27)*.

Traditionally, the thermodynamic nonideality term is expanded in a virial series:

$$1 + \frac{\partial \ln(y)}{\partial \ln c} = 1 + 2BM_1 c + Oc^2 + \ldots. \tag{4.16}$$

The term arising from the Donnan effect, $2BM_1$, for a monomer dimer system is given by *(28)*

$$2BM_i = \frac{Z_i^2}{M_i m_3}, \tag{4.17}$$

where Z_i is the charge on the protein, M_i is the molar mass of the protein, and m_3 is the molality of the salt contributing to the ionic strength.

2.6. Curve Fitting to Sedimentation Velocity Profiles

Nonlinear curve fitting to sedimentation profiles requires generating model boundary profiles as a function of time for each set of parameter guesses. These curves are compared to the data and the root mean squared deviation (rmsd) is computed. The parameters are varied systematically until the rmsd is minimized. A fit is considered "good" if the rmsd is of the same magnitude as the noise level of the data and the deviations between the data curves and the fitted curves are random with no systematic trends.

2.6.1. Numerical Solutions to the Lamm Equation

The continuity equation for sedimentation processes, first published by Lamm in 1929 *(29)*, is basically a statement of the conservation of mass during sedimentation in a sector-shaped cell.

In cylindrical coordinates it can be represented by the following differential equation:

$$\left(\frac{\partial c}{\partial t}\right)_r = -2\frac{\partial}{\partial \xi}\left[\omega^2 \xi s c - \xi D \left(\frac{\partial c}{\partial \xi}\right)_t\right], \tag{4.18}$$

where $\xi = r^2/2$ and the other parameters have their usual meaning.

Solution of the Lamm partial differential equation can be achieved by numerical methods. A particularly rapid method of solving the Lamm equation was published by Claverie, Dreux, and Cohen in the mid 1970s (30, 31) and has been employed since then by many investigators for curve fitting AUC data.

Most notable was the first application of Claverie's method to curve fitting published by Todd and Haschemeyer in 1981 and 1983 (32, 33). Before the use of numerical solutions, several investigators used approximate solutions for linear least-squares curve fitting. The first of these was a program called SEDFIT whose use was first published in 1979 by Les Holladay (34, 35). Since then there are several others who have published similar methods: Philo has developed a program called Svedberg (36) and Behlke has developed a program called Lamm (37). Both of these latter methods employ highly accurate approximate solutions to the Lamm equation.

Several software packages have been developed for the analysis of sedimentation data employing solutions to the Lamm equation as their basis. These will be considered below after the presentation of examples of several types of noninteracting and interacting systems – both ideal and nonideal. It should be noted that the two types of system must be analyzed in very different ways.

3. Examples of Noninteracting and Interacting Systems Analyzed by Sedimentation Velocity

For the purposes of this discussion, $g(s)$ patterns will be used to demonstrate various points since they preserve the true shapes of the sedimenting boundary. The $g(s)$ patterns are essentially concentration gradient curves with respect to the radial axis expressed in svedberg units, and therefore, represent the true shapes of the concentration distribution at specific times of sedimentation. For an ideal, noninteracting system the $g(s)$ curves include and preserve the effects of both sedimentation and diffusion. In the case of ideal, interacting systems, they include, in addition to the effects of sedimentation and diffusion, the effects that the rapidly reversible interaction has on the shape of the boundary. The shapes of "diffusion-free" reaction boundaries for interacting systems were first presented in 1950s by Gilbert and Gilbert and Jenkins (38–40). Moreover, it should be stressed that

rigorous analysis of interacting systems (both ideal and nonideal) requires curve fitting to numerical solutions of the Lamm equations in which the reversible interactions and nonideality are specifically taken into account by including the appropriate interaction scheme and type of nonideality in the model being fitted.

3.1. Noninteracting System

3.1.1. Ideal Monomer–Dimer, Noninteracting:

In an ideal, noninteracting system upon dilution, the $g(s)$ patterns (left ordinate) are similar geometrically and the peaks (and other features of the boundary) do not shift with concentration (**Fig. 4.1**). This is the hallmark of an ideal, noninteracting system: normalized plots will all superimpose since the boundary shapes differ only in their amplitudes. The slight splitting of the $c(s)$ peak at the monomer position (at 4.0S) results because the fit uses the same average value of f/f_o for both species. This approximation is reasonably close in this case but because the fit is dominated by the value of f/f_o of the dimer (since it is present at twice the mass concentration) the fit is not as good as it could have been had the values of f/f_o had been allowed to float independently for each species. For further information on the use and limitations of $c(s)$ analysis see the SEDFIT website *(41)*.
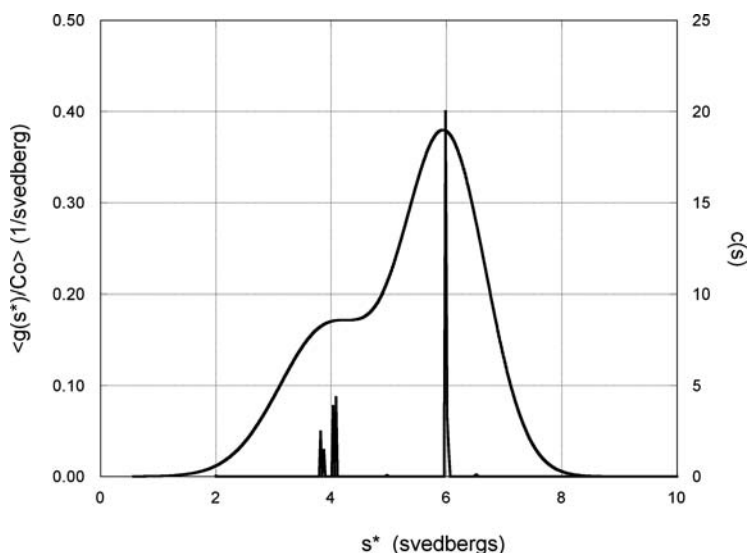

Fig. 4.1. The *left-hand* ordinate is a plot of $g(s^*)$ vs. s^* and the *right-hand* ordinate is a plot of $c(s)$ vs s^* over the same time interval as for $g(s^*)$ and gives the expected sharp delta-function-like peaks centered at the values of the sedimentation coefficients of the two species in this mixture. As mentioned in the text, in this case s^* is the radial coordinate expressed in units of svedbergs.

<table>
<tr><td>

3.1.2. Nonideal
Noninteracting
Monomer–Dimer
System

</td><td>

Nonideality, on the other hand, results in a very different behavior that must be dealt with by direct fitting of the concentration profiles using numerical solutions to the Lamm equation. The available fitting techniques will be discussed in more detail below. For the time being, we will consider the behavior to be expected from several types of system likely to be encountered in practice.

Figure 4.2. shows $g(s)$ plots of the same system as in **Fig. 4.1** under nonideal conditions with a value of $K_s = 0.1$ L/g and BM $= 0.1$ L/g for each species (*see* **Eqs. (4.14)** and **(4.15)**) as the loading concentration is varied from 0.05 g/L to 15 g/L for the monomer species in an equimolar mixture to a monomer (50,000 g/mol) and dimer. Notice that the dimer is swept up together with the monomer into a single boundary. This kind of nonideal behavior makes it extremely difficult, if not impossible, to detect aggregates under nonideal conditions, particularly at low ionic strength, if the molecules carry significant charge.
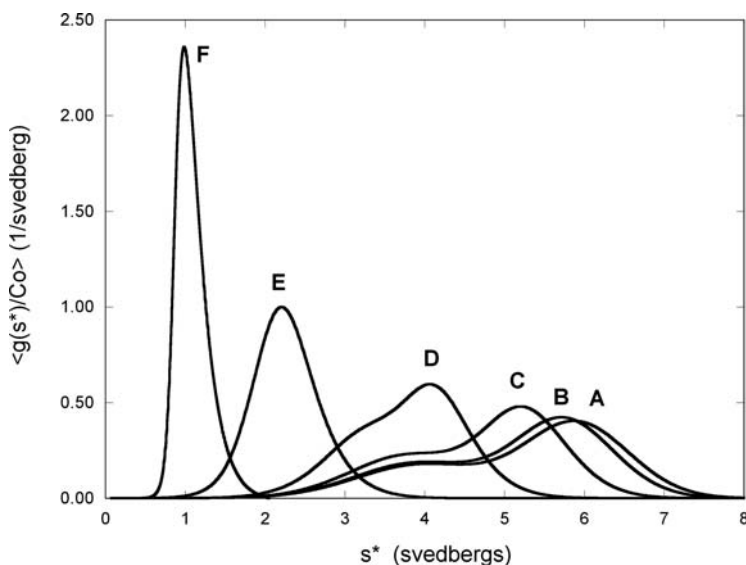
</td></tr>
</table>

Fig. 4.2. Nonideal, noninteracting system: $g(s)$ vs s^*. Equimolar mixture of the same monomer–dimer system shown in **Fig. 4.1**. (A) 0.05 g/L, (B) 0.15 g/L, (C) 0.50 g/L, (D) 1.5 g/L, (E) 5.0 g/L, and (F) 15.0 g/L loading concentration of monomer with $K_s = 0.1$ L/g and $BM_1 = 0.1$ L/g. Note that the curves shift to lower s^* values due to the hydrodynamic nonideality (**Eqs. (4.14)** and **(4.15)**).

<table>
<tr><td>

***3.2. Ideal Reversibly
Interacting Systems***

3.2.1. Reversible
Monomer–Dimer

</td><td>

First we will consider a rapidly reversible, ideal monomer–dimer system, the simplest reversible interacting system. The reaction
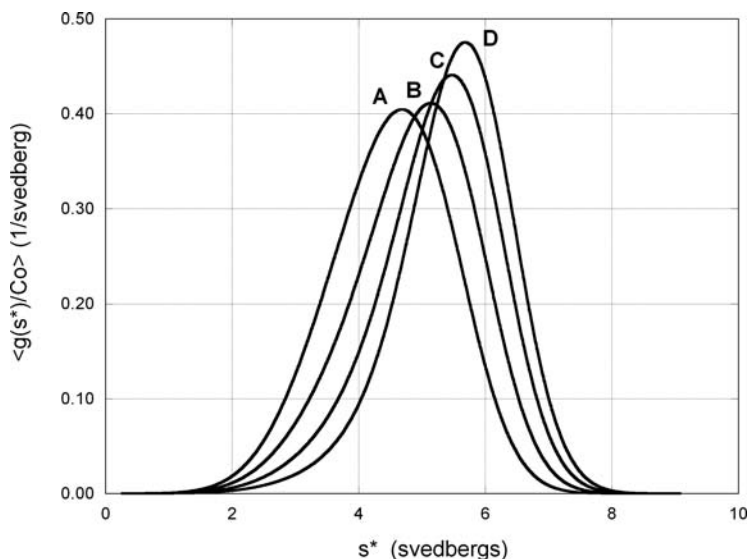
</td></tr>
</table>

Fig 4.3. Monomer–dimer reversible system with $K_{1-2} = 2.5 \times 10^5$ M^{-1}; $M_1 = 50000$; $s_1 = 4.0$S; $s_2 = 6.0$S; $\omega^2 t = 2.1 \times 10^{11}$ rad^2/sec; 50,000 rpm plotted at several loading concentrations. The normalized curves shift to lower s* values upon dilution. Loading concentrations: (A) 1.33 μM, (B) 4 μM, (C) 12 μM, and (D) 36 μM.

boundary for a monomer–dimer system will exhibit a single asymmetric peak that shifts with loading concentration *(42)* (**Fig. 4.3**) The gradient plot from a monomer–dimer system will always be unimodal whereas those for higher stoichiometries will in general be bimodal (*see* **Figs. 4.7–4.9** below) *(42)*.

In **Fig. 4.3** we have a monomer–dimer reversible system with $K_{1-2} = 2.5 \times 10^5$ M^{-1}; $M_1 = 50,000$; $s_1 = 4.0$S; $s_2 = 6.0$S; $\omega^2 t = 2.1 \times 10^{11}$, plotted at several loading concentrations. Note that the normalized curves shift to lower *s* values upon dilution. The loading concentration for each curve is indicated in the figure legend.

Figure 4.4 shows a comparison of *g*(*s*) and *c*(*s*) curves at 0.2 mg/ml (4×10^{-6}M) from **Fig. 4.3**. Left-hand ordinate is the *g*(*s*) plot, which is essentially a plot of the concentration gradient in the cell at the time point indicated, $\omega^2 t = 2.1 \times 10^{11}$. The right-hand ordinate is *c*(*s*), with no smoothing (i.e., regularization = 0.0), from the same narrow time span as for the *g*(*s*) plot. The three spikes represent the values of *s* along with a single value of f/f_o from the Lamm equation solutions required to fit this interacting system to a set of noninteracting Lamm equation solutions.

In this interacting system the monomer and dimer concentrations at each point in the reaction boundary are determined by the equilibrium constant and the total concentration at each point in the boundary (**Fig. 4.5**).
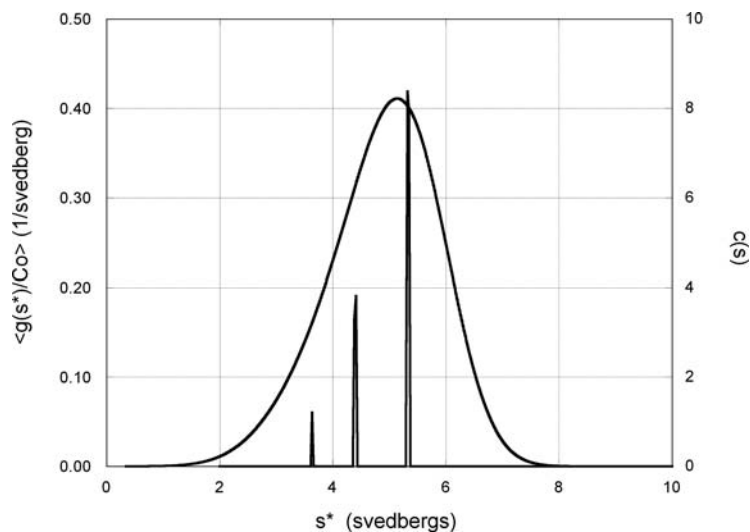
Fig. 4.4. Comparison of $g(s^*)$ and $c(s)$ curves at 0.2 mg/ml (4×10^{-6} M) from **Fig. 4.3**. *Left-hand* ordinate is the $g(s^*)$ plot, which is essentially a plot of the concentration gradient in the cell at the time point indicated, $\omega^2 t = 2.1 \times 10^{11}$ rad^2/sec. The *right-hand* ordinate is $c(s)$, with no smoothing (i.e., regularization $= 0.0$), from the same narrow time span as for the $g(s^*)$ plot. The three spikes represent the values of s^*, along with a single value of f/f_0, required to fit this interacting system to solutions of noninteracting Lamm equation solutions.

When the species concentration gradient distribution is expressed as $g(s)$ for each species in the reaction boundary (**Fig. 4.6**), it becomes clear that the s values at the maximum of each peak are not related to the sedimentation coefficients of the
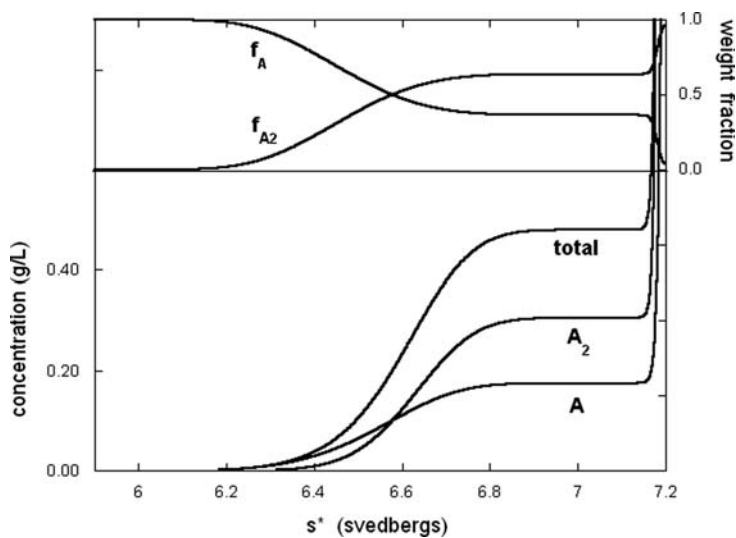

Fig. 4.5. (*Bottom*) Concentration profiles of the monomer (A) and dimer (A2) species in the reaction boundary (total). (*Top*) Weight fraction of monomer (f_A) and dimer (f_{A2}) across the boundary.
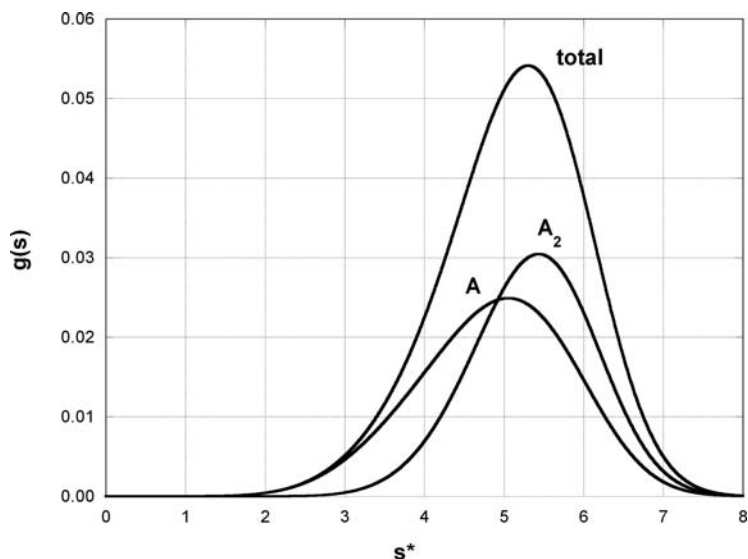
Fig. 4.6. Species concentration gradient distribution expressed as $g(s^*)$ for each species in the reaction boundary for the monomer–dimer system at same time point as in **Fig. 4.5**.

individual species, 4S and 6S, respectively. In addition neither of the concentration gradient curves for A or A_2 is symmetrical, and, therefore, could not be represented by the sum of simple single-species Lamm equation solutions. When this type of data is fit with the sum of noninteracting species using SEDFIT's c(s) the result is shown in **Fig. 4.4**.

3.2.2. Reversible Monomer–Tetramer System

Consider a monomer–tetramer system $M_1 = 30,000$, $s_1 = 3S$, $s_4 = 7.5S$, at 60,000 rpm with $K_a = 1 \times 10^{15}$ M^{-3} (Fig. 4.7). Note that the concentration gradient of monomer is positive throughout the boundary and that the monomer concentration continuously increases across the boundary. **Figure 4.7** shows the total concentration distribution as well as that of free monomer and tetramer across the boundary, expressed as $G(s^*)$ vs. s^*, for the loading concentration of 100 μM. **Figure 4.8** shows the species distributions as $g(s^*)$ vs. s^*.

3.2.3. Hetero-Associating: 2:1 Complex Formation

Now we consider a more complicated hetero-associating system: $A + B = AB$; $AB + B = AB_2$: $K_1 = 2 \times 10^6$; $K_2 = 5 \times 10^5$; $s_A = 4.0S$; $s_B = 6.0S$; $s_C = 7.0S$; and $s_D = 10S$. Initial molar ratio of B to A = 2.0. Loading concentrations for component A are (**Fig. 4.9**). (A) 0.1 μM, (B) 0.3 μM, (C) 1.0 μM, (D) 3.0 μM, and (E) 10.0 μM.

Figure 4.10 shows $g(s^*)$ and $c(s)$ patterns from the reaction boundary obtained for the hetero-associating system shown in **Fig. 4.11**. As for the monomer–dimer system, the series of spikes is the distribution computed with $c(s)$ by allowing f/f_o to float and with no smoothing (i.e., regularization was set to 0.0) These
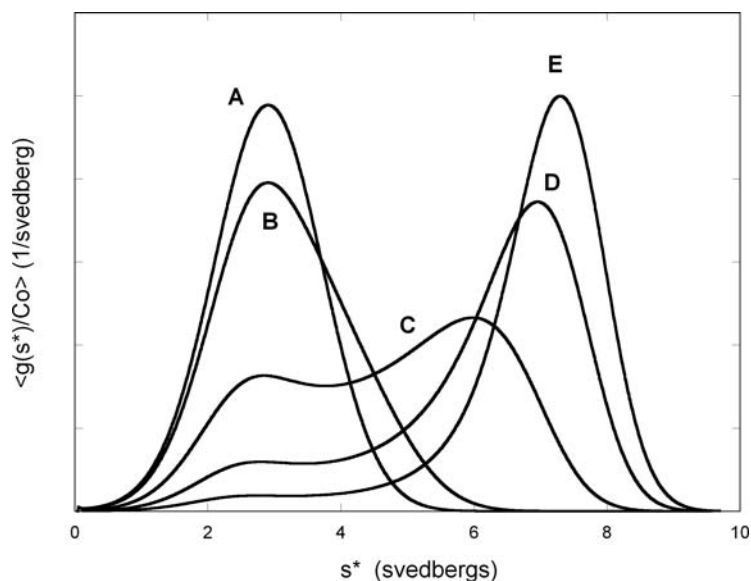
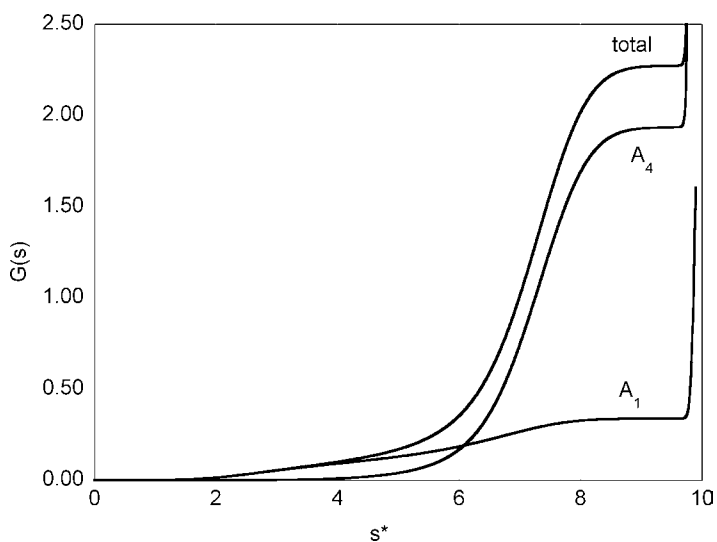Fig. 4.7. Monomer tetramer system as a function of loading concentration. Plot of $g(s)$ vs. s^*.

Fig. 4.8. Reversible monomer tetramer system. Plot of species concentration distribution as $G(s^*)$ vs. S^*.

four spikes represent the values of s to which the Lamm solutions were corresponded and their heights represent the amplitudes (i.e., the loading concentrations) of those four Lamm equation solutions.

As one can readily see, the positions of the spikes bear little relation to the values of s corresponding to the species (4S, 6S, 7S, and 10S) that comprise this reaction boundary. This is because
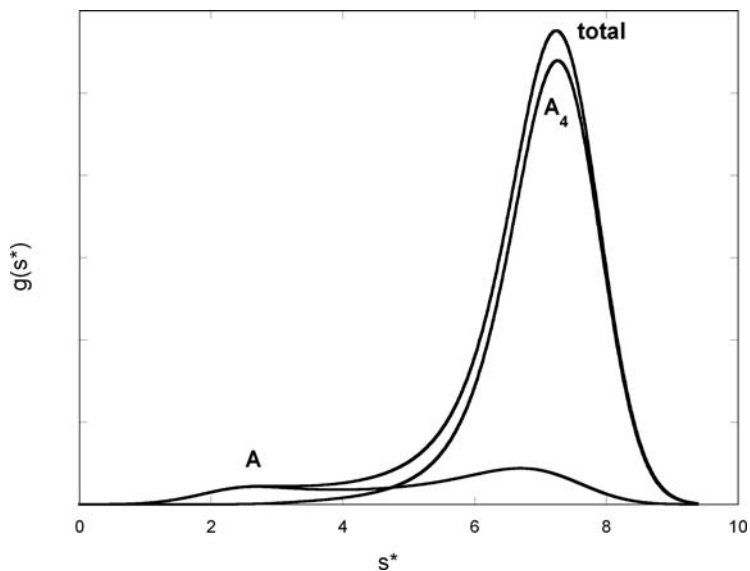
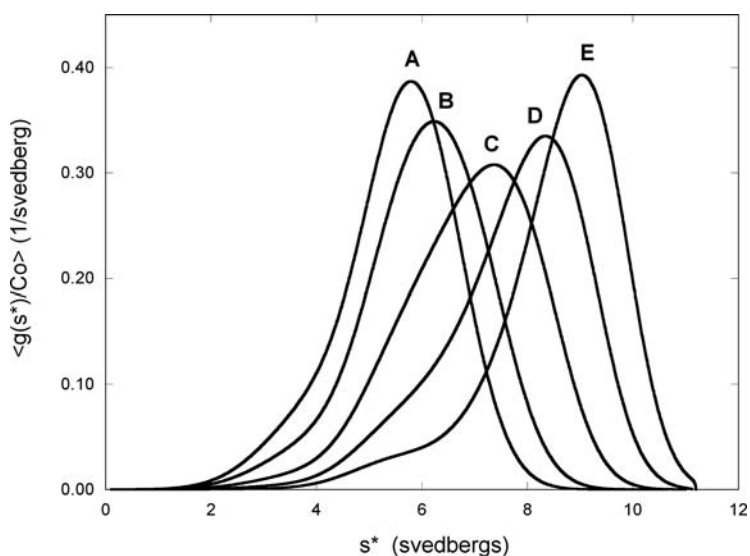Fig. 4.9. Species distribution for the reversible monomer–tetramer system expressed as $g(s^*)$ vs. s.

Fig. 4.10. Hetero-associating system: $A+B=AB$; $AB+B=AB_2$: $K_1 = 2 \times 10^6$ M^{-1}; $K_2 = 5 \times 10^5$ M^{-1}; $s_A = 4.0$S; $s_B = 6.0$S; $s_C = 7.0$S; and $s_D = 10$.S. Initial molar ratio of B to A = 2.0. Loading concentrations of A were (A) 1×10^{-7} M, (B) 3×10^{-7} M, (C) 1×10^{-6} M (D) 3×10^{-6} M and (E) 1×10^{-5} M.

even though there is about 11%(w/w) D present in this sample, there is no feature of the boundary that can be represented by $c(s)$, and, therefore, no single-species Lamm solution is added that corresponds to the complex. Also, not shown here, the residuals
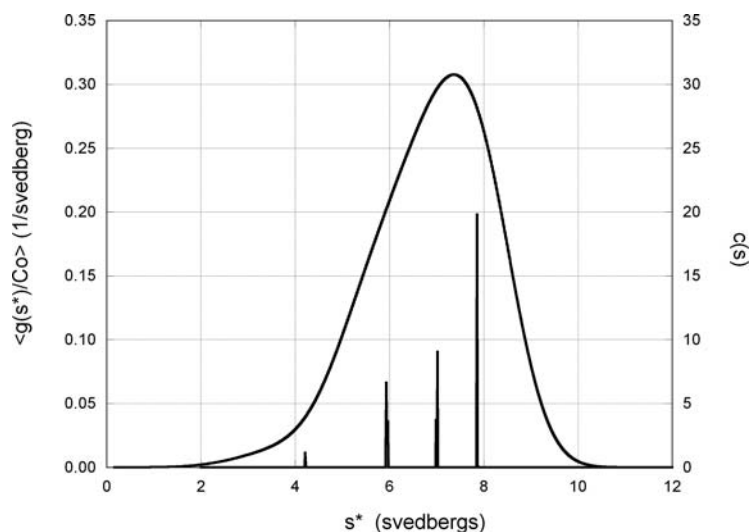
Fig. 4.11. A $g(s^*)$ and $c(s)$ patterns for the simulated hetero-associating system shown in **Fig. 4.10**, curve C at a loading concentrations of $[A]_o = 1$ μM and $[B]_o = 2$ μM.

obtained by fitting $c(s)$ to an interacting system (i.e., wrong model) are usually quite large and systematic. That observation alone should be taken as a clue that a more rigorous method should be used.

Figure 4.12 shows the concentration distribution of each species present in the reaction boundary shown in **Fig. 4.10**. Note that the concentration of A is higher in the presence of
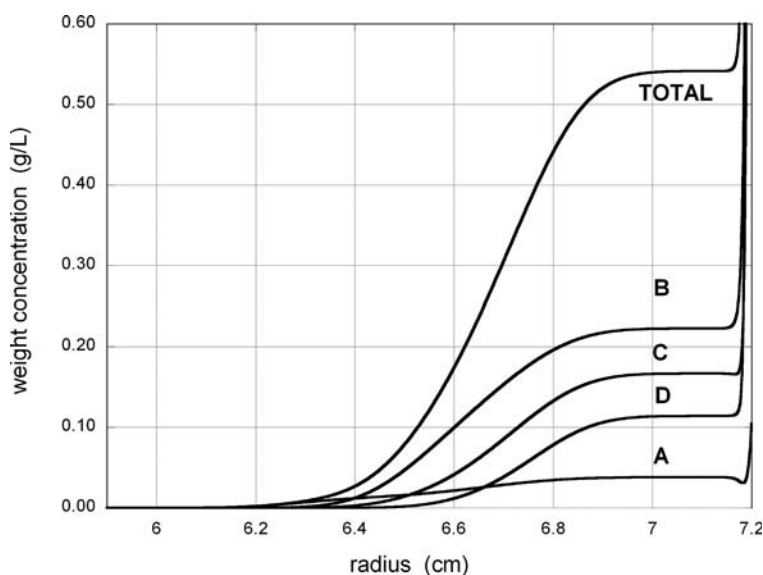

Fig. 4.12. Concentration distribution of each species present in the reaction boundary for the simulated hetero-associating system shown in **Fig. 4.10**.

complex than in the regions depleted in complex. This is a requirement of the law of mass action (*see* also **Fig. 4.13**.). In general, the concentration of the reactants will always increase as the total concentration increases, even though the weight fraction is decreasing. This is a fact that is often not appreciated. This behavior can be seen in **Figs. 4.6**, **4.7**, **4.8**, **4.13**, **4.14**, and **4.18**.
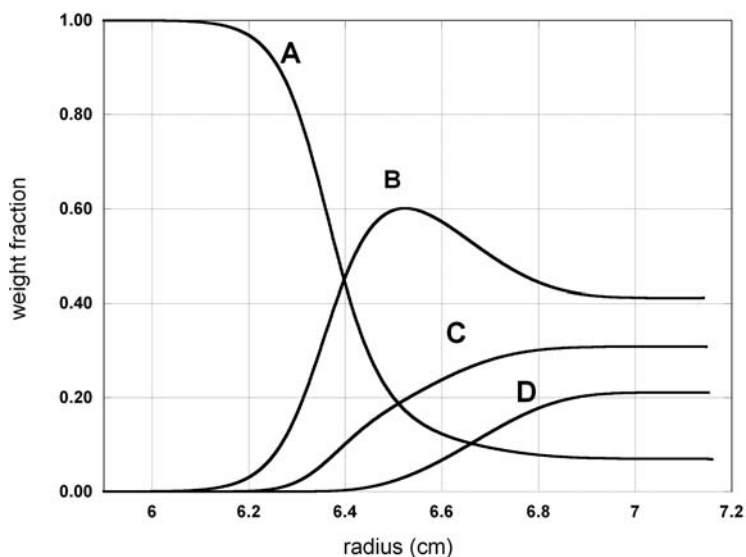

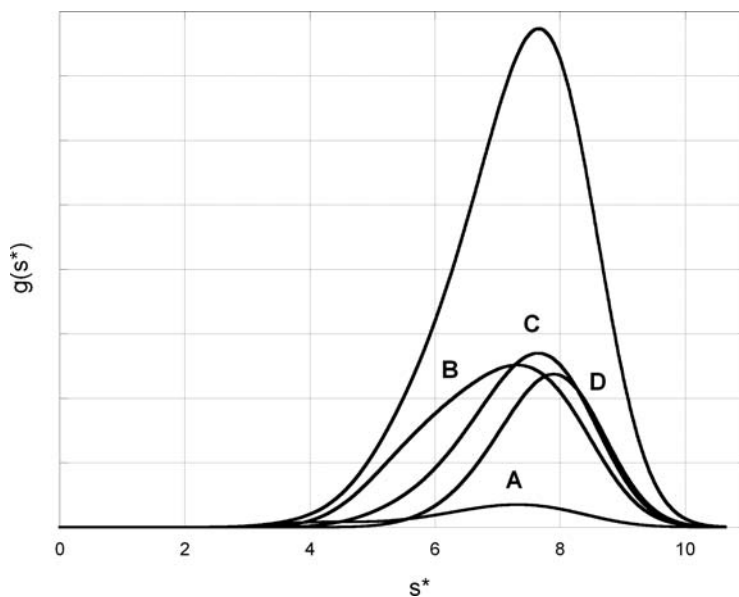Fig. 4.13. Weight fraction of each species within the boundary shown in **Fig. 4.10**.

Fig. 4.14. Gradient curves for each species expressed as $g(s^*)$ for the boundary shown in **Fig. 4.10**.
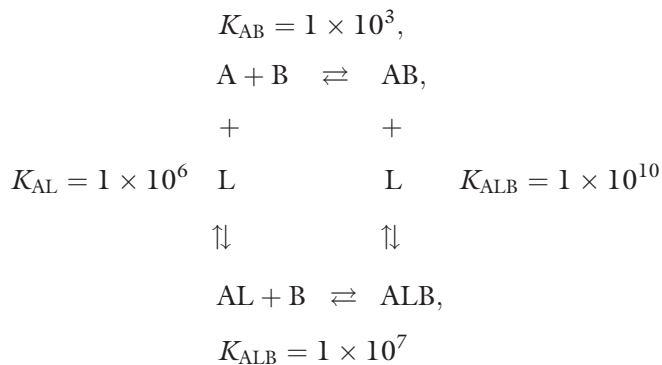
Figure 4.13 shows the weight fraction of each species shown in **Fig. 4.12**, plotted as a function of radius. Note the relative increase of species B near 6.5 cm. In this region of the boundary, excess B is starting to become incorporated into the final complex, D.

Figure 4.14 shows gradient curves for each species expressed as $g(s)$. Note the lack of correspondence of the peak positions in the gradient curves with the s values reported by $c(s)$. The point of showing this series is to point out graphically that the species A, B, C, and D do not sediment independently just as in the case of the reversible monomer–dimer system above. Since their local concentrations are governed by the law of mass action, their sedimentation behavior cannot be described as the sum of ordinary solutions to the Lamm equation. And since that is true, any sedimentation spectral analysis, such as $c(s)$ using SEDFIT, of an interacting system will produce peaks in the distribution that have no meaning other than that they represent the positions of what are essentially Gaussians that give the best fit of the data. The peak values of s returned by the $c(s)$ function have no physical meaning and do not represent the sedimentation of the individual interacting species within the reaction boundary.

Recently, Dam et al. *(43)* have proposed to use $c(s)$ in conjunction with a so-called constant bath approximation, to analyze this type of system. Since the constant bath approximation relies on the assumption that the concentration gradient of the slowest species is negligible over the entire boundary region, and since this is a condition that is frequently not satisfied in most heterologous associations, extreme caution should be exercised in the use of this method and should probably be avoided altogether. A more rigorous and reliable approach would be to fit the data directly using one of the available programs like SEDPHAT, SEDANAL, or UltraScan that explicitly include the appropriate association reaction scheme in the numerical solutions to the Lamm equation, as we will see below.

3.2.4. Ligand Binding to a Hetero-Associating System: Ligand-Induced Association

Consider the following ligand-induced system:

$$K_{AB} = 1 \times 10^3,$$

$$A + B \quad \rightleftarrows \quad AB,$$

$$+ \qquad\qquad +$$

$$K_{AL} = 1 \times 10^6 \quad L \qquad\qquad L \qquad K_{ALB} = 1 \times 10^{10}$$

$$\updownarrow \qquad\qquad\quad \updownarrow$$

$$AL + B \quad \rightleftarrows \quad ALB,$$
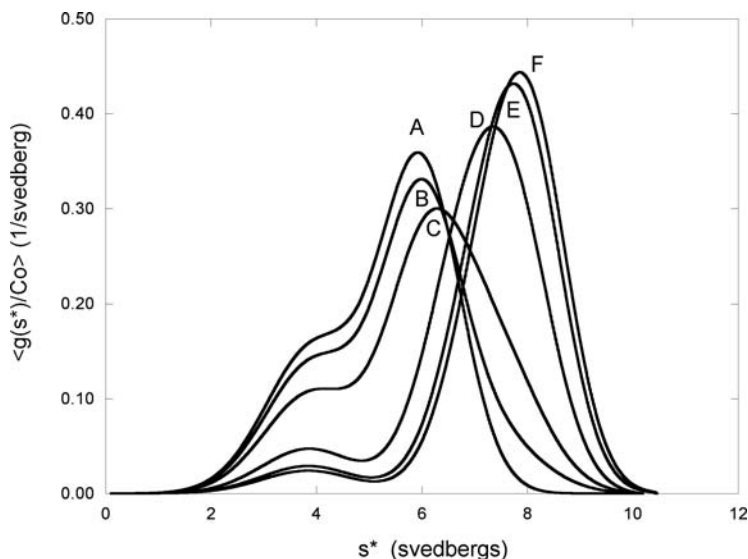
$$K_{ALB} = 1 \times 10^7$$

Fig. 4.15. Ligand-induced association between a 4.0S and a 6.0S component to produce an 8.5S liganded complex. Curves are $g(s^*)$ vs. s^* plotted as a function of ligand concentration, [L] (A) 0.01 μM, (B) 0.03 μM, (C) 0.1 μM, (D) 0.3 μM, (E) 1.0 μM, and (F) 3.0 μM.

Species A is 50,000 g/mol, 4.0S; species B, 100,000 g/mol, 6.0S; and the complex, AB, is 8.0S; The ligand is 300 g/mol with a sedimentation coefficient of 0.14S. The liganded A, AL, is 50,300 g/mol, 4.0S; and the liganded complex, ALB is 150,300 g/mol and 8.5S. The association constant between unliganded A and B is $K_{AB} = 1 \times 10^3 M^{-1}$. The ligand-binding association constant to A is $K_{AL} = 1 \times 10^6 \ M^{-1}$ and the association constant of binding of liganded A to B is $K_{ALB} = 1 \times 10^7 M^{-1}$. The hetero-interaction is very weak in the absence of ligand. The implied constant for binding of ligand, L, to the complex, AB (indicated by square brackets), is $1 \times 10^{10} \ M^{-1}$. There is significant redistribution of ligand during the sedimentation. **Figure 4.15** shows $g(s)$ curves plotted as a function of ligand concentration, spanning a range from 10.0 pM to 3.0 μM after 6800 seconds at 50,000 rpm($\omega^2 t = 1.86 \times 10^{11}$).

3.3. Nonideal, Reversibly Interacting Systems

3.3.1. Nonideal, Reversible Monomer–Dimer System

Consider the same monomer–dimer system as shown above (**Fig. 4.3**) but with added nonideality typical of what one might expect at low ionic strength for globular proteins or for a highly asymmetric protein. The amount of nonideality used in this simulation is of a magnitude typical of what might be observed for
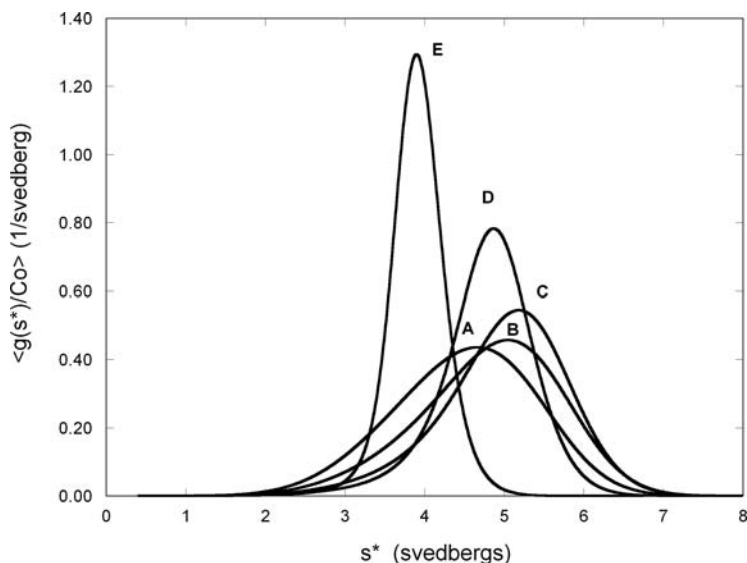
Fig. 4.16. Nonideal reversible monomer–dimer system. $M = 50{,}000$, $s_1 = 4.0S$, $s_2 = 6.0S$, $K_s = 0.1$ L/g, and BM1 $= 0.1$ L/g; $K_{1-2} = 2.5 \times 10^5$ M. Normalized plots of $g(s^*)$ vs. s^* for various loading concentrations: (A) 1.33 µM, (B) 4.0 µM, (C) 12.0 µM, (D) 36.0 µM, and (E) 108 µM.

charged proteins at low ionic strength. The term BM_1 arising from the Donnan effect for a monomer–dimer system is given by **Eq. (4.17)**. For a protein of molar mass 50,000 g/mol with an effective charge of ±7 at an ionic strength of 10 mM, the value of BM_1 would be about 0.1 L/g.

There are two features of which one should take note in **Fig. 4.16**.: the peak of the gradient curves initially increases from about 4.6S to 5.2S before starting to decrease due to the nonideality which becomes more significant at the higher concentrations. As the peak value decreases at the higher concentrations, the peaks also become narrower due to the self-sharpening effect which results because of the hydrodynamic concentration dependence, which causes the molecules at higher concentrations to sediment more slowly than those at lower concentrations. This effect is expressed through K_s. As one can see from this example, nonideality can completely obscure evidence of an interaction (**Fig. 4.16**).

3.3.2. Nonideal Hetero-Associating System

We will consider the same hetero-associating system as shown in **Fig. 4.7**, but now under simulated low-ionic-strength conditions (**Fig. 4.17**): $A+B = AB$; $AB+B = AB_2$; $K_1 = 2 \times 10^6$ M^{-1}; $K_2 = 5 \times 10^5$ M^{-1}; $s_A = 4.0S$; $s_B = 6.0S$; $s_C = 7.0S$; and $s_D = 10.S$. Molar ratio of B to A $= 2.0$. Loading concentrations of A were (A) 1.e-7, (B) 3.33e-7 M (C) 1.e-6 M (D) 3.e-6 M, (E) 9e-6 M, (F) 2.7e-5 M, and (G) 8.1e-5 M. Nonideality is $K_s = 0.1$ L/g and $BM_i = 0.1$ L/g.
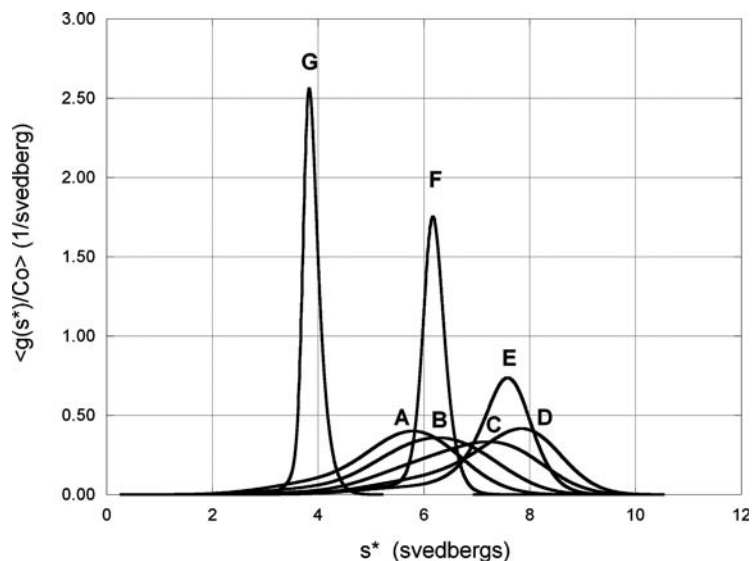
Fig. 4.17. Nonideal hetero-associating system $A+B=AB$ $AB+B=AB_2$: $K_A = 2.5 \times 10^5$, $s_A = 4.0S$, $s_B = 6.0S$; $s_C = 7.0S$, and $s_D = 10.S$. Molar ratio of B to A = 2.0. Loading concentrations of A were $\times$ (A) 1×10^{-7} M, (B) 3.33×10^{-7} M, (C) 1×10^{-6} M, (D) 3×10^{-6} M, (E) 9×10^{-6} M, (F) 2.7×10^{-5} M, and (G) 8.1×10^{-5}M. Nonideality was $K_s = 0.1$ L/g and $BM_i = 0.1$L/g.

Fig. 4.18. Nonideal hetero-associating system $A+B=AB$ $AB+B=AB_2$. Plot of the species distribution within the boundary whose $g(s)$ curve is show in **Fig. 4.14**, curve G, at 8.1×10^{-5}M. Note that although this boundary is sedimenting with a peak s^* value of somewhat less than the 4.0S reactant A, it is composed mainly of doubly liganded complex, AB_2 (curve D).

As can be seen again in this example, nonideality can completely obscure evidence of an interaction (**Fig. 4.17**.). The amount of nonideality used in this simulation is of a magnitude typical of what might be observed for charged proteins at low ionic strength. **Figure 4.18** is a plot of the species d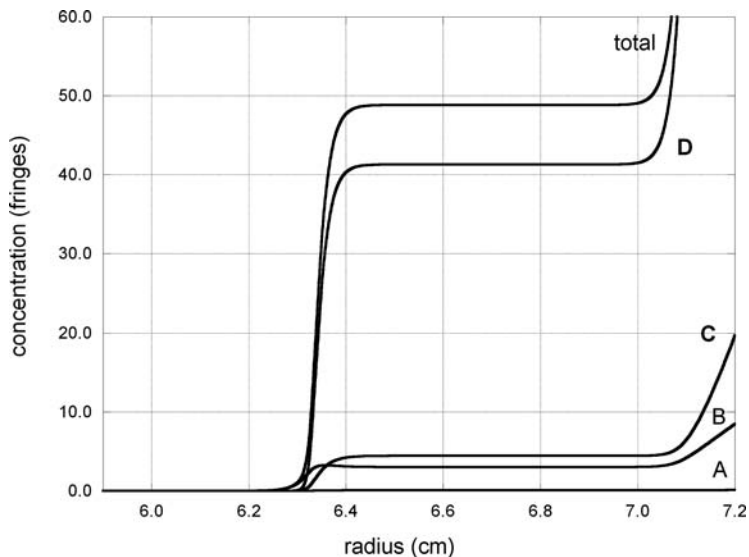istribution within the boundary whose $g(s)$ curve is shown in **Fig. 4.17**, curve G, at 8.1×10^{-5} M. Note that although this boundary is sedimenting with a peak s value of somewhat less than 4.0S, it is composed mainly of doubly liganded complex, AB_2 (curve D).

4. Analysis by Curve Fitting Data with Solutions to the Lamm Equation

These complex systems can be analyzed successfully by modeling the sedimenting reaction boundaries using nonlinear curve-fitting methods. Numerical solutions to the Lamm equation with step-by-step computation of the redistribution of species according to the law of mass action are computed for various guesses of the parameters. The procedure is repeated until a set of guesses that give the least RMS residual (L-2 Norm) or least average magnitude of the residuals (L-1 Norm) is found. Both rapidly reversible and kinetically limited interactions can be treated while taking nonideality into account. Moreover, one can combine data from multiple optical systems to allow discrimination between species. In general, one should sample the widest range of concentration possible in order to populate significantly all species in the model being fitted.

There are several popular software packages that can be used rigorously to analyze interaction systems. For the specific application of these packages, you are referred to the authors' websites and publications. The program SEDANAL *(12)* can be found at http://SEDANAL.bbri.org/; the programs SEDFIT and SEDPHAT *(16)* can be found at http://www.analyticalultracentrifugation.com/, and the program UltraScan *(44)* can be sound at http://ultrascan.uthscsa.edu/. Other useful AUC analysis software can be found at http://rasmb.bbri.org/rasmb/

References

1. Svensson, H. (1954) The second order aberrations in the interferometric measurement of concentration gradients. *Optica Acta* **1**, 25–32.

2. Svensson, H. (1954) The second order aberrations in the interferomentric measurement of concentration gradients. II. Experimental verification of theory. *Optica Acta* **1**, 90–93.

3. Svensson, H. (1956) The third order aberrations in the interferometric measurement of concentration gradients. *Optica Acta* **3**, 164–168.

4. Stafford, W. F. (unpublished observation).

5. Richards, E. G., Teller, D., Schachman, H. K. (1971) Alignment of Schlieren and Rayleigh optical systems in the ultracentrifuge. I. Focusing of the camera and cylindrical lenses. *Anal Biochem* **41**, 189–214.

6. Richards, E. G., Teller, D. C., Hoagland, V. J., et al. (1971) Alignment of Schlieren and Rayleigh optical systems in the ultracentrifuge. II. A general procedure. *Anal Biochem* **41**, 215–247.

7. Richards, E. G., Bell, C. J., Kirschner, M., et al. (1972) Alignment of Schlieren and Rayleigh optical systems in the ultracentrifuge. 3. Design, construction, and placement of Rayleigh mask. *Anal Biochem* **46**, 295–331.

8. Casassa, E. F., Eisenberg, H. (1964) Thermodynamic analysis of multicomponent solutions. *Adv Protein Chem* **19**, 287–395.

9. Kar, S. R., Kingsbury, J. S., Lewis, M. S., et al. (2000) Analysis of transport experiments using pseudo-absorbance data. *Anal Biochem* **285**, 135–142.

10. Schuck, P., Demeler, B. (1999) Direct sedimentation analysis of interference optical data in analytical ultracentrifugation. *Biophys J* **76**, 2288–2296.

11. Stafford, W. F. (1992) Boundary analysis in sedimentation transport experiments: a procedure for obtaining sedimentation coefficient distributions using the time derivative of the concentration profile. *Anal Biochem* **203**, 295–301.

12. Stafford, W. F., Sherwood, P. J. (2004) Analysis of heterologous interacting systems by sedimentation velocity: Curve fitting algorithms for estimation of sedimentation coefficients, equilibrium and rate constants. *Biophys Chem* **108**, 231–243.

13. Rivas, G., Stafford, W. F., Minton, A. P. (1999) Characterization of heterologous protein–protein interaction via analytical ultracentrifugation. *Methods: A Companion to Methods in Enzymology*.

14. Stafford, W. F. (1998) Time difference sedimentation velocity analysis of rapidly reversible interacting systems: determination of equilibrium constants by non-linear curve fitting procedures. *Biophys J* **74**, A301.

15. Schuck, P. (1999) Sedimentation equilibrium analysis of interference optical data by systematic noise decomposition. *Anal Biochem* **272**, 199–208.

16. Schuck, P. (2000) Size-distribution analysis of macromolecules by sedimentation velocity ultracentrifugation and Lamm equation modeling. *Biophys J* **78**, 1606–1619.

17. Johnson, M., Faunt, L. (1992) Parameter estimation by least-squares methods. *Methods in Enzymology* **210**, 1–37.

18. Johnson, M. L. (1992) Why, when, and how biochemists should use least squares, *Anal Biochem* **206**, 215–225.

19. Schuck, P., Perugini, M. A., Gonzales, N. R., et al. (2002) Size-distribution analysis of proteins by analytical ultracentrifugation: strategies and application to model systems, *Biophys J* **82**, 1096–1111.

20. Svedberg, T., Pederson, K. O. (1940) *The Ultracentrifuge*, Oxford University Press, New York.

21. Schachman, H. K. (1959) . Academic Press, New York.

22. Williams, J. W., Van Holde, K. E., Baldwin, R. L., et al. (1958) The theory of sedimentation analysis. *Chem Rev* **58**, 715–806.

23. Fujita, H. (1962) *Mathematical Theory of Sedimentation Analysis*. Academic Press, New York.

24. Fujita, H. (1976) *Foundations of Ultracentrifugal Analysis*. John Wiley & Sons, New York.

25. Tanford, C. (1961) *Physical Chemistry of Macromolecules*, p. 710. John Wiley & Sons, New York.

26. Harding, S. E., Johnson, P. (1985) The concentration-dependence of macromolecular parameters, *Biochem J* **231**, 543–547.

27. Solovyova, A., Schuck, P., Costenaro, L., Ebel, C. (2001) Non-ideality by sedimentation velocity of halophilic malate dehydrogenase in complex solvents, *Biophys J* **81**, 1868–1880.

28. Roark, D. E., Yphantis, D. A. (1971) Equilibrium centrifugation of nonideal systems. The Donnan effect in self-associating systems. *Biochemistry* **10**, 3241–328149.

29. Lamm, O. (1929) Die Differentialgleichung der Ultrazentrifugierung. *Arkiv Math. Astron. Fysik* **21B, No.2**, 1–4.

30. Claverie, J.-M. (1976) Sedimentation of generalized systems of interacting particles III. Concentration dependent sedimentation

and extension to other transport methods. *Biopolymers* **15**, 843–857.

31. Claverie, J. M., Dreux, H., Cohen, R. (1975) Sedimentation of generalized systems of interacting particles. I. Solution of systems of complete Lamm equations. *Biopolymers* **14**, 1685–1700.

32. Todd, G. P. Haschemeyer, R. H. (1981) General solution to the inverse problem of the differentia17l equation of the ultracentrifuge. *Proc Natl Acad Sci U S A* **78**, 6739–6743.

33. Todd, G., Haschemeyer, R. (1983) Generalized finite element solution to one-dimensional flux problems. *Biophys Chem* **17**, 321–326.

34. Holladay, L. (1980) Simultaneous rapid estimation of sedimentation coefficient and molecular weight. *Biophys Chem* **11**, 303–308.

35. Holladay, L. (1979) An approximate solution to the Lamm equation. *Biophys Chem* **10**, 187–190.

36. Philo, J. S. (1997) An improved function for fitting sedimentation velocity data for low-molecular-weight solutes. *Biophys J* **72**, 435–444.

37. Behlke, J., Ristau, O. (2002) A new approximate whole boundary solution of the Lamm differential equation for the analysis of sedimentation velocity experiments. *Biophys Chem* **95**, 59–68.

38. Gilbert, G. A. (1955) The physical chemistry of enzymes – general discussion. Discuss. *Farad Soc* **20**, 65–77.

39. Gilbert, G. A. (1959) Sedimentation and electrophoresis of interacting substances .1. Idealized boundary shape for a single substance aggregating reversibly. *Proc R Soc* **A253**, 377–388.

40. Gilbert, G. A., Jenkins, R. C. (1959) Sedimentation and electrophoresis of interacting substances .2. Asymptotic boundary shape for 2 substances interacting reversibly, *Proc. R Soc* **A253**, 420–437.

41. Schuck, P. (www.analyticalultracentrifugation.com/references.htm.).

42. Cann, J. R. (1970) **89** *Interacting Macromolecules.* New York: Academic Press.

43. Dam, J., Velikovsky, C. A., Mariuzza, R. A., et al. (2005) Sedimentation velocity analysis of heterogeneous protein–protein interactions: Lamm equation modeling and sedimentation coefficient distributions $c(s)$, *Biophys J*, 619–34.

44. Demeler, B. (2005) *UltraScan A Comprehensive Data Analysis Software Package for Analytical Ultracentrifugation Experiments, in Modern Analytical Ultracentrifugation: Techniques and Methods*, S.E.H.a.A.J.R. D. J. Scott, Editor. 2005, Royal Society of Chemistry, UK. p. 210–229.

Chapter 5

Monitoring Molecular Interactions by NMR

James M. Lipchock and J. Patrick Loria

Abstract

The ability of proteins to interact with small molecules or other proteins is essential in all aspects of biology. In many cases these interactions cause detectable changes in NMR chemical shifts, lineshapes, and relaxation rates and therefore provide a means by which to study these biologically important phenomena. Here we review the theory upon which this analysis is based, provide several illustrative examples, and highlight potential problems in the study of binding interactions by solution NMR.

Key words: Conformational exchange, relaxation dispersion, protein binding, protein dynamics, relaxation-compensated CPMG, spin-relaxation.

1. Introduction

Life requires the successful interaction between molecules. The most simple and fundamental biological processes would be impossible without them. The study of a subset of these interactions, protein–protein and protein–ligand, by solution nuclear magnetic resonance (NMR) spectroscopy is the subject of this chapter. Many excellent reviews exist that analyze the effects that a binding partner has on internal protein dynamics *(1, 2)*. In contrast, here we focus on the use of NMR methods to monitor binding events and, in particular, characterize their kinetics. First, **(Section 2.1)**, we cover the theory of longitudinal and transverse relaxation rates as they apply to the study of protein–protein interactions. Next, the effects of macromolecular binding on NMR lineshapes and transverse relaxation rates are reviewed **(Section 2.2)**. Finally, we illustrate a few applications and the limitations of these techniques through examination of some published examples **(Sections 3** and **4)**.

2. Theory

2.1. Spin-Relaxation Rates and Molecular Motion

All of the examples described below are for an isolated, hetero-nuclear two-spin (I-S) system comprised of two spin-$1/2$ nuclei. Under these restrictions, longitudinal (S_z) and transverse ($S_{x,y}$) magnetization, respectively, decays or relaxes back to its Boltzmann equilibrium value according to *(3)*

$$R_1 = d[3J(\omega_S) + J(\omega_I - \omega_S) + 6J(\omega_I + \omega_S)] + cJ(\omega_S) \quad (5.1)$$

and

$$R_2 = \frac{d}{2}[4J(0) + 3J(\omega_S) + J(\omega_I - \omega_S) + 6J(\omega_I) + 6J(\omega_I + \omega_S)]$$
$$+ \frac{c}{6}[4J(0) + 3J(\omega_S)] + R_{ex,} \quad (5.2)$$

where $d = (1/2)(\mu_0/4\pi)^2 \hbar^2 \gamma_I^2 \gamma_S^2 \langle r_{IS}^{-6} \rangle$ is the dipolar coupling constant and $c = (1/3)\Delta\sigma^2 \omega_S^2$; μ_0 is the permeability of free space, $\hbar$ is Planck's constant divided by 2π, $\gamma_{I(S)}$ are the gyromagnetic ratios of the I and S nuclei, r_{IS} is the average internuclear I–S bond length, $\omega_{I(S)}$ is the Larmor frequency of the I(S) nuclei, $\Delta\sigma$ is the chemical shift anisotropy (CSA) of the S nucleus, and R_{ex} is the contribution due to conformational or chemical exchange on the chemical shift timescale. For I and S, referring to either amide ^1H-^{15}N or ^1H-$^{13}C^\alpha$ spin systems, the CSA and dipolar I–S interactions are assumed to be collinear. $J(\omega)$ is the spectral density function expressed as the cosine transform of the autocorrelation function ($C(t)$) of the I–S bond vector, such that *(3)*

$$J(\omega) = 2\int_0^\infty C(t)\cos\omega t\,dt. \quad (5.3)$$

Under the assumption that intramolecular motion is more rapid and uncorrelated with the macromolecular rotational tumbling, the autocorrelation function for the system can be written as the product of two autocorrelation functions *(4)*:

$$C(t) = C_O(t)C_I(t) \quad (5.4)$$

where C_O and C_I are the correlation functions for the rotational and internal motions, respectively. If the macromolecule is spherical and undergoes isotropic rotation, then C_O decays in a single exponential fashion, such that

$$C_O(t) = \frac{1}{5}e^{-t/\tau_c} \quad (5.5)$$

where τ_c, the rotational correlation time of the macromolecule, is related to the isotropic diffusion constant and equals $(6D_{iso})^{-1}$. If rotational diffusion is axially symmetric, the overall correlation function is given by *(5)*

$$C_O(t) = \frac{1}{5}\left(A_1 e^{-t/\tau_1} + A_2 e^{-t/\tau_2} + A_3 e^{-t/\tau_3}\right), \qquad (5.6)$$

where $A_1 = (3\cos^2\theta - 1)^2/4$, $A_2 = 3\sin^2\theta\cos^2\theta$, and $A_3 = 0.75 \sin^4\theta$, with θ defined as the angle between the principal axis of the rotational diffusion tensor and the I–S bond vector. The diffusion correlation times given in **Eq. (5.6)** are $\tau_1^{-1} = 6D_\perp$, $\tau_2^{-1} = D_P + 5D_\perp$, and $\tau_3^{-1} = 4D_P + 2D_\perp$, where the diagonal elements of the rotational diffusion tensor (D_{xx}, D_{yy}, and D_{zz}) can be defined: $D_{xx} = D_{yy} = D_\perp$ and $D_{zz} = D_P$. The correlation function for internal motion is

$$C_I(t) = \langle P_2(\hat{\mu}(0) \cdot \hat{\mu}(t))\rangle, \qquad (5.7)$$

in which the orientation of the I–S vector in the molecular frame $\hat{\mu}$ is described by the second Legendre polynomial, $P_2(x) = (3x^2 - 1)/2$. For bond vectors experiencing rapid, small-amplitude intramolecular motions, the R_2/R_1 ratio is primarily determined by the overall rotational correlation time and, to a first approximation, is independent of the internal bond vector motions. Thus the R_2/R_1 ratio can be used to estimate τ_c because *(6–8)*

$$\frac{R_2}{R_1} =$$

$$\frac{[4J(0) + 3J(\omega_S) + J(\omega_I - \omega_S) + 6J(\omega_I) + 6J(\omega_I + \omega_S)] + \frac{c}{3d}[4J(0) + 3J(\omega_S)]}{[6J(\omega_S) + 2J(\omega_I - \omega_S) + 12J(\omega_I + \omega_S)] + 2(c/d)J(\omega_S)}$$

$$(5.8)$$

and for isotropic overall rotation the spectral density is independent of the orientation of the I–S bond vector, such that

$$J(\omega) = \frac{\tau_c}{1 + \omega^2\tau_c^2}. \qquad (5.9)$$

For the case of axially symmetric rotational correlation with two unique diffusion coefficients the spectral density function for the ith I–S bond vector is given by

$$J_i(\omega) = \sum_{j=1}^{3} A_{ji} \frac{\tau_j}{1 + \omega^2\tau_j^2}, \qquad (5.10)$$

where the prefactor, A, and correlation times are given by **Eq. (5.6)**. Thus, in the isotropic case the rotational correlation time can be obtained from the ratio of R_2 and R_1, providing a measure of the size or oligomeric state of the molecule under study. For axially symmetric rotational diffusion, the R_2/R_1 ratio and some knowledge of the hydrodynamic properties of the protein can also lead to insight into the aggregation state of the protein. This analysis assumes that chemical (conformational) exchange is negligible, that is, $R_{ex} = 0$, for the sites under investigation.

However, motions that give rise to conformational exchange can also be utilized to assess protein–protein or protein–ligand

interactions. Conformational exchange transfers the nuclear spin between distinct magnetically inequivalent environments on the μs–ms timescale. Protein–protein or protein–ligand binding processes can be represented by the following respective equations:

$$nA \underset{k_{-1}}{\overset{k_1}{\rightleftharpoons}} B \qquad (5.11)$$

and

$$A + L \underset{k_{-1}}{\overset{k_1}{\rightleftharpoons}} A \bullet L. \qquad (5.12)$$

In **Eq. (5.11)**, A signifies the monomer unit, associating to form an *n-mer* (B). In **Eq. (5.12)** protein (A) binds to ligand (L). The conformational exchange rate constant that characterizes these processes is $k_{ex} = k_1' + k_{-1}$. In **Eq. (5.11)**, for a monomer-dimer equilibrium, $k_1' = 2k_1[A]$, whereas in **Eq. (5.12)**, $k_1' = k_1[L]$. The primary effect of μs–ms motions is to broaden the NMR resonance and increase the transverse relaxation rate, R_2, as indicated by the R_{ex} term in **Eq. (5.2)**. Complex magnetization, under free-precession conditions, that is, exchanging between two distinct magnetic environments, is described by the coupled differential equation known as the Bloch–McConnell equation *(9)*:

$$\frac{\mathrm{d}}{\mathrm{d}t} \begin{bmatrix} M_A^+ \\ M_B^+ \end{bmatrix} = \begin{bmatrix} -i\Omega_A - R_{2A}^0 - p_B k_{ex} & p_A k_{ex} \\ p_B k_{ex} & -i\Omega_B - R_{2B}^0 - p_A k_{ex} \end{bmatrix} \begin{bmatrix} M_A^+ \\ M_B^+ \end{bmatrix}, (5.13)$$

where $p_{A(B)}$ are the fractional populations of site $A(B)$, $R_{2A(B)}^0$ is the exchange-free transverse relaxation rate in site $A(B)$ and $\Omega_{A(B)}$ is the NMR resonance frequency for each site. The Fourier transform of the solution to **Eq. (5.13)** yields the NMR spectrum. The effect of exchange is to broaden the NMR resonance and, more subtly, to shift the resonance position to its population weighted value, $\Omega = p_A\Omega_A + p_B\Omega_B$.

2.2. NMR and Conformational Exchange

The effect of conformational exchange on the transverse relaxation rate can be monitored using Carr–Purcell–Meiboom–Gill (CPMG) spin-echo measurements *(10–14)*. Here, the exchange-induced increase in R_2 depends on the pulse spacing, τ_{cp}, in the spin-echo period (*see* **Fig. 5.1**) as shown mathematically: *(15–17)*
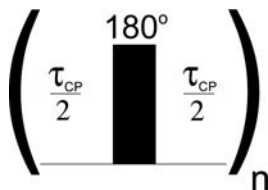

Fig. 5.1. Spin-echo pulse element. The 180° radio frequency pulse is flanked by delays. The total length of the relaxation period is determined by the value of τ_{cp} and n.

$$R_2(1/\tau_{cp}) = \frac{1}{2}\left(R_{2A}^0 + R_{2B}^0 + k_{ex} - \frac{1}{\tau_{cp}}\cosh^{-1}[D_+\cosh(\eta_+) - D_-\cos(\eta_-)]\right),$$
(5.14)

where

$$D_\pm = \frac{1}{2}\left[\pm1 + \frac{\Psi + 2\Delta\omega^2}{\left(\Psi^2 + \zeta^2\right)^{1/2}}\right]^{1/2},$$
(5.15)

$$\eta_\pm = \frac{\tau_{cp}}{2}\left[\pm\Psi + (\Psi^2 + \zeta^2)^{1/2}\right]^{1/2},$$
(5.16)

$$\Psi = k_{ex}^2 + \Delta\omega^2,$$
(5.17)

$$\zeta = -2\Delta\omega \ \ k_{ex}(P_A - P_B)$$
(5.18)

and $\Delta\omega = |\Omega_A - \Omega_B|$, with the remaining terms as defined previously.

When studying protein–ligand interactions by NMR line-shape analysis, the Bloch–McConnell equations describe the chemical exchange contribution to the NMR resonance *(9)*. Under equilibrium conditions for a case of n chemically exchanging sites

$$S(\nu) = \text{Im}\left\{ic\,\vec{1}(\mathbf{R} - i\Omega - \mathbf{K} - i2\pi\nu\mathbf{E})^{-1}\vec{p}\right\},$$
(5.19)

where $S(\nu)$ is the intensity of the spectrum at frequency, ν *(18)*. In **Eq. (5.19)**, c is a normalization factor and $\vec{1}$ is an $1 \times n$ row vector with all values equal to unity. The value $\vec{p}$ is a $n \times 1$ column vector where the entry p_n is the fractional population of the nth site. The matrix $\mathbf{E}$ is an identity matrix of dimension n. R and Ω are $n \times n$ diagonal matrices where the elements $R_{n,n}$ and $\Omega_{n,n}$ equal the apparent transverse relaxation rate, R_2^*, and the angular frequency of the spin in the nth site, respectively. The matrix $\mathbf{K}$ encapsulates the kinetics of the exchange process. The diagonal element $K_{n,n}$ is the sum $\sum\limits_{j=1}^{n} -k_{n,j}$, where $k_{n,j}$ is the rate constant describing the conversion from the nth site to the jth site. The nondiagonal elements of this matrix, $K_{n,m}$, where $n \neq m$, are equal to the rate constants describing the conversion from the mth site to the nth site.

The discussion above demonstrates that if protein oligomerization significantly changes the hydrodynamic properties of the protein, it can be monitored by measuring the variation in R_2/R_1, lineshape, or $R_2(1/\tau_{cp})$. Likewise, protein–ligand interactions can be characterized by lineshape analysis or the aforementioned τ_{cp} dependence of R_2. Applications of these methods to study protein–protein interactions are discussed in **Section 3** and protein–ligand binding is dealt with in **Section 4**. The NMR pulse sequences utilized in these methods are well established and are

not the subject of this Chapter *(19–23)*. Here we discuss their application, by noting specific examples, for uncovering novel insight into biological function. In each section the specific assumptions required and the problems the experimentalist may typically encounter are highlighted.

3. Methods

3.1. Protein–Protein Interactions by NMR Spin-Relaxation (See Note 1)

Weak protein–protein association reactions are typically difficult to characterize because many of the spectroscopic observables resemble those of the dominant monomer species. However, in the case of nuclear spin-relaxation techniques, the minor oligomeric species contributes significantly to the observed relaxation rate **(Section 2)** *(24–27)*. If the lifetime of the associated complex is longer than the rotational diffusion time, an population-weighted average relaxation rate is measured:

$$R^{\mathrm{avg}} = \sum_i p_i R_i. \qquad (5.20)$$

As shown (*see* **Fig. 5.2**), even a small amount of dimer species measurably contributes to the apparent relaxation rate, R_{app}. Given the usual uncertainties in R_2 and R_1 of 1–4% for a protein of molecular weight 20 kDa, a dimer fractional population of 0.02
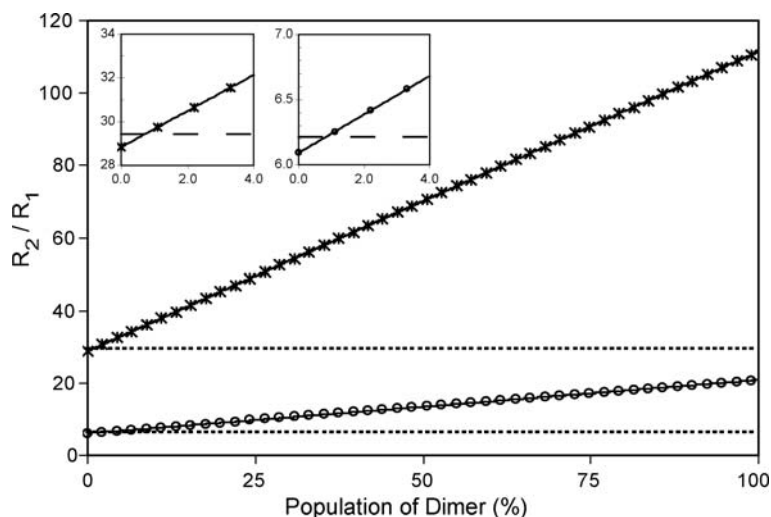
Fig. 5.2. Relaxation rate dependence on protein oligomerization state. R_2/R_1 ratio for ^{15}N (*circles*) and ^{13}C (*crosses*) positions in a protein with a monomer molecular weight 20 kDa. Relaxation rates are plotted as a function of percentage dimer formation. The dashed lines indicate the upper 2% error bound in the experimental rates. The inset shows a magnified view of this ratio at the low dimer population region. The data were simulated for a spherical protein at 298 K and 14.1 T.

(2%) would be readily detectable as an increase in R_2/R_1. Therefore, measurement of R_2/R_1 as a function of protein concentration allows for the determination of the equilibrium constant for the binding reaction as

$$(R_2/R_1)^{\text{avg}} = p_A(R_2^A/R_1^A) + (1 - p_A)(R_2^B/R_1^B). \qquad (5.21)$$

The measurement of longitudinal and transverse relaxation rates, as with any experiment, requires care in instrument setup and calibration *(23)*. Peak intensities in two-dimensional NMR spectra are determined by any of a variety of NMR processing/viewing programs. These intensities are determined for varying lengths of the R_1 and R_2 relaxation periods. The relaxation rates are then calculated by fitting a single exponential decay function to the NMR peak intensities, as they decrease with increasing relaxation delay time in spin-echo *(28)* and inversion recovery type experiments. The relaxation delay is increased in each successive two-dimensional experiment by keeping the interpulse delay constant (*see* **Fig. 5.1**) and increasing *n*. The details of these protocols are beyond the scope of this chapter, but are covered in detail in a previous edition of this book series *(23)*. Below we use specific examples from the literature to illustrate what can be learned about protein–protein interactions using NMR spin-relaxation rates.

3.1.1. Low-Molecular-Weight Protein Tyrosine Phosphatase (PTP)

The NMR pulse sequences used to measure R_2 and R_1 rates are the standard sensitivity-enhanced sequences commonly employed *(29–31)*. The task of extracting binding information from relaxation rates is aided by knowledge of or the ability to model the hydrodynamic properties on the oligomeric species involved. Bernado, et al. *(24)* used HydroNMR *(32)* to calculate relaxation rates for the self-associating PTP monomers. These calculated values are then compared to the measured relaxation rates and the self-association model is adjusted until suitable agreement between experimental and calculated data is achieved (*see* **Fig. 5.3**). The best fit indicates that PTP exists in equilibrium between distinct monomeric, dimeric, and tetrameric states. This modeling allows for estimation of the association constant for the oligomerization process.

3.1.2. Experimental Considerations

As noted in Bernado et al. *(24)* it is imperative to carefully select the relaxation data utilized in this type of analysis. Strictly, only rigid sites, absent of conformational exchange effects, are considered for inclusion in the R_2/R_1 ratio and subsequent analysis *(7)*.

First, amino acid sites with R_2 and R_1 relaxation rates greater than 1.5 standard deviations from the protein-wide mean value are excluded from analysis. Often, additional paring of the relaxation dataset is performed by exclusion of residues with heteronuclear NOE values less than 0.7. This trimmed dataset of R_2/R_1 ratios, at least in the case of isotropically rotating macromolecules,
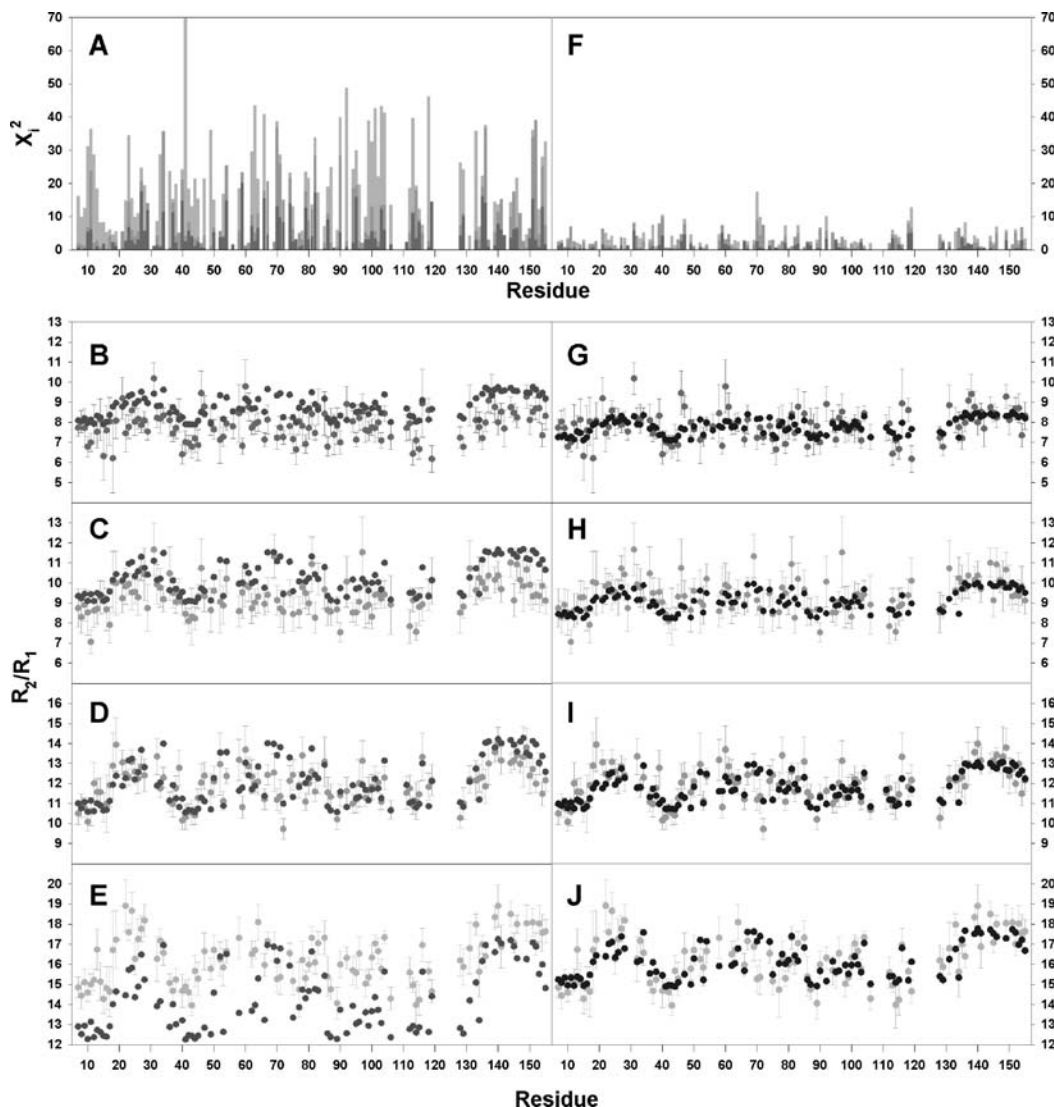
Fig. 5.3. Oligomerization from R_2/R_1. Experimental (*light gray*) and calculated (*dark gray*) values of R_2/R_1 for low-molecular-weight-protein tyrosine phosphatase. Experimental R_2/R_1 values at different concentrations are shown with their error bars B and G, 0.17 ± 0.02 mM; C and H, 0.34 ± 0.03 mM; D and I, 0.66 ± 0.07 mM; E and J, 1.24 ± 0.07 mM. In B–E calculated R_2/R_1 are for the monomer–dimer model and in G–J calculated values are for the monomer–dimer–tetramer model. Residuals for each NH are shown in panels A (monomer–dimer model) and F (monomer–dimer–tetramer model), respectively. Contributions to the residuals from experimental data at different concentrations follow the same color code as in panels B–E. Reproduced from **Ref.** *(24)* with permission from the American Chemical Society.

is a good estimate of rotational correlation time, as any residues undergoing conformational exchange processes or residues experiencing large-amplitude fast motions are usually eliminated by this method. However, in the case of anisotropic rotation, this method may not be ideal. In cases such as these, measurement of transverse (η_{xy}) and longitudinal (η_z) cross-correlation rates are

used to aid in identifying atomic sites that are subject to conformational exchange phenomena. In either case, the relaxation data should be trimmed to reflect only those residues experiencing low-amplitude rapid internal motions.

Another potential problem, highlighted in **Section 3.1.1**, is the absence of a suitable structural model for higher-order oligomers. As can be seen from **Eqs. (5.9)** and **(5.10)** the hydrodynamic shape of the macromolecule can have significant effects on $J(\omega)$ values and hence on the measured relaxation rates. When the structural model and, therefore, the relaxation rates for a given state are unknown, determination of the different population states requires one to fit for the unknown relaxation rates in addition to the populations. One method to offset these additional variables, utilized by Bernado et al. *(24)* in the case of PTP, is to collect relaxation rates across a range of macromolecular concentrations. In this example, it was found that the previously accepted monomer–dimer association model did not fit the experimental relaxation rates across the concentration series. Rather, a model that includes an additional dimer oligomerization to form a structurally uncharacterized tetramer is necessary. Careful analysis of relaxation rates not only yielded the relative populations for each of the species and the relaxation rates for the unknown state, but also a likely structural model for the tetramer, as a patch of residues on the surface was found to have elevated R_2/R_1 rates, typical of macromolecular interfaces due to increased exchange broadening and reduced dynamic fluctuations.

Finally, consideration of the bead size to be used in the hydrodynamic modeling plays an important role in correctly characterizing aggregation phenomena. The program HydroNMR *(32)* can be used for modeling the diffusion properties of the macromolecule. In the HydroNMR program *(32)*, a bead of radius a is used to replace all heavy atoms in the macromolecule to create an initial hydrodynamic model. A shell is then created by covering the initial model with tangentially intersecting spheres of radius σ. The hydrodynamic properties for a given molecule are determined by calculating the properties for a series of decreasing σ values and extrapolating to $\sigma = 0$. The only variable in the process is the bead size, a, which is optimized in HydroNMR to yield relaxation rates consistent with the experimentally measured rates. Bernado et al. *(33)* present that for proteins and small nucleic acids the average optimal bead size is 3.3 Å, which corresponds well with the solvent accessible surface area, and has a range extending from 2.6 Å to 4.8 Å. Additionally, deviation from the average optimal value tends to reveal something about the nature of the macromolecule under study. Macromolecules with depressed optimal bead sizes tend to be more dynamic, while those with elevated values likely undergo transition with higher-order oligomeric states. For example, full-length ubiquitin has an optimal a value of 2.2 Å; however, removing the three, highly

flexible, C-terminal residues from the modeling yields an optimal *a* value of 3.05 Å *(33)*. Conversely, an optimal bead size of 4.35 Å is necessary to fit the experimental relaxation rates for monomeric cytochrome c, whereas a bead size of 3.3 Å reproduces the data equally well for the monomer in equilibrium with the crystallography measured dimeric form.

As such, it is clear how intimately bead size influences the quantitation of macromolecular aggregation and oligomerization. The population of a monomer species, for example, can be artificially increased or decreased by selecting a larger or smaller bead size. Additionally, the populations can become even more biased if protein motions differ greatly between oligomeric states.

3.2. Protein–Protein Methods by CPMG Dispersion

Characterization of the physicochemical parameters of conformational or chemical exchange phenomena by CPMG dispersion experiments requires an additional experimental dimension relative to measurement of a single R_2 value as described in **Section 3.1**. In CPMG dispersion experiments, a series of R_2 values are measured at multiple τ_{cp} values as shown (*see* **Fig. 5.4a**). These R_2 values are obtained as a function of τ_{cp} and are plotted versus $1/\tau_{cp}$ (*see* **Fig. 5.4b**). Subsequently, **Eq. (5.14)** is fit to these experimental data to extract the exchange parameters, which describe the motional process. In addition to the normal experimental requirements the ability to successfully detect and measure chemical exchange necessitates that $\Delta\omega > 0$ and the population of the minor conformation be at least 1% *(23)*. If these two requirements are not met, the amplitude of the dispersion curves, (*see* **Fig. 5.4b**), will be nearly or completely flat, thereby precluding assessment of the exchange parameters *(34)*. Normally, for intramolecular processes, manipulation of $\Delta\omega$ and/or p_A is not easily
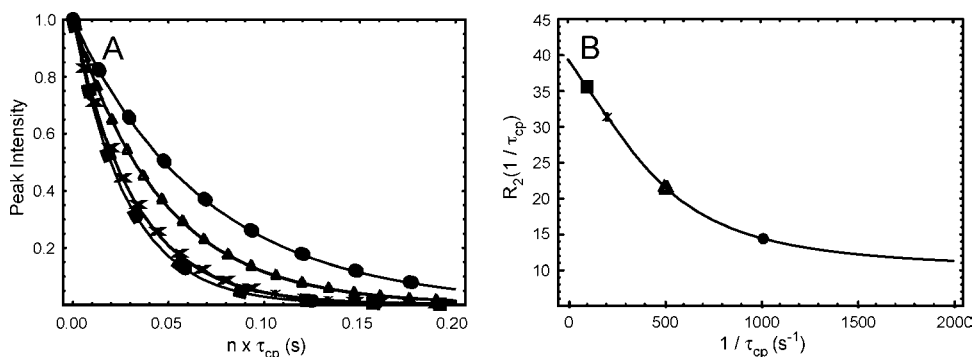

Fig. 5.4. Constructing a CPMG dispersion curve. Transverse relaxation rates ($R_2(1/\tau_{cp})$) are determined from single exponential decays in (**A**) as a function of pulse spacing ($\tau_{cp} = 1, 2, 5, 10$ ms for circles, triangles, crosses, and squares, respectively) as shown (*see* **Fig. 5.1**). The rates in (**A**) are plotted as shown in (**B**), in which the symbols in (**B**) represent the curve in (**A**) from which the rates were taken. Equation (5.14) is fit to the $R_2(1/\tau_{cp})$ values to obtain the exchange parameters. The simulated data assumed $\Delta\omega = 700 \text{ s}^{-1}$, $k_{ex} = 1500 \text{ s}^{-1}$, $R_2^0 = 10 \text{ s}^{-1}$, and $p_a = 0.90$.

achieved. However, for protein–protein or protein–ligand interactions, the equilibrium populations are readily controlled through careful adjustment of the protein or ligand concentrations. The goal is to set up the intermolecular reaction such that the equilibrium described by **Eqs. (5.11) or (5.12)** does not lie far to the right or left. Two examples that demonstrate the characterization of protein–protein interactions by CPMG dispersion measurements are provided below (**Sections 3.2.1** and **3.2.2**).

3.2.1. Coupled Folding/Dimerization

The presence of intermolecular conformational exchange ($R_{ex} > 0$) due to protein association can be exploited to study the physical properties of oligomer formation. Hill et al. *(35)* made use of intramolecular exchange contributions to the backbone transverse relaxation rates to study the coupled folding and dimerization of the engineered protein $\alpha_2 D$. For this protein, folding and dimerization cause measurable chemical shift perturbations ($\Delta\omega > 0$) upon conversion from the unfolded monomer. Transverse relaxation rates as a function of the 180° pulse spacing (*see* **Fig. 5.1**) are measured with CPMG relaxation dispersion experiments *(14)* at the $^{13}C^\alpha$ positions of four leucine residues. The resulting dispersion curves are shown (*see* **Fig. 5.5**). Analysis is facilitated by the
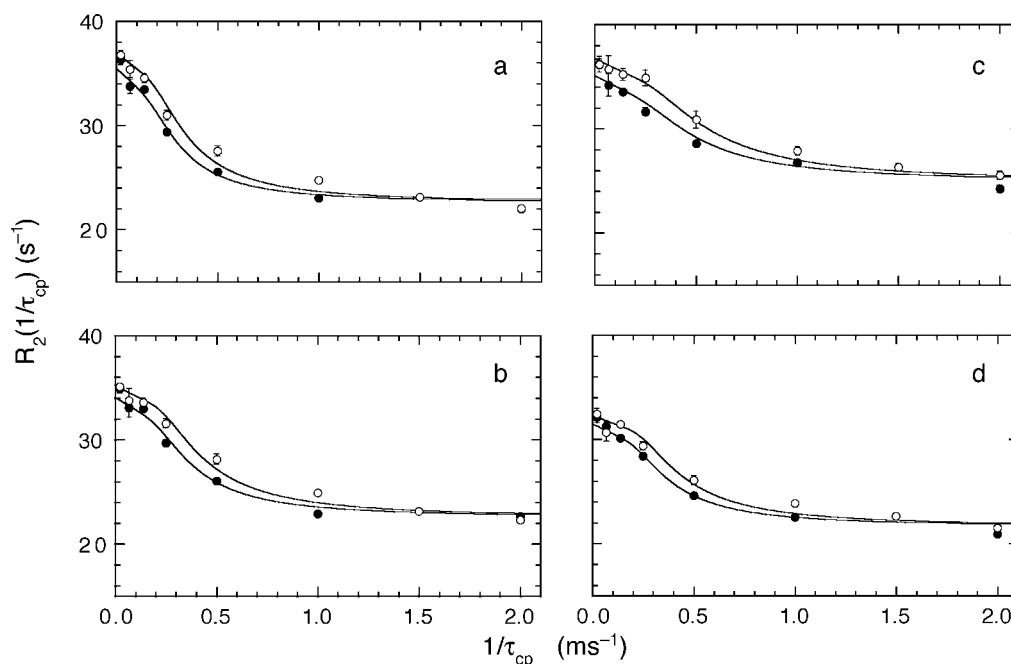

Fig. 5.5. Dispersion curves for protein folding. Determination of protein folding parameters for $\alpha_2 D$ from the field dependence of CPMG relaxation dispersion. Values of $R_2(1/\tau_{cp})$ measured at (*filled circles*) $B_0 = 11.7$ T and (*open circles*) $B_0 = 14.1$ T are plotted versus $1/\tau_{cp}$ for (**a**) Leu 6, (**b**) Leu 13, (**c**) Leu 25, and (**d**) Leu 32. Solid lines are the best global nonlinear least-squares fits to **Eq. (5.14)**. Values of χ^2 are (**a**) 7.77, (**b**) 5.93, (**c**) 5.88, and (**d**) 5.41. Reproduced from **Ref.** *(35)* with permission from the American Chemical Society.

acquisition of dispersion data at two or more static magnetic fields, which allows estimation of the chemical exchange time-scale *(36, 37)*. Under the conditions studied, a fit of **Eq. (5.14)** to the dispersion data provides an exchange rate constant, k_{ex}, of approximately $500–600\,s^{-1}$ and an equilibrium population of monomer around 3%. As such, conformational exchange is slow on the chemical shift timescale ($k_{ex} < \Delta\omega$); therefore, both the populations of the exchanging species and $\Delta\omega$ can be obtained. The obvious benefit of knowing the populations is that the forward and reverse rate constants, k_1 and k_{-1}, can be obtained via $k_{ex} = k_1'/p_B = k_{-1}/p_A$. However, if k_{ex} is greater than $\Delta\omega$ (fast exchange), then estimation of the individual rate constants requires independent characterization of the equilibrium populations.

When exchange is in the slow regime $\Delta\omega$ can be a particularly powerful and useful piece of information, as it provides insight into the chemical shifts of the interconverting species. In the study of $\alpha_2 D$, $\Delta\omega$ values of approximately 1 ppm are measured for the folding/dimerization process, which are significantly less than those expected for a typical random-coil to α-helix transformation ($\sim$2 ppm). The conclusion, based on these results, is that the unfolded monomer populates partially structured helical conformational space and is not entirely random coil.

3.2.2. Protein–Protein Intersubunit Interactions

CPMG dispersion experiments were used to address the nature of the intersubunit interfaces in the *Escherichia coli* 0157 cytotoxin B subunit from the AB$_5$ class of homopentameric toxins *(38)*. Previous NMR experiments found this pentameric structure to be symmetric in the apoenzyme form, contrary to the crystal structure model obtained for this protein. Additionally, significant conformational exchange broadening of residues in the interface, including V22, K23, and V50 (*see* **Fig. 5.6**), is observed. These dispersion profiles are flat in the presence of a subunit-bridging bivalent inhibitor called P^k dimer, indicating that ligand binding quenches this conformational motion. Interestingly, the exchange rates obtained by fitting the dispersion data to **Eq. (5.14)** reveal similar exchange rate constants for all of the affected residues, suggesting a concerted process. Again, the authors exploit the ability to estimate $\Delta\omega$ for the assumed two-site conformational exchange process in the attempt to identify the structure of the lowly populated conformer. However, unlike the example in **Section 3.2.1,** there is no reasonable reference chemical shift value for the lowly populated state of cytotoxin B. In cases such as this, the crystal structure can be used as a model for the minor conformation and the ^{15}N chemical shifts can be calculated for the crystal and NMR structures via the method developed by Xu and Case *(39)*. The differences between the calculated chemical shifts for the two conformations can then be compared to the
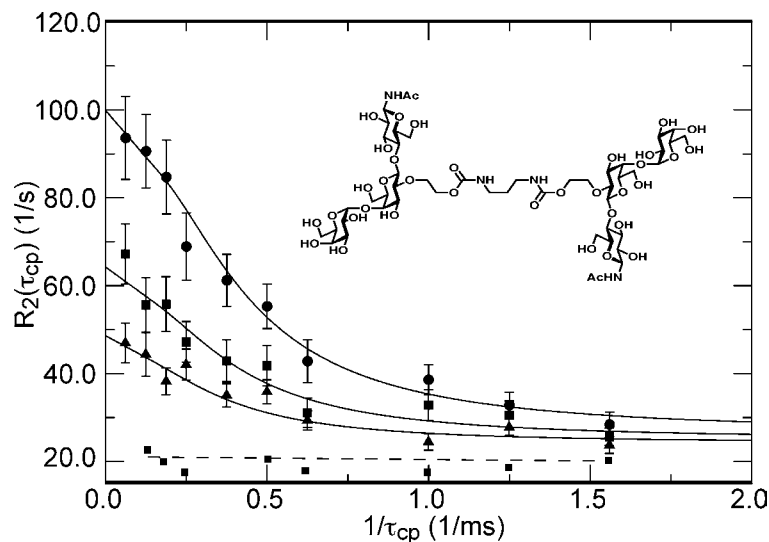
Fig. 5.6. Relaxation dispersion curves. Typical ^{15}N relaxation dispersion profiles for the amide nitrogens of Val50 (●), Val22 (■), and Lys23 (▲) in VTB. The relaxation dispersion profile for Val50 in the presence of fivefold molar excess of inhibitor P^k dimer (inset) is shown by the broken line. Solid lines represent the best fit to the data with the equation appropriate for all exchange timescales with $k_{ex} = 1000\,s^{-1}$. Reproduced from **Ref.** *(38)* with permission from the American Chemical Society.

experimentally determined $\Delta\omega$ values. A high level of agreement between the $\Delta\omega$ values obtained in this manner would suggest that the structure of the minor conformation was accurately represented. In the example of subunit B, there is a reasonable correlation between these chemical shift differences, suggesting that the apo symmetric pentamer conformation is sampling the low abundance, asymmetric, crystallographic conformation. This information, coupled with the localization of the mobile residues at the subunit interface, implies an innate ability of this pentamer structure to reorganize its subunit contacts.

3.2.3. Additional Experimental Considerations

Commonly, the exchange-free transverse relaxation rates in **Eq. (5.14)** are assumed to be equal ($R_{2A}^0 - R_{2B}^0 = 0$), thereby decreasing the number of parameters that must be determined through fitting (i.e., $R_2^0, k_{ex}, \Delta\omega$, and $p_A p_B$). In cases in which the experimental focus is on determination of relaxation rates in a protein in the presence and absence of ligand, this assumption is likely to be of little consequence to the fitted exchange parameters, because ligand binding is not likely to significantly alter the molecular weight of the protein of interest. However, for protein association reactions where the size of the studied macromolecule is significantly different as a result of protein–protein binding, this is often an invalid assumption; that is, $R_{2A}^0 - R_{2B}^0 \neq 0$. Ishima and Torchia investigated this scenario

and found that for $R_{2A}^0 - R_{2B}^0 = 15 s^{-1}$, the deviation of the fitted values from the true value can be as high as 14% for the populations and 6% for the exchange rate constant *(40)*. The value of $\Delta\omega$ is not affected by incorrectly assuming equivalent R_2 values. However, Ishima and Torchia note that in cases where R_2^0 values are not equivalent, but $\left(|R_{2A}^0 - R_{2B}^0| \times k_{ex}^{-1}\right)^2 \ll 1$, **Eq. (5.14)** remains accurate. Outside of this requirement and in the case of $R_{2A}^0 - R_{2B}^0 \neq 0$, errors in the fitted parameters can occur.

3.3. Protein–Ligand Methods by CPMG Dispersion

Early in the history of biological NMR, the interactions between proteins and ligands were preferably studied by monitoring the ligand signal *(41)*. In the absence of high magnetic fields and heteronuclear isotopic labeling techniques, the ^1H signals of the ligand were vastly superior to those of the protein in terms of signal-to-noise (S/N) and lineshape *(16, 42, 43)*. However, with routine access to high-field magnets and a variety of isotopic labeling protocols, observation of the NMR resonances from the protein has become relatively straightforward. The obvious benefit of this advance is an often significant increase in the number of observable signals affording insight into ligand binding. In some cases, however, ligand binding can be effectively studied with an easily labeled *(44)* or unlabeled ligand *(41, 45–49)* and these more traditional methods should not be dismissed.

As should now be clear, the ability of CPMG dispersion methods to monitor chemical exchange phenomena that result from macromolecular interactions relies on a change in chemical shift between the exchanging conformers and a significantly populated (>1%) minor conformation. As shown (*see* **Fig. 5.7**), the amplitude of the exchange effect on the dispersion curves diminishes with more highly skewed population distributions. From an experimental standpoint, the more shallow the dispersion amplitude, the more difficult it becomes to accurately measure the rate of exchange, populations, and chemical shift differences. Therefore, when measuring binding kinetics by
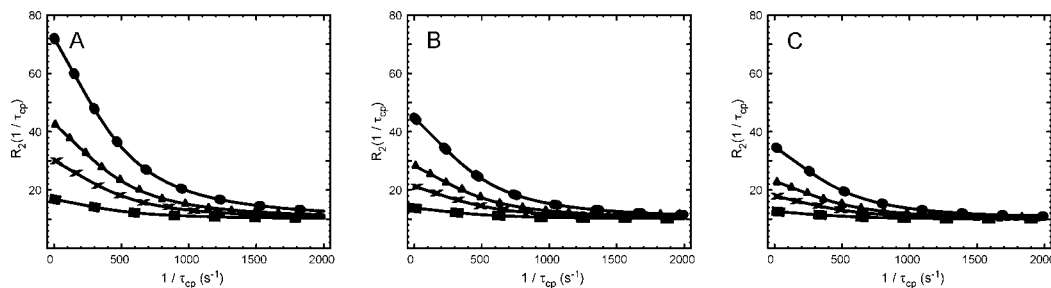

Fig. 5.7. Population effect on dispersion curves. CPMG dispersion curves were simulated for exchange parameters $k_{ex} = 1500 s^{-1}$ and $R_2^0 = 10 s^{-1}$ with $\Delta\omega = 2.0$ ppm at three fields: (**A**) 18.8 T, $\Delta\omega = 1019 s^{-1}$, (**B**) 14.1 T, $\Delta\omega = 764 s^{-1}$, and (**C**) 11.7 T, $\Delta\omega = 637 s^{-1}$ and four populations: (●) $p_a = 0.90$, (▲) $p_a = 0.95$, (x) $p_a = 0.97$, and (■) $p_a = 0.99$.

NMR, it is important to carefully adjust and control the equilibrium populations such that the dispersion amplitude lies within the window where it can be most accurately measured. The desired equilibrium populations can be achieved through manipulation of the ligand and protein concentrations, based on knowledge or estimation of the protein–ligand dissociation constant.

Below in **Sections 3.3.1 and 3.4** the use of CPMG dispersion and lineshape methods, respectively, are addressed for their application to protein–ligand interactions.

3.3.1. Phosphatidylinositide 3-Kinase (PI3K) SH2 Domain Binding to Phosphotyrosine Peptide

CPMG dispersion experiments were utilized by Gunther and co-workers to address dynamics in PI3K and its interaction with a phosphorylated peptide, MT8 *(50)*. Because the K_d for ligand binding is small (8 μM), at low concentrations of MT8 nearly all of this peptide is in the bound conformation and, therefore, the k_{ex} values determined from the dispersion experiments are quite close to the ligand off-rate constant (k_{-1}), as $[L] \approx 0$ and $k_{ex} = k_{-1} + k'_1[L] \approx k_{-1}$. The authors found that the experiments performed at 5% saturation of PI3K with MT8 yielded populations such that $p_a p_b = 0.048$, which afforded significant magnitude for reasonable dispersion profiles. Generally, there is no clear rule for which experimental conditions will provide the optimal magnitude of the dispersion curves, as both the populations and $\Delta\omega$ factor into the amplitudes *(37)*. As such, this often requires a degree of trial and error. The data obtained under these conditions revealed that all of the residues near the MT8 binding site for which dispersion was measured (Arg 340, Arg 358, Ser 339, and Glu 341) seem to report on the same binding event, as the individually measured off-rates are very similar ($1345\,\text{s}^{-1}$, $1252\,\text{s}^{-1}$, $1478\,\text{s}^{-1}$, and $1252\,\text{s}^{-1}$, respectively). Synchrony of this degree affords a much more robust method to quantitate the ligand off-rate because all residues can be fit with a single global model with far fewer adjustable parameters. Additionally, knowledge of the populations of free and bound protein from the K_d aids in fitting of the data, as it reduces the parameters that must be determined from the dispersion experiments.

3.4. Protein–Ligand Methods by NMR Lineshape Analysis

Ligand-binding reactions can be studied by analyzing the NMR lineshapes as a function of the protein:ligand ratio for a series of two-dimensional ^1H-^{15}N HSQC experiments collected on a ^{15}N-labeled protein. Typically, this is achieved by titrating small aliquots of a concentrated ligand solution into the protein. The titration series is followed by monitoring the chemical shift perturbations in the HSQC spectra. Knowledge of the ligand dissociation constant facilitates analysis in two ways: (1) the equilibrium concentrations of the ligand, protein, and protein–ligand complex can be calculated; (2) the total number of parameters to be determined in the fitting process can be reduced, because K_d is the ratio of the on- and off-rate constants. As such, this beneficially
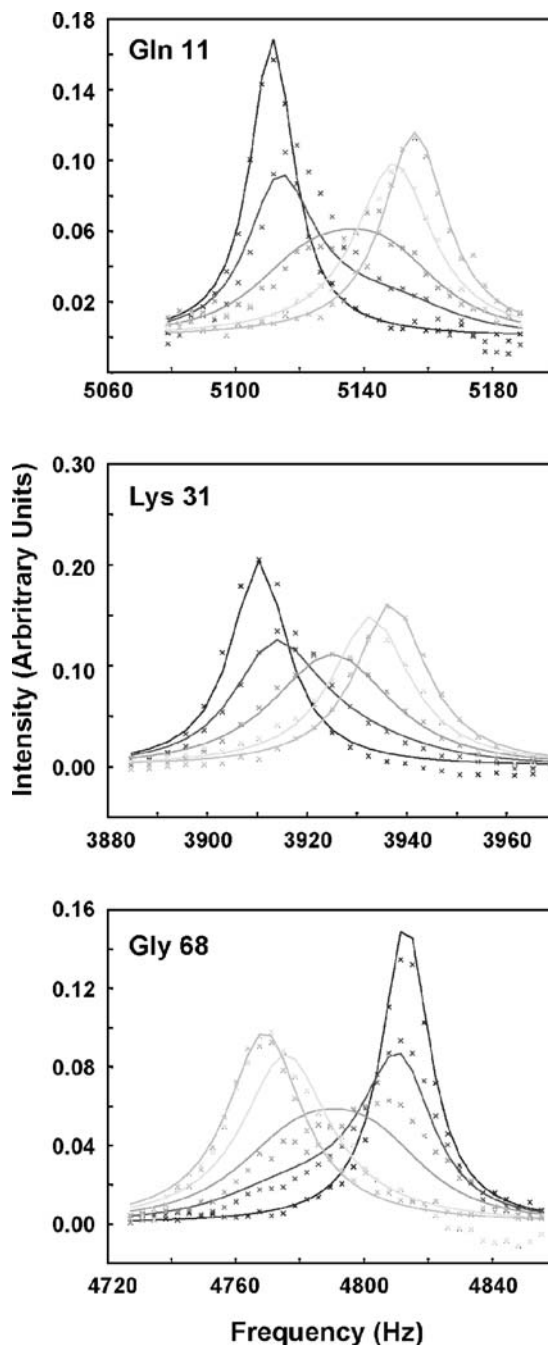
Fig. 5.8. Lineshape fitting results for the pTppAp titration. Titration data is shown for residues Gln 11, Lys 31, and Gly 68. Experimental data points are shown along with the line representing the best fit using best fits to **Eq. (5.19)**. The curves represent the proton chemical shift dependence and peak intensity at 0.0, 0.3, 0.6, 0.9, 1.2 (left-to-right for (Gln11 and Lys31) and right-to-left for (Gly68)) equivalents of pTppAp. (Reproduced from **Ref.** *(51)* with permission from the American Chemical Society).

minimizes the fitting problem to a two-dimensional search for k_{-1} and the normalization factor, c, from **Eq. (5.19)**. The protocol is described below in an application to Ribonuclease A (RNase A) *(51, 52)*.

The kinetics of ligand binding to its protein partner is measured by titration of ligand into a solution of ^{15}N-labeled protein. After each of the 10 titration steps, a high-resolution ^{1}H–^{15}N HSQC spectrum is acquired. The NMR data can be processed with an array of available software, the choice of which is at the experimenter's discretion. In the following example, the data is initially processed with NMRPipe and converted to text format with in-house scripts before final analysis with MATLAB (Mathworks, Inc.).

For RNase A, a total of 12 well-resolved peaks with noticeable changes in resonance shape and chemical shift during the ligand titration are selected. The two-dimensional peaks are first integrated across the ^{15}N dimension. The resulting one-dimensional peak shapes for the free enzyme and ligand-saturated RNase A were fit to a Lorentzian to determine the apparent transverse relaxation rate, R_2^*, and the resonance frequency of the free and bound states. These data are then used to construct the matrices **R**, **K,** and **Ω** and the vector $\vec{p}$ as shown in **Eq. (5.19)**. Each of the 10 titration points for all 12 residues are fit individually. Once it is determined that all residues gave essentially the same result, all 12 amino acid resonances are fit simultaneously using a Levenberg–Marquardt algorithm *(53)* to determine the required normalization factor, c, and the rate for ligand dissociation, k_{-1}. A subset of these data and the resulting fits are shown (*see* **Fig. 5.8**).

A simple two-site binding model is the best description of the RNase A/ligand titration experiment. All affected residues report similar fits and therefore all data are simultaneously fit to a two-site exchange model. For the substrate analog, phospho-thymidine pyrophosphoryl adenosine phosphate (pTppAp) the dissociation rate constant at 298 K was determined to be $80 \pm 5\,\mathrm{s}^{-1}$ with $k_1 = 4.9 \pm 0.6 \times 10^9\,\mathrm{M}^{-1}\mathrm{s}^{-1}$ *(52)*. For the product analog, cytidine monophosphate(CMP), similar experiments provided $k_{-1} = 1700\,\mathrm{s}^{-1}$ and $k_1 = 8.1 \pm 0.7 \times 10^6\,\mathrm{M}^{-1}\mathrm{s}^{-1}$ *(51)*.

4. Notes

1. It is imperative in all experiments described to maintain constant pH during the ligand or protein titration reactions. This is best achieved with a micro-pH electrode that can be directly inserted into the NMR tube. The pH can then be adjusted with each titration by addition of the desired acid or base. Typically, these acid or base solutions should be concentrated enough

such that volume changes are minimal but not so concentrated that large local pH changes occur prior to mixing. This can result in protein or ligand denaturation in the volume surrounding the pipette. Our suggestion is to use strong acids or bases around 100 mM.

5. Summary and Conclusions

Over the past 25 years, NMR spectroscopy has afforded much insight into the structure and biological activity of enzymes. While the techniques discussed here are often used to study the role of internal dynamics in enzymatic function, we hope we have shown they are equally powerful and applicable in understanding the critical and often complex events of ligand binding and protein–protein interactions. NMR spectroscopy is unique in its ability to measure site-specific information for the quantitation of and structural insight into these often transient interactions. As the techniques NMR spectroscopists employ continue to improve and expand, it is certain that new windows of understanding will be opened into these molecules so essential for all forms of life.

Acknowledgements

References

1. Palmer, A. G., 3rd. (2004) NMR characterization of the dynamics of biomacromolecules. *Chem Rev* **104**, 3623–3640.
2. Jarymowycz, V. A., Stone, M. J. (2006) Fast time scale dynamics of protein backbones: NMR relaxation methods, applications, and functional consequences. *Chem Rev* **106**, 1624–1671.
3. Abragam, A. (1961) *Principles of Nuclear Magnetism*, Clarendon Press, Oxford.
4. Wallach, D. (1967) Effect of internal rotation on angular correlation functions. *J Chem Phys* **47**, 5258–5268.
5. Woessner, D. E. (1962) Nuclear spin relaxation in ellipsoids undergoing rotational Brownian motion. *J Chem Phys* **37**, 647–654.
6. Kay, L. E., Torchia, D. A., Bax, A. (1989) Backbone dynamics of proteins as studied by nitrogen-15 inverse detected heteronuclear NMR spectroscopy: application to staphylococcal nuclease. *Biochemistry* **28**, 8972–8979.
7. Tjandra, N., Feller, S. E., Pastor, R. W., et al. (1995) Rotational diffusion anisotropy of human ubiquitin from ^{15}N NMR relaxation. *J Am Chem Soc* **117**, 12562–12566.

8. Zheng, Z., Czaplicki, J., Jardetzky, O. (1995) Backbone dynamics of *trp* repressor studied by 15 N NMR relaxation. *Biochemistry* **34**, 5212–5223.

9. McConnell, H. M. (1958) Reaction rates by nuclear magnetic resonance. *J Chem Phys* **28**, 430–431.

10. Meiboom, S., Gill, D. (1958) Modified spin-echo method for measuring nuclear spin relaxation times. *Rev Sci Instrum* **29**, 688–691.

11. Carr, H. Y., Purcell, E. M. (1954) Effects of diffusion on free precession in nuclear magnetic resonance experiments. *Phys Rev* **94**, 630–638.

12. Orekhov, V. Y., Pervushin, K. V., Arseniev, A. S. (1994) Backbone dynamics of (1-71) bacteriorhodopsin studied by two-dimensional ^{1}H-^{15}N NMR spectroscopy. *Eur J Biochem* **219**, 887–896.

13. Allerhand, A., Gutowsky, H. S. (1964) Spin-echo NMR studies of chemical exchange. I. Some general aspects. *J Chem Phys* **41**, 2115–2126.

14. Loria, J. P., Rance, M., Palmer, A. G. (1999) A relaxation-compensated Carr–Purcell–Meiboom–Gill sequence for characterizing chemical exchange by NMR spectroscopy. *J Am Chem Soc* **121**, 2331–2332.

15. Carver, J. P., Richards, R. E. (1972) A general two-site solution for the chemical exchange produced dependence of T_2 upon the Carr–Purcell pulse separation. *J Mag Res* **6**, 89–105.

16. Davis, D. G., Perlman, M. E., London, R. E. (1994) Direct measurements of the dissociation-rate constant for inhibitor-enzyme complexes via the $T_{1\rho}$ and T_2 (CPMG) methods, *J Magn Reson Ser B* **104**, 266–275.

17. Jen, J. (1978) Chemical exchange and NMR T_2 relaxation – the multisite case. *J Magn Reson* **30**, 111–128.

18. Reeves, L. W., Shaw, K. N. (1970) Nuclear magnetic resonance studies of multi-site exchange. I. Matrix formulation of the Bloch equations. *Can J Chem* **48**, 3641–3653.

19. Palmer, A. G., Williams, J., McDermott, A. (1996) Nuclear magnetic resonance studies of biopolymer dynamics. *J Phys Chem* **100**, 13293–13310.

20. Palmer, A. G., Bracken, C. (1999) in (Pons, M., Ed.) *NMR in Supramolecular Chemistry,* pp. 171–190, Kluwer Academic Publishers, Netherlands.

21. Palmer, A. G., Kroenke, C. D., Loria, J. P. (2001) Nuclear magnetic resonance methods for quantifying microsecond-to-millisecond motions in biological macromolecules. *Meth. Enzymol* **339 Part B**, 204–238.

22. Palmer, A. G. (2001) NMR probes of molecular dynamics: Overview and comparison with other techniques. *Annu Rev Biophys Biomol Struct* **30**, 129–155.

23. Kempf, J. G., Loria, J. P. (2004) in (Downing, A. K., ed.) *Protein NMR Techniques,* pp. 185–231, Humana Press, Totowa.

24. Bernado, P., Akerud, T., Garcia de la Torre, J., et al. (2003) Combined use of NMR relaxation measurements and hydrodynamic calculations to study protein association. Evidence for tetramers of low molecular weight protein tyrosine phosphatase in solution, *J Am Chem Soc* **125**, 916–923.

25. Fushman, D., Cahill, S., Cowburn, D. (1997) The main-chain dynamics of the dynamin pleckstrin homology (PH) domain in solution: analysis of 15 N relaxation with monomer/dimer equilibration. *J Mol Biol* **266**, 173–194.

26. Pfuhl, M., Chen, H. A., Kristensen, S. M., et al. (1999) NMR exchange broadening arising from specific low affinity protein self-association: analysis of nitrogen-15 nuclear relaxation for rat CD2 domain 1, *J Biomol NMR* **14**, 307–320.

27. Mercier, P., Spyracopoulos, L., Sykes, B. D. (2001) Structure, dynamics, and thermodynamics of the structural domain of troponin C in complex with the regulatory peptide 1-40 of troponin I. *Biochemistry* **40**, 10063–10077.

28. Hahn, E. L. (1950) Spin echoes. *Phys Rev* **80**, 580–594.

29. Skelton, N. J., Palmer, A. G., Akke, M., et al. (1993) Practical aspects of two-dimensional proton-detected ^{15}N spin relaxation measurements. *J Magn Reson, Ser B* **102**, 253–264.

30. Kay, L. E., Keifer, P., Saarinen, T. (1992) Pure absorption gradient enhanced heteronuclear single quantum correlation spectroscopy with improved sensitivity. *J Am Chem Soc* **114**, 10663–10665.

31. Palmer, A. G., Cavanagh, J., Wright, P. E., Rance, M. (1991) Sensitivity improvement in proton-detected two-dimensional heteronuclear correlation NMR spectroscopy. *J Magn Reson* **93**, 151–170.

32. Garcia de la Torre, J., Huertas, M. L., Carrasco, B. (2000) HYDRONMR: prediction of NMR relaxation of globular proteins from atomic-level structures and hydrodynamic calculations. *J Magn Reson* **147**, 138–146.

33. Bernado, P., Garcia de la Torre, J., Pons, M. (2002) Interpretation of 15 N NMR relaxation data of globular proteins using hydrodynamic calculations with HYDRONMR, *J Biomol NMR* **23**, 139–150.

34. Kempf, J. G., Loria, J. P. (2002) Protein dynamics from solution NMR: Theory and applications. *Cell Biochem Biophys* **39**, 187–212.

35. Hill, R. B., Bracken, C., DeGrado, W. F., et al. (2000) Molecular motions and protein folding: Characterization of the backbone dynamics and folding equilibrium of alpha D-2 using C-13 NMR spin relaxation. *J Am Chem Soc* **122**, 11610–11619.

36. Millet, O. M., Loria, J. P., Kroenke, C. D., et al. (2000) The static magnetic field dependence of chemical exchange linebroadening defines the NMR chemical shift time scale. *J Am Chem Soc* **122**, 2867–2877.

37. Kovrigin, E. L., Kempf, J. G., Grey, M., et al. (2006) Faithful estimation of dynamics parameters from CPMG relaxation dispersion measurements. *J Magn Reson* **180**, 93–104.

38. Yung, A., Turnbull, W. B., Kalverda, A. P., et al. (2003) Large-scale millisecond intersubunit dynamics in the B subunit homopentamer of the toxin derived from *Escherichia coli* O157. *J Am Chem Soc* **125**, 13058–13062.

39. Xu, X. P., and Case, D. A. (2001) Automated prediction of 15 N, 13Calpha, 13Cbeta and 13C' chemical shifts in proteins using a density functional database. *J Biomol NMR* **21**, 321–333.

40. Ishima, R., Torchia, D. A. (2006) Accuracy of optimized chemical-exchange parameters derived by fitting CPMG R2 dispersion profiles when R2(0a) not = R2(0b). *J Biomol NMR* **34**, 209–219.

41. Lee, G. C., Chan, S. I. (1971) A 31P NMR study of the association of uridine-3'-monophosphate to ribonuclease A. *Biochem Biophys Res Commun* **43**, 142–148.

42. Raftery, M. A., Dahlquist, F. W., Chan, S. I., et al. (1968) A proton magnetic resonance study of the association of lysozyme with monosaccharide inhibitors. *J Biol Chem* **243**, 4175–4180.

43. Lanir, A., Navon, G. (1971) Nuclear magnetic resonance studies of bovine carbonic anhydrase. Binding of sulfonamides to the zinc enzyme. *Biochemistry* **10**, 1024–1032.

44. Tolkatchev, D., Xu, P., Ni, F. (2003) Probing the kinetic landscape of transient peptide–protein interactions by use of peptide (15)n NMR relaxation dispersion spectroscopy: binding of an antithrombin peptide to human prothrombin. *J Am Chem Soc* **125**, 12432–12442.

45. Dubois, B. W., Evers, A. S. (1992) 19F-NMR spin-spin relaxation (T2) method for characterizing volatile anesthetic binding to proteins. Analysis of isoflurane binding to serum albumin, *Biochemistry* **31**, 7069–7076.

46. Rozovsky, S., Jogl, G., Tong, L., et al. (2001) Solution-state NMR investigations of triosephosphate isomerase active site loop motion: ligand release in relation to active site loop dynamics. *J Mol Biol* **310**, 271–280.

47. Rozovsky, S., McDermott, A. E. (2001) The time scale of the catalytic loop motion in triosephosphate isomerase. *J Mol Biol* **310**, 259–270.

48. Gerig, J. T., Halley, B. A., Loehr, D. T., Reimer, J. A. (1979) NMR studies of ortho and meta-fluorocinnamate alpha chymotrypsin complexes. *Org Magn Reson* **12**, 352–356.

49. Gerig, J. T., Stock, A. D. (1975) Studies of kinetics of interaction between N-trifluoroacetyl-D-tryptophan and alph-chymotrypsin by pulsed nuclear magnetic resonance. *Org Magn Reson* **7**, 249–255.

50. Mittag, T., Schaffhausen, B., Gunther, U. L. (2003) Direct observation of protein–ligand interaction kinetics. *Biochemistry* **42**, 11128–11136.

51. Beach, H., Cole, R., Gill, M., et al. (2005) Conservation of μs–ms enzyme motions in the apo- and substrate-mimicked state. *J Am Chem Soc* **127**, 9167–9176.

52. Kovrigin, E. L., Loria, J. P. (2006) Enzyme dynamics along the reaction coordinate: critical role of a conserved residue. *Biochemistry* **45**, 2636–2647.

53. Marquardt, D. W. (1963) An algorithm for least-squares estimation of nonlinear parameters. *J Soc Indust App Math* **11**, 431–441.

Chapter 6

Ligand-Binding Interactions and Stability

John W. Shriver and Stephen P. Edmondson

Abstract

The reversible interaction or binding of ligands to biological macromolecules is fundamental to nearly every aspect of biochemistry and cell biology. Binding events typically do not occur in isolation in biochemistry, and are almost always coupled or linked to other reactions such as protonation changes, other ligand-binding interactions, structural transitions, and folding. It is rarely sufficient to simply state that something binds. An understanding of binding requires a measure of affinity, stoichiometry, and the contributions of linked reactions. Emphasis is placed here on defining binding and the influence of linkage on binding and stability using both spectroscopic and calorimetric data.

Key Words: Binding, linkage, association constant, dissociation constant, protonation, folding, calorimetry, ITC, DSC, fluorescence.

1. Introduction

Binding in biochemistry involves the facile, reversible, noncovalent interaction between a macromolecule (such as a protein or a nucleic acid) and another molecule which may be a small molecule or ion (e.g., a sugar, a hormone, a metal ion, or a proton) or another macromolecule *(1–3)*. The smaller species is usually referred to as the ligand, the term coming from the Latin *ligare (2)*. The association of multiple macromolecules is treated similarly (e.g., protein–protein interactions, or protein–DNA binding), and in such cases the choice of which is the ligand is arbitrary. Ligand binding often influences other equilibria involving all the binding

species, including the binding of other ligands and macromolecular folding (stability).

An understanding of binding requires a description of the thermodynamics and kinetics of both the primary binding reaction of interest as well as the linked reactions. We will focus here on the energetics of the reactions and linkages, and assume that the binding kinetics are rapid on the timescale of the binding measurements. To adequately understand the energetics of a binding process it is necessary to know the number of binding sites on each macromolecule (stoichiometry), the strength of binding at each site (binding affinity), and if there are linkages to other binding events and structural transitions.

The emphasis here is on providing a quantitative, practical description of ligand binding and the effects of linkage. Examples are provided which can be readily expanded to treat more complicated processes. Interactive *Mathematica* (Wolfram) Notebooks which can be used in conjunction with this text can be downloaded from http://daffy.uah.edu/thermo/ These provide the ability to conveniently simulate and fit binding data with linkages that typically occur in biochemistry.

2. Binding Without Linkage

2.1. Single-Site Binding

For a single-site binding reaction where N represents a macromolecule such as a protein or nucleic acid and L represents a ligand, binding results in a complex indicated by NL:

$$N + L \xrightleftharpoons{K_a} NL$$

This is a reversible reaction, and the equilibrium constant for the binding can be expressed as an association or binding constant:

$$K_a = \frac{[NL]}{[N][L]_f}. \qquad (6.1)$$

The brackets indicate concentration or activity. The subscript "f" on the concentration of L is included to stress that this is the concentration of free ligand and does not include that bound to N (i.e., NL), and it is not the total concentration of ligand added. A dissociation constant is given by the inverse of the binding constant:

$$K_d = \frac{[N][L]_f}{[NL]} \qquad (6.2)$$

or $K_d = 1/K_a$. Strong binding is typically associated with a K_d less than 10^{-6} M, while weak binding is associated with a K_d greater than 10^{-3} M. The use of K_d is often preferred since it is the concentration of free ligand required to obtain filling of half the binding sites on the macromolecule (see below).

Binding is not an "all-or-nothing" phenomenon. Each ligand and macromolecule is either bound or free, but the solution always contains both (100% saturation is physically impossible). The fraction of the protein sites containing bound L (i.e., the fraction of the sites filled) is given by

$$\nu = \frac{[NL]}{[NL] + [N]}, \qquad (6.3)$$

where $[NL] + [N]$ is the total concentration of sites available, $[N]_t$. ν is referred to as the binding density, and can be viewed as a measure of the progress of the binding reaction. Rearranging **Eq. (6.2)**, we obtain

$$[NL] = \frac{[N][L]_f}{K_d} \qquad (6.4)$$

and substituting into **Eq. (6.3)** provides one of the fundamental equations describing binding:

$$\nu = \frac{[L]_f}{[L]_f + K_d} \qquad (6.5)$$

Equation (6.5) defines the fraction of sites filled as a function of the dissociation constant and the concentration of free ligand. Note that the concentration of the macromolecule does not occur in the expression. The equation describes a rectangular hyperbola, and is analogous to the Michaelis–Menten equation *(1, 4)*.

2.2. Direct Plots and Free Ligand Concentration–Binding In Vivo

The curve defined by **Eq. (6.5)** is commonly referred to as a "binding isotherm", and a plot of ν vs. $[L]_f$ is a "direct" plot of the data (**Fig. 6.1**) (*see* **Note 1**). The K_d may be directly estimated by noting that ν is 0.5 when $[L]_f = K_d$. However, binding affinities are best determined by fitting the binding isotherm over a range of ligand concentrations to properly define the precision with which the binding constant is determined, as well as to determine the accuracy of the binding model. Note that filling, or saturation, of the sites can be difficult to obtain, especially with weaker binding. **Figure 6.2** shows how the shape of the binding isotherm is affected by the dissociation constant (*see* **Note 2**). Tighter binding leads to a rapid rise of ν with free ligand concentration, whereas for weaker binding much higher concentrations of free ligand are required to
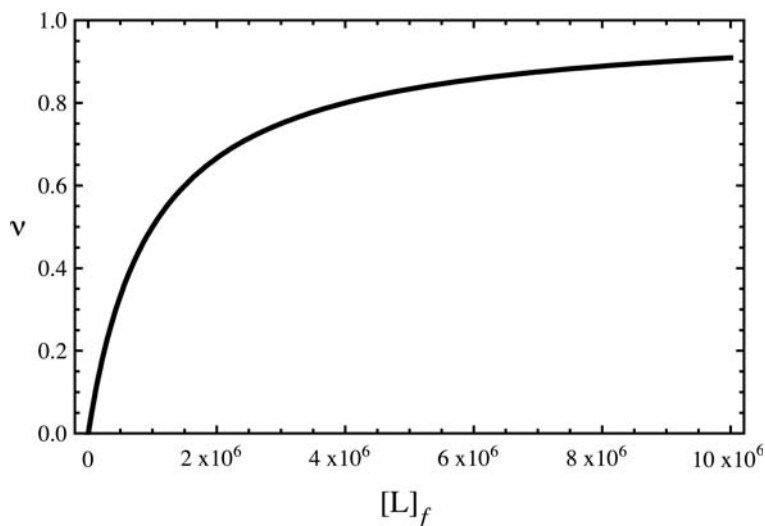
Fig. 6.1. A simulated binding isotherm showing the dependence of the binding density, ν (i.e., the fraction of the binding sites filled) as a function of the free concentration of ligand. The binding isotherm is defined by **Eq. (6.5)** with a dissociation constant of 10^{-6} M, and the free ligand concentration is varied from 0 M to 10^5 M. Half-saturation of the binding sites is attained when the free ligand concentration is equal to the K_d.
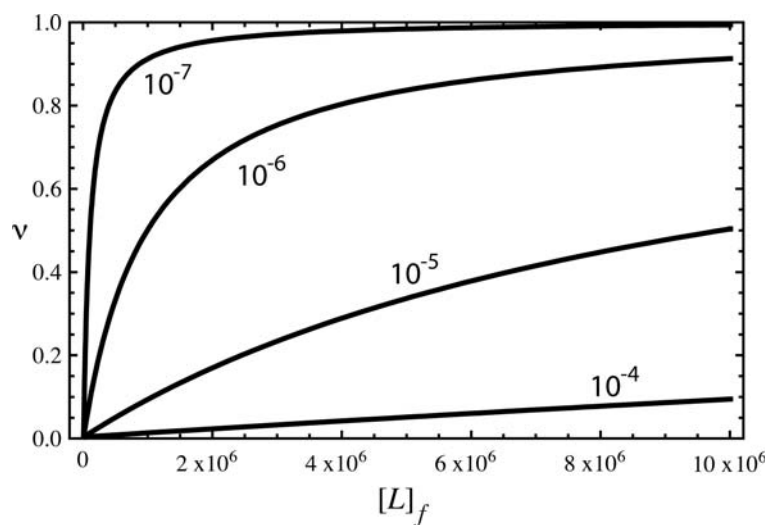

Fig. 6.2. The effect of the dissociation constant on the shape of the binding isotherm. With decreasing K_d, the binding curve approaches the y-axis without limit.

fill the sites (the lower curve). However, even for weak binding, near-saturation of the sites can be achieved if high enough concentrations of free ligand can be achieved. Most importantly, to know the extent to which something binds in vivo, one must know the K_d and the physiological concentrations of free ligand.

2.3. Direct Plots and Total Ligand Concentration

It is sometimes necessary to plot the fraction of sites filled as a function of the total ligand added (i.e., $[L]_f$ plus $[NL]$). This is especially true when studying binding indirectly, for example, using spectroscopic or calorimetric methods. The free ligand concentration is

$$[L]_f = [L]_{total} - [NL] \qquad (6.6)$$

and total $[N]$ is

$$[N]_{total} = [NL] + [N]. \qquad (6.7)$$

From the definition of the binding constant we can write

$$[N] = \frac{[NL]}{K_a * [L]_f}. \qquad (6.8)$$

Substitution of **Eq. (6.6)** into **(6.8)**, and **Eq. (6.8)** into **(6.7)** yields

$$[N]_{total} = [NL] + \frac{[NL]}{K_a([L]_{total} - [NL])}. \qquad (6.9)$$

Solving for $[NL]$,

$$[NL] = \frac{1 + K_a[N]_{total} + K_a[L]_{total} - \sqrt{-4K_a^2[N]_{total}[L]_{total} + (1 + K_a[N]_{total} + K_a[L]_{total})^2}}{2K_a}. \qquad (6.10)$$

Equation (6.10) describes the dependence of the concentration of the complex on the total concentrations of N and L, as well as the binding constant (note:K_a and not K_d). The free concentration of L does not appear anywhere in this equation. The binding density is obtained from $\nu = [NL]/[N]_{total}$:

$$\nu = \frac{1 + K_a[N]_{total} + K_a[L]_{total} - \sqrt{-4K_a^2[N]_{total}[L]_{total} + (1 + K_a[N]_{total} + K_a[L]_{total})^2}}{2K_a[N]_{total}}. \qquad (6.11)$$

Simulations of the binding density for various values of the binding constant are shown in **Fig. 6.3**, with the total ligand concentration plotted on the abscissa rather than the free ligand concentration (*see* **Note 3**). Note that under conditions of tight binding, this plot contains a sharp break that occurs where the concentration of total ligand equals the concentration of sites. This allows the number of sites (i.e., the stoichiometry) to be estimated directly from the plot (and precisely determined by a nonlinear least-squares fit, see below).

Equation (6.11) is often more useful than **Eq. (6.5)** since in a typical titration experiment the amount of free ligand may be difficult to determine, but the total amount of ligand added is almost always known. The fraction of sites filled, ν, is not always directly measured. It can be followed indirectly by using a spectroscopic signal that changes with binding, for example, a change
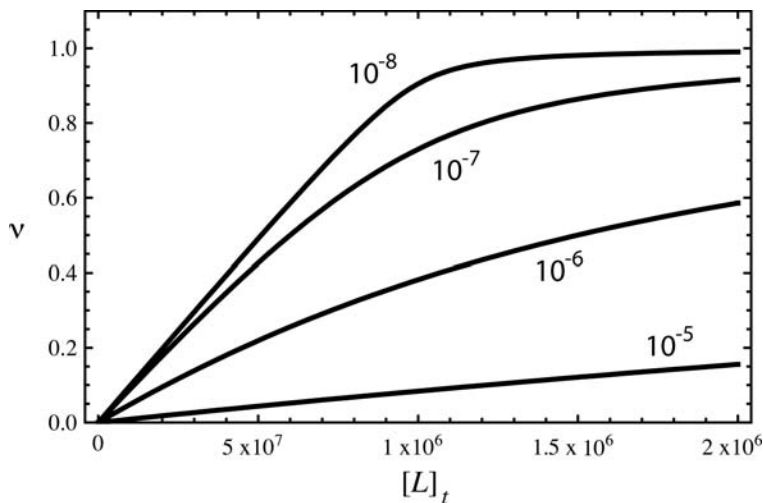
Fig. 6.3. The dependence of the binding density on total ligand concentration. With decreasing K_d (increased affinity) the binding curve shows a "break" which corresponds to the total concentration of binding sites. Such a plot is useful for defining the stoichiometry of a binding reaction.

in the fluorescence intensity of the protein, or a change in NMR chemical shift. The observed signal, S_{obs}, is then given by

$$S_{obs} = S_{max} \times \nu, \qquad (6.12)$$

where S_{max} is the maximal signal change observed when ν approaches 1.0.

2.4. Titration Plots – Importance of the Concentration Range of Free Ligand

Equation (6.5) may be rearranged to

$$K_d = [L]_f \frac{(1 - \nu)}{\nu}. \qquad (6.13)$$

Taking the log of both sides and rearranging, we obtain

$$-\log[L]_f = -\log K_d + \log \frac{(1 - \nu)}{\nu}, \qquad (6.14)$$

which is reminiscent of the Henderson–Haselbalch equation *(5)*. In fact, protonation can be viewed as a binding reaction since association of the proton with the conjugate base is facile and reversible *(1, 2)*. **Equation (6.14)** can be rearranged so that ν is expressed as a function of $\log[L]_f$, and a plot of such a function is shown in **Fig. 6.5**. This is a "titration" plot, or a Bjerrum plot (*see* **Note 4**). The midpoint is obtained where the titration is half complete, i.e., half the sites are filled, and $p[L]_f$ is equal to pK_d. Titration plots of the data presented in **Fig. 6.2** are shown in **Fig. 6.4**. Titration plots are useful for presenting data over a wide concentration range, and especially when there is more than one binding site with differing affinities (*see* **Note 5**). The
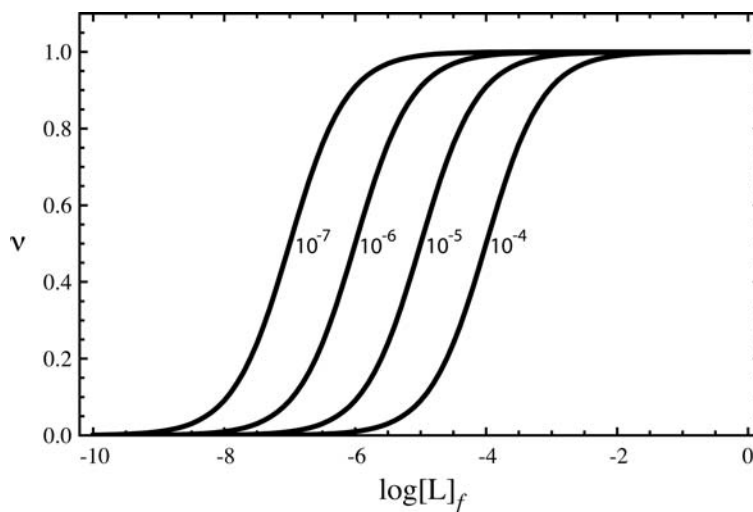
Fig. 6.4. A titration plot of the binding density as a function of the free ligand concentration. Note that the shape of the binding curve is independent of the K_d (varied from 10^{-4} M to 10^{-7} M). A titration plot is convenient for presentation of binding data over a wide concentration range, especially when more than one site occurs with widely differing affinities.

titration plot also nicely demonstrates that the most significant change in binding density occurs when the concentration of ligand (free) is comparable to the dissociation constant, an important consideration if binding is suspected to regulate the activity of a protein in vivo. Also, it demonstrates that to experimentally define a binding constant, the free concentration of ligand must be varied over a rangse comparable to the dissociation constant. This may be difficult under conditions of very tight binding.

2.5. Scatchard Plots

Equation (6.5) can also be rearranged to obtain

$$\frac{\nu}{[L]_f} = -\frac{1}{K_d}\nu + \frac{1}{K_d}, \tag{6.15}$$

which is the Scatchard equation for single-site binding *(1)*. A plot of $\nu/[L]_f$ as a function of ν provides a straight line with a *y*-intercept of $-K_a$, and an *x*-intercept of 1, indicating a stoichiometry of 1 (*see* **Note 6**). The Scatchard equation represents a coordinate transformation to obtain a linearization of **Eq. (6.5)**. Scatchard plots were popular at one time so that parameters could be estimated by plotting data by hand. Given the ability to easily perform nonlinear least-squares fitting of data and error analysis with personal computers, Scatchard analysis is no longer advisable. Analysis of binding data is discussed in **Sections 4.5 and 4.6.**

3. Multiple Equilibria and Linkage

The equations describing linkage are relatively easy to obtain using the molecular partition function. We introduce the method here and apply it to single-site binding (**Sections 3.1–3.2**). We also summarize the equations describing protein stability and unfolding thermodynamics (**Section 3.3**), and then describe three linkage examples in detail (**Section 3.4–3.6**).

3.1. The Molecular Partition Function

Macromolecules which can exist in more than one state will populate each state at equilibrium according to the Boltzman distribution, where the probability or fractional population of each state i is (**3, 5**):

$$f_i = \frac{e^{-G_i/RT}}{\sum\limits_j e^{-G_j/RT}}.$$
(6.16)

The state with the highest probability of being occupied is that with the lowest energy, but all states are populated to some extent at equilibrium with the probability decreasing exponentially with increasing free energy. The sum in the denominator is referred to as the molecular partition function, commonly symbolized by Q *(3, 5)*. It can be shown that the partition function is given by the sum of the concentrations of each species, divided by the concentration of the reference state. As an example, consider a reversible, two-state equilibrium, $A \Leftrightarrow B$, with equilibrium constant $K = [B]/[A]$. The molecular partition function is

$$Q = \frac{[A] + [B]}{[A]} = 1 + K.$$
(6.17)

The fractional population of each state at equilibrium is given by the corresponding term in the partition function divided by the partition function:

$$f_A = \frac{1}{1 + K},$$
$$f_B = \frac{K}{1 + K}.$$
(6.18)

3.2. Binding and the Molecular Partition Function

Following the above definitions, the molecular partition function for the binding of ligand L to N is *(5)*

$$Q = \frac{[N] + [N.L]}{[N]} = 1 + K_a[L]_f.$$
(6.19)

The partition function for a binding reaction is sometimes referred to as the binding polynomial *(3)*. The fractional populations of the two N states at equilibrium are

$$f_N = \frac{1}{1 + K[L]_f},$$

$$f_{N.L} = \frac{K[L]_f}{1 + K[L]_f}.$$

(6.20)

The concept of the molecular partition function is especially useful in multiple equilibrium problems, including the linkage of binding to other reactions such as folding and other binding reactions.

3.3. Protein Folding

We summarize here the basic equations describing protein folding which will be useful in a description of the linkage of binding to folding. For simplicity, we assume that folding can be described as the reversible unfolding of a monomer in a two-state reaction (6–9):

$$N \underset{}{\overset{K_{un}}{\rightleftharpoons}} U$$

More complicated examples can be found in **Chapter 3** and these can be readily utilized when appropriate by modifying the linkage analysis below. The native protein, N, can unfold to U with an equilibrium constant K_{un}, which is related to the free energy of unfolding (5):

$$K_{un} = e^{-\Delta G/RT}.$$

(6.21)

ΔG is given by (5, 10)

$$\Delta G = \Delta H - T\Delta S,$$

$$\Delta H = \Delta H(T_m) + \Delta C_p(T - T_m),$$

$$\Delta G = \Delta H(T_m)\left(1 - \frac{T}{T_m}\right) + \Delta C_p\left((T - T_m) + T\ln\frac{T_m}{T}\right),$$

(6.22)

where $\Delta H(T_m)$ is the heat of unfolding at the midpoint temperature, T_m, and ΔC_p is the change in heat capacity of unfolding at the T_m. A plot of ΔG as a function of T is referred to as the protein stability curve (11) (see **Chapter 3** and **Note 7**). The fractional population of the native and unfolded species in the absence of linkage is given by

$$f_N = \frac{1}{1 + K_{un}},$$

$$f_U = \frac{K_{un}}{1 + K_{un}}.$$

(6.23)

The unfolding of the protein can be followed spectroscopically (e.g., by CD, fluorescence, or NMR), or calorimetrically (e.g., by DSC). A spectroscopic signal as a function of temperature is given by a weighted sum of the signals of the native and unfolded species, with the weights given by **Eq. (6.23)** (*see* **Note 8**).

$$S_{obs} = \alpha_N S_N + \alpha_U S_U. \tag{6.24}$$

A DSC endotherm is given by the derivative of the excess enthalpy due to the unfolding reaction, ΔH_{excess}, as a function of temperature, where *(12)*
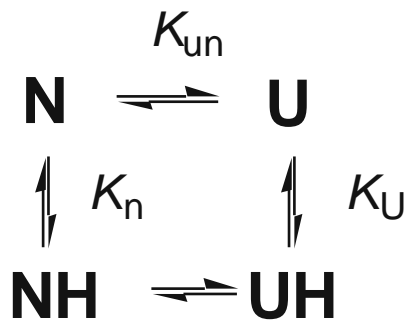
$$\Delta H_{excess} = f_U \Delta H. \tag{6.25}$$

The DSC data can be fit by nonlinear least squares to obtain the T_m and ΔH (*see* **Note 9**).

3.4. Protein Folding Linked to Protonation

Electrostatic interactions are important in controlling protein structure, stability, and interactions *(13–16)*. The effect of pH on stability can be used to quantitatively probe the location and importance of these interactions *(17–19)*. Ionic interactions must lead to perturbation of the pKs of the groups involved from those observed in isolated model compounds. The effect of pH on folding is described here, and the effect on binding in **Section 3.5**.

pH can only affect stability if the pK of an ionizing group is linked to folding, which requires that at least one pK must differ significantly in the folded and unfolded states *(14)*. We model this here with a single protonation site linked to folding. This does not imply that there is only a single ionizing group on the protein, but only that one affects protein stability to a significant extent. The pK_a of a single titrating group is perturbed by folding such that in N the pK_a is $\log(K_n)$, where K_n is the association constant for proton binding (e.g., to a carboxylate). In the unfolded state the pK_a of the group is $\log(K_u)$, where K_u is the proton association constant for the linked group in the unfolded form.

$$
\begin{array}{ccc}
 & K_{un} & \\
N & \rightleftharpoons & U \\
\big\updownarrow K_n & & \big\updownarrow K_U \\
NH & \rightleftharpoons & UH
\end{array}
$$

The binding polynomial describes proton binding, and is a function of the hydrogen ion concentration:

$$Q = 1 + K_{un} + K_n \cdot [H] + K_{un} \cdot K_u \cdot [H]. \qquad (6.26)$$

From this we can write expressions for the pH dependence of the fractions of each of the species at equilibrium:

$$
\begin{aligned}
f_N &= 1/Q, \\
f_{NH} &= K_n \cdot [H]/Q, \\
f_U &= K_{un}/Q, \\
f_{UH} &= K_{un} \cdot K_u \cdot [H]/Q.
\end{aligned}
\qquad (6.27)
$$

Progress curves showing the dependence of folding (or unfolding) on pH can be obtained by summing the fractions of the native (or unfolded) species:

$$
\begin{aligned}
\alpha_N &= \frac{1 + K_n \cdot [H]}{Q}, \\
\alpha_U &= \frac{K_{un}(1 + K_u \cdot [H])}{Q}.
\end{aligned}
\qquad (6.28)
$$

A plot of α_N as a function of pH is shown in **Fig. 6.5a** (*see* **Note 10**), and the effect of varying temperature on the pH dependence of folding is shown in **Fig. 6.5b**. Cross-sections through the surface in **Fig. 6.5b** at constant pH represent thermal "melts" which might be observed if folding were followed as a function of temperature by a spectroscopic method. The pH dependence of folding that might be observed with a spectroscopic technique such as CD is given by a weighted sum of the spectroscopic signals for the N and U species **(Eq. (6.24))**, with the weights given by the α_N and α_U values in **Eq. (6.28)** (*see* **Note 11**).

Finally, the pH dependence of protein stability can be found from the pH dependence of the effective equilibrium constant for unfolding, K_{un}^{eff}, given by

$$K_{un}^{eff} = \frac{f_U + f_{UH}}{f_N + f_{NH}}. \qquad (6.29)$$

Thus, in the presence of linkage, it is **Eq. (6.29)** which defines the observed equilibrium between folded and unfolded species, and not K_{un}, the intrinsic unfolding reaction equilibrium constant. Fitting data which reflects the equilibrium between folded and unfolded protein as a function of pH to **Eq. (6.29)** permits a deconvolution of the effects of protonation from the intrinsic equilibrium and determination of K_{un}.

The combined temperature and pH dependence of the free energy of unfolding is given by $\Delta G = -RT \ln K_{un}^{eff}$ and is shown in **Fig. 6.6a**. The pH dependence of the intersection of the free energy surface with the zero plane represents the pH dependence of the T_m, and is shown in **Fig. 6.6b**. The sigmoidal curve does
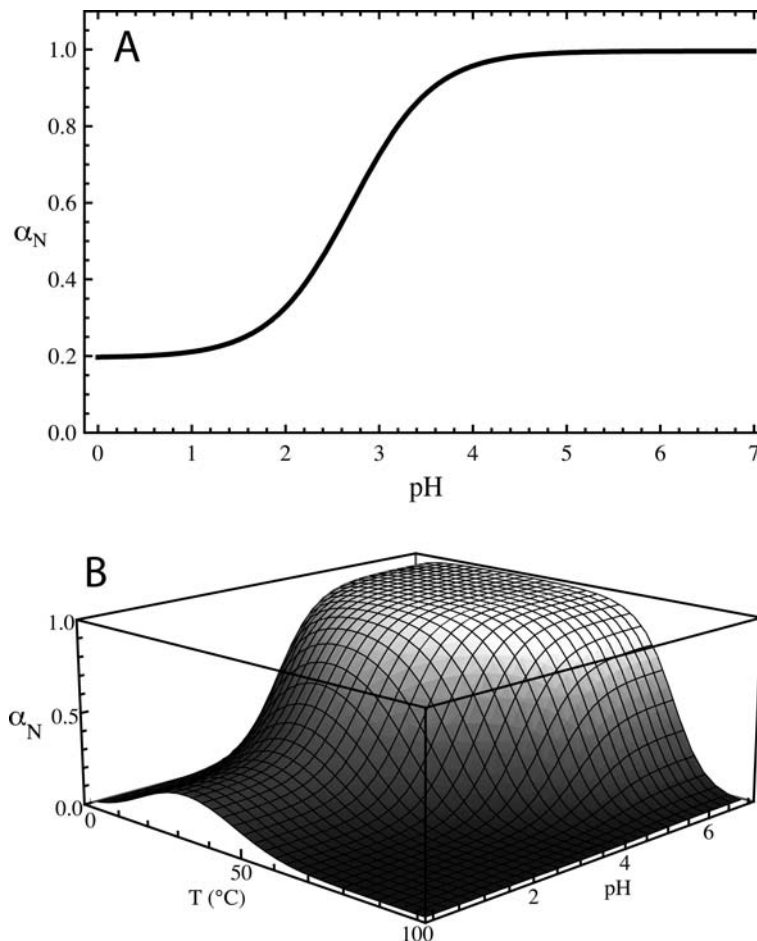
Fig. 6.5. Simulations of the dependence of the extent of protein folding on temperature and pH due to linkage of folding to protonation. Panel A shows the dependence of α_N on pH at 25°C. The curve is a cross-section through the surface in Panel B which shows the effect of both temperature and pH. Cross-sections perpendicular to this at constant pH represent thermal "melts". Note at lower pH maximal folding is observed around 25°C, with increased unfolding occurring not only with increasing temperature, but also at temperatures below this (cold denaturation). The thermodynamic parameters for protein folding were $T_m = 80°C$, $\Delta H(T_m) = 50$ kcal/mol, and $\Delta C_p = 1000$ cal/deg/mol. The pKs for the single titrating group linked to folding were 2 in the native protein, and 5 in the unfolded.

not represent a titration curve, but the upper and lower limits are defined by the pKs of the linked group in the native and unfolded species. The magnitude of the decrease in stability with pH depends on the difference in the pKs.

In order to define the dependence of DSC data on pH, the total excess enthalpy of the system relative to an arbitrary state (typically, the native species N) is required:

$$H_{excess} = f_U \Delta H_{un} + f_{UH}(\Delta H_{un} + \Delta H_{UH}) + f_{NH}\Delta H_{NH} - N_o\Delta H_b, \quad (6.30)$$

which is a weighted sum of the enthalpies of each state (relative to N), with the weights given by the fractional occupations of the
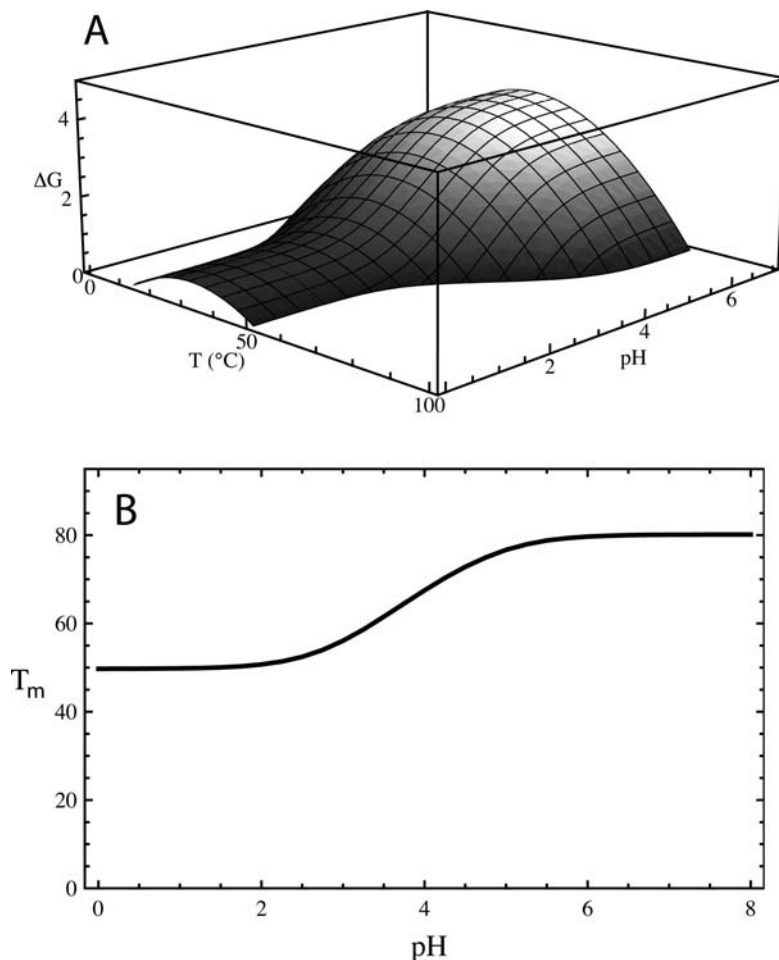
Fig. 6.6. Simulation of the pH dependence of protein stability due to the linkage of folding to the protonation of the protein. Panel A shows the dependence of the free energy of unfolding as a function of temperature and pH. The intersection of the surface with the zero plane defines the pH dependence of the T_m in Panel B (since $K = 1$ when $\Delta G = 0$). The thermodynamic parameters for the intrinsic protein folding were $T_m = 80°C$, $\Delta H(T_m) = 50$ kcal/mol, and $\Delta C_p = 1000$ cal/deg/mol. The pKs for the single titrating group linked to folding were 3 in the native protein, and 5 in the unfolded.

respective states. The last term is the contribution to the heat due to release of protons taken up by the buffer with a heat of protonation ΔH_b. N_o is the number of protons taken up with unfolding given by the fraction of the U states in the protonated form minus the fraction of the N states in the protonated form:

$$N_o = f_{UH} - f_{NH} \qquad (6.31)$$

The DSC endotherm is given by the temperature dependence of the excess heat capacity, which is the total derivative of H_{excess} with respect to temperature and includes the changes in enthalpies as well as the fractional occupations of the states. This can be calculated numerically by calculating the change in H_{excess} with a small
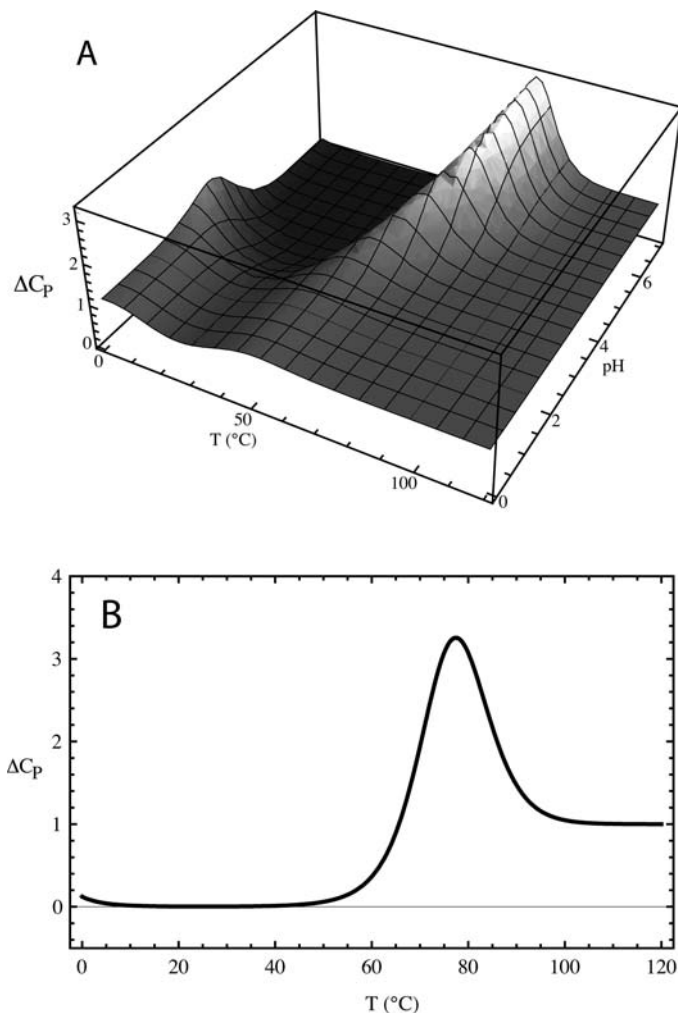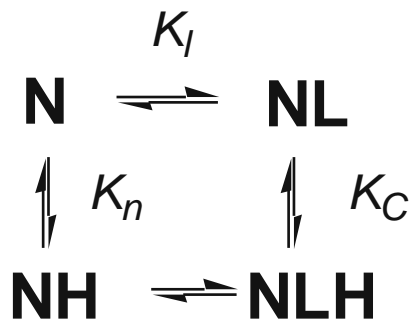
Fig. 6.7. Simulations of the dependence of DSC on pH due to the linkage of protein folding to the protonation of a protein side chain. Panel A shows the dependence of the excess heat capacity of the system on temperature and pH. Panel B is a cross-section through this surface at pH 7 showing the DSC expected for unfolding. The thermodynamic parameters for protein folding were $T_m = 75^{\circ}C$, $\Delta H(T_m) = 50$ kcal/mol, and $\Delta C_p = 1000$ cal/deg/mol. The pKs for the single titrating group linked to folding were 2 in the native protein, and 5 in the unfolded.

change in temperature. A simulation of the pH dependence of the DSC of a protein is shown in **Fig. 6.7**. DSC data collected as a function of pH can be fit globally by nonlinear least squares (*see* **Note 12**).

3.5. Binding Linked to Changes in Protonation

Ligand binding may be linked to changes in ionization of the protein *(20)*. Binding is characterized by the binding constant K_l, and protonation of the free and ligand-bound protein is described by proton-binding constants K_n and K_C, respectively (given by 10^{pKa} of the titrating group).

$$
\begin{array}{ccc}
& K_l & \\
\mathbf{N} & \rightleftharpoons & \mathbf{NL} \\
\Big\updownarrow K_n & & \Big\updownarrow K_C \\
\mathbf{NH} & \rightleftharpoons & \mathbf{NLH}
\end{array}
$$

The fractional occupation of the four species is given by

$$
\begin{aligned}
f_{\mathrm{N}} &= 1/Q, \\
f_{\mathrm{NH}} &= K_n[H^+]/Q, \\
f_{\mathrm{NL}} &= K_l[L]/Q, \\
f_{\mathrm{NLH}} &= K_C K_l[H^+][L]/Q, \\
Q &= 1 + K_l[L] + K_n[H^+] + K_l K_n[L][H^+].
\end{aligned}
\tag{6.32}
$$

The binding progress is described by sum of the fractional populations of the ligand-bound species:

$$
\alpha_{\mathrm{NL}} = K_l[L](1 + K_c[H^+])/Q.
\tag{6.33}
$$

The equilibrium constant for binding is given by the sum of the fractions of bound species divided by the sum of the unbound:

$$
K_{\mathrm{obs}} = \frac{K_l(1 + K_c[H^+])}{1 + K_n[H^+]}.
\tag{6.34}
$$

The binding affinity at various values of pH can be measured by both spectroscopic or calorimetric (ITC) methods. ITC is especially useful since it also provides the heat of ligand binding. The observed heat is given not only by the intrinsic heat of binding, but also contains contributions from the heat of protonation of free protein, the heat of protonation of the complex (each weighted by the fractions of the N and NL species which are protonated), and protonation of the buffer:

$$
\Delta H_{\mathrm{obs}} = \Delta H_c - f_{\mathrm{N(H)}}\Delta H_n + f_{\mathrm{NL(H)}}\Delta H_c + N_{\mathrm{H}}\Delta H_b,
\tag{6.35}
$$

where the changes in the number of protons bound upon binding ligand are

$$
\begin{aligned}
N_{\mathrm{H}} &= f_{\mathrm{NL(H)}} - f_{\mathrm{N(H)}}, \\
f_{\mathrm{NL(H)}} &= \frac{K_c[H^+]}{1 + K_c[H^+]}, \\
f_{\mathrm{N(H)}} &= \frac{K_n[H^+]}{1 + K_n[H^+]}.
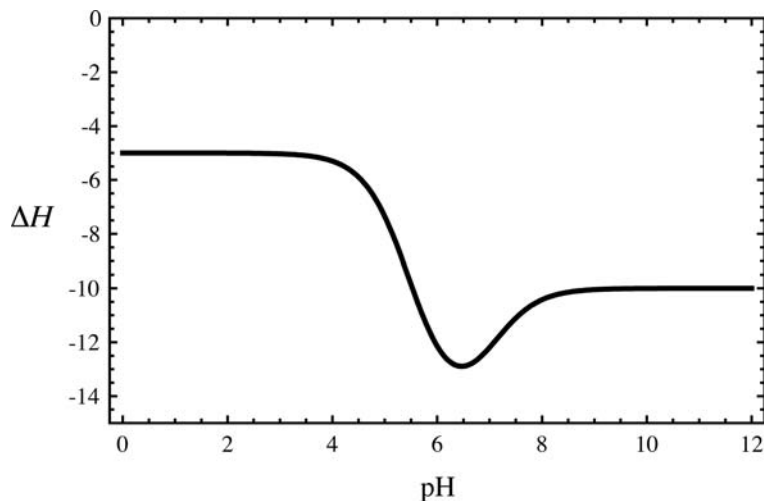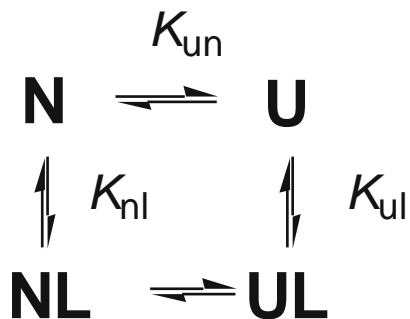\end{aligned}
\tag{6.36}
$$

Fig. 6.8. Simulation of the heat of ligand binding as a function of pH with linkage to the protonation of a single side chain in the protein. The pK_a of the linked group was 7 in the ligand-free protein, and shifted to 5.5 upon ligand binding. The K_d for ligand binding was 10^{-8} M and was associated with a heat of −10 kcal. The heats of protonation of the protein side chain were −20 kcal/mol in the ligand-free form, and −15 kcal/mol in the complex The heat of protonation of the buffer was 25 kcal/mol.

$f_{NL(H)}$ and $f_{N(H)}$ are the fractions of the bound and free N states, respectively, which are in the protonated form. An example of the unusual effects expected for the pH dependence of the heat of ligand binding is shown in **Fig. 6.8** (*see* **Note 13**). Additional presentations of the effects of linked protonation have been provided by Baker and Murphy *(20)*.

3.6. Binding Linked to Folding and Stability

Finally, we consider the effect of ligand binding on protein folding and stability. The intrinsic unfolding reaction of N ⇔ U is described above (**Section 3.3**) by an equilibrium constant K_{un} (and the associated ΔH_{un}, ΔC_p, and T_m). This describes the temperature dependence of the intrinsic stability (the protein stability curve). In addition, we consider the linkage of ligand binding to both the native and unfolded species, with binding constants K_{nl} and K_{ul}, respectively.

$$
\begin{array}{ccc}
 & K_{un} & \\
\mathbf{N} & \rightleftharpoons & \mathbf{U} \\
\Big\updownarrow\, K_{nl} & & \Big\updownarrow\, K_{ul} \\
\mathbf{NL} & \rightleftharpoons & \mathbf{UL}
\end{array}
$$

Ligand binding is described by a binding affinity and enthalpy (at a reference temperature, e.g., $25°C$) and a ΔC_p of binding (temperature independent). The temperature dependence of the binding enthalpy, entropy, free energy, and affinity are given by *(1, 5)*

$$\Delta H(T) = \Delta H(25) + \Delta C_P(T - 298), \qquad (6.37)$$

$$\Delta S(25) = (\Delta H(25) - \Delta G(25))/298, \qquad (6.38)$$

$$\Delta G(T) = \Delta H(T) - T\Delta S(T), \qquad (6.39)$$

$$K = e^{-\Delta G(T)/RT}. \qquad (6.40)$$

The concentration of NL and UL in terms of total protein and ligand concentration can be approximated by

$$[NL] = \frac{1 + K_{nl}[N]_t + K_{nl}[L]_t - \sqrt{-4K_{nl}^2[N]_t[L]_t + (1 + K_{nl}[N]_t + K_{nl}[L]_t)^2}}{2K_{nl}}, \qquad (6.41)$$

$$[UL] = \frac{1 + K_{ul}[N]_t + K_{ul}[L]_t - \sqrt{-4K_{ul}^2[N]_t[L]_t + (1 + K_{ul}[N]_t + K_{ul}[L]_t)^2}}{2K_{ul}}, \qquad (6.42)$$

which were derived above (**Section 2.3**). They are approximate since **Eq. (6.6)** is not valid in this case with two complexes present, but that is circumvented as follows. The concentration of free ligand is

$$[L]_f = [L]_t - [NL] - [UL]. \qquad (6.43)$$

The fractional population of the four states are given by

$$f_N = 1/Q,$$

$$f_U = K_{un}/Q,$$

$$f_{NL} = K_{nl}[L]_f, \qquad (6.44)$$

$$f_{UL} = K_{un}K_{ul}[L]_f,$$

$$Q = 1 + K_{un} + K_{nl}[L]_f + K_{un}K_{ul}[L]_f.$$

The concentrations of NL and UL can be expressed in terms of these fractions and **Eq. (6.43)** can be rearranged to

$$[L]_t - [N]_t f_{NL} - [N]_t f_{UL} - [L]_f = 0. \qquad (6.45)$$

The concentration of free ligand is then obtained by finding the value of $[L]_f$ which satisfies the equation (i.e., the root). $[L]_f$ is then used to define the fractional populations of the four states
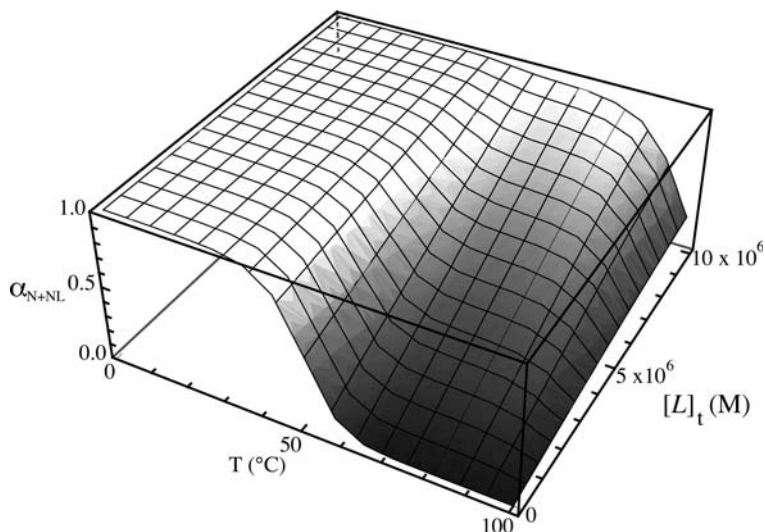
Fig. 6.9. Simulation of the effect of temperature and ligand concentration on the extent of folding due to the linkage of folding to ligand binding. The thermodynamic parameters for protein folding were $T_m = 50\ °C$, $\Delta H(T_m) = 50$ kcal/mol, and $\Delta C_p = 1000$ cal/deg/mol. The dissociation constants were 10^{-7} M for the native and 10^{-4} M for the unfolded protein.

using **Eq. (6.44)**. These define the dependence of folding on temperature and ligand concentration and may be used to define thermal melting profiles as a function of ligand concentration (**Fig. 6.9**).

The unfolding equilibrium constant in the presence of linkage is then

$$K_{obs} = \frac{f_U + f_{UL}}{f_N + f_{NL}}, \tag{6.46}$$

and the free energy of unfolding, ΔG_{obs}, is $-RT\ln(K_{obs})$. The dependence of the T_m on ligand concentration may be found from the ligand dependence of the temperature at which ΔG_{obs} is zero (i.e., the root of $\Delta G_{obs} = 0$) (*see* **Fig. 6.10**). Note that T_m increases with increasing ligand concentration without limit. A T_m cannot be given without stating the ligand concentration.

To define the expected DSC data as a function of ligand concentration, we express the total excess enthalpy of the system relative to a reference state (typically N) in terms of a weighted sum of the enthalpies of the four states (N being set to 0):

$$H_{excess} = f_U \Delta H_{un} + f_{UL}(\Delta H_{un} + \Delta H_{ul}) + f_{NL}\Delta H_{nl}, \tag{6.47}$$
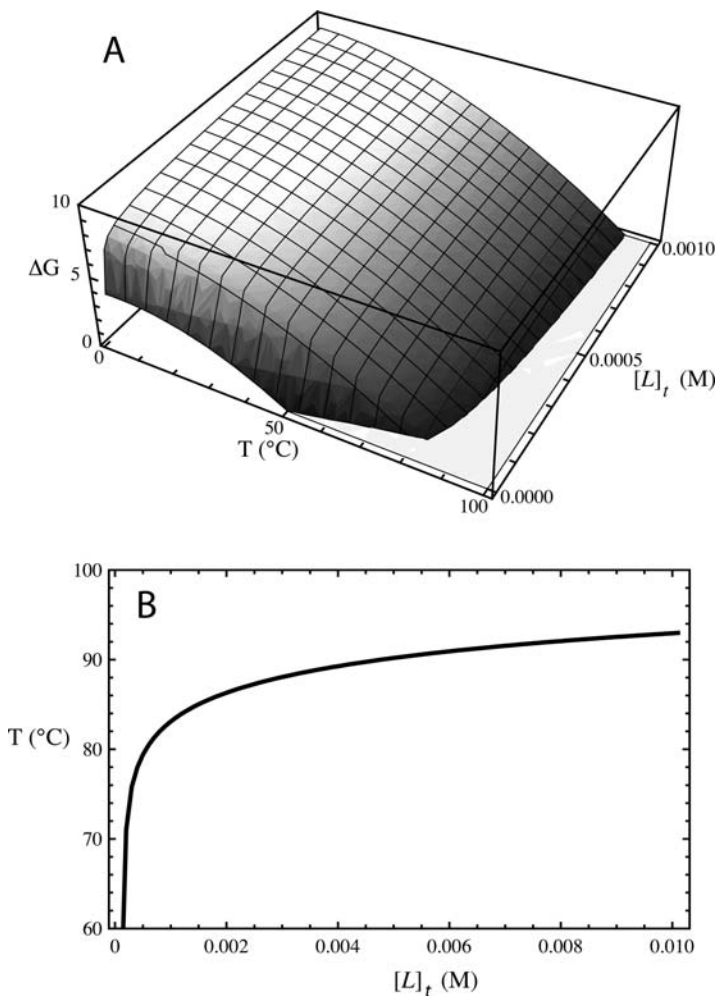
Fig. 6.10. Simulation of the effect of ligand concentration on protein stability due to the linkage of ligand binding to protein folding. Panel A shows the temperature and ligand concentration dependence of the free energy of unfolding. The intersection of the surface with the zero plane provides the dependence of the T_m on ligand concentration shown in Panel B. The thermodynamic parameters for protein folding were $T_m = 50°C$, $\Delta H(T_m) = 50$ kcal/mol, and $\Delta C_p = 1000$ cal/deg/mol. The dissociation constants were 10^{-7} M for the native and 10^0 for the unfolded protein.

and the DSC is the excess heat capacity given by the total derivative of H_{excess} with respect to temperature:

$$C_{p,\,excess} = \frac{\partial H_{excess}}{\partial T}, \tag{6.48}$$

which may be calculated numerically by dividing the change in H_{excess} due to a small increment (e.g., $0.01°C$) in temperature by the magnitude of the increment (*see* **Fig. 6.11**).
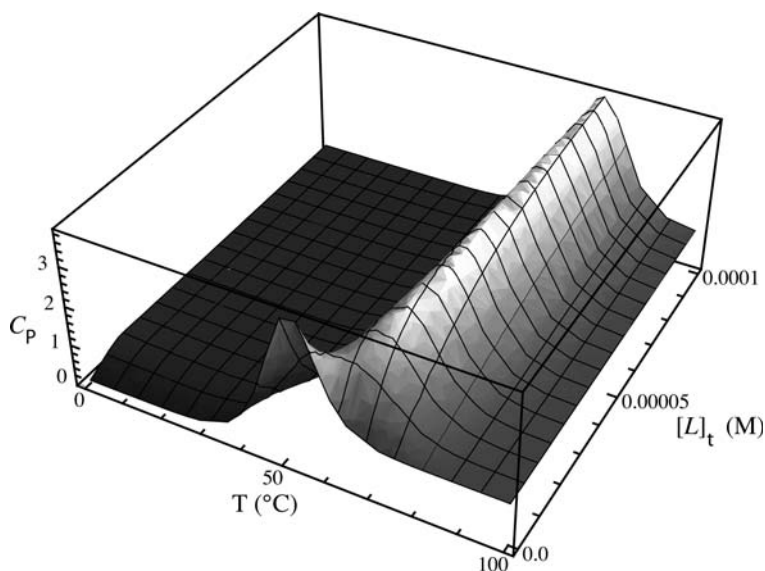
Fig. 6.11. Simulations of the effect of temperature and ligand concentration on the excess heat capacity due to linkage of protein folding to ligand binding. Thermodynamic parameters were as in **Fig. 6.10**.

4. Methods

4.1. Experimental Design

Linkages are revealed and analyzed by performing an array of binding experiments with not only varying concentrations of the ligand of interest, but also by varying other factors which may be important in linked reactions, for example, pH, additional ligand (known and unknown) concentrations, and temperature. As wide a range of experimental conditions as possible should be utilized to permit the observation and accurate description of linkage effects. For example, upon decreasing the pH below 4 in the presence of 0.3 M NaCl, the T_m of the protein Sac7d decreases *(21)* similar to that observed for most proteins, and is indicative of the linkage of folding to side-chain ionization (*see* **Fig. 6.6**). However, below pH 2, the T_m increases. This is not expected by simple linkage of protonation and folding, and indicates the additional linkage of anion binding. Had the data above pH 2 been fit with a model that only described the linkage of folding and protonation, the analysis would have been incomplete and incorrect. Additional data indicated that in the absence of salt, the DSC endotherm shifts to low temperature with decreasing pH and disappears entirely at pH 2 (similar to **Fig. 6.7**). It then reappears with a further decrease in pH and shifts back to higher temperature. Although there is little or no endotherm at pH 2, circular dichroism shows that about 25% of Sac7d is folded at pH 2 and that heating leads to a cooperative transition. Only by varying a

wide range of experimental parameters and observing the binding and folding progress with multiple techniques was it possible to observe these linkages and isolate each of the intrinsic reactions of interest *(22, 23)*.

Reliable extraction of thermodynamic parameters for systems which involve linkages requires multidimensional binding data (e.g., spectroscopic and ITC binding data) and stability or folding data (e.g., the temperature dependence of folding followed spectroscopically and by DSC as a function of pH and ligand concentration). Each reaction in the linkage model (binding, ionization (including buffer ionization), and folding and other structural transitions) is characterized by an equilibrium constant at a reference temperature (or alternatively simply the T_m), and a ΔH and ΔC_p. As a result, the number of parameters even in a simple model can be quite large. Many parameters can be fixed to minimize the complexity of the problem: for example, those for the buffer can be set to literature values; ΔH and ΔC_p for the ionizing groups can be set to values for model compounds, as can the pKs in the unfolded state; and those in the native state can be determined by NMR. In addition, the effects of some parameters can be eliminated by adjustment to appropriate limits. The advantage of an explicit linkage model is that it clearly indicates the assumptions made. In the presence of linkages, it is certainly better than modeling the binding with a simple model.

4.2. Spectroscopic Methods

Binding can be monitored indirectly with any spectroscopic method which shows a change in signal upon binding. Examples include a change in the intrinsic CD or fluorescence of protein, or the shifting of one or more NMR resonances upon ligand binding. Although indirect methods typically require significantly less material than direct methods, they suffer from the fact that it is assumed that the signal is directly proportional to the number of sites occupied. While methods exist to test the validity of this assumption, the time required for such analysis may be prohibitive and the assumption of direct proportionality is often stated in the data analysis.

4.2.1. Sample Preparation

Titrations are conducted such that the molecule providing the spectroscopic signal is held at essentially constant concentration (with adjustment for dilution during the titration) and the ligand is titrated incrementally with small aliquots of a stock solution of sufficiently high concentration (e.g., ×100) to minimize dilution of the observed molecule. Both are dissolved in the same buffer, preferably with extensive dialysis, and temperature is measured and maintained as precisely as possible. Concentrations of all solutions are determined spectroscopically with accurate extinction coefficients using calibrated spectrophotometers (*see* **Note 14**).

4.2.2. Data Collection

Data is collected following the directions of the spectrophotometer manufacturer. It is important to collect sufficient data to provide

complete coverage of the titration curve. This requires not only definition of the maximal response, but also the shape of the binding isotherm in the vicinity of regions of maximal change (e.g., near inflection and break points). In fluorescence data collection, particular attention should be placed on allowing for the possibility of an inner filter effect, as well as photobleaching of the sample *(24)*.

4.2.3. Data Analysis

The dependence of the signal change as a function of total ligand concentration is fit to **Eq. (6.12)** with the binding density defined
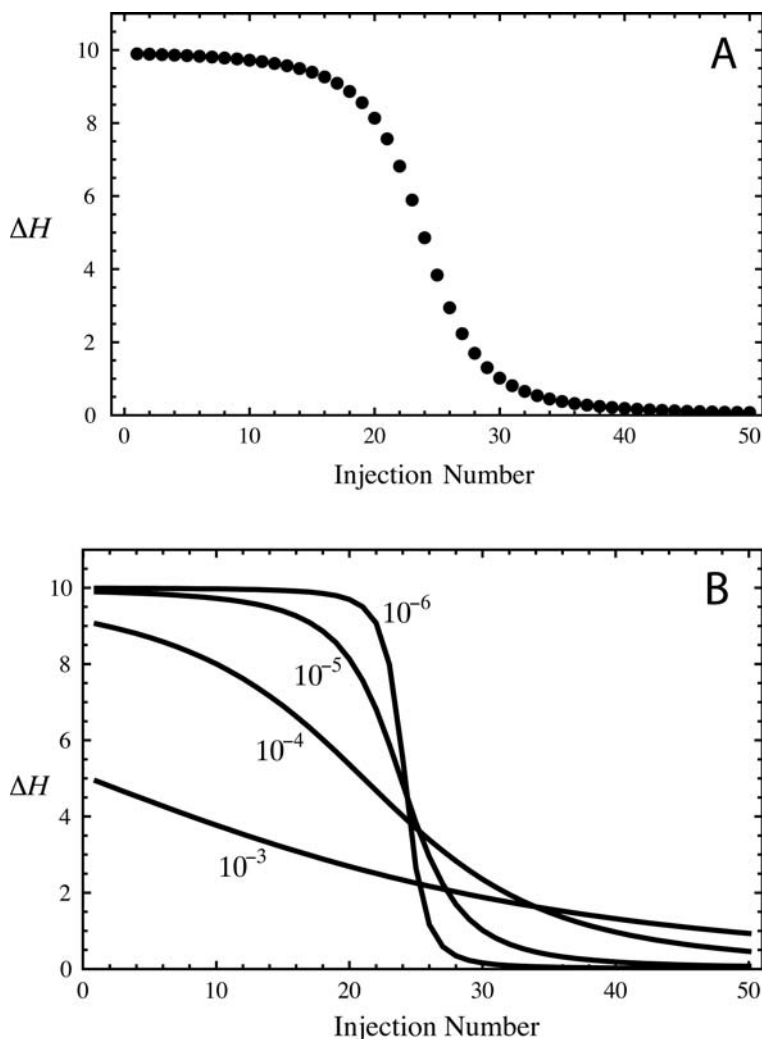

Fig. 6.12. Simulations of the heat of binding expected for ITC titrations. Panel A shows the molar heat of binding observed with each injection of ligand (50 injections total). The K_d was 10^{-5} M and the binding heat was 10 kcal/mol. The simulations in Panel B demonstrate that at higher affinity, the data cannot define the binding constant since there are insufficient data points at the equivalence point to define the shape of the curve. At low affinity, the molar-binding heat cannot be defined due to insufficient binding. ITC is best used when the product $[P]_t \cdot K$ is in the range of 50–1000 *(25)*.

by **Eq. (6.11)**. The fitted parameters include the maximal signal change, S_{max}, and the binding constant, K_a. Errors in the parameters should be reported to indicate the quality of the fit. Ideally, a representative plot of a fitted curve on the data should also be presented.

4.3. Isothermal Titration Calorimetry (ITC)

4.3.1. Overview

ITC can be used to directly measure the heat change associated with a binding reaction at a specified (constant) temperature *(25–28)*. By performing a series of binding experiments at different temperatures, the change in heat capacity of the reaction can also be defined $(\Delta C_p = (\partial \Delta H / \partial T)_p)$. In general there is no better method for obtaining both ΔH and ΔC_p of binding. Small aliquots of one of the binding species (e.g., ligand) are titrated into a solution of the remaining species (e.g., macromolecule) at constant temperature, and the heat associated with each injection is measured. The heat change associated with binding modifies the amount of heat required to maintain constant temperature (exothermic reactions lead to a decrease in heat required and endothermic reactions require more), and the deviation from the baseline level of heat flow provides the heat associated with binding of the aliquot injected. With reasonably tight binding, most of the titrant in the first few injections is largely bound, and normalization of the heat change by the number of moles of complex formed provides the molar heat of binding. As the titration proceeds, the available binding sites are depleted until no further heat change is observed (except possibly for a heat of dilution of the titrant).

4.3.2. Experimental Design

The product $[P]_t \bullet K_a$ must be in the range of 50–1000 to obtain useful data to define both the binding affinity and heat of binding by ITC *(25)*. Higher values lead to data which cannot reliably define the binding affinity, yet reliable heats can still be measured (see Fig. 6.12). Note that for very tight binding it is necessary to lower the protein concentration to the point that the signal-to-noise ratio becomes too low. The concentration of the protein and ligand should be set so that the midpoint of the titration appears about midway through the titration in order to define the shape of the titration curve before and after equivalence. The stock titrant concentration in the syringe is typically on the order of 100 times more concentrated than the solution being titrated; thus, solubility limits may dictate the macromolecule concentration. Simulations using estimates of the binding parameters are useful for designing ITC experiments, and programs are available from the manufacturers of the instruments.

4.3.3. Sample Preparation

It is essential that the sample and titrant solutions are well matched to prevent large heats of dilution. This can be

accomplished by extensive dialysis against the same buffer solution. Both reference and sample solutions are degassed with stirring under a slight vacuum. MicroCal provides a device that also includes a timer for reproducible degassing. The choice of buffer is nontrivial since changes in ionization will lead to heat contributions from buffer protonation/ionization. Buffer heats of protonation must be considered if binding is associated with ionization changes, and methods for removing the effects of protonation using linkage analysis have been described *(20)*.

4.3.4. Instrumental Considerations

The detailed design of an ITC instrument has been described *(25)*. An instrument designed for biochemical studies is composed of two matched metal cells for containing the sample to be titrated, and a reference which contains buffer and is not altered during the course of a titration. The cells are made of a metal which is inert under most biochemical conditions, but caution must be taken to prevent modification of the cells (e.g., chemical changes due to corrosion, or mechanical damage due to mishandling or freezing). A computer-controlled, motor-driven syringe injects the titrant into the sample cell, and with at least one manufacturer it is also used to stir the reaction mixture (MicroCal, Inc.) with minimal perturbation of the baseline during the titration.

Optimum performance is obtained if an ITC instrument is powered by a line conditioner and preferably an isolated electrical circuit with a true isolated ground. Cells are meticulously cleaned using procedures described by the manufacturer. Instrument calibration must be performed using procedures supplied by the manufacturer, typically with defined heat pulses. It is important to calibrate the instrument at each temperature in variable temperature work. Most ITC experiments are performed with overfilled cells, and therefore the cell volume of the calorimeter can be defined using a reaction of known heat (e.g., titration of 18-crown-6 ether with Ba^{+2} *(29)*). The binding of 2'-CMP to RNase A is a common reaction used to test the performance of calorimeters *(25)*. The temperature limit of currently available instruments appropriate for biochemical studies ranges from about 0°C to 100°C.

4.3.5. Data Collection

Data collection is under computer control with typically 20–30 injections of 5–10 μl each. Data collection should not be started until baseline stability has been attained. With the best instruments currently available (e.g., the MicroCal VP-ITC) this is obtained within one hour of setup including placement of the injection syringe into the sample cell and initiation of stirring. Each injection is followed by heat absorption or release depending on whether or not the binding is endothermic or exothermic. A small heat change is also typically associated with heat of dilution of the ligand and can be seen at the end of the injection series after saturation of the binding sites. Sufficient time between injections

must be allowed to permit definition of the baseline during the titration. The total titration requires about 1–2 h. Note that the first data point is usually unusable due to leakage from the syringe needle during instrument equilibration.

4.3.6. Data Analysis

Software supplied by the instrument manufacturers can be used to perform straightforward integration of the peaks following each injection and binding analysis. More complicated models can also be added as user-defined external modules. However, there is a considerable advantage to writing your own software for fitting ITC data. This is especially true if closed-form expressions cannot be written for the concentration of complex in terms of ligand concentration, binding affinity, and number of sites. The basic equations for analyzing ITC data are described here. These can be easily utilized with any binding model.

The binding of a ligand L to a macromolecule N is studied by injecting L into N. The cell is overfilled and therefore the reaction volume observed by the calorimeter remains constant. With the ith injection of L of volume Δv into a constant cell volume c, the concentration of N decreases due to displacement of a volume equal to the injection volume, so that the concentration of macromolecule after the ith injection is given in discrete numerical form by

$$N_i = N_{i-1} - \frac{\Delta v}{c} N_{i-1}. \tag{6.49}$$

In differential form this becomes

$$\frac{\partial N}{N} = -\frac{\partial v}{c}, \tag{6.50}$$

which can be integrated to give *(27)*

$$N_i = N_o\, e^{-\frac{i*\Delta v}{c}}, \tag{6.51}$$

where N_{o} is the starting concentration of macromolecule in the cell. During the titration, the concentration of the ligand increases with each injection i, but a slight amount is also lost due to displacement of the cell contents with each injection. The concentration of ligand after the ith injection is given by

$$L_i = L_{i-1} + L_o \frac{\Delta v}{c} - L_{i-1} \frac{\Delta v}{c}, \tag{6.52}$$

where L_{o} is the stock ligand concentration in the syringe. In differential form this is

$$\frac{\partial (L - L_o)}{(L - L_o)} = -\frac{\partial v}{c} \tag{6.53}$$

so that

$$L_i = L_o(1 - e^{-\frac{i*\Delta v}{c}}). \tag{6.54}$$

The amount of heat generated with each injection is proportional to the amount of new NL generated (i.e. $NL_i - NL_{i-1}$) plus the amount of complex lost due to extrusion that accompanies the injection. Since the displacement does not take place instantaneously and efficient mixing is occurring continuously, the amount lost is taken as the average of the concentrations at the beginning and end of the injection:

$$\Delta NL_i = NL_i - NL_{i-1} + 0.5\frac{\Delta v}{c}(NL_{i-1} + NL_i). \qquad (6.55)$$

The heat generated in the cell is given by the molar enthalpy times the incremental change in complex times the cell volume plus a heat of dilution *(27)*:

$$Q_j = c\,\Delta H\,\Delta NL_i + q_i. \qquad (6.56)$$

In some situations the heat generated is normalized by the concentration increment of the ligand titrated. The change in complex per incremental increase in total ligand concentration is given by

$$\frac{\Delta NL_i}{\Delta L_i} = (NL_i - NL_{i-1} + 0.5\frac{\Delta v}{c}(NL_{i-1} + NL_i))/(L_i - L_{i-1} + 0.5\frac{\Delta v}{c}(L_{i-1} + L_i)),$$

$$(6.57)$$

so that the molar heat change is given by

$$\overline{Q_j} = \Delta H\,\frac{\Delta NL_i}{\Delta L_i} + q_i. \qquad (6.58)$$

The fitting of ITC data requires a model to permit the calculation of the change in complex concentration for each incremental increase in ligand concentration. For single-site binding with a binding constant K, the concentration of complex is given by:

$$NL_i = \frac{1 + K\,N_i + K\,L_i - \sqrt{-4\,K^2\,N_i\,L_i + (1 + K\,N_i + K\,L_i)^2}}{2\,K} \qquad (6.59)$$

For more complicated binding models, an equation similar to **Eq. (6.59)** must be obtained to define the concentration of complex. Thus, ITC data for single-site binding can be fit by nonlinear regression with **Eqs. (6.56)** and **(6.59)** (or a similar equation) with adjustable parameters ΔH, K, and q_i.

4.4. Differential Scanning Calorimetry

DSC data collection and analysis is described in Chapter 6.

4.5. Nonlinear Least-Squares Fitting of Binding Data

The fitting of experimental data by nonlinear regression is readily accomplished in any situation where artificial data can be simulated with a mathematical function and an adjustable set of parameters *(30)*. Data which is intrinsically nonlinear should not be linearized (*see* **Note 15**). The simulated and observed data are compared, and the parameters are adjusted by a nonlinear fitting

program to minimize the differences between the observed and simulated datasets (i.e., the residuals) (*see* **Note 16**). Most importantly, the fitting provides not only the parameters, but also estimates of the errors in the parameters (*see* **Note 17**).

4.6. Global Nonlinear Regression

Multiple datasets collected using different conditions (e.g., different ligand concentrations, pH, and temperature) as well as with different methods (e.g., spectroscopy, ITC, and DSC) are fit simultaneously using global nonlinear regression methods which permit the sharing of common parameters during the refinement and minimization of the combined residuals *(31)*. This can prove to be computationally intensive and efficient optimization routines are essential. The IGOR software package (Wavementrics) is especially useful for globally fitting multidimensional datasets. The individual datasets are fit to the respective equations as described above, and the parameters which are common to each are indicated and optimized globally.

5. Notes

1. *Mathematic* Notebooks containing interactive simulations of binding and linkage as well as data analysis examples can be downloaded from http://daffy.uah.edu/thermo/ See Binding and Linkage Notebook – A (Simple Binding), **Section 1.1** for a direct plot of binding density vs. free ligand concentration.
2. *Mathematica* Notebook A, **Section 1.2**, permits the visualization of the effect of K_d on the binding isotherm by interactively manipulating K_d.
3. Notebook A, **Section 1.4**, allows the visualization of the influence of K_d on a plot of binding density as a function of total ligand concentration.
4. Notebook A, **Section 1.6** shows a titration plot of binding data with the ability to interactively manipulate the effect of K_d on the plot. Note that the shape of the curve does not change with a change in K_d: the curve only shifts. This is in contrast to what is observed with both of the direct plots in 1.2 and 1.4.
5. Binding curves for two sites with identical and differing affinities are shown in Notebook A, **Section 1.8–1.12**. The advantages of titration plots are shown with the ability to interactively manipulate two dissociation constants in 1.10.
6. A Scatchard plot is provided in Binding and Linkage – A (Simple Binding), **Section 1.7**. They should be avoided for data fitting because of the non-Gaussian noise distribution

that results from the coordinate transformation. They may be useful in some situations for presentations and initial estimates of parameters.

7. Interactive plots of protein stability curves are presented in *Mathematica*Notebook Protein Folding Notebook – Melts and DSC, **Section 1**. The influence of ΔH, T_m, and ΔC_p on the stability of the protein as well as the extent of unfolding as a function of temperature can be investigated.

8. Indirect data representing the temperature dependence of protein folding (e.g., fluorescence intensity as a function of temperature) will be given by a weighted sum of the signal intensities of pure native and unfolded protein. The weights are given by the fractional occupation of the native and unfolded species. An interactive simulation is provided in the Protein Folding Notebook – Melts and DSC, **Section 1.2**, along with a nonlinear least-squares fitting of such data to obtain the thermodynamic parameters describing folding in **Section 1.3**. These simulations and fits allow the intrinsic signals of the pure species to be linearly temperature dependent, with two additional parameters for each (slopes and *y*-intercepts).

9. Fitting of DSC data can be done either by directly obtaining the ΔC_p from the offset of the pre- and post-transition baselines, or by first removing the ΔC_p from the data, and then fitting the remaining excess enthalpy contribution to obtain T_m and ΔH. Because an accurate ΔC_p is rarely obtained from DSC baselines, the latter is the preferred method. An example is provided in Protein Folding Notebook – Melts and DSC, **Section 1.6**.

10. An interactive plot of the pH dependence of folding due to linkage of ionization of a single titrating group to folding is provided in Binding and Linkage Notebook C (Linkage), **Section 2.1**. Note that the sigmoidal curve does not represent a titration curve and that the midpoint does not correspond to a pK_a of a titrating group.

11. As in Note 8, the intrinsic signals of the pure species are most likely temperature dependent, and can be described with two additional parameters for each (slope *m* and *y*-intercept *b*); for example, $S_N = S_N^b + S_N^m T \; and \; S_U = S_U^b + S_U^m T..$

12. Simulations of the heat changes associated with changes in folding and protonation can be found in Binding and Linkage Notebook – C (Linkage), **Section 2.2**.

13. Simulations of the effect of pH on the heat of ligand binding are presented in the Notebook B, **Section 4.3**. These include the effect of pH and ligand concentration on the amount of complex, as well as the heat of ligand binding as a function of pH.

14. Wavelength and absorbance calibration of spectrophotometers is essential for binding studies since errors in

concentration measurements will be propogated into errors in all the binding parameters. Procedures for calibration of both are found in reference *(32)*.

15. Data should not be transformed into a linear form to permit a linear least-squares fit. This usually results in distortion of the Gaussian distribution of the noise, and violates one of the basic assumptions of least-squares fitting. Nonlinear data must be fit directly using a nonlinear least-squares routine.

16. Nonlinear regression of binding isotherm is presented in Notebook A, **Section 1.3**. Artificial data is simulated with Gaussian distributed noise, and the "data" fit to obtain both the K_d, and the error in the parameter.

17. Nonlinear regression of indirect binding data, where the signal is obtained as a function of the total ligand concentration, is presented in Notebook A, **Section 1.5**. The fitting provides the K_d as well as the maximal signal change at infinite ligand concentration (along with errors for both parameters). In general, an asymptotic value at infinite ligand concentration should be obtained from the nonlinear fitting, and not by arbitrarily selecting a single data point at high ligand concentration.

Acknowledgments

References

1. Edsall, J. T., Gutreund, H. (1983) Biothermodynamics, John Wiley and Sons, New York.
2. Conners, K. A. (1987) Binding Constants: The Measurement of Molecular Complex Stability, John Wiley, New York.
3. Wyman, J., Gill, S. J. (1990) Binding and Linkage: Functional Chemistry of Biological Macromolecules, University Science Books, Mill Valley, CA.
4. Marshall, A. G. (1978) Biophysical Chemistry, John Wiley & Sons, New York.
5. Eisenberg, D., Crothers, D. (1979) Physical Chemistry with Applications to the Life Sciences, Benjamin/Cummings, Menlo Park, CA.
6. Lumry, R., Biltonen, R., Brandts, J. (1966) Validity of the "two-state" hypothesis for conformational transitions of proteins, Biopolymers 4, 917–944.
7. Biltonen, R. L., Freire, E. (1978) Thermodynamic characterization of conformational states of biological macromolecules using differential scanning calorimetry. CRC Crit Rev Biochem 5, 85–124.
8. Privalov, P. (1979) Stability of proteins. Small globular proteins. Adv. Protein. Chem. 33, 167–241.
9. Freire, E. (1995) in (Shirley, B., Ed.) Protein Stability and Folding, Humana Press, Totowa, N.J.
10. Makhatadze, G., Privalov, P. L. (1995) Energetics of protein structure. Adv Protein Chem 47, 308–425.
11. Becktel, W., Schellman, J. (1987) Protein stability curves. Biopolymers 26, 1859-1877.
12. Brandts, J. F., Lin, L.-N. (1990) Study of strong to ultratight protein interactions using differential scanning calorimetry. Biochemistry 29, 6927–6940.

13. Edsall, J. T., Wyman, J. (1958) Biophysical Chemistry, Academic Press, New York.

14. Tanford, C. (1970) Protein denaturation. Part C: Theoretical models for the mechanism of denaturation. Adv Protein Chem 24, 1–95.

15. Perutz, M. F. (1978) Electrostatic effects in proteins. Science 201, 1187–1191.

16. Honig, B., Nicholls, A. (1995) Classical electrostatics in biology and chemistry. Science 268, 1144–1149.

17. Yang, A. -S., Honig, B. (1993) On the pH dependence of protein stability. J Mol Biol 231, 459–474.

18. Garcia-Moreno E. B. (1995) Probing structural and physical basis of protein energetics linked to protons and salt. Meth. Enzymol. 259, 512–538.

19. Antosiewicz, J., McCammon, J. A., Gilson, M. K. (1996) The determinants of pK_as in proteins, Biochemistry 35, 7819–7833.

20. Baker, B. M., Murphy, K. P. (1996) Evaluation of linked protonation effects in protein binding reactions using isothermal titration calorimetry. Biohphysical J 71, 2049–2055.

21. McCrary, B. S., Edmondson, S. P., Shriver, J. W. (1996) Hyperthermophile protein folding thermodynamics: Differential scanning calorimetry and chemical denaturation of Sac7d. J Mol Biol 264, 784–805.

22. McCrary, B. S., Bedell, J., Edmondson, S. P., et al. (1998) Linkage of protonation and anion binding to the folding of Sac7d. J Mol Biol 276, 203–224.

23. Clark, A., McCrary, B. S., Edmondson, S., et al. (2004) Thermodynamics of core hydrophobicity and packing in the hyperthermophile proteins Sac7d and Sso7d. Biochemistry 43, 2840–2853.

24. Lakowicz, J. (1999) Principles of Fluorescence Spectroscopy. Springer, New York.

25. Wiseman, T., Williston, S., Brandts, J. F., et al. (1989) Rapid measurement of binding constants and heats of binding using a new titration calorimeter. Anal Biochem 179, 131–137.

26. Breslauer, K. J., Freire, E., Straume, M. (1992) Calorimetry: A tool for DNA and ligand–DNA Studies. Meth Enzymol 211, 533–567.

27. Bundle, D. R., Sigurskjold, B. W. (1994) Determination of accurate thermodynamics of binding by titration microcalorimetry. Meth Enzymol 247, 288–305.

28. Lopez, M. M., Makhatadze, G. I. (2002) Isothermal titration calorimetry. Methods Mol Biol 173, 121–126.

29. Wang, P., Izatt, R. M., Gillespie, S. E., et al. (1995) Thermodynamics of the Interaction of 18-crown-6 with K+, Tl+, Ba+2, Sr+2 and Pb+2 from 323.15 to 398.15 K, J Chem Soc Faraday Trans 91, 4207–4213.

30. Bevington, P. (1969) Data Reduction and Error Analysis for the Physical Sciences, McGraw-Hill, Inc., New York.

31. Beechem, J. M. (1992) Global analysis of biochemical and biophysical data. Methods Enzymol 210, 37–54.

32. Gordon, A., Ford, R. (1972) The Chemist's Companion: A Handbook of Practical Data, Techniques, and References, John Wiley, New York, N.Y.

Chapter 7

A Method for Direct Measurement of Protein Stability In Vivo

Zoya Ignatova and Lila M. Gierasch

Abstract

The stability of proteins is tuned by evolution to enable them to perform their cellular functions for the success of an organism. Yet, most of the arsenal of biophysical techniques at our disposal to characterize the thermodynamic stability of proteins is limited to in vitro samples. We describe an approach that we have developed to observe a protein directly in a cell and to monitor a fluorescence signal that reports the unfolding transition of the protein, yielding quantitatively interpretable stability data in vivo. The method is based on incorporation of structurally nonperturbing, specific binding motifs for a bis-arsenical fluorescein derivative in sites that result in dye fluorescence differences between the folded and unfolded states of the protein under study. This fluorescence labeling approach makes possible the determination of thermodynamic stability by direct urea titration in *Escherichia coli* cells. The specific case study we describe was carried out on the predominantly β-sheet intracellular lipid-binding protein, cellular retinoic acid-binding protein (CRABP), expressed in *E. coli*.

Key words: Protein stability, in-cell urea titration, FlAsH labeling, fluorescence, microscopy, CRABP.

1. Introduction

Optimal thermodynamic stability of proteins is crucial to their physiological functions and activities. Reduced protein stability can be detrimental, leading to misfolding pathologies such as the neurodegenerative diseases – Alzheimer's, Parkinson's, and other amyloid diseases *(1, 2)*. Conversely, overly stable proteins may lose the ability to respond to allosteric modulators. Therefore, a molecular understanding of a protein requires analysis of its thermodynamic stability. A wide array of informative and sophisticated in vitro approaches yields quantitative descriptions of stability under a given set of experimental conditions. For many studies, these stabilities have been assumed to be applicable also in

vivo. The crowded cellular environment, however, will modulate conformational flexibility of a protein and adds complexity to folding and unfolding pathways *(3, 4)*. The thermodynamic stability of a protein is very likely to be altered by macromolecular crowding, which in turn will influence both folding and aggregation reactions. Additionally, molecular chaperones interact with a large fraction of the cellular proteome, as do many small ligands that are present in a cell *(5)*; these interactions, along with changes in the oxidative potential due to responses to oxidative stress *(6)*, can influence the thermodynamic stability of a protein in the cellular environment. Therefore, it is highly desirable to develop methods to measure protein stability directly in cells.

Technical challenges make the goal of measuring protein stability in cells extremely difficult, and only a few groups have reported in vivo stabilities. Oas and colleagues applied amide hydrogen exchange detected by MALDI mass spectrometry in a pioneering study to provide the first direct measurements of in vivo protein stability in the *Escherichia coli* cytoplasm *(7)*. Their results showed the thermodynamic stability of the small monomeric λ repressor in the cell to be the same as in the test tube. However, in this method cells are lysed prior to mass spectrometry measurement. Consequently, this approach cannot readily be used to explore directly how different physiological states alter thermodynamic stabilities in the cell. Similarly, the pulse proteolysis approach recently introduced by Marqusee and coworkers *(8)*, which is based on selective digestion of unfolded proteins in equilibrium mixtures of folded and unfolded proteins, requires conversion of intact cells into lysates. For maximum versatility, a method to measure protein stability directly in the cell, during different physiological situations, would be very advantageous.

A variety of qualitative in vivo approaches have been designed that monitor folding and solubility (which is generally reliant on proper folding) of expressed proteins. For example, one strategy is based on the necessity for correct folding for successful structural complementation of a reporter protein *(9)*. Here, the reporter protein is split into two parts that must recombine to function, providing an efficient way of screening for folding-competent and soluble mutants. Another approach is based on reading out the efficiency of fluorescence resonance energy transfer (FRET) between an N-terminal blue fluorescent protein and a C-terminal green fluorescent protein *(10)*. FRET efficiency will be enhanced when the fusion protein folds to the compact native state. Fusion of a protein of interest to chloramphenicol acetyltransferase was used to identify well-folded mutants on the assumption that only these would be soluble and confer resistance to chloramphenicol *(11)*. However, all of these approaches are limited in their ability to provide a quantitative measure of protein stability.

We have developed a fluorescence-based approach to determine protein stability in vivo *(12, 13)* using a well-behaved model system – the 136-amino-acid cellular retinoic acid-binding protein (CRABP) *(14)*. CRABP is visualized in the context of all macromolecules present in the cell using the membrane-permeable bis-arsenical fluorescein-based dye 'FlAsH' *(15)*. This fluorescent dye ligates to a genetically engineered tetracysteine motif (Cys-Cys-Xxx-Yyy-Cys-Cys); the extremely rare occurrence of this motif in the cellular proteome ensures high specificity of labeling *(15)*. By engineering the specific tetracysteine sequence (here Cys-Cys-Gly-Pro-Cys-Cys) into the internal Ω-loop of CRABP (incorporating the native Gly-Pro present in this loop), we created a tetra-Cys CRABP variant that binds FlAsH and yields a fluorescent emission intensity sensitive to the conformational state of the protein, with the denatured ensemble hyperfluorescent compared to the native state *(13)*. FlAsH fluorescence can therefore be used to follow the transition from native to unfolded CRABP during unfolding by chemical denaturant. This approach enables determination of the free energy of unfolding in vivo; FlAsH fluorescence can be used as a direct read-out to monitor the urea-induced unfolding of tetra-Cys CRABP directly in the cell. The complexity of the cellular environment demands cautious interpretation of the thermodynamic data obtained, as many cellular components may be perturbed by the urea treatment. Nonetheless, direct observations in cells will provide new insights. Fulfilling a requirement for its use in these measurements, tetra-Cys CRABP is soluble and indistinguishable in structure and function from its native counterpart whether FlAsH-labeled or unlabeled *(13)*. The FlAsH labeling approach has also been applied to mutants of CRABP in order to explore the effects of specific residue substitutions: for example, mutation of the helix-terminating residue Pro39 to Ala was known to retard the folding and unfolding of CRABP *(16)*, and P39A tetra-Cys CRABP shows a high tendency to form aggregates in vitro *(17)*. By incorporating the tetra-Cys motif into P39A CRABP, we could follow formation of aggregates in real time in vivo *(13)*.

The sensitivity of the FlAsH quantum yield to the conformational state of the protein is the premise for the application of this approach to directly measure in vivo stability. Application of this strategy to other proteins necessitates a careful structure-directed choice of a sequence from the target protein, so that incorporation of the tetra-Cys motif is tolerated without structural perturbation, and also that the FlAsH quantum yield is sensitive to the folding of the protein host. In addition to the overall structural constraints each protein provides for incorporation of the tetra-Cys sequence, the geometric properties of the binding sites are crucial to the FlAsH fluorescence characteristics (B. Krishnan and L. Gierasch, manuscript in preparation). Although the successful design of a

FlAsH-binding tetracysteine tag into a given protein might require multiple trials, a clear advantage provided by this system is the direct read-out of stability in intact cells.

2. Materials

1. DIFCO^{TM} Luria Bertani (LB) medium (BD Biosciences, San Jose, CA) (10 g/L tryptone, 5 g/L yeast extract, 10 g/L NaCl, pH 7.5)
2. Ampicillin (Sigma, St. Louis, MO) is dissolved in water at 100 mg/mL, sterile-filtered (0.2 μm cut-off), and stored in 1 mL aliquots at –20°C. It is added to the culture medium to a final concentration of 100 μg/mL.
3. Isopropyl-β-D-thiogalactoside (IPTG) (Gold Bio-Technology, St. Louis, MO) is dissolved in water at 400 mM, sterile-filtered (0.2 μm cut-off), and stored in 1 mL aliquots at –20°C. It is added to the culture medium at the time of induction in the appropriate amount for a final concentration of 0.4 mM.
4. Stock solution of lysozyme (500 mg/mL) (ICN Biomedicals, Irvine, CA) and DNase (100 mg/mL) (Roche Diagnostics, Indianapolis, IN) are stored in 500 μL aliquots at –20°C.
5. FlAsH-EDT$_2$ (marketed as Lumio^{TM} by Invitrogen, Carlsbad, CA) in its commercial stock concentration of 2 mM was stored at –20°C. Ethanedithiol (Sigma) is aliquoted in DMSO to 10 mM and is diluted fresh prior to each experiment.
6. Urea stock solution (9 M in 10 mM Tris HCl buffer, pH 7.5) (MP Biomedicals, Solon, OH) is freshly made before use, and sterile-filtered (0.2 μm cut-off).
7. 3x SDS-loading buffer contains 187.5 mM Tris HCl, pH 6.8, 6% (w/w) SDS, 30% glycerol, and 0.03% (w/v) bromophenol blue, and is stored at room temperature.

3. Methods

This article describes an approach that we recently developed to determine in vivo protein stability using a high-copy-number plasmid for the expression of the protein of interest in *E. coli* BL21(DE3) cells. Our results show that other *E. coli* mutant strains WG710 and WG708 *(18)* give comparable and reproducible results to the *E. coli* BL21(DE3) cells *(19, 20)*. This provides evidence for the general applicability of the procedure to any *E. coli* strain. To obtain reliable and reproducible results it is important to start the urea titrations at a time point after induction when a sufficient protein amount is already synthesized in the cell.

The use of high-copynumber plasmids yields adequate protein as soon as one hour after induction. One might consider using low-copy-plasmids as well; ultimately, the starting point of the urea titration should be established in any particular case depending on the rate and yield of protein biosynthesis for the plasmid used.

3.1. In-Cell Urea Titration

1. Tetra-Cys CRABP or P39A tetra-Cys CRABP (**Note 1**) is cloned into the pET16b (Amp^R) plasmid under the T7 promoter, and the resulting plasmids are transformed into *E. coli* BL21(DE3) cells, carrying the DE3 lysogen for high-level expression of T7 polymerase. Only freshly transformed cells should be used for expression.

2. A small volume culture is inoculated with a single colony in LB medium containing 100 μg/mL ampicillin and grown overnight at 30°C with constant shaking at 200 rpm. The lower temperature retards the growth of bacteria and provides a more viable culture (with fewer dead cells).

3. Sterile harvested cells (2060 X g, 15 min, 4°C) are carefully resuspended in fresh medium and brought up to 25× the original volume in fresh sterile LB medium containing 100 μg/mL ampicillin. This culture is grown at 37°C until the OD$_{600}$ = 0.5 (**Note 2**) and then treated with lysozyme (final concentration 50 ng/mL) for 10 min on ice. While the inner membrane is freely permeable to the FlAsH dye *(15)*, lysozyme enhances the permeability of the outer membrane of the bacterial host cell to FlAsH. This gentle lysozyme pretreatment has no deleterious effect on the viability and growth of the cells *(13)*. After removal of the lysozyme-containing medium by centrifugation (2060 × g, 15 min, 4°C), the cell pellet is resuspended in the same amount of fresh sterile LB medium containing 100 μg/mL ampicillin along with FlAsH dye and EDT (**Note 3**). EDT suppresses the labeling of endogenous cysteine pairs *(15)* and ensures that the FlAsH-fluorescence signal is a result of specific ligation to the tetracysteine motifs. In the usual protocol, cell aliquots of 1 mL are labeled with 0.2 μM FlAsH-EDT$_2$ and 1 μM EDT. The volume of the aliquots can be adjusted depending on the needs of the subsequent experiments. FlAsH and EDT remain in the medium during the entire time of cultivation.

4. After one generation, at OD$_{600}$ = 1.0, protein synthesis is induced by adding IPTG to 0.4 mM. To establish the behavior of the protein under study, a time course of fluorescence increase for the cell culture is obtained: every 15 min, 150-μl aliquots are withdrawn and subjected to fluorescence measurements in bulk at 530 nm (excitation 500 nm). The temperature of the cuvette holder is maintained at 37°C. Fluorescence of cells with a plasmid bearing the wild-type CRABP without the tetra-Cys motif and labeled with FlAsH, is used as a blank, and

the value is subtracted from each point. The observed increase in fluorescence reports on a combination of increased numbers of cells, increased concentration of expressed protein, and any onset of protein aggregation (**Note 4**). In experiments with any new protein, one should ensure that the fluorescence results only from labeled protein of interest residing within the cells; therefore, the following controls are advisable to demonstrate that the fluorescence signal is due to intracellular species: *(1)* Spin down 150-μl aliquots at 1503 X *g* for 5 min and check the fluorescence of the supernatant at 530 nm. *(2)* Rinse cells once with 50 mM Hepes, pH 7.5, and resuspend in the same amount of buffer. Measure fluorescence again. For any cellular protein, the measured fluorescence values of unwashed and washed cells should be within the measurement error, and the fluorescence of the supernatant should be comparable to the fluorescence of the supernatant of the control CRABP protein without a tetra-Cys binding motif. Hyperfluorescent supernatants are indicative of protein released into the medium or cell membrane debris that binds FlAsH nonspecifically.

5. To monitor the thermodynamic stability of the expressed protein in vivo, 2 h after induction the culture is split into equal aliquots (usually between 250 μL and 350 μL) and urea from a sterile stock (9 M urea in 10 mM Tris HCl buffer, pH 7.5) is added to each aliquot to various final concentrations (not higher than 3 M). Cells retain their viability in urea concentrations up to ~3 M urea *(7,13)*, which should be the highest urea concentration used in in vivo urea titrations. The volumes of all samples in one urea titration set should be adjusted to equal amounts with sterile LB medium containing 100 μg/mL ampicillin. The samples are incubated at 37°C for at least 75 min to insure the equilibrium between folded and unfolded populations (**Note 5**) with constant shaking (longer incubation is also possible, but no longer than 120 min), and subjected to fluorescence measurements (emission at 530 nm; excitation 500 nm). Fluorescence of cells containing a plasmid bearing the wild-type CRABP without the tetra-Cys motif (labeled with FlAsH and under the same urea concentrations) is used as a blank, and the measured value at each urea concentration is subtracted from each point in the urea titration set. A representative result is shown in **Fig. 7.1**. To derive thermodynamic parameters, the urea denaturation curves were fitted to a two-state model *(21)* (**Note 6**) (**Table 7.1**). The actual urea concentration of each sample is determined using the measured index of refraction of the supernatant (after centrifugation of the cells at 1503 X *g* for 15 min) *(22)*. In the urea titration experiment, the control experiments described above in step 4 (measuring the fluorescence of the supernatant and of washed
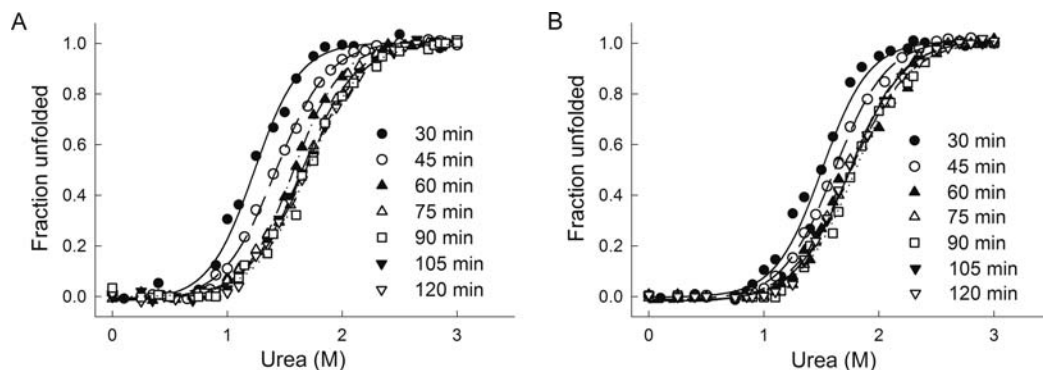
Fig. 7.1. Urea titrations of FlAsH-labeled protein in vivo as a function of the incubation time: (**A**) tetra-Cys CRABP and (**B**) P39A tetra-Cys CRABP, after sample incubation for the indicated times in urea, monitored by FlAsH fluorescence. (Reproduced from **Ref.** *(12)* with permission from Willey InterScience.)

Table 7.1
Thermodynamic stability of tetra-Cys CRABP in vitro and in vivo. (Reproduced from Ref. *(12)* **with permission from Wiley InterScience.)**

	ΔG (kcal.mol^{-1})	m (kcal.mol^{-1}.M^{-1})	C_m (M)
In vivo (incubated 75 min)	5.2 ± 0.1	-3.4 ± 0.1	1.52 ± 0.05
In vitro (incubated 360 min)	6.5 ± 0.3	-1.8 ± 0.1	3.68 ± 0.06

and resuspended cells) are advisable to ensure that an observed increase in the fluorescence signal arises only from unfolding of the protein within the cell and is not a result of protein release into medium or hyperfluorescent cell debris.

3.2. Cell Viability

Cell viability and changes in the cell number during the incubation times in urea (**Note 7**) were qualitatively assessed by measuring the optical density at 600 nm (**Fig. 7.2**), using LB medium as a blank. This method alone, while rapid, is not sufficient to observe a potential deleterious effect of urea on cell viability, since dead cells can also contribute to the bulk absorbance at 600 nm. For more careful assessment of viability, the fraction of viable cells should be determined on solid nutrient medium by taking one µL samples of the cell suspension, diluting them 10,000-fold in fresh sterile LB medium, plating them on LB-agar (LB medium solidified by addition of 15 g/L agar), and incubating the plates at 37°C overnight. Colonies are then counted, and the number of the viable cells is calculated per mL (**Fig. 7.2**).
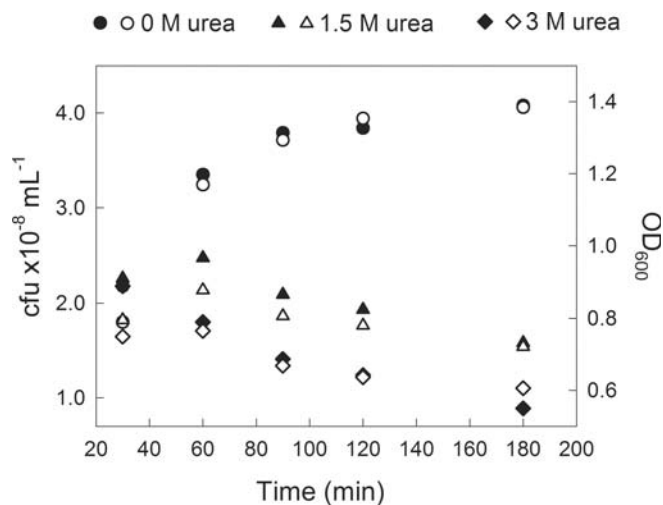
Fig. 7.2. Cell viability. Change in the viability of the host cells as a function of the time of incubation in 0 M, 1.5 M, and 3 M urea. The viability was quantified by measuring the number of cells capable of forming colonies (*left axis, closed circles*) and optical density at 600 nm (*right axis, open symbols*).

3.3. Cell Fractionation

It is essential for the determination of in vivo stability that the protein under study remain soluble throughout the measurement. Hence, we recommend a control to insure that the measured FlAsH signal arises from soluble protein; separation of soluble and insoluble protein by fractionation gives direct information on how the protein under study behaves in the expression system used. In comparing the behavior of different proteins and mutants of any given protein under study, it may be of interest to assess the extent to which a given protein partitions to the insoluble (pellet) fraction, and this same protocol can be used for this goal.

1. The 5 mL overnight culture prepared from freshly transformed *E. coli* BL21(DE3) cells with either tetra-Cys CRABP or P39A tetra-Cys CRABP plasmids is used to inoculate 100 mL of LB medium containing 100 µg/mL ampicillin and grown at 37°C with constant shaking (200 rpm). At $OD_{600} = 1.0$, IPTG is added to 0.4 mM to induce the T7 promoter-based expression of tetra-Cys CRABP or P39A tetra-Cys CRABP. At different time points, 10 mL aliquots are withdrawn with sterile handling, and bacteria are harvested by centrifugation at 2060 X g for 15 min at 4°C. All steps after the aliquot withdrawal may be carried out under nonsterile conditions.

2. Cells are resuspended in 1.5 mL of 50 mM phosphate buffer at pH 8.0 containing 300-mM NaCl. Cells are disrupted by lysozyme (at a final concentration of 500 µg/mL) for 30 min (**Note 8**) and DNase (at a final concentration of 50 µg/mL) treatment on ice for 15 min, followed by sonication on ice with 20 s bursts per minute for 3 min (30% duty cycle). The cell lysates are

fractionated into soluble and insoluble fractions by centrifugation at 27,000 X g at 5°C in a tabletop centrifuge for 30 min. The insoluble pellet fraction is resuspended into 1.5 mL of 10 mM Tris HCl buffer, pH 8.0, containing 8 M urea. A volume of 20-μL aliquots of each fraction are mixed with 10 μL 3x SDS-loading buffer and preheated for 3 min at 95°C, then loaded onto an SDS-PAGE gel (12% acrylamide), and the tetra-Cys CRABP content in each fraction is quantified by optical densitometry. The density is related to a density of a standard sample containing purified tetra-Cys CRABP at 1 mg/mL.

3.4. Fluorescence Microscopy

During the time course of growth or urea incubation of the labeled cells expressing either tetra-Cys CRABP or P39A tetra-Cys CRABP (see **Section 3.1**), 20 μL of cell suspension is withdrawn and concentrated twice by centrifugation at 7,297 X g for 3 min and subsequent resuspension in 50 mM Hepes buffer, pH 7.5. A volume of 2 μL of this concentrated suspension is immobilized in 1% agarose in LB and imaged with a fluorescent microscope (Nikon Eclipse E600, Melville, NY) with excitation at 485 nm and a 510-nm emission cut-on filter. The images are processed with the Openlabs software (Improvision, Lexington, MA). Examples of micrographs are shown in **Fig. 7.3**.

3.5. In vitro FlAsH-labeling and urea titration

1. Tetra-Cys CRABP contains an N-terminal His-tag, enabling it to be purified from the soluble fraction of the *E. coli* cell lysate using Ni^{2+}-NTA (Qiagen, Valencia, CA) affinity resin *(14)*. The purification is monitored on 12% SDS-PAGE as above (3.3.2). The purest protein fraction appears between 175 mM and 260 mM imidazole. A typical purification of a completely soluble CRABP variant like tetra-Cys CRABP yields 7–10 mg of pure protein from 1L culture.
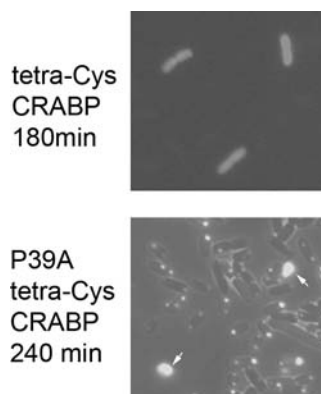
Fig. 7.3. Fluorescence microscopy images showing uniformly distributed fluorescence of tetra-Cys CRABP (180 min after induction) and hyperfluorescent dense aggregates of P39A tetra-Cys CRABP at the poles of the cells (at 240 min after induction). Hyperfluorescent impurities in the extracellular medium are marked by an arrow.

2. The fractions with pure protein are collected and dialyzed over-
    night at 4°C in 15 kDa MW cut-off dialysis tubing against 10 mM
    Tris HCl, pH 8.0, containing 2 mM β-mercaptoethanol (BME).
    BME is used to minimize oxidation of tetra-Cys-binding sites
    (15). The dialyzed protein is filtered through a Nalgene 0.45-μm
    syringe filter, and protein concentration is determined spectro-
    photometrically using the ϵ_{280} of 21,750 M^{-1} cm^{-1} for tetra-Cys
    CRABP *(14)*. Purified proteins could be stored in aliquots up to
    200 μM (preferably 100 μM) at 4°C for use within 2 weeks. When
    higher concentrations are desired, protein should be concentrated
    prior to the experiment using a Centricon system (molecular mass
    cut-off of 10 kDa) at 4°C.

3. Tetra-Cys CRABP from the purification stocks is diluted to the
    desired concentration in 10-mM HEPES pH 7.5, containing
    1-mM tris(carboxyethyl)phosphine (TCEP) and labeled with
    FlAsH and ethanedithiol (FlAsH:EDT ratio 1:5) at room tem-
    perature for 2 h in the dark. The usual ratio of FlAsH:protein
    used is 2:1. The labeled tetra-Cys protein is stable for several
    days at 4°C. A typical labeling mixture for urea titration in vitro
    contains 7-μM labeled protein.

4. Labeled protein is aliquoted and mixed with various urea
    concentrations. After equilibration at 37°C for a minimum of
    6 h, the aliquots are subjected to fluorescence measurements
    either using the intrinsic Trp signal (excitation 280 nm, 2-nm
    bandwidth; monitoring emission from 300 nm to 380 nm with
    a 2-nm bandwidth) or using the FlAsH signal (as described).
    The temperature of the cuvette holder is maintained at 37°C
    with a water bath. Representative results for tetra-Cys CRABP
    and P39A tetra-Cys CRABP (isolated using the same protocol)
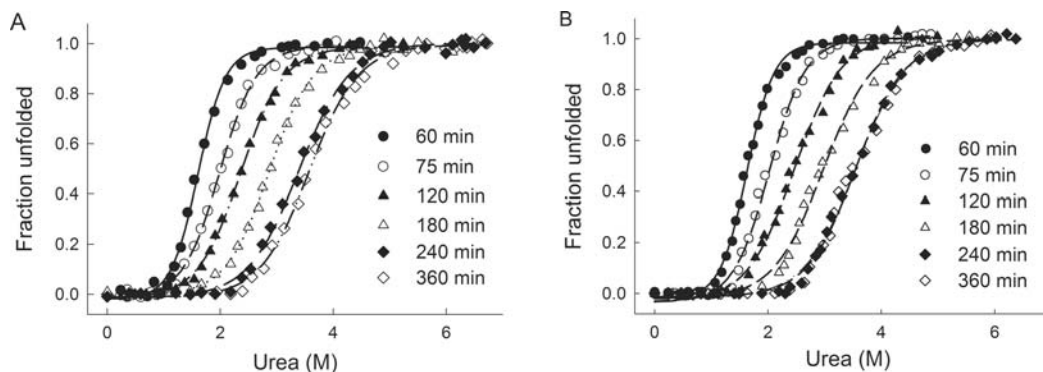   are shown in **Fig. 7.4**.

Fig. 7.4. Urea titrations of FlAsH-labeled protein in vitro as a function of the incubation time (monitored by Trp fluorescence): (**A**) tetra-Cys CRABP and (**B**) P39A tetra-Cys CRABP. The actual urea concentration was determined by measuring the refractive index, and data are curve-fit to a two-state model. (Reproduced from **Ref.** *(12)* with permission from Willey InterScience.)

4. Notes

1. This protocol can be adapted to any protein provided that a successful design of a FlAsH-binding motif that is sensitive to global conformational changes can be achieved. In addition, the engineered tetra-Cys sequence should not perturb the structural integrity and thermodynamic stability of the protein host. Moreover, the system can be used to compare the destabilizing effect of mutations before a time-costly and potentially low yield purification is undertaken.

2. LB absorbs at 600 nm (OD_{600} is between 0.07 and 0.09), and fresh LB is used as a blank in the OD measurements.

3. The EDT stock solution (10 mM in DMSO) is best stored at $-20°C$ and is freshly diluted prior to each labeling experiment. EDT generates an extremely unpleasant thiol smell, and the initial aliquoting and addition to the culture needs to be handled exclusively under the hood. Containers with tight-fitting lids (i.e., falcon tubes, Eppendorf tubes, or Schott bottles) should be used instead of common flasks or culture tubes for cultivation of the cells. The used pipette tips or other plastic materials should be collected in a tightly closed container (preferably stored under the hood) and then discarded according to safety regulations.

4. Different fluorescence patterns are observed upon induction of soluble and aggregation-prone proteins; the signal of a soluble protein reports on the steady increase of its amount during protein synthesis, while that for an aggregation-prone variant may show an altered signal reporting on aggregate formation. In the case of FlAsH-labeled tetra-Cys P39A CRABP, aggregates are hyperfluorescent, leading to a pronounced upswing in fluorescence of bulk cell samples upon initiation of aggregation *(13)*. Fluorescence microscopy images confirm these results: Whereas the fluorescence is spread uniformly throughout the cytoplasm in cells expressing the soluble tetra-Cys CRABP, in cells expressing aggregation-prone P39A tetra-Cys CRABP hyperfluorescent aggregates are observed near the poles (**Fig. 7.3**) *(13)*. In parallel, cell fractionation studies reveal the partitioning of the protein between the soluble and insoluble fractions.

5. We observed that the incubation time required for establishment of equilibrium between folded and unfolded populations of CRABP in vivo is significantly shorter than in vitro (**Figs. 7.1** and **7.4**). Based on our preliminary measurements, we believe that acceleration of the unfolding rate is the most likely factor leading to faster equilibration in vivo *(12)*, but studies are underway to dissect all possible factors. Our initial approach to measuring stability in vivo used a short incubation time of the cells in different urea concentrations (30 min) with a goal of minimizing the negative impact on viability of the cells at higher

urea concentrations *(13)*. However, follow-up studies on the incubation time dependence of quantitative in vivo stability experiments clearly indicate that the minimum time required for equilibration for either tetra-Cys CRABP or P39A tetra-Cys CRABP in vivo is 75 min, as indicated by the absence of further change in the urea melt as incubation time is increased (**Fig. 7.1A** and **B**) *(12)*. The time dependence of establishing an equilibrium between folded and unfolded populations in vivo can vary significantly (i.e., fast-folding proteins might require shorter incubation times), and the optimal incubation time needs to be determined for each protein by monitoring in parallel the cell viability and the approach of the observed fluorescence to a constant value at any given urea concentration.

6. To extract any thermodynamic data from the stability curves, the urea melts need to be reversible. In our case, the melts are reversible only for the completely soluble tetra-Cys CRABP protein (**Fig. 7.5**). To measure the stability of aggregation-prone proteins, which form detergent-resistant aggregates (i.e., amyloid aggregates), one might consider shorter induction times or lower expression levels in order to carry out the urea melt before insoluble structures are formed.

7. Longer incubation times are accompanied by losses in cell viability (**Fig. 7.2**). To offset the impact of cell loss, prior to FlAsH-fluorescence measurements the optical density (OD_{600}) is recorded, and the OD_{600} of all the samples is normalized to the optical density of the 3-M urea sample by addition of fresh LB medium at the appropriate urea concentration.
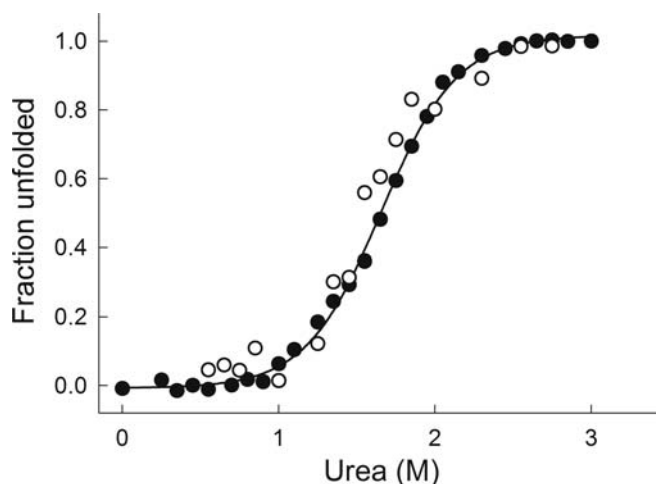
Fig. 7.5. Reversibility of the in vivo urea titrations. FlAsH-labeled tetra-Cys CRABP-expressing cells were treated with 3 M urea for 75 min, and then refolding was initiated by dilution of aliquots into fresh LB medium containing 100 μg/mL ampicillin. After incubation of the cells for 60 min, the extent of return of the FlAsH signal, as a measure of refolding, was monitored by FlAsH fluorescence (*open symbols*). A urea melt of FlAsH-labeled tetra-Cys CRABP incubated for 75 min is given for comparison (*closed symbols*).

8. The lysozyme treatment converts the cell pellet into a very viscous suspension due to the release of DNA. The subsequent hydrolysis with DNase reduces the viscosity of the solution.

Acknowledgments

References

1. Chiti, F., Stefani, M., Taddei, N., et al. (2003) Rationalization of the effects of mutations on peptide and protein aggregation rates. Nature **424**, 805–808.

2. Dobson, C. M. (2003) Protein folding and misfolding. Nature **426**, 884–890

3. Evans, M. S., Clarke, T. F. IV, Clark, P. L. (2005) Conformations of co-translational folding intermediates. Protein Pept Lett **12**, 189–195.

4. Minton, A. P. (2006) How can biochemical reactions within cells differ from those in test tubes? J Cell Sci **119**, 2863–2869.

5. Pace, C. N., McGrath, T. (1980) Substrate stabilization of lysozyme to thermal and guanidine hydrochloride denaturation. J Biol Chem **255**, 3862–3865.

6. Frand, A. R., Cuozzo, J. W., Kaiser, C. A. (2000) Pathways for protein disulphide bond formation. Trends Cell Biol **10**, 203–210.

7. Ghaemmaghami, S., Oas, T. G. (2001) Quantitative protein stability measurement in vivo. Nat Struct Biol **8**, 879–882.

8. Park, C., Marqusee, S. (2005) Pulse proteolysis: a simple method for quantitative determination of protein stability and ligand binding. Nat. Methods **2**, 207–212.

9. Wigley, W. C., Stidham, R. D., Smith, N. M., et al. (2001) Protein solubility and folding monitored in vivo by structural complementation of a genetic marker protein. Nat Biotechnol **19**, 131–136.

10. Philipps, B., Hennecke, J., Glockshuber, R. (2003) FRET-based in vivo screening for protein folding and increased protein stability. J Mol Biol **327**, 239–249.

11. Maxwell, K. L., Mittermaier, A. K., Forman-Kay, J. D., et al. (1999) A simple in vivo assay for increased protein solubility. Protein Sci **8**, 1908–1911.

12. Ignatova, Z., Krishnan, B., Bombardier, J. P., et al. (2007) From the test tube to the cell: Exploring the folding and aggregation of a β-clam protein. Biopolymers **88**, 157–163.

13. Ignatova, Z., Gierasch, L. M. (2004) Monitoring protein stability and aggregation in vivo by real-time fluorescent labeling. Proc Natl Acad Sci USA **101**, 523–528.

14. Clark, P. L., Weston, B. F., Gierasch, L. M. (1998) Probing the folding pathway of a beta-clam protein with single-tryptophan constructs. Fold. Des. **3**, 401–412.

15. Griffin, B. A., Adams, S. R., Jones, J., Tsien, R. Y. (2000) Fluorescent labeling of recombinant proteins in living cells with FlAsH. Methods Enzymol. **327**, 565–578.

16. Eyles, S. J., Gierasch, L. M. (2000) Multiple roles of prolyl residues in structure and folding. J Mol Biol **301**, 737–747.

17. Ignatova, Z., Gierasch, L. M. (2005) Aggregation of a slow-folding mutant of a β-clam protein proceeds through a monomeric nucleus. Biochemistry **44**, 7266–7274.

18. Racher, K. I., Culham, D. E., Wood, J. M. (2001) Requirements for osmosensing and osmotic activation of transporter ProP from Escherichia coli. Biochemistry **40**, 7324–7333.

19. Ignatova, Z., Gierasch, L. M. (2006) Inhibition of protein aggregation in vitro and in vivo by a natural osmoprotectant. Proc Natl Acad Sci USA **103**, 13357–13361.

20. Ignatova, Z., Gierasch, L. M. (2007) Effects of osmolytes on protein folding and aggregation in cells. Meth Enzymol **428**, 355–372.

21. Fersht, A. (1999) Structure and Mechanism in Protein Science, Freeman, New York, pp. 508–539.

22. Pace, C. N., Shirley, B.A., Thompson, J.A. (1987) In (Creighton, T.E., ed.), Protein structure: A practical approach, IRL, Oxford pp. 311–330.

Chapter 8

Quantifying the Roles of Water and Solutes (Denaturants, Osmolytes, and Hofmeister Salts) in Protein and Model Processes Using the Solute Partitioning Model

Laurel M. Pegram and M. Thomas Record, Jr.

Abstract

Salts and uncharged solutes in aqueous solution exert effects on a wide range of processes in which large amounts of biopolymer surface are buried or exposed (folding/unfolding, complexation/dissociation, or precipitation/dissolution). A simple two-state solute partitioning model (SPM, where the solute is partitioned between the bulk and surface water) allows the interpretation and prediction of the thermodynamic effects of various uncharged solutes (e.g., urea, glycine betaine) on protein and nucleic acid processes in terms of structural information. The correlation of solute effects with various coarse-grained types of biopolymer surface exposed or buried in a process provides a novel probe for investigation of large-scale conformational changes. Solutes that are fully excluded from one or more types of biopolymer surface are useful to quantify changes in water of hydration of these surfaces in biopolymer processes. Additionally, application of the SPM to the analysis of non-Coulombic salt effects on various model processes provides an estimate for the hydration layer at surfaces and shows that ion effects are additive and independent of the nature of the counterion.

Key words: Solute partitioning model (SPM), solute effects, Hofmeister salts.

1. Introduction

Nonuniform distributions of small solutes and salt ions near surfaces are responsible for the often large effects of concentration of these solutes on a very wide range of processes in water, including formation or disruption of biopolymer–water interfaces, molecular solute–water interfaces, and macroscopic air–water interfaces *(1–3)*. To what extent can one predict solute effects from structural data, or use solute effects on the steps of a process to deduce structural information regarding surfaces buried or exposed in

those steps, and the concomitant release or uptake of water and solutes? To interpret the significant observation of Myers, Pace, and Scholtz *(4)* that protein unfolding *m*-values in urea and GuHCl are approximately proportional to the change in accessible surface area (ΔASA), we developed the solute partitioning model (SPM) *(5)*. This model allows us to quantitatively test the hypothesis *(1, 2)* that salt ions and uncharged solutes exert their effects depending on whether they are accumulated in, or excluded from, the water of hydration at the biopolymer surface exposed (or buried) in a particular process.

This thermodynamic and two-state SPM interprets the preferential accumulation or exclusion of solutes in terms of partitioning between a thermodynamically defined interfacial microphase and the bulk solution. This model has been applied to analyze the effects of denaturants and osmolytes on the thermal stability of a small globular protein *(6, 7)*, the effects of electrolytes (acids, bases, Hofmeister salts) on the surface tension of water *(8, 9)*, as well as to quantify the interactions of selected solutes with various types of biopolymer surface *(10,13)*. The well-characterized solutes urea and glycine betaine (GB) have been used as probes to predict and quantify interface formation and coupled conformational changes in lac repressor–lac operator binding *(13)* and in the individual steps of the mechanism of open complex formation by *Escherichia coli* RNA polymerase *(14)*.

2. Background

Thermodynamic effects of changes in concentration of an uncharged solute on a protein process (or other process with a ΔASA) are rigorously interpreted in terms of partitioning of the solute between the bulk solution and a local domain (microphase) characterized by the water of hydration of the surface defined by ΔASA *(7–14)*:

$$-\frac{1}{RT}\frac{\partial \Delta G^{\circ}_{\text{obs}}}{\partial m_3} = \frac{\partial \ln K_{\text{obs}}}{\partial m_3} = (1+\varepsilon_3)\frac{b_1 \Delta\text{ASA}(K_{\text{p},3}-1)}{m_1^{\bullet}}, \quad (8.1)$$

where the partition coefficient $K_{\text{p},3}$ is defined as the ratio of molal concentrations of solute in the local and bulk domains (i.e., $K_{\text{p},3} \equiv m_3^{\text{local}}/m_3^{\text{bulk}}$). Though the molal concentration scale is the appropriate one to use to develop the SPM, the molar scale is usually the better choice for the analysis of experimental data because $\Delta G^{\circ}_{\text{obs}}$ and $\ln K_{\text{obs}}$ are typically more linear functions of molar solute concentration (*see* **Note 1**). The quantity $b_1 \equiv n_1/A$

is the number of water molecules per unit surface area in the local biopolymer domain defined by ΔASA, and $m_1^\bullet$ is the solvent molality (55.5 mol/kg for H_2O). The term $(1 + \varepsilon_3)$ is a nonideality correction (typically $|\varepsilon_3| \ll 1$) that enters in the conversion from solute activity to molal concentration (*see* **Note 2**).

For a process involving an uncharged biopolymer process in a solution at salt concentration m_3 (or for protein processes at high enough salt concentration so Coulombic interactions make no net contribution to ΔG_{obs}°):

$$-\frac{1}{RT}\frac{\partial \Delta G_{obs}^\circ}{\partial m_3} = \frac{\partial \ln K_{obs}}{\partial m_3} = (1+\varepsilon_\pm)\frac{\nu b_1 \Delta ASA}{m_1^\bullet}\left(\frac{\nu_+ K_{p,+} + \nu_- K_{p,-}}{\nu} - 1\right), \quad (8.2)$$

where $\nu \equiv \nu_+ + \nu_-$ is the number of ions per formula unit of the salt and the partition coefficient $K_{p,3}$ of the salt component in **Eq. 8.1** is replaced by the appropriate stoichiometric combination of cation and anion partition coefficients *(1, 11)*. The validity and utility of the above equations have been directly tested through the application of the SPM to model processes.

3. Applications of the SPM

Here we review some recent applications of the SPM to interpret the thermodynamic effects of solutes (nonelectrolytes) on protein folding *(6, 7, 11)*, and protein–DNA binding *(13, 14)* and of electrolytes (acids, bases, salts spanning the Hofmeister series) on creation of an air–water interface (surface tension, *8, 9*). We also briefly preview ongoing applications of the SPM, including the interpretation of high-concentration salt effects on protein folding and protein–DNA interactions *(17)*.

3.1. Obtaining $b_1(K_{p,3} - 1$ for Interactions of Urea with the Homologous Series of Surfaces Exposed in Unfolding Globular Proteins of Different Sizes

In unfolding, different globular proteins expose different total amounts of surface (different ΔASA), but the coarse-grained composition of the surface exposed in unfolding is very similar (65–75% nonpolar, 15–20% polar amide). Hence, these unfolding surfaces form a homologous series, and the SPM predicts that determination of the intrinsic quantity $b_1(K_{p,3} - 1)$ (cf. **Eq. 8.1**) for the effect of a particular solute on stability of one protein is sufficient to predict its effect on any member of this homologous series of globular proteins. Empirical precedent for this prediction was provided by the analysis of Myers et al. of effects of urea and GuHCl on unfolding of globular proteins *(3)*. Myers and coworkers found that urea and GuHCl "*m*-values"

(i.e., derivatives of the standard free energy of unfolding with respect to denaturant concentration) are approximately proportional to the change in accessible surface area. Analysis of the current dataset *(13, 18)* **reveals that** $b_1(K_{p,3} - 1)$ for the interaction of urea with the surface exposed in unfolding a typical globular protein is 0.015 ± 0.002 (cf. **Fig. 8.1**), allowing the prediction of the *m*-value for urea denaturation of any protein where an estimate of the ΔASA is available. The composite quantity $b_1(K_{p,3} - 1) = 0.015 \pm 0.002$ for the interaction of urea with the surface exposed in unfolding globular proteins is positive, indicating that urea is locally accumulated in the water of hydration of this surface ($K_{p,3} > 1$); if an average $b_1 = 0.2$ $H_2O/\text{Å}^2$ is assumed (cf. **Section 3.5**), then $K_{p,\text{urea}} = 1.075 \pm 0.010$. On average, the local urea concentration in the vicinity of the protein surface exposed in unfolding exceeds the bulk urea concentration by only 7.5%; this relatively small extent of accumulation of urea (*local* concentration gradient) is thermodynamically sufficient to destabilize the native state and drive unfolding at molar concentrations of urea.
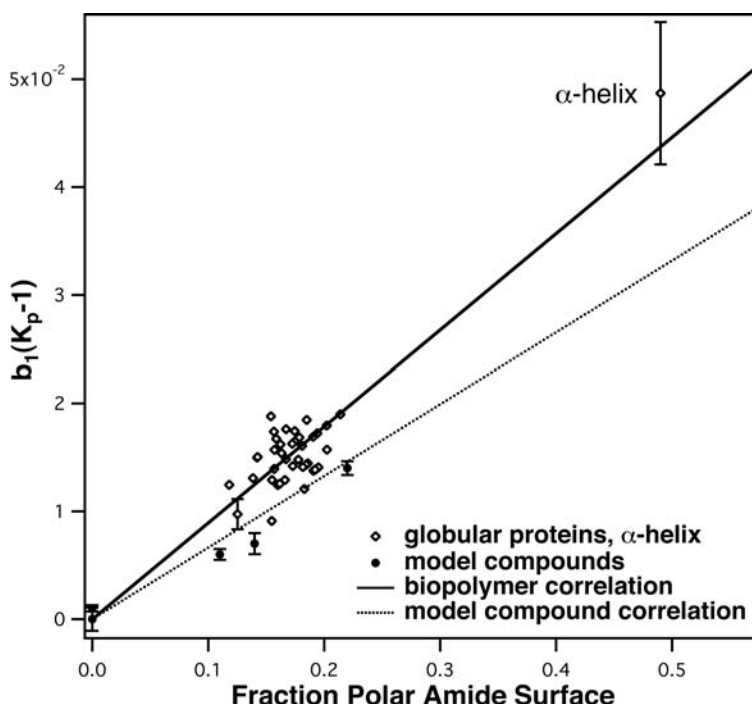
Fig. 8.1. Surface area-normalized degree of urea accumulation as a function of fractional polar amide surface. *Open symbols* represent biopolymer melting data; for globular proteins, values of $b_1(K_{p,3} - 1)$ are clustered around 0.015. The melting of an alanine-based α-helical peptide exposes a much greater fractional amount of polar amide surface than protein unfolding, and the *m*-value for this process yields a $b_1(K_{p,3} - 1)$ value of 0.049 *(13, 19)*.

3.2. Interpretation of Urea m -Values Using a Coarse-Grained Decomposition of Accessible Surface Area

The above application of the SPM to the effect of urea on unfolding of the homologous series of globular proteins does not provide molecular detail regarding the extent of accumulation of urea at chemically different parts of the protein surface exposed in unfolding (15–20% polar amide, 65–75% nonpolar). Insight into this coarse-grained molecular detail can be obtained by investigating the interactions of urea with different native biopolymers and the effects of urea on processes involving biopolymers or model compounds in which the ΔASA differs in surface composition. This information is then correlated with amounts of various coarse-grained types of biopolymer surface (e.g., anionic, polar amide, nonpolar, etc). For urea, **Fig. 8.1** shows that the degree of urea accumulation per unit surface area (expressed as the composite quantity $b_1(K_{p,3} - 1)$) is proportional to the fraction of that surface which is polar amide (O and N accessible surface of backbone and side-chain amides). Plotted biopolymer data (open diamonds) are obtained from m-values for unfolding of globular proteins and an alanine-based α-helix *(13, 19)*. Model compound data (closed circles) are obtained from analysis of isopiestic distillation data for aqueous solutions of urea and amino acids (glycine, alanine) or short peptides of these amino acids *(18)*, where both the model compound and urea are extrapolated to low concentrations (to match the conditions of the biopolymer data; *see* **Note 3**). For interactions of urea with these surfaces, the proportionality of $b_1(K_{p,3} - 1)$ to the fraction of polar amide surface, together with the lack of evidence for significant contributions of other biopolymer surface types to urea preferential interactions (*see* **Note 4**), led to a general relationship between the urea concentration dependence of a biopolymer process and the change in polar amide ASA, valid in the range of low to moderate c_3 (typically < 1 M, a range where ln K_{obs} is a linear function of c_3):

$$\frac{\partial \ln K_{obs}}{\partial c_3} = (1.4 \pm 0.3) \cdot 10^{-3} \Delta ASA_{\text{polar amide}}$$

$$(c_3 < 1\text{M})$$

(8.3)

Calibration of the use of this equation to quantify burial of polar amide surface in protein–nucleic acid interactions using thermodynamic data for the lac repressor–operator interaction is described in **Section 3.4**.

Currently relationships analogous to that developed for urea in **Eq. 8.3** are available only for GB (completely excluded from two layers of water at anionic surfaces *(12, 13)*, see below) and at a higher level of approximation for GuHCl (more strongly accumulated near polar amide surface than urea) *(7, 11)*. Studies with trehalose and TMAO are in progress (J. Cannon, unpublished). Once a library of suitable solutes is developed and their interactions with the range of biopolymer surfaces are quantified,

determinations of the effects of these solutes on the kinetics and equilibria of the steps of biopolymer processes will provide new dimensions of thermodynamic, structural, and mechanistic insight. In particular, these solutes will provide powerful probes of large-scale coupled folding and other large-scale conformational changes as well as on the extent of interface formation and water uptake or release.

3.3. Using GB (N, N, N - trimethyl glycine) to Quantify Changes in Hydration of Anionic Biopolymer Surface in Processes

To date, the most promising solute to quantify changes in water of hydration of any type of biopolymer surface in processes is GB, which behaves thermodynamically as if completely excluded from approximately two layers of water in the vicinity of anionic surface (e.g., partially anionic oxygens of carboxylate and phosphate groups of proteins and nucleic acids, respectively) *(12,13)*. For protein–nucleic acid interactions in which anionic surface of DNA phosphate groups is buried in forming the interface and water of hydration of these phosphate oxygens is displaced, GB is predicted to favor binding. If this is the only significant effect of GB (*see* **Note 4**), then the initial slope of the dependence of the binding constant K_{obs} on GB concentration ($d \ln K_{obs}/d[GB]$ as $[GB] \to 0$) is related to the number of waters released ($n_{1,\text{anionic}} = -b_{1,\text{anionic}} \Delta ASA_{\text{anionic}}$) from anionic phosphate oxygens by

$$n_{1,\text{anionic}} \approx 55.5 \, d \ln K_{obs}/d[GB] \qquad (8.4)$$

Analyses of effects of urea and GB on binding of lac repressor to lac operator DNA using **Eqs. 8.1, 8.2, 8.3, 8.4** are described below.

3.4. Calibrating and Interpreting Solute Effects on Protein–DNA Interactions; Probes for Interface Formation and Large-scale Conformational Changes

Hong et al. *(13)* quantified the large effects of urea and GB on specific binding of lac repressor tetramer to the lac operator site on plasmid DNA using repressor titrations of operator DNA at different solute concentrations, performed with the nitrocellulose membrane filter assay. For this system, the ΔASA of formation of the specific complex, known from structural data, consists of three different interfaces (cf. **Fig. 8.2**): the interface between the folded DNA-binding domains (DBDs) of repressor and operator DNA and two protein interfaces, one from folding the hinge helices and the other from docking the folded, operator-bound DBD on the core of repressor. Approximately 500 Å^2 of polar amide protein surface is buried in each of these three interfaces; ~600 Å^2 of anionic surface is also buried, all of it from anionic DNA phosphate oxygens in the protein–DNA interface. Values of $\ln K_{obs}$ as a function of solute concentration are plotted in **Fig. 8.3**. From quadratic fits to these data, and application of significant empirical corrections to constant salt activity, limiting experimental values of $\partial \ln K_{obs}/\partial m_3$ of –2.1 ± 0.2 for urea and +1.9 ± 0.2 for GB

Fig. 8.2. Illustration of the three interfaces formed on lac repressor–operator binding: the interface between the folded DNA-binding domains (DBDs) of repressor and operator DNA (*black*) and the protein interfaces formed from hinge helices folding (*black cyllinders*) and from docking the folded, operator-bound DBD on the repressor core (*gray*). This figure is based on PDB file 1EFA and was created using VMD *(20)*.

were obtained *(13)*. From **Eq. 8.3**, the limiting slope in urea yields $\Delta\text{ASA}_{\text{polar amide}} = (1.5 \pm 0.3)\times 10^3 \text{ Å}^2$, in agreement with the structural value. From **Eq. 8.4**, the limiting slope in GB yields $\Delta\text{ASA anionic} = (4.8 \pm 1.0)\times 10^2 \text{ Å}^2$, similar but not equal to the structural result (*see* **Note 5**).

Kontur et al. *(14)* used urea and GB to investigate the formation of protein–DNA interfaces (by GB detection of burial of anionic DNA phosphates) and large-scale coupled folding (by urea detection of polar amide surface burial) in the steps of the mechanism of formation of a specific "open" promoter complex by *E. coli* RNA polymerase at the bacteriophage λP_R promoter. At least three steps are involved: (1) initial binding and wrapping of duplex promoter DNA (approximately 100 base pairs) on RNA polymerase to form a "closed" complex designated I_1, the first kinetically significant intermediate, in which the DNA of the transcription start site is inserted in a closed (duplex) state, high in the massive active site cleft of RNA polymerase; (2) a relatively slow (rate-determining) conformational change to a second
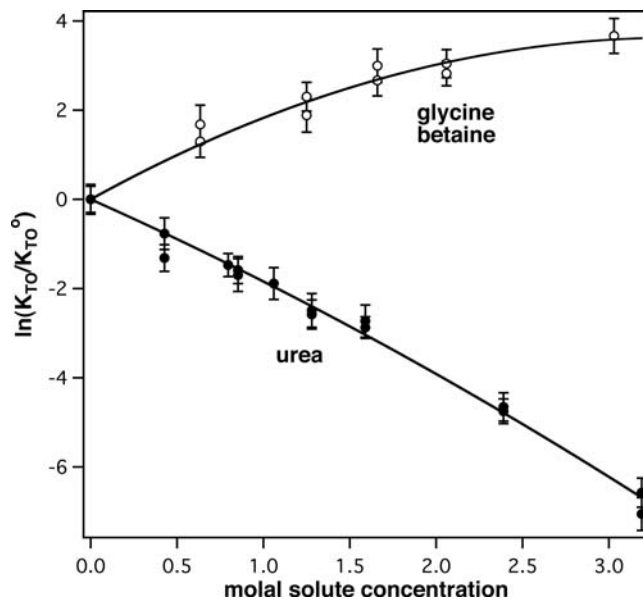
Fig. 8.3. Equilibrium binding constant for the repressor–operator complex (cf. **Fig. 8.2**) as a function of urea or glycine betaine concentration *(13)*. From **Eq. 8.3**, the limiting slope in urea yields $\Delta ASA_{polaramide} = 1500$ Å^2, in agreement with the structural value. From **Eq. 8.4**, the limiting slope in GB yields ΔASA anionic $= 480$ Å^2, similar, but not equal, to the structural result. (Unpublished GB solute titrations containing more data at low GB concentrations provide a more accurate description of the curvature and yield closer quantitative agreement with the structural prediction (M. Capp, unpublished).)

kinetically significant intermediate (I_2, not yet characterized at any promoter); and (3) conversion of I_2 to the initiation-competent open complex (RP_o) in which 14 base pairs of DNA are open in the vicinity of the transcription start site and in which the template strand has descended to place the start site base in the catalytic site of the polymerase. The first and third steps equilibrate rapidly on the timescale of the relevant direction of the second step; currently information is available regarding the urea and GB concentration dependences of K_1, the equilibrium constant for the initial binding–wrapping step, k_2, the rate constant for conversion of I_1 to I_2, and the overall dissociation rate constant k_d, approximately equal to the quotient k_{-2}/K_3, where k_{-2} is the rate constant for conversion of I_2 to I_1 and K_3 is the equilibrium constant for the conversion of I_2 to RP_o.

Data for the effects of urea and GB on K_1, k_2, and $1/k_d$ (to express the information in the direction of RP_o formation instead of dissociation) are summarized in **Fig. 8.4**. GB has a large stabilizing effect on K_1, indicating the release of water from anionic DNA phosphate surface in this step (**Eq. 8.4**). Surprisingly, GB exerts a still-larger effect on the kinetically significant steps of dissociation, interpreted as the formation of a large polymerase–DNA interface
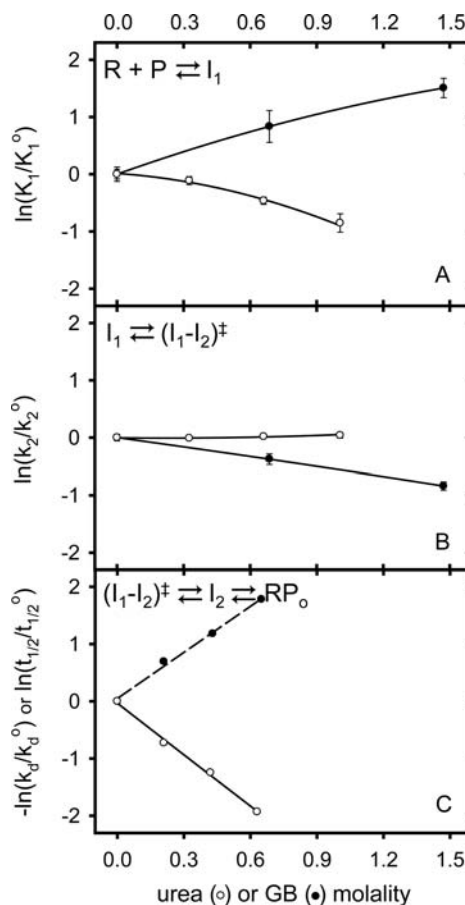
Fig. 8.4. Effects of urea and glycine betaine on K_1, k_2, and $1/k_d$ for RP_o formation. The large stabilization effects seen for GB on K_1 and especially $1/k_d$ (**panels A and C**) indicate the release of water from anionic DNA phosphate surface in these steps (**Eq. 8.4**). The initial effect of urea on K_1 is small, consistent with formation of a protein–DNA interface which buries little polar amide surface. By contrast, urea exerts a very large effect on the late steps of the mechanism, consistent with the burial of amide surface in folding of more than 100 residues of polymerase. The unusual effect of GB on k_2 implies the exposure of anionic surface during this slow and very significant conformational change in I_1 to I_2.

in the last step of RP_o formation. (Both K_1 and $1/k_d$ exhibit large dependences on salt concentration *(21)* which are consistent with DNA–protein interface formation.) The initial effect of urea on K_1 is very small, consistent with formation of a protein–DNA interface that buries little polar amide surface; at higher urea, a larger effect of urea on K_1 is observed which may result from urea-induced desta-bilization of the quaternary structure (sigma-core interaction) of free RNA polymerase. By contrast, urea exerts a very large effect on the late steps of the mechanism, consistent with the burial of amide surface in folding of more than 100 residues of polymerase. Taken together with the large effects of GB and salt on the dissociation rate constant, we interpreted this urea effect to indicate folding of

the "downstream clamp" of RNA polymerase; binding of the folded clamp to DNA gives rise to the GB and salt effects. Most intriguing, perhaps, is the unusual effect of GB on k_2. This slow and very significant conformational change in I_1 to I_2 must therefore expose anionic surface; two candidates are the release of the DNA-mimic region of the sigma subunit (region 1.1) from the active site cleft to allow binding of single-stranded (template) DNA, and/or the unwrapping of upstream DNA from the backside of polymerase. Both these conformational changes must occur between I_1 and RP_o; studies with DNA truncations and a region 1.1 deletion of polymerase are in progress to test whether these variants exhibit different effects of GB, urea, and salt.

3.5. Hofmeister Effects of Salts on Surface Tension and on Biopolymer Processes Arise from Partitioning of Individual Salt Ions Between the Interfacial Region and Bulk Water: SPM Analysis

Surface tension is the work (or ΔG_{obs}°) required to create a unit area of surface, where the underlying process is the transfer of water molecules from bulk water to the surface environment. Surface-active solutes that partition into surface water (i.e., accumulate at local concentrations that exceed their bulk concentration) lower surface tension by reducing the work of transferring water to the surface. Excluded solutes increase the work of transferring water from bulk to surface, and thus increase the surface tension, because the transferred water must be "unmixed" from the solution (as in freezing point depression or other colligative processes). Similarly, solute effects on the solubility of sparingly soluble model compounds (e.g., hydrocarbons, nucleic acid bases, amino acids with nonpolar side chains, end-blocked amino acids) are interpretable in terms of partitioning of solute molecules between the bulk solution and the local phase of water of hydration at the molecular surface of the model compound. Accumulated solutes increase the aqueous solubility; excluded solutes decrease the solubility. Where the solute is an electrolyte, the partition coefficient is predicted, by an extension of the SPM, to be the stoichiometrically weighted sum of the partition coefficients of the individual ions (cf. **Eq. 8.2**). In the absence of Coulombic effects of salt concentration, the individual ion partition coefficients obtained by application of the SPM to surface tension increments (STIs) of electrolytes are expected to be independent of the other ion(s) present and to be additive. The rank order of effects of salts on surface tension has long been known to follow the Hofmeister series established for protein processes. We recently established that "Hofmeister" effects of salts on surface tension are interpretable using the SPM and that these effects arise from partitioning of individual salt ions between bulk water and the local region of water at the air–water interface *(8, 9)*.

From analyses of surface tension *(8, 9)* increments ($d\gamma/dm_3$; cf. **Fig. 8.5**), we have obtained composite thermodynamic quantities $b_1(K_{p,3} - 1)$ for a wide range of salts. By assuming Na_2SO_4 is completely excluded from the air–water surface (*see* **Note 5**), we obtain a lower-bound estimate of b_1 (the local water) of ~ 0.19
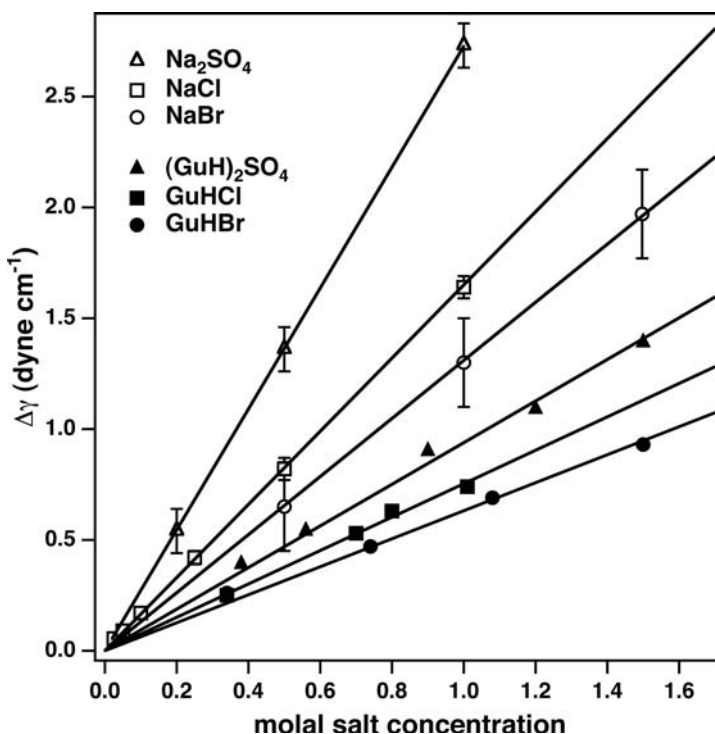
Fig. 8.5. Representative surface tension data for selected Hofmeister salts. *Open symbols* represent sodium salts *(22)*, while the corresponding *filled symbol* denotes the guanidinium salt of the same anion *(23)*.

water molecules/Å^2 (or $\sim$2 layers) *(8, 9)*. As mentioned in **Section 3.3**, SPM analysis of the effects of GB on various biopolymer processes indicates a minimum b_1 value of 0.22 $H_2O/\text{Å}^2$ for anionic oxygen surface. These similar values for different surfaces suggest that a local region of approximately two layers of water ($b_1 \cong 0.2\ H_2O/\text{Å}^2$) might be appropriate for any type of surface being investigated.

The results of the surface tension analysis using the SPM are shown in **Fig. 8.6**. The partition coefficients obtained for the air–water surface are shown on the left, and the qualitative rankings of cations and anions based on their effects on protein unfolding are shown on the right. One striking feature is the disparity in the placements of the alkali metal cations; while these cations are strongly excluded from the air–water *(8, 9, 24)* and nonpolar surfaces, they are generally inferred to be neutral ($K_p \sim 1$) with respect to protein folding. Single-ion partition coefficients are shown to be additive and independent, and qualitative agreement with recent surface-sensitive spectroscopy experiments and molecular dynamics simulations is attained *(24)*. With this demonstration that "Hofmeister" effects on surface tension are quantitatively interpreted using the SPM, continuation of this
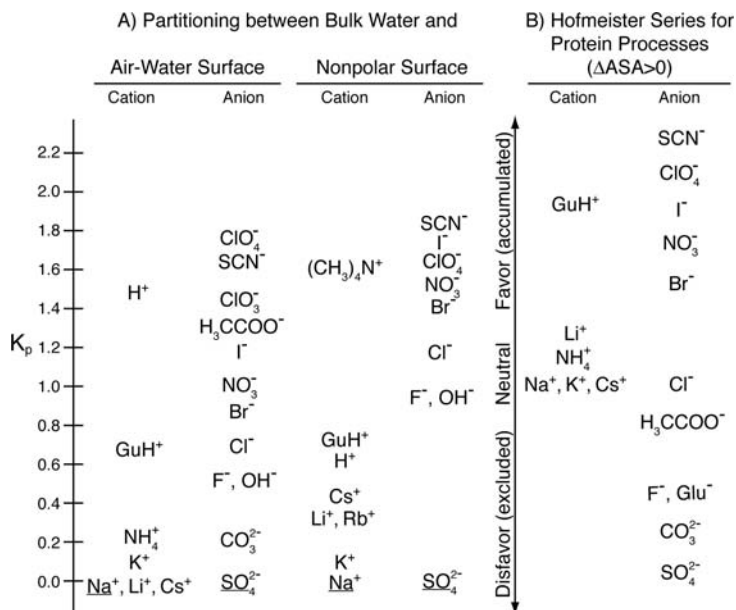
Fig. 8.6. (**A**) Comparison of single-ion partition coefficients $K_{p,i}$ for partitioning between bulk water and water at the air–water interface or molecular hydrocarbon surface. (**B**) Inferred placements of Hofmeister cations and anions based on salt effects on protein processes in which surface is exposed to water.

work includes analysis of salt effects on sparingly soluble uncharged model compounds in terms of ion partitioning between the bulk solution and water of hydration at the molecular surface.

When hydrocarbon solubility data *(25)* are analyzed via the SPM (**Eq. 8.1**) similar trends to those seen for the air–water interface are observed (cf. **Fig. 8.6**). The alkali metal cations are all quite highly excluded, with clustered partition coefficients, whereas the different anions exhibit a wide range of partitioning behavior (from strong exclusion of sulfate to strong accumulation of thiocyanate), which follows the order of the Hofmeister series. The alkali metal cations must be moderately accumulated at some other type of protein surface to compensate for their strong exclusion from nonpolar surface and explain their intermediate (relatively nonperturbing) position in the Hofmeister series. Preliminary analysis of solubility and distribution coefficient data for model peptides *(26)* indicates that Hofmeister salts are accumulated at polar amide surface and that differences between different salts are relatively small in comparison to the situation observed with hydrocarbon surface *(27)*. Since protein unfolding and other protein processes involve mostly changes in exposure of nonpolar and amide protein surface, the above interpretation of model compound data quantitatively confirms the previous proposal

(3) that the Hofmeister salt series observed for biopolymer processes results from the compensation between highly salt-specific net exclusion from nonpolar surface and net accumulation at amide surface.

3.6. Future Directions: Separating and Interpreting Coulombic and Hofmeister-osmotic Effects of Salts on Protein Folding and Protein–Nucleic Acid Interactions

With the determination of partition coefficients characterizing the interactions of cations and anions of the Hofmeister series with nonpolar and polar amide surface, it should be possible to predict the Hofmeister and osmotic contributions to salt-induced stabilization or destabilization of a folded protein (or protein complex) from structural information. Nonlinear Poisson–Boltzmann calculations should be useful to calculate the Coulombic component of the stabilization, dominant at low salt concentration, and **Eq. 8.1**, with the coarse-grained surface area breakdown for the system being studied, should be applicable to interpret the linear dependence of ΔG°_{obs} and its temperature derivatives on salt concentration observed at moderate to high salt concentrations. This analysis is currently being tested using unfolding of the lac repressor DBD and the melting of a DNA oligomer duplex as model systems. Additionally, the ion-specific dependences of the equilibrium constant, enthalpy, and heat capacity of specific binding of integration host factor (IHF) protein to DNA are being interpreted using the SPM *(17)*.

4. Notes

1. For analysis of experimental data, the molar concentration scale is preferred; the limiting slopes of the solute concentration dependences on the molar and molal scales are the same, but $\Delta G^\circ_{obs} = -RT \ln K_{obs}$ for a biopolymer or model process as a function of molar solute concentration is experimentally found to be linear, with the limiting (low [solute]) slope, over a wider range of solute concentration.

2. The nonideality correction $(1 + \varepsilon_3)$ is directly evaluated from the concentration dependence of the osmolality $(Osm = \nu\phi m_3)$ of the two-component solution: $dOsm/dm_3 \equiv \nu(1 + \varepsilon_3)$. Here, ν is the number of solute components $(\nu = 1$ for an uncharged solute, $\nu = 2$ for a 1:1 salt), and the osmotic coefficients ϕ can be readily obtained from the literature (e.g. *15, 16*).

3. The model compound data, unlike the biopolymer results, are quite urea concentration-dependent, with attenuation of the urea–amide interaction occurring at high concentrations; the reasons for this difference are not clear.

4. Model compound data indicate a significant accumulation of urea at aromatic hydrocarbon surface, but this interaction appears to be weaker than that between urea and polar amide

surface (L. Pegram, unpublished). Since GB also appears to interact favorably with (accumulate at) GC bases in single-stranded DNA, **Eqs. 8.3** and **8.4** are not suitable for use with single-stranded GC-containing DNA or other systems with large amounts of aromatic surface. Additionally, GB affects salt activity so a correction to constant salt activity may be needed; reference *(13)* contains the necessary equation (Eq. A6) to make this correction (although the sign on the right-hand side of the equation should be negative and not positive).

5. Unpublished GB solute titrations containing more data at low GB concentrations provide a more accurate description of the curvature at low GB concentration and yield an initial slope which, after correction to constant salt activity, is in closer quantitative agreement with that predicted from the structure (M. Capp, unpublished).

6. Because Na_2SO_4 has the largest STI of the salts we investigated, we assume it is completely excluded from the air–water interface. If a salt with a larger STI is used as a reference, b_1 will increase and the resulting partition coefficients will be shifted, but the qualitative conclusions remain unchanged.

Acknowledgements

References

1. Record, M. T. Jr., Zhang, W., Anderson, C. F. (1998) Analysis of effects of salts and uncharged solutes on protein and nucleic acid equilibria and processes: A practical guide to recognizing and interpreting polyelectrolyte effects, Hofmeister effects, and osmotic effects of salts. Adv Protein Chem 51, 281–353.

2. Timasheff, S. N. (1998) Control of protein stability and reactions by weakly interacting cosolvents: The simplicity of the complicated. Adv Protein Chem 51, 355–432.

3. Baldwin, R. L. (1996) How Hofmeister ion interactions affect protein stability. Biophys J 71, 2056–2063.

4. Myers, J. K., Pace, C. N., Scholtz, J. M. (1995) Denaturant *m*-values and heat capacity changes: Relation to changes in

accessible surface areas of protein unfolding. Protein Sci 4, 2138–2148.

5. Record, M. T. Jr., Anderson, C. F. (1995) Interpretation of preferential interaction coefficients of nonelectrolytes and of electrolyte ions in terms of a two-domain model. Biophys J 68, 786–794.

6. Felitsky, D. J., Record, M. T. Jr. (2004) Application of the local-bulk partitioning and competitive binding models to interpret preferential interactions of glycine betaine and urea with protein surface. Biochemistry 43, 9276–9288.

7. Courtenay, E. S., Capp, M. W., Saecker, R. M., et al. (2000) Thermodynamic analysis of interactions between denaturants and protein surface exposed on unfolding: Interpretation of urea and guanidinium chloride

m-values and their correlation with changes in accessible surface area (ASA) using preferential interaction coefficients and the local-bulk domain. Proteins 41, 72–85.

8. Pegram, L. M., Record, M. T. Jr. (2006) Partitioning of atmospherically relevant ions between bulk water and the water/vapor interface. Proc Natl Acad Sci USA 103, 14278–14281.

9. Pegram, L. M., Record, M. T. Jr. (2007) Hofmeister effects on surface tension arise from partitioning of cations and anions between bulk water and the air–water interface. J Phys Chem B 111, 5411–5417.

10. Courtenay, E. S., Capp, M. W., Anderson, C. F., et al. (2000) Vapor pressure osmometry studies of osmolyte–protein interactions: Implications for the action of osmoprotectants in vivo and for the interpretation of "osmotic stress" experiments in vitro. Biochemistry 39, 4455–4471.

11. Courtenay, E. S., Capp, M. W., Record, M. T. Jr. (2001) Thermodynamics of interactions of urea and guanidinium salts with protein surface: Relationship between solute effects on protein processes and changes in water-accessible surface area. Protein Sci 10, 2485–2497.

12. Felitsky, D. J., Cannon, J. G., Capp, M. W., et al. (2004) The exclusion of glycine betaine from anionic biopolymer surface: Why glycine betaine is an effective osmoprotectant but also a compatible solute. Biochemistry 43, 14732–14743.

13. Hong, J., Capp, M. W., Saecker, R. M., et al. (2005) Use of urea and glycine betaine to quantify coupled folding and probe the burial of DNA phosphates in Lac Repressor–Lac Operator binding. Biochemistry 44, 16896–16911.

14. Kontur, W. S., Saecker, R. M., Davis, C. A., et al. (2006) Solute probes of conformational changes in open complex (RP_o) formation by *Escherichia coli* RNA polymerase at the λP_R promoter: Evidence for unmasking of the active site in the isomerization step and for large-scale coupled folding in the subsequent conversion to RP_o. Biochemistry 45, 2161–2177.

15. Scatchard, G., Hamer, W. J., Wood, S. E. (1938) Isotonic solutions. I. The chemical potential of water in aqueous solutions of sodium chloride, potassium chloride, sulfuric acid, sucrose, urea and glycerol at 25°C. J Am Chem Soc 60, 3061–3070.

16. Robinson, R. A., Stokes, R. H. (1959) Electrolyte Solutions. Butterworths, London, England.

17. Vander Meulen, K., Saecker, R. M., Record, M. T. Jr. (2008) Formation of a wrapped protein–DNA interface: FRET and ITC characterization of large contributions of ions and water to the thermodynamics of binding IHF to H'DNA. J Mol Biol 377, 9–27.

18. Cannon, J. G., Anderson, C. F., Record, M. T. Jr. (2007) Urea–amide preferential interactions in water: Quantitative comparison of model compound data with biopolymer results using water accessible surface areas. J Phys Chem B 111, 9675–9685.

19. Scholtz, J. M., Barrick, D., York, E. J., et al. (1995) Urea unfolding of peptide helices as a model for interpreting protein unfolding. Proc Natl Acad Sci USA 92, 185–189.

20. Humphrey, W., Dalke, A., Schulten, K. (1996) VMD – Visual molecular dynamics. J Molec Graphics 14, 33–38.

21. Roe, J. H., Record, M. T. Jr. (1985) Regulation of the kinetics of the interaction of *Escherichia coli* RNA polymerase with the λP_R promoter by salt concentration. Biochemistry 24, 4721–4726.

22. Washburn, E. W. (ed.) (2003) International Critical Tables of Numerical Data, Physics, Chemistry, and Technology, 1st electronic ed. Knovel, Norwich, NY.

23. Kumar, A. (2001) Aqueous guanidinium salts Part II. Isopiestic osmotic coefficients of guanidinium sulphate and viscosity and surface tension of guanidinium chloride, bromide, acetate, perchlorate, and sulphate solutions at 298.15 K. Fluid Phase Equilib 180, 195–204.

24. Petersen, P. B., Saykally, R. J. (2006) On the nature of ions at the liquid water surface. Annu Rev Phys Chem 57, 333–364.

25. Long, F. A., McDevit, W. F. (1952) Activity coefficients of nonelectrolyte solutes in aqueous salt solutions. Chem Rev 51, 119–169.

26. Nandi, P. K., Robinson, D. R. (1972) The effects of salts on the free energy of the peptide group. J Am Chem Soc 94, 1299–1308.

27. Pegram, L. M., Record, M. T. Jr. (2008) Thermodynamic Origin of Hofmeister ion effects. J Phys Chem B 112, 9428–9436.

Chapter 9

Molecular Crowding and Solvation: Direct and Indirect Impact on Protein Reactions

Jörg Rösgen

Abstract

The typical environment for biomolecules in vivo is highly crowded. Under such conditions chemical activities, rather than simply concentrations, govern the behavior of the molecules. In this chapter we discuss the underlying solvation principles that give rise to the chemical activities. We focus on simple experimentally accessible examples, macromolecular crowding, protein folding, and ligand binding under crowded conditions. We discuss effects of high concentrations of both macromolecules and small molecules in terms of the Kirkwood–Buff theory, which couples solution structure to thermodynamics.

Key words: Solvation, crowding, protein stability, unfolding, ligand binding, Kirkwood–Buff theory.

1. Introduction

On the molecular level, life is governed chiefly by the chemical activities of the compounds an organism is composed of *(1)*. **(Note 1)** Chemical activities are at the basis of fundamental biochemical phenomena as diverse as interaction affinities, kinetic rates of chemical reactions, and diffusion. It is therefore of utmost importance to understand how chemical activities originate from the behavior of a given set of molecules, and what are the consequences of altering the solution composition. In dilute solution this is a simple task, because under such "ideal" conditions chemical activities are proportional to concentrations. Life, however, does not typically deal with dilute conditions. For instance, anyone who has opened a raw egg knows that cellular contents are far from being ideally dilute, as the contents are quite viscous and concentrated. Such concentrated, nonideal conditions can lead to

chemical activities that deviate by orders of magnitude from their "ideal" behavior (simple proportionality with concentration).

In this chapter we investigate how specific and nonspecific interactions between biomolecules affect their chemical activities, and how this relates to their equilibrium behavior – such as protein folding and ligand binding. Special emphasis will be given to osmolytes, which are small organic molecules that are used by essentially all organisms to counteract cellular stresses *(2)*.

Interest in the mutual roles of water and cosolute on protein behavior developed early on after Tanford noted that co-solute effects are actually a balance between protein・cosolute interactions on the one hand and protein・water interactions on the other hand *(3)*. This finding lead to Schellman's exchange concept *(4)*, which states that cosolute interacting with the protein automatically replaces water, and interacting water molecules replace cosolute. At that stage of research, however, it was only possible to quantify the overall effect of this exchange. The actual numbers of water and cosolute molecules were inaccessible to quantification. Naturally this lead to the development of model assumptions and speculations about the specific roles of water and cosolute. To get beyond the level of models and speculations a rigorous theory was needed. Such a theory was developed by Ben-Naim *(5, 6)*, unnoticed by much of the biophysical and biochemical community. This so-called inverse Kirkwood–Buff theory is based on first principles and yields the mutual solvation of all solution species, including macromolecular hydration and solvation by the cosolutes. Only recently has this theory been popularized for the use with proteins, originally by Smith and by Shimizu *(7–12)*. Here we present some aspects of the Kirkwood–Buff theory that are essential for the use of experimental data in determining the relative roles of hydration, cosolute solvation, and other interactions in biomolecular energetics.

2. Background: Molecular Solvation

This section provides the theoretical background that is necessary to fully understand the application section below. **Section 2.1** gives an introduction to the structure of a solution in terms of pair correlation functions, and serves as an extended figure legend to **Fig. 9.1**. The reader may initially skip **Sections 2.2** and **2.3**, as they focus on details of the calculations performed in the application **Section 3**. **Section 2.2** presents essential aspects of the Kirkwood–Buff theory *(13)*, which allows calculating
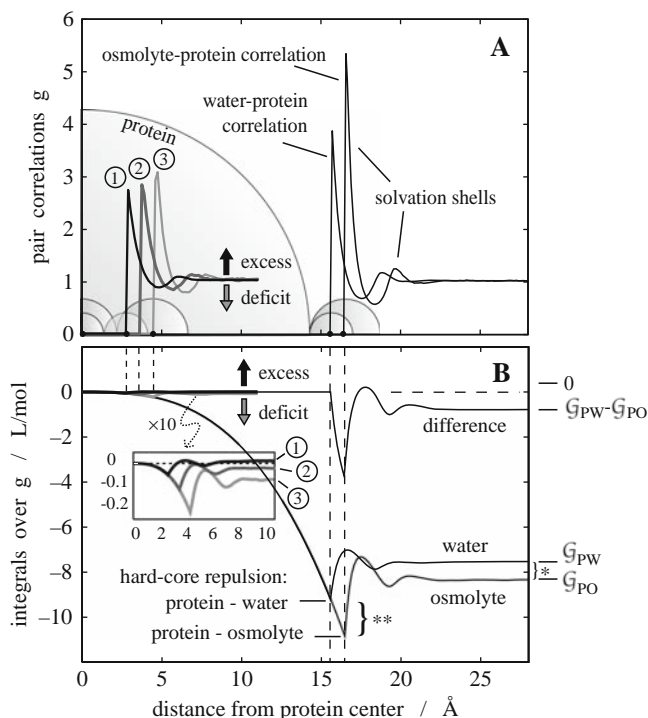
Fig. 9.1. Solvation in a three-component hard-sphere mixture. The radii of the spheres are modeled to roughly resemble water, the osmolyte TMAO, and protein. Sphere sizes are indicated in the upper panel for clarity. (**A**) Pair correlation functions between all molecules, from left to right: Water self-hydration (labeled 1), osmolyte hydration (labeled 2), osmolyte self-solvation (labeled 3), protein hydration, and protein–osmolyte solvation. Values of unity correspond to bulk density. Note the region of direct steric exclusion (inability of molecules to overlap), where pair correlations are zero. Spheres are drawn to illustrate steric exclusion. (**B**) Integrals over the deviation of g (panel A) from bulk density. The final value of these integrals is the overall solvation $G_{ij} = \int (g_{ij} - 1) \mathrm{d}V$ shown on the right side of panel B for protein solvation. Solvation effects of the small molecules are minute in comparison and are shown tenfold enlarged in the insert. The overall water self-hydration G_{WW}, osmolyte hydration G_{OW}, and osmolyte self-solvation G_{OO} are labeled 1, 2, and 3, respectively. Note that the solvation shells partially or totally offset the effect of steric exclusion, depending on the kind of interaction pairs (G_{PW}, G_{PO}, G_{WW}, etc.), and whether or not solvation differences ($G_{PW} - G_{PO}$) are considered. Thus, the preferential solvation $G_{PW} - G_{PO}$ of the protein has a smaller magnitude than expected from the direct mutually excluded volume (see single and double asterisk).

thermodynamic properties of a solution from its structural features. Kirkwod–Buff theory is among the first and foremost examples for structural thermodynamics. **Section 2.3** is about the reverse process, namely deriving structural information from solution thermodynamics, named inverse Kirkwood–Buff theory *(5)*.

2.1. Overall Solvation and the Structure of a Solution

2.1.1. Structure of a Solution

The overall goal of this chapter is to discuss and analyze nonideal solution effects (crowding and solvation) on protein reactions, and this requires analyzing chemical activities. The task of analyzing chemical activities can be subdivided into two aspects, investigation of (1) the absolute value of the chemical activity under a given set of conditions, such as ideal dilution, and (2) the change in chemical activity caused by the addition of a single compound or several compounds. In this chapter, we discuss the latter aspect, that is, slopes of chemical activities vs. the concentrations of the solution components. These slopes can be expressed in terms of the structure of the solution, given by pairwise correlations between the different molecular species *(13)*. As an illustration, **Fig. 9.1A** schematically shows such pair correlations g_{ij} for a simplified case of spherical molecules, representing protein, water, and some osmolyte. These g_{ij} functions give the concentration of molecules of type j around molecules of type i relative to the bulk concentration. So, values larger than 1 indicate an excess of molecule-type j around i, and values smaller than 1 a deficit. The pair correlations are distance dependent, and regions of high local concentration (peaks) are called solvation shells, which are often most pronounced at contact distance. **Figure 9.1A** shows the sizes of all involved molecules for illustration. For instance, the large sphere represents a protein, and the two smaller spheres at surface contact with this protein represent water and osmolyte. The function g_{PW} (the water–protein correlation) shows how the average water density around protein spheres behaves relative to the bulk water density. The slightly larger osmolyte molecule gives rise to a peak in the osmolyte–protein correlation g_{PO} at slightly larger distances from the protein's center of mass. Also shown are correlations between the smaller molecules (bold lines on the left side of **Fig. 9.1A**). Since molecules cannot mutually overlap, all pair correlations g_{ij} are zero up to their contact distance (**Fig. 9.1A**, left side). Far away in the bulk solution the presence of the first molecule is not felt any more, and so g_{ij} becomes unity further towards the right side of **Fig. 9.1A**. Between these two limits, the pair correlations g_{ij} show some characteristic solvation features that strongly depend on the chemical nature and concentration of all solution components. Effects of molecular size are quite obvious comparing a series of g_{ij}, namely the g_{WW} (labeled 1) of the smaller water, the g_{OO} (labeled 3) of the larger osmolyte, and the osmolyte–protein correlation, which displays the largest solvation peak.

2.1.2. The Overall Solvation

The local deviations from bulk density lead to overall correlations between molecules as shown in **Fig. 9.1B**. Here, the deviations of all g_{ij} from unity are integrated over the space around the central

molecule to yield the overall correlations $G_{ij} = \int (g_{ij} - 1) dV$. (**Note 2**) The overall correlations, G_{ij} (final values at the right side of **Fig. 9.1B**, and on the right side of the insert), have contributions from the different features seen in **Fig. 9.1A**, such as direct steric exclusion and solvation shells. Note that solvation shells can overcompensate the anticorrelation between particles that is always given by the direct steric exclusion. Such solvation shells can originate from attractive interactions, but also from packing effects in the absence of any attractive interactions *(14)*. In fact, the simulation that was used to generate **Fig. 9.1** was based on hard-core repulsion as the only force between molecules. Thus, the solvation peaks in **Fig. 9.1** originate from hard-core repulsion, rather than from attractive interactions.

The themodynamics of the systems discussed below is solely based on overall correlations G_{ij}, that is, the final values of the integration in **Fig. 9.1**B; but it can be useful to go beyond the overall effect and discuss G_{ij} in terms of the integrated solvation features g_{ij}. The actual shape of the g_{ij} functions in a multicomponent system is inaccessible by experiment and can only be derived from computer simulation. However, simulations are not yet accurate and precise enough to calculate thermodynamic information from g_{ij}. The practical approach to linking structure and thermodynamics must therefore be based on experimental data that are used to derive the integrated g_{ij}, that is, the overall correlations G_{ij}. This procedure is outlined in the following (**Sections 2.2** and **2.3**).

2.2. Calculation of Thermodynamic Functions from the Structure of the Solution

2.2.1. Kirkwood–Buff Equations Expressing Thermodynamics in Terms of Structure

This **Section 2.2** and the following **Section 2.3** deal with the forward and backward directions, respectively, of deriving thermodynamic data from the structural information. There are many ways to define the term "structure of a solution", and the appropriate definition will always depend on the context. In the context of thermodynamics, the structure of a solution is given by the pair correlation functions g_{ij} that we discussed above *(13)*. The actual connection to thermodynamics, however, is on the level of the integrated g_{ij}, the so-called Kirkwood–Buff integrals G_{ij}. These overall correlations between particles of type i and j are the final value of the integration of $g_{ij} - 1$. For the purpose of thermodynamic calculations, all of these pairwise correlations are summarized in a matrix with the elements

$$B_{ik} = c_i(\delta_{ik} + c_k G_{ik}), \qquad (9.1)$$

where c represents molar concentrations, and δ_{ik} is the Kronecker delta ($\delta_{ik} = 1$ for $i = k$, and $\delta_{ik} = 0$ otherwise). Generally, the thermodynamic data can be calculated from the determinant $|B|$ of this matrix, and its cofactors $|B|_{ij}$. (**Note 3**) The resulting slope of the chemical activity $\ln a_k$ with particle number N_i is then *(13)*

$$\left(\frac{\partial \ln a_k}{\partial N_i}\right)_{T,p} = \frac{|B|_{ik}}{V|B|} - \frac{\bar{v}_i \bar{v}_k}{RT\kappa V} \tag{9.2}$$

where the partial volumes are given by

$$\bar{v}_i = \frac{\sum_k c_k |B|_{ik}}{\sum_{k,l} c_k c_l |B|_{kl}}, \tag{9.3}$$

and the compressibility is

$$\kappa RT = \frac{|B|}{\sum_{k,l} c_k c_l |B|_{kl}}. \tag{9.4}$$

2.2.2. Switching from Particle Numbers to Concentrations

Equation 9.2 contains particle numbers N_i, which is inconvenient. Transforming the equation to regular concentration scales results in

$$\left(\frac{\partial \ln a_k}{\partial m_i}\right)_{T,p} = 1000 \frac{c_W}{M_W}\left(\frac{|B|_{ik}}{|B|} - \frac{\bar{v}_i \bar{v}_k}{RT\kappa}\right), \tag{9.5}$$

where M_W is the molecular weight of water, and the factor of 1000 originates from the conversion between g and kg of water in m_i. This equation still contains two different kinds of concentration scales, namely, the molal scale m (moles per kg of water) and the molar scale c (moles per liter of solution). This is not a problem if the density of the solution is known. However, the molar scale turns out to be the preferred one for purposes of data interpretation *(15–17)*. It is therefore desirable to convert **Eq. 9.5** uniformly to the molar scale as the concentration scale of interest. While this is no problem in principle, it can be cumbersome. Therefore we only give the solution for simple cases in the examples discussed in the sections below.

Conversion to molar concentrations is especially easy in a two-component solution:

$$\left(\frac{\partial}{\partial N}\right)_{T,p} = \left(\frac{\partial c}{\partial N}\right)_{T,p}\left(\frac{\partial}{\partial c}\right)_{T,p} = \left[\frac{1}{V} - \frac{N}{V^2}\left(\frac{\partial V}{\partial N}\right)_{T,p}\right]\left(\frac{\partial}{\partial c}\right)_{T,p}, \tag{9.6}$$

where we used $c = N/V$. The derivative of the volume with respect to the number of particles equals the partial molar volume. Thus the result is

$$\left(\frac{\partial}{\partial N}\right)_{T,p} = \frac{1 - c\bar{v}}{V}\left(\frac{\partial}{\partial c}\right)_{T,p} = \frac{c_W \bar{v}_W}{V}\left(\frac{\partial}{\partial c}\right)_{T,p}, \tag{9.7}$$

where the volume fractions of water $c_W \bar{v}_W$ and solute $c\bar{v}$ add up to unity.

Another equation that we will use was originally presented by Ben-Naim [18], and recently generalized by Smith et al. [19]

$$\bar{v}_k = \kappa RT - \sum_i \bar{v}_i c_i G_{ik} \approx - \sum_i \bar{v}_i c_i G_{ik}. \qquad (9.8)$$

The approximation of $\kappa RT \approx 0$ is normally permissible for aqueous solutions.

2.2.3. Usage of the Equations

Equations of the type of **Eqs. 9.2** through **9.8** can be used to calculate the overall solvation given by the Kirkwood–Buff integrals G_{ij}. For this purpose we need for each G_{ij} one of the experimental properties contained in **Eqs. 9.2** through **9.8**. This set of equations can then be solved for all G_{ij}. Solving for the G_{ij} can become a tedious task, because the number of different G_{ij} increases rapidly with increasing number of solution components. An n-component system has n^2 different G_{ij}. For symmetry reasons, however, many of these are equal, because $G_{ij} = G_{ji}$ [18]. Thus the problem is reduced from n^2 to $n(n+1)/2$. Further simplifications may be possible depending on the specific conditions, for example, low concentrations of some components, such as proteins, specific ligands, etc.

Pursuing this general strategy of deriving the G_{ij} from equations of the type of **Eqs. 9.2** through **9.8** leads to expressions whose interpretation is especially straightforward. This is because the resulting equations are in terms of molar concentrations, which is the preferred scale for data interpretation for several reasons. Firstly, the nonideality of osmolyte solutions can be expressed in very simple terms if the molar scale is used. This is valid for the normally constant slope of protein stability with osmolyte concentration [20–28], as well as for the nonideality of the osmolyte solution itself, given by activity coefficients [15, 16]. Secondly, the molar scale is preferred for reasons rooted in solution theory (*see* **Refs.** *17* and *29* for details).

2.3. Calculation of the Structure of the Solution from Thermodynamic Functions

The approach in the previous subsection was to calculate thermodynamic properties in terms of Kirkwood–Buff integrals G_{ij}. These equations could be either used to understand how solvation impacts thermodynamics, or to solve multiple equations simultaneously for the G_{ij}. This latter procedure can be very cumbersome in systems that contain many components, and so we show now how to obtain the G_{ij} directly from the experimental thermodynamics.

The overall solvation, that is, the Kirkwood–Buff integrals, G_{ij}, can be directly calculated from experimental data using the relation [13]

$$G_{ik} = \frac{|A|_{ik}}{|A|} \frac{1}{c_i c_k} - \frac{\delta_{ik}}{c_i}, \qquad (9.9)$$

where the matrix A has as its elements

$$A_{ik} = a_{ik} + \frac{\bar{v}_i \bar{v}_k}{\kappa RT},\qquad (9.10)$$

and the slope of the chemical activity of component i with regard to the number of particles of type k is

$$a_{ik} = V \left(\frac{\partial \ln a_i}{\partial N_k} \right)_{T,p} = \frac{1000}{c_W M_W} \left(\frac{\partial \ln a_i}{\partial m_k} \right)_{T,p},\qquad (9.11)$$

where c_W and M_W are molarity and molecular weight of water. In applying these equations for the calculation of all G_{ij} there are n^2 derivatives a_{ij} required for an n component system. Again, we do not need to measure all of them, because of the symmetry

$$a_{ij} = a_{ji}.\qquad (9.12)$$

Moreover, applying the Gibbs–Duhem relation

$$\sum_i m_i \left(\frac{\partial \ln a_i}{\partial m_k} \right)_{T,p} = 0\qquad (9.13)$$

for each component k further reduces the number of a_{ij} by n. So, altogether $n(n-1)/2$ derivatives a_{ij} are needed in an n component system to calculate all G_{ij}. The partial molar volumes $\bar{v}_i$ are obtained from density measurements, and the compressibility can be measured separately. For aqueous systems it is often permissible to set the compressibility to zero. **Equation 9.10** seems to prohibit this step, but using **Eq. 9.10** in the context of **Eq. 9.9** renders this step possible, and the resulting equation is well-defined even in the limit of zero compressibility. The calculation of the G_{ij} is cumbersome if done by hand, but software such as *Mathematica*® (Wolfram Research) greatly simplifies this task.

In the following sections we focus on solvation under crowded conditions. Further information about experimental *(30)* and mathematical *(31)* aspects is available elsewhere.

3. Application

3.1. Macromolecular Crowding and Confinement

Hard-core repulsion is the dominant force for macromolecules in the absence of significant attractive interactions and long-range electrostatic repulsion between macromolecules. Such systems have their classical representation in hard-sphere models. Several decades ago it was shown that hemoglobin molecules in aqueous

solution behave like a gas of hard-spheres *(32)*. Hemoglobin is roughly spherical, is net-neutral around pH 7, and is highly soluble in its net-neutral state. These features make hemoglobin the perfect experimental example for the effects of pure macromolecular crowding, as represented by uncharged hard-spheres. We proceed now to discuss such hard-core repulsion – the most fundamental contribution to concentration-dependent solution behavior – using hemoglobin as an example. After that, we discuss important conceptual points that experimentators should keep in mind when dealing with macromolecular crowding.

3.1.1. One-Component Hard-Sphere Gas as a Representation of Hemoglobin

In a simple one-component system the connection between thermodyamics and structure (given by the correlations between hard-spheres G_{HH}) is straightforward. The dependence of the chemical potential on the concentration of the single component (**Note 4**)

$$\left(\frac{\partial \ln a}{\partial \ln c}\right)_{T,V} = 1 - \frac{c G_{HH}}{1 + c G_{HH}} \tag{9.14}$$

contains two parts. Firstly, the ideal part is unity and reflects that under ideal dilute conditions the chemical activity a is proportional to concentration c. Secondly, the Kirkwood–Buff integral G_{HH} gives the deviation from ideality. For hard-spheres $c G_{HH}$ starts at zero for $c = 0$, and decreases towards –1 as c increases. Thus, the nonideal (crowding) term $-c G_{HH}/(1 + c G_{HH})$ starts at zero and hyperbolically increases with c. Solving **Eq. 9.14** for G_{HH} is straightforward, and using the chemical activity of a hard-sphere gas *(33)* for $(\partial \ln a/\partial \ln c)_{T,V}$ results in the self-solvation G_{HH} shown in **Fig. 9.2** (continuous line) along with the analogous results when taking into account the presence of water. The calculation was done for hemoglobin-sized spheres. G_{HH} in this one-component system equals $G_{HH} - G_{WH}$ in the corresponding two-component system including water (*see* **Section 3.1.2**). Note that the mutual exclusion of protein molecules decreases as their concentration increases. This is because the solvation peaks (*see e.g.* **Fig. 9.1**) in a hard-sphere gas become larger as the concentration increases (enhanced packing of macromolecules).

In addition to the chemical activity the compressibility equation

$$\kappa_T = \frac{1 + c G_{HH}}{c R T} \tag{9.15}$$

is also very simple, and the partial molar volume in a one-component system

$$\bar{v} = \frac{1}{c} \tag{9.16}$$
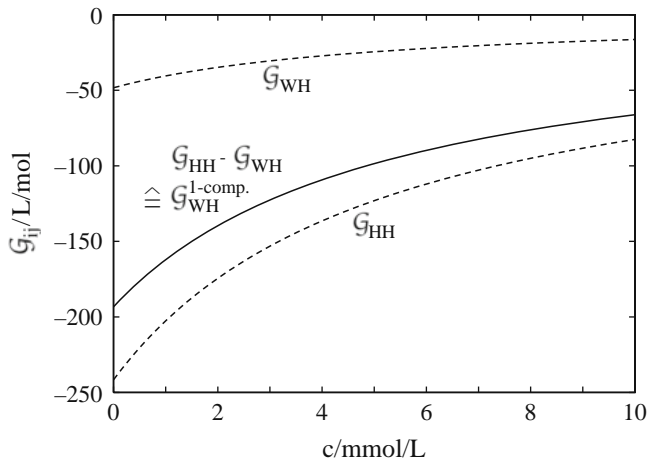
Fig. 9.2. Solvation of aqueous hemoglobin, calculated from **Eqs. 9.26** and **9.27**. The water self-hydration (**Eq. 9.28**) is not displayed, because it is essentially zero compared to the shown Kirkwood–Buff integrals. The continuous line also represents the one-component G_{HH} (*see* **Eq. 9.14**). For evaluation of these equations both the slope of the chemical activity $(\partial \ln a / \partial \ln c)_{T,V}$ and the partial volume of hemoglobin are needed. The chemical activity of hemoglobin is closely approximated by the chemical activity of a hard-sphere gas *(34)*, and we calculated $(\partial \ln a / \partial \ln c)_{T,V}$ according to Carnahan & Starling *(33)*. The volume was chosen to be –48 L/mol – the approximate volume of hemoglobin *(119)*.

does not contain a Kirkwood–Buff integral. In the current case of a one-component system, however, these equations are of limited practical usefulness, unless the compressibility is known.

3.1.2. Two-Component Hard-Sphere Gas

3.1.2.1. Hemoglobin Solvation

Curiously, the chemical activity of hemoglobin as a function of its own concentration in aqueous solution matches the simple behavior of *a gas* that contains a single component, while the water is not included in the thermodynamic analysis *(34)*. This appears puzzling on first sight, since an aqueous hemoglobin solution is clearly not a gas. However, the Kirkwood–Buff expressions for one- and two-component systems are very similar, and thus the one-component approach is valid as discussed now. The slope of the chemical activity of the hemoglobin in water is (**Note 5**)

$$\left(\frac{\partial \ln a_H}{\partial \ln c} \right)_{T,p} = 1 - \frac{c(G_{HH} - G_{WH})}{1 + c(G_{HH} - G_{WH})}, \qquad (9.17)$$

where G_{WH} is the hemoglobin–water correlation, that is, the hydration of the protein. The only difference between this equation and the one for the single-component system is the subtraction of the hemoglobin hydration G_{WH} from the hemoglobin self-solvation G_{HH}. **Figure 9.2** shows these two solvation parameters along with their difference for hemoglobin – modeled using hard-sphere

activity coefficients. Remember that the continuous line is not only the solvation difference between hemoglobin hydration and self-solvation, but also corresponds to the apparent hemoglobin self-solvation itself, if water is neglected. In this case it is permissible to neglect some details (the hemoglobin hydration), as long as it is recognized that effective solvation properties, rather than true solvation properties result. In the given example, the hard-sphere size of hemoglobin from G_{HH} appears to be smaller than it really is if the presence of water is ignored.

3.1.2.2. Macromolecular Crowding Is Self-ameliorating

Figure 9.2 also shows that all solvation parameters become less negative as the concentration of hemoglobin increases. The initial value of G_{HH} at 0 M corresponds to the mutual sterically excluded volume of two hemoglobin molecules. It is only at these low concentrations at which the molecules can distribute randomly in solution that G_{HH} equals this mutual sterically excluded volume. As the protein concentration increases, less free space remains available. As a consequence random distribution is impeded, and the molecules force each other to pack more efficiently. Such self-alleviation of the severity of macromolecular crowding is one of its inherent properties. This example serves to demonstrate that it is instructive not only to know that hemoglobin behaves as hard-spheres, but also what the implications are in terms of the self-solvation G_{HH} and other solvation properties. Without the increase in packing efficiency that comes with macromolecular crowding, hemoglobin would have the hyperbolically escalating activity- and osmotic coefficients that many osmolytes exhibit (*see* **Section 3.2.2**, and **Ref.*16***). At nearly 50% hemoglobin in red blood cells, such extreme osmotic coefficients would lead to water gushing into the erythrocytes, resulting in an instant and complete hemolysis. Our life depends on hemoglobin showing "only" steric macromolecular crowding that implies the strongly concentration-dependent solvation details displayed in **Fig. 9.2**.

3.1.3. Macromolecular Crowding Is Not the Whole Story

There is no question that such simple macromolecular crowding and confinement plays a major role for the energetics of many systems, but other effects contribute in addition. Among these are soft interactions between macromolecules such as the biologically ubiquitous electrostatics *(35)*, hydrophobic interactions between protein molecules that can destabilize proteins *(36)*, the geometry and size of the available space *(37–39)*, the compact or coiled nature of the macromolecules *(40)*, and interaction with surrounding molecules or structures *(41, 42)*. So, on the one hand, it is not surprising that crowding and confinement are effective both in simulation *(43, 44)*, and experiment *(45–47)*.

On the other hand, it should be understood that sometimes crowding conditions can do the opposite of stabilizing proteins. Such conditions serve as a means to maintain disorder, as shown

for the model system of synuclein expressed into bacterial peri-plasm *(48)*. The heavily crowded conditions in living cells may have no effect on cytoplasmic protein stability *(49, 50)*. Moreover, even in vitro the effect of macromolecular crowding can be disappointingly small, or actually of opposite sign compared to the effects that small molecules exert. For example, a slightly destabilizing effect of ficoll on protein folding was recently reported *(51)*, in contrast to expectations of finding stabilization by macromolecular crowding. Also, folding of TCAM, an intrinsically unstable variant of RNase T1, is much more strongly promoted by the small organic osmolytes TMAO and sarcosine than by either of dextran 70, ficoll 70, and BSA *(52)*. The *m*-value for forced folding of TCAM is 63 J/mol/(g/L) in sarcosine, and 14 J/mol/(g/L) in dextran 70. *m*-values are a measure for the response of a biochemical equilibrium to osmolyte concentration (see below, and Chapter 2). Such modest effects are actually not too surprising, since the unfolded chain may be able to explore interstitial voids between crowders which are inaccessible to the native molecules *(53)*.

3.1.4. Use of and Alternatives for Crowding Agents in Experiment

These considerations should make obvious that the phenomenon of molecular crowding can not only be complex in itself, but is usually not separable from other "secondary" effects. Even if crowding agents are carefully selected, such secondary effects are operative. Experimental observations on crowding are therefore expected to depend on the specific crowding agent chosen, and only in exceptional cases as the self-crowding of hemoglobin, the absence of side-effects may be expected. The choice of a specific crowding agent for an experiment will depend strongly on the purpose for which this cosolute is added, and we will shortly discuss a few in the following.

(1) "Protein stabilization" may be achieved with crowding agents. However, small organic molecules may be more efficient than classical macromolecular crowding agents, as mentioned above. Generally, modifications of the concentration of small molecules is a promising approach to improving protein stability and solubility. Protein stability profiling *(54)* and empirical phase diagrams *(55, 56)* have recently demonstrated the usefulness of this approach for drug and formulation development. Other types of protein research can equally well benefit from alterations in solution compositions, and the addition of macromolecular crowding agents should be viewed as only one possibility among others.

(2) Crowding agents have been employed for "solvation analysis" using the osmotic stress method *(57, 58)*. This method is especially useful for its original application with systems that completely exclude the crowding agent *(59–62)*, or for which the minimum crowder's size can be determined *(63, 64)*. Typically, large crowders would be selected for this method, such as

high-molecular-weight PEGs, ficoll, and similar polymers. Note, however, that in general the solvation of a biomolecule is expected to have energetic contributions from both water and the added crowding agent *(57, 65)*. This makes it especially important to make sure that the crowder is completely excluded from the investigated biomolecules, or that the observed effects are completely independent of the choice of the crowding agent. Otherwise, the number of excluding waters obtained from the osmotic stress method includes non-water contributions. Further below we will discuss this method more, and unify its results with the approach of using preferential interactions in general. This can be done using the Kirkwood–Buff theory.

(3) The use of crowding agents to create a more physiological environment is not a straightforward approach. The cytoplasm contains a large number of different kinds of macromolecules of different charge, different surface characteristics, different tendencies to interact with one another and the investigated molecule. Given these facts, it may appear an insurmountable challenge to produce a realistic mimic of cytoplasmic crowding. Still, it seems that comparisons between NMR measurements in the cytoplasm and in vitro indicate it is possible to make proteins behave similarly under both conditions by measures as seemingly blunt as adding 300 mg/ml BSA *(66)*. It may thus be that the addition of random crowding agents gives a realistic mimic of the cell in terms of structure and dynamics. We already discussed above that protein stability, in contrast, can be unaffected by cellular crowding, and that different crowding agents can have a stabilizing or destabilizing effect on proteins. With regard to protein stability it is therefore advisable to keep in mind that adding a crowder does not necessarily make the solution more "physiologic."

Overall, we can see that the crowded conditions may produce a broad spectrum of effects. The sign and magnitude of the effects will depend on the system and its molecular components. Much research remains to be done to gain a good understanding of crowded systems that contain more than just a few components. Kirkwood–Buff theory will play an important role in finally understanding the complex mixed effects of steric crowding and attractive plus repulsive interactions. This is because it provides the link between thermodynamic experiment and the relative arrangement of molecules in solution that is so important in understanding molecular crowding. Computer simulation is able to provide such molecular detail, but the calculations have to be benchmarked against experimental data. The comparison of hemoglobin thermodynamics with results from research on hard-spheres *(32)* was based on a similar idea. Modern computer simulations linked to experiment via the Kirkwood–Buff theory provide new capabilities, which are recently being explored using small molecules *(17, 67–71)*.

Such combination of computer simulation and experiment is likely to also shed more light on macromolecular crowding in the future.

On the experimental side, we do not have to wait for these advances in simulation and theory. Application of Kirkwood–Buff theory to experimental data can already now yield the overall solvation of all solution components. We discuss this approach now in more detail using small molecules as a convenient example.

3.2. Solvation by Small Molecules

3.2.1. Small-Molecule Steric Crowding

Molecular crowding is not limited to macromolecules. Also the impact of small molecules on protein thermodynamics, stability, and binding interactions has been attributed to crowding *(72–76)*, as in the case of macromolecules. It is unlikely that such crowding is the only significant force in general. Normally it should be expected that both crowding and attractive/repulsive interactions play a significant role *(77–80)*. Moreover, although a separation of the effects of volume exclusion and further solvation may appear desirable *(81–83)*, they are, strictly speaking, all part of the solvation of the solution species *(84)*. Thus, solvation shells and crowding are part of one single phenomenon that is rigorously captured by the statistical mechanical Kirkwood–Buff approach. The different approaches of crowding, preferential interaction *(3, 85)*, osmotic stress *(58)*, transfer model *(86, 87)*, local domain model *(24)*, and other models of preferential interaction *(88)*, can all be unified in the Kirkwood–Buff theory. Most of these approaches are designed to understand the experimental results in terms of the molecular solvation. However, only the rigorous Kirkwood–Buff theory requires no model assumptions for deriving these solvation data. In the following sections we discuss several examples for effects of added small molecules on solution components.

3.2.2. General Solvation: Osmolytes

Binary solutions of water and small organic osmolytes are especially good as an introductory example of solvation effects, because their solvation behavior has been found to be very simple *(15, 89)*. The partial molar volumes of the two solution components can be directly calculated from **Eq. 9.3:**

$$
\begin{aligned}
\bar{v}_O &= \frac{c_W|B|_{WO} + c_O|B|_{OO}}{c_O c_O|B|_{OO} + 2c_W c_O|B|_{WO} + c_W c_W|B|_{WW}} \\
&= \frac{1 + c_W(G_{WW} - G_{WO})}{c_W + c_O + c_O c_W(G_{WW} + G_{OO} - 2G_{WO})},
\end{aligned}
\tag{9.18}
$$

$$
\bar{v}_W = \frac{1 + c_O(G_{OO} - G_{WO})}{c_W + c_O + c_O c_W(G_{WW} + G_{OO} - 2G_{WO})},
\tag{9.19}
$$

and the compressibility from **Eq. 9.4**

$$\kappa RT = \frac{c_W(1 + c_W G_{WW})c_O(1 + c_O G_{OO}) - (c_O c_W G_{OW})^2}{c_W + c_O + c_O c_W(G_{WW} + G_{OO} - 2G_{WO})}. \quad (9.20)$$

The partial molar volumes of osmolytes do not vary much with concentration *(16)* and the compressibility of aqueous solutions is close to zero *(90)*. Therefore, the strongly concentration-dependent chemical activity is of primary interest in the present context. It is calculated as explained in **Note 5**, which yields

$$\left(\frac{\partial \ln a_O}{\partial c_0}\right) = \frac{1}{c_O} + \frac{G_{WO} - G_{OO}}{1 - (G_{WO} - G_{OO})c_O}. \quad (9.21)$$

As can be seen from **Eq. 9.21**, the difference between the overall hydration G_{WO} and the overall self-solvation G_{OO} of osmolyte can be directly calculated, solving **Eq. 9.21** for $G_{WO} - G_{OO}$. Separate calculation of these solvation parameters requires an additional step. Application of **Eq. 9.8** to the present case of a two-component system yields two equations one of which is

$$\bar{v}_O = \kappa RT - \bar{v}_W c_W G_{WO} - \bar{v}_O c_O G_{OO} \approx -\bar{v}_W c_W G_{WO} - \bar{v}_O c_O G_{OO}. (9.22)$$

Thus, G_{WO} and G_{OO} can be directly calculated from **Eqs. 9.21** and **9.22**, which yields *(89)*

$$G_{WO} = RT\kappa - \frac{\bar{v}_O}{a_{OO}} \quad (9.23)$$

for osmolyte hydration (which also equals solvation of water by osmolyte for symmetry reasons),

$$G_{OO} = RT\kappa - \frac{\bar{v}_O}{a_{OO}} + \frac{1 - a_{OO}}{a_{OO} c_O} \quad (9.24)$$

for osmolyte self-solvation, and

$$G_{WW} = RT\kappa - \frac{1}{c_W} + \frac{\bar{v}_O}{a_{OO}} \cdot \frac{\bar{v}_O c_O}{1 - \bar{v}_O c_O} \quad (9.25)$$

for water self-hydration, where $a_{OO} = (\partial \ln a_O / \partial \ln c_O)$. The peculiar property of most of the organic osmolytes investigated so far is that the difference $G_{WO} - G_{OO}$ is roughly constant *(15, 89)*. This difference is shown in **Fig. 9.3**, where several special cases are pointed out. Most osmolytes (monosaccharides, polyols, and several amino acids) have a roughly constant difference $G_{WO} - G_{OO}$ between 50 mL/mol and 200 mL/mol. These constant values might be considered "effectively occupied volumes" within a partition-function based approach to solution nonideality *(16, 91)*. (**Note 6**) Urea is the most outstanding example for simple solvation behavior shown in **Fig. 9.3**. Its solvation difference $G_{WO} - G_{OO}$ is about constant and about zero. This simplifies **Eq. 9.21** to

$$\left(\frac{\partial \ln a_O}{\partial c_0}\right) \approx \frac{1}{c_O}, \quad (9.26)$$
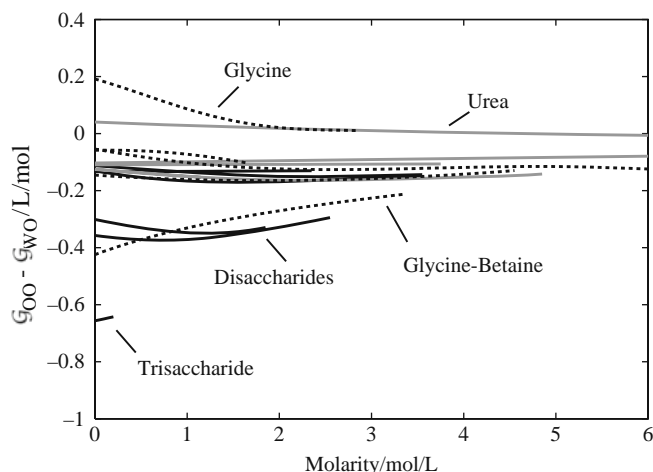
Fig. 9.3. Solvation preference of osmolytes in aqueous osmolyte solution. *Continuous black lines*: saccharides; *continuous gray lines*: polyols and urea; *dashed lines*: amino acids, and derivatives.

which is ideal solution behavior, that is, direct proportionality between osmolyte activity a_O and concentration c_O. The only two osmolytes with distinctly non-constant solvation are glycine and glycine-betaine (trimethyl glycine). The disaccharides sucrose and trehalose, as well as a couple of amino acids, have a nearly constant solvation.

Overall, the generally constant solvation behavior of osmolytes appears to be a characteristic that distinguishes osmolytes from nonosmolytes. Alcohols, for example, display very variable solvation *(92)*. It makes sense that organisms use compounds with predictable and constant solvation (osmolytes) to fine-tune their biochemistry under conditions of stress *(15, 89)*. This allows the cells to "dial in" the desired protecting effect by merely regulating the concentration of a given compound. Using organic compounds that are not employed as osmolytes in nature could wreak havoc on cells, because the solvation character of the compound may change rapidly as its concentration is slightly shifted. This effect might contribute to the toxicity of alcohols.

3.2.3. General Solvation: Proteins

3.2.3.1. Preferential Interaction

Solvation of proteins by a variety of organic and inorganic cosolutes has traditionally been expressed in terms of preferential interaction coefficients. These coefficients are a measure of the deviation of the solution composition around a protein from bulk composition. Even without giving an exhaustive list, numerous examples are available for data obtained by density measurements *(93)*, centrifugation *(94)*, isopiestic distillation *(95)*, and vapor

pressure osmometry (96). There are many different definitions of preferential interaction parameters (see e.g. **Ref. 97**), and it is beyond the scope of this chapter to discuss all of these. However, because preferential interaction and solvation are closely related, we give the simplest example for a direct connection between the overall solvation (Kirkwood–Buff integrals) and one of the preferential interaction parameters (98)

$$\Gamma_{O(P\rightarrow 0)} = -(G_{PW} - G_{PO})c_O = -\left(X_W \frac{c_O}{c_W} - X_O\right), \quad (9.27)$$

matched for protein solvation in dilute protein solution. $X_W = G_{PW}c_W$ is the excess number of water molecules (W) around the protein (P), relative to the bulk density, and $X_O = G_{PO}c_O$ the excess of osmolytes (O).

3.2.3.2. Kirkwood–Buff Equations

Applying **Eq. 9.2** to this example yields a very similar equation (**Note 7**)

$$\left(\frac{\partial \ln a_P}{\partial \ln c_O}\right)_{p,T} = \frac{(G_{PW} - G_{PO})c_O}{1 - (G_{WO} - G_{OO})c_O}, \quad (9.28)$$

which is identical to **Eq. 9.27** if the osmolyte is dilute ($c_O \rightarrow 0$). These two equations (**Eqs. 9.27** and **9.28**) express in a quantitative manner, how the addition of osmolyte affects the chemical activity of dilute aqueous protein. Both G_{PW} and G_{PO} contain the several contributions discussed in **Section 2.1** and **Fig. 9.1**. The first and always present contribution is the exclusion of water and osmolyte due to their inability to overlap with protein atoms. Because **Eq. 9.28** contains Kirkwood–Buff integrals only as differences, much of this excluded volume is subtracted out. Note, however, that in other instances the G_{ij} occur by themselves rather than as a difference. For example, the overall hydration of dilute protein in water G_{PW} equals the negative partial molar volume of the protein. Recent attempts to subtract out the core excluded volume (81, 99) may therefore be ultimately misleading (84). Beyond the hard core excluded volume anything that alters the frequency of occurrence of each solution component is of importance. This includes the solvation peaks due to packing shown in **Fig. 9.1**, repulsions beyond hard-core effects, nonspecific binding, specific binding, etc.

It is especially straightforward to measure the slope given by **Eq. 9.28** if we consider differences between protein states, such as native and denatured. Then **Eq. 9.28** becomes (31)

$$\frac{m}{RT} = \left(\frac{\partial \Delta \ln a_P}{\partial c_O}\right)_{p,T} = \frac{\Delta(G_{PW} - G_{PO})}{1 - (G_{WO} - G_{OO})c_O}, \quad (9.29)$$

where the Δ denotes the difference between the two states, and the m-value is defined as the slope of the Gibbs free energy of the

transition $-RT\partial \ln K/\partial c_O$. It is intriguing that the m-value is normally a constant when urea or other osmolytes without net-charge are used *(20–28)*. Often also other compounds (salts, polymers, etc.) give rise to a constant slope of preferential inter-action parameters *(57)*. This is equivalent to a constant m-value – at least at the submolar concentrations of cosolutes that are often used, because then the denominator in **Eqs. 9.28** and **9.29** is close to unity.

3.2.3.3. Issues in Classically Understanding m-Values

The finding of constant m-values is not expected based on classical thermodynamic considerations *(100)*. The reason why such find-ings are puzzling is that normally the Gibbs free energy depends on the concentration of additives (1) not at all, (2) as a square-root, or (3) logarithmically. Case 2 is taken to be indicative of electrostatics, and case 3 of binding. A linear dependence of the Gibbs free energy on osmolyte concentration does not fit into any of these classical categories. However, it was noted that the che-mical activity of water normally changes logarithmically with a linear variation of the concentration of an additive. Thus, constant m-values, and linear preferential interaction parameters are expected if the Gibbs free energy depends logarithmically on water, suggesting a strong involvement of protein–water interac-tions in the process. For these reasons, such phenomena have been called "water effect" *(57)*.

Such apparently strong involvement of water is to be expected already on the sole basis of a simple fact: the presence of osmolyte at a certain point on the protein surface automatically implies absence of water, and presence of water results in the absence of osmolyte. This simple fact, the "exchange concept" *(4, 101)*, is important to remem-ber. Based on **Eq. 9.27** it is straightforward to see that the participa-tion of water in this solvent exchange $X_W \frac{c_O}{c_W}$ will contribute to the protein energetics only if c_O is sufficiently large. Typical experiments of specific high-affinity ligand binding take place at extremely low concentration of additive c_O, and thus the water contribution is suppressed. In contrast, osmolyte concentrations often go up to the molar region, both in vivo *(2)* and in vitro. Consequently, the hydration has to be considered in a typical osmolyte experiment.

This is not to say that the hydration term that is "dialed in" at elevated osmolyte concentration will always be significant. Rather, its importance will always depend on the specific system. There are cases in which water appears to be solely responsible for the observed effects *(102–105)*, in others hydration changes seem to be insignif-icant *(15, 89, 106)*. We will discuss this further in **Section 3.2.4**.

3.2.3.4. Protein Solvation in Terms of Thermodynamics

There are some general conclusions that can be drawn from the observations that (1) m-values for protein folding are usually constant, and (2) the volume change upon unfolding $\Delta \bar{v}_P$ is

usually very small. These observations can be utilized by way of **Eq. 9.29** and a version of **Eq. 9.8** that is adapted to the situation of the difference of two states.

$$\Delta \bar{v}_P \approx -\bar{v}_W c_W \Delta G_{PW} - \bar{v}_O c_O \Delta G_{PO}, \quad (9.30)$$

where we skipped the protein term $-\bar{v}_P c_P \Delta G_{PP}$, because the protein was assumed to be dilute ($c_P \approx 0$). **Equations 9.29** and **9.30** are two equations with two unknowns, resulting in *(15)*

$$\Delta(G_{PW}) = -\Delta \bar{v}_P + \bar{v}_O c_O \frac{m/RT}{(\partial \ln a_O / \partial \ln c_O)} \quad (9.31)$$

and

$$\Delta(G_{PO}) = -\Delta \bar{v}_P - (1 - \bar{v}_O c_O) \frac{m/RT}{(\partial \ln a_O / \partial \ln c_O)}. \quad (9.32)$$

Employing now the above-mentioned observations leaves for $\Delta(G_{PW})$ and $\Delta(G_{PO})$ only bulk solution properties that are independent of the protein ($\bar{v}_O c_O$ and a_{OO}), and a constant, protein-dependent factor of m. Thus, the first general conclusion is that the shape of the $\Delta(G_{PW})$ and $\Delta(G_{PO})$ curves mostly depend on the bulk properties of the binary osmolyte solution in the absence of protein. These properties are the volume fraction of osmolyte $\bar{v}_O c_O$ and the dependence of the osmolyte chemical activity on its concentration ($\partial \ln a_O / \partial \ln c_O$). These values are known for many osmolytes *(15, 16, 89)*. Actually plotting the protein-independent part of **Eqs. 9.31** and **9.32** results in the second general conclusion *(89)*: The contribution of hydration to the impact of osmolytes on protein folding is small and is very similar for all osmolytes we investigated so far.

Figure 9.4 illustrates these principles for the example of TCAM (reduced and carboxyamidated ribonuclease T1). Panel A shows how the protein solvation by osmolyte changes upon unfolding. (**Note 8**) Urea solvates the denatured state more than the native state ($\Delta(G_{PO}) = G_{PO}^{denatured} - G_{PO}^{native} > 0$), whereas the protecting osmolytes sorbitol and sarcosine do the opposite, as reflected by their opposite sign in **Fig. 9.4**A. Unfolding of TCAM accommodates an increased amount of urea in the protein's vicinity. Specifically, this amount is equivalent to an additional space of two to three liters of bulk urea solution per mole of protein (*see* **Fig. 9.4**A). Multiplying this number by the concentration of urea yields the actual difference in the number of urea molecules around denatured and native TCAM. It is noteworthy that the change in urea number upon unfolding is very small – about 3 urea molecules per protein at 1 M, and 12 urea molecules per protein at 6 M. This is the contribution of the urea to the change in preferential interaction upon unfolding (*see* **Eq. 9.27**). One striking difference between urea and the protecting osmolytes sorbitol and sarcosine is the concentration dependence of solvation. For urea,
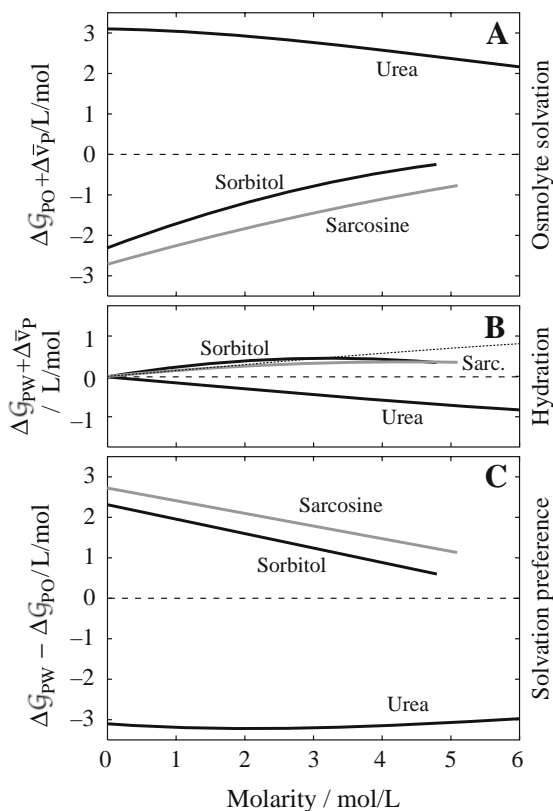
Fig. 9.4. Solvation of TCAM in osmolyte solutions *(89)*. (**A**) Protein osmolation change upon unfolding, offset by the negligibly small $\Delta \bar{v}_P$. (**B**) Protein hydration change upon unfolding, also offset by $\Delta \bar{v}_P$. (**C**) Change in protein solvation preference upon unfolding.

$\Delta(G_{PO})$ changes by less than 30% between 0 M and 5 M, whereas the change is more than threefold for sarcosine and about tenfold for sorbitol. Besides the sign of $\Delta(G_{PO})$, such differences in slope seem to be a characteristic distinction between protecting and nonprotecting osmolytes *(15, 89)*.

Panel B of **Fig. 9.4** shows the change in TCAM hydration upon unfolding $\Delta(G_{PW})$. It is evident that the hydration changes are small compared to the "osmolation" changes. (**Note 9**) Also, the magnitude of $\Delta(G_{PW})$ is very similar for protecting- and nonprotecting osmolytes, though their sign is different. For purposes of comparison the urea $\Delta(G_{PW})$ value is displayed also with inverted sign in Panel B (thin dotted line). We therefore see that hydration changes upon unfolding have surprisingly little sensitivity towards the kind of osmolyte and its concentration.

Panel C shows the difference of the solvation properties displayed in the other two panels. The linearity in the solvation difference for the protecting osmolytes is a direct consequence of the first-order behavior (*see* **Note 6**). This is because the solvation

difference is given by the difference between **Eqs. 9.31** and **9.32**, resulting in $m/RT/(\partial \ln a_O/\partial \ln c_O)$. Inserting the first-order activity (**Eq. 9.36**) leaves the linear equation $m(1 - c/c_1)/RT$. Also the unchanged solvation preference $\Delta(G_{PW} - G_{PO})$ in the presence of urea is a consequence of its nearly ideal behavior (the derivative $(\partial \ln a_O/\partial \ln c_O)$ is about unity).

3.2.4. General Solvation: Ligands

Investigation of ligand-binding reactions adds another level of complexity to the system. Folding involves a minimum of two species, native and denatured. In case of ligand binding there are three species involved in the reaction, bound protein state, unbound protein state, and free ligand. If the ligand is small, the protein naturally draws the researcher's interest most. However, it turns out that solvation effects of small ligands may be larger than the effects of protein solvation *(107)*. Before going into these details we first have a look on the general overall response of ligand-binding equilibria to the presence of cosolutes, including osmolytes.

3.2.4.1. Kirkwood–Buff Equation for m-Values of Ligand Binding

The Gibbs free energy of binding often depends linearly on the concentration of additives. An incomplete list of examples includes the binding of glucose to hexokinase in the presence of PEG *(108)*, protein–DNA interaction in the presence of various additives *(104, 109)*, protein dimerization in the presence of sugars *(79)*, drug binding to protein in the presence of triethylene-glycol *(110)*, binding of FAD to glycogen phosphorylase b in different osmolytes *(111)*, and the binding of cyclodextrin and adamanthane in various salts and osmolytes *(112)*. The widely found linearity suggests that ligand binding in the presence of osmolytes is somehow thermodynamically similar to protein folding, which also displays the same linear change of the Gibbs free energy with osmolyte concentration. Indeed, applying the Kirkwood–Buff apporach (**Eqs. 9.2–9.8**) to the case of dilute ligand binding to dilute protein results in *(31)*

$$-\left(\frac{\partial \ln K}{\partial c_O}\right) = \frac{\Delta(G_{PW} - G_{PO}) - (G_{LW} - G_{LO})}{1 - (G_{WO} - G_{OO})c_O}, \qquad (9.33)$$

a result that is very similar to the one found for folding (**Eq. 9.29**). The hydration G_{LW} and osmolation G_{LO} of the ligand constitutes the only difference between these equations.

Now, we could continue the analogy between folding and binding, and state that hydration is generally expected to contribute very little to the thermodynamics of ligand binding in osmolyte solution. On first sight this seems to contradict many investigations in which release of water was found to be the major event in the binding reaction. For example, the settling of EcoR1 restriction enzyme from a nonspecifically bound state into

its specifically bound state is independent of the type of osmolyte used *(104)*, suggesting that it is the water and not the osmolyte that is the main player in the solvation process. Based on a comparison with crystal structures, it has been proposed that the protein "squeezes water out" that is trapped between the non-specifically bound state and the DNA *(104)*.

3.2.4.2. Mechanistic vs. Thermodynamic Role of Hydration

A short idealized discussion of this situation with EcoR1 will show that there is no contradiction at all between this experimental finding and the theoretical expectations. Given the situation depicted in **Fig. 9.5**, the main event in the transition is the settling of the protein with concomitant water release from the water pocket of volume V_{water}. In terms of the overall hydration G_{PW} we note that the space available to water does not change, that is, $\Delta G_{PW} = 0$. In contrast to that, the settling makes available space to the osmolyte that was not available before, and thus $\Delta G_{PO} = V_{water}$. Consequently, the water does not play any role thermodynamically, while the osmolyte does not contribute directly to the mechanism. To recover the number of water molecules from the thermodynamic data, the change in solvation balance $\Delta(G_{PW} - G_{PO})$ has to be multiplied with the water molarity c_W, which yields back $-V_{water} c_W$ – the number of water molecules in a volume V_{water}. So, the surprising result is that in a situation where mechanistically the water is solely responsible for the observed effect, the changes in solvation and energetics originate exclusively from the osmolyte. Moreover, from the change in protein–osmolyte solvation we can recover the change in the number of displaced water molecules around the protein.

Note, that in general ΔG_{PW} is not zero, even if it is small *(89)*. Therefore, we have to normally expect changes in both osmolyte and water number around protein that contribute to $c_W \Delta(G_{PW} - G_{PO})$. The use of the term "excluding water molecules" (as opposed to just "water molecules") *(57)* is meant to indicate this fact. If, however, the response of the binding reaction is essentially independent of the type of osmolyte, it is likely that
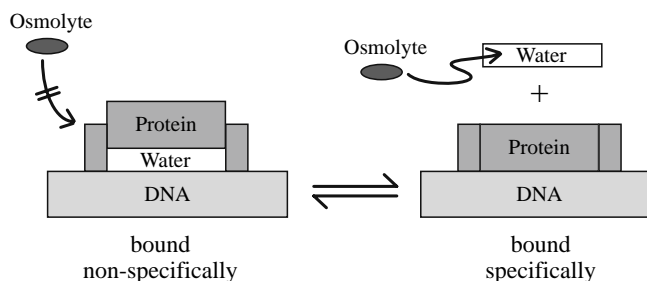
Fig. 9.5. Idealized picture for the transition from nonspecifically DNA-bound EcoR1 to the specifically bound state. Note that the volume available to water does not change. However, the volume available to osmolyte increases upon settling of the protein onto the DNA while going from the nonspecifically bound state to the specifically bound state.

the change in the number of "excluding water molecules" equals the change in the number of "water molecules" *(57)*. This situation is a limiting case of the discussed "water effects" *(113)*.

3.2.4.3. Experimental Example: Non-constant m-Value of Ligand Binding

We pointed out in **Section 3.2.3** that *m*-values are normally constant for protein folding. It is therefore to be expected that the protein part of **Eq. 9.33** should also yield a constant *m*-value. However the ligand solvation ($G_{LW} - G_{LO}$) could make nonlinear contributions to the *m*-value *(107)*. Such nonlinear effect was found for the interaction between ATP and urea *(114)*. In fact, it was even found that protein at mM concentrations can significantly change the chemical activity of a ligand *(115)*.

Figure 9.6 shows a case in which a concentration-dependent *m*-value of CMP binding to RNase A was observed *(107)*. The figure shows the phase separation lines (50% population size) between the three principal species in solution as a function of ligand and urea concentrations. The *m*-value of unfolding is constant, as judged by the linear slope of the phase separation line between native liganded and denatured. However, the phase separation line between the native and native liganded states is curved; that is, the *m*-value of ligand binding is not constant. The dashed lines in **Fig. 9.6** serve as a guide to the eye to demonstrate the change in slope between 0 M and 3 M urea. Remarkably, the initial *m*-value at 0 M urea is an order of magnitude larger than the calculated *m*-value based on the protein surface exposure change upon binding *(107)*. Also, the *m*-value is an order of magnitude
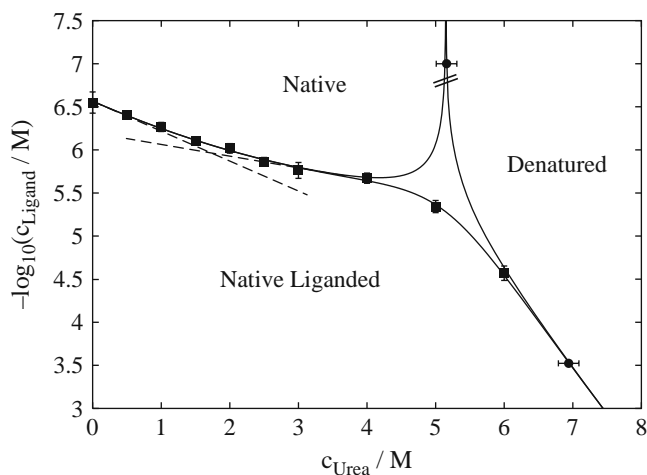
Fig. 9.6. Ligand binding and denaturation of RNase A as a function of urea concentration *(107)*. The continuous lines are phase separation lines (50% population size), the symbols are pK values of CMP dissociation (*squares*) and midpoint concentrations of urea-induced unfolding. Note the change in slope of the ligand-dissociation phase separation line (indicated by the *dashed line*), which corresponds to a strongly urea-concentration-dependent *m*-value.

larger than is calculated from a formula that is based on macromolecular nucleic acid properties *(116)*. In contrast, the change of nucleotide activity coefficient in urea *(115)* is in the right order of magnitude to account for essentially the entire effect.

3.2.4.4. Independence of Protein and Ligand Effects

At low protein and ligand concentration the protein solvation, free ligand solvation, and bulk osmolyte solvation can be analyzed separately, just as demonstrated for the case of protein folding. This is because the *m*-value of binding (*cf*. **Eq. 9.33**) can be split into additive terms

$$\frac{m}{RT} = \frac{\Delta(G_{PW} - G_{PO})}{1 - (G_{WO} - G_{OO})c_O} - \frac{(G_{LW} - G_{LO})}{1 - (G_{WO} - G_{OO})c_O} \quad (9.34)$$

and the denominators solely depend on the bulk osmolyte properties. The indirect impact of osmolytes on the affinity of proteins for ligands, given by the second term on the right-hand side of **Eq. 9.34**, exists independently of the presence of proteins. It is general and affects all protein reactions that use the same kind of ligand in the identical way. Given that the chemical activity of nucleotides can change by more than half an order of magnitude in the presence of renal physiological concentrations of urea, all cellular processes that involve nucleotides will be strongly affected by the high and fluctuating urea concentrations of the kidney. Because essentially all cellular processes depend on nucleotides, this poses a severe challenge. How do renal cells survive such daily, or even hourly, assaults? Further research on the solvation properties of renal osmolytes and their mixtures should provide an answer to this question.

Beyond this most blatant example of the importance of solvation in renal osmoregulation, osmolytes are also used in many other mammalian organs, and in living organisms in general. This makes clear that molecular solvation has to be investigated to understand cellular biochemistry.

4. Notes

1: Often, chemical activities are considered "effective concentrations". This is because of the appealingly simple proportionality between concentration and chemical activities in dilute solution. Although this is a useful working concept, it should be taken with a grain of salt. Chemical activities are the driving force that levels concentration gradients, just as temperature is the driving force that levels heat (internal energy) gradients. Yet, nobody would call internal energy an "effective temperature". So, the reader should be aware that the term "effective concentration" is ultimately a nonscientific expression. Though, it can be

linguistically useful because there is no matching expression for "chemical activity" in common language.

2: The integration over the volume dV corresponds to a weighted integration over the distance given as abscissa in **Fig. 9.1**: $dV = 4\pi r^2 dr$. Therefore, upon integration the smaller solvation peaks (to the right side of each of the pair correlations drawn in **Fig. 9.1**A) are weighted more than the large peaks that occur at contact distance (the first two solvation shells are indicated for the osmolyte–protein correlation). As a consequence, even small and seemingly insignificant solvation features that are beyond the first or second solvation shell can significantly contribute to the overall solvation.

3: The cofactor of a matrix B is defined as $|B|_{ij} = \frac{\partial}{\partial B_{ij}}|B|$. For instance,

$$B = \begin{pmatrix} B_{11} & B_{12} \\ B_{21} & B_{22} \end{pmatrix}, \quad |B|_{12} = \frac{\partial}{\partial B_{12}}|B| = \frac{\partial}{\partial B_{12}}(B_{11}B_{22} - B_{12}B_{21}) = -B_{21}. \quad (9.35)$$

The determinant for this small matrix is given by the difference $|B| = (B_{11}B_{22} - B_{12}B_{21})$, as used in the previous equation.

4: We used **Eq. 9.2** to calculate this result. Note that the derivative is taken at constant volume, because in a single-component solution the conversion to molar concentrations is problematic at constant pressure. This is because the system size is not defined if all variables are either intensive (T and p), or extensive but normalized ($c = N/V$). At constant volume the second term on the right-hand side of **Eq. 9.2** disappears. Application of **Eq. 9.2** is straightforward in a one-component system, because the matrix B contains only one element, namely, $B_{11} = c_1 + c_1^2 G_{11}$. Its determinant equals this element, and the sole cofactor is unity. **Equation 9.14** is then obtained after a simple rearrangement of the result. **Equations 9.15** and **9.16** are similarly simple.

5: For a two-component system the matrix B has four elements. Its determinant is given in **Note 3**, along with an explanation how to calculate its cofactors. **Equation 9.17** is obtained by inserting **Eqs. 9.3** and **9.4** into **Eq. 9.2** and applying the transformation given by **Eq. 9.7**. The calculation is lengthy, unless appropriate software for symbolic calculations is used, such as Mathematica®.

6: We have recently shown that chemical activities of naturally occurring osmolytes follow a remarkably simple first- or second-order behavior; that is, the partition function has a linear or quadratic dependence on their chemical activity *(16, 91)*. In a literal interpretation the fitting parameters could be considered as effective volumes and interaction affinities. However, interpreting the observations in terms of molecular solvation (as done here and elsewhere *(15, 89)*) is the more rigorous approach. This is because a linear or quadratic form of the

partition function could arise from a summation of a large number of terms, rather than only one or two. In that case, the literal interpretation would not be strictly correct.

The first- and second-order equations that properly capture the chemical activities of naturally occurring osmolytes are

$$a_{O,1st} = \frac{c_O}{1 - c_O/c_1} \tag{9.36}$$

and

$$\frac{a_{O,2nd}}{c_O} = \frac{g_{2,c}/2c_O}{2 - c_O/c_2}\left[-1 + c_O/c_1 + \sqrt{(1 - c_O/c_1)^2 + 4c_O(1 - c_O/c_2)^2/g_{2,c}}\right] \tag{9.37}$$

where c_1, c_2, and $g_{2,c}$ are parameters that have been tabulated *(15, 16)*.

7: The calculation in three concentration dimensions requires an additional transform that is not included in **Eq. 9.2**. There are several strategies to do the transform to the molar scale. Application of **Eq. 9.6** does this for one dimension (e.g., the osmolyte concentration). The second transformation can be applied to the next dimension after the same pattern, taking into account the rules of base transforms of partial derivatives (in the "tangential space") given by *(117)*

$$\left(\frac{\partial}{\partial x_i}\right)_{x_{k \neq i}} = \sum_l \left(\frac{\partial y_l}{\partial x_i}\right)_{x_{k \neq i}} \left(\frac{\partial}{\partial y_l}\right)_{y_{m \neq l}}. \tag{9.38}$$

Of course, the whole transform can also be done in one step using this base-transform rule. An alternative strategy was presented by Smith *(19)*.

8: **Figure 9.4**, panels A and B, show $\Delta(G_{PO}) + \Delta\bar{v}_P$ and $\Delta(G_{PW}) + \Delta\bar{v}_P$, rather than $\Delta(G_{PO})$ and $\Delta(G_{PW})$. The difference between the overall solvation including and excluding the volume change upon unfolding $\Delta\bar{v}_P$ is normally negligible, because $\Delta\bar{v}_P$ is usually in the order of less than ±1% of the protein volume *(118)*. In the given example of TCAM this corresponds to 0.1 L/mol at the very most, and thus does not change the figure significantly.

9: Just as hydration (from greek *hudor* – water) is used to mean solvation by water, we may use osmolation as an analog concise expression to refer to solvation by osmolyte.

Acknowledgements

References

1. Ostwald, W. (1893). On chemical energy. *J Am Chem Soc* 15, 421–430.

2. Hochachka, P. W., Somero, G. N. (2002). *Biochemical Adaptation. Mechanism and Process in Physiological Evolution.* Oxford University Press, Oxford.

3. Tanford, C. (1969). Extension of the theory of linked functions to incorporate the effects of protein hydration. *J Mol Biol* 39, 539–44.

4. Schellman, J. A. (1994). The thermodynamics of solvent exchange. *Biopolymers* 34, 1015–26.

5. Ben-Naim, A. (1977). Inversion of Kirkwood–Buff theory of solutions – Application to water–ethanol system. *J Chem Phys* 67, 4884–4890.

6. Ben-Naim, A. (1988). Theory of preferential solvation of nonelectrolytes. *Cell Biophysics* 12, 255–269.

7. Abui, M., Smith, P. E. (2004). A combined simulation and Kirkwood–Buff approach to quantify cosolvent effects on the conformational preferences of peptides in solution. *Journal of Physical Chemistry B* 108, 7382–7388.

8. Shimizu, S. (2004). Estimating hydration changes upon biomolecular reactions from osmotic stress, high pressure, and preferential hydration experiments. *Proc Nat Acad Sci USA* 101, 1195–1199.

9. Shimizu, S., Boon, C. L. (2004). The Kirkwood–Buff theory and the effect of cosolvents on biochemical reactions. *J Chem Phys* 121, 9147–9155.

10. Shimizu, S., Smith, D. J. (2004). Preferential hydration and the exclusion of cosolvents from protein surfaces. *J Chem Phys* 121, 1148–54.

11. Smith, P. E. (2004). Local chemical potential equalization model for cosolvent effects on biomolecular equilibria. *J Phys Chem B* 108, 16271–16278.

12. Smith, P. E. (2004). Cosolvent interactions with biomolecules: Relating computer simulation data to experimental thermodynamic data. *J Phys Chem B* 108, 18716–18724.

13. Kirkwood, J. G., Buff, F. P. (1951). The statistical mechanical theory of solutions. I. *J Chem Phys* 19, 774–777.

14. Hansen, J. P., McDonald, I. R. (1986). *Theory of Simple Liquids.* Academic Press, London.

15. Rösgen, J., Pettitt, B. M., Bolen, D. W. (2005). Protein folding, stability, and solvation structure in osmolyte solutions. *Biophys J* 89, 2988–97.

16. Rösgen, J., Pettitt, B. M., Bolen, D. W. (2004). Uncovering the basis for nonideal behavior of biological molecules. *Biochemistry* 43, 14472–14484.

17. Kokubo, H., Rösgen, J., Bolen, D. W., et al. (2007). Molecular basis of the apparent near ideality of urea solutions. *Biophys J* 93, 3392–3407.

18. Ben-Naim, A. (1992). *Statistical Thermodynamics for Chemists and Biochemists.* Plenum, NewYork.

19. Smith, P. E. (2006). Chemical potential derivatives and preferential interaction parameters in biological systems from Kirkwood–Buff theory. *Biophys J* 91, 849–56.

20. Mello, C. C., Barrick, D. (2003). Measuring the stability of partly folded proteins using TMAO. *Protein Sci* 12, 1522–9.

21. Holthauzen, L. M., Bolen, D. W. (2007). Mixed osmolytes: The degree to which one osmolyte affects the protein stabilizing ability of another. *Protein Sci* 16, 293–8.

22. Ferreon, A. C., Bolen, D. W. (2004). Thermodynamics of denaturant-induced unfolding of a protein that exhibits variable two-state denaturation. *Biochemistry* 43, 13357–69.

23. Timasheff, S. N., Xie, G. (2003). Preferential interactions of urea with lysozyme and their linkage to protein denaturation. *Biophys Chem* 105, 421–48.

24. Courtenay, E. S., Capp, M. W., Saecker, R. M., et al. (2000). Thermodynamic analysis of interactions between denaturants and protein surface exposed on unfolding: interpretation of urea and guanidinium chloride *m*-values and their correlation with changes in accessible surface area (ASA) using preferential interaction coefficients and the local-bulk domain model. *Proteins* Suppl. 4, 72–85.

25. Makhatadze, G. I. (1999). Thermodynamics of protein interactions with urea and guanidinium hydrochloride. *J Phys Chem B* 103, 4781–4785.

26. Santoro, M. M., Bolen, D. W. (1988). Unfolding free energy changes determined

by the linear extrapolation method. 1. Unfolding of phenylmethanesulfonyl alpha-chymotrypsin using different denaturants. *Biochemistry* 27, 8063–8.

27. Greene, R. F., Jr., Pace, C. N. (1974). Urea and guanidine hydrochloride denaturation of ribonuclease, lysozyme, alpha-chymotrypsin, and beta-lactoglobulin. *J Biol Chem* 249, 5388–93.

28. Felitsky, D. J., Record, M. T., Jr. (2004). Application of the local-bulk partitioning and competitive binding models to interpret preferential interactions of glycine betaine and urea with protein surface. *Biochemistry* 43, 9276–88.

29. Ben-Naim, A. (1978). Standard thermodynamics of transfer – Uses and misuses. *J Phys Chem* 82, 792–803.

30. Harries, D., Rösgen, J. (2008). A practical guide on how osmolytes modulate macromolecular properties, in (Correia, J. J., Detrich, H. W., eds.) *Methods in Cell Biology* 84, 679–735. Elsevier, New York.

31. Rösgen, J. (2007). Molecular basis of osmolyte effects on protein and metabolites, in (Häussinger, D., Sies, H., eds.) *Methods in Enzymology: Osmosensing and Osmosignalling*, Vol. 428, pp. 459–486. Academic Press, New York.

32. Ross, P. D., Minton, A. P. (1977). Analysis of non-ideal behavior in concentrated hemoglobin solutions. *J Mol Biol* 112, 437–52.

33. Carnahan, N. F., Starling, K. E. (1969). Equation of state for nonattracting rigid spheres. *J Chem Phys* 51, 635–636.

34. Ross, P. D., Minton, A. P. (1977). Hard quasispherical model for the viscosity of hemoglobin solutions. *Biochem Biophys Res Commun* 76, 971–6.

35. Minton, A. P. (1995). A molecular-model for the dependence of the osmotic-pressure of bovine serum-albumin upon concentration and pH. *Biophys Chem* 57, 65–70.

36. Cheung, J. K., Truskett, T. M. (2005). Coarse-grained strategy for modeling protein stability in concentrated solutions. *Biophys J* 89, 2372–84.

37. Zhou, H. X., Dill, K. A. (2001). Stabilization of proteins in confined spaces. *Biochemistry* 40, 11289–93.

38. Ziv, G., Haran, G., Thirumalai, D. (2005). Ribosome exit tunnel can entropically

stabilize alpha-helices. *Proc Natl Acad Sci USA* 102, 18956–61.

39. Minton, A. P. (1992). Confinement as a determinant of macromolecular structure and reactivity. *Biophys J* 63, 1090–100.

40. Wills, P. R., Georgalis, Y., Dijk, J., et al. (1995). Measurement of thermodynamic nonideality arising from volume-exclusion interactions between proteins and polymers. *Biophys Chem* 57, 37–46.

41. Cheung, M. S., Thirumalai, D. (2006). Nanopore–protein interactions dramatically alter stability and yield of the native state in restricted spaces. *J Mol Biol* 357, 632–43.

42. Minton, A. P. (1995). Confinement as a determinant of macromolecular structure and reactivity. 2. Effects of weakly attractive interactions between confined macrosolutes and confining structures. *Biophys J* 68, 1311–1322.

43. Takagi, F., Koga, N., Takada, S. (2003). How protein thermodynamics and folding mechanisms are altered by the chaperonin cage: molecular simulations. *Proc Natl Acad Sci USA* 100, 11367–72.

44. Cheung, M. S., Klimov, D., Thirumalai, D. (2005). Molecular crowding enhances native state stability and refolding rates of globular proteins. *Proc Natl Acad Sci USA* 102, 4753–8.

45. Eggers, D. K., Valentine, J. S. (2001). Crowding and hydration effects on protein conformation: a study with sol-gel encapsulated proteins. *J Mol Biol* 314, 911–22.

46. Ravindra, R., Zhao, S., Gies, H., et al. (2004). Protein Encapsulation in mesoporous silicate: The effects of confinement on protein stability, hydration, and volumetric properties. *J Am Chem Soc* 126, 12224–12225.

47. Minton, A. P., Wilf, J. (1981). Effect of macromolecular crowding upon the structure and function of an enzyme: glyceraldehyde-3-phosphate dehydrogenase. *Biochemistry* 20, 4821–6.

48. McNulty, B. C., Young, G. B., Pielak, G. J. (2006). Macromolecular crowding in the *Escherichia coli* periplasm maintains alpha-Synuclein disorder. *J Mol Biol* 355, 893–7.

49. Ghaemmaghami, S., Oas, T. G. (2001). Quantitative protein stability measurement in vivo. *Nat Struct Biol* 8, 879–82.

50. Ignatova, Z., Gierasch, L. M. (2004). Monitoring protein stability and aggregation in

vivo by real-time fluorescent labeling. *Proc Natl Acad Sci USA* 101, 523–8.

51. Ignatova, Z., Krishnan, B., Bombardier, J. P., et al. (2007). From the test tube to the cell: Exploring the flooding and aggregation of a beta-clam protein. *Biopolymers* 88, 157–163.

52. Qu, Y., Bolen, D. W. (2002). Efficacy of macromolecular crowding in forcing proteins to fold. *Biophys Chem* 101–102, 155–65.

53. Zhou, H. X. (2004). Protein folding and binding in confined spaces and in crowded solutions. *J Mol Recognit* 17, 368–75.

54. Mezzasalma, T. M., Kranz, J. K., Chan, W., et al. (2007). Enhancing recombinant protein quality and yield by protein stability profiling. *J Biomol Screen* 12, 418–428.

55. Kueltzo, L. A., Ersoy, B., Ralston, J. P., et al. (2003). Derivative absorbance spectroscopy and protein phase diagrams as tools for comprehensive protein characterization: a bGCSF case study. *J Pharm Sci* 92, 1805–20.

56. Tsai, P. K., Volkin, D. B., Dabora, J. M., et al. (1993). Formulation design of acidic fibroblast growth factor. *Pharm Res* 10, 649–59.

57. Parsegian, V. A. (2002). Protein–water interactions. *Int Rev Cytol* 215, 1–31.

58. Parsegian, V. A., Rand, R. P., Fuller, N. L., et al. (1986). Osmotic stress for the direct measurement of intermolecular forces. *Methods Enzymol* 127, 400–16.

59. Leikin, S., Parsegian, V. A., Rau, D. C., et al. (1993). Hydration forces. *Ann Rev Phys Chem* 44, 369–395.

60. Rand, R. P., Parsegian, V. A. (1992). The forces between interacting bilayer membranes and the hydration of phospholipid assemblies, in (Yeagle, P. ed.) *The Structure of Biological Membranes*, pp. 251–306. CRC Press, Boca Raton.

61. Rand, R. P., Fuller, N. L., Gruner, S. M., et al. (1990). Membrane curvature, lipid segregation, and structural transitions for phospholipids under dual-solvent stress. *Biochemistry* 29, 76–87.

62. Petrache, H. I., Tristram-Nagle, S., Harries, D., et al. (2006). Swelling of phospholipids by monovalent salt. *J Lipid Res* 47, 302–9.

63. Rostovtseva, T. K., Nestorovich, E. M., Bezrukov, S. M. (2002). Partitioning of differently sized poly(ethylene glycol)s into OmpF porin. *Biophys J* 82, 160–169.

64. Vodyanoy, I., Bezrukov, S. M., Parsegian, V. A. (1993). Probing alamethicin channels with water-soluble polymers. Size-modulated osmotic action. *Biophys J* 65, 2097–105.

65. Timasheff, S. N. (1992). Solvent effects on protein stability. *Curr Opin Struct Biol* 2, 34–39.

66. Selenko, P., Serber, Z., Gadea, B., et al. (2006). Quantitative NMR analysis of the protein G B1 domain in *Xenopus laevis* egg extracts and intact oocytes. *Proc Natl Acad Sci USA* 103, 11904–9.

67. Weerasinghe, S., Smith, P. E. (2003). Kirkwood–Buff derived force field for mixtures of acetone and water. *J Chem Phys* 118, 10663–10670.

68. Weerasinghe, S., Smith, P. E. (2003). A Kirkwood–Buff derived force field for mixtures of urea and water. *J Phys Chem B* 107, 3891–3898.

69. Weerasinghe, S., Smith, P. E. (2004). A Kirkwood–Buff derived force field for the simulation of aqueous guanidinium chloride solutions. *J Chem Phys* 121, 2180–6.

70. Kang, M., Smith, P. E. (2006). A Kirkwood–Buff derived force field for amides. *J Comput Chem* 27, 1477–1485.

71. Kokubo, H., Pettitt, B. M. (2007). Preferential solvation in urea solutions at different concentrations: properties from simulation studies. *J Phys Chem B* 111, 5233–42.

72. Winzor, D. J., Wills, P. R. (1995). Thermodynamic nonideality of enzyme solutions supplemented with inert solutes – Yeast hexokinase revisited. *Biophys Chem* 57, 103–110.

73. Jacobsen, M. P., Wills, P. R., Winzor, D. J. (1996). Thermodynamic analysis of the effects of small inert cosolutes in the ultracentrifugation of noninteracting proteins. *Biochemistry* 35, 13173–9.

74. Poon, J., Bailey, M., Winzor, D. J., et al. (1997). Effects of molecular crowding on the interaction between DNA and the *Escherichia coli* regulatory protein TyrR. *Biophys J* 73, 3257–64.

75. Lonhienne, T. G., Winzor, D. J. (2001). Interpretation of the reversible inhibition of adenosine deaminase by small cosolutes in terms of molecular crowding. *Biochemistry* 40, 9618–22.

76. Schachman, H. K., Luffer, M. A. (1949). The hydration, size and shape of tobacco mosaic virus. *J Am Chem Soc* 71, 536–541.

77. Morar, A. S., Wang, X., Pielak, G. J. (2001). Effects of crowding by mono-, di-, and tetrasaccharides on cytochrome c-cytochrome c peroxidase binding: comparing experiment to theory. *Biochemistry* 40, 281–5.

78. Weatherly, G. T., Pielak, G. J. (2001). Second virial coefficients as a measure of protein–osmolyte interactions. *Protein Sci* 10, 12–6.

79. Patel, C. N., Noble, S. M., Weatherly, G. T., et al. (2002). Effects of molecular crowding by saccharides on alpha-chymotrypsin dimerization. *Protein Sci* 11, 997–1003.

80. Arakawa, T., Timasheff, S. N. (1982). Stabilization of protein structure by sugars. *Biochemistry* 21, 6536–6544.

81. Matteoli, E. (1997). A study on Kirkwood–Buff integrals and preferential solvation in mixtures with small deviations from ideality and/or with size mismatch of components. Importance of a proper reference system. *J Phys Chem B* 101, 9800–9810.

82. Shulgin, I. L., Ruckenstein, E. (2006). The Kirkwood–Buff theory of solutions and the local composition of liquid mixtures. *J Phys Chem B* 110, 12707–13.

83. Schellman, J. A. (2003). Protein stability in mixed solvents: a balance of contact interaction and excluded volume. *Biophys J* 85, 108–25.

84. Ben-Naim, A. (2007). A critique of some recent suggestions to correct the Kirkwood–Buff integrals. *J Phys Chem B* 111, 2896–2902.

85. Timasheff, S. N. (1992). Water as ligand – Preferential binding and exclusion of denaturants in protein unfolding. *Biochemistry* 31, 9857–9864.

86. Auton, M., Bolen, D. W. (2005). Predicting the energetics of osmolyte-induced protein folding/unfolding. *Proc Natl Acad Sci USA* 102, 15065–15068.

87. Nozaki, Y., Tanford, C. (1963). The solubility of amino acids and related compounds in aqueous urea solutions. *J Biol Chem* 238, 4074–4081.

88. Reisler, E., Haik, Y., Eisenberg, H. (1977). Bovine serum albumin and aqueous guanidine hydrochloride solutions. Preferential and absolute interactions and comparison with other systems. *Biochemistry* 16, 197–203.

89. Rösgen, J., Pettitt, B. M., Bolen, D. W. (2007). An analysis of the molecular origin of osmolyte-dependent protein stability. *Protein Sci* 16, 733–743.

90. Lide, D. R. (2004). *CRC Handbook of Chemistry and Physics*. CRC Press, Boca Raton, FL.

91. Rösgen, J., Pettitt, B. M., Perkyns, J., et al. (2004). Statistical thermodynamic approach to the chemical activities in two-component solutions. *J Phys Chem B* 108, 2048–2055.

92. Matteoli, E., Lepori, L. (1984). Solute–solute interactions in water. 2. An analysis through the Kirkwood–Buff integrals for 14 organic solutes. *J Chem Phys* 80, 2856–2863.

93. Timasheff, S. N. (1998). Control of protein stability and reactions by weakly interacting cosolvents: the simplicity of the complicated. *Adv Protein Chem* 51, 355–432.

94. Ebel, C., Eisenberg, H., Ghirlando, R. (2000). Probing protein–sugar interactions. *Biophys J* 78, 385–93.

95. Hade, E. P. K., Tanford, C. (1967). Isopiestic compositions as a measure of preferential interactions of macromolecules in two-component solvents. Application to proteins in concentrated aqueous cesium chloride and guanidine hydrochloride. *J Am Chem Soc* 89, 5034–5040.

96. Zhang, W., Capp, M. W., Bond, J. P., et al. (1996). Thermodynamic characterization of interactions of native bovine serum albumin with highly excluded (glycine betaine) and moderately accumulated (urea) solutes by a novel application of vapor pressure osmometry. *Biochemistry* 35, 10506–16.

97. Anderson, C. F., Courtenay, E. S., Record, M. T. (2002). Thermodynamic expressions relating different types of preferential interaction coefficients in solutions containing two solute components. *J Phys Chem B* 106, 418–433.

98. Schurr, J. M., Rangel, D. P., Aragon, S. R. (2005). A contribution to the theory of preferential interaction coefficients. *Biophys J* 89, 2258–76.

99. Shulgin, I. L., Ruckenstein, E. (2005). A protein molecule in an aqueous mixed solvent: fluctuation theory outlook. *J Chem Phys* 123, 054909.

100. Tanford, C. (1968). Protein denaturation. *Adv Protein Chem* 23, 121–282.

101. Timasheff, S. N. (2002). Thermodynamic binding and site occupancy in the light of the Schellman exchange concept. *Biophys Chem* 101, 99–111.

102. Sidorova, N. Y., Rau, D. C. (1996). Differences in water release for the binding of EcoRI to specific and nonspecific DNA sequences. *Proc Natl Acad Sci USA* 93, 12272–7.

103. Parsegian, V. A., Rand, R. P., Rau, D. C. (2000). Osmotic stress, crowding, preferential hydration, and binding: A comparison of perspectives. *Proc Natl Acad Sci USA* 97, 3987–92.

104. Sidorova, N. Y., Rau, D. C. (2004). Differences between EcoRI nonspecific and "star" sequence complexes revealed by osmotic stress. *Biophys J* 87, 2564–76.

105. Rau, D. C. (2006). Sequestered water and binding energy are coupled in complexes of lambda Cro repressor with non-consensus binding sequences. *J Mol Biol* 361, 352–61.

106. Shimizu, S. (2004). Estimation of excess solvation numbers of water and cosolvents from preferential interaction and volumetric experiments. *J Chem Phys* 120, 4989–4990.

107. Ferreon, A. C., Ferreon, J. C., Bolen, D. W., et al. (2007). Protein phase diagrams II: Nonideal behavior of biochemical reactions in the presence of osmolytes. *Biophys J* 92, 245–56.

108. Rand, R. P., Fuller, N. L., Butko, P., et al. (1993). Measured change in protein solvation with substrate binding and turnover. *Biochemistry* 32, 5925–9.

109. Vossen, K. M., Wolz, R., Daugherty, M. A., et al. (1997). Role of macromolecular hydration in the binding of the *Escherichia coli* cyclic AMP receptor to DNA. *Biochemistry* 36, 11640–7.

110. Kiser, J. R., Monk, R. W., Smalls, R. L., et al. (2005). Hydration changes in the association of Hoechst 33258 with DNA. *Biochemistry* 44, 16988–97.

111. Chebotareva, N. A., Kurganov, B. I., Harding, S. E., et al. (2005). Effect of osmolytes on the interaction of flavin adenine dinucleotide with muscle glycogen phosphorylase b. *Biophys Chem* 113, 61–6.

112. Harries, D., Rau, D. C., Parsegian, V. A. (2005). Solutes probe hydration in specific association of cyclodextrin and adamantane. *J Am Chem Soc* 127, 2184–2190.

113. Timasheff, S. N. (1998). In disperse solution, "osmotic stress" is a restricted case of preferential interactions. *Proc Nat Acad Sci USA* 95, 7363–7367.

114. Sinha, R, Kundu, K. K. (1998). Transfer Gibbs energies of ATP in aqueous mixtures of non-ionic glycerol and urea and ionic $NaNO_3$. *Indian J Chem Sect A* 37, 789–794.

115. Shearwin, K. E., Winzor, D. J. (1990). Allowance for thermodynamic nonideality and Donnan effects in binding studies. Activity coefficients of charged ligands in the presence of albumin. *Biophys Chem* 36, 235–43.

116. Hong, J., Capp, M. W., Anderson, C. F., et al. (2004). Preferential interactions of glycine betaine and of urea with DNA: Implications for DNA hydration and for effects of these solutes on DNA stability. *Biochemistry* 43, 14744–58.

117. Warner, F. W. (1983). *Foundations of Differentiable Manifolds and Lie Groups.* Springer, New York.

118. Chalikian, T. V. (2003). Volumetric properties of proteins. *Annu Rev Biophys Biomol Struct* 32, 207–235.

119. Durchschlag, H. (1986). Specific volumes of biological macromolecules and some other molecules of biological interest, in (Hinz, H.-J., ed.)*Thermodynamic Data for Biochemistry and Biotechnology*, pp. 45–128. Springer, Berlin.

Chapter 10

Defining the Role of Salt Bridges in Protein Stability

Ilian Jelesarov and Andrey Karshikoff

Abstract

Although the energetic balance of forces stabilizing proteins has been established qualitatively over the last decades, quantification of the energetic contribution of particular interactions still poses serious problems. The reasons are the strong cooperativity and the interdependence of noncovalent interactions. Salt bridges are a typical example. One expects that ionizable side chains frequently form ion pairs in innumerable crystal structures. Since electrostatic attraction between opposite charges is strong *per se*, salt bridges can intuitively be regarded as an important factor stabilizing the native structure. Is that really so? In this chapter we critically reassess the available methods to delineate the role of electrostatic interactions and salt bridges to protein stability, and discuss the progress and the obstacles in this endeavor. The basic problem is that formation of salt bridges depends on the ionization properties of the participating groups, which is significantly influenced by the protein environment. Furthermore, salt bridges experience thermal fluctuations, continuously break and re-form, and their lifespan in solution is governed by the flexibility of the protein. Finally, electrostatic interactions are long-range and might be significant in the unfolded state, thus seriously influencing the energetic profile. Elimination of salt bridges by protonation/deprotonation at extreme pH or by mutation provides only rough energetic estimates, since there is no way to account for the nonadditive response of the protein moiety. From what we know so far, the strength of electrostatic interactions is strongly context-dependent, yet it is unlikely that salt bridges are dominant factors governing protein stability. Nevertheless, proteins from thermophiles and hyperthermophiles exhibit more, and frequently networked, salt bridges than proteins from the mesophilic counterparts. Increasing the thermal (not the thermodynamic) stability of proteins by optimization of charge–charge interactions is a good example for an evolutionary solution utilizing physical factors.

Key words: Electrostatic interactions, salt bridge, protein stability, thermal stability, denatured state, pK, protein unfolding.

1. Introduction

The stability and functionality of proteins is the result of the delicate balance between different types of noncovalent interactions and thermodynamic forces. Among them, electrostatic

interactions were the first to be considered as a factor responsible for stabilizing the folded protein. Already in the first decades of the twentieth century it was recognized that proteins exhibit properties reminiscent of the properties of water-soluble, charged colloid particles with a compact structure. Protein stabilization by electrostatic interactions became the dominating concept after the work of Linderstrøm-Lang *(1)*, who in 1924 published his seminal theory providing for the first time quantitative explanation/description of proton titration curves and pH-induced denaturation. The ideas of Linderstrøm-Lang are the basis of the present understanding of electrostatic interactions, although they were introduced even before all amino acid types constituting proteins were known. In the following decades, in parallel with the rapidly accumulating information on the spatial structure of proteins, the importance of hydrogen bonds in stabilizing regular secondary structure elements and tertiary folds was identified *(2, 3)*. In his famous review published in 1959 Kauzmann emphasized the fact that about half of the amino acids found in proteins have hydrophobic, nonpolar side chains, and argued that the hydrophobic effect is the major factor stabilizing proteins *(4)*.

Although more than 40,000 protein structures are deposited in the Protein Data Bank at present, and this number grows exponentially, a wide spectrum of questions related to the stability and the functionality of proteins awaits answers. The quantitative assessment of the contribution of weak noncovalent bonds to protein folding and stability is a major goal of modern protein science; yet, in many cases the interpretation of available data is controversial *(5)*. In this chapter we present approaches aiming at estimation of the contribution of electrostatic interactions, particularly of salt bridges, to the unfolding free energy, and discuss the present-day views about their role in protein stability and function. The very nature of charge–charge interactions poses difficulties in quantitative description and defining their importance. In contrast to the other types of noncovalent interactions they are short-range and long-range and depend on ionization equilibria, which in turn are governed by electrostatic interactions themselves. The correct understanding of the interplay of electrostatic interactions with all other noncovalent interactions is of prime importance in developing robust strategies for rational design of proteins with desired properties for medical and biotechnological applications. The material presented is largely focused on theoretical approaches. Computational studies of electrostatic interactions enjoy growing popularity since they provide the unique opportunity to analyze pairwise interactions in atomistic detail and to delineate discrete energy terms, information which is not available from "wet" experiments.

2. Definitions, Concepts, and Formalism

2.1. Electrostatic Interactions and Salt Bridges

In protein science, the term "electrostatic interactions" is used as a generic term in referring to interactions between charged groups, whose ionization state depends on pH and on the specific environment, including the interactions with the partial charges of polar but nonionizable groups (dipoles). When protonated, the imidazole group (histidine), amino groups (ε-amino group of lysine and the N-terminal amino group), and the guanidinium group (arginine) are positively charged. Carboxyl groups (aspartic acid, glutamic acid, the C-terminal carboxylate), the thiol group (cysteine), and the hydroxyl group of the phenol ring (tyrosine) are negatively charged in their deprotonated forms. Usually, charged groups tend to be accessible to the solvent. In many cases, oppositely charged groups are close to each other, thus forming ionic pairs or salt bridges. A salt bridge is defined as a hydrogen-bonded pair of charges of opposite sign. Obviously, the formation of a salt bridge depends on the protonation state of the partners and hence on pH. It should be noted that charge–charge attraction or repulsion could be significant even if the geometrical centers of the functional groups are separated by distances larger than 4 Å, the distance usually used to identify a salt bridge. Long-range electrostatic effects are important not only for the stability of proteins but also for their functionality (ligand binding, substrate tunneling, catalysis, etc).

2.2. Folding/Unfolding Equilibrium and Electrostatic Interactions

The stability of a protein molecule at given conditions is defined by the difference in the free energies between its unfolded (denatured) and folded (native) states. The same is valid for the electrostatic term of the free energy:

$$\Delta G^{\text{el}} = \Delta G^{\text{U,el}} - \Delta G^{\text{F,el}}, \qquad (10.1)$$

$\Delta G^{\text{U,el}}$ and $\Delta G^{\text{F,el}}$ are the electrostatic free energies corresponding to the unfolded and folded state of the protein, respectively. It is commonly accepted that ΔG^{el} originates mainly from the changes in interactions that the ionizable groups are involved in. Perhaps the most prominent manifestation of the influence of electrostatic interactions (and salt bridges in particular) in protein stability is the phenomenon of pH-induced denaturation (see **Section 4**). Assuming that only the electrostatic interactions are changed by pH variation, **Eq. 10.1** can be written as

$$\Delta G^{\text{el}}(\text{pH}) = 2.3RT \int\limits_{\text{pH}_0}^{\text{pH}} \left(\nu^{\text{U}}(\text{pH}) - \nu^{\text{F}}(\text{pH}) \right) d\text{pH}, \qquad (10.2)$$

where

$$\nu^{\mathrm{U,F}}(\mathrm{pH}) = \sum_{i=1}^{N} \theta_i^{\mathrm{U,F}}(\mathrm{pH}), \qquad (10.3)$$

is the average number of protons bound to the protein in the unfolded (U) and in the folded (F) state, respectively, whilst θ_i is the degree of protonation of titratable site i, often referred to as "titration curve" of this site. The total number of titratable (ionizable) sites is N. **Equation 10.2** can be obtained in terms of protonation/deprotonation equilibria *(6)* or from a statistical mechanics treatment *(7)*. The bottom line is that the quantitative evaluation of the role of electrostatic interactions in the stabilization of the native protein structure requires knowledge, experimentally obtained or theoretically predicted, of the ionization equilibria in both the unfolded and the folded state. The experimental approaches to the problem are discussed in **Section 4**.

2.3. Ionization Equilibria

The ionization behavior of each titratable site is described by the proton dissociation constant, often designated as K_a, which is linked to the free energy according to $\Delta G_a = -2.3RT \log K_a = 2.3RT\mathrm{p}K_a$. ΔG_a can be dramatically influenced by the rest of the protein moiety. (Henceforth, we omit the subscripts "a" for clarity of notation). In other words, individual, chemically identical titratable sites experience the influence of different environments and could have very different ionization properties. The most relevant factors regulating the ionization equilibria are listed in **Table 10.1**. For the moment we consider a fixed spatial organization of titratable sites (single conformer). The very important influence of the conformational flexibility (factor 4 in **Table 10.1**) will be discussed in **Section 3.1.2**. The influence of the desolvation (factor 1 in **Table 10.1**) on the ionization equilibrium constant of a given site can be evaluated by the thermodynamic cycle illustrated in **Fig. 10.1**. The term $\Delta G_{p\to d}^{\mathrm{S}} = 2.3RT(\mathrm{p}K_{\mathrm{mod}} - \mathrm{pH})$ is the energy of deprotonation of the considered group when the influence of the protein moiety is completely ignored, that is, the group is considered as model compound dissolved in water. Obviously, $\Delta G_{p\to d}^{\mathrm{S}}$ can be obtained just by knowing the deprotonation constants of the relevant model compounds (K_{mod}), for instance acetyl-X-amide, where X stands for different titratable groups (**Table 10.2**). According to the cycle, the quantity of interest, the free energy of deprotonation, $\Delta G_{p\to d}^{\mathrm{P}}$, of a given site in the protein is related to the deprotonation energy of the model compound $\Delta G_{p\to d}^{\mathrm{S}}$ by

$$\Delta G_{p\to d}^{\mathrm{P}} = \Delta G_{p\to d}^{\mathrm{S}} + \Delta G_{d}^{\mathrm{S\to P}} - \Delta G_{p}^{\mathrm{S\to P}}$$

$$= 2.3RT(\mathrm{p}K_{\mathrm{mod}} - \mathrm{pH}) + \Delta G_{\mathrm{sol}}. \qquad (10.4)$$

Table 10.1
Major factors determining the ionization equilibria of titratable groups in proteins

	Factor	Comments
1	*Desolvation penalty (ΔG_{sol})*	This is the energy of transfer of a titratable group or a model compound from solvent to its fixed location in the protein molecule.
2	*Electrostatic interaction of the titratable groups with the permanent protein charges (charge–dipole interactions; ΔG_{pc}).*	For instance, these are the interactions of a given titratable group with the charge dipoles of the polypeptide backbone.
3	*Electrostatic interaction between titratable groups (charge–charge interactions; ΔG_{tc}))*	These interactions determine the cooperative character of the ionization equilibria in proteins.
4	*Conformational flexibility*	Native proteins can adopt different conformations at different conditions. For instance, conformational changes may occur upon the ionization of a given titratable group. Also, at certain conditions more than one conformation of the protein molecule can be in equilibrium. This factor essentially influences factors 1–3.
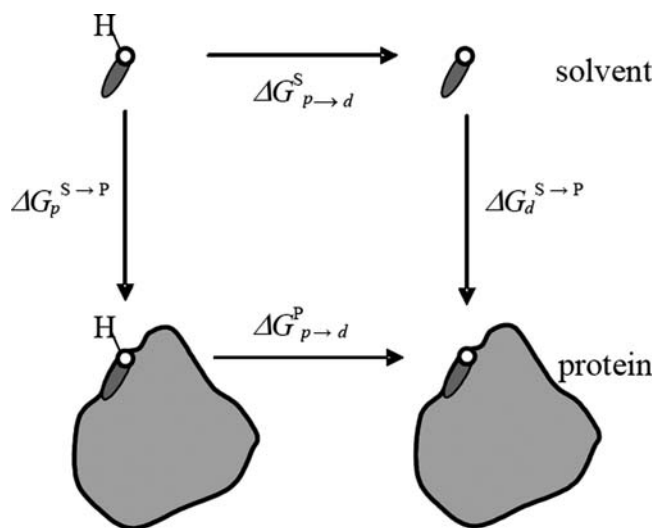
Fig. 10.1. Thermodynamic cycle for the calculation of the pK values of the titratable sites in proteins. The upper and lower horizontal branches represent the deprotonation of the considered titratable group free in solution or in its fixed location in the protein, respectively. The left and right vertical branches describe the change in solvation which the protonated and deprotonated forms experience upon transfer from the bulk solution (model compound, fully solvent-accessible) to the protein (residue, partially or completely solvent-inaccessible), respectively. The free energy changes associated with each process are indicated.

Table 10.2
Standard pK values of model compounds, pK$_{mod}$, representing the commonly ionizable sites in proteins. Source references are given in parentheses after the pK values

Titratable group	pK$_{mod}$		
C-terminus	3.8 *(8)*,	3.6 *(9)*,	3.63 *(10)*
Asp	4.0 *(8, 9)*		
Glu	4.4 *(8)*,	4.5 *(9)*	
His	6.3 *(8)*,	6.4 *(9)*	
His, deprotonation of N$_{\delta 1}$ (N$_{\varepsilon 2}$ - methylated)	6.6 *(11)*,		
His, deprotonation of N$_{\varepsilon 2}$ (N$_{\delta 1}$ - methylated)	7.0 *(11)*		
N-terminus	7.5 *(8)*,	8.0 *(9)*	
Cys	9.5 *(8)*,	9.0 *(9)*,	8.3 *(12,13)*
Tyr	9.6 *(8)*,	10.0 *(9)*	
Lys	10.4 *(8, 9)*		
His (2-nd deprotonation)	10.8 *(9)*		
Arg	12.0 *(8, 9)*		

The difference $\Delta G_{\text{sol}} = \Delta G_d^{\text{S}\rightarrow\text{P}} - \Delta G_p^{\text{S}\rightarrow\text{P}}$ is the desolvation energy (factor 1 in **Table 10.1**), which represents the difference of $\Delta G_d^{\text{S}\rightarrow\text{P}}$ and $\Delta G_p^{\text{S}\rightarrow\text{P}}$, the free energies of transfer of the titratable site (as a model compound) from the solution to its location in the protein in the deprotonated state and in the protonated state, respectively. As defined here, ΔG_{sol} is related to the process of deprotonation of a given group, rather than to its ionization. For groups which become ionized upon protonation the desolvation energy has the opposite sign.

Among alternatives, $\Delta G_{p\rightarrow d}^{\text{P}}$ according to **Eq. 10.4** is most frequently evaluated computationally using continuum electrostatics models. In these models the protein molecule is presented as a material with low dielectric constant immersed in the high dielectric medium of the solvent. For this system the Poisson–Boltzmann equation is solved *(14, 15)*. The following assumptions are implicit in the continuum electrostatics calculations. (1) The protein is represented by a single conformer. Any conformational changes that may occur upon ionization are neglected.

(2) $\Delta G_{\mathrm{sol}} = \Delta G_d^{\mathrm{S \to P}} - \Delta G_p^{\mathrm{S \to P}}$ is electrostatic in nature, which simplifies the model and is reasonable in the context of (1). (3) The interaction between any pair of charges does not depend on the presence of other charges. In such a way, the different contributions to the electrostatic energy can be considered separately. In other words, the total electrostatic energy is assumed to be an additive sum of independent energy terms that correspond to different sources of the electrostatic field.

With the above assumptions, the energy of deprotonation of a given site, i, can be presented as a sum of the different electrostatic contributions corresponding to factors 1–3 listed in **Table 10.1**:

$$\Delta G_{p \to d, i}^{P} = 2.3RT(\mathrm{p}K_{\mathrm{mod},i} - \mathrm{pH})$$
$$+ \Delta G_{\mathrm{sol},i} + \Delta G_{\mathrm{pc},i} + \Delta G_{\mathrm{tc},i} \tag{10.5}$$

The term $\Delta G_{\mathrm{pc},i}$ is the change of the electrostatic energy of interaction between the charges of site i and the protein permanent, pH-independent charges (dipoles) upon deprotonation of this site (factor 2 in **Table 10.1**). Metal ions coordinated by the protein structure are also considered permanent if their valence is not changed in parallel with the change of the protonation state of the protein.

The last term in **Eq. 10.5**, $\Delta G_{\mathrm{tc},i}$, accounts for the charge–charge interactions of the ith site with the rest of the titratable sites (factor 3 in **Table 10.1**). This energy obviously depends on the protonation state of all titratable sites. At different pH values, the titratable sites will be in different protonation states, depending on their chemical nature and environment, that is, the protein will be characterized by different charge constellations. If the charge constellation corresponding to an arbitrary pH is known, the task of calculating titration curves of the individual sites, θ_i (pH), and hence of $\nu^{\mathrm{F}}(\mathrm{pH})$, is solved (see **Eq. 10.3**). The solution of this problem is provided by statistical mechanics formulations, first introduced for pK calculations by Bashford and Karplus (16). A single protonation state of a protein molecule with N ionizable sites is completely described by an N-component vector, $\mathbf{x} = (x_1, x_2, \ldots x_i, \ldots x_N)$, whose ith component, x_i, has value of 0 or 1 depending on whether the ith group is protonated or deprotonated. Thus, at given state $\mathbf{x}$ of the protein and pH, the energy of the protein-solvent system can be expressed as

$$\Delta G(\mathbf{x}, \mathrm{pH})2 = 2.3RT \sum_i x_i(\mathrm{p}K_{\mathrm{int},i} - \mathrm{pH})2$$
$$+ \frac{1}{2} \sum_i \sum_{j \neq i} W_{ix_i, jx_j}. \tag{10.6}$$

Indices i and j enumerate all titratable sites, and W_{ix_i, jx_j} is the charge–charge interaction energy between site i in microscopic

state x_i and site j in microscopic state x_j. The average value of any variable x_i coincides with the degree of deprotonation and is given by the Boltzmann statistical sum:

$$\alpha_i(\mathrm{pH}) = \langle x_i \rangle = \frac{\sum\limits_{\{\mathbf{x}\}} x_i e^{-\Delta G(\mathbf{x},\mathrm{pH})/RT}}{\sum\limits_{\{\mathbf{x}\}} e^{-\Delta G(\mathbf{x},\mathrm{pH})/RT}}. \qquad (10.7)$$

The summations in the above equation are over all 2^N possible protonation states $\{\mathbf{x}\}$. The calculation of $\alpha_i(\mathrm{pH})$ is, in fact, equivalent to calculating $\theta_i(\mathrm{pH}) = 1 - \alpha_i(\mathrm{pH})$, which can be used in **Eq. 10.3** for calculation of the protein titration curve. It should be noted that **Eq. 10.7** is adequate only within the limits of the implicit assumptions of the continuum model, as discussed above. In principle, **Eq. 10.7** can be extended to a more general case by including other features and properties that can influence the ionization equilibria, for example for redox sites or ligand binding *(17)*. Without violation of the main assumptions stated above, another extension has been proposed *(18, 19)* accounting for alternative proton binding on the titratable groups and for alternative orientation of the polar hydrogens of the nontitratable groups, that is, for tautomers and rotamers. Although these extensions improve the description of the ionization behavior of the protein molecule, they remain within the limits of a single conformer representation.

3. Electrostatic Properties of Proteins

Proteins exist as a mixture of states separated by free energy barriers. In the simplest case described here, only the native (folded) and the denatured (unfolded) states are thermodynamically relevant. The energetic difference between these states arises from differences in the balance of noncovalent interactions, interactions with the solvent, and entropic factors. We consider separately the electrostatic properties of folded and unfolded proteins for clarity, bearing in mind that both states are equally important in describing protein energetics.

3.1. Ionization Equilibria in Folded Proteins

As already pointed out, the steric and chemical properties of the surroundings of titratable groups could profoundly change their ionization properties. This is very important in the context of folded proteins, since the position of charges is fixed by the global fold and re-adjustment of charge–charge distances is limited by

rotation around side chain bonds. In this section we discuss the influence of the factors listed in **Table 10.1** on the ionization behavior.

3.1.1. Solvent Accessibility and Charge–Dipole Interactions

Since $\Delta G_{\mathrm{pc},i}$ and $\Delta G_{\mathrm{sol},i}$ of **Eq. 10.5** depend only on the protein structure (i.e., on how the particular group is situated in the protein) but not on the charge–charge interactions with other titratable sites, it is convenient to introduce the quantity intrinsic pK for the individual sites:

$$pK_{\mathrm{int},i} = pK_{\mathrm{mod},i} + (2.3RT)^{-1}(\Delta G_{\mathrm{sol},i} + \Delta G_{\mathrm{pc},i}). \qquad (10.8)$$

Similarly to $pK_{i,\,\mathrm{mod}}$, $pK_{\mathrm{int},i}$ is pH independent. Knowledge of the intrinsic pK is useful in different aspects. One of them is that it already provides information about the role of the individual components of electrostatic interactions in the stabilization of the native protein structure. The most significant influence has the term $\Delta G_{\mathrm{sol},i}$. The effect of burial of the titratable sites is manifested by stabilization of their neutral form (increasing pK of acidic groups and decreasing pK of basic groups). Due to the desolvation energy, a group completely buried in the protein interior may shift its pK value by up to 25 pH units *(21)*. Taking into account that $\Delta G_{\mathrm{sol},i}$ is unfavorable if the deprotonation is related to charging of site i, it becomes clear that the desolvation penalizes charge burial. Buried titratable groups are usually surrounded by polar environment, so that the term $\Delta G_{\mathrm{pc},i}$ tends to partially compensate the desolvation penalty *(21, 22)*. An illustration of the effect of compensation of these two factors is given in **Fig. 10.2**, where the combined results of pK calculations on Asp121 in *Bacillus circulans* xylanase and MD simulations are presented *(23)*. During the first 300 ps of the simulation,
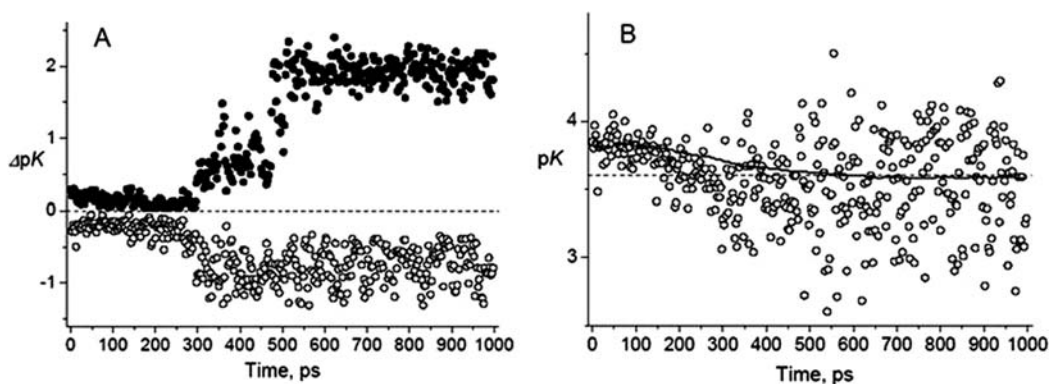
Fig. 10.2. Molecular dynamic simulation and pK calculations on Asp121 from *Bacillus circulans* xylanase. **A**: Time evolution of the snapshot ΔpK_{sol} values due to desolvation (*solid circles*) and due to electrostatic interactions with the peptide dipoles, ΔpK_{pc}, (*open circles*). **B**: Snapshot pK values of Asp121 taken in 5 ps intervals. The time evolution of the average pK is indicated as a *continuous line*. The *dashed line* corresponds to the experimental pK value of 3.6 *(20)*.

the carboxyl group of Asp121 is accessible to the solvent which is reflected by the low $\Delta pK_{sol} = \Delta G_{sol}/(2.3RT)$ and $\Delta pK_{pc} = \Delta G_{pc}/(2.3RT)$ values calculated for trajectory snapshots. After about 400 ps the carboxyl group of Asp121 becomes partially buried. As a result, ΔpK_{sol} increases, thereby stabilizing the neutral form of the carboxyl group. At the same time, the energy of interactions with the peptide dipoles from the surrounding becomes more favorable, thereby stabilizing the charged form. This compensatory effect is typical and reflects the chemical properties of proteins as polypeptides *(24)*.

3.1.2. Conformational Flexibility

Proteins are flexible entities. The amplitude of thermal motions can be significant. Moreover, changes in the chemical composition of the solvent and physical–chemical parameters can introduce conformational changes on a local or global scale. Since the formalism outlined in **Section 2** is adequate only for fixed atomic positions, the assessments of the ionization equilibria based on a single protein conformer (usually determined by X-ray crystallography) are correct either only for a set of sites with limited flexibility, or only in a narrow pH interval, for which the corresponding structure is relevant. The X-ray structure does not necessarily represent the ensemble of structures of the protein in solution. Due to crystal contacts the protein molecule may adopt conformations which are negligibly populated in solution. Also, conformational changes may occur due to changes of the protonation state of the protein. To give an example, the experimentally observed pK values of Glu28 and Asp29 from RNase T$_1$ can be reproduced only if the nearby Lys25 is considered flexible *(25)*. The conformational flexibility is perhaps the key factor providing coupling between electrostatic interactions and other noncovalent interactions in proteins.

Different approaches have been devised to deal with protein flexibility in electrostatic calculations. Flexibility can be implicitly accounted for by adjusting the protein dielectric constant in continuum PB calculations *(26–28)*. Although such methods generally make pK predictions closer to the experiment, being still based on a single conformer, they are incapable to reveal any correlation between protonation and structural changes. Other approaches attempt an explicit treatment *(14, 17, 29)*. However, it is computationally demanding, which practically prohibits its application in full. The reduction of the complexity is most commonly made by using a limited, but representative, number of conformations.

The ionization free energy depends primarily on local environmental effects. A large number of studies have focused on description and analysis of local conformational flexibility effects on ionization equilibria of individual titratable sites *(18, 19, 30–35)*. For example, the conformational space defined by the

side-chain torsion angles can be systematically explored *(31)*. Alternatively, side-chain conformations with maximized solvent accessibility could be considered along with the "native" conformer as seen by X-ray crystallography *(32)*.

Information about conformational flexibility can be extracted from ensembles of NMR structures, which are presumed to give a good representation of protein structural diversity in solution. An overall improvement of pK towards the experimental data can be achieved by averaging the pK values calculated using all members of the NMR ensemble *(36)*. However, since NMR ensembles typically consists of only 10–50 conformers, averaging is arithmetic, that is, all conformers are given equal statistical weights, an assumption which has no rigorous physical ground. It was also demonstrated that in regions where NMR and X-ray structures differ significantly the pK values calculated on the basis of the X-ray structures are in better agreement with the experimental data *(37)*. For solvent-exposed residues, however, a better agreement with the experimental results has been obtained using NMR structures. One can speculate that crystal contacts, as it was pointed out above, are one of the main sources for failing to correctly predict the ionization equilibria in proteins.

Alternative approaches to account for the conformational flexibility is to collect ensembles of structures generated by molecular dynamics simulations. Various protocols combining calculations of ionization equilibria with simulated protein flexibility have been elaborated. In different approaches, the considered structural changes rank from involving only polar hydrogen atoms *(18, 19, 30, 33)*, to side-chain fluctuations *(31, 32, 34, 35, 38)*, to global structural motions *(6, 23, 28, 39–42)*. Overall, pK values from MD ensemble averages were closer to the experimental values in most cases. However, the pKs of buried titratable groups were still badly captured by continuum methods *(28)*. The intuitive explanation is the (still) limited sampling time. During a few hundreds of picoseconds solvent-exposed side chains can visit many alternative conformations with similar pK. This time might be insufficient for a buried, conformationally restrained side chain to visit fewer conformations with very different pK, since the transition might require global conformational rearrangements, which occur on longer timescales. Below we briefly summarize several interesting conclusions that can be made from MD-based studies of the ionization properties of proteins. (1) Longer simulation times are required to achieve approximately constant average pK. For example, simulations of at least 500 ps were necessary to collect ensembles reproducing the experiment for the majority of titratable sites in *Bacillus circulans* xylanase, but for some sites sampling for more than 1 ns was required. *(23)*. An illustration is given in the lower panel of **Fig. 10.3**, showing the time evolution of pK of Asp121. (2) Multiple shorter MD trajectories (starting
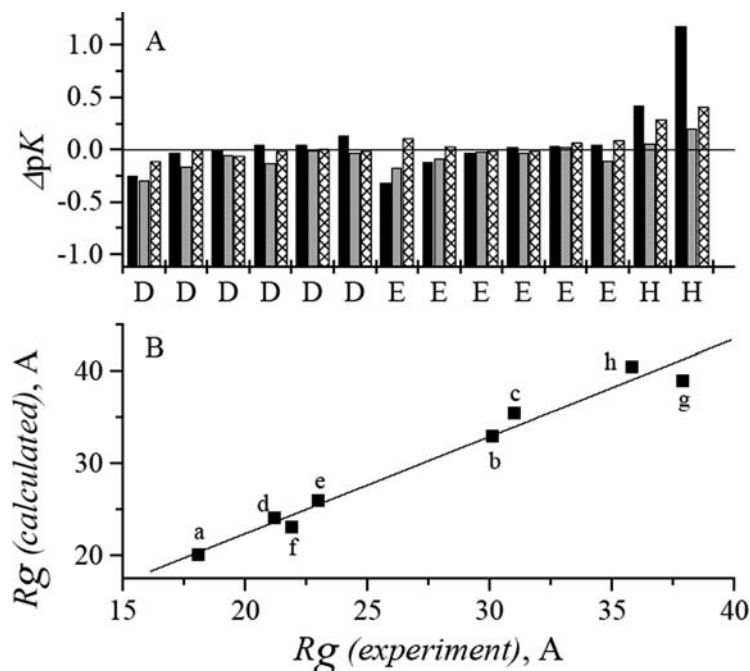
Fig. 10. 3. Recent success in prediction of the properties of the denatured state. **A**: Comparison of experimental and calculated pK values of titratable sites in *Drosophila* protein drk. The data are presented as $\Delta pK = pK - pK_{mod}$. The experimental data (*black bars*) are taken from ref. *(55)* for the carboxyl groups and from ref. *(56)* for the histidines. The *gray bars* and the *hatched bars* are theoretical predictions according to the models described in ref. *(53)* and in ref. *(58)*, respectively. **B**: Experimental and predicted radius of gyration of three unfolded proteins. The letters refer to the protein and the experimental conditions. a, Cyt C at pH 3 *(59)*; b, Cyt C at pH<2 *(60)*; c, Cyt C at pH 7 in 4 M GdmCl *(61)*; d, truncated SNAse at pH 7.5 *(62)*; e, SNAse at pH 5.5 *(63)*; f, Lysozyme at pH 5.2 *(64)*; g, Lysozyme at pH 2 *(65)*; h, lysozyme at pH 2 in 4 M GdmCl *(65)*. The calculated radii of gyration are from ref. *(66)*.

from the same initial structure) might be superior to a single MD trajectory of the same total length *(41)*. (3) The initial structure is likely to influence the results of continuum pK predictions *(23)*, although this is not always the case *(43)*. It appears that, again, the extent of sampling is more important. Also, even with different initial structures, the ionization of buried residues (including active site residues) is not well reproduced. (4) The calculated pK values are likely to be biased by the choice of the initial protonation state. The problem could be overcome by collecting conformers from two independent molecular dynamics runs: one with all titratable sites charged and one with all sites neutral *(6, 40)*. In this case, however, the benefit of the ergodic hypothesis is lost. In view of the ever-growing computational power and the refinement of force fields, one can say that the combination of pK calculations and molecular dynamics simulation is currently the most promising approach for analysis the influence of

conformational flexibility on the ionization equilibria in proteins. It will be illustrated in the next section that considering and understanding of this influence is of prime importance for evaluation of the role of electrostatic interactions in protein stability.

3.2. Ionization Equilibria in Unfolded Proteins

Because the unfolded state is by definition an unstructured and fully solvated state, the easiest and often used way of handling electrostatic interactions in denatured proteins is to ignore them. This so-called null approximation can be (but must not be) justified for extreme cases where electrostatic interactions are screened, for instance, by denaturing agents such as GdmCl. In all other cases (denatured states induced by heat, nonionic denaturants, or pressure), the assumption of nonexistent electrostatic interactions is unjustified for prediction of the electrostatic term of unfolding energy *(44)*. Indeed, experimental work has occasionally identified pK shifts from the model values (pK_{mod}), indicating non-zero electrostatic interactions *(45–47)*. There is no reason to believe that the cited cases are an exception and electrostatic interactions in other unfolded proteins should be neglected.

The question is then, could electrostatic interactions in denatured proteins be considered quantitatively? Since experimental studies with denatured proteins are difficult and are severely limited by the low population of that state at benign conditions, theoretical approaches to the problem are indispensable. Many attempts have been made to find a solution. The denatured state has been modeled with an extended backbone and side-chain conformation, assuming complete hydration and maximized charge–charge distances *(27)*. Another approximation is to project side-chain charges on the backbone of a simplified polypeptide chain, thus reducing charge–charge interactions to interactions between sequentially neighboring charges *(48)*. Others modeled the denatured state as having native-like topology, yet being "swelled", reflecting the increased hydrodynamic radius of and the generally increased charge–charge distances in denatured proteins *(49)*. Continuum pK calculations using the mentioned models have demonstrated good agreement with the experimental data. However, they all are designed to solve specific tasks. They also have a major limitation, namely, only one possible (and fixed) distribution of charges is assumed. Such a situation is physically unrealistic, since denatured proteins exist as large ensembles of rapidly interconverting conformers.

Recently, more realistic models have been devised. According to Zhou, the denatured state is represented by a virtual Gaussian chain connecting titratable sites *(50–53)*. The distance between charges is not fixed and exists as a distribution, which depends on the bond length and the number of bonds separating the virtual polymer elements. Another approach based on the continuum dielectric model and ideologically very close to that of Zhou represents the unfolded protein as a material with low dielectric

constant ($\varepsilon_p = 30$–40) immersed in the high-permittivity medium of the solvent *(54)*. The shape of the dielectric cavity can be considered as an average over all possible conformations of a flexible chain, which results in a sphere inside which most of the protein atoms reside. The radius of this sphere can be the radius of gyration of an unfolded protein *(54)*. In equilibrium, the charges are located on the surface of the dielectric cavity. The conformational heterogeneity of the unfolded ensemble is modeled by different charge configurations on the surface of the dielectric cavity, which can be calculated by Monte Carlo simulation. The fundamental advantage of these models is that the charge–charge distances are variable. The adequacy of the two similar approaches to predict the electrostatic properties of unfolded proteins was convincingly demonstrated by comparison of calculated pK values with experimental data. Recently, the pK values of some titratable groups in unfolded proteins were directly measured *(55–57)*. These studies provided sound evidence that the considered pKs are discrete and distinguishable from those of model compounds. As seen in **Fig. 10.3**, the two sets of calculated values agree fairy well with the experiment, the maximal deviation being 0.4 pH units. Although the measured or calculated pK shifts (in a still very limited number of denatured states) are smaller than those usually observed in folded proteins, these shifts are large enough to have detectable influence on the pH dependence of protein stability.

4. Defining the Role of Salt Bridges in Protein Stability by Experiment, Computation, and Structural Analysis

4.1. Experimental Estimates of the Electrostatic Contribution to Protein Stability

The classical way to estimate the contribution of salt bridges to protein thermodynamic stability is to measure the free energy of unfolding (ΔG_U) as a function of pH. The idea is simple. Since the charged form of the groups participating in salt bridges depend on protonation/deprotonation, increasing or decreasing the proton concentration will eliminate the negative charges or the positive charges, respectively, thereby disrupting the salt bridges. The measured difference in ΔG_U relative to a pH, where the native and denatured states are identically protonated corresponds to the electrostatic contribution of salt bridges to stability. The experiment can be performed in various ways. Thermal melting experiments at different pH values yield the unfolding enthalpy

(ΔH_m) and the midpoint of thermal denaturation (T_m). If the unfolding heat capacity change (ΔC_p) is known either from direct measurements by heat capacity calorimetry (DSC) or from Kirchoff's plots $(\Delta H_m$ vs. $T_m)$, ΔG_U at any temperature can be calculated from the Gibbs–Helmholtz equation:

$$\Delta G_U(pH) = \Delta H_m(pH)\left[1 - \frac{T}{T_m}\right]$$

$$- \Delta C_p\left[T - T_m - T\ln\left(\frac{T}{T_m}\right)\right] - RT\ln K_m(pH). \quad (10.9)$$

Alternatively, ΔG_U can be assessed at benign temperature from isothermal denaturant-induced unfolding experiments using the linear extrapolation method (LEM) according to

$$\Delta G_U(pH) = -m(pH)[den]_{1/2} - RT\ln K_{den\ 1/2}(pH). \quad (10.10)$$

The mid-point of denaturation is $[den]_{1/2}$. At this denaturant concentration the fraction of unfolded protein (f_U) is 0.5. The term $m(pH) = d\Delta G(den, pH)/d[den]$ (units of $kJ^{-1}mol^{-1}M^{-1}$) describes the linear dependence of the unfolding free energy on the denaturant concentration in a narrow range of denaturant concentrations, where $0.4 < f_U < 0.6$. For unfolding of monomeric proteins, $K_m(pH)$ and $K_{den_{1/2}}(pH)$ equal 1. For multimeric proteins, if unfolding is coupled to simultaneous dissociation to subunits, $K_m(pH) = K_{den1/2}(pH) = \frac{nf_U^n M_{tot}^{n-1}}{1-f_u}$, where n is the number of subunits and M_{tot} is the total concentration of subunits. Both methods have advantages and disadvantages, but the pH-dependence of ΔG_U has been determined with high precision for many proteins. In the vast majority of cases, the acidic pH region is explored, since at the high pH required to protonate basic side chains chemical modifications occur. The typical outcome is shown in **Fig. 10.4A** where protonation of acidic side chains is destabilizing. Although dozens of proteins get less stable at low pH this is not necessarily always the case (**Fig. 10.4B**). There are proteins which are not very sensitive to low pH, or even gain thermodynamic stability at low pH. The decrease in stability at low pH can be pronounced. Given that the typical stability of globular protein domains is 5–15 kcal mol^{-1}, pH-induced destabilization by as much as 10–15 kcal mol^{-1} is dramatic. The protonation of acidic groups affects not only the folded state. Neglecting the residual charge–charge interactions in the denatured states of barnase (**Fig. 10.4A**), the N-terminal domain of the ribosomal protein L9 from *B. stearothermophilus,* and some other proteins according to the null approximation (see **Section 3.2**) largely overestimates the pH effect on ΔG_U *(50, 51, 67)*. The choice of physical agent used to shift the equilibrium between folded and unfolded protein in order to calculate ΔG_U has in many cases critical influence on the
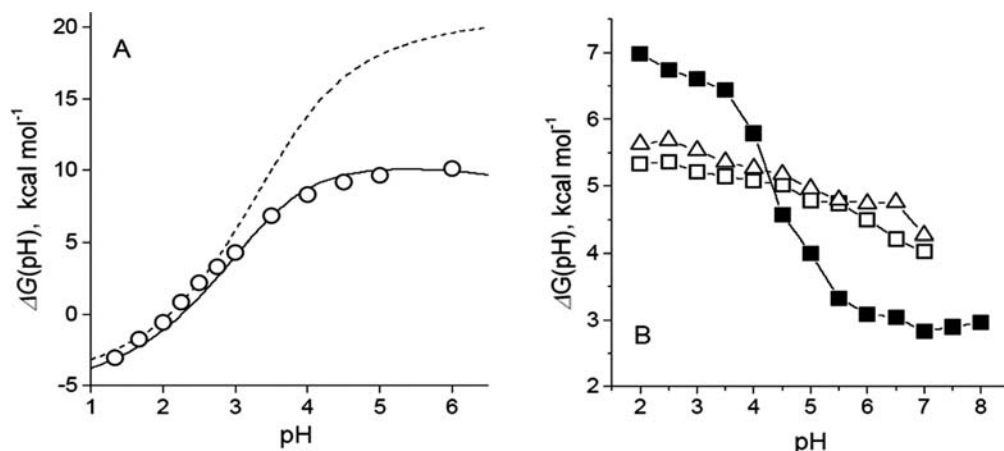
Fig. 10.4. pH dependence of the denaturation free energy. **A:** Barnase. Experimental data *(45)* are compared with the theoretical curves *(54, 67)* obtained by taking into account electrostatic interactions in the unfolded state (*continuous line*) and with the pK_{mod} values from **Table 10.2** (*dashed line*). Practically identical results are obtained for the same protein by Zhou *(50)*. **B:** A dimeric leucine zipper engineered to maximize the interhelical electrostatic interactions *(68)*. The symbols represent the unfolding free energy measured by heat denaturation (*open squares*), urea-induced denaturation (*triangles*), and GdmCl-induced denaturation (*filled squares*).

resulting $\Delta G_U(pH)$ function, as illustrated in **Fig. 10.4B**. It is now a well established fact that the results of GdmCl-induced unfolding are frequently at odds with the $\Delta G_U(pH)$ profiles collected by urea-induced and thermal unfolding experiments *(69, 70)*. GdmCl acts as a dissociated salt and screens charge–charge interactions. Possibly, salt bridges are mostly affected, yet there is no way to justify this widespread belief. Various effects could arise, depending on the charge constellation. If salt bridges stabilize the native state (and there are no residual charge-charge interactions in the denatured state), around neutral pH the stability of the protein will be apparently lower when measured by GdmCl-induced unfolding in comparison to urea/heat denaturation. At low pH, where only positive charges are present, the effect of GdmCl could be stabilizing, since Coulombic repulsion will be attenuated. The picture is indeed more complicated, due to the fact that the denatured state is not an electrostatic "dummy" and charge–charge interactions in that state will also be modulated by salt. Moreover, apart from the charge screening effect, different denaturants (and heat) might change the structure of both the native and denatured proteins in different ways. Given the long-range nature of electrostatic interactions, even small structural perturbations might have serious consequences on the experimentally estimated $\Delta G_U(pH)$. This point was clearly demonstrated by comparisons of $\Delta G_U(pH)$ profiles constructed by following nonthermodynamic variables (spectroscopic signals) or by following genuine thermodynamic variables (proton inventory) *(70)*.

Equations 10.2 and **10.3** build the basis of another approach to measure $\Delta G_U(pH)$ experimentally. The difference of protons bound to the native and unfolded state with reference to an arbitrary chosen $pH, \Delta\nu = \nu^U - \nu^F$, can be directly measured by potentiometric titration. In principle, this is the method of choice since $\Delta\nu$ is obtained in a model-independent manner, but application is hampered by the relatively high protein concentrations required to collect high-precision data. From thermal unfolding data $\Delta\nu$ is also accessible according to

$$\Delta\nu = \frac{d(\ln K_U)}{d[H^+]} = \frac{1}{2.303}\frac{d(\ln K_U)}{dT}\frac{dT_m}{dpH} = \frac{1}{2.303}\frac{\Delta H_m}{RT_m^2}\frac{dT_m}{dpH}. \quad (10.11)$$

Since differentiation is involved, the experimental errors are often too large to allow reliable estimates of $\Delta\nu$. Alternatively, the pK values can be measured directly by NMR spectroscopy. In the ideal case, if pK_i^F and pK_i^U are available, the degrees of protonation, $\theta_i^{U,F}(pH)$, can be obtained by the Henderson–Hasselbalch equation

$$\theta_i(pH) = \frac{10^{(pK_i - pH)}}{1 + 10^{(pK_i - pH)}}, \quad (10.12)$$

and **Eq. 10.2** and **10.3** can be employed to calculate $\Delta\nu$. Unfortunately, the method is not free of problems. First, the proteins for which ionization equilibria can be measured in both the folded and unfolded states are still rare. Secondly, the evaluation of pK_i^F itself is often not straightforward. The extraction of pKs from the pH-dependence of the chemical shift is made by fitting the same Henderson–Hasselbalch equation to the data *(71)*:

$$\delta(pH) = \delta_b + \frac{\delta_a 10^{n(pK - pH)}}{1 + 10^{n(pK - pH)}}, \quad (10.13)$$

where n is the Hill coefficient, reflecting the mutual dependence of the ionization of titratable sites. $\delta(pH)$ is the observed chemical shift of the reporting nucleus at given pH, while δ_a and δ_b are the limiting chemical shifts at the acidic and the basic flanks of $\delta(pH)$. For some groups complete titration curves cannot be measured. Therefore, either δ_a or δ_b remains undefined, which introduce uncertainty in fitted value of pK_i^F. Often, $\delta(pH)$ exhibits a multistep sigmoidal shape. In such cases the appropriate fitting expression is *(72, 73)*

$$\delta(pH) = \delta_b + \sum_{I=1}^{j}\frac{C_i(\delta_a - \delta_b)10^{(pK_I - pH)}}{1 + 10^{(pK_I - pH)}}, \quad (10.14)$$

where $\sum_{i=1}^{j} C_i = 1$ and $j = 1, 2 \ldots$ counts the number of inflections of $\delta(pH)$. In **Fig. 10.5** a two-step titration curve is illustrated. **Eq. 10.14** presumes that such a curve reflects the titration of two sites and since in this case $j = 2$, two pK values are obtained and assigned to two different groups. The very same shape can
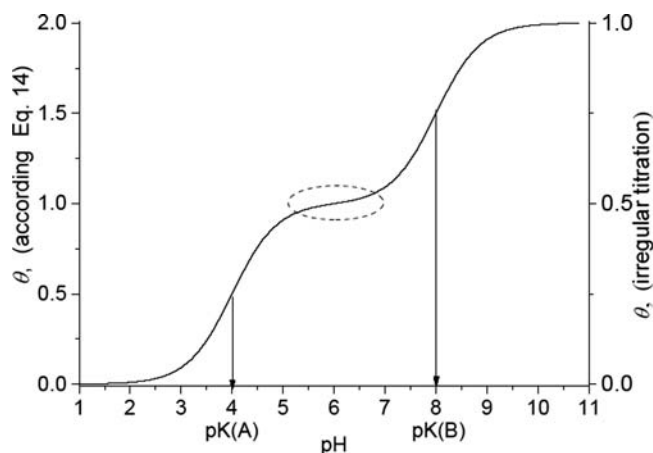
Fig. 10.5. Simulated two-step sigmoidal titration curve. On the *left ordinate*: degree of deprotonation according **Eq. (10.14)**. Two p*K* values are assigned to two different sites, A and B. In this case two p*K* values are derived (*pointed by arrows*) and the change of the total charge is 2. On the *right ordinate*: degree of deprotonation of a single titratable site whose ionization is coupled with the ionization of another site. The ellipse marks the region of the plateau typical for irregular titration curves.

however be obtained for the titration of a single group if its ionization is coupled with the ionization of another group. This phenomenon is referred to as cooperative or irregular titration *(74)* and the conditions leading to irregular titration behavior were deduced theoretically *(75)*. As far as **Eq. 10.2** uses integral quantities (i.e., the difference between protein titration curves), the interpretation of $\delta(pH)$ curves with multistep sigmoidal shape does not influence the calculation of the electrostatic contribution to unfolding free energy.

4.2. Assessing the Contribution of Salt Bridges by Mutation

Numerous attempts have been undertaken to probe for the contribution of salt bridges by mutation. There are many examples of removing the charge from one of the salt bridge partners by mutation, leading to destabilization. However, the loss of free energy upon mutation cannot be equated with the reduction of the overall charge–charge interactions energy due to the loss of the salt bridge. The situation is basically the same as in pH-variation experiments. Depending on the nature of replacement, desolvation, charge–dipole interactions, and charge–charge interaction with neighboring charges are modified. Some mutations could also remove van der Waals contacts made by the nonpolar moiety of the replaced salt bridge partner with other groups. Introduction of smaller side chains creates space for side-chain rearrangements. Charge reversal changes dramatically the charge constellation in the vicinity of the parent salt bridge. Moreover, the conformational flexibility and hence the dynamic properties of the region can change, which has impact on the energetics of the system.

It is believed that the use of double-mutant cycles can provide more detailed information about the energetics of salt bridges *(76)*. A double-mutant cycle yields the so-called "coupling free energy" of a salt bridge by mutating each group separately and both groups simultaneously. If the two mutated residues are noninteracting, the effect of mutating either residue is independent of mutating the other residue. However, if the mutated residues are interacting with each other, the effect of substituting one residue will depend on the residue at the other position. Hence, to determine the coupling free energy of a salt bridge, the free energy of unfolding, ΔG_U, of the wild-type protein, the two single mutants and the double mutant have to be determined. The double-mutant cycle is designed to cancel all effects except those from the direct interaction between the two mutated residues. It follows that in an ideal double-mutant cycle the coupling free energy is due only to the direct interaction between the mutated residues. This is true if rather restrictive assumptions are made. First, one assumes that there is no significant conformational change upon either mutation, so that van der Waals packing is not influenced. Second, the mutations do not significantly alter electrostatic interactions in the unfolded state. As we have shown, the second assumption is often untrue. To summarize, double-mutant cycles provide valuable information about the contribution of *a priori*-selected salt bridges to protein stability in terms of the coupling free energies. It is currently the only experimental approach to obtain a semiquantitative estimate of the free energy of pairwise charge–charge interaction. Although information from double-mutant cycles could be a useful guide for rational design and molecular modeling, the two assumptions mentioned above should be kept in mind.

4.3. Do Proteins Benefit from Salt Bridges?

Structural stabilization of proteins at different environmental conditions can be considered a prime functional solution. Are salt bridges involved in this solution? A prominent salt bridge network links the two subunits of the disulfide oxidoreductase from *Pyrococcus furiosus* (**Fig. 10.6**). The network consists of 10 functional groups. The total number of bonds is 14, out of which 6 are connecting the two subunits. More than half of the bonds are made within the same subunit, thus facilitating the appropriate conformation and orientation of neighboring functional groups. Taking into account that this protein is from a hyperthermophilic organism (optimal growth temperature above 80°C) one might presume that these salt bridges essentially contribute to the stability of the dimer and to the conformation of the subunits at the interface region. Many other examples of this kind can be given, yet a general statement about the role of salt bridges cannot be made. In view of the aforementioned difficulties to obtain reliable knowledge about the energetic contribution of salt bridges, it is
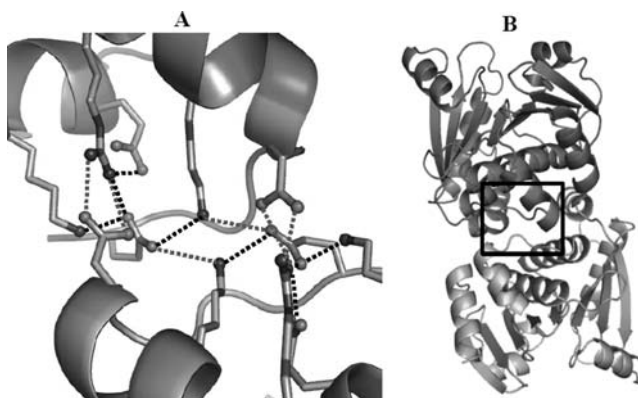
Fig. 10. 6. **A**: Salt bridge network connecting two subunits of disulfide oxidoreductase from *Pyrococcus furiosus (78)*. *Black lines*: salt bridges connecting the subunits; *grey lines*: intrasubunit salt bridges. **B**: Cartoon presentation of the two subunits (*in different shading*) of the native protein. The region of the salt bridge network is indicated.

not surprising to find in the literature rather polarized opinions: from stating that salt bridges could be a destabilizing factor *(68)*, or have only modest contribution to stability *(77)*, to claiming a central role of ion pairs in the stabilization of the native protein structure *(78)*. In energy terms, the stabilizing contribution of individual salt bridges has been evaluated to occur over a wide range: from 0.5 kcal mol^{-1} *(79)* to 3–5 kcal mol^{-1} *(80)*. Of course, since these are focused on different proteins exhibiting different structural and functional features, these and similar reports should not be considered contradictory. Neither can they serve as a basis for general conclusions.

The spatial distribution of the ionizable residues in proteins is of special interest in many aspects. To minimize the desolvation penalty, charged groups are "expelled" to the protein surface. Formally, the first benefit of this effect is a better solubility and prevention of nonspecific association and aggregation of protein molecules, a feature of critical importance for maintaining the native structure and the functional properties of proteins in the "crowded" environment of living cells. On the other hand, charge distribution on the protein surface should guarantee specific binding if needed. Multimeric proteins are a typical example: subunits interact in a unique arrangement often driven by formation of salt bridges and salt bridge networks linking the individual subunits, as just discussed in the example above. Furthermore, an appropriate arrangement of the charges can facilitate binding by electrostatic steering of charged or polar ligands, substrates, and other macromolecules.

One of the possible ways to estimate the structural significance of electrostatic interactions is to study the three-dimensional distribution of ionizable sites in folded proteins representing different structural and functional classes *(81)*. Since favorable electrostatic interactions (stabilizing the native structure) arise from attraction

between opposite charges, one could expect distribution of surface charges to be nonrandom. It turns out, however, that the number of salt bridges in native proteins does not differ statistically from the number expected from a distribution created by a random process *(82)*. Hence, salt bridges do not appear to be utilized as stabilizers of the native structure. On the other hand, repulsive contacts are significantly rejected, so that in most of the native structures there are none at all, or else just one repulsive contact. It follows that the electrostatic term of the free energy of a folded protein is effectively minimized by avoiding electrostatic repulsion, rather than by optimizing the network of attractive interactions. In other words, electrostatic stabilization is not linked to the evolutionary appearance of additional salt bridges. It should be noted that this conclusion does apply to thermo- and especially to hyperthermostable proteins (see **Section 4.4**).

Surprising as it might appear, the apparent lack of evolutionary pressure for maximizing the number of salt bridges can perhaps be explained by the fact that salt bridges are dynamic formations and are strongly influenced by the local and overall conformational flexibility. In solution, salt bridges break and reform. Sometimes charged side chains fluctuate within alternative salt bridge arrangements. The effect of the conformational flexibility on the ionization equilibria of the charged side chains involved in salt bridges is illustrated in **Fig. 10.7**, where the dynamics and the energetics of the Asp15/Lys52 salt bridge in
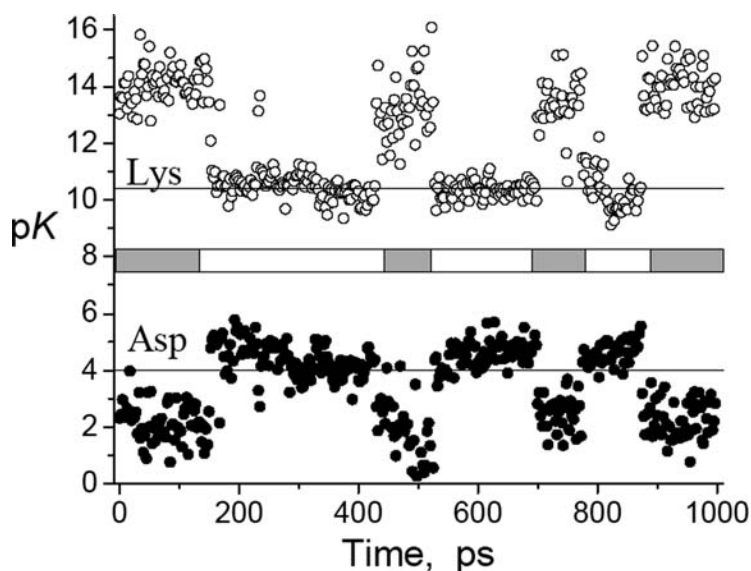
Fig. 10.7. Snapshot pK values of Lys52 (*open circles*) and Asp15 (*solid circles*) from *Bacillus agaradhaerens* xylanase calculated by means of combination of molecular dynamic simulation and electrostatic calculations *(23)*. The time intervals at which the two residues form a salt bridge are marked with *gray* segments in the *horizontal bar*. The *straight lines* indicate pK$_{mod}$ of Asp and Lys.

B. agaradhaerens xylanase is presented *(23)*. In the time intervals within which Asp15 and Lys52 do not form salt bridge, their pK values are close to the standard ones (pK_{mod}), indicating that these groups do not contribute to the electrostatic stabilization of the protein. In contrast, whenever the salt bridge is formed, the pKs shift significantly from pK_{mod}, indicating a stabilization effect. On average, the salt bridge is broken about 50% of the total simulation time. Hence, the contribution of the Asp15/Lys52 salt bridge is half of that expected from a "stable", non-fluctuating ion pair. Similar observations have been reported for the dynamic properties of the triplet Asp8/Arg110/Asp12 in barnase, which has a relatively short lifetime and marginal stabilization effect *(83)*. Concerning the thermodynamic stability of proteins, one can hypothesize that surface-exposed salt bridges "pass unnoticed" by evolution due to the inefficient energetic contribution of many of them.

The short lifetime and frequent formation/disruption of salt bridges is not a general rule. Estimates made by MD simulation have shown that salt bridges can exist unbroken substantially longer than 1 ns, even as long as 200 ns *(42, 84, 85)*. A representative example can be given with the case of the Braun's *Escherichia coli* outer membrane lipoprotein protein (Lpp-56). It is a homotrimeric, parallel coiled coil, which contains many salt bridges organized in five rings girdling the three-helix bundle of the molecule (**Fig. 10.8A**). The number of simultaneously existing salt bridges is 15 during a 7-nm MD simulation; 12 salt bridges are interhelical. The protein (168 residues) thus contains twice as many salt bridges than the expected number from a random distribution. This suggests that the charge–charge interactions in this protein should be involved in the stabilization of the native structure. Indeed, in the course of 7-ns MD simulation, the prevailing majority of salt bridges do not, or only seldom break *(86)*. An example of a long-living salt bridge is given in **Fig. 10.8B**. This salt bridge is interhelical and belongs to the C-terminal ring 5 (**Fig. 10.8A**). The salt bridge is broken only during the first 400 ps and in the time interval 1500–2200 ps. After this time it remains intact (**Fig. 10.8C**). The integrity of this salt bridge is supported by an additional hydrogen bond between the carboxyl group and a tyrosine (**Fig.10.8B**). The hydrogen bond seems to play a twofold role: besides maintaining the appropriate conformation of the C-terminal residue and, hence, the appropriate orientation of the C-terminal carboxyl group, it is an interhelical link, contributing to the stability of the bundle. The population of conformers with intact salt bridges within ring 5 is between 85% and 95%. The high occupancy, in contrast to the example form **Fig.10.7**, leads to a large average shift of the pK values of the participating groups. The calculated average values of the C-terminal carboxyl
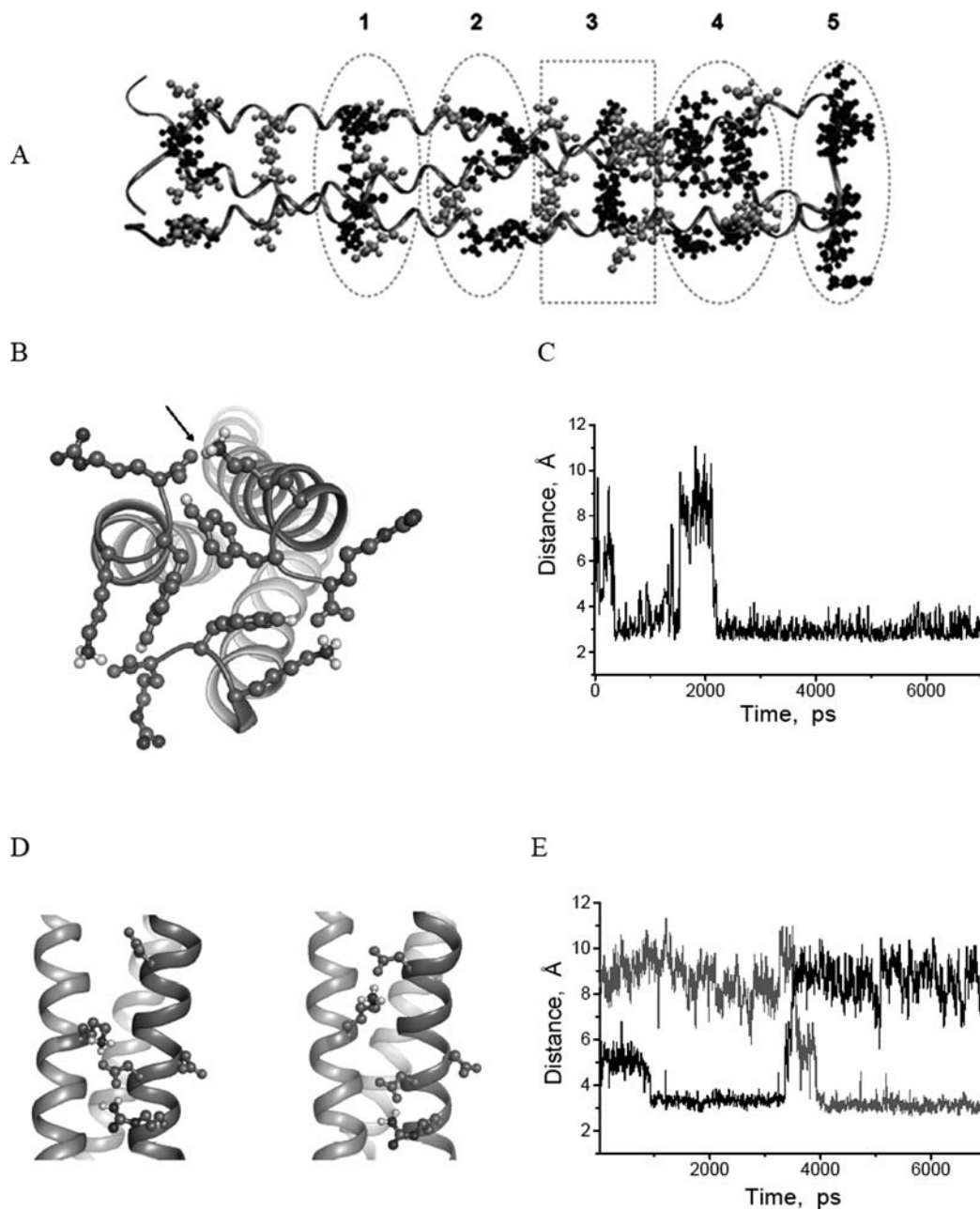
Fig. 10.8. Overall organization and dynamics of particular salt bridges in the Lpp-56 protein. **A**: An overview of the salt bridges in Lpp-56. The three helices are shaded differently. The prominent rings of salt bridges are numbered. Side chains participating in the salt bridge rings are drawn as ball-and-sticks. All other side chains are not shown. The N-terminus is on the *left*. **B**: Interhelical salt bridge between the C-terminal carboxyl group and the ε-amino group of Lys54. The side chain of Tyr54 forming a hydrogen bond with the C-terminal carboxylic group is also shown. **C**: Time evolution of the distance between the C-terminal carboxyl group and Lys54. **D**: Lys38 forms alternative salt bridges with Asp34 or Asp40 of the adjacent α-helix. **E**: Time course of the existence of the alternative Lys54/Asp34 (*gray*) and Lys54/Asp40 (*black*) salt bridges. The data were collected by a 7-ns MD simulation in explicit water.

groups and of the three lysines at position 54 are 3.2 and 13.0, respectively, which is a source of a significant stabilizing contribution. Rings 2 and 4 (see **Fig. 10.8A**) are also characterized with extremely high population of intact salt bridges, 99% and 69%, respectively. Another example of achieving electrostatic stabilization is Ring 3 (**Fig. 10.8D,E**). The side chain of lysine at position 38 can alternatively form intrahelical salt bridges with two aspartic acids from the adjacent helix (**Fig. 10.8D**). During one-third of the simulation time Lys38 is bound to Asp40. Thereafter, Lys38 is involved in an alternative salt bridge with Asp33 from the same adjacent helix. Thus, the link between the two helices of the bundle is intact for ~80% of the time, and is likely to confer a valuable contribution to the stability of the molecule.

The contrasting dynamic behavior of the salt bridges illustrated in **Fig. 10.7** and **Fig. 10.8** poses a question about the factors dictating the frequency of formation/disruption. One can presume that the number of hydrogen bonds involved in the salt bridge is a factor increasing its lifetime. Indeed, rings 2 and 4 in Lpp-56 consist of salt bridges composed by identical functional groups (guanidinium and carboxyl groups) but linked by different numbers of hydrogen bonds. The salt bridges in ring 2 are linked by two hydrogen bonds, whereas those in ring 4 are linked by one. Correspondingly, salt bridges within ring 4 have shorter lifetimes. Another important factor is the local environment. An example is ring 5 (**Fig. 10.8C,D**), where a third partner is involved, maintaining the most appropriate spatial arrangement of the functional groups forming the salt bridge. The dominating factor seems, however, to be the conformational flexibility of the molecule. It may or may not tolerate conformational freedom of the charged side chains and in this way regulate the salt bridge lifetime. Hence, the contribution of the salt bridges to protein stability is function of their lifetimes, and depends on the dynamic properties of the protein molecule on a local or even global scale. This property cannot be identified in a single, say X-ray structure. For instance, according to the X-ray structure of Lpp-56 *(87)* the salt bridges in ring 1 are well defined, whereas the MD simulation suggests a negligible average population of these salt bridges (about 1%). In contrast, the salt bridges in ring 2 are well defined in the MD trajectory, yet are not present in the X-ray structure.

4.4. Electrostatic Contribution to Protein Thermal Stability

In the last few decades a series of discoveries changed our understanding of the environmental limits of life. For example, living organisms have been found in hot springs and around the deep-ocean volcanic vents where the temperature reaches, or even exceeds, the boiling point of water. Obviously, the proteins constituting thermo- and hyperthermophiles organisms must maintain their native structure at temperatures at which their homologues in mesophilic organisms are unfolded. Indeed, some proteins have

denaturation temperature of about 150°C *(88)*. Comparisons of X-ray structures of functionally homologous proteins from thermo-/hyperthermophilic organisms and from mesophilic organisms revealed the striking fact that they do not differ in fold, and generally speaking, exhibit only minor structural variation. This observation challenges our understanding of the fine-tuning of noncovalent interactions, since very subtle structural differences appear responsible for large difference in the physical–chemical properties of proteins.

Recently, an increasing number of observations strengthen the view that electrostatic interactions are an important factor conferring thermostability to proteins, although opposite views also exist *(89–94)*. The overall trend of an increased number of salt bridges in proteins from organisms with higher optimal growth temperature is illustrated in **Fig. 10.9** and in **Table 10.3**.

Hyperthermostable proteins clearly confirm this trend. One can argue that it is a side effect. Glutamine and asparagine side chains in some sequential and spatial arrangements are labile and tend to get deamidated at higher temperatures. It is not surprising, therefore, that hyperthermostable proteins contain less asparagine and especially glutamine in comparison to the mesophilic counterparts. Due to the environmental pressure the unstable and solvent-accessible glutamine and asparagine are substituted by glutamic and aspartic acid. In parallel, to preserve the charge balance, the number of positively charged residues, especially lysine, increases *(97–99)*. If this hypothesis is correct, it follows that the increased number of charged groups is driven by the chemical character of asparagine and the glutamine, not by the necessity to search for additional sources of thermal stability.
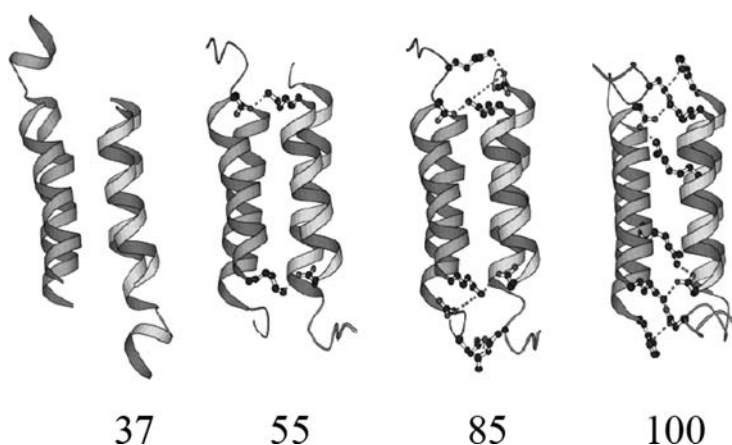
Fig. 10.9. Salt bridges at the subunits interface of the citrate synthase dimers from different organisms *(95)*: pig (optimal temperature 37°C), *Thermotoga maritima* (55°C), *Sulfolobus solfataricus* (85°C), *Pyrococcus furiosus* (100°C). The figure was kindly provided by Prof. M. J. Danson, University of Bath, Centre for Extremophile Research, UK.

Table 10.3
Number of salt bridges in thermo- and hyperthermostable proteins from different functional classes compared with their counterparts from mesophilic organisms (96)

Protein and organism [a]	Optimal temperature	Salt bridges in native structure	expected [b]
Rubredoxin			
Pyrococcus furiosus	100	**4**	4.2
Desulfovibrio desulforicans		0	1.1
Desulfovibrio vulgaris		1	3.4
Desulfovibrio gigas		1	3.9
Clostridium pasteurianum		2	3.6
Superoxide dismutase (Mn,Fe)			
Thermus thermophilus	75	**10**	10.1
Pseudomonas ovalis		6	6.2
Escherichia coli		4	6.6
Malate dehydrogenase			
Thermus flavus	75	**17**	16.7
porcine		15	17.7
Phosphoglycerate kinase			
Bacillus stearothermophilus	55	**32**	30.4
Saccharomyces cerevisiae		8	20.8
Phosphofructokinase			
Bacillus stearothermophilus	55	**15**	15.2
Escherichia coli		10	15.8
Lactate dehydrogenase			
Bacillus stearothermophilus	55	**21**	15.4
Lactobacillus casei		12	14.2
dogfish		19	14.6
porcine		13	13.0

Table 10.3

(continued)

Protein and organism [a]	Optimal temperature	Salt bridges in native structure	expected [b]
D-glyceraldehyde-3-phosphate			
dehydrogenase			
Bacillus stearothermophilus	55	**16**	19.5
lobster		15	13.3

[a] The thermophilic organism is underlined.
[b] Calculated according to Spassov et al. _(82)_

Indeed, as seen in **Table 10.3** the number of salt bridges in thermostable proteins is around that expected for a random distribution. In some cases, however, electrostatic stabilization is gained through an increased number of salt bridges _(80, 100)_.

Nevertheless, even if the increased charge content is a side effect, thermo- and especially hyperthermostable proteins are expected to gain stabilization energy from electrostatic interactions. A sizeable energy barrier exists for the solvation (disintegrating) of a salt bridge and the height of this barrier increases with temperature, as demonstrated by high-temperature, continuum-solvent MD simulations of a prototypical ion-pair model _(100)_. The sole presence of such energy barrier suggests an apparent role of ion pairs in increasing the kinetic barrier for thermal unfolding. Indirect evidence for the stabilizing role of salt bridges at high temperatures comes also from experimental studies. Variants of the cold shock protein _Bs_-Csp from _B. subtilis_ (a mesophile) were generated by directed evolution approaches _(101)_. The most stable variant had an unfolding temperature of 82.2°C and resembled the thermophilic counterpart protein (_Bc_-Csp from _B. caldolyticus_) and also in stability as function of the salt concentration.

Another striking property of thermostable and especially of hyperthermostable proteins is the increase of the size and the number of salt bridge networks _(78, 92, 102–108)_. A typical salt bridge network connecting the subunits of the hyperthermostable protein disulfide oxidoreductase from _Pyrococcus furiosus_ is shown in **Fig. 10.6**. The contribution of surface salt bridge networks to protein stability has been tested occasionally by experiment. For example, in the triad Arg190-Glu231-Lys193 of the NADP$^+$-binding domain of the _Thermotoga maritima_ glutamate dehydrogenase the contribution of each charge–charge pair is reduced by 1.1 kcal mol^{-1} in the absence of the third partner _(109)_. Very similar results were previously obtained for the triad Asp8-Asp12-Arg110 in the mesostable protein barnase _(110)_.

This effect, referred to as cooperative interactions within ion pairs *(109)*, is due to the environment created by each of the members of the network, which being polar, is appropriate for stabilizing the ionized forms of the other partners. In addition, the conformational flexibility is possibly reduced within a salt bridge network, leading to longer salt bridge lifetimes, hence to an increase in stability, as discussed in the previous section.

The examples considered above are a small part of the huge body of structural and experimental observations suggesting that the increased thermal stability of thermophile proteins and the increased content of salt bridges are related. The most obvious physical reason for an increased contribution of salt bridges to thermal stabilization is the reduction of the dielectric constant of water at higher temperatures. The direct consequence is the reduction of the desolvation penalty for the formation of a salt bridge when the temperature increases. At the same time, the charge–charge interactions increase in magnitude. These two factors act in parallel towards stabilizing the charged form of the functional groups participating in salt bridges, and oppose the effect of thermal motions which disfavor salt bridge formation. Thus, the electrostatic term of free energy becomes increasingly less sensitive to the temperature. One can hypothesize that the long lifespan of salt bridges in salt bridge networks, supported by the reduced desolvation penalty and increased charge–charge interactions at high temperatures, both of which help to withstand the thermal motion, is one of the key factors for increasing the thermal stability of proteins.

5. Conclusions

Elucidation of the contribution of electrostatic interactions and salt bridges to protein stability is key to understanding the physics of proteins and their central position in the molecular machinery of living organisms. Many attempts have been made to determine the energetic contribution of salt bridges to protein stability, yet the issue remains contentious. The reason is that the favorable charge–charge attraction within a salt bridge is opposed by the unfavorable free energy of desolvation of charges and is further modulated by charge–dipole interactions and by the ionization behavior of nearby charged groups. Salt bridges are dynamic. Being mostly surface-exposed they experience large thermal motions, continuously breaking and re-forming. Therefore, the total energetic contribution of isolated salt bridges is governed by their lifespan, which in turn is a function of the overall flexibility of the protein molecule.

There is still no well-accepted view about the energetic role of salt bridges. Contrasting opinions mirror the conceptual difficulty

to account for the cooperativity and strong interdependence of noncovalent forces. Since absolute energy cannot be measured, the strength of a salt bridge is evaluated from the energy difference between states with the salt bridge being formed or destroyed. The total electrostatic contribution to protein stability can be estimated by disrupting attractive charge–charge interactions through protonation/deprotonation. However, this is the energy relative to states, where the charge balance is severely altered in comparison to the native charge constellation. Individual salt bridges can be targeted by mutation. Even carefully designed and executed double-mutant studies provide only the coupling energy between charged side chains, yet it is impossible to filter out nonadditive energetic terms arising from the structural changes introduced by mutation. Theoretical methods provide detailed description of the discrete energy contributions influencing the stability of salt bridges, but the accuracy of computational estimates suffer from the still incomplete description of the physical properties of protein. In the past, both experimental and theoretical studies have largely neglected the electrostatic interactions in denatured proteins. It is now clear that the denatured state must be carefully considered if the goal is to quantify protein stability. As in many other branches of modern protein science, understanding the role of salt bridges in proteins requires the combined efforts of structural, experimental, and theoretical approaches.

Acknowledgments

References

1. Linderstrøm-Lang, K. (1924) On the Ionization of Proteins. *C R Trav Lab Carlsberg* 15, 1–29.

2. Pauling, L., Corey, R.B., Branson, H.R. (1951) The structure of proteins: Two hydrogen-bonded helical configurations of the polypeptide chain. *Proc Natl Acad Sci USA* 37, 205–211.

3. Pauling, L., Mirsky, A.E. (1936) On the structure of native, denatured, and coagulated Proteins. *Proc Natl Acad Sci USA* 22, 439–447.

4. Kauzmann, W. (1959) Some factors in the interpretation of protein denaturation. *Adv Protein Chem* 14, 1–63.

5. Rose, G.D., Fleming, P.J., Banavar, J.R., et al. (2006) A backbone-based theory of protein folding. *Proc Natl Acad Sci USA* 103, 16623–16633.

6. Yang, A.-S., Honig, B. (1993) On the pH dependence of protein stability. *J Mol Biol* 231, 459–474.

7. Kundrotas, P., Karshikoff, A. (2004) Electrostatic interactions in unfolded proteins.

Implication for protein stability, in (Richard, R., ed.) *Current Topics in Peptide & Protein Research*. Research Trends, Poojapura. pp. 21–35.

8. Nozaki, Y., Tanford, C. (1967) Examination of titration behaviour. *Meth Enzymol* 11, 715–734.

9. Matthew, J.B. (1985) Electrostatic effects in proteins. *Annu Rev Biophys Biomol Struct* 14, 387–417.

10. Lide, D.R. (1999) *CRC Handbook of Chemistry and Physics*. CRC Press, Boca Raton.

11. Tanokura, M. (1983) 1H-NMR study on the tautomerism of the imidasole ring of histidine residues. 1. Microscopic pK values and molar ratios of tautomerism in histidine-containing peptides. *Biochim Biophys Acta* 742, 576–585.

12. Demchuk, E., Wade, R.C. (1996) Improving the continuum dielectric approach to calculating pK_as of ionizable groups in proteins. *J Phys Chem* 100, 17373–17387.

13. Raquet, X., Lounnas, V., Lamotte-Brasseur, J., et al. (1997) pK_a calculations for class A α-lactamases: Methodological and mechanistic implications. *Biophys J* 73, 2416–2426.

14. Ullmann, G.M., Knapp, E.W. (1999) Electrostatic models for computing protonation and redox equilibria in proteins. *Eur Biophys J* 28, 533–551.

15. Fogolari, F., Brigo, A., Molinari, H. (2002) The Poisson–Boltzmann equation for biomolecular electrostatics: a tool for structural biology. *J Mol Recognit* 15, 377–392.

16. Bashford, D., Karplus, M. (1990) pK_as of ionizable groups in proteins: Atomic detail from a continuum electrostatic model. *Biochemistry* 29, 10219–10225.

17. Spassov, V.Z., Bashford, D. (1999) Multiple-site ligand binding to flexible macromolecules: Separation of global and local conformational change and an iterative mobile clustering approach. *J Comput Chem* 20, 1091–1111.

18. Koumanov, A., Rüterjans, H., Karshikoff, A. (2002) Continuum electrostatic analysis of irregular ionization and proton allocation in proteins. *Proteins* 46, 85–96.

19. Koumanov, A., Benach, J., Atrian, S., et al. (2003) The catalytic mechanism of *Drosophila* alcohol dehydrogenase: Evidence for a proton relay modulated by the coupled ionization of the active site lysine/tyrosine pair and a NAD+ ribose OH switch. *Proteins* 51, 289–298.

20. Joshi, M., Hedberg, A., McIntosh, L. (1997) Complete measurement of the pK(a) values of the carboxyl and imidazole groups in *Bacillus circulans* xylanase. *Protein Sci* 6, 2667–2670.

21. Warshel, A., Russell, S.T., Churg, A.K. (1984) Macroscopic models for studies of electrostatic interactions in proteins: Limitations and applicability. *Proc Natl Acad Sci USA* 81, 4785–4789.

22. Warshel, A., Russell, S.T. (1984) Calculations of electrostatic interactions in biological systems and in solutions. *Q Rev Biophys* 17, 283–422.

23. Koumanov, A., Karshikoff, A., Friis, E.P., et al. (2001) Conformational averaging in pK calculations. Improvement and limitations in prediction of ionization properties of proteins. *J Phys Chem B* 105, 9339–9344.

24. Spassov, V.Z., Ladenstein, R., Karshikoff, A. (1997) Optimization of the electrostatic interactions between ionized groups and peptide dipoles in proteins. *Protein Sci* 6, 1190–1196.

25. Koumanov, A., Spitzner, N., Rüterjans, H. et al. (2001) Ionisation properties of titratable groups in ribonuclease T_1. II. Electrostatic analysis. *Eur Biophys J* 30, 198–206.

26. Antosiewicz, J., McCammon, J.A., Gilson, M.K. (1994) Prediction of pH-dependent properties of proteins. *J Mol Biol* 238, 415–436.

27. Schaefer, M., Sommer, M., Karplus, M. (1997) pH-dependence of protein stability: Absolute electrostatic free energy difference between conformations. *J Phys Chem B* 101, 1663–1683.

28. van Vlijmen, H.W.T., Schaefer, M., Karplus, M. (1998) Improving the accuracy of protein pK_a calculations – conformational averaging versus the average structure. *Proteins* 33, 145–158.

29. Beroza, P., Case, D.A. (1998) Calculations of proton-binding thermodynamics in proteins. *Meth Enzymol* 295, 170–189.

30. Bashford, D., Case, D.A., Dalvit, C., et al. (1993) Electrostatic calculations of side-chain pK_a values in myoglobin and comparison with NMR data for histidine. *Biochemistry* 32, 8045–8056.

31. You, T.J., Bashford, D. (1995) Conformation and hydrogen ion titration of proteins: A continuum electrostatic model with conformational flexibility. *Biophys J* 69, 1721–1733.

32. Beroza, P., Case, D.A. (1996) Including side chain flexibility in continuum electrostatic calculations of protein titration. *J Phys Chem* 100, 20156–20163.

33. Alexov, E., Gunner, M.R. (1997) Incorporating protein conformational flexibility into the calculation of pH-dependent protein properties. *Biophys J* 72, 2075–2093.

34. Georgescu, R.E., Alexov, E., Gunner, M.R. (2002) Combining conformational flexibility and continuum electrostatics for calculating pKas in proteins. *Biophys J* 83, 1731–1748.

35. Alexov, E. (2003) Role of the protein side-chain fluctuations on the strength of pairwise electrostatic interactions: comparing experimental with computed pKas. *Proteins* 50, 94–103.

36. Antosiewicz, J., McCammon, J.A., Gilson, M.K. (1996) The determination of pKas in proteins. *Biochemistry* 35, 7819–7833.

37. Khare, D., Alexander, P., Antosiewich, J., et al. (1997) pKa measurements from nuclear magnetic resonance for B1 and B2 immunoglobin G-binding domain of protein G: comparison with calculated values for nuclear magnetic resonance and X-ray structures. *Biochemistry* 36, 3580–3589.

38. Alexov, E.G., Gunner, M.R. (1999) Calculated protein and protonmotion coupled to electron transfer: Electron transfer from Q_A-Q_B to Q_B in bacterial photosynthetic reaction centers. *Biochemistry* 38, 8253–8270.

39. Bashford, D., Gerwert, K. (1992) Electrostatic calculations of the pKa values of ionizable groups in bacteriorhodopsin. *J Mol Biol* 224, 473–486.

40. Yang, A.-S., Honig, B. (1994) Structural origin of pH and ionic strength effects on protein stability. Acid denaturation of sperm whale apomyoglobin. *J Mol Biol* 237, 602–614.

41. Gorfe, A.A., Ferrara, P., Caflisch, A., et al. (2002) Calculation of protein ionization equilibria with conformational sampling pKa of a model leucine zipper, GCN4 and barnase. *Proteins* 46, 41–60.

42. Huang, X.Q., Zhou, H.X. (2006) Similarity and difference in the unfolding of thermophilic and mesophilic cold shock proteins studied by molecular dynamics. *Biophys J* 91, 2451–2463.

43. Wlodek, S.T., Antosiewicz, J., McCammon, J.A. (1997) Prediction of titration properties of structures of a protein derived from molecular dynamics trajectories. *Protein Sci* 6, 373–382.

44. Pace, C.N., Alston, R.W., Shaw, K.L. (2000) Charge–charge interactions influence the denatured state ensemble and contribute to protein stability. *Protein Sci* 9, 1395–1398.

45. Oliveberg, M., Arcus, V.L., Fersht, A.R. (1995) pKa values of carboxyl groups in the native and denatured state of barnase: The pKa values of the denatured state are on 0.4 units lower than those of model compounds. *Biochemistry* 34, 9424–9433.

46. Swint-Kruse, L., Robertson, A.D. (1995) Hydrogen bonds and the pH dependence of ovomucoid third domain stability. *Biochemistry* 34, 4724–4732.

47. Whitten, S.T., Garcia-Moreno, B. (2000) pH dependence of stability of staphylococcal nuclease: Evidence of substantial electrostatic interactions in the denatured state. *Biochemistry* 39, 14292–14304.

48. Warwicker, J. (1999) Simplified methods for pK(a) and acid pH-dependent stability estimation in proteins: Removing dielectric and counterion boundaries. *Protein Sci* 8, 418–425.

49. Elcock, A.H. (1999) Realistic modeling of the denatured states of proteins allows accurate calculations of the pH dependence of protein stability. *J Mol Biol* 294, 1051–1062.

50. Zhou, H.-X. (2002) A Gaussian-chain model for treating residual charge–charge interactions in the unfolded state of proteins. *Proc Natl Acad Sci USA* 99, 3569–3574.

51. Zhou, H.-X. (2002) Residual electrostatic effects in the unfolded state of the N-terminal domain of L9 can be attributed to nonspecific nonlocal charge–charge interactions. *Biochemistry* 41, 6533–6538.

52. Zhou, H.X. (2002) Dimensions of denatured protein chains from hydrodynamic data. *J Phys Chem B* 106, 5769–5775.

53. Zhou, H.-X. (2003) Direct test of the Gaussian-chain model for treating residual charge–charge interactions in the unfolded state of proteins. *J Am Chem Soc* 125, 2060–2061.

54. Kundrotas, P.J., Karshikoff, A. (2002) Model for calculations of electrostatic interactions in unfolded proteins. *Phys Rev E* 65, Art No 011901.

55. Tollinger, M., Forman-Kay, J.D., Kay, L.E. (2002) Measurement of side-chain carboxyl pKa values of glutamate and aspartate residues in an unfolded protein by multinuclear NMR spectroscopy. *J Am Chem Soc* 124, 5714–5717.

56. Tollinger, M., Crowhurst, K.A., Kay, L.E., et al. (2003) Site-specific contributions to the pH dependence of protein stability. *Proc Natl Acad Sci USA* 100, 4545–4550.

57. Cho, J.H., Raleigh, D.P. (2006) Electrostatic interactions in the denatured state and in the transition state for protein folding: Effects of denatured state interactions on the analysis of transition state structure. *J Mol Biol* 359, 1437–1446.

58. Kundrotas, P.J., Karshikoff, A. (2004) Charge sequence coding in statistical modeling of unfolded proteins. *Biochim Biophys Acta* 1702, 1–8.

59. Pollack, L., Tate, M.W., Darnton, N.C., et al. (1999) Compactness of the denatured state of a fast-folding protein measured by submillisecond small-angle X-ray scattering. *Proc Natl Acad Sci USA* 96, 10115–10115.

60. Kamatari, Y.O., Konno, T., Kataoka, M., et al. (1996) The methanol-induced globular and expanded denatured states of cytochrome c: A study by CD fluorescence, NMR and small-angle X-ray scattering. *J Mol Biol* 512, 512–523.

61. Segel, D.J., Fink, A.L., Hodgson, K.O. et al. (1998) Protein denaturation: A small-angle X-ray scattering study of the ensemble of unfolded states of cytochrome c *Biochemistry* 37, 12443–12451.

62. Flanagan, J.M., Kataoka, M., Shortle, D., et al. (1992) Truncated staphylococcal nuclease is compact but disordered. *Proc Natl Acad Sci USA* 89, 748–752.

63. Panick, G., Malessa, R., Winter, R., et al. (1998) Structural characterization of the pressure-denatured state and unfolding/refolding kinetics of staphylococcal nuclease by synchrotron small-angle X-ray scattering and Fourier-transform infrared spectroscopy. *J Mol Biol* 275, 389–402.

64. IbarraMolero, B., SanchezRuiz, J.M. (1997) Are there equilibrium intermediate states in the urea-induced unfolding of hen egg-white lysozyme? *Biochemistry* 36, 9616–9624.

65. Hoshino, M., Hagihara, Y., Hamada, D., et al. (1997) Trifluoroethanol-induced conformational transition of hen egg-white lysozyme studied by small-angle X-ray scattering. *FEBS Lett* 416, 72–76.

66. Kundrotas, P.J., Karshikoff, A. (2003) Effects of electrostatic interactions on dimensions of unfolded polypeptide chains with various charge distributions: Monte Carlo study. *J Chem Phys* 119, 3574–3581.

67. Kundrotas, P.J., Karshikoff, A. (2002) Modeling of denatured state for calculations of electrostatic contribution to protein stability. *Protein Sci* 11, 1681–1686.

68. Phelan, P., Gorfe, A.A., Jelesarov, I., et al. (2002) Salt bridges destabilize a leucine zipper designed for maximized ion pairing between helices. *Biochemistry* 41, 2998–3008.

69. Ibarra-Molero, B., Loladze, V.V., Makhatadze, G.I. et al. (1999) Thermal versus guanidine-induced unfolding of ubiquitin. An analysis in terms of the contributions from charge–charge interactions to protein stability. *Biochemistry* 38, 8138–8149.

70. Bolen, D.W., Yang, M. (2000) Effects of guanidine hydrochloride on the proton inventory of proteins: Implications on interpretations of protein stability. *Biochemistry* 39, 15208–15216.

71. Marklay, J.L. (1975) Observation of histidine residues in proteins by means of nuclear magnetic resonance spectroscopy. *Acc Chem Res* 8, 70–80.

72. Shrager, R.I., Barker, P.B., Freeman, R. (1972) Computer-optimized decoupling scheme for wideband application and low-level operation. *J Magn Reson* 11, 541–547.

73. Blomberg, F., Mauer, W., Rüterjans, H. (1977) Nuclear magnetic resonance investigation of ^{15}N-labeled histidine in aqueous solution. *J Am Chem Soc* 39, 8149–8159.

74. Yang, A.-S., Gunner, M.R., Sampogna, R., et al. (1993) On the calculation of pK$_a$s in proteins. *Proteins* 15, 252–265.

75. Koumanov, A., Ladenstein, R., Karshikoff, A. (2001) Electrostatic interactions in proteins: Contribution to structure–function relationships and stability, in (Pandalai, R., ed.) *Recent Research Developments in Protein Engineering*. Research Signpost, Trivandrum. pp. 123–148.

76. Horovitz, A., Serrano, L., Avron, B., et al. (1990) Strength and cooperativity of contributions of surface salt bridges to protein stability. *J Mol Biol* 216, 1031–1044.

77. Xue, W.F., Szczepankiewicz, O., Bajer, M. C., et al. (2006) Intra- versus intermolecular interactions in monellin: Contribution of surface charges to protein assembly. *J Mol Biol* 358, 1244–1255.

78. Ren, B., Tibbelin, G., Pascale, D., et al. (1998) A protein disulfide oxidoreductase from the archaeon *Pyrococcus furiosus* contains two thioredoxin fold units. *Nat Struct Biol* 5, 602–611.

79. Lyu, P.C.C., Gans, P.J., Kallenbach, N.R. (1992) Energetic contribution of solvent-exposed ion-pairs to alpha-helix structure. *J Mol Biol* 223, 343–350.

80. Anderson, D.E., Becktel, W.J., Dahlquist, F.W. (1990) pH-Induced denaturation of proteins: a single salt bridge contributes 3–5 kcal/mol to the free energy of folding of T4 lysozyme. *Biochemistry* 29, 2403–22408.

81. Spassov, V.Z., Atanasov, B.P. (1994) Spatial optimization of electrostatic interactions between the ionized groups in globular proteins. *Proteins* 19, 222–229.

82. Spassov, V.Z., Karshikoff, A.D., Ladenstein, R. (1994) The optimisation of the electrostatic interactions in proteins of different functional and folding type. *Protein Sci* 3, 1556–1569.

83. Caflisch, A. and M. Karplus (1995) Acid and thermal denaturation of barnase investigated by molecular dynamics simulation. *J Mol Biol* 252, 627–708.

84. Sheldahl, C., Harvey, S.C. (1999) Molecular dynamics on a model for nascent high-density lipoprotein: Role of salt bridges. *Biophys J* 76, 1190–1198.

85. Gruia, A.D., Fischer, S., Smith, J.C. (2004) Kinetics of breaking a salt-bridge critical in protein unfolding. *Chem Phys Lett* 385, 337–340.

86. Bjelic, S., Wieninger, S., Jelesarov, I., et al. (2008) Electrostatic contribution to the thermodynamic and kinetic stability of the homotrimeric coiled coil Lpp-56: A computational study. *Proteins 70*, 810–822.

87. Shu, W., Liu, J., Ji, H., et al. (2000) Core structure of the outer membrane lipoprotein from *Escherichia coli* at 1.9 Å resolution. *J Mol Biol* 299, 1101–1112.

88. Tanaka, T., Sawano, M., Ogasahara, K., et al. (2006) Hyper-thermostability of CutA1 protein, with a denaturation temperature of nearly $150°C$. *FEBS Lett* 580, 4224–4230.

89. Waldburger, C.D., Schildbach, J.F., Sauer, R.T. (1995) Are buried salt bridges important for protein stability and conformational specificity? *Struct Biol* 2, 122–128.

90. Magyar, C., Szilagyi, A., Zavodszky, P. (1996) Relationship between thermal stability and 3-D structure in a homology model of 3-isopropylmalate dehydrogenase from *Escherichia coli*. *Protein Eng* 9, 663–670.

91. Karlsson, E.N., Crennell, S.J., Higgins, C., et al. (2003) Citrate synthase from *Thermus aquaticus*: a thermostable bacterial enzyme with a five membered inter-subunit ionic network. *Extremophiles* 7, 9–16.

92. Karlstrom, M., Steen, I.H., Madern, D., et al. (2006) The crystal structure of a hyperthermostable subfamily II isocitrate dehydrogenase from *Thermotoga maritima*. *FEBS J* 273, 2851–2868.

93. Sciacca, M.F.M., Milardi, D., Pappalardo, M., et al. (2006) Role of electrostatics in the thermal stability of ubiquitin – A combined DSC and MM study. *J Therm Anal Calor* 86, 311–314.

94. Robinson-Rechavi, M., Alibes, A., Godzik, A. (2006) Contribution of electrostatic interactions, compactness and quaternary structure to protein thermostability: Lessons from structural genomics of *Thermotoga maritima*. *J Mol Biol* 356, 547–557.

95. Bell, G.S., Russell, R.J.M., Connaris, H., et al. (2002) Stepwise adaptations of citrate synthase to survival at life's extremes – From psychrophile to hyperthermophile. *Biochemistry* 269, 6250–6260.

96. Spassov, V.Z., Karshikoff, A.D., Ladenstein, R. (1995) The optimization of protein–solvent interactions. Thermostability and the role of hydrophobic and electrostatic interactions. *Protein Sci* 4, 1516–1527.

97. Berezovsky, I.N., Chen, W.W., Choi, P.J., et al. (2005) Entropic stabilization of proteins and its proteomic consequences. *PLoS Comput Biol* 1, 322–332.

98. Lee, D.Y., Kim, K.A., Yu, Y.G., et al. (2004) Substitution of aspartic acid with glutamic acid increases the unfolding transition temperature of a protein. *Biochem Biophys Res Commun* 320, 900–906.

99. Greaves, R.B., Warwicker, J. (2007) *BMC Struct Biol* 7, 18.

100. Elcock, A.H. (1998) The stability of salt bridges at high temperatures – implications for hyperthermophilic proteins. *J Mol Biol* 284, 489–502.

101. Martin, A., Sieber, V., Schmid, F.X. (2001) In vitro selection of highly stabilized protein variants with optimized surface. *J Mol Biol* 309, 717–726.

102. Chan, M.K., Mukund, S., Kletzin, A., et al. (1995) Structure of a hyperthermophilic tungstopterin enzyme, aldehyde ferredoxin oxidoreductase. *Science* 267, 1463–1469.

103. Knapp, S., de Vos, W.M., Rice, D., et al. (1997) Crystal structure of glutamate dehydrogenase from the hyperthermophilic eubacterium *Thermotoga maritima* at 2.5 Å resolution. *J Mol Biol* 267, 916–932.

104. Korndörfer, I., Steipe, B., Huber, R., et al. (1997) The crystal structure of holo-glyceraldehyde-3-phosphate dehydrogenase from the hyperthermophilic bacterium *Thermotoga maritima* at 2.5 Å resolution. *J Mol Biol* 246, 511–521.

105. Yip, K.S.P., Britton, K.L., Stillman, T.J., et al. (1998) Insights into the molecular basis of thermal stability from the analysis of ion-pair networks in the glutamate dehydrogenase family. *Eur J Biochem* 255, 336–346.

106. Danson, M.J., Hough, D.W., Russell, R.J.M., et al. (1996) Enzyme thermostability and thermoactivity. *Protein Eng* 9, 629–630.

107. Ishikawa, K., Okumura, M., Katayanagi, K., et al. (1993) Crystal structure of ribonuclease H from *Thermus thermophilus* HB8 refined at 2.8 Å resolution. *J Mol Biol* 230, 529–542.

108. Henning, M., Sterner, R., Kirschner, K., et al. (1997) Crystal structure ar 2.0 Å resolution of phosphoribosil anthranilate isomerase from the hyperthermophile *Thermotoga maritima*: Possible determinants of protein stability. *Biochemistry* 36, 6009–6016.

109. Lebbink, J.H.G., Consalvi, V., Chiaraluce, R., et al. (2002) Structural and thermodynamic studies on a salt-bridge triad in the NADP-binding domain of glutamate dehydrogenase from *Thermotoga maritima*: cooperativity and electrostatic contribution to stability. *Biochemistry* 41, 15524–15535.

110. Horovitz, A., Fersht, A.R. (1990) Strategy for analysing the co-operativity of intramolecular interactions in peptides and proteins. *J Mol Biol* 214, 613–617.

Chapter 11

Protein Stabilization by the Rational Design of Surface Charge–Charge Interactions

Katrina L. Schweiker and George I. Makhatadze

Abstract

The design of proteins with increased stability has many important applications in biotechnology. In recent years, strategies involving directed evolution, sequence-based design, or computational design have proven successful for generating stabilized proteins. A brief overview of the various methods that have been used to increase protein stability is presented, followed by a detailed example of how the rational design of surface charge–charge interactions has provided a robust method for protein stabilization.

Key words: Protein stability, computational design, surface charge–charge interactions.

1. Introduction

The ability to design stable proteins is of great importance to biotechnology and other industries. In order to design or engineer proteins with increased stability, it is necessary to have a fundamental understanding of the intramolecular forces that contribute to stabilizing the native conformation. The protein core is stabilized by hydrophobic interactions between buried nonpolar side chains *(1–3)*. Burial of polar residues in the core is unfavorable due to the high energetic cost of desolvation *(4, 5)*. This energetic penalty can be offset by forming hydrogen bonds with other polar groups or buried water molecules. The core residues are further stabilized by van der Waals (packing) interactions *(4, 6–8)*. Hydrogen bonding and packing interactions in the protein core have been demonstrated to be as important as hydrophobicity for stability *(8–10)*. More recently it has been shown that surface residues are also modulating the stability of a protein *(11–16)*.

The term "protein stability" can have different meanings depending on the focus of the research being performed. Protein stability can refer to the change in Gibbs free energy upon unfolding (ΔG), thermostability (T_m), rates of folding or unfolding, in vivo degradation rates, or retention of activity after being exposed to harsh chemical or thermal conditions. The transition temperature and Gibbs free energy are measures of thermodynamic stability. They are interrelated in such a way that it is possible to alter the stability (ΔG) of a protein without affecting the thermostability *(17)* and vice-versa *(15)* (**Fig. 11.1**). This is a result of the relationship between ΔG, T_m, and the other thermodynamic parameters of enthalpy (ΔH), entropy (ΔS), and change in heat capacity upon unfolding (ΔC_p). The thermodynamic stability (ΔG) for a protein that unfolds via a two-state transition, N↔U, can be described by the equilibrium constant, K_{eq}, which is the ratio of the fraction of folded protein (F_N) to the fraction of unfolded protein (F_U) in a sample.

$$\Delta G = -RT \cdot \ln(K_{eq}) = -RT \cdot \ln\left(\frac{F_U}{F_N}\right). \qquad (11.1)$$

The change in stability (ΔG) at any temperature, T, is related to the thermostability (T_m) of the protein via the Gibbs–Helmholtz equation.

$$\Delta G(T) = \Delta H(T_m) + \Delta C_P \cdot (T - T_m) - T \cdot \left[\frac{\Delta H(T_m)}{T_m} + \Delta C_P \cdot \ln\left(\frac{T}{T_m}\right)\right],$$
$$(11.2)$$

where $\Delta H(T_m)$ is the enthalpy of unfolding at T_m and ΔC_p is the change in heat capacity upon unfolding that characterizes the temperature dependence of both the enthalpy and entropy functions. Equation 2 assumes temperature-independent ΔC_p. The transition temperature, T_m, is the temperature where 50% of the protein is unfolded. The enthalpy and entropy at any temperature, T, are $\Delta H(T) = \Delta H(T_m) + \Delta C_p(T - T_m)$ and $\Delta S(T) = \Delta H(T_m)/T_m + \Delta C_p \cdot \ln(T/T_m)$, respectively. Changes in the heat capacity, enthalpy, and entropy of unfolding due to amino acid substitutions in the protein define the thermodynamic mechanisms by which T_m and/or ΔG are increased.

1.1. Thermodynamic Mechanisms of Stabilization

The stability function, $\Delta G(T)$, defined by the Gibbs–Helmholtz equation (**Eq. 11.2**) is a bell-shaped curve (**Fig. 11.1A**), because the ΔC_p for protein unfolding is positive. The stability of a protein is equal to zero when 50% of the molecules are folded and 50% are unfolded. This occurs at two temperatures: T_m is the heat-denaturation transition temperature and T_c is the cold-denaturation transition temperature. The stability function has a maximum (ΔG_{max}) at the temperature where the entropic
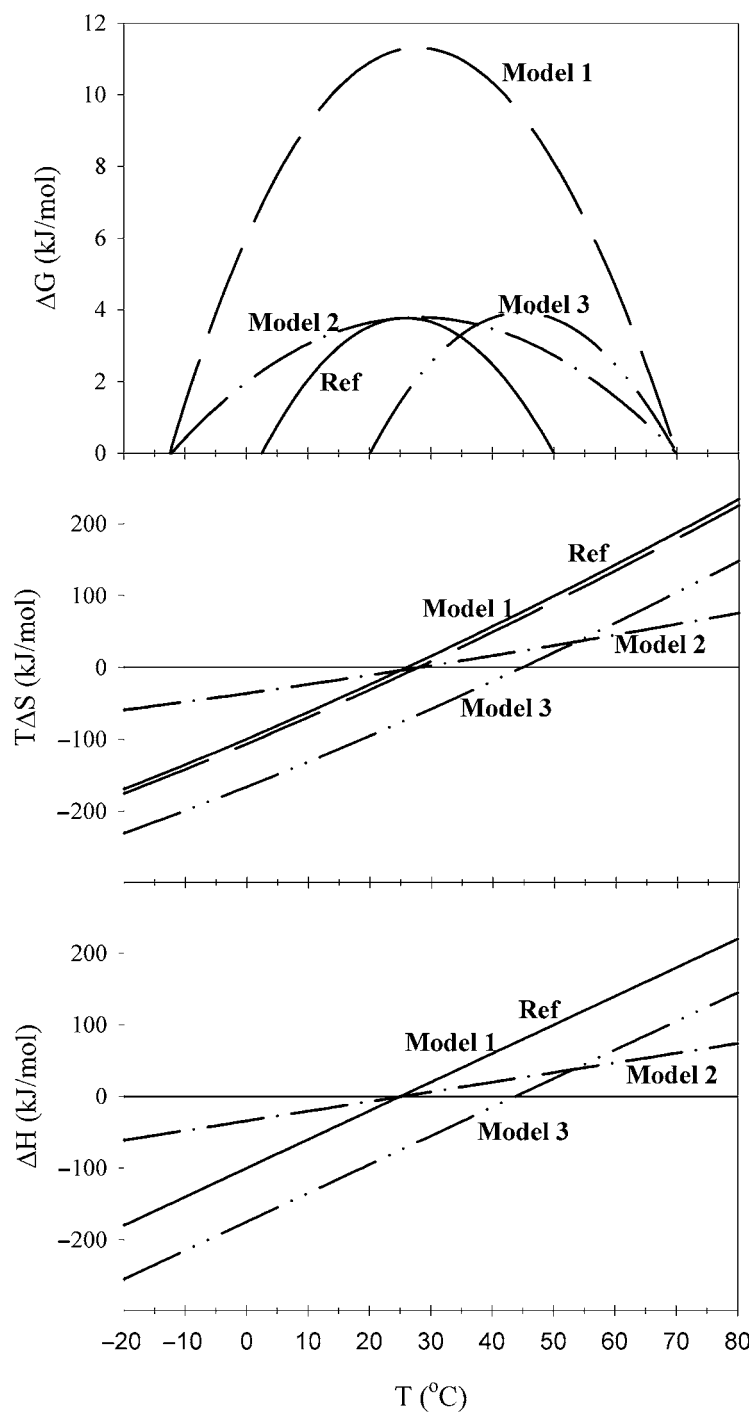
Fig. 11.1. Three thermodynamic mechanisms of thermostabilization. To highlight the differences more clearly, extreme examples of each mechanism of stabilization have been modeled. In each panel, different thermodynamic mechanisms are represented by the following lines: solid – Reference State; dashed – Mechanism 1; dash-dot-dashed – Mechanism 2; dash-dot-dot-dashed – Mechanism 3. **A.** The Gibbs free energy as a function of temperature. **B.** The temperature dependence of the entropy. **C.** The temperature dependence of the enthalpy function. Reproduced from **Ref** *(15)* with permission from Elsevier.

contribution is equal to zero (T_{max}). The changes ΔH, ΔS, and ΔC_p, in response to substitutions within the protein, will have an effect on the transition temperature and will define the thermodynamic mechanism by which the protein thermostability is increased or decreased. **Figure 11.1** illustrates three possible thermodynamic mechanisms of thermostabilization. Large changes in the relevant thermodynamic parameters for each mechanism have been modeled to make the differences among them clearer. In practice, however, combinations of these models are more appropriate for explaining experimental observations. Stabilization by the first mechanism results in a large increase in both the maximum stability (ΔG_{max}) and the thermostability (T_m) of the protein (**Fig. 11.1A**) caused by a small decrease in the entropy of unfolding (**Fig. 11.1B**). However, the enthalpy function (**Fig. 11.1C**) and heat capacity are unchanged. In the second model, a decrease in ΔC_p results in a ΔG function with decreased temperature dependence, ultimately causing an increase in T_m, without affecting T_{max} or the absolute value of ΔG_{max}. The third mechanism causes the entire ΔG function to shift to higher temperatures. This shift is a result of a large decrease in both the enthalpy and entropy of unfolding, which increases both T_m and T_{max} without affecting the absolute value of ΔG_{max}. In all three models the overall stability of the protein at room temperature is affected differently. In both the first and third mechanisms, the stability at room temperature (ΔG_{RT}) changes relative to the reference state. ΔG_{RT} increases in Model 1 and decreases in Model 3 (**Fig. 11.1A**). The second mechanism illustrates how the thermostability of a protein can be altered without affecting the overall stability at room temperature. By understanding the underlying mechanisms of stabilization, proteins can in principle be designed to meet desired thermodynamic criteria.

1.2. Protein Stabilization Approaches

The approaches to stabilizing proteins can be grouped into three major categories: directed evolution, sequence-based design, and computational design. Each has its own advantages and disadvantages that should be considered when deciding which to use for the design of stable proteins. A few of the factors to be considered include the amount of prior information required (i.e., sequence vs. 3D structure) to carry out the design, how quickly the result can be obtained, and the universal applicability of the method. A brief comparison of the three design categories in terms of these issues is provided below and summarized in **Table 11.1**.

1.2.1. Directed Evolution

Directed evolution uses random mutagenesis, targeted mutagenesis, or homologous recombination to introduce mutations into a gene of interest *(18, 19)*. Random mutagenesis is the simplest approach, in the sense that it requires virtually no prior information about the protein. Combining error-prone PCR with screening

Table 11. 1
Comparison of the different approaches used to design/engineer stable proteins

	Directed evolution	Sequence-based design	Computational design
3D Structure	No	No	Yes
Speed	Slow	Fast	Fast
Labor intensive	Yes	No	No
Guaranteed results	Maybe	No	No
Universal	No	Maybe	Yes
Mechanism of stabilization	Unknown *	Unknown *	Thermodynamic *

* Computational design approaches model and optimize specific intramolecular interactions, increasing protein stability via thermodynamic mechanisms. On the other hand, the selection pressures used in directed evolution and sequence-based design lack specificity in terms of which interactions are optimized. As a result, the primary mechanism of stabilization could be a slower unfolding rate (kinetic mechanism), the optimization of specific intramolecular interactions (thermodynamic mechanism), or both.

and selection has been effective for altering the function *(20)*, the stability *(21)*, or both *(22)* of various proteins. Targeted mutagenesis is most effective for instances where it would be difficult to find the best mutations using random mutagenesis, such as significantly changing the function of a protein *(23)*. In this case, it is necessary to have some structural or biochemical information about the protein so that mutagenesis can be directed to the appropriate active site residues. Homologous recombination between proteins with a very high sequence identity can be used to introduce more diversity into the sequence library than is possible through random mutagenesis. It has been used to create proteins with improved activity *(21, 22, 24, 25)*, higher thermostability *(21, 22, 24, 26, 27)*, or entirely new functions *(28)*. Recombination has been demonstrated to be a successful approach not only when used alone *(24, 27, 28)*, but also when applied in combination with targeted or random mutagenesis *(21, 22, 25, 26)*. Regardless of which directed evolution approaches are used, the first, and arguably most important, step is to create a diverse library of sequences. Then selection pressure is applied to the library and it is screened for proteins that retain desired properties under the selected conditions. Examples of selection pressure include increasing temperature, antibiotic concentrations, or protease concentrations. Selection can also occur in a thermophilic host, which forces the protein to evolve in a biological context *(29)*. The advantage of this type of selection is that the protein will not lose its natural function during the evolutionary

process. Multiple rounds of mutation, screening, and selection are often necessary before the best protein variant can be identified.

Several different proteins have been stabilized using directed evolution *(29–32)*. Subtilisins and *p*-nitrobenzyl esterase (PNE) were stabilized using random mutagenesis and then selecting for both stability at high temperatures and function at lower temperatures, with the result that thermostable variants maintained activity across a broader range of temperatures than naturally evolved enzymes *(22, 29)*. These experiments suggested that stability and function are not mutually exclusive parameters. In the case of the subtilisin family of proteins, most of the stabilizing substitutions that occurred as a result of directed evolution were not found in the thermophilic proteins, and therefore would not have been selected using sequence-based approaches *(29)*. One disadvantage of the method used to stabilize the subtilisins and PNE is that new functional assays had to be developed for each protein. A way to circumvent this requirement is to link selection directly to the ability of a protein to fold, rather than the ability to maintain activity *(30–38)*. The PROSIDE method *(30)*, developed by Schmid and coworkers does just that. It links the protease resistance of a protein to phage infectivity, and relies on the assumption that a stable protein will be more resistant to protease. Three different proteins, RNase T1 *(30)*, CspB *(31, 35, 37)*, and Gβ1 *(32, 38)* have been successfully stabilized using this method. Recently, a similar phage display approach was used to increase the thermostability of an antibody by 9°C *(36)*.

Directed evolution is advantageous over computational design in the sense that no prior information about the protein structure is required. It is only necessary to know the protein sequence so it can be cloned appropriately and whether stability can be easily assayed. Moreover, as long as appropriate constraints are applied, stability and function can be enhanced simultaneously *(22)*. The major disadvantage is that obtaining the final product can be slow because it takes time to construct libraries that are sufficiently diverse and to develop appropriate selection criteria and functional assays. In addition, important properties of the protein can be lost if they are not selected for directly *(39)*. The screening process is also very labor-intensive, and often the most time-consuming step *(29)*. Another disadvantage is that there is no way to know *a priori* the mechanisms of stabilization. Also, it is not possible to know whether all substitutions are important since multiple random substitutions are simultaneously introduced into the sequence. As a result, it will be difficult to learn more about why these particular substitutions were stabilizing for these proteins. Furthermore, directed evolution is not a universal approach and needs to be customized for each individual protein as a different set of sequence libraries and selection criteria must be developed for each protein.

1.2.2. Sequence-Based Design

Sequence-based design refers to approaches that use the information contained in multiple sequence alignments to create more stable protein variants. The premise for these methods is that since the primary structure of a protein encodes all the information needed for folding into the native tertiary structure, it also contains information about stability. In natural evolution, proteins tend to be selected for function. In addition, the proteins need to be able to be easily degraded when they are no longer needed, so there is little evolutionary pressure for proteins to have high stabilities. As a result, the consensus sequence that can be obtained from a multiple sequence alignment is not always the most stable. More sophisticated statistical analyses, however, have made it possible to identify stabilizing properties from multiple sequence alignments *(40, 41)*.

One of the sequence-based design approaches is based on the hypothesis that since, arguably, life originated in an extremely hot environment, the last common ancestor of all organisms is hyperthermophilic. Therefore, substituting a residue that was present in the last common ancestor into a modern protein should increase its thermostability *(42)*. Since the ancestral residues are often also the consensus residue for a particular position, it raises the question: can the observed changes in stability be explained by the statistical free energy of the residue (the consensus approach), or are they due to the presence of an ancestral residue? To address this question, the enzyme 3-isopropylmalate dehydrogenase (IPMDH) was redesigned using phylogenetic analysis *(42)*. The stabilities of 12 protein variants containing single site substitutions of amino acids to their ancestral residue were characterized. Eight of the ancestral residues were the same as the consensus and four were not. However, both categories had the same success rates – half of the substitutions yielded protein variants that were more stable than the wild-type *(42)*. These results suggest that stabilization by ancestral substitutions is not simply due to the statistical free energies of the residues.

Sequence-based approaches have also been used to design stable variants by making multiple substitutions simultaneously. In one example, two Bayesian statistical approaches were used to analyze a multiple sequence alignment of the subtilisin protein family. The first method, PROBE *(43)* identified a set of conserved domains that is characteristic to the protein family. Then Classifier *(44)* was used to find a smaller subset of important residues based on specific sequence motifs. By coupling PROBE and Classifier, it was possible to identify a sequence motif that was present in some of the thermophilic subtilisins, but not the mesophilic proteins. To test whether this 16-residue motif was responsible for the increased stabilities of the thermophilic enzymes, the sequence was inserted into a mesophilic subtilisin, and the stability and activity of the variant were characterized. The variant had an

increased thermostability of 13°C relative to the wild-type enzyme, and was able to retain some activity at 90°C, a temperature where the wild-type subtilisin is completely inactive *(45)*.

Sequence-based design methods are advantageous over computational design methods because no three-dimensional structure is required for design. They are less time-consuming than directed evolution because diverse in vivo sequence libraries do not need to be developed and multiple rounds of selection do not need to be performed for each protein to be optimized. The successful redesign of the two different enzymes described above highlights the potential of sequence-based design to be a universal approach to protein stabilization. One of the disadvantages of sequence-based design is that the hypothesis that the ancestral protein is hyperthermophilic might not be correct for all proteins *(46)*. In this case, the substitutions selected based on the ancestral protein sequence may not necessarily lead to increases in thermostability since the ancestral sequence is mesophilic. Another disadvantage of this approach is that the statistical analysis of multiple sequence alignments requires a large number of sequences. If a given protein family does not contain enough sequences to generate a statistically meaningful alignment, then it might not be possible to appropriately identify the ancestral gene. As a result, the selected substitutions might not actually be present in the ancestral protein sequence and, therefore, would not lead to increased thermostability.

1.2.3. Computational Design

Computational design methods use known three-dimensional structures of proteins to model the energetics of native-state interactions. If an NMR or X-ray crystal structure is not available for a given protein, but it has a high degree of homology to proteins for which structures are available, then the protein can be redesigned using homology modeling. Computational approaches have tended to focus on optimizing interactions in the protein core *(6, 47–51)*. However, attempts to increase the stability of proteins by redesigning the core have yielded mixed results *(6, 7, 51, 52)*. Core redesign is challenging for a couple of reasons. First, the protein core is tightly packed, suggesting that interactions within it have already been optimized. In order to further improve the interactions within the core, precise modeling of the positions of the side chains is required. Second, most core redesign methods use a fixed backbone in the modeling process *(6, 49, 53)*. While this assumption is necessary to minimize the search space, it has been demonstrated that the backbone does indeed shift to accommodate substitutions *(52)*. The flexibility of the backbone makes it difficult to predict the effects of multiple core substitutions on protein stability *(52)*.

One way to overcome the challenges associated with redesigning the core of the protein is to focus on optimizing interactions

on the protein surface. Surface redesign is advantageous over core redesign because residues on the surface have greater conformational flexibility than those in the core. As a result, the modeling of surface side chains does not have to be as precise to yield a good description of surface interactions. Recent work has provided experimental evidence that surface residues provide an effective means for modulating protein stability *(11–16, 54–56)*. Further support for surface redesign comes from a theoretical study on the physical origin of stability. This study suggested that in response to evolutionary pressure, mesophilic proteins obtain higher thermostability by increasing the number of charged residues *(46)*, which are more likely to be found on the protein surface than in the core.

A major advantage of computational design methods over directed evolution or sequence-based design approaches is that they have been demonstrated to be universal *(16)*. Computational design, like the sequence-based design approaches, is faster than directed evolution because the energetic calculations can be performed more quickly than multiple rounds of screening and selection. It is also possible to qualitatively predict the stabilities of proteins using computational design *(11, 15, 16)*. Furthermore, these approaches have the potential to be developed into algorithms that can quantitatively predict the stabilities of the designed sequences. The main disadvantage of computational design is that three-dimensional structures are required to model the intramolecular interactions in the native state, so proteins that are not homologous to any known structures cannot be redesigned using computational methods.

2. Rational Design of Surface Charge–Charge Interactions

An approach to generate stable proteins through the rational design of surface charge–charge interactions has recently been developed *(11, 15, 16)*. In this method, the energies of charge–charge interactions on the protein surface are calculated using the Tanford–Kirkwood model corrected for solvent accessibility (TK-SA) *(57–60)*. The TK-SA model treats proteins as hard spheres from which solvent ions are excluded. The ionizable groups in the protein are modeled as point charges that occupy fixed positions, and it is assumed that the interaction between the surface charges is the only type of interaction between the groups

(57). The interaction energies between the surface charges of residues i and j are calculated as

$$E_{ij} = \varepsilon^2 \left(\frac{A_{ij} - B_{ij}}{2b} - \frac{C_{ij}}{2a} \right) \cdot (1 - SA_{ij}), \qquad (11.4)$$

where ε is the unit charge; b is the radius of the sphere representing the protein is derived from its specific volume; and a is the radius of the sphere from which solvent ions are excluded. A_{ij}, B_{ij}, and C_{ij} are functions of the positions of the charges, the dielectric constants of the protein and solvent, as defined previously by Tanford and Kirkwood *(57)*. C_{ij} is also a function of the ionic strength of the solvent. The term SA_{ij} is the average solvent accessibility of groups i and j and is calculated as previously described *(61, 62)*.

The contribution of charge–charge interaction energies to the Gibbs free energy of unfolding is determined from changes in pKa values of the protein upon substitution relative to model compounds. The energy of a given protonation state (χ) in the native sate of a protein is

$$\Delta G_N(\chi) = -RT(\ln 10) \sum_{i=1}^{n} (q_i + x_i) pK_{\mathrm{int},i} + \frac{1}{2} \sum_{i,j=1}^{n} E_{ij}(q_i + x_i)(q_j + x_j), \qquad (11.5)$$

where x_i, and x_j are equal to –1, 0, or +1 depending on the protonation state of groups i and j; q_i is the charge of group i in the unprotonated state; and the intrinsic pK, $pK_{int,i}$, is the pK of group i if all other groups had zero charge and is determined from model compounds. Since it is assumed that there are no charge–charge interactions in the unfolded state, the energy of the protonation state, χ, in the unfolded state of a protein is defined by the intrinsic pK values:

$$\Delta G_U(\chi) = -RT(\ln 10) \sum_{i=1}^{n} (q_i + x_i) pK_{\mathrm{int},i}. \qquad (11.6)$$

These energies can be used to define the partition functions Z_N and Z_U for the native and unfolded states, respectively:

$$Z_N = \sum_{\chi} \exp\left(-\frac{\Delta G_N(\chi)}{RT} - \nu(\chi)(\ln 10) pH \right), \qquad (11.7)$$

$$Z_U = \sum_{\chi} \exp\left(-\frac{\Delta G_U(\chi)}{RT} - \nu(\chi)(\ln 10) pH \right), \qquad (11.8)$$

where $\nu(\chi)$ represents the number of protonated ionizable groups in the protonation state, χ. The neutral forms of the native and unfolded states $(\Delta G_N(\chi) = 0$ and $\Delta G_U(\chi) = 0)$ are the reference states for both Z_N and Z_U, so the overall contribution of charge–charge interactions to the Gibbs free energy of unfolding is

$$\Delta G_{qq} = -RT \ln\left(\frac{Z_U}{Z_N}\right). \qquad (11.9)$$

To account for the flexibility of side chains on the protein surface in the calculations of charge–charge interaction energies (ΔG_{qq}), an ensemble of different structures is generated by homology modeling using Modeller v. 7.7 *(63)*. **Figure 11.2A** illustrates the results of the TK-SA calculations for wild-type ubiquitin. The value of ΔG_{qq} for any given residue represents the energy of the interactions between that residue and every other charged residue in the protein. Positive values of ΔG_{qq} indicate that these residues participate in unfavorable interactions, while negative values indicate the interactions are favorable. Ubiquitin has several residues that participate in unfavorable interactions, leading to the hypothesis that the stability can be increased by neutralizing or reversing the charges of residues participating in unfavorable interactions. Furthermore, it should be possible to gain larger increases in stability through charge reversal than neutralization *(11)*.

To test this hypothesis, nine single substitutions were made in the ubiquitin model system. Three variants that neutralized the charges at unfavorable positions (K6Q, H68Q, and R72Q) and three that reversed the charges at unfavorable positions (K6E, R42E, and H68E) were constructed. As a control, three variants that neutralized the charges at positions predicted to contribute favorably to stability (K27Q, K29Q, and K29N) were also constructed. Since thermal denaturation of ubiquitin at neutral pH is irreversible *(64)*, the stabilities of these variants were measured by monitoring changes in secondary structure as a function of denaturant concentration using far-UV circular dichroism spectroscopy (CD) *(65)*. It was observed that neutralization of the unfavorable charges was indeed stabilizing, as predicted. Moreover, charge reversal yielded further increases in stability of approximately 1 kJ/mol. Importantly, when the charges predicted to contribute favorably were neutralized, the stability of the ubiquitin variants was significantly decreased relative to the wild-type.

The robustness of this model was tested using six proteins: RNaseSA, peripheral subunit binding domain (Psbd41), rubredoxin, L30e, α-lactalbumin, and the bacterial cold shock protein (CspB). In the initial test, the calculated values of ΔG_{qq} were compared to the experimental stabilities reported in the literature for three of the model systems: RNaseSa *(12)*, Psbd41 *(13)*, and rubredoxin *(66)*. The changes in both the thermostabilities (ΔT_m) and stabilities ($\Delta\Delta G_{exp}$) of the substituted variants relative to their respective wild-type proteins were compared to the changes in charge–charge interaction energy ($\Delta\Delta G_{qq}$) expected from the substitutions *(67)*. It was observed that the changes in thermostability and stability for these proteins could be predicted from the calculated changes in ΔG_{qq}.
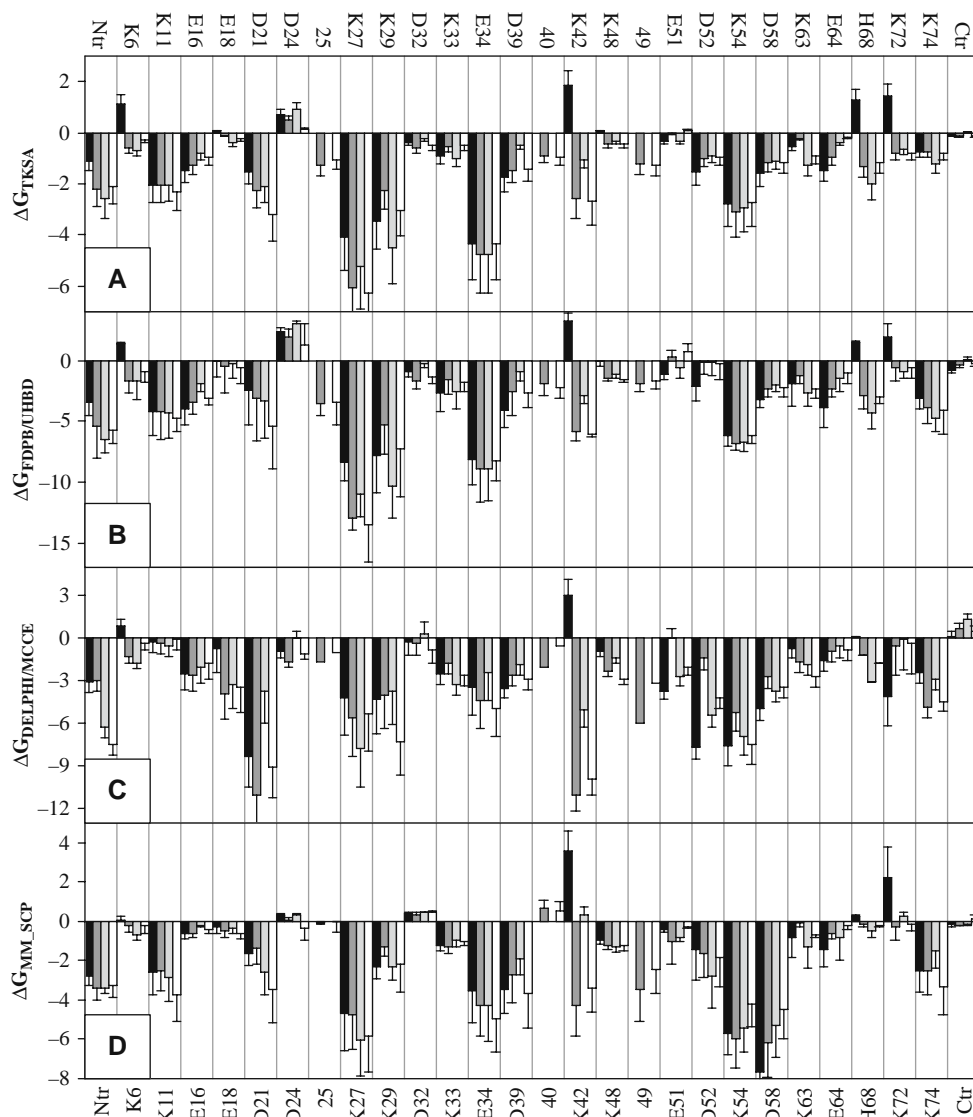
Fig. 11.2. Surface charge–charge interaction energies (ΔG_{qq}) for wild-type and designed variants of ubiquitin at pH 5.5. The charge–charge interactions were calculated using four different models. (**A**) TK-SA, (**B**) FDPB-UHBD, (**C**) MMCE, (**D**) MM_SCP. Each bar represents the total energy of charge–charge interactions of the corresponding residue with every other residue in the protein, averaged over an ensemble of 11 structures. Positive values of ΔG_{qq} are indicative of unfavorable interactions, while negative values correspond to favorable interactions. *Black bars* – wild-type ubiquitin; *dark grey bars* – UBQ-GA#1; *light grey bars* – UBQ-GA#2; and *white bars* – UBQ-GA#3, represent designed sequences that were identified by the genetic algorithm. UBQ-GA#1 and UBQ-GA#3 included uncharged polar residues in the optimization, while UBQ-GA#2 did not. Reproduced from **Ref.** *(16)* with permission from the American Chemical Society.

The ribosomal protein L30e from *Thermococcus celer* provided an opportunity to determine the extent to which surface charge–charge interactions affect protein stability. In this experiment, the effects of charge to alanine substitutions were predicted using the

TK-SA model for 26 positions on the surface of L30e. Alanine substitutions alter side chain packing interactions, hydrophobicity, and secondary structure propensity, in addition to eliminating charges. If these other interactions contribute significantly to stabilization at these positions, then it would be expected that the calculated values of ΔG_{qq} would not be able to predict the experimentally observed changes in stability. However, the experimental changes in stability were correctly predicted for almost all of the positions. The six positions that were predicted incorrectly were all located at the N or C termini of α-helices, and are therefore likely to be participating in specific interactions at the helix ends. The identity of the residues in helix-capping positions has been previously demonstrated to be important for thermodynamic stability (68–74). It is likely that the nonelectrostatic interactions important for capping motifs have a larger contribution to stability than the charge–charge interactions at these positions.

α-Lactalbumin is a small calcium-binding protein found in milk that has recently been observed to bind highly basic proteins and histones through electrostatic interactions. The *apo* form was predicted to have many unfavorable surface charge–charge interactions (75). The conformational change induced by calcium binding does not appear to significantly affect the unfavorable interactions. However, the presence of the calcium ion does create favorable interactions for the residues directly involved in binding, although residues far from the binding loop maintained unfavorable interactions. It was possible to predict the effects of the single site substitutions in α-lactalbumin through changes in the surface charge–charge interaction energies, and it was found that the changes in thermostability directly correlate to changes in the calcium affinity of the protein. Importantly, not only was this the first attempt at rational design for α-lactalbumin, but it was also the first successful stabilization of this protein (75).

To learn more about the nature of protein stabilization through the rational design of surface charges, the CspB bacterial cold shock protein was used as a model system. The calculated surface charge–charge interaction energies from the mesophilic *Bacillus subtilis* (CspB-Bs), the thermophilic *B. caldolyticus* (CspB-Bc), and the hyperthermophilic *Themotoga maritima* (CspB-Tm) were compared (15, 67). Although the sequences are highly homologous, the surface charge distributions of these three proteins are very different. It was observed that CspB-Bs has more unfavorable interactions than either CspB-Bc or CspB-Tm and that CspB-Bc has fewer favorable interactions than CspB-Tm, which correlates with the relative thermostabilities of these proteins. A cold shock protein (CspB-TB) was designed that contained the same core residues as CspB-Bs but the surface charge distribution of CspB-Tm to determine whether an increased number of favorable surface charge–charge interactions does increase the stability of

the protein. The thermal stabilities of CspB-Bs and CspB-TB were measured using CD and it was observed that the thermostability of the designed protein was increased by 20°C *(15)*.

CspB-Bs and CspB-TB are structurally similar, but have very different surface charge distributions. Making the same substitutions in these proteins provided a unique opportunity to learn more about how the electrostatic contributions in the unfolded state affect protein stability and whether the substitutions are affecting interactions other than those between charges. Comparison of the predicted ($\Delta\Delta G_{qq}$) and experimentally measured changes in stability ($\Delta\Delta G_{exp}$) showed that it was possible to predict the effects of most substitutions. Those that were predicted incorrectly were located in a β-hairpin, suggesting that charge–charge interactions in the unfolded state could be affecting the contributions of these residues to protein stability. However, the correlation was not improved when the Gaussian chain model *(76)* of the unfolded state was used to account for possible charge–charge interactions in the unfolded state or when the putative unfolded state structure was disrupted. These residues were actually part of a complex network of charge–charge interactions, and when this network was disrupted, the experimental results agreed with the predictions *(77)*. Therefore, it appears that including electrostatic contributions in the unfolded state does not significantly improve the agreement between the calculations and experiments.

In order to truly analyze the effects of changes in charge–charge interactions on protein stability, it would be ideal to make substitutions that affect the charge of a side chain without also affecting the size, hydrophobicity, or packing interactions. Because of the limitation imposed by a small number of naturally occurring amino acids, however, it is often easier to use the natural amino acids lysine and glutamic acid for reversal of existing charges and glutamine and asparagine are used for charge neutralization. As a result, the changes in stability due to charge reversal or neutralization could actually be due to other factors such as hydrophobicity, secondary structure propensity, packing, or changes in hydrogen bonding patterns. It is also possible that they could be affecting stability altering short-range (salt bridges) rather than long-range charge–charge interactions. Since long-range and short-range electrostatic interactions are affected differently by increasing concentrations of ionic strength, it should be possible to determine how stability is being affected by making the same substitutions in different charge environments. Long-range interactions tend to become weaker with increasing salt concentrations, while short-range interactions tend to persist. If the substitutions are affecting long-range electrostatic interactions, then there should be an inverse correlation between the changes in stability and changes in the halophilicity of the protein. For most substitutions, this behavior was observed *(77)*. The substitutions that deviated from

the correlation between stability and halophilicity occurred at the same position in both CspB-Bs and CspB-TB, and suggested that hydrophobic interactions have a larger contribution than charge–charge interactions at this position. The studies on CspB made it possible to understand the nature of how proteins are stabilized through optimized surface charge–charge interactions.

In addition to providing a means to study the details about how changes in surface charge–charge interactions affect the stability of a protein, the successful thermostabilization of CspB-Bs by altering its surface charge distribution led to the idea that it should be possible to develop a computational algorithm to identify the optimal surface charge distribution for any given protein. Ideally, this would be accomplished by performing exhaustive calculations that would sample every possible ionization state for each residue in the protein. However, for a protein with n surface positions and three possible ionization states (positive, neutral, and negative), 3^n calculations would need to be performed in order to identify all possible charge distributions. A small protein like ubiquitin, which has only 23 surface residues (greater than 50% solvent accessibility), would require $3^{23} \approx 10^{11}$ calculations, making exhaustive calculations computationally prohibitive for rational design approaches. The genetic algorithm *(16, 78, 79)* is a faster method to determine the optimal distribution of charges on the surface of a protein because it is based on the idea that it is not necessary to find all of the best sequences, but rather it is sufficient to identify some of the sequences that are among the most favorable. For ubiquitin, the genetic algorithm required approximately 5×10^4 calculations, allowing for a significant reduction in computational resources compared to exhaustive calculations.

The genetic algorithm has been previously described in great detail *(16, 78–80)*, but will be briefly discussed here. The first step of the genetic algorithm is to generate an initial population of charge distributions, each of which is represented by a "chromosome." A certain number of "chromosomes" have randomly generated charge distributions, and the rest have the wild-type charge distribution. It is important to note that only charged residues with a solvent accessibility greater than 50% are included in optimization. Next, a probability score is assigned to each charge distribution, based on the energies of charge–charge interactions calculated by the TK-SA model, and the lowest-energy "chromosomes" are sent to the next generation. Then, probabilistic crossover events between the remaining "chromosomes" are used to finish populating the next generation. Once the second generation is fully populated, random point "mutations" are allowed to occur with a predetermined probability. An energy penalty helps to minimize the number of "mutations." This process is repeated until the lowest energy sequences have remained unchanged for a set number of cycles.
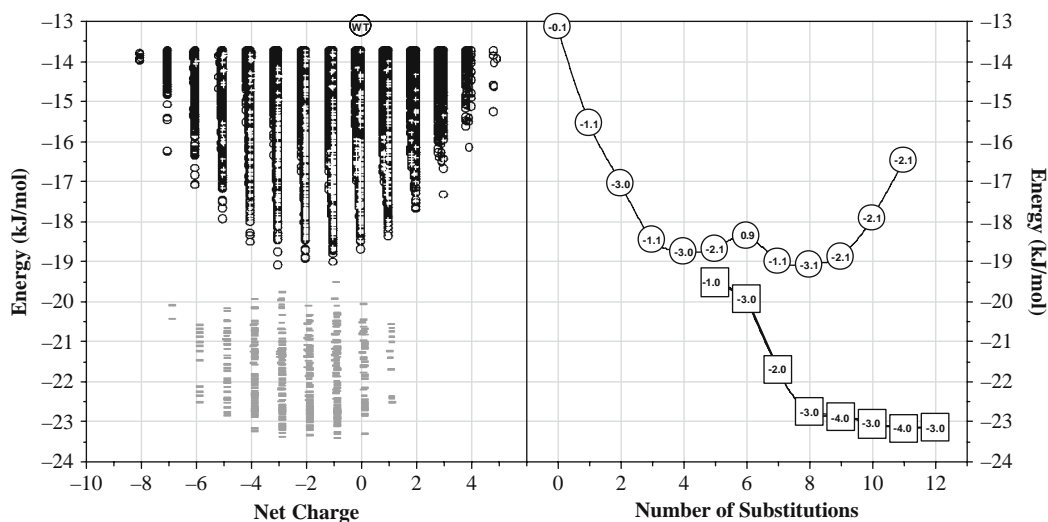
Fig. 11.3. Analysis of the ability of the genetic algorithm to find the optimal sequence of ubiquitin. The charge–charge interaction energies were calculated at pH 5.5 using the TK-SA model. Each sequence is characterized by the energy, net charge, and number of substitutions relative to the wild-type protein. (**A**) The ability of the genetic algorithm to effectively sample the sequence space searched by more exhaustive calculations is assessed. The *open black circles* represent results of exhaustive calculations. The *gray* crosshair represents the genetic algorithm. The *light gray hash marks* (energies below −19 kJ/mol) represent the results of the genetic algorithm when previously uncharged surface residues were also included in optimization. (**B**) The relationship between the number of substitutions in the sequence and the energy of the lowest sequence with that number of substitutions. The *open circles* correspond to the *gray* crosshairs in **A**, while the *open squares* represent the *gray* hash marks in **A**. The numbers within the symbol are the net charges of those sequences at pH 5.5. Reproduced from **Ref.** *(16)* with permission from the American Chemical Society.

Figure 11.3A highlights the ability of the genetic algorithm to appropriately sample the sequence space covered by exhaustive calculations. When optimizing only residues that were charged in the wild-type sequence, the genetic algorithm was able to identify several sequences that had increased favorable charge–charge interaction energies relative to the wild-type. Further increases in favorable interactions were identified when uncharged polar residues on the protein surface were also included in the optimization. The relationship between the charge–charge interaction energies and the number of substitutions shows that the increase in favorable energy is a nonlinear function (**Fig. 11.3B**). After eight or ten substitutions, the gain in favorable energy per substitution becomes very small. This suggests that it is possible to increase protein stability with only a few substitutions, making computational design of surface charges a practical tool for generating stable proteins.

The robustness of the rational design of surface charge–charge interactions has been tested using six model proteins (acyl-phosphatase, procarboxypeptidase, tenascin, U1A, ubiquitin, and the Fyn SH3 domain) which varied in size, shape, and secondary structure composition *(16, 81)*. For each protein, the energies of

surface charge–charge interactions were calculated using the TK-SA model, and then the optimal distributions were identified using the genetic algorithm. As an example, **Fig. 11.2A** shows the results of the TK-SA calculations for the wild-type and designed variants of ubiquitin. Two of the designed variants included neutral polar residues in the optimization procedure, while a third optimized only the existing charges. The number of unfavorable interactions, relative to wild-type ubiquitin, is decreased in each of the designed variants. In addition to the designed variants, other ubiquitin variants were constructed to remove unfavorable charges at individual positions. One reversed the unfavorable charge at position 6 (UBQ-6), one reversed the charge at position 72 (UBQ-72), and one contained two substitutions to reverse the charges at both positions simultaneously (UBQ-6/72). The stabilities of ubiquitin variants were characterized using urea-induced unfolding, as previously described *(65)*. It was observed that UBQ-6 and UBQ-72 both had increased stabilities relative to the wild-type, and UBQ-6/72 was more stable than the single variants. Furthermore, all three designed sequences were more stable (with $\Delta\Delta G$ relative to the wild type of 13.2 kJ/mol, 18.4 kJ/mol, and 17.7 kJ/mol) than the double variant ($\Delta\Delta G = 5.2$ kJ/mol), providing experimental evidence that optimization of surface charge–charge interactions is a viable approach for increasing protein stability. The flexibility of the design process, evidenced by achieving stabilization with three different designed sequences, will make it possible to redesign proteins without affecting functional properties. The stabilities of the other model systems were also measured using either CD or differential scanning calorimetry (DSC) *(82–84)*. The designed sequences of all six model systems had stabilities that were increased relative to their wild-type protein. Recently, CDC42 was also redesigned through the optimization of surface charge–charge interactions. At 190 amino acid residues, CDC42 is the largest protein to be redesigned by this approach, and served to test the robustness of the method for large proteins. The thermostability of the designed CDC42 variant was increased by 10°C relative to the wild-type *(85)*, which is quite remarkable for such a large protein. Furthermore, the successful stabilization of several proteins with different sizes, tertiary structures, and secondary structure composition provides evidence that this approach is a viable, universal method for generating thermostable proteins.

In order for any protein design approach to be truly successful, the designed variants must be able to retain their function. To determine whether the optimization of surface charge–charge interactions alters protein function, activity assays were performed on CspB, acylphosphatase, and CDC42. CspB is expressed by *B. subtilis* when the bacterium is exposed to colder temperatures. While the exact mechanism by which CspB protects cells from

cold shock has been the subject of much debate, it is known to bind single-stranded DNA (ssDNA) with a preference for poly-pyrimidine sequences *(86, 87)*. The binding of ssDNA templates to CspB-Bs and the designed CspB-TB (which is 23°C more thermostable than CspB-Bs) were compared using fluorescence spectroscopy. It was found that not only could CspB-TB bind ssDNA better than CspB-Bs at higher temperatures (37°C), but it could also bind ssDNA with a higher affinity than CspB-Bs at lower temperatures (25°C) *(15)*. Although the physiological function of acylphosphatase is still unknown, it has been shown to catalyze the hydrolysis of acylphosphates. The catalytic activity of the wild-type and designed acylphosphatase variants was measured with a continuous UV absorption assay using benzoylphosphate as a substrate. The designed variant was able to maintain hydrolytic activity at higher temperatures than the wild-type enzyme *(85)*. CDC42 is a member of the Rho family of GTP-binding proteins. The hydrolysis of GTP by CDC42 can be monitored by a colorimetric assay that detects the amount of free phosphate released during the reaction. The thermal inactivation of CDC42 is irreversible, so the functional properties were measured as the residual activity after incubation at high temperatures (~10°C higher than the wild type) The designed variant had similar activity to the wild-type after incubation at lower temperatures and was able to maintain its activity after incubation at temperatures where the wild-type enzyme was inactivated *(85)*. These results suggest that stabilizing proteins through redesign of surface charges does not lead to loss of functional activity.

3. Practical Considerations

The TK-SA model is a simple model of electrostatics that is effective for calculating qualitative changes in the energies of interactions between charges on the protein surface. However, there are a few issues to consider regarding its implementation in the rational design of stable proteins. First, a major assumption of the model is that the protein is spherical. For globular proteins, this appears to be valid, even when the shape deviates from a sphere. For example, tenascin has more of a cylindrical shape, yet this model was able to be used to predict stabilizing substitutions *(16)*. Second, the TK-SA model assumes that the interaction between charges is the only type of electrostatic interaction in the native state. This is clearly an oversimplification, since it is known that hydrogen bonding and partial dipoles also play a role in electrostatic interaction energies. For this reason, surface side

chains that are involved in intramolecular hydrogen bonds should not be included in optimization procedures that use TK-SA. Finally, it has been noted that this model ignores important parameters such as self-energy and solvation *(88–90)*. Nevertheless, when the results of the TK-SA calculations for the surface charge–charge interactions are compared to results from other continuum models, such as the finite difference solution of the Poisson–Boltzmann equation (FDPB/UHBD) *(91, 92)* performed on a single structure, the Multi-Conformer Continuum Electrostatic model (MCCE) performed on multiple conformers, or the microenvironment modulated screened Coulomb potential (MM_SCP) model, all results are qualitatively similar (**Fig. 11.2**). The only advantage of TK-SA over these other models is that it is less computationally demanding.

Another concern regarding the rational optimization of the surface charge–charge interactions is that it is not possible to quantitatively predict the stabilities of the proteins. This is due to the fact that only the native-state interactions between surface charges are being considered. Important factors for protein stability, such as side chain hydrophobicity, secondary structure propensity, hydrogen bonding, packing interactions, and unfolded state effects *(4, 5, 9, 56, 93–99)* are not considered. Nevertheless, this approach does provide very good qualitative predictions of protein stability. In order to become quantitative, these other factors will need to be accounted for in the computational algorithm. Key questions that will need to be addressed in the future development of this approach are: which factors are the most important for modulating stability, and how quantitative does the algorithm need to be in order to be practical? It is likely that including just a few of the parameters mentioned here will allow the algorithm to quantitatively predict the stability of the designed sequences within the errors of experimental techniques.

Acknowledgements

References

1. Kauzmann, W. (1959). Some factors in the interpretation of protein denaturation. *Adv Protein Chem* 14, 1–63.

2. Dill, K. A. (1990). Dominant forces in protein folding. *Biochemistry* 29, 7133–155.

3. Matthews, B. W. (1995). Studies on protein stability with T4 lysozyme. *Adv Protein Chem* 46, 249–278.

4. Serrano, L., Kellis, J. T., Jr., Cann, P., et al. (1992). The folding of an enzyme. II. Substructure of barnase and the contribution of different interactions to protein stability. *J Mol Biol* 224, 783–804.

5. Makhatadze, G. I., Privalov, P. L. (1995). Energetics of protein structure. *Adv Protein Chem* 47, 307–425.

6. Desjarlais, J. R., Handel, T. M. (1995). De novo design of the hydrophobic cores of proteins. *Protein Sci* 4, 2006–2018.

7. Lazar, G. A., Desjarlais, J. R., Handel, T. M. (1997). De novo design of the hydrophobic core of ubiquitin. *Protein Sci* 6, 1167–1178.

8. Loladze, V. V., Ermolenko, D. N., Makhatadze, G. I. (2002). Thermodynamic consequences of burial of polar and non-polar amino acid residues in the protein interior. *J Mol Biol* 320, 343–357.

9. Pace, C. N., Shirley, B. A., McNutt, M., et al. (1996). Forces contributing to the conformational stability of proteins. *Faseb J* 10, 75–83.

10. Griko, Y. V., Makhatadze, G. I., Privalov, P. L., et al. (1994). Thermodynamics of barnase unfolding. *Protein Sci* 3, 669–676.

11. Loladze, V. V., Ibarra-Molero, B., Sanchez-Ruiz, J. M., et al. (1999). Engineering a thermostable protein via optimization of charge–charge interactions on the protein surface. *Biochemistry* 38, 16419–16423.

12. Grimsley, G. R., Shaw, K. L., Fee, L. R., et al. (1999). Increasing protein stability by altering long-range Coulombic interactions. *Protein Sci* 8, 1843–1849.

13. Spector, S., Wang, M., Carp, S. A., et al. (2000). Rational modification of protein stability by the mutation of charged surface residues. *Biochemistry* 39, 872–879.

14. Perl, D., Mueller, U., Heinemann, U., et al. (2000). Two exposed amino acid residues confer thermostability on a cold shock protein. *Nat Struct Biol* 7, 380–383.

15. Makhatadze, G. I., Loladze, V. V., Gribenko, A. V., et al. (2004). Mechanism of thermostabilization in a designed cold shock protein with optimized surface electrostatic interactions. *J Mol Biol* 336, 929–942.

16. Strickler, S. S., Gribenko, A. V., Gribenko, A. V., et al.. (2006). Protein stability and surface electrostatics: a charged relationship. *Biochemistry* 45, 2761–2766.

17. Loladze, V. V., Ermolenko, D. N., Makhatadze, G. I. (2001). Heat capacity changes upon burial of polar and nonpolar groups in proteins. *Protein Sci* 10, 1343–1352.

18. Farinas, E. T., Bulter, T., Arnold, F. H. (2001). Directed enzyme evolution. *Curr Opin Biotechnol* 12, 545–551.

19. Bloom, J. D., Meyer, M. M., Meinhold, P., et al. (2005). Evolving strategies for enzyme engineering. *Curr Opin Struct Biol* 15, 447–452.

20. Kumar, S., Chen, C. S., Waxman, D. J., et al. (2005). Directed evolution of mammalian cytochrome P450 2B1: mutations outside of the active site enhance the metabolism of several substrates, including the anticancer prodrugs cyclophosphamide and ifosfamide. *J Biol Chem* 280, 19569–19575.

21. Morawski, B., Quan, S., Arnold, F. H. (2001). Functional expression and stabilization of horseradish peroxidase by directed evolution in Saccharomyces cerevisiae. *Biotechnol Bioeng* 76, 99–107.

22. Giver, L., Gershenson, A., Freskgard, P. O., et al. (1998). Directed evolution of a thermostable esterase. *Proc Natl Acad Sci USA* 95, 12809–12813.

23. Hill, C. M., Li, W. S., Thoden, J. B., et al. (2003). Enhanced degradation of chemical warfare agents through molecular engineering of the phosphotriesterase active site. *J Am Chem Soc* 125, 8990–8991.

24. Ness, J. E., Welch, M., Giver, L., et al. (1999). DNA shuffling of subgenomic sequences of subtilisin. *Nat Biotechnol* 17, 893–896.

25. Bulter, T., Alcalde, M., Sieber, V., et al. (2003). Functional expression of a fungal laccase in Saccharomyces cerevisiae by directed evolution. *Appl Environ Microbiol* 69, 987–995.

26. Cherry, J. R., Lamsa, M. H., Schneider, P., et al. (1999). Directed evolution of a fungal peroxidase. *Nat Biotechnol* 17, 379–384.

27. Murashima, K., Kosugi, A., Doi, R. H. (2002). Thermostabilization of cellulosomal endoglucanase EngB from Clostridium cellulovorans by in vitro DNA recombination with non-cellulosomal endoglucanase EngD. *Mol Microbiol* 45, 617–626.

28. Hopfner, K. P., Kopetzki, E., Kresse, G. B., et al. (1998). New enzyme lineages by

subdomain shuffling. *Proc Natl Acad Sci USA* 95, 9813–9818.

29. Wintrode, P. L., Arnold, F. H. (2000). Temperature adaptation of enzymes: lessons from laboratory evolution. *Adv Protein Chem* 55, 161–225.

30. Sieber, V., Pluckthun, A., Schmid, F. X. (1998). Selecting proteins with improved stability by a phage-based method. *Nat Biotechnol* 16, 955–960.

31. Martin, A., Sieber, V., Schmid, F. X. (2001). In-vitro selection of highly stabilized protein variants with optimized surface. *J Mol Biol* 309, 717–726.

32. Wunderlich, M., Schmid, F. X. (2006). In vitro evolution of a hyperstable Gbeta1 variant. J Mol Biol 363, 545–557.

33. Finucane, M. D., Tuna, M., Lees, J. H., et al. (1999). Core-directed protein design. I. An experimental method for selecting stable proteins from *combinatorial libraries. Biochemistry* 38, 11604–11612.

34. Finucane, M. D., Woolfson, D. N. (1999). Core-directed protein design. II. Rescue of a multiply mutated and destabilized variant of ubiquitin. *Biochemistry* 38, 11613–11623.

35. Perl, D., Schmid, F. X. (2001). Electrostatic stabilization of a thermophilic cold shock protein. *J Mol Biol* 313, 343–357.

36. Brockmann, E. C., Cooper, M., Stromsten, N., et al. (2005). Selecting for antibody scFv fragments with improved stability using phage display with denaturation under reducing conditions. *J Immunol Methods* 296, 159–170.

37. Wunderlich, M., Martin, A., Schmid, F. X. (2005). Stabilization of the cold shock protein CspB from Bacillus subtilis by evolutionary optimization of Coulombic interactions. *J Mol Biol* 347, 1063–1076.

38. Wunderlich, M., Martin, A., Staab, C. A., et al. (2005). Evolutionary protein stabilization in comparison with computational design. *J Mol Biol* 351, 1160–1168.

39. Tao, H., Cornish, V. W. (2002). Milestones in directed enzyme evolution. *Curr Opin Chem Biol* 6, 858–864.

40. Fukuchi, S., Nishikawa, K. (2001). Protein surface amino acid compositions distinctively differ between thermophilic and mesophilic bacteria. *J Mol Biol* 309, 835–843.

41. Alsop, E., Silver, M., Livesay, D. R. (2003). Optimized electrostatic surfaces parallel increased thermostability: A structural bioinformatic analysis. *Protein Eng* 16, 871–874.

42. Watanabe, K., Ohkuri, T., Yokobori, S., et al. (2006). Designing thermostable proteins: ancestral mutants of 3-isopropylmalate dehydrogenase designed by using a phylogenetic tree. *J Mol Biol* 355, 664–674.

43. Neuwald, A. F., Liu, J. S., Lipman, D. J., et al. (1997). Extracting protein alignment models from the sequence database. Nucleic Acids Res 25, 1665–1677.

44. Shaw, E., Dordick, J. S. (2002). Predicting amino acid residues responsible for enzyme specificity solely from protein sequences. *Biotechnol Bioeng* 79, 295–300.

45. DiTursi, M. K., Kwon, S. J., Reeder, P. J., et al. (2006). Bioinformatics-driven, rational engineering of protein thermostability. *Protein Eng Des Sel* 19, 517–524.

46. Berezovsky, I. N., Shakhnovich, E. I. (2005). Physics and evolution of thermophilic adaptation. *Proc Natl Acad Sci USA* 102, 12742–12747.

47. DeGrado, W. F., Summa, C. M., Pavone, V., et al. (1999). De novo design and structural characterization of proteins and metalloproteins. *Annu Rev Biochem* 68, 779–819.

48. Street, A. G., Mayo, S. L. (1999). Computational protein design. Structure 7, R105–R109.

49. Pokala, N., Handel, T. M. (2001). Review: protein design – where we were, where we are, where we're going. *J Struct Biol* 134, 269–281.

50. Dantas, G., Kuhlman, B., Callender, D., et al. (2003). A large scale test of computational protein design: folding and stability of nine completely redesigned globular proteins. *J Mol Biol* 332, 449–460.

51. Korkegian, A., Black, M. E., Baker, D., et al. (2005). Computational thermostabilization of an enzyme. Science 308, 857–860.

52. Hurley, J. H., Baase, W. A., Matthews, B. W. (1992). Design and structural analysis of alternative hydrophobic core packing arrangements in bacteriophage T4 lysozyme. *J Mol Biol* 224, 1143–1159.

53. Kuhlman, B., Baker, D. (2000). Native protein sequences are close to optimal for their structures. *Proc Natl Acad Sci* USA 97, 10383–10388.

54. Predki, P. F., Agrawal, V., Brunger, A. T., et al. (1996). Amino-acid substitutions in a

surface turn modulate protein stability. *Nat Struct Biol* 3, 54–58.

55. Nagi, A. D., Regan, L. (1997). An inverse correlation between loop length and stability in a four-helix-bundle protein. *Fold Des* 2, 67–75.

56. Fernandez, A. M., Villegas, V., Martinez, J. C., et al. (2000). Thermodynamic analysis of helix-engineered forms of the activation domain of human procarboxypeptidase A2. *Eur J Biochem* 267, 5891–5899.

57. Tanford, C., Kirkwood, J. G. (1957). Theory of protein titration curves. I. General equations for impenetrable spheres. *J Am Chem Soc* 79, 5333–5339.

58. Matthew, J. B., Gurd, F. R., Garcia-Moreno, B., et al. (1985). pH-dependent processes in proteins. *CRC Crit Rev Biochem* 18, 91–197.

59. Matthew, J. B., Gurd, F. R. (1986). Stabilization and destabilization of protein structure by charge interactions. *Meth Enzymol* 130, 437–453.

60. Matthew, J. B., Gurd, F. R. (1986). Calculation of electrostatic interactions in proteins. *Meth Enzymol* 130, 413–436.

61. Richmond, T. J. (1984). Solvent accessible surface area and excluded volume in proteins. Analytical equations for overlapping spheres and implications for the hydrophobic effect. *J Mol Biol* 178, 63–89.

62. Ibarra-Molero, B., Loladze, V. V., Makhatadze, G. I., et al. (1999). Thermal versus guanidine-induced unfolding of ubiquitin. An analysis in terms of the contributions from charge–charge interactions to protein stability. *Biochemistry* 38, 8138–8149.

63. Marti-Renom, M. A., Stuart, A. C., Fiser, A., et al. (2000). Comparative protein structure modeling of genes and genomes. *Annu Rev Biophys Biomol Struct* 29, 291–325.

64. Wintrode, P. L., Makhatadze, G. I., Privalov, P. L. (1994). Thermodynamics of ubiquitin unfolding. *Proteins* 18, 246–253.

65. Pace, C. N. (1986). Determination and analysis of urea and guanidine hydrochloride denaturation curves. *Meth Enzymol* 131, 266–280.

66. Strop, P., Mayo, S. L. (2000). Contribution of surface salt bridges to protein stability. *Biochemistry* 39, 1251–1255.

67. Sanchez-Ruiz, J. M., Makhatadze, G. I. (2001). To charge or not to charge? *Trends Biotechnol* 19, 132–135.

68. Chakrabartty, A., Doig, A. J., Baldwin, R. L. (1993). Helix capping propensities in peptides parallel those in proteins. *Proc Natl Acad Sci USA* 90, 11332–11336.

69. Doig, A. J., Baldwin, R. L. (1995). N- and C-capping preferences for all 20 amino acids in alpha-helical peptides. *Protein Sci* 4, 1325–1336.

70. Gong, Y., Zhou, H. X., Guo, M., et al. (1995). Structural analysis of the N- and C-termini in a peptide with consensus sequence. *Protein Sci* 4, 1446–1456.

71. Viguera, A. R., Serrano, L. (1995). Experimental analysis of the Schellman motif. *J Mol Biol* 251, 150–160.

72. Thomas, S. T., Loladze, V. V., Makhatadze, G. I. (2001). Hydration of the peptide backbone largely defines the thermodynamic propensity scale of residues at the C' position of the C-capping box of alpha-helices. Proc *Natl Acad Sci USA* 98, 10670–10675.

73. Ermolenko, D. N., Thomas, S. T., Aurora, R., et al. (2002). Hydrophobic interactions at the Ccap position of the C-capping motif of alpha-helices. J Mol Biol 322, 123–135.

74. Marshall, S. A., Morgan, C. S., Mayo, S. L. (2002). Electrostatics significantly affect the stability of designed homeodomain variants. *J Mol Biol* 316, 189–199.

75. Permyakov, S. E., Makhatadze, G. I., Owenius, R., et al. (2005). How to improve nature: study of the electrostatic properties of the surface of alpha-lactalbumin. *Protein Eng Des Sel* 18, 425–433.

76. Zhou, H. X. (2002). A Gaussian-chain model for treating residual charge–charge interactions in the unfolded state of proteins. *Proc Natl Acad Sci USA* 99, 3569–3574.

77. Gribenko, A. V., Makhatadze, G. I. (2007). Role of the charge–charge interactions in defining stability and halophilicity of the CspB proteins. *J Mol Biol* 366, 842–856.

78. Ibarra-Molero, B., Sanchez-Ruiz, J. M. (2002). Genetic algorithm to design stabilizing surface-charge distributions in proteins. *J Phys Chem B* 106, 6609–6613.

79. Godoy-Ruiz, R., Perez-Jimenez, R., Garcia-Mira, M. M., et al. (2005). Empirical parametrization of pK values for carboxylic acids in proteins using a genetic algorithm. *Biophys Chem* 115, 263–266.

80. Obitko, M. (1998). Genetic algorithms. http://cs.felk.cvut.cz/~xobitko/ga/.

81. Schweiker, K. L., Zarrine-Afsar, A., Davidson, A. R., et al. (2007). Computational design of the Fyn SH3 domain with increased stability through optimization of surface charge–charge interactions. *Protein Sci* 16, 2694–2702.

82. Makhatadze, G. I. (1998). Measuring protein thermostability by differential scanning calorimetry, in (Wiley, T. J., ed.) *Current Protocols in Protein Chemistry, 2.* John *Wiley & Sons*, New York.

83. Lopez, M. M., Makhatadze, G. I. (2002). Differential scanning calorimetry. *Methods Mol Biol* 173, 113–119.

84. Streicher, W. W., Makhatadze, G. I. (2007). Advances in the analysis of conformational transitions in peptides using differential scanning calorimetry. *Meth Mol Biol* 350, 105–113.

85. Gribenko, A. V., Patel, M . M., Makhatadze, G. I. (2008). to be published.

86. Lopez, M. M., Yutani, K., Makhatadze, G. I. (1999). Interactions of the major cold shock protein of Bacillus subtilis CspB with single-stranded DNA templates of different base composition. *J Biol Chem* 274, 33601–33608.

87. Lopez, M. M., Yutani, K., Makhatadze, G. I. (2001). Interactions of the cold shock protein CspB from Bacillus subtilis with single-stranded DNA. Importance of the T base content and position within the template. *J Biol Chem* 276, 15511–15518.

88. Schutz, C. N., Warshel, A. (2001). What are the dielectric "constants" of proteins and how to validate electrostatic models? *Proteins* 44, 400–417.

89. Warshel, A. (2003). Computer simulations of enzyme catalysis: methods, progress, and insights. Annu Rev Biophys Biomol Struct 32, 425–443.

90. Garcia-Moreno, E. B., Fitch, C. A. (2004). Structural interpretation of pH and salt-dependent processes in proteins with computational methods. Methods Enzymol 380, 20–51.

91. Antosiewicz, J., McCammon, J. A., Gilson, M. K. (1994). Prediction of pH-dependent properties of proteins. *J Mol Biol* 238, 415–436.

92. Antosiewicz, J., McCammon, J. A., Gilson, M. K. (1996). The determinants of pKas in proteins. *Biochemistry 35*, 7819–7833.

93. Oliveberg, M., Arcus, V. L., Fersht, A. R. (1995). pKA values of carboxyl groups in the native and denatured states of barnase: the pKA values of the denatured state are on average 0.4 units lower than those of model compounds. *Biochemistry* 34, 9424–9433.

94. Kuhlman, B., Luisi, D. L., Young, P., et al. (1999). pKa values and the pH dependent stability of the N-terminal domain of L9 as probes of electrostatic interactions in the denatured state. Differentiation between local and nonlocal interactions. *Biochemistry* 38, 4896–4903.

95. Cho, J. H., Raleigh, D. P. (2005). Mutational analysis demonstrates that specific electrostatic interactions can play a key role in the denatured state ensemble of proteins. *J Mol Biol* 353, 174–185.

96. Trefethen, J. M., Pace, C. N., Scholtz, J. M., et al. (2005). Charge–charge interactions in the denatured state influence the folding kinetics of ribonuclease Sa. *Protein Sci* 14, 1934–1938.

97. Fersht, A., Winter, G. (1992). Protein engineering. Trends Biochem Sci 17, 292–295.

98. Baldwin, E. P., Matthews, B. W. (1994). Core-packing constraints, hydrophobicity and protein design. *Curr Opin Biotechnol* 5, 396–402.

99. Loladze, V. V., Makhatadze, G. I. (2005). Both helical propensity and side-chain hydrophobicity at a partially exposed site in alpha-helix contribute to the thermodynamic stability of ubiquitin. *Proteins* 58, 1–6.

Chapter 12

NMR Analysis of Native-State Protein Conformational Flexibility by Hydrogen Exchange

Griselda Hernández and David M. LeMaster

Abstract

The rate of hydrogen exchange for the most protected amides of a protein is widely used to provide an estimate of global conformational stability by analyzing the exchange kinetics in the unfolded state in terms of model peptide exchange rates. The exchange behavior of the other amides of the protein which do not exchange via a global unfolding mechanism can provide insight into the smaller-scale conformational transitions that facilitate access to solvent as required for the exchange reaction. However, since the residual tertiary structure in the exchange-competent conformation can modulate the chemistry of the exchange reaction, equilibrium values estimated from normalization with model peptide rates are open to question. To overcome this limitation, the most robust approaches utilize differential analyses as a function of experimental variables such as denaturant concentration, temperature, pH, and mutational variation. Practical aspects of these various differential analysis techniques are considered with illustrations drawn from the literature.

Key words: Hydrogen exchange, protein dynamics, conformational flexibility, NMR.

1. Introduction

Ever since the 1950s when Linderstrom-Lang and coworkers *(1)* used infrared spectroscopy to demonstrate that the amide protons of a protein exchange with deuterium from the bulk solvent phase with rates that span many orders of magnitude, hydrogen exchange has been the most widely used technique to monitor protein conformational flexibility. A large proportion of these applications have made use of only a qualitative interpretation of the exchange rates. Amide hydrogen exchange provided early evidence of the dramatic changes in conformational flexibility of enzymes that can arise upon substrate/inhibitor binding *(2)* which, combined with advances in mass spectrometry, have

recently offered extensive insights into protein–ligand interactions *(3,4)*. This series *(5)* and others *(6,7)* have reviewed the critical role in protein folding studies provided by NMR-monitored quenched-flow techniques by following the temporal development of protection from hydrogen exchange at individual residue positions throughout the backbone. Combining such pulse labeling techniques with the increased sensitivity and molecular weight range provided by mass spectrometry enables characterization of both normal and misfolded intermediates in the protein folding process *(8–10)* with the added benefit that by monitoring the mass of individual protein molecules as a function of deuterium exchange one can determine whether or not groups of amide protons are exchanging in a concerted fashion *(11)*. In each of these cases, the relevant conclusions regarding conformational flexibility can often be drawn without interpreting the exchange rates of the individual amide protons by a quantitative kinetic model. The present review focuses upon the techniques involved and the issues that arise when a more precise interpretation of the exchange data is applied to study protein conformational dynamics in the native state.

2. Hydrogen Exchange as a Monitor of Conformational Equilibria

Quantitative interpretation of hydrogen exchange kinetics is standardly based on the protection analysis described by Hvidt and Nielsen *(12)*, as represented by the following equation:

$$\text{closed} \; \underset{k_{cl}}{\overset{k_{op}}{\rightleftharpoons}} \; \text{open} \; \overset{k_{ch}}{\rightarrow} \; \text{exchanged}$$
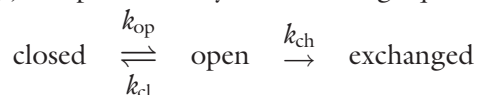
In the first of the two limiting conditions, the rate of the closing reaction is slow compared to the rate of the chemical exchange step (i.e., $k_{cl} << k_{ch}$). In this case, essentially every conformational opening transition leads to a hydrogen exchange reaction so that the observed rate $k_{ex} = k_{op}$, commonly referred to as the EX1 condition. As a result, the kinetics of exchange under EX1 conditions provides a direct monitor of the rate for the underlying conformational transition. However, observation of such EX1 kinetics generally requires the use of high pH in order to selectively accelerate the chemical exchange step. Closer to physiological conditions, the rate of the closing reaction is usually rapid compared to that of the chemical exchange step which occurs from the open-state conformation (i.e., $k_{cl} >> k_{ch}$). As a result, a pre-equilibrium of the open and closed conformational states is established and the overall exchange rate constant equals $(k_{op}/k_{cl}) \, k_{ch}$, where k_{op}/k_{cl} is

the equilibrium constant for the conformational opening transition. This condition is referred to as exhibiting EX2 kinetics.

Experimental access to the equilibrium constant for the conformational opening transition requires estimation of the rate constant for the chemical exchange step k_{ch}. As Hvidt and Nielsen *(12)* pointed out, the most straightforward interpretation depends upon whether or not the residual conformational structure of the protein in the exchange-competent state significantly modulates the kinetics of the chemical exchange. If the effects of the residual conformational structure are negligible, then the k_{ch} rate constant can be estimated from the exchange behavior of simple model peptides under the same experimental conditions. The pros *(13)* and cons *(14)* of this peptide normalization assumption have been actively debated ever since under the rubric of the local unfolding *(15)* and the solvent penetration *(16)* models. Although much of this discussion has focused on estimating the spatial extent of the conformational transition needed to generate efficient hydrogen exchange *(17)*, it should be emphasized that the central kinetic question for the quantitative interpretation of hydrogen exchange rates in the EX2 limit remains whether the residual conformation significantly modulates the chemical exchange step.

The validity of the peptide normalization assumption can be directly tested for amides that only exchange their protons via a global unfolding of the protein structure, since the ΔG value deduced from the conformational pre-equilibrium formed during the hydrogen exchange reaction can be directly compared to the free energy of stability measured by calorimetric or spectroscopic means. The practical aspects of using hydrogen exchange to estimate protein conformational stability have been presented previously in this series *(18)*. Allowing for the effects of incomplete equilibration of cis–trans isomerization of prolines and solvent isotope effects on conformational stability, most proteins studied to date yield ΔG values estimated from hydrogen exchange experiments that agree quite well with the independently determined values, although exceptions have been noted *(19–21)*.

3. The Role of Electrostatics in Modulating Hydrogen Exchange Kinetics

By definition, amides which exchange via a transition that does not involve global unfolding retain residual conformational structure in their exchange-competent state. As these smaller-scale

conformational fluctuations generally cannot be characterized by independent experimental techniques, the analogous test of the peptide normalization assumption cannot be made. As a result, the potential role of this residual conformational structure in modulating the chemical exchange rates must be considered. Electrostatic interactions with charged and polar groups in the residual conformational structure provide the most commonly discussed mechanism by which the rate of the chemical exchange step for a given amide may be altered, relative to the reference model peptide values *(22–26)*.

Above pH 4, most peptide groups exchange essentially exclusively by hydroxide ion-catalyzed removal of the amide proton. As with the more familiar ionization of the weak acids and bases on the protein side chains, the acidity of the peptide nitrogen is modulated by the local electrostatic potential that (de)stabilizes the peptide anion state. The pK values for simple model peptides are approximately two units above that of water. Since these model peptides act as normal Eigen acids *(27)* such that their kinetic acidity directly reflects their thermodynamic acidity, hydroxide-catalyzed exchange occurs at ∼1% of the diffusion-limited rate. When the local electrostatic potential is negative, the acidity of the peptide unit will be decreased, resulting in a proportionately slower exchange rate. Conversely, when the local electrostatic potential is positive, the peptide anion state is stabilized. In this case, the exchange rate increases up until the pK of the peptide matches that of water at which point a diffusion-limited rate is observed *(28–30)*.

Although ionization of protein side chain groups can directly alter hydrogen exchange rates by modulating the local electrostatic potential, it is often problematic to exclude the interpretation that such side chain ionizations alter the energetics of the local conformational equilibria and thus affect the hydrogen exchange rates indirectly. Solvent-exposed amides offer the most straightforward test of electrostatic effects since they need not require any conformational transition in order to exchange with the bulk solvent. The groups of Wüthrich *(31)* and Woodward *(23)* have reported that a number of the solvent-exposed amide hydrogens of bovine pancreatic trypsin inhibitor have exchange rates which are several hundred-fold slower than the corresponding model peptide values. Although the physical basis of these decreased exchange rates has not been fully rationalized, their dependence on ionic strength indicates a substantial electrostatic component *(32)*. More recently, we *(33)* have found that within the active site in the **a** domain of the human protein disulfide isomerase the amide hydrogens at the N-terminus of the α_2 helix undergo hydroxide-catalyzed exchange at the diffusion-limited rate. By increasing the acidity of these amides up to that of water, the positive electrostatic potential at the end of the helix

renders these amides susceptible to general base catalysis. Indeed below pH 8, the exchange of the His 38 amide is predominantly catalyzed by the neutral imidazole form of its own side chain with a rate that is more than a million-fold above the neutral water-catalyzed reaction.

Quantitative analysis of the electrostatic modulation of hydrogen exchange is not limited to the solvent-exposed residues. The charge of the tetracysteine-coordinated active site metal in the rubredoxin from *Pyrococcus furiosus* can be altered by substitution of Zn(II), Ga(III), and Ge(IV) without a significant change in conformational stability *(34,35)*. Up to a million-fold acceleration in hydrogen exchange rates was observed for the amide protons that arise largely, if not exclusively, from the resultant modulation of the electrostatic potential at the individual peptide sites. If instead this variation in hydrogen exchange rates is interpreted in terms of a change in conformational stability, the values for the predicted differential free energies extend up to 8 kcal/mol. Poisson–Boltzmann calculations *(36,37)* on the native-state structure of *Pf* rubredoxin faithfully predict the changes in acidity of the amide nitrogens needed to fit the differential hydrogen exchange rates using an effective internal protein dielectric constant value of 6. The consistency of the electrostatic modeling of the differential hydrogen exchange rates based on the X-ray structure of *Pf* rubredoxin indicates that the exchange-competent conformations must closely resemble the native-state structure.

4. Differential Analysis of Subglobal Hydrogen Exchange

Given the degree to which hydrogen exchange kinetics can be modulated by electrostatic effects, estimation of conformational equilibria by normalization against model peptide values for hydrogen exchange reactions that do not occur via global unfolding is open to question. To help circumvent this limitation, the most robust approaches utilize differential analyses. The rate of hydrogen exchange for individual amide protons can be assessed as a function of experimental variables such as denaturant concentration, temperature, and mutational variation. In this case, quantitative interpretations depend upon the considerably weaker assumption that the residual conformational structure does not differentially affect the rate of the chemical exchange step as a function of the experimental condition being varied.

A central issue for any such differential analysis is how to assess whether or not the conformational transitions that underlie the hydrogen exchange process are changing as a function of the experimental condition being varied. To determine the contribution of native-state conformational flexibility to the observed hydrogen exchange data, one must first identify the degree to which global unfolding might also contribute. This distinction can often be established by making use of the fact that the fraction of exchange which occurs via global unfolding is generally strongly dependent on temperature and denaturant concentration.

Determining the degree to which a global unfolding transition contributes to the observed hydrogen exchange rates is particularly germane to the actively debated question of whether increased conformational rigidity underlies the heightened thermal stability observed for proteins obtained from thermophilic organisms. Hydrogen exchange measurements have provided much of the experimental basis used to justify a correlation between conformational rigidity and global stability *(38–40)*. However, if the global unfolding transition contributes significantly to the observed hydrogen exchange rates for either the thermophile protein or its mesophile homolog being compared under a given set of conditions, no clear conclusion can be drawn for this question. To argue otherwise necessarily assumes that "flexibility" includes the global unfolding transition, in which case the correlation between conformational rigidity and global stability becomes true by definition.

5. Methods

5.1. Denaturant Dependence of Hydrogen Exchange

The hydroxide-catalyzed exchange rate constant of poly-D,L-alanine linearly decreases with increasing urea concentrations with a fourfold retardation at 8 M *(41)*. The analogous measurements as a function of guanidinium chloride (GdmCl) exhibits a maximum near 4 M with an overall variation that is less than twofold. The denaturant dependence of hydrogen exchange for the various charged residues in model peptides has not been reported. The large changes in ionic strength arising from variation in GdmCl concentration can be counterbalanced by addition of sodium chloride *(42)*, although more commonly the standard peptide normalization values are applied independently of guanidinium concentration.

The global stability of a protein commonly varies linearly with urea or GdmCl concentration *(43)*. This proportionality constant, the *m*-value, is in turn approximately proportional to the protein

surface area that becomes exposed during the unfolding process. Increasing concentrations of denaturant serves not only to increase the population of the globally unfolded species, it also serves to increase the population of partially unfolded states. The dependence of protein hydrogen exchange rates as a function of GdmCl provides a means of characterizing the spatial extent of the exchange-competent conformational transition(s) *(44)*.

For a number of proteins, all of the monitored amides appear to exhibit only two general types of denaturant-dependent rates *(42,45)*. At lower levels of denaturant, many amides exhibit exchange rates that are essentially independent of denaturant concentration, consistent with a small fraction of buried surface exposure in the exchange-competent state. At higher denaturant concentrations, the *m*-value rapidly rises to a value consistent with that of global unfolding. However, most notably in the example of horse cytochrome c, Englander and coworkers *(46)* have observed that clusters of amides exhibit phases in the GdmCl dependence curves with *m*-values that are intermediate between the flat segment characterizing exchange via local fluctuations and the steepest slope at high denaturant concentrations, consistent with exchange via global unfolding. As illustrated in **Fig. 12.1**, at low guanidinium concentrations, the hydrogen exchange rate of Phe
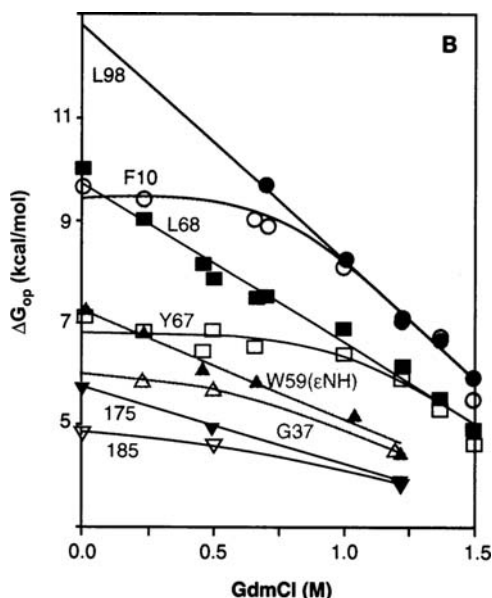
Fig.12.1. Guanidinium chloride-dependent hydrogen exchange of selected amides in cytochrome c. The limiting slope for Phe 10 and Leu 98 reflect the transition to global unfolding. Decreased slopes consistent with subglobal hydrogen exchange transitions are seen for Tyr 67 and Leu 68 of the 60 s helix, Gly 37 and Trp 59 H$^{\varepsilon 1}$ of the 36–61 loop, and Ile 75 and Ile 85 of the omega loop lying over the plane of the heme. Reprinted with permission from **Fig. 1B** of Yawen Bai et al., Science 269:192–197 (14 July 1995). Copyright AAAS.

10 (representative of residues in the N-terminal α-helix) is nearly concentration independent. However, as 1.0-M GdmCl is approached, the exchange rate of Phe 10 increases and converges with that exhibited by Leu 98 of the C-terminal α-helix which appears to exchange via global unfolding throughout the GdmCl concentration range. Although residues Tyr 67 and Leu 68 of the 6 s helix exhibit a qualitatively similar pattern, the limiting slope of their common *m*-value at high GdmCl concentrations is less than that for Phe 10 and Leu 98. A yet smaller limiting slope is observed for the Ile 75 and Ile 85 residues that lie in the neck of a small omega loop segment that is positioned over the plane of the heme in the native structure.

The hydrogen exchange behavior for a set of residues that exhibit a similar limiting denaturant dependence can be plausibly interpreted in terms of a collective conformational transition if these residues form a spatially contiguous region of the protein that is structurally consistent with such a subglobal transition. The common *m*-value for these residues provides an estimate of the amount of surface exposure in the exchange-competent state, relative to the global unfolding transition, which in turn can be compared to the spatial extent of the structural region defined by these residues *(46)*. Interpretation as a subglobal transition requires that the corresponding *m*-value be unambiguously less than that for the global unfolding transition. Otherwise, complications in the peptide normalization analysis can generate the appearance of multiphase stability behavior *(47,48)*.

5.2. Temperature Dependence of Hydrogen Exchange

The activation energy of hydroxide-catalyzed exchange for poly-D,L-alanine is +17 kcal/mol *(49)*. The temperature dependence of water ionization and the resulting variation in hydroxide ion concentration accounts for +14 kcal/mol, while the exchange reaction itself is characterized by a kinetic barrier of +3 kcal/mol, similar to that of hydroxide exchange within the bulk water phase *(50)*. In order to extract apparent thermodynamic values from the temperature dependence of hydrogen exchange, correction must also be made for the temperature dependence of ionization for the buffer. Although the ionization enthalpy for acetate (–0.1 kcal/mol) *(51)*, phosphate (–1.9 kcal/mol for K_1, +0.8 kcal/mol for K_2 and +3.5 kcal/mol for K_3) *(51)*, and borate (+3.5 kcal/mol) *(52)* buffers are relatively small, that of Tris is +11.3 kcal/mol *(53)*.

The variation of hydrogen exchange rate with temperature provided the first direct evidence that the efficient exchange-competent conformation(s) for individual amides can undergo a transition from a smaller scale "local fluctuation" to exchange via global unfolding as the thermal transition of the protein is approached. As summarized in **Fig. 12.2** *(54)*, the groups of Wüthrich *(55)* and of Woodward *(56)* reported temperature-dependence studies on individual slowly exchanging amides of bovine pancreatic trypsin inhibitor. Above 70°C, the three residues illustrated exhibit similar
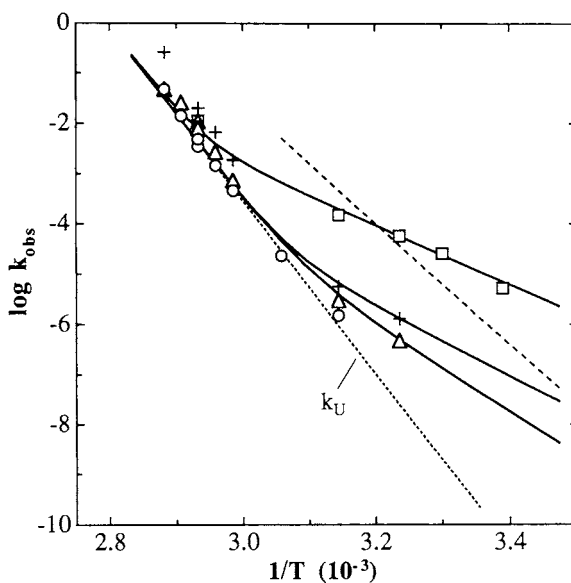
Fig.12.2. Temperature dependence of amide hydrogen exchange rates for Gln 31, Phe 45, and Met 52 of bovine pancreatic trypsin inhibitor at pH 3.6. The "dotted line" indicates the extrapolated rate of global unfolding. The common slope observed at high temperature corresponds to an activation energy near 80 kcal/mol, while at lower temperatures the activation energies of the three residues decrease by varying amounts. Reprinted with permission from **Fig. 3** of K. S. Kim et al., Biochemistry 32, 9609–9613 (1993). Copyright American Chemical Society.

kinetics with an apparent activation energy near 80 kcal/mol, consistent with hydrogen exchange via global unfolding. However, at lower temperatures further from the global thermal transition, the slopes of the Arrhenius plots for these three residues diverge to yield apparent activation energy values ranging from 27 kcal/mol to 40 kcal/mol.

To complement their earlier pressure dependence studies *(57)*, Bryant and coworkers *(58)* determined the activation enthalpies for hydrogen–deuterium exchange in bacteriophage T4 lysozyme for a temperature range more than 30° below the reversible thermal transition. As seen in **Fig. 12.3**, these activation enthalpy estimates exhibit substantial variation along the protein backbone, varying from 7 kcal/mol to 34 kcal/mol. The authors concluded that the variations in activation energy values for residues that are structurally close together in the folded protein suggest that there may be a variety of energetically distinct pathways for the access of solvent to these structurally related exchange sites.

Within the EX2 kinetic limit, the temperature dependence of the hydrogen exchange arises both from the variation in the conformational equilibrium between the conformational ground state and the exchange-competent state(s) and from the temperature dependence of the chemical exchange step in the exchange-competent state.
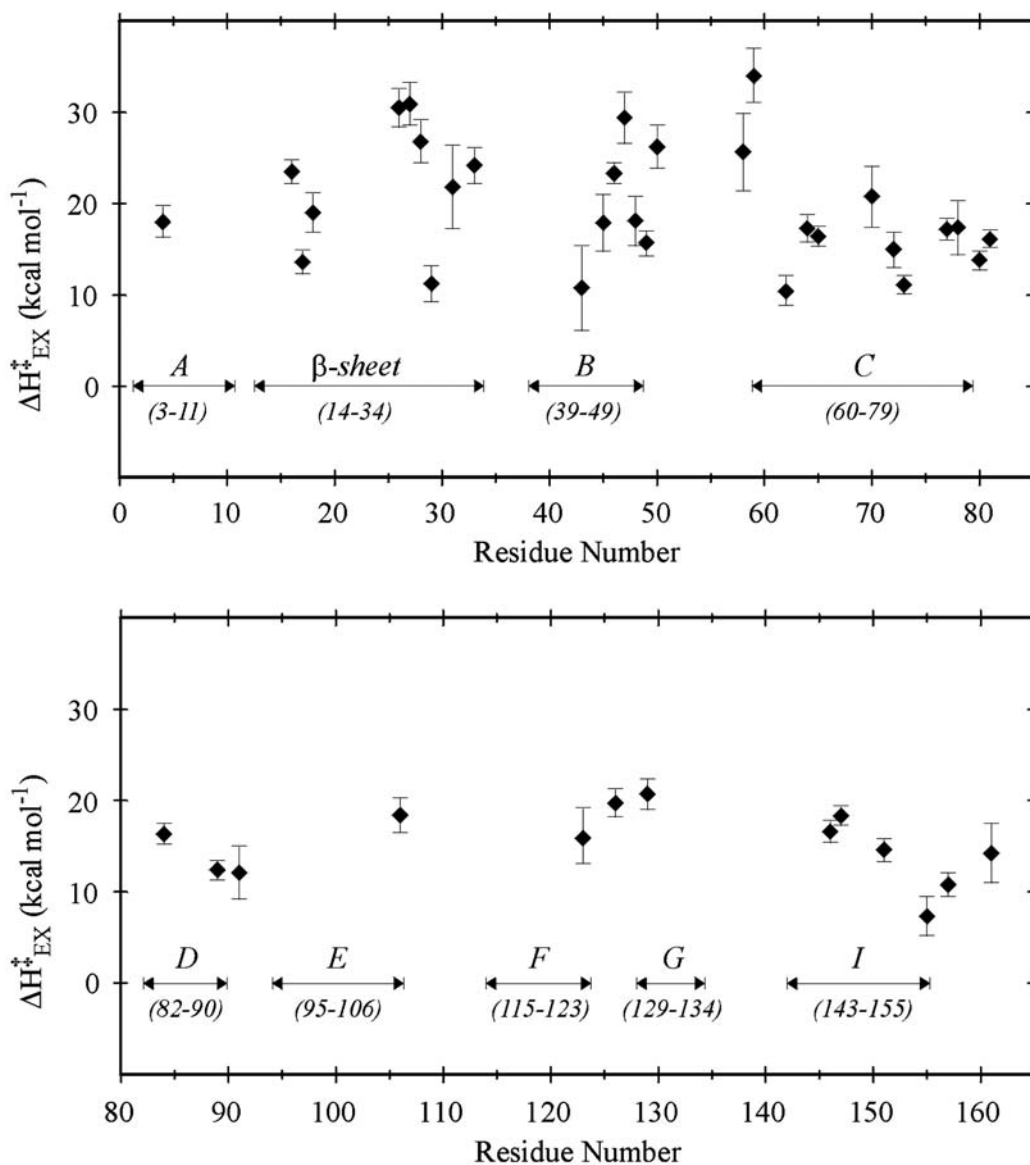
Fig.12.3. Activation enthalpies for hydrogen–deuterium exchange of bacteriophage T4 lysozyme determined over the temperature interval of 280–305 K. "Error bars" indicate a 67% confidence interval of the fit. Letters represent each of the nine helices. Reprinted with permission from **Fig. 1** of M. E. Dixon et al., Biochemistry 39, 248–254 (2000). Copyright American Chemical Society.

Interpretation of the conformational equilibria can be obtained via a differential analysis under the comparatively weak assumption of a similar temperature dependence for the chemical exchange step between the amides being compared. In this analysis, the observed differential temperature dependence of the hydrogen exchange yields the differential enthalpy of the conformational equilibrium according to

$$\mathrm{d}(\ln(k_{\mathrm{ex1}}/k_{\mathrm{ex2}}))/\mathrm{d}(1/T) = \mathrm{d}(\ln \Delta K_{\mathrm{eq}})/\mathrm{d}(1/T) = -\Delta\Delta H/R.$$

In measuring the hydroxide-catalyzed exchange rate constants for the rubredoxins from the hyperthermophilic *Pyrococcus furiosus* (*Pf*) and the mesophilic *Clostridium pasteurianum* (*Cp*), we observed that nine of the amides in the so-called multi-turn segment *(59)* exchange at similar rates near room temperature for both proteins (**Fig. 12.4**) *(60)*. As discussed in more detail below, magnetization transfer-based experiments enabled the measurement of the hydrogen exchange kinetics of nearly all backbone amide positions in the rubredoxins. When the ratio of the exchange rates for the *Cp* and *Pf* rubredoxins at each amide of this segment are plotted against the inverse temperature, all nine of these slowly exchanging positions yield slopes consistent with a differential conformational enthalpy of 6–8 kcal/mol (**Fig. 12.5**). In contrast, all of the more rapidly exchanging amides in this segment exhibit no significant differential temperature dependence. The similarity in the magnitude and temperature dependence for these slowly exchanging amides are consistent with a collective conformational opening of the multi-turn segment that is hydrogen exchange-competent at temperatures 100° below the thermal transition for these proteins *(48)*. Furthermore, below room temperature the amides in this segment of the hyperthermophilic *Pf* rubredoxin become exposed to solvent for exchange
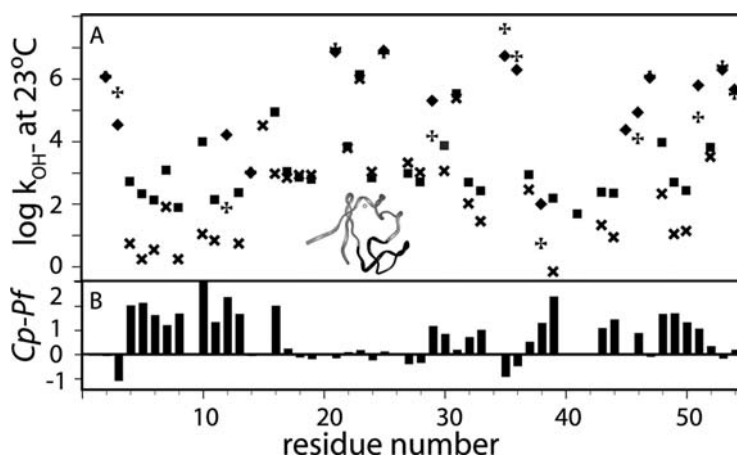
Fig.12.4. Hydroxide-catalyzed amide exchange rate constants for *Clostridium pasteurianum* and *Pyrococcus furiosus* rubredoxins at 23°C. The log k_{OH}^- value for poly-D,L-alanine is 8.3 under these conditions *(61,83)*. Nearly all of residues exhibit rate constants for *Pf* rubredoxin (+ and ×) that are equal to or less than those for *Cp* rubredoxin (■ and ◆) at this temperature. For both proteins the exchange rate constants of the most slowly exchanging amides in the multi-turn segment are highly similar. The inserted backbone structure of rubredoxin highlights this segment. Reprinted with permission from **Fig. 2** of G. Hernández et al., Biochemistry 40, 14384–14391 (2001). Copyright American Chemical Society.
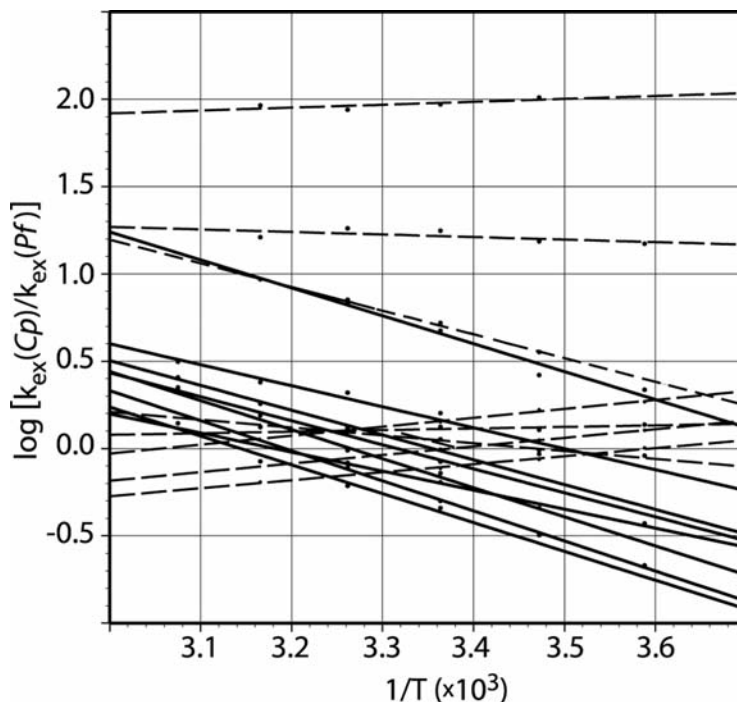
Fig.12.5. Arrhenius plot of the differential amide exchange kinetics for the multi-turn residues of *Cp* and *Pf* rubredoxin. The "solid lines" indicate all of the residues for which the *Cp* rubredoxin log k_{OH}^- value is less than 3.0 at 23°C, while the "dashed lines" indicate the data for the more rapidly exchanging residues. With the exception of Phe 30, with a log k_{OH}^- value less than 3.0 in *Pf* rubredoxin, only the set of slowly exchanging amides exhibit significant differential temperature-dependent exchange rates that are consistent with $\Delta\Delta H$ values between 6 kcal/mol and 8 kcal/mol. Reprinted with permission from **Fig. 6** of G. Hernández et al., Biochemistry 40, 14384–14391 (2001). Copyright American Chemical Society.

for a larger fraction of the time than does the corresponding segment in the mesophilic homolog. These data provided the first demonstration that a defined structural region in a thermophile protein can be more flexible than the corresponding region in a mesophile homolog under identical conditions.

5.3. pH Dependence of Hydrogen Exchange

The sensitivity of hydrogen exchange rates to variations in pH is central to many of the applications of this technique. Above pH 4, model peptides generally exhibit hydrogen exchange rates that are directly proportional to the hydroxide ion concentration. These hydroxide-catalyzed exchange rate constants depend upon the identities of the side chains on either side of the peptide linkage *(61)*. For ionizable side chains, the neutral and charged forms differ in their exchange rate constant contributions, consistent with the electrostatic interaction between the side chain and the peptide nitrogen anion intermediate formed during the exchange reaction. An analogous set of exchange rate constants characterize the hydronium

ion-catalyzed exchange that is generally dominant below pH 3. A modest contribution from neutral water-catalyzed exchange is observed only near the exchange minimum (i.e., pH 3–4). It should be noted that the standard peptide reference rates *(61)* were measured in 0.5 M KCl in order to suppress electrostatic effects. Although exchange measurements on poly-d,l-alanine as a function of ionic strength suggest a small effect for neutral residues, these authors noted that the exchange rates for charged residues differ by roughly 30% at more typical salt concentrations.

Probably the most common reason for studying the pH dependence of hydrogen exchange is to discriminate between the EX1 and EX2 kinetic conditions. In the idealized case of a protein for which the conformational dynamics (and any indirect charge effects) are pH independent, EX1-type exchange will also be pH independent, since under these conditions the exchange reaction is completed each time the transition to the exchange-competent state occurs. On the other hand, when the conformational equilibrium is established rapidly as compared to the chemical exchange step, exchange rates proportional to the hydroxide-ion should occur. Needless to say, since protein conformational stability does vary with pH and titration of ionizable side chains can affect hydrogen exchange kinetics, discrimination between EX1 and EX2 kinetics based on pH variation is sometimes ambiguous.

Of particular utility is the ability to observe a pH-dependent transition between EX1 and EX2 conditions by exploiting the fact that at higher pH values the chemical exchange step can sometimes be sufficiently accelerated so as to compete with the conformational closing transition. Robertson and coworkers have used this approach to characterize the kinetics of global unfolding for the ovomucoid third domain *(62)* and ubiquitin *(63)*. Subglobal conformational transitions have also been characterized by this approach as illustrated in the example of the *Borrelia burgdorferi* outer surface protein OspA. The X-ray analysis of this protein *(64)* revealed a highly extended anti-parallel β-sheet structure with 21 strands followed by the single α-helix at the C-terminus. Koide and coworkers *(65)* reported hydrogen exchange measurements as a function of pH on this protein. The experimental hydrogen exchange rates for amides within segments of the protein are plotted in **Fig. 12.6** against a range of reference peptide rates generated by varying pH and denaturant concentration, adjusted for the differences among the individual dipeptide sequences. The central portion of the protein (strands 9–13) destabilize before the transition to the EX1 regime. However, both the N-terminal β1-8 and the C-terminal β14-α exhibit a change in slope, indicative of passing from the EX2 condition into that of EX1 kinetics. As a result, the rate of unfolding for these protein segments can be directly estimated.

Carrying out a series of conventional hydrogen–deuterium exchange reactions in parallel presents several technical
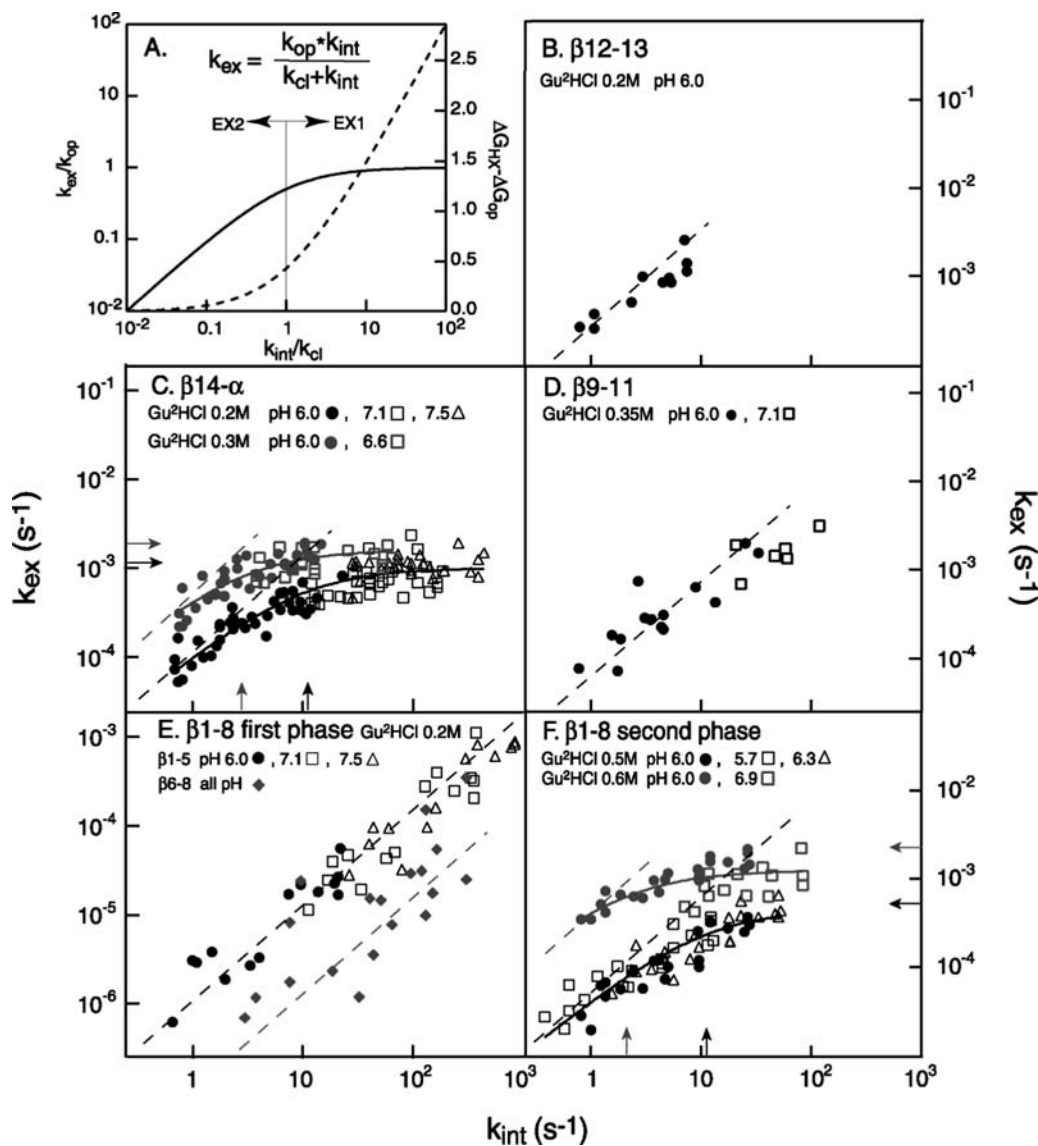
Fig.12.6. The transition from EX2 to EX1 kinetics for the β-sheet segments of *Borrelia burgdorferi* OspA. Panel A indicates the theoretical dependence of k_{ex} on the model peptide reference values k_{int} across the transition between EX2 and EX1 kinetics. The other panels present the experimental hydrogen exchange data from portions of the extended β-sheet structure. The "straight dashed lines" indicate simple EX2 dependence, while the "curved lines" of panel C and F represent the dependence anticipated for a transition to EX1 kinetics. Reprinted from **Fig. 4** of S. Yan et al., J. Mol. Biol. 323, 363–375 (2002) with permission from Elsevier.

complications. Given the acute sensitivity of the hydrogen exchange rates to changes in pH and temperature, minimizing undesired variations among the samples can be challenging. In order to observe the more rapidly exchanging peaks, the time between the introduction of the deuterated solvent and commencement of NMR data collection is generally kept to a

minimum. As a result, the sample pH is commonly not measured until the end of the experiment which is often of the order of months. In many types of experimental measurements, internal calibration standards are used to compensate for such sample-to-sample variation. In order for such an internal standard to be of use for referencing a typical protein hydrogen exchange experiment, it would require a hydroxide-catalyzed exchange rate that is 10^4–10^7-fold slower than that of simple model peptides with a similar temperature dependence. In general, O-bound and N-bound hydrogens act as "normal" acids in the Eigen formalism of acid–base kinetics *(27)*. In this case, the kinetic acidity is determined by the difference between the pK_a value of the acid and that of water, based on the assumption that proton transfer within the hydrogen-bonded collision complex is sufficiently rapid so that thermodynamic equilibrium is established before dissociation. Hence, to achieve the desired decrease in hydroxide-catalyzed rates, a 4–7-unit increase in the pK_a value would be needed (i.e., pK_a of ~21–25). Since O-bound and N-bound protons also undergo acid-catalyzed hydrogen exchange, it is problematic to obtain such a weak acidity while maintaining predominantly base-catalyzed exchange kinetics near neutral pH.

Carbon acids can exhibit such a high pK value (and much higher) with no significant competition from an acid-catalyzed exchange reaction. However, a large proportion of carbon acids do not conform to normal acid behavior. Rather, they exhibit kinetic acidities that are substantially weaker than would be predicted from their thermodynamic pK_a values. As illustrated in the familiar example of the thiazolium ring *(66)*, which serves as the reactive core of vitamin B_1, normal carbon acid behavior can be achieved through localization of the negative charge density to the primary carbon and through minimization of the heavy atom reorganization required by the transition to the carbanion state *(67)*.

Drawing upon the recent demonstration that the C-2 position of 1,3-dimethylimidazolium (**Fig. 12.7A**) has a pK_a of 23.0 *(68)*, we *(69)* have demonstrated that the hydroxide-catalyzed exchange of the H-2 proton occurs with an apparent log protection factor of 5.58 at 23°C in a buffered solution containing 100 mM sodium chloride. Signal decay rate constants can be readily determined with uncertainties of 1–2% from 2D ^1H–^{13}C correlation spectra
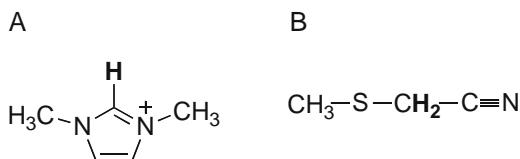
Fig.12.7. 1,3-dimethylimidazolium and methylthioacetonitrile. The positions that ionize with the kinetics of a normal Eigen acid are indicated in bold.

of [2-^{13}C] 1,3-dimethylimidazolium iodide at submillimolar concentrations in the analogous fashion used to monitor amide exchange rates in ^{15}N-labeled protein samples. This normal carbon acid internal referencing approach was used to determine the pH values in real time during the hydrogen exchange experiments on the metal-substituted *Pf* rubredoxins discussed above *(35)* under these same solution conditions. A related series of imidazolium cations are reported to have activation energies for exchange of 21 kcal/mol, *(70)* modestly higher than that reported for model peptide exchange, indicating a similar temperature dependence. Although quaternization of the ring nitrogens eliminates the metal-binding properties associated with neutral imidazole, the net positive charge of the imidazolium cation results in an appreciable ionic strength dependence for the hydrogen exchange rates. For situations in which variations in ionic strength are potentially problematic, the neutral normal carbon acid [methylene-^{13}C]thiomethylacetonitrile (**Fig. 12.7B**) with an apparent log protection factor of 6.76 at 23°C offers a useful alternative *(69)*.

5.4. Time Dependence of Hydrogen Exchange

In the standard protection analysis, the observed rate of hydrogen exchange k_{ex} represents the lower limit for the rate of conformational opening transition. By shortening the time frame during which exchange occurs, tighter constraints can be obtained for the underlying conformational transitions. Quenched-flow techniques similar to those used to analyze the folding reaction are potentially applicable to studying conformational transitions within the native state. As noted above, for several different proteins, an increase in pH has resulted in the transition from EX2 to EX1 exchange kinetics for the most protected amides. In these conventional hydrogen–deuterium exchange experiments, introduction of the deuterated solvent and initiation of NMR data collection generally requires several minutes. Particularly at high pH values, the large majority of the peptide amides are often fully exchanged within this dead time. However as illustrated by Arrington and Robertson in their analysis of the ovomucoid third domain *(71)*, rapid mixing at high pH followed by quenching to lower pH to suppress further exchange during the subsequent data collection can provide near-millisecond temporal resolution (**Fig. 12.8**). Each of the six panels shows the peak amplitudes for a residue that begins to exhibit significant hydrogen exchange in 12 ms at pH values near 10. The dashed curves represent the exchange behavior expected for simple EX2 kinetics, leading the authors to conclude that a switch toward EX1 behavior is occurring for these residues which are exchanging via a subglobal conformational transition.

A similar time frame of hydrogen exchange kinetics can be monitored under equilibrium conditions making use of magnetization transfer techniques. Rather than following the interchange
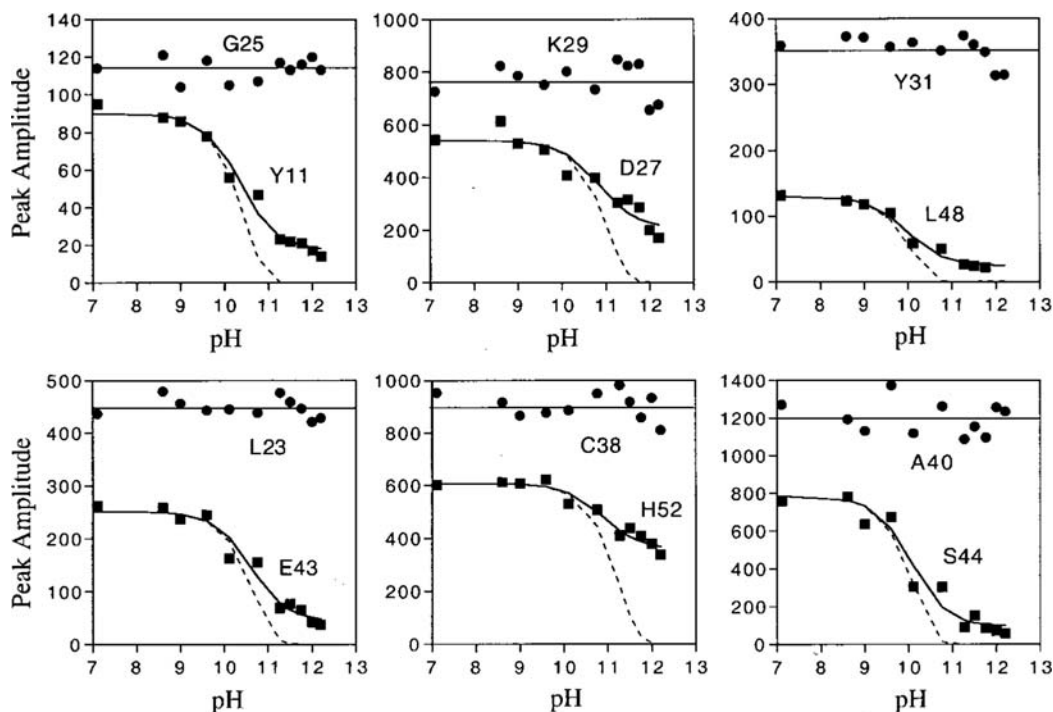
Fig.12.8. The pH dependence of TOCSY crosspeak amplitudes for NH groups in ovomucoid third domain after 12 ms of hydrogen–deuterium exchange. Residues Leu 23, Gly 25, Lys 29, Tyr 31, Cys 38, and Ala 40 were previously shown to exchange via global unfolding *(62)*, and little if any decrease in peak intensity is observed under the present conditions. In contrast, the amide resonances from the other six residues decrease markedly as the pH is increased. However, in each case this decrease is less abrupt than that predicted for simple EX2 kinetic behavior (*dashed lines*). Reprinted from **Fig. 2** of C. B. Arrington et al., J. Mol. Biol. 296, 1307–1317 (2000) with permission from Elsevier.

of hydrogen isotopomers from the solvent phase, the magnetic spins of the ^1H resonance of water are selectively excited and the migration of those excited nuclei is monitored during their chemical exchange into the protein peptide units. As a result, the upper limit of the time frame monitored by these experiments is determined by the nuclear relaxation of the solvent proton resonance. The lower time limit of the detection is determined by the frequency separation between the amide and the water resonances, or more commonly in protein studies by the ^1H–^{15}N coupling constant (90–95 Hz) when heteronuclear correlation experiments are used to observe the amide resonances in a ^{15}N-labeled sample.

One of the most robust magnetization transfer experiments developed to accurately measure protein hydrogen exchange rates is the CLEANEX-PM pulse sequence *(72)* which efficiently suppresses artifactual intensity arising from TOCSY contributions and both intramolecular and exchange-relayed NOE/ROE contributions. This pulse sequence was initially applied to the analysis of rapidly exchanging amides on the protein surface *(73)*. However,

increasing the pH and temperature causes the exchange rates of more strongly protected amides to move into the time window for which the CLEANEX-PM experiment is sensitive. As illustrated in **Fig. 12.9**, we *(74)* have used this approach to demonstrate that the amides throughout the backbone of *Pf* rubredoxin open up to solvent in the millisecond time frame near room temperature, indicating a substantial degree of conformational flexibility for this protein which exhibits the highest reported reversible thermal transition temperature for a monomeric species *(48)*. The right-hand side panels present the reference FHSQC *(75)* spectra in which peaks arise from magnetization that originates and remains on the amide resonances throughout the pulse sequence. On the left is a series of CLEANEX-PM spectra indicating magnetization which originated in the selectively excited water resonance and then, during a variable length mixing period, chemically exchange onto the amide positions where they are subsequently detected. The similarity between the bottom pair of spectra indicate that substantial exchange from water is occurring at each remaining amide resonance during the mixing period.

One limitation of the original CLEANEX-PM experiment is that the buildup of intensity as a function of the length of the mix time rapidly deviates from linearity due to the T_2 relaxation of the protein amide resonances. Due to this effect, the original authors based their exchange rate determinations on initial slope analysis *(73)*. To increase the range of useful mix times and hence the sensitivity of the experiment, we *(76)* proposed a relaxation-compensated version of the CLEANEX-PM experiment which makes use of a reference experiment in which the water-selective e-PHOSGY *(77)* component is replaced with a nonselective hard pulse. When combined with perdeuteration, hydrogen exchange rates can be accurately measured over a range of at least $0.2 –70 \, s^{-1}$ *(78)*.

5.5. Mutational Variation in the Study of Hydrogen Exchange

Difference analysis-based hydrogen exchange studies can be effectively applied to the protein itself by systematic mutation. Except at the site of mutation, all of the peptide normalization factors cancel out for the remainder of the sequence in such a difference comparison. In general, mutation introduces perturbations that result from removing a set of native-like interactions and introducing another set of non-native-type interactions. It is often not straightforward to quantitatively deconvolute the contributions from the non-native-type interactions so as to gain maximal insight into the interactions that are native to the parental protein.

Comparative studies of structurally homologous proteins offer a potentially robust approach to this problem. Complementary pairs of hybrid proteins can be derived from two parental sequences by interchanging one or more nonconserved residues. Given a pair of homologous proteins, as for the *Pf* and *Cp* rubredoxins that differ significantly in both their thermal stabilities and
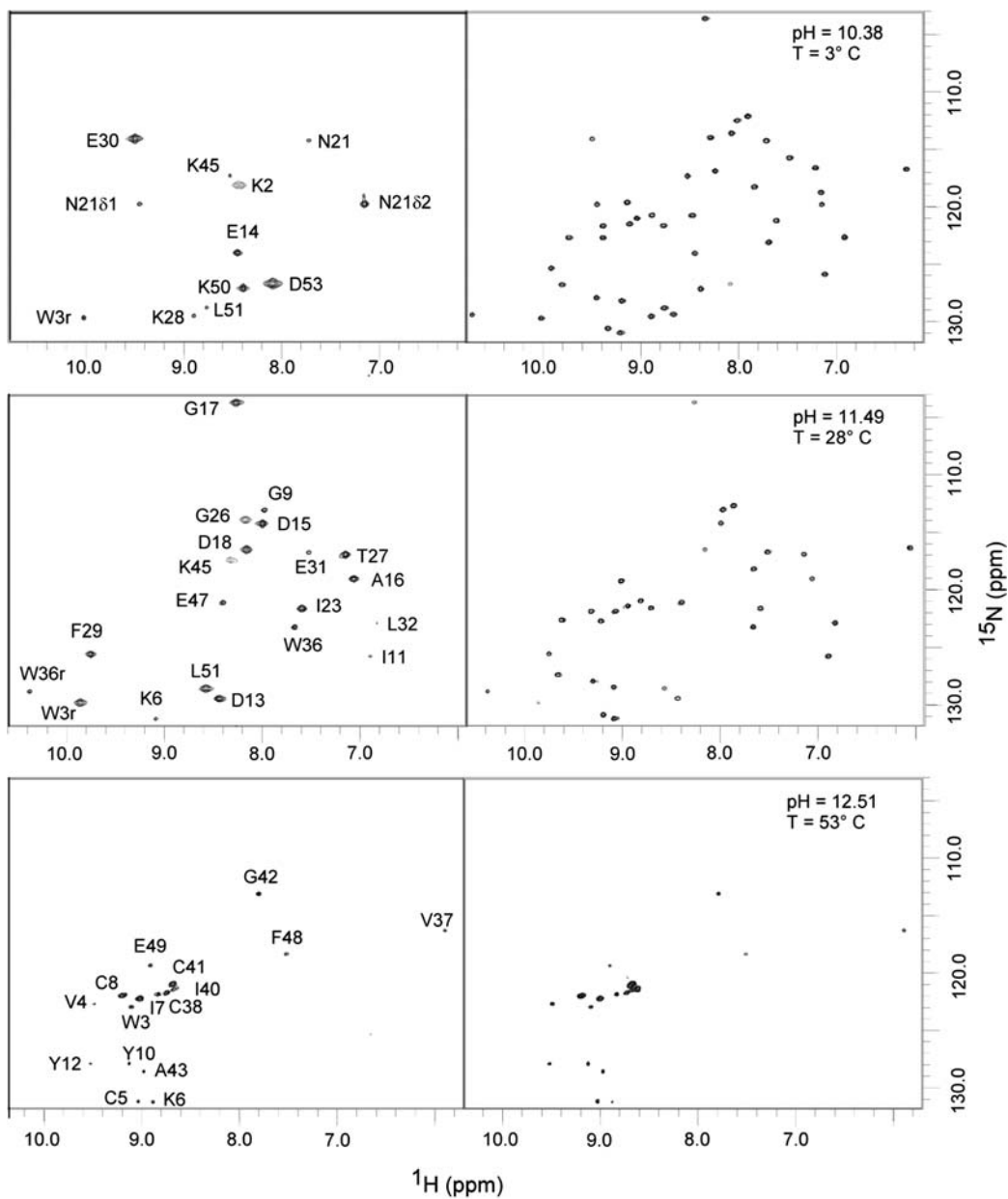
Fig.12.9. Magnetization transfer-based hydrogen exchange measurements on *Pyrococcus furiosus* rubredoxin as a function of pH and temperature. The CLEANEX-PM *(73)* spectra *(left)* monitor magnetization that originates in the ^{1}H solvent resonance and then exchanges into the amide proton position during the mixing period. The reference FHSQC *(75)* spectra *(right)* monitor magnetization that originates in the protein amide resonances and remains there throughout the pulse sequence. Reprinted from **Fig. 1** of G. Hernández et al., Proc. Natl. Acad. Sci. USA. 97, 3166–3170 (2000) with permission from the National Academy of Sciences, U.S.A. Copyright (2000) National Academy of Sciences, U.S.A.

their hydrogen exchange behavior, pairs of complementary hybrids can yield valuable insights into how such differences are spatially partitioned within the protein structure. As discussed above, the multi-turn segment in both *Cp* and *Pf* rubredoxins exhibits a collective mode of hydrogen exchange at temperatures that are well below the thermal unfolding transition. By interchanging the sequence for this segment between the two parental rubredoxins, we *(78)* found that exchange rates at 23°C for each of the amides within both the *Cp* and *Pf* multi-turn segments differed by less than a factor of 2.5 between the parental protein and the hybrid protein in which this segment is attached to the core of the other parental rubredoxin. Furthermore, the differential temperature dependence of hydrogen exchange for the slowly exchanging residues of the hyperthermophile vs. mesophile multi-turn segment seen for the parental rubredoxins was largely preserved when these segments were attached to the protein core of the other parental rubredoxin.

Particularly revealing are the differential exchange rates for the amides within a given protein core when the multi-turn segment from either the *Pf* or *Cp* rubredoxin sequence is attached. Despite the fact that the slowest exchanging amides surround the metal-binding site which lies on the opposite face of the protein, when the hyperthermophile multi-turn sequence is introduced into *Cp* rubredoxin, the reversible thermal transition temperature is increased 12° *(79)*. Yet, for no amide in the protein core did the hydrogen exchange rate at 23°C decrease by as much as a factor of 3 upon introducing the thermostabilizing *Pf* multi-turn sequence *(78)*. On the other hand, the slowly exchanging core residues Tyr 4 and Glu 50 accelerate their exchange by more than a factor of 3 in the more thermostable hybrid, indicating that this hybrid has equivalent if not increased room temperature conformational flexibility, relative to the mesophile *Cp* rubredoxin parent, as monitored by these exchange measurements. When the temperature dependence of the differential hydrogen exchange is monitored for the core residues of the parental *Cp* rubredoxin and the *Pf* multi-turn *Cp* hybrid, six residues were found to have exchange rates within the range of the slowly exchanging positions in the multi-turn segment as well as elevated differential enthalpy values for exchange similar to those seen within the multi-turn segment (**Fig. 12.10**). In contrast, for seven other core residues that exchange even more slowly, none have $\Delta\Delta H$ values above 1.5 kcal/mol, near the uncertainty limit of these data. These results are consistent with these six core residues sharing exchange-competent conformational transitions with the residues of the multi-turn segment. As seen in **Fig. 12.11**, these six residues form a compact region of the core that would appear to predominantly interact with the slowly exchanging residues of the multi-turn segment via the aromatic ring stacking of Tyr 4 and Phe 30.

The degree to which the differential hydrogen exchange behavior in such a pair of protein hybrids reflects conformational
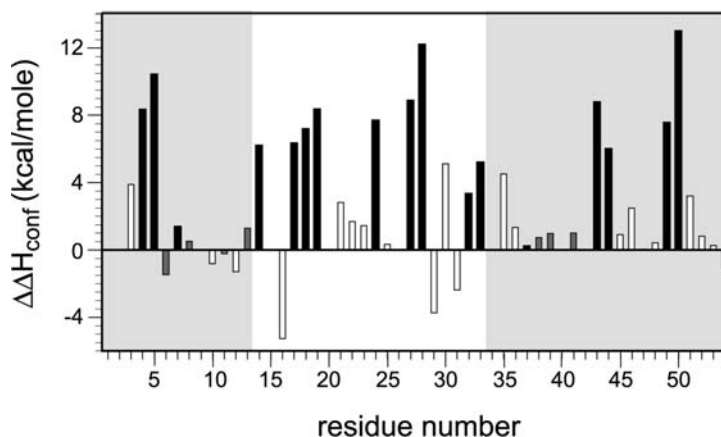
Fig.12.10. Differential enthalpy of amide hydrogen exchange arising from interchanging the multi-turn sequence ("light background") from *Pf* rubredoxin onto the protein core ("gray background") of *Cp* rubredoxin. The slowly exchanging amides of the multi-turn segment are indicated in black as are the amides of the core that lie within the same range of exchange rates. More rapidly exchanging amides are indicated with "open bars", while the more slowly exchanging amides of the protein core are denoted in "gray". Six residues of the core (Tyr 4, Thr 5, Gly 43, Val 44, Phe 49, and Glu 50) exhibit both similar hydrogen exchange rates and similar differential enthalpies of exchange to those of the multi-turn segment. None of the amides of the protein core that exchange more slowly than the amides of the multi-turn segment exhibit $\Delta\Delta H$ values above 1.5 kcal/mol. Note that although Phe 30 of the multi-turn segment has an exchange rate that is approximately 10-fold higher than those residues marked in "black", nevertheless it exhibits a moderately elevated differential enthalpy of exchange. Reprinted with permission as adapted from **Fig. 4** of D. M. LeMaster et al., Proteins 61, 608–616 (2005). Copyright Wiley & Sons.

transitions characteristic of the parental proteins can be expected to depend upon the degree to which the interactions along the hybridization interface mimic those found in the parental protein structures. Using such a design criterion *(80)*, another pair of complementary hybrids of *Cp* and *Pf* rubredoxins was formed by interchanging the seven nonconserved residues in the active-site metal-binding region. The sum of the thermodynamic stabilities of these two metal-binding site-swapped rubredoxins was found to be equal to the sum of the thermodynamic stabilities of the parental *Cp* and *Pf* rubredoxins *(81)*. These rubredoxin chimera provide the first example of a complementary pair of hybrids systematically designed from known parental protein structures which exhibit full thermodynamic additivity upon exchanging a cluster of mutually interacting nonconserved residues that define a substantial hybridization interface (360 Å²) across the core of a protein domain. Throughout the amino acid sequence, the differential exchange kinetics induced by the substitution of the seven hyperthermophile residues into the metal-binding site region of *Cp* rubredoxin are generally of equivalent intensity but opposite sign to the differential kinetics resulting from the complementary
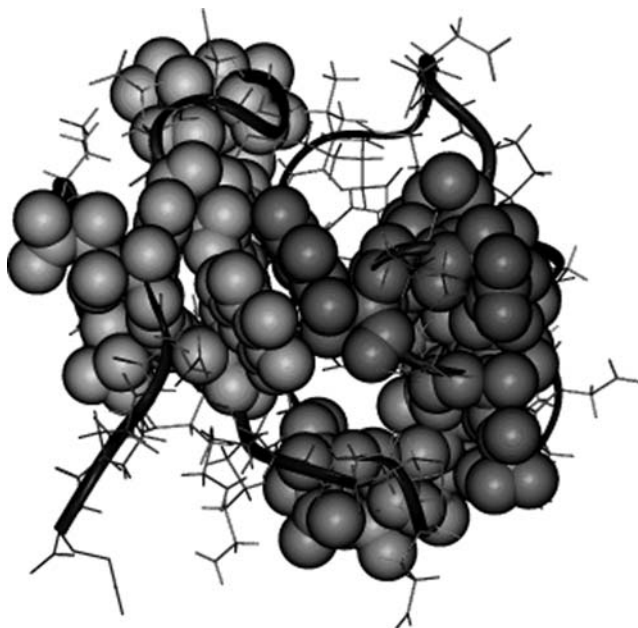
Fig.12.11. Spatial distribution of differential enthalpy of the exchange-competent conformational opening in the protein core of *Cp* rubredoxin upon substitution of the multi-turn sequence from *Pf* rubredoxin. The six residues of the protein core exhibiting hydrogen exchange kinetics similar to that of the multi-turn segment are highlighted in light gray in the upper left region of the figure. The slowly exchanging residues of the multi-turn segment are indicated in dark gray in the lower right. These two clusters of residues appear to primarily interact via the aromatic ring stacking of Tyr 4 and Phe 30. Reprinted with permission as adapted from **Fig. 5** of D. M. LeMaster et al., Proteins 61, 608–616 (2005). Copyright Wiley & Sons.

residue exchange *(82)*. These data indicate that the alterations in the exchange-competent conformational transitions that result from substitution of the hyperthermophile residues into *Cp* rubredoxin are closely mirrored by those which arise from the mesophile substitutions into the hyperthermophile sequence. The amides which exhibit more than a threefold change in differential exchange rate due to the residue substitutions around the metal site are almost exclusively from structurally buried residues with their side chains forming a connected set of interactions, penetrating well across the protein interior.

6. Conclusions

For over 50 years amide hydrogen exchange measurements have continued to provide valuable insights into the conformational dynamics of proteins. Although in some applications only a

qualitative interpretation of the exchange rates is sufficient for drawing useful conclusions, in many situations a quantitative analysis of these rates is critical to the physical understanding of the data. In such analyses it has been commonly assumed that the residual conformational structure of the protein in the exchange-competent state has no effect on the rate of the chemical exchange step. Although this assumption appears to be often well justified for amide groups that exchange via a global unfolding transition, contradictions to this assumption have been demonstrated for hydrogen exchange that occurs by more localized conformational fluctuations. Suitable design of difference analysis studies can provide an effective approach to this issue whenever the differential effect of the residual conformational structure on the chemical exchange step is either independent of the experimental condition being varied or else depends upon this variable in a predictable fashion. Electrostatic effects have often been treated as an undesired complication to interpreting hydrogen exchange rates in terms of conformational equilibria. However, the systematic modulation of the acidity of the peptide nitrogen acidities by variation of the electrostatic field potential can provide valuable insight into the electrostatic interactions of the protein interior, offering an additional pathway to broadening the utility of hydrogen exchange measurements.

References

1. Hvidt, A., Linderstrøm-Lang, K. (1954) Exchange of hydrogen atoms in insulin with deuterium atoms in aqueous solutions, *Biochim Biophys Acta* 14, 574–575.

2. Schechter, A. N., Moravek, L., Anfinsen, C. B. (1968) Suppression of hydrogen exchange in *Staphylococcal* nuclease by ligands, *Proc Nat Acad Sci USA* 61, 1478–1485.

3. Busenlehner, L. S., Armstrong, R. N. (2005) Insights into enzyme structure and dynamics elucidated by amide H/D exchange mass spectrometry, *Arch Biochem Biophys* 433, 34–46.

4. Borch, J., Jorgensen, T. J. D., Roepstorff, P. (2005) Mass spectrometric analysis of protein interactions, *Curr Opin Chem Biol* 9, 509–516.

5. Scholtz, J., Robertson, A. D. (1995) Hydrogen exchange techniques, in (Shirley, B.A., ed.) *Protein Stability and Folding*, Vol. 40, pp. 291–312, Humana Press, Clifton, NJ.

6. Roder, H. (1989) Structural characterization of protein folding intermediates by proton magnetic resonance and hydrogen exchange, *Meth Enzymol* 176, 446–473.

7. Krishna, M. M. G., Hoang, L., Lin, Y., et al. (2004) Hydrogen exchange methods to study protein folding, *Methods* 34, 51–64.

8. Konermann, L., Simmons, D. A. (2003) Protein-folding kinetics and mechanisms studied by pulse-labeling and mass spectrometry, *Mass Spectr Rev* 22, 1–26.

9. Nazabal, A., Schmitter, J. M. (2006) Hydrogen–deuterium exchange analyzed by matrix-assisted laser desorption-ionization mass spectrometry and the HET-s prion model, *Meth Enzymol* 413, 167–181.

10. Kheterpal, I., Wetzel, R. (2006) Hydrogen/deuterium exchange mass spectrometry – A window into amyloid structure, *Acc Chem Res* 39, 584–593.

11. Miranker, A., Robinson, C. V., Radford, S. E., et al. (1996) Investigation of protein folding by mass spectrometry, *FASEB J* 10, 93–101.

12. Hvidt, A., Nielsen, S. O. (1966) Hydrogen exchange in proteins, *Adv Protein Chem* 21, 287–386.

13. Englander, S. W. (1967) Hydrogen exchange, in (Fasman, G., ed.) *Poly-a-amino*

acids, pp. 339–367. Marcel Dekker, Inc., New York.

14. Woodward, C. K., Rosenberg, A. (1971) Studies of hydrogen exchange in proteins. V. The correlation of ribonuclease exchange kinetics with the temperature-induced transition, *J Biol Chem* 246, 4105–4113.

15. Englander, S. W., Kallenbach, N. R. (1984) Hydrogen exchange and structural dynamics of proteins and nucleic acids, *Q Rev Biophys* 16, 521–655.

16. Woodward, C., Simon, I., Tüchsen, E. (1982) Hydrogen exchange and the dynamics of proteins, *Mol Cell Biochem* 48, 135–160.

17. Miller, D. W., Dill, K. A. (1995) A statistical mechanical model for hydrogen exchange in globular proteins, *Prot Sci* 4, 1860–1873.

18. Huyghues-Despointes, B. M. P., Pace, C. N., Englander, S. W., et al. (2001) Measuring the conformational stability of a protein by hydrogen exchange, in (Murphy, K.P., ed.) *Protein Structure, Stability and Folding*, Vol. 168, pp. 69–92. Humana Press, Totowa, NJ.

19. Arrington, C. B., Robertson, A. D. (2000) Correlated motions in native proteins from MS analysis of NH exchange: Evidence for a manifold of unfolding reactions in ovomucoid third domain, *J Mol Biol* 300, 221–232.

20. Wildes, D., Anderson, L. M., Sabogal, A., et al. (2006) Native state energetics of the Src SH2 domain: Evidence for a partially structured state in the denatured ensemble, *Prot Sci* 15, 1769–1779.

21. Bowler, B. E. (2007) Thermodynamics of protein denatured states, *Mol Biosystems* 3, 88–99.

22. Kim, P.S., Baldwin, R.L. (1982) Influence of charge on the rate of amide proton exchange, *Biochemistry* 21, 1–5.

23. Tüchsen, E., Woodward, C. (1985) Hydrogen kinetics of peptide amide protons at the bovine pancreatic trypsin inhibitor protein-solvent interface, *J Mol Biol* 185, 405–419.

24. Delepierre, M., Dobson, C. M., Karplus, M., et al.. (1987) Electrostatic effects and hydrogen exchange behavior in proteins. The pH dependence of exchange rates in lysozyme, *J Mol Biol* 197, 111–130.

25. Dempsey, C. E. (1988) pH Dependence of hydrogen exchange from backbone peptide amides of Melittin in methanol, *Biochemistry* 27, 6893–6901.

26. Fogolari, F., Esposito, G., Vigino, P., et al. (1998) pKa shift effects on backbone amide base-catalyzed hydrogen exchange rates in peptides, *J Am Chem Soc* 120, 3735–3738.

27. Eigen, M. (1964) Proton transfer, acid–base catalysis, and enzymic hydrolysis. (I) Elementary processes, *Angew Chem Int Ed* 3, 1–72.

28. Molday, R. S., Kallen, R. G. (1972) Substituent effects on amide hydrogen exchange rates in aqueous solution, *J Am Chem Soc* 94, 6739–6745.

29. Wang, W. H., Cheng, C. C. (1994) General base catalyzed proton exchange in amides, *Bull Chem Soc Jpn* 67, 1054–1057.

30. Wang, W. H., Cheng, C. C. (1995) Erratum: general base catalyzed proton exchange in amides, *Bull Chem Soc Jpn* 68, 2767–2767.

31. Wagner, G., Wüthrich, K. (1982) Amide proton exchange and surface conformation of the basic pancreatic trypsin inhibitor in solution, *J Mol Biol* 160, 343–361.

32. Christoffersen, M., Bolvig, S., Tüchsen, E. (1996) Salt effects on the amide hydrogen exchange of bovine pancreatic trypsin inhibitor, *Biochemistry* 35, 2309–2315.

33. Hernández, G., Anderson, J.S., LeMaster, D.M. (2008) Electrostatic stabilization and general base catalysis in the active site of the human protein disulfide isomerase **a** domain monitored by hydrogen exchange, *ChemBioChem* 9, 768–778 .

34. LeMaster, D. M., Minnich, M., Parsons, P. J., et al. (2006) Tetrathiolate coordination of germanium(IV) in a protein active site, *J Inorg Biochem* 100, 1410–1412.

35. LeMaster, D. M., Anderson, J. S., Hernández, G. (2006) Role of native-state structure in rubredoxin native-state hydrogen exchange, *Biochemistry* 45, 9956–9963.

36. Anderson, J. S., LeMaster, D. M., Hernandez, G. (2006) Electrostatic potential energy within a protein monitored by metal charge-dependent hydrogen exchange, *Biophys J* 91, L93–L95.

37. LeMaster, D. M., Anderson, J. S., Hernández, G. (2007) Spatial distribution of dielectric shielding in the interior of *Pyrococcus furiosus* rubredoxin as sampled in the subnanosecond timeframe by hydrogen exchange, *Biophys Chemist* 129, 43–48.

38. Wrba, A., Schweiger, A., Schultes, V., et al. (1990) Extremely thermostable D-glyceraldehyde-3-phosphate dehydrogenase from the eubacterium *Thermotoga maritima*, *Biochemistry* 29, 7584–7592.

39. Bonisch, H., Backmann, J., Kath, T., et al. (1996) Adenylate kinase from *Sulfolobus acidocaldarius*: Expression in *Escherichia coli* and characterization by Fourier transform infrared spectroscopy, *Arch Biochem Biophys* 333, 75–84.

40. Zavodszky, P., Kardos, J., Svingor, A., et al. (1998) Adjustment of conformational flexibility is a key event in the thermal adaptation of proteins, *Proc Natl Acad Sci USA* 95, 7406–7411.

41. Loftus, D., Gbenle, G. O., Kim, P. S., et al. (1986) Effects of denaturants on amide proton exchange rates: A test for structure in protein fragments and folding intermediates, *Biochemistry* 25, 1428–1436.

42. Itzhaki, L. S., Neira, J. L., Fersht, A. R. (1997) Hydrogen exchange in chymotrypsin inhibitor 2 probed by denaturants and temperature, *J Mol Biol* 270, 88–89.

43. Pace, C. N. (1986) Determination and analysis of urea and guanidine hydrochloride denaturation curves, *Meth Enzymol* 131, 266–280.

44. Mayo, S. L., Baldwin, R. L. (1993) Guanidinium chloride induction of partial unfolding in the amide proton exchange in RNase A, *Science* 262, 873–876.

45. Loh, S. N., Rohl, C. A., Kpefhaber, T., et al. (1996) A general two-process model describes the hydrogen exchange behavior of RNase A in unfolding conditions, *Proc Natl Acad Sci USA* 93, 1982–1987.

46. Bai, Y., Sosnick, T. R., Mayne, L., et al. (1995) Protein folding intermediates: native-state hydrogen exchange, *Science* 269, 192–197.

47. Hiller, R., Zhou, Z. H., Adams, M. W. W., et al. (1997) Stability and dynamics in a hyperthermophilic protein with melting temperature close to 200 degrees C, *Proc Natl Acad Sci USA* 94, 11329–11332.

48. LeMaster, D. M., Tang, J., Hernández, G. (2004) Absence of kinetic thermal stabilization in a hyperthermophile rubredoxin indicated by 40 microsecond folding in the presence of irreversible denaturation, *Proteins* 57, 118–127.

49. Englander, J. J., Calhoun, D. B., Englander, S. W. (1979) Measurement and calibration of peptide group hydrogen–deuterium exchange by ultraviolet spectroscopy, *Anal Biochem* 92, 517–524.

50. Wraight, C. A. (2006) Chance and Design – Proton transfer in water, channels and bioenergetic proteins, *Biochim Biophys Acta* 1757, 886–912.

51. Pitzer, K. S. (1937) The heats of ionization of water, ammonium hydroxide, carbonic, phosphoric and sulfuric acids., *J Am Chem Soc* 59, 2365–2371.

52. Barres, M., Redoute, J. P., Romanetti, R., et al. (1973) Calorimetry of complexes in solution, *C R Acad Sci Ser C* 276, 363–366.

53. Harned, H .S., Owen, B. B. (1950) *Physical Chemistry of Electrolyte Solutions, ACS Monograph*, p. 514. Reinhold Publishers, New York.

54. Kim, K. S., Woodward, C. (1993) Protein internal flexibility and global stability: Effect of urea on hydrogen exchange rates of bovine pancreatic trypsin inhibitor, *Biochemistry* 32, 9609–9613.

55. Richarz, R., Sehr, P., Wagner, G., et al. (1979) Kinetics of the exchange of individual amide protons in the basic pancreatic trypsin inhibitor, *J Mol Biol* 130, 19–30.

56. Woodward, C. K., Hilton, B. D. (1980) Hydrogen isotope exchange kinetics of single protons in bovine pancreatic trypsin inhibitor, *Biophys J* 32, 561–575.

57. Hitchens, T. K., Bryant, R. G. (1998) Pressure dependence of amide hydrogen–deuterium exchange rates for individual sites in T4 lysozyme, *Biochemistry* 37, 5878–5887.

58. Dixon, M. E., Hitchens, T. K., Bryant, R. G. (2000) Comparison of pressure and temperature activation parameters for amide hydrogen exchange in T4 lysozyme, *Biochemistry* 39, 248–254.

59. Watenpaugh, K. D., Sieker, L. C., Jensen, L. H. (1980) Crystallographic refinement of rubredoxin at 1.2 Å resolution, *J Mol Biol* 138, 615–633.

60. Hernández, G., LeMaster, D. M. (2001) Reduced temperature dependence of collective conformational opening in a hyperthermophile rubredoxin, *Biochemistry* 40, 14384–14391.

61. Bai, Y. W., Milne, J. S., Mayne, L., et al. (1993) Primary structure effects on peptide group hydrogen-exchange, *Proteins: Struct, Funct, Genet* 17, 75–86.

62. Arrington, C. B., Robertson, A. D. (1997) Microsecond protein folding kinetics from native-state hydrogen exchange, *Biochemistry* 36, 8686–8691.

63. Sivaraman, T., Arrington, C. B., Robertson, A. D. (2001) Kinetics of unfolding and

folding from amide hydrogen exchange in native ubiquitin, *Nat Struct Biol* 8, 331–333.

64. Li, H., Dunn, J. J., Luft, B. J., Lawson, C. L. (1997) Crystal structure of Lyme disease antigen outer surface protein A complexed with an Fab, *Proc Natl Acad Sci USA* 94, 3584–3589.

65. Yan, S., Kennedy, S. D., Koide, S. (2002) Thermodynamic and kinetic exploration of the energy landscape of *Borrelia burgdorferi* OspA by native-state hydrogen exchange, *J Mol Biol* 323, 363–375.

66. Washabaugh, M. W., Jencks, W. P. (1989) Thiazolium C(2)-Proton exchange: Isotope effects, internal return, and a small intrinsic barrier, *J Am Chem Soc* 111, 683–692.

67. Costentin, C., Saveant, J. M. (2004) Why are proton transfers at carbon slow? Self-exchange Reactions, *J Am Chem Soc* 126, 14787–14795.

68. Amyes, T. L., Diver, S. T., Richard, J. P., et al. (2004) Formation and stability of N-heterocyclic carbenes in water: The carbon acid pKa of imidazolium cations in aqueous solution, *J Am Chem Soc* 126, 4366–4374.

69. LeMaster, D. M., Anderson, J. S., Hernández, G. (2007) Normal carbon acid referencing for protein amide hydrogen exchange, *Magn Reson Chem* 45, in press.

70. Noszal, B., Rabenstein, D. L. (1991) Nitrogen-protonation microequilibria and C(2)-deprotonation microkinetics of histidine, histamine, and related compounds, *J Phys Chem* 95, 4761–4765.

71. Arrington, C. B., Robertson, A. D. (2000) Microsecond to minute dynamics revealed by EX1-type hydrogen exchange at nearly every backbone hydrogen bond in a native protein, *J Mol Biol* 296, 1307–1317.

72. Hwang, T. L., Mori, S., Shaka, A. J., et al. (1997) Application of phase-modulated CLEAN Chemical EXchange Spectroscopy (CLEANEX-PM) to detect water-protein proton exchange and intermolecular NOEs, *J Am Chem Soc* 119, 6203–6204.

73. Hwang, T. L., vanZijl, P. C. M., Mori, S. (1998) Accurate quantitation of water-amide proton exchange rates using the phase-modulated CLEAN chemical EXchange (CLEANEX-PM) approach with a Fast-HSQC (FHSQC) detection scheme, *J Biomol NMR* 11, 221–226.

74. Hernández, G., Jenney, F. E., Adams, M.W.W., and LeMaster, D.M. (2000) Millisecond time scale conformational flexibility in a hyperthermophile protein at ambient temperature, *Proc Natl Acad Sci USA* 97, 3166–3170.

75. Mori, S., Abeygunawardana, C., Johnson, M. O., et al. (1995) Improved sensitivity of HSQC spectra of exchanging protons at short interscan delays using a new fast HSQC (FHSQC) detection scheme that avoids water saturation, *J Magn Reson B* 108, 94–98.

76. Hernández, G., LeMaster, D. M. (2003) Relaxation compensation in chemical exchange measurements for the quantitation of amide hydrogen exchange in larger proteins, *Magn Reson Chem* 41, 699–702.

77. Dalvit, C., Hommel, U. (1995) Sensitivity-improved detection of protein hydration and its extension to the assignment of fast-exchanging resonances, *J Magn Reson B* 109, 334–338.

78. LeMaster, D. M., Tang, J., Paredes, D. I., et al. (2005) Enhanced thermal stability achieved without increased conformational rigidity at physiological temperatures: Spatial propagation of differential flexibility in rubredoxin hybrids, *Proteins* 61, 608–616.

79. LeMaster, D. M., Tang, J., Paredes, D. I., et al. (2005) Contribution of the multi-turn segment in the reversible thermal stability of hyperthermophile rubredoxin: NMR thermal chemical exchange analysis of sequence hybrids, *Biophys Chem* 116, 57–65.

80. Hernández, G., LeMaster, D.M. (2005) Hybrid native partitioning of interactions among nonconserved residues in chimeric proteins, *Proteins* 60, 723–731.

81. LeMaster, D. M., Hernández, G. (2005) Additivity in both thermodynamic stability and thermal transition temperature for rubredoxin chimeras via hybrid native partitioning, *Structure* 13, 1153–1163.

82. LeMaster, D. M., Hernández, G. (2006) Additivity of differential conformational dynamics in hyperthermophile/mesophile rubredoxin chimeras as monitored by hydrogen exchange, *ChemBioChem* 7, 1886–1889.

83. Connelly, G. P., Bai, Y. W., Jeng, M. F., et al. (1993) Isotope effects in peptide group hydrogen-exchange, *Proteins* 17, 87–92.

Chapter 13

Single-Molecule Fluorescence Studies of Protein Folding

G. Ulrich Nienhaus

Abstract

The structural and dynamic details of protein folding are still widely unexplored due to the enormous level of heterogeneity intrinsic to this process. The unfolded polypeptide chain can assume a vast number of possible conformations, and many complex pathways lead from the ensemble of unfolded conformations to the ensemble of native conformations in an overall funnel-shaped energy landscape. Classical experimental methods involve measurements on bulk samples and usually yield only average values characteristic of the entire molecular ensemble under study. The observation of individual molecules avoids this averaging and allows, in principle, microscopic distributions of conformations and folding trajectories to be revealed. Fluorescence-based techniques are arguably the most versatile single-molecule methods at present, and Förster resonance energy transfer (FRET) between two dye molecules specifically attached to the protein of interest provides a means of studying the inter-dye distance and, thereby, the conformation of folding polypeptide chains in real time. This chapter focuses on practical aspects and different experimental realizations for protein folding investigations by using single-molecule fluorescence.

Key words: Protein folding, single-molecule fluorescence spectroscopy, single-molecule fluorescence microscopy, Förster resonance energy transfer (FRET), protein immobilization, biofunctionalized surfaces, protein diffusion, folding trajectories.

1. Introduction

Protein folding, the intriguing process by which the polypeptide chain acquires its proper three-dimensional architecture, is a simple example of biological self-organization that has challenged theorists and experimentalists for many years. The basic interactions causing the polypeptide chain to fold are well understood; yet, the prediction of the three-dimensional structure of a protein from its specific amino acid sequence is still not generally feasible. In early work, folding of the polypeptide chain was believed to occur via a unique pathway, as represented by a simple kinetic

scheme with a few discrete intermediate states *(1, 2)*. Recent years have witnessed enormous advances in our theoretical understanding of protein folding, which led to an appreciation of the enormous complexity of this process. The polypeptide samples many different substates in a complex energy landscape and can pursue many different, parallel trajectories on its way to the compact, folded conformation *(3–6)*.

To explore the heterogeneous dynamics of the polypeptide en route to the native state, folding transitions can be synchronously induced in large ensembles of proteins by sudden external perturbations such as laser flashes, and the ensuing changes can be followed by time-resolved spectroscopy over all timescales relevant to the problem *(7–9)*. However, due to the heterogeneous, multistep nature of protein folding, the synchronization gets lost so that bulk experiments can only provide ensemble-averaged information on folding pathways. Single-molecule techniques, by contrast, avoid ensemble averaging and allow one to assess the properties of individual molecules or subpopulations. Already in the 1970s, Neher and Sakmann demonstrated the power of single-molecule detection for the elucidation of biomolecular dynamics by patch-clamp recording of currents from individual ion channels *(10)*. In the last decade, novel experimental techniques have been applied to the study of biomolecular dynamics at the single-molecule level, including atomic force microscopy *(11)*, optical tweezers *(12, 13)*, and single-molecule fluorescence spectroscopy *(14–18)*, which have yielded exciting new insights. Here we will focus on applications of the latter technique in protein folding studies, with an emphasis on using Förster resonance energy transfer (FRET) as a structure-sensitive probe *(19–21)*. FRET is based on the nonradiative coupling of two dye molecules referred to as donor and acceptor that are specifically attached to the protein of interest. FRET depends on the inverse sixth power of the donor–acceptor distance, which makes it an exquisitely sensitive tool for examining structural and dynamic properties of individual molecules with atomic-scale resolution. A variety of single-pair FRET experiments have proven the applicability of the method in protein folding studies to analyze structural properties of unfolded proteins in equilibrium in the presence of denaturant *(22–24)*, to observe time trajectories of folding pathways in real time *(25, 26)*, and to measure folding kinetics under nonequilibrium conditions *(27)*.

1.1. Single-Molecule Fluorescence Instrumentation

Instrumentation for single-molecule fluorescence spectroscopy has recently become commercially available *(28)*, so researchers interested in its application no longer have to build their own sophisticated apparatus. Here we restrict ourselves to the essentials of the method; detailed descriptions of single-molecule

fluorescence spectroscopy and microscopy apparatus can be found in books and review articles *(14, 15, 29)*.

A severe limitation inherent to the method is the finite amount of photons that can be collected from a single fluorophore due to photodestruction. Therefore, one often aims to maximize the information retrievable with each photon, which is its wavelength (spectral information), its polarization (orientational information), the location from where it was emitted (position information), its real time of arrival (intensity information), and the delay between excitation and fluorescence emission (fluorescence lifetime information).

To achieve single-molecule sensitivity with high signal-to-noise ratio, photons have to be collected with optimal efficiency. Still, less than 1 in 20 photons are registered in typical state-of-the-art setups. Furthermore, it is necessary to rigorously restrict the volume from which fluorescence is collected so that the signals from the molecule under study are not overwhelmed by background fluorescence from impurities. The two main approaches are (1) confocal laser scanning microscopy (CLSM), with fluorescence excitation by pulsed or continuous-wave lasers (*see* **Note 1**) and detection by low-background avalanche photodiodes (APDs), and (2) wide-field microscopy with laser excitation and two-dimensional detection using highly sensitive, intensifying (ICCD) or electron-multiplying charge-coupled device (EMCCD) cameras. In wide-field microscopy, optimal signal-to-noise ratio is achieved using evanescent wave excitation. This variant is commonly referred to as total internal reflection fluorescence (TIRF) microscopy.

Confocal imaging with APDs enables observation of single molecules with high (submicrosecond) time resolution. Data are collected one molecule at a time, and signals from many molecules are recorded in sequence to build up a statistically significant molecular ensemble. By contrast, up to a few hundred molecules are registered in parallel when using wide-field imaging, and, therefore, this technique is particularly useful for experiments involving irreversible processes, for example, chemical reactions initiated by fast mixing with reagents, which require a fresh sample for each measurement. However, the time resolution of wide-field imaging is limited to millisecond frame integration times of CCD cameras.

In **Fig. 13.1**, the essential features of the two single-molecule microscopy designs are depicted schematically. In the confocal geometry in **Fig. 13.1A**, a laser beam is focused to a diffraction-limited spot (~0.3–0.5 μm diameter) by using a high-numerical-aperture objective lens that also serves to collect the emission from the fluorescently labeled molecules. A suitably chosen dichroic mirror passes the red-shifted fluorescence light and reflects back-scattered excitation light. The confocal pinhole in the detection

pathway provides axial sectioning as it transmits only light emanating within $\sim$0.5–1 μm from the focal plane. For experiments on freely diffusing fluorescent molecules, the laser light is simply focused into the solution, and light bursts are recorded as labeled molecules briefly visit the sensitive volume. As the observation time is limited by the $\sim$1-ms diffusion time of a protein molecule through the tiny detection volume of the microscope, measurements over longer periods of time require surface immobilization of the molecules. A piezoelectric stage scanner allows one to move the sample with respect to the confocal spot so that images can be acquired by raster scanning.

Figure13.1B is a schematic depiction of a TIRF microscope, in which an evanescent field is created by total reflection of laser light at the surface to the aqueous medium by means of a prism. In an alternative design, the sample is excited through the objective lens, which has the advantage that the sample can be accessed
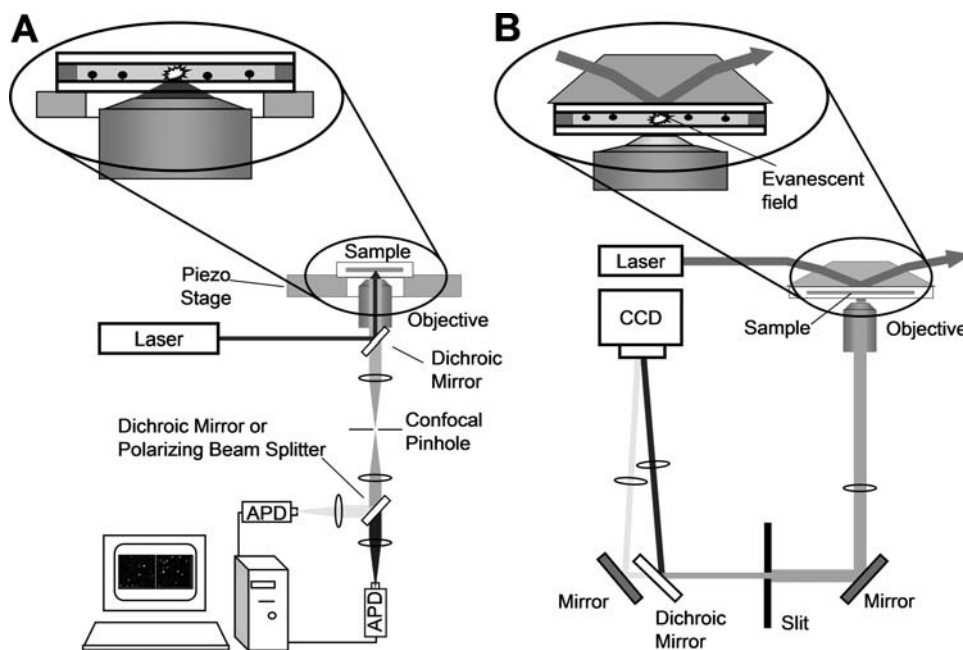
Fig. 13.1. Schematic depictions of fluorescence microscopy techniques for single-molecule experiments. (**A**) Confocal laser scanning fluorescence microscope (CLSM). A laser beam is reflected by a dichroic mirror and focused by a high-numerical-aperture objective to produce a tight focal spot in the sample, from where fluorescence emission is detected by the same objective. A confocal pinhole is inserted into the emission path to provide sectioning along the optical axis. The fluorescence beam is separated into two colors or orthogonal polarizations by using a dichroic mirror or polarizing cube. Two photon-counting APD detectors register incoming photons with high efficiency and submicrosecond time resolution. A piezo stage allows the sample to be moved across the focus for collection of images. (**B**) Total internal reflection fluorescence microscope (TIRFM). A laser beam is directed through a quartz prism and reflected at the quartz–water interface so as to create an evanescent wave that extends $\sim$100 nm into the aqueous solution. The fluorescence emission by protein molecules immobilized at this surface is collected by a high-numerical-aperture objective. Part of the image is passed through a slit and separated by a dichroic mirror into two images associated with the two color channels. Both images are combined on the CCD camera chip.

freely from the upper side. However, separation of excitation and emission light is more critical in this variant so that the signal-to-noise ratio may be compromised.

In both confocal and wide-field designs, the emitted fluorescence is usually detected in two or more separate detection channels. For FRET experiments, the emission is split by a dichroic mirror into two color channels appropriately designed for efficient collection of donor and acceptor emission and optimal cross-talk rejection. Moreover, efficient blocking filters for the exciting laser line and possibly additional band-shaping filters are inserted into the individual detection paths. Instead of the dichroic mirror, a polarizing beam splitter is employed in measurements of molecular rotation using polarization anisotropy, which separates the emission into perpendicular and parallel polarization components. Both detection modes can be combined in a four-channel system *(30)* (*see* **Note 2**).

1.2. Single-Molecule Fluorescence Intensity Fluctuation Analysis

Using a single-molecule fluorescence setup, trajectories of the fluorescence emission from single molecules are recorded in real time, from which detailed dynamics information can be obtained by stochastic analysis *(31)*. In the simplest case, a time correlation analysis is performed on the intensity fluctuations arising from fluorescently labeled protein molecules freely diffusing through the confocal volume. This method, commonly referred to as fluorescence correlation spectroscopy (FCS), may become very popular for probing protein–ligand interactions and protein aggregation *(32, 33)*. The photon events are directly fed into a hardware correlator for on-line computation of the autocorrelation function (ACF), defined as

$$G(\tau) = \frac{\langle \delta F(t) \cdot \delta F(t+\tau) \rangle}{\langle F(t) \rangle^2},$$ (13.1)

where F denotes the fluorescence intensity, δF its fluctuations around the average value, t and τ represent real time and correlation time, respectively, and the angular brackets denote the time average. The ACF quantifies the probability to detect a photon at some time $(t+\tau)$ if there was a photon at time t. Instead of using on-line correlation, the photon arrival times can also be recorded in the computer, and the ACF is calculated afterwards (*see* **Note 3**). Analysis of the ACF allows one to determine the sample concentration, the translational diffusion coefficient, and the timescales of conformational fluctuations in the range $\sim 1~\mu s$–1 ms *(34, 35)*. The emission intensity of many fluorescent dyes depends sensitively on their environment; for example, the excitation of Alexa Fluor 488 can be quenched upon contact with certain amino acid side chains. Therefore, FCS measurements can provide information on submillisecond-range polypeptide fluctuations

under denaturing conditions, that is, in the presence of chemical denaturants (GdmCl, urea, protons). Moreover, binding of denaturant molecules is known to cause an expansion of the protein molecule, which affects its translational diffusion coefficient. However, these variations are comparatively small and cannot be resolved by standard FCS. Further complications arise from the fact that chemical denaturants (except for protons) change the viscosity and the refractive index of the medium, and both effects will need to be accounted for in the analysis. A recent modification of the FCS technique, 2-focus FCS (2fFCS) *(36)*, promises a substantially improved precision of FCS and is, therefore, likely to find broad application in the measurement of structural properties of proteins under denaturing conditions.

Measurements of intensity fluctuations on freely diffusing fluorophores are limited by the duration of the molecular transit through the detection volume. Therefore, dynamics on longer timescales can only be observed with surface-immobilized biomolecules, as will be discussed below.

1.3. Single-Pair FRET Experiments

The basic idea of a protein folding experiment using FRET is rather simple. Two different dyes are attached to specific residues of a protein such that they are in close proximity in the folded state (**Fig. 13.2A**). One of the dyes absorbs at a shorter wavelength and is referred to as the "green dye", or "donor dye" in the following. The other dye absorbs at longer wavelengths and is called the "red dye", or "acceptor dye". An individual protein molecule is
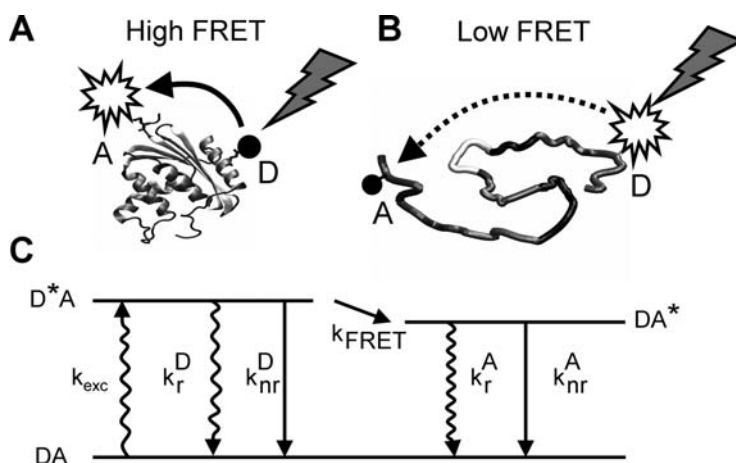
Fig. 13.2. Principle of a FRET measurement of distance fluctuations. (**A**) In the folded state, the donor (D) and acceptor (A) dyes are in close proximity. Excitation of the donor results in efficient energy transfer to the acceptor. (**B**) In the unfolded state, the inter-dye distance increases, and concomitantly, the energy transfer decreases. (**C**) The Jablonski diagram depicts the energy levels and transitions of a donor–acceptor pair, with transition rate coefficients for excitation, k_{exc}, radiative and nonradiative deexcitation, k_r, and k_{nr}, respectively, and Förster transfer, k_{FRET}.

illuminated by laser light with a wavelength suitable for donor excitation. In the folded state, the excited donor efficiently transfers its energy to the acceptor because their close proximity leads to strong nonradiative coupling. Consequently, red fluorescence from the acceptor is predominant, and the direct green fluorescence from the donor is very weak. Upon protein unfolding, the distance between the donor and acceptor dyes increases on average (**Fig. 13.2B**). As a result, the probability of energy transfer is decreased; more green photons from the donor are detected and less red ones from the acceptor. The relative intensities from donor and acceptor thus allow different conformational states of a protein to be distinguished.

The Jablonski diagram (**Fig. 13.2C**) shows the ground-state and first excited-state energy levels of donor and acceptor, and transitions between them are indicated by arrows. Upon absorption of a photon by the donor with rate coefficient k_{exc}, its electronic system is promoted to an excited state, with a lifetime given by

$$\tau = \frac{1}{k_r + k_{nr} + k_{FRET}}, \tag{13.2}$$

where k_r, k_{nr}, and k_{FRET} are the rate coefficients for radiative, nonradiative (excluding FRET), and FRET deexcitation, respectively. The latter rate coefficient arises from the presence of the acceptor dye in the vicinity of the donor. According to Förster's theory *(19, 37)*, k_{FRET} varies strongly with the inter-dye distance, r, according to

$$k_{FRET} = \frac{1}{\tau_0} \left(\frac{R_0}{r} \right)^6. \tag{13.3}$$

The Förster radius, R_0, is in the range 20–80 Å for common dye pairs such as Cy3/Cy5 and Alexa Fluor 546/Alexa Fluor 647 *(38)*. Its value depends on the orientation factor, κ^2, the donor quantum yield, Φ_D, the donor–acceptor spectral overlap integral, J (in M^{-1} cm^{-3}), and the refractive index, n, of the medium through which donor and acceptor interact:

$$R_0 = (8.79 \times 10^{23} \kappa^2 \Phi_D J\, n^{-4})^{1/6} \quad \text{(in Å)}, \tag{13.4}$$

with

$$\kappa^2 = (\cos \theta_T - 3 \cos \theta_D \cos \theta_A)^2 \tag{13.5}$$

and

$$J = \int_0^\infty f_D(\lambda) \varepsilon_A(\lambda) \lambda^4 d\lambda. \tag{13.6}$$

In **Eq. 13.5**, θ_T denotes the angle between the donor emission dipole and the acceptor absorption dipole, and θ_D and θ_A are,

respectively, the angles between the donor and acceptor emission dipoles and the line connecting donor and acceptor. In general, κ^2 is time-dependent due to rotational motions of the dyes. However, if donor emission and acceptor absorption dipoles reorient so quickly that the orientational dependence of the coupling is completely averaged within the donor fluorescence lifetime τ, the average value, $\langle \kappa^2 \rangle = 2/3$, can be introduced in **Eq. 13.4**. The spectral overlap integral J depends on the normalized fluorescence emission spectrum of the donor, $f_D(\lambda)$, and the molar extinction coefficient spectrum of the acceptor, $\varepsilon_A(\lambda)$.

With **Eqs. 13.2** and **13.3**, the probability of energy transfer to the acceptor after donor excitation, the FRET efficiency, E, is calculated as

$$E = \frac{k_{\text{FRET}}}{k_r + k_{nr} + k_{\text{FRET}}} = \frac{R_0^6}{r^6 + R_0^6}. \tag{13.7}$$

This simple relation between a spectroscopic observable, E, and a structural parameter, r, shown as the solid line in **Fig. 13.3**, makes the FRET method a "spectroscopic ruler" *(39)* that is widely applicable to measurements of structural changes associated with biomolecular interactions and conformational dynamics.

The FRET efficiency E can be determined ratiometrically from measurements of the donor and acceptor fluorescence intensities, I_D and I_A,
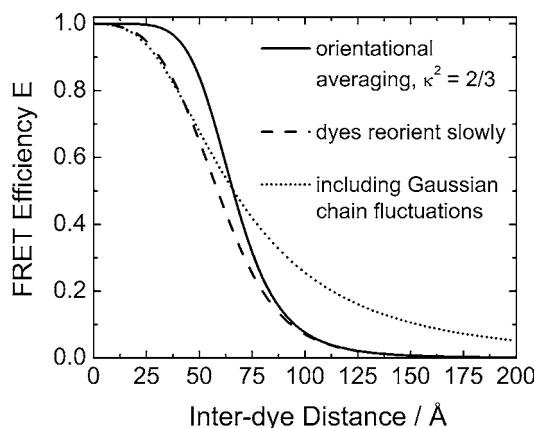
Fig. 13.3. Dependence of the FRET efficiency *E* on the inter-dye distance (for the FRET dye pair Alexa Fluor 546/Alexa Fluor 647). The "solid line" represents the dependence according to Förster's theory, assuming a fixed inter-dye distance and complete orientational averaging within the donor's fluorescence lifetime. The "dashed line" depicts the average FRET efficiency at a fixed distance, *r*, assuming isotropic transition dipoles with reorientation slower than the donor's fluorescence lifetime. The "dotted line" represents the average FRET efficiency of a fluctuating Gaussian chain with slow dye orientation, as a function of the root-mean-square average distance between the dyes.

$$E = \frac{I_A}{(I_A + \gamma I_D)}. \qquad (13.8)$$

Here, the parameter γ takes differences in the donor and acceptor quantum yields, Φ, and the detection efficiencies of both channels, η, into account,

$$\gamma = \frac{\eta_A \Phi_A}{\eta_D \Phi_D}. \qquad (13.9)$$

The FRET efficiency E can also be calculated from measurements of the donor fluorescence lifetime:

$$E = 1 - \frac{\tau}{\tau_0}. \qquad (13.10)$$

Here, τ and τ_0 are the donor lifetimes in the presence and absence of an acceptor dye, respectively. FRET analyses from donor lifetimes have the clear advantage that they are not subject to background and instrumental corrections of the donor and acceptor intensities.

Single-molecule FRET is an excellent technique for measuring changes in donor–acceptor distances, but deriving absolute distances from FRET data requires utmost care *(40–42)*. Determination of R_0 is not straightforward because the interaction of dyes with the protein may affect their (1) fluorescence properties (spectra, fluorescence lifetime) and (2) rotational dynamics, and (3) the proper refractive index of the medium through which the dyes interact may be difficult to assign. For example, in aqueous buffer with refractive index $n = 1.33$, $R_0 = 71$ Å for the dye pair Alexa Fluor 546/Alexa Fluor 647 (assuming $\kappa^2 = 2/3$). For a FRET pair bound to a protein, the latter is also part of the coupling medium. From experiment, $n \approx 1.47$ has been suggested as suitable for a hydrated protein *(43)*. With this value, $R_0 = 66$ Å in buffer and $R_0 = 63$ Å in 6 M GdmCl *(22)*. Another problem especially pertinent in protein folding experiments is that the FRET distance r is not constant but varies incessantly as the polypeptide chain fluctuates among many different conformations. In this case, the measurement yields a FRET-weighted average distance for the corresponding time interval.

If rotational averaging of the dye molecules is incomplete during the donor lifetime, **Eq. 13.7** cannot be used to calculate the FRET distance. Instead, one has to calculate an average over all possible dye orientations on the timescale of the FRET measurement, which leads to the dashed curve in **Fig. 13.3**. If large-scale chain fluctuations are present, one has to average also over all possible chain configurations *(25, 44)*. For a simple Gaussian-chain polymer model, the dependence of the average FRET efficiency on the average inter-dye distance is shown as a dotted line in **Fig. 13.3**.

1.4. Single-Molecule Experiments Using Pulsed Laser Excitation

Laser excitation sources that deliver pulses shorter than the fluorescence lifetime enable us to measure, in addition to the real time of photon arrival, the delay between fluorophore excitation and its subsequent fluorescence emission. This method, time-correlated single-photon counting (TCSPC), allows time traces of the fluorescence lifetimes from single molecules to be determined, which provides an independent measurement of the FRET efficiency according to **Eq. 13.10**. In the simplest case, the distribution of delay times in a certain time interval exhibits an exponential decay, and the statistical mean of the distribution is the single-molecule fluorescence lifetime.

In FRET experiments, the occurrence of low FRET values poses the problem that it either indicates weak FRET coupling or the absence of a functional acceptor. By excitation with alternating green and red laser pulses on the microsecond (alternating laser excitation, ALEX) *(45)* or nanosecond (pulse interleaved excitation, PIE) *(46)* timescale, these two cases can be unambiguously distinguished. The 2fFCS method (*see* **Section 1.2.**) also involves pulsed laser excitation. By applying picosecond laser pulses switching every 25 ns between two orthogonal polarizations, the two foci can be illuminated in an alternating fashion by using a Nomarski prism *(36)*.

2. Materials

2.1. Buffer Solutions

Highest-purity reagents are required for single-molecule experiments to minimize the background fluorescence. The usual buffer salts can be obtained in excellent purity from most major suppliers (e.g., Sigma Aldrich) at spectrophotometric grade. Fluorescent impurities may also be removed from solutions by using activated charcoal (e.g., Darco, granular, 12–20 mesh, Sigma Aldrich). Water from ion-exchange water purification systems (MilliQ 18.2 MΩ) is in general suitable, but needs to be monitored continuously for fluorescent contaminations. As a general rule, all solutes have to be tested for fluorescent impurities prior to use.

Buffer A: 20 mM TrisHCl, 100 mM KCl, 10 mM $MgCl_2$, pH 7.4.

2.2. Reagents for Protein Labeling with Fluorophores and Biotin

Fluorophores should be chosen so as to have a large extinction coefficient ($\sim 10^5$ $M^{-1}cm^{-1}$) at the wavelength of the excitation laser line, a high fluorescence quantum yield, a high photostability, and weak intrinsic intensity fluctuations, which arise from transitions between bright and dark states. For FRET experiments, the Förster radius must be suitable for the experiment (*see* **Section 1.3.**), and donor and acceptor emission must be

spectrally well separated to minimize direct acceptor excitation and cross-talk between the detection channels. Finally, the dyes must be well soluble in water and available with functional groups that allow for specific protein labeling. Currently, Alexa *(47)* and Cy *(48)* dyes are among the most popular dyes for single-molecule fluorescence studies.

2.2.1. Amine-Reactive Labels	1. Fluorophores such as Cy3 and Cy5 succinimidyl ester (GE Healthcare, Chalfont St. Giles, UK) or Alexa Fluor 546 succinimidyl ester (Molecular Probes Europe BV, Leiden, the Netherlands). 2. Biotin succinimidyl ester (Sigma-Aldrich, Munich, Germany).
2.2.2. Cysteine-Reactive Labels	1. Fluorophores such as Cy3 and Cy5 maleimide (GE Healthcare, Chalfont St. Giles, UK) or Alexa Fluor 546 and Alexa Fluor 647 maleimide (Molecular Probes).
2.3. Reagents for Surface Preparation	1. Bovine serum albumin (BSA), biotinylated BSA (Sigma Aldrich). 2. Methoxy-PEG-succinimidyl propionate (mPEG-SPA), MW 5000 and 2000 (Nektar Therapeutics, Huntsville, AL). 3. Methoxy-PEG-succinimidyl α-methylbutanoate (mPEG-SMB-5000) (Nektar Therapeutics). 4. Biotin-PEG-succinimidyl ester (biotin-PEG-NHS), MW 3400, (Nektar Therapeutics). 5. Six-armed, isocyanate-terminated star polymers (backbone: 80% ethylene oxide, 20% propylene oxide; average MW 12000 g/mol; SusTech GmbH, Darmstadt, Germany). 6. Star PEGs (SunBio, Orinda, CA, USA). 7. Biocytin (biotinyl-L-lysine) (Toronto Research Chemicals, North York, ON, Canada).

3. Methods

3.1. Overall Strategy for Single-Molecule Folding Studies	Shorter peptides can be produced by solid-phase chemical synthesis, in which non-natural amino acids and protection groups can be introduced to provide specific labeling sites for fluorophores. Although this approach offers great flexibility, it is more convenient to produce proteins by heterologous recombinant expression. In this procedure, amino acids for selective dye derivatization are introduced by site-directed mutagenesis. From the three-dimensional structure, suitable dye attachment sites should be identified that promise high labeling efficiencies. For FRET experiments, two labeling sites should be selected for dye derivatization such that the expected inter-dye distance change

produces a large FRET efficiency change for the chosen dye pair. It is usually not required that the two labeling sites differ in their chemical functionalities. Random derivatization leads to labeled species containing zero, one, and two labels. By choosing the proper reaction conditions, it is ensured that we obtain essentially only doubly labeled species, from which there are four distinguishable subspecies: donor–donor, donor–acceptor, acceptor–donor, and acceptor–acceptor. The singly and doubly acceptor-derivatized species cannot be detected by donor excitation, and the singly and doubly donor-derivatized species lack FRET. These species are also identifiable by using ALEX or PIE excitation schemes (*see* **Section 1.4.**). For the two mixed species (donor–acceptor, acceptor–donor), one reasonably assumes that they do not differ in their FRET efficiency. Moreover, incorrectly labeled species can also be separated by high-performance or fast-performance liquid chromatography, HPLC or FPLC, respectively.

Thiol and amino groups of cysteine and lysine side chains, respectively, and the free α-amino group of the N-terminal amino acid provide reactive sites for dye labeling. However, multiple occurrences of cysteine and especially lysine residues in a typical polypeptide chain prevent the specific attachment of exactly one or two label(s) to the native protein. Currently, the most popular approach is to derivatize cysteine because of its lower natural abundance. Unwanted cysteine residues in the natural sequence are replaced with other amino acids by using site-directed mutagenesis, and new cysteines can be introduced at locations where they appear suitable for FRET studies and are likely to bind maleimide or haloacetamide derivatives of fluorescent dyes. Alternative methods are available *(49–53)*, but they are currently not as popular as simple cysteine ligation.

The labeled constructs should be examined in bulk folding experiments to assess if the observed FRET changes are as anticipated and if the overall stability of the protein is not compromised by dye derivatization. Afterwards, single-molecule experiments can be performed, either on molecules freely diffusing or bound to surfaces for long-time observation. For the latter experiment, it is also advisable to perform additional solution studies to examine the presence of surface interactions.

3.2. Derivatization of Primary Amines

Multiple occurrences of lysine residues in a typical polypeptide chain limit their use for site-specific attachment of labels via amine derivatization. Still, this approach provides an easy method to fluorescently label a protein and/or to attach a surface anchor (e.g., biotin) to test for specific or unspecific adsorption of the target protein onto the prepared surface.

1. The protein (typical concentration: 1–100 μM) and the succinimidyl ester of the dye or biotin are mixed in a 1:1 molar ratio in 50 mM carbonate buffer, pH 8.2.

2. The mixture is left to react overnight at 4°C.

3. The protein is purified from unbound labels by gel filtration using Performa-DTR cartridges (Edge Biosystems, Gaithersburg, MD).

3.3. Derivatization of Cysteine Residues

For random FRET pair labeling of two cysteine residues, conditions are chosen such that equal amounts of donor and acceptor dye bind to the protein to maximize the fraction of FRET pair-labeled species.

1. The protein is dissolved at 50 μM in PBS, pH 7.5. A volume of 60 μl of the solution is reacted with a 10× molar excess of a 50 mM Tris(2-carboxyethyl)phosphin (TCEP) stock solution for 15 min to reduce all cysteine side chains.

2. The reduced double cysteine mutant (e.g., RNase H K3C E135C), Alexa Fluor 546 maleimide, and Alexa Fluor 647 maleimide (Molecular Probes) in a molar ratio 1:1:3 are reacted overnight at 4°C in 20 mM phosphate buffer, pH 7.0.

3. The protein solution is applied to a cation exchange column (RESOURCE S, Äkta-System, Amersham Pharmacia, Little Chalfont, UK) and eluted with a linear gradient of 0–1 M NaCl in 20 mM sodium phosphate buffer (pH 7.0) to separate protein molecules labeled with both a donor and an acceptor dye molecule from the other labeled variants. The fraction of interest is eluted at ∼0.13 M NaCl.

4. The purified, doubly labeled protein is biotinylated by reaction with biotin succinimidyl ester in a molar ratio 1:0.5 to minimize multiple biotinylation (*see* **Section 3.2.**).

3.4. Protein Immobilization

Observing freely diffusing protein molecules has the clear advantage that perturbations of protein folding and/or function from surface interactions can be excluded. However, since diffusion through the confocal volume limits the observation time to ∼1 ms, it is often desirable to extend the time window by immobilizing the protein of interest. Control experiments should be carried out to ensure that immobilization does not interfere with the intrinsic polypeptide dynamics *(26, 54–56)*.

Several methods have been introduced for biomolecule immobilization on solid supports *(57)*. Some methods are based on the specific single-point attachment of the protein to silylated *(58)* or polymer-coated glass surfaces *(55, 57, 59)*. **Figure 13.4A** schematically shows protein attachment to a glass surface coated with a layer of protein molecules (BSA, streptavidin) physisorbed to the glass, which can be crosslinked additionally by using EDC. **Figures 13.4B** and **13.4C** depict protein functionalization of surfaces coated with linear and star-shaped PEG molecules. Surface attachment is particularly challenging for protein folding experiments as compared to functional studies on native proteins. A folded globular protein is hydrophilic on the outside
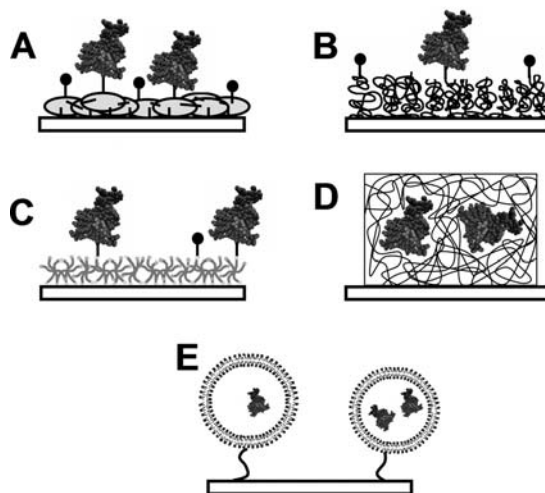
Fig. 13.4. Schematic illustration of surface preparations suitable for specific immobilization of biomolecules. (**A**) Protein-coated surface prepared by physisorption and crosslinking. (**B**) Polymer-coated surface prepared from linear PEG chains. (**C**) Polymer-coated surface prepared from six-armed, crosslinked PEG star polymers. (**D**) Polymer matrices for entrapment of biomolecules (e.g., PVA, agarose, or silica). (**E**) Surface-tethered lipid vesicles.

and hydrophobic in its core. Upon unfolding, its hydrophobic moieties become exposed. However, the surface needs to be inert toward both folded and unfolded states of the protein. Indeed, in our hands, only the derivatization with isocyanate end-functionalized, crosslinked star-PEGs yielded surfaces that allowed reversible unfolding and refolding of proteins *(55,60)*. Other techniques rely on the confinement of the protein inside porous (gel) matrices such as polyacrylamide *(61)* or agarose *(62)*, as sketched in **Fig. 13.4D**, or inside phospholipid vesicles (**Fig. 13.4E**). In the latter procedure, solvent conditions are fixed at the time of immobilization and cannot be altered in a simple fashion *(54, 63)*.

3.5. Sample Cell

A simple, disposable sample holder for single-molecule microscopy is a sandwich cell made from glass coverslips. Two pieces of double-sided adhesive tape are fixed on a glass coverslip ($24 \times 32 \text{ mm}^2$) to form a channel with a width of ~ 2 mm. A second glass coverslip ($20 \times 20 \text{ mm}^2$) is attached to form a sandwich. The measurements are performed in the channel. The typical sample volume is 4 µl; the sample thickness (~ 100 µm) can be adjusted by the thickness of the tape.

3.5.1. Cleaning and Aminosilanization of Glass Coverslips

1. Glass coverslips ($24 \times 32 \text{ mm}^2$ and $20 \times 20 \text{ mm}^2$ (Menzel, Braunschweig, Germany) are exposed to an O_2/ozone plasma for 10 min.
2. The slides are immersed for 5 min in acetone (Selectipure grade, Merck).

3. The slides are reacted with a commercial aminosilane (Vecta-bond, Vector Laboratories, Burlingame, CA) by immersion for 5 min in a Vectabond/acetone solution (2.8 ml Vectabond in 140 ml acetone).

4. The slides are immersed in 18-MΩ Millipore water and dried under a nitrogen flow.

3.5.2. Protein-Coated Surfaces

Physisorption and chemisorption of protein layers is performed directly in the channels of the sandwich-cells.

1. For physisorption, a 1 mg/ml solution of biotinylated BSA or streptavidin (both from Sigma) in 100 mM sodium phosphate buffer (pH 7.4) is filled into the channel of a sandwich made from cleaned, nonfunctionalized glass.

2. The solution is incubated for 10 min to allow the protein to adsorb on the glass.

3. The channel is rinsed with sodium phosphate buffer.

4. For chemisorption, the sandwiches are made from freshly prepared aminosilanized glass slides (*see* **Section 3.5.1.**). A 10-fold molar excess of 1-ethyl-3-[3-dimethylamino-propyl]carbodiimide hydrochloride (EDC) (Fluka Chemicals, Buchs SG, Switzerland) is added to a 1 mg/ml BSA or streptavidin solution in 100 mM sodium phosphate buffer (pH 7.4). The reaction mixture is filled into the channel and left to react for 2 h.

5. Unbound protein is flushed out with 100 mM Tris (2-amino-2-(hydroxymethyl)propane-1,3-diol) buffer, pH 7.4. Any remaining activated carboxylic groups are passivated by incubation with Tris buffer for an additional 15 min.

3.5.3. Surfaces Coated with Linear PEGs

1. To provide anchors for specific protein immobilization via biotin/streptavidin linkage, a 100 mg/ml solution of mPEG-SPA 5000, mPEG-SPA 2000, or mPEG-SMB-5000 in 50 mM sodium carbonate buffer (pH 8.2) is mixed with a 100 mg/ml biotin-PEG-succinimidyl ester solution at a 99%/1% w/w ratio.

2. The solution is incubated in an aminosilanized sandwich channel for 2 h.

3. The channel is thoroughly flushed with 18-MΩ MilliQ water.

3.5.4. Star PEG Surfaces

We have developed an immobilization method in which the protein molecules are attached via a streptavidin–biotin linkage to glass surfaces covered with a self-assembled monolayer of star-shaped PEG polymers on an aminoalkylsilylated glass surface (**Fig. 13.4C**) *(55, 60)*. Isocyanate groups on the ends of the six-armed star polymers (1) bind to the underlying self-assembled aminosilane monolayer, (2) crosslink with neighboring stars, and (3) provide amino groups (by hydrolysis) for further functionalization of the polymer coating with biotin or other specific linkers.

1. 1 mg star-shaped polymer (6-armed; isocyanate-terminated; backbone: 80% ethylene oxide, 20% propylene oxide; average MW 12000 g/mol; SusTech GmbH, Darmstadt, Germany) is dissolved in 1 ml of anhydrous THF.

2. Add 9 ml of deionized H_2O. For biotinylation of the star polymer surfaces, 1 mg biocytin is dissolved before adding the H_2O to the star polymers.

3. The mixture is left to react for 5 min.

4. The solution is filtered (20-nm pore filter, Whatman, Maidstone, UK) and immediately spin-coated on aminosilanized glass surfaces (2500 rpm, 40 s).

5. The films are left overnight at ambient atmosphere before sandwich cells are prepared from the surfaces.

6. If the star polymers are extremely reactive and polymerize immediately after adding H_2O (**step 3**), they are dissolved in 10 ml of anhydrous THF instead. The solution is filtered (20-nm pore filter) and spin-coated on aminosilanized glass surfaces (2500 rpm, 40 s). The films are left overnight at ambient atmosphere before biocytin is spin-coated onto the star polymer film (1 mg biocytin in 200 µl THF/10 ml H_2O, 2500 rpm, 40 s).

7. A sample cell is prepared.

8. For storage at –20°C, the channel is filled with water or 100 mM sodium phosphate buffer, pH 7.

3.5.5. Protein Binding on PEG-Coated Surfaces

1. A solution of 200 µg/ml streptavidin in 100 mM sodium phosphate buffer is filled into the channel coated with biotinylated protein or PEG surfaces.

2. After incubation for 10 min, the channel is flushed with 100 mM sodium phosphate buffer.

3. The fluorescently labeled and biotinylated protein (300 pM) is introduced into the channel and incubated for 10 min. Typical buffer solution: 100 mM sodium phosphate buffer. RNase H buffer: 20 mM Tris, pH 8; 50 mM KCl; 50 mM $MgCl_2$.

4. The channel is flushed with buffer to remove any unbound protein.

3.5.6. Oxygen Scavenging

Photobleaching of the fluorescent dyes sets strong limitations to the overall time during which a single molecule can be observed. Typically, it arises from a reaction of the dye in the excited states with reactants in solution. For a variety of dyes (e.g., Cy5), the removal of dioxygen from the solution greatly reduces photobleaching. An oxygen removal system based on the enzymes glucose oxidase (GOD) and catalase in the presence of D-glucose is widely used for single-molecule assays under native conditions *(64)*. When using this system, the sample holders are normally sealed with epoxy glue to minimize oxygen diffusion from the ambient air as the enzyme system causes acidification of the

solution. In the presence of chemical denaturants, however, one has to resort to other methods for oxygen depletion *(65)*.

4. Applications

4.1. Single-Molecule Fluorescence Studies on Protein Solutions

The conceptually simplest single-molecule experiment is to focus the excitation beam into a dilute sample solution in a confocal microscope (**Fig. 13.1A**). The typical size of the volume from which the fluorescence emission is collected is ∼1 fl, and, consequently, by diluting the sample to a concentration of <100 pM, one ensures that the probability of having more than one molecule in the confocal volume at the same time is negligible (provided that they do not interact strongly). For autocorrelation analysis, the signals from the APDs are registered with <1 μs time resolution and preferentially submitted to on-line correlation analysis to avoid storing huge amounts of data. For FRET experiments, a time resolution of 0.1–1 ms is appropriate for observing isolated single-molecule bursts, for which the FRET efficiency can be evaluated. As an example, **Fig. 13.5** shows time traces of photon counts from an RNase H solution (∼500 pM in buffer A). The protein molecules were fluorescently labeled with a green donor dye (Alexa Fluor 546) and a red acceptor dye (Alexa Fluor 647) by coupling their maleimide derivatives to cysteine residues introduced at position 3 and 135 of the polypeptide sequence (*see* **Section 3.3.**). Fluorescence was excited with an Ar-ion laser (514 nm, 100 μW). In **Fig. 13.5**, the number of photons collected within 1-ms bins are
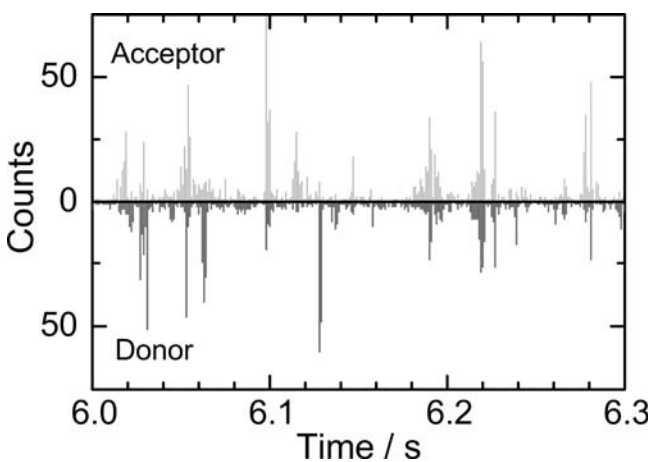
Fig. 13.5. Part of an intensity time trace of FRET-pair labeled RNase H freely diffusing in buffer solution. The plot shows the number of photons detected within 1-ms intervals over a period of 300 ms.

plotted for the time interval between 6.0 s and 6.3 s. Within a few tens of minutes, data from thousands of molecules transiting the focus can be collected. In the data analysis, only large bursts are selected so that background fluorescence and weak bursts associated with peripheral trajectories are rejected. The total number of detected photons within a burst is a few ten up to ∼200 counts. To obtain the FRET efficiency from the photon counts using **Eq. 13.8**, the background must be subtracted; differences in the quantum yields of donor and acceptor, cross-talk between the channels, and direct acceptor excitation also need to be accounted for. A proper procedure for these corrections has been presented by Schuler *(66)*. With TCSPC (*see* **Section 1.4.**), fluorescence lifetimes can also be determined for individual bursts, from which the FRET efficiency is obtained with **Eq. 13.10** (*see* **Note 4**). The FRET efficiency data are usually presented in histograms, in which the number of molecules within a certain interval of FRET efficiency (typically, $\Delta E \approx 0.02$–0.05) is plotted versus the FRET efficiency (*see examples in* **Section 4.2.**). From the small photon number in a single burst, it is obvious that the FRET efficiencies obtained from freely diffusing molecules have considerable statistical errors and contribute markedly to the width of the FRET efficiency distributions.

Frequently, it is helpful to simultaneously analyze the emitted fluorescence intensity with respect to wavelength (color), polarization, and fluorescence lifetime *(67)*. This multi-parameter fluorescence detection (MFD) approach in combination with multidimensional analysis of the data allows subpopulations with different photophysical properties to be resolved much more easily *(30)*.

4.2. Imaging of Surface-Immobilized, FRET-Pair Labeled Proteins

Since tracking of individual molecules over extended periods of time is technically not feasible at the present time, surface immobilization is required for long-time observations. This approach is challenging in single-molecule studies of protein function because nonspecific interactions with the surface can easily disturb protein structure and dynamics. For protein folding, the problem is even more severe because the surface needs to be inert toward both folded and unfolded proteins. In addition to nonspecific interactions, the presence of a covalent linker between a surface and the protein molecule may also affect the folding process *(68)*.

A simple approach to studying protein folding is to collect raster scan or wide-field images of immobilized preparations under varying denaturant conditions so as to probe equilibrium properties. The emitted fluorescence can be measured over longer periods of time, so photon statistics is not as much of a problem as in solution experiments. **Figure 13.6A** displays individual RNase H molecules in a confocal scan image of 128×128 pixels covering an area of $18 \times 18\ \mu m^2$. The image was acquired with a dwell time of 5 ms per pixel,
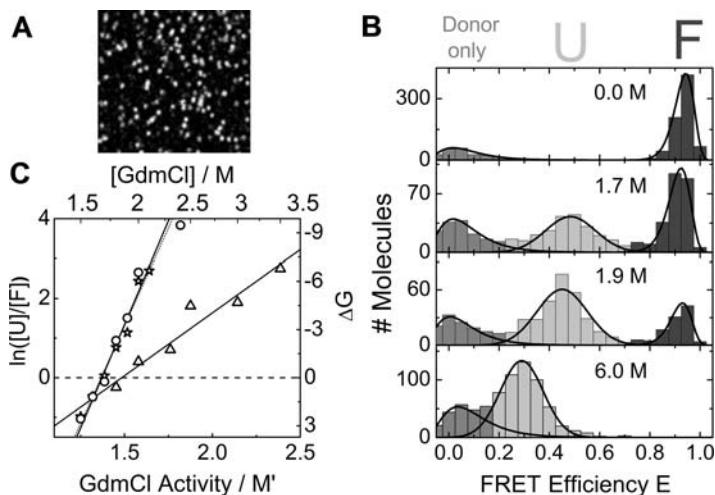
Fig. 13.6. Single-molecule FRET data on RNase H molecules, labeled with a FRET pair of dyes and immobilized on a star-PEG coated glass surface. (**A**) Scan image (18 × 18 μm^2); each spot represents a single RNase H molecule. (**B**) Histograms of FRET efficiency values E at four different GdmCl concentrations, averaged over single-molecule spots. Three populations can be distinguished, folded molecules (F), unfolded molecules (U), and molecules without a functional acceptor (Donor only). The "solid lines" represent fits with two log-normal and one Gaussian (unfolded population) distributions. (**C**) Logarithm of population ratios and resulting free energy differences between folded and unfolded conformations, ΔG_{FU}, plotted as a function of GdmCl concentration, of RNase H in buffer solution (*spheres*), RNase H immobilized on star-polymer ("stars") and physisorbed BSA ("triangles") surfaces.

using 514-nm excitation with an Ar-ion laser. The RNase H molecules were specifically FRET-labeled (*see* **Section 3.3.**) and immobilized on a star-polymer surface (*see* **Section 3.5.4.**). Sparse surface coverage ensures that only a single protein molecule is contained in the diffraction-limited confocal spot (*see* **Note 5**). There are a variety of ways to test if interactions with the surface are present. Obviously, a quantitative comparison of results obtained with immobilized samples and those on freely diffusing molecules should yield consistent results. Moreover, single-molecule polarization measurements can be performed to study if the proteins are free to rotate when immobilized on the surface *(25, 63)*. There should also be complete folding–unfolding reversibility *(55)*, and the effect of denaturant concentration on the equilibrium between unfolded and folded states should not be affected by surface immobilization (see below).

To study the dependence on denaturant, a number of images are collected for each GdmCl concentration, so that a few hundred spots can be analyzed. The donor and acceptor intensity signals (photon numbers) are corrected for (local) background, and FRET efficiency values are calculated (*see* **Note 6**). The molecules are grouped in FRET efficiency intervals; histograms with the interval $\Delta E = 0.05$ are shown in **Fig. 13.6B** for [GdmCl] = 0 M,

1.7 M, 1.9 M, and 6.0 M. From these histograms, three FRET distributions, centered on different average FRET values, $\langle E \rangle$, can be distinguished – folded molecules (denoted by F, $\langle E \rangle \approx 0.9$), unfolded molecules (denoted by U, $0.3 < \langle E \rangle < 0.5$), and molecules lacking the acceptor dye (donor only, $\langle E \rangle \approx 0.0$). The distribution associated with the folded molecules changes its relative area with GdmCl concentration, but not its peak position and width, reflecting the fact that the folded state is structurally well defined. By contrast, the FRET distribution of unfolded substates is much broader, and a pronounced shift to lower FRET values with increasing GdmCl concentration signals a significant expansion of the molecules as more and more GdmCl molecules bind to the polypeptide chain. A thermodynamic model was developed that describes the observed expansion of the protein molecules with denaturant concentration *(22)*. In addition to the folded state, it involves a continuum of unfolded substates, $U_N ... U_1 \leftrightarrow F$. Based on this model, thermodynamic and structural properties of these substates were extracted from many histograms measured in the GdmCl concentration range 0–6 M.

Also shown are fits of the histograms with two log-normal and one Gaussian (unfolded species) distributions to determine the relative population (area), average FRET efficiency, and distribution width for each species (*see* **Note 7**). This procedure is obviously necessary to enable the decomposition of overlapping subpopulations. From the relative populations, we obtain the equilibrium coefficient, K_{UF}, which is connected to the free energy difference between the two species, ΔG_{UF}, by the Boltzmann relation

$$K_{\mathrm{UF}} = \frac{[U]}{[F]} = \exp\left(-\frac{\Delta G_{\mathrm{UF}}(D)}{RT}\right). \qquad (13.11)$$

The free energy difference depends in a linear fashion on the denaturant concentration, or more precisely, the activity, D (*see* **Note 8**). In **Fig. 13.6C**, the logarithm of the population ratio and the free energy change are plotted as a function of the GdmCl concentration for different samples. The data for RNase H on BSA-coated surfaces (triangles) exhibit a markedly different slope in the linear dependence as compared to a solution sample (spheres), indicating a modified response of the surface-immobilized proteins to denaturant. By contrast, RNase H prepared on star-PEG surfaces (*see* **Section 3.5.4.**) behaves essentially identical to RNase H in solution. This observation suggests that interactions between the immobilized protein molecules and the star-PEG hydrogel surface are indeed minimal.

4.3. Observing Single-Molecule Time Trajectories

While imaging is convenient, collection of single-molecule time trajectories with high time resolution offers the highest data content. Molecules are identified on a raster scan image, and afterwards, the confocal spot is moved to the molecule, and the

emission is recorded with submicrosecond time resolution until both FRET labels are photobleached. The single-molecule FRET time trajectories directly reveal conformational dynamics within the folded and unfolded states as well as folding–unfolding transitions. By choosing the experimental conditions (temperature, pH, chemical denaturants) such that the free energies of the folded and unfolded states are similar, reversible transitions between unfolded and folded states occur frequently enough that they can be conveniently studied. In **Fig. 13.7**, two examples of time trajectories of the donor and acceptor fluorescence emission intensities are shown together with the calculated FRET efficiencies for labeled RNase H, immobilized on star-PEG surfaces in the
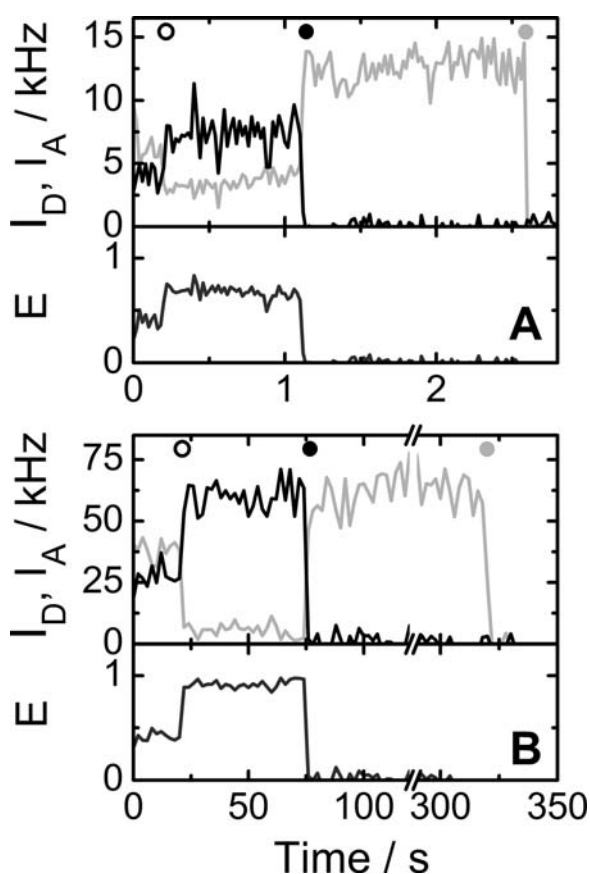
Fig. 13.7. Fluorescence intensity time traces of FRET-pair labeled RNase H immobilized on a crosslinked star-PEG surface, with [GdmCl] = 1.7 M. Grey and black lines represent donor and acceptor fluorescence intensities, respectively, corrected for background, cross-talk and different quantum yields and detection efficiencies of the dyes; the resulting FRET efficiency is shown in the lower panel. Open, solid black and grey dots indicate transitions in FRET efficiency and photobleaching of the red and green dye, respectively. (**A**) Continuous excitation with 1-ms binning time (plotted here with 20 ms averaging for presentation). (**B**) Time lapse excitation (20 ms every 2 s) to extend the observation time by a factor of 100.

presence of 1.7 M GdmCl. Symbols on top of the diagram mark the times at which significant changes in FRET (open circles) and photobleaching of donor (grey circles) and acceptor (black circles) are observed. Identifying FRET changes in noisy data is a subtle issue that requires a careful statistical analysis of the data *(25)*. The data in **Fig. 13.7A** were recorded during continuous excitation of the molecule, which limits the total observation time to a few seconds due to photobleaching of the dyes. **Figure 13.7B** shows data taken with time-lapse excitation (20 ms every 2 s). Thereby, longer timescales are accessible, albeit at lower time resolution.

Time-lapse experiments were carried out on a few hundred RNase H molecules for comparison with previous bulk measurements of the denaturation transition by circular dichroism *(69)* and tryptophan fluorescence *(70)*. They revealed an apparent rate coefficient $k_{app} \approx 1.9 \times 10^{-2}$ s^{-1} (at 1.7 M GdmCl and 25°C), corresponding to an apparent lifetime of ~50 s, which is in excellent agreement with bulk data *(25)*. This result also suggests that the protein is negligibly perturbed by the immobilization.

These observed changes in FRET efficiency can be classified into four categories, $U \rightarrow U$, $F \rightarrow F$, $U \rightarrow F$, and $F \rightarrow U$, as judged by the FRET efficiency E before and after each step, where, based on the analysis of the FRET histograms, $E > 0.72$ was taken to indicate the folded state. The detailed analysis of more than 500 steps between an initial and a final FRET value revealed that the jumps extend over the entire accessible range *(25)*. There is a slight preference for small FRET jumps, suggesting that transitions between similar peptide folds are somewhat more likely to occur, but otherwise, there is a high diversity of accessible folded and unfolded substates among which transitions can happen, as was also suggested from single-molecule unfolding studies of adenylate kinase *(54)*. In contrast to that study, however, we did not find any indication of slow transitions, but only sudden steps on the millisecond timescale. In our work, the presence of FRET efficiency transitions on the second timescale within the unfolded state of RNase H was quite surprising. Normally, the unfolded polypeptide chain is assumed to fluctuate among many different states rather than to reside in particular conformations for fairly long times.

5. Notes

1. Instead of exciting the fluorescence with the appropriate energy/wavelength for resonant absorption of a single photon, one may also perform simultaneous absorption of two photons with half the energy. However, for efficient two-photon excitation, one needs high temporal and spatial photon density, which requires the use of picosecond (or

femtosecond) pulsed infrared lasers and tight focusing. Since the photon density is only high enough close to the focus, two-photon excitation features an intrinsic depth sectioning so that confocal optics is not necessary.

2. Even for single-channel FCS experiments (*see* **Section 1.2.**), one frequently employs a 50% beam splitter and photon detection with two APDs. Instead of autocorrelating the signals from a single APD, one cross-correlates the signals of the two APDs, which also yields the ACF of the emitted photons. However, spurious signals (afterpulsing) produced by the detectors are rejected in this detection scheme.

3. Recording intensity fluctuations with high time resolution over extended periods of time produces large amounts of data, whereas on-line calculation of the ACF is a convenient means of data reduction. It comes at the expense of information loss, however.

4. The experimental effort for TCSPC data collection is significantly higher than for measuring fluorescence emission intensities. Still, the possibility of extracting FRET efficiencies in two independent ways increases the reliability of the data.

5. Two or more molecules may still occur within the same spot with a low probability. They can be identified by an atypically high emission. In the measurement of time trajectories (*see* **Section 4.3.**), these cases are easily identified by multistep bleaching.

6. Imaging individual spots is a convenient way of collecting data from a large number of molecules. However, the time resolution is set by the dwell time of a single pixel in raster scanning (or longer if one decides to combine pixels in the analysis) or the frame rate of the CCD camera. Therefore, dynamics occurring on a faster timescale is averaged out. By contrast, measurement of time trajectories with microsecond time resolution reveals fast conformational fluctuations. There is another important advantage: often the acceptor photobleaches first; the subsequent increase of the donor emission and its leakage into the detector channel provides a direct measurement of the γ factor and cross-talk. Finally, after bleaching of both donor and acceptor, the background noise remains.

7. In addition to the photon counting statistics, flickering of the dye labels and heterogeneity within the unfolded state contribute to the width of the observed FRET distribution. Only if all subconformations within the unfolded state interconvert fast on the experimental timescale (i.e., the time over which photons are collected ($\sim$1 ms in burst analysis)), an average FRET efficiency value will result. If subconformations interconvert slowly, however, they will be measured with their different FRET efficiency values and thus contribute to an additional broadening of the overall FRET distribution.

8. The dependence of folding–unfolding equilibria on the concentration of chemical denaturants is usually modeled by a linear free energy relationship:

$$\Delta G_{\mathrm{UF}}(D) = \Delta G_{\mathrm{UF}}(0) + m_{\mathrm{UF}} D. \qquad (13.12)$$

Here, D represents the activity, which is used in lieu of the concentration to remove the intrinsic nonlinearity observed for GdmCl. It is calculated from the molar concentration according to the empirical expression *(71, 72)*

$$D = \frac{C_{0.5[\mathrm{GdmCl}]}}{C_{0.5} + [\mathrm{GdmCl}]}, \qquad (13.13)$$

with the experimentally determined denaturation coefficient $C_{0.5} = 7.5$ M. Note that the upper and lower horizontal axes in **Fig. 13.7C** are labeled with GdmCl concentration and activity D, respectively.

Acknowledgments

References

1. Levinthal, C. (1968) Are there pathways for protein folding?, *J Chim Phys* 65, 44–45.

2. Baldwin, R. L. (1995) The nature of protein folding pathways: The classical versus the new view, *J Biomol NMR* 5, 103–109.

3. Onuchic, J. N., Wolynes, P. G. (2004) Theory of protein folding, *Curr Opin Struct Biol* 14, 70–75.

4. Wolynes, P. G., Onuchic, J. N., Thirumalai, D. (1995) Navigating the folding routes, *Science* 267, 1619–1620.

5. Onuchic, J. N., Nymeyer, H., Garcia, A. E., et al. (2000) The energy landscape theory of protein folding: Insights into folding mechanisms and scenarios, *Adv Protein Chem* 53, 87–152.

6. Dill, K. A., Chan, H. S. (1997) From Levinthal to pathways to funnels, *Nat Struct Biol* 4, 10–19.

7. Callender, R. H., Dyer, R. B., Gilmanshin, R., et al. (1998) Fast events in protein folding: The time evolution of primary processes, *Annu Rev Phys Chem* 49, 173–202.

8. Eaton, W. A., Munoz, V., Hagen, S. J., et al. (2000) Fast kinetics and mechanisms in protein folding, *Annu Rev Biophys Biomol Struct* 29, 327–359.

9. Gruebele, M. (1999) The fast protein folding problem, *Annu Rev Phys Chem* 50, 485–516.

10. Neher, E., Sakmann, B. (1976) Single-channel currents recorded from membrane of

denervated frog muscle fibres, *Nature* 260, 799–802.

11. Rief, M., Gautel, M., Oesterhelt, F., et al. (1997) Reversible unfolding of individual titin immunoglobulin domains by AFM, *Science* 276, 1109–1112.

12. Cecconi, C., Shank, E. A., Bustamante, C., et al. (2005) Direct observation of the three-state folding of a single protein molecule, *Science* 23, 2057–2060.

13. Kellermayer, M. S., Smith, S. B., Granzier, H. L., et al. (1997) Folding–unfolding transitions in single titin molecules characterized with laser tweezers, *Science* 276, 1112–1116.

14. Michalet, X., Kapanidis, A. N., Laurence, T., et al. (2003) The power and prospects of fluorescence microscopies and spectroscopies, *Annu Rev Biophys Biomol Struct* 32, 161–182.

15. Böhmer, M., Enderlein, J. (2003) Fluorescence spectroscopy of single molecules under ambient conditions: Methodology and technology, *ChemPhysChem* 4, 793–808.

16. Haran, G. (2003) Single-molecule fluorescence spectroscopy of biomolecular folding, *J. Phys Condens Matter* 15, R1219–R1317.

17. Schuler, B. (2005) Single-molecule fluorescence spectroscopy of protein folding, *ChemPhysChem* 6, 1206–1220.

18. Nienhaus, G. U. (2006) Exploring protein structure and dynamics under denaturing conditions by single-molecule FRET analysis, *Macromol Biosci* 6, 907–922.

19. Förster, T. (1948) Zwischenmolekulare Energiewanderung und Fluoreszenz, *Ann Physik* (Leipzig) 437, 55–75 (Translated in: Biological Physics, edited by Mielczarek, E.V., Greenbaum, E., Knox, R.S., American Institute of Physics, New York, 1993, pp. 1148–1160).

20. Ha, T., Enderle, T., Ogletree, D. F., et al. (1996) Probing the interaction between two single molecules: Fluorescence resonance energy transfer between a single donor and a single acceptor, *Proc Natl Acad Sci USA* 93, 6264–6268.

21. Selvin, P. R. (2000) The renaissance of fluorescence energy transfer, *Nat Struct Biol* 7, 730–734.

22. Kuzmenkina, E. V., Heyes, C. D., Nienhaus, G. U. (2006) Single-molecule FRET study of denaturant induced unfolding of RNase H, *J Mol Biol* 327, 313–324.

23. Schuler, B., Lipman, E. A., Eaton, W. A. (2002) Probing the free-energy surface for protein folding with single-molecule fluorescence spectroscopy, *Nature* 419, 743–747.

24. McCarney, E. R., Werner, J. H., Bernstein, S. L., et al. (2005) Site-specific dimensions across a highly denatured protein: a single molecule study, *J Mol Biol* 352, 672–682.

25. Kuzmenkina, E. V., Heyes, C. D., Nienhaus, G. U. (2005) Single molecule Förster resonance energy transfer study of protein dynamics under denaturing conditions, *Proc Natl Acad Sci USA* 102, 15471–15476.

26. Rhoades, E., Cohen, M., Schuler, B., et al. (2004) Two-state folding observed in individual protein molecules, *J Am Chem Soc* 126, 14686–14687.

27. Lipman, E. A., Schuler, B., Bakajin, O., et al. (2003) Single-molecule measurement of protein folding kinetics, *Science* 301, 1233–1235.

28. Wahl, M., Koberling, F., Patting, M., et al. (2004) Time-resolved confocal fluorescence imaging and spectroscopy system with single molecule sensitivity and sub-micrometer resolution, *Curr Pharm Biotechnol* 5, 299–308.

29. Ha, T. (2001) Single molecule flourescence resonance transfer, *Methods* 25, 78–86.

30. Widengren, J., Kudryavtsev, V., Antonik, M., et al. (2006) Single-molecule detection and identification of multiple species by multi-parameter fluorescence detection, *Anal Chem* 78, 2039–2050.

31. Flomenbom, O., Klafter, J., Szabo, A. (2005) What can one learn from two-state single-molecule trajectories?, *Biophys* J 88, 3780–3783.

32. Zemanová, L., Schenk, A., Valler, M. J., et al. (2005) High-throughput screening of interactions between G protein-coupled receptors and ligands using confocal optics microscopy, *Methods Mol Biol* 305, 365–384.

33. Hazlett, T. L., Ruan, Q., Tetin, S. Y. (2005) Application of fluorescence correlation spectroscopy to hapten–antibody binding, *Methods Mol Biol* 305, 415–438.

34. Haustein, E., Schwille, P. (2003) Ultrasensitive investigations of biological systems by fluorescence correlation spectroscopy, *Methods* 29, 153–166.

35. Lamb, D. C., Schenk, A., Röcker, C., et al. (2000) Sensitivity enhancement in fluorescence correlation spectroscopy of multiple

species using time-gated detection, *Biophys J* 79, 1129–1138.

36. Dertinger, T., Pacheco, V., von der Hocht, I., et al. (2007) Two-focus fluorescence correlation spectroscopy: A new tool for accurate and absolute diffusion measurements, *ChemPhysChem* 8, 433–443.

37. Clegg, R. M. (1996) in (Wang, X. F., and Herman, B., eds.) Fluorescence imaging spectroscopy and microscopy, pp 180–252. John Wiley & Sons.

38. Van der Meer, B. W., Coker III, G., Chen, S.-Y. S. (1994) Resonance energy transfer: Theory and data, VCH Publishers, Inc., New York, Weinheim, Cambridge.

39. Stryer, L., Haugland, R. P. (1967) Energy transfer: A spectroscopic ruler, *Proc Natl Acad Sci USA* 58, 719–726.

40. Rasnik, I., McKinney, S. A., Ha, T. (2005) Surfaces and orientations: Much to fret about?, *Acc Chem Res* 38, 542–548.

41. Coban, O., Lamb, D. C., Zaychikov, E., et al. (2006) Conformational heterogeneity in RNA polymerase observed by single-pair FRET microscopy, *Biophys J* 90, 4605–4617.

42. Majumdar, Z. K., Hickerson, R., Noller, H. F., et al. (2005) Measurements of internal distance changes of the 30S ribosome using FRET with multiple donor–acceptor pairs: Quantitative spectroscopic methods, *J Mol Biol* 351, 1123–1145.

43. Vörös, J. (2004) The density and refractive index of adsorbing protein layers, *Biophys J* 87, 553–561.

44. Schuler, B., Lipman, E. A., Steinbach, P. J., et al. (2005) Polyproline and the "spectroscopic ruler" revisited with single-molecule fluorescence, *Proc Natl Acad Sci USA* 102, 2754–2759.

45. Kapanidis, A. N., Lee, N. K., Laurence, T. A., et al. (2004) Fluorescence-aided molecule sorting: Analysis of structure and interactions by alternating-laser excitation of single molecules, *Proc Natl Acad Sci USA* 101, 8936–8941.

46. Müller, B. K., Zaychikov, E., Bräuchle, C., et al. (2005) Pulsed interleaved excitation, *Biophys J* 89, 3508–3522.

47. Panchuk-Voloshina, N., Haugland, R. P., Bishop-Stewart, J., et al. (1999) Alexa dyes, a series of new fluorescent dyes that yield exceptionally bright, photostable conjugates, *J Histochem Cytochem* 47, 1179–1188.

48. Mujumdar, R. B., Ernst, L. A., Mujumdar, S. R., et al. (1993) Cyanine dye labeling reagents: Sulfoindocyanine succinimidyl esters, *Bioconjug Chem* 4, 105–111.

49. Schuler, B., Pannell, L. K. (2002) Specific labeling of polypeptides at amino-terminal cysteine residues using Cy5-benzyl thioester, *Bioconjug Chem* 13, 1039–1043.

50. Yamaguchi, J., Nemoto, N., Sasaki, T., et al. (2001) Rapid functional analysis of protein–protein interactions by fluorescent C-terminal labeling and single-molecule imaging, *FEBS Lett* 502, 79–83.

51. Cropp, T. A., Schultz, P. G. (2004) An expanding genetic code, *Trends Genet* 20, 625–630.

52. David, R., Richter, M. P., Beck-Sickinger, A. G. (2004) Expressed protein ligation. Method and applications, *Eur J Biochem* 271, 663–677.

53. Kapanidis, A. N., Weiss, S. (2002) Fluorescent probes and bioconjugation chemistries for single-molecule fluorescence analysis of biomolecules, *J Chem Phys* 117, 10953–10964.

54. Rhoades, E., Gussakovsky, E., Haran, G. (2003) Watching proteins fold one molecule at a time, *Proc Natl Acad Sci USA* 100, 3197–3202.

55. Amirgoulova, E. V., Groll, J., Heyes, C. D., et al. (2004) Biofunctionalized polymer surfaces exhibit minimal interaction towards immobilized proteins, *ChemPhysChem* 5, 552–555.

56. Talaga, D. S., Lau, W. L., Roder, H., et al. (2000) Dynamics and folding of single two-stranded coiled-coil peptides studied by fluorescent energy transfer confocal microscopy, *Proc Natl Acad Sci USA* 97, 13021–13026.

57. Rasnik, I., Myong, S., Cheng, W., et al. (2004) DNA-binding orientation and domain conformation of the *E. coli* rep helicase monomer bound to a partial duplex junction: Single molecule studies of fluorescently labeled enzymes, *J Mol Biol* 336, 395–408.

58. Wennmalm, S., Edman, L., Rigler, R. (1997) Conformational fluctuations in single DNA molecules, *Proc Natl Acad Sci USA* 94, 10641–10646.

59. Ha, T., Rasnik, I., Cheng, W., et al. (2002) Initiation and re-initiation of DNA unwinding by the Escherichia coli rep helicase, *Nature* 419, 638–641.

60. Groll, J., Amirgoulova, E., Ameringer, T., et al. (2004) Biofunctionalized, ultrathin coatings of cross-linked star-shaped poly(ethylene oxide) allow reversible folding of immobilized proteins, *J Am Chem Soc* 126, 4234–4239.

61. Dickson, R. M., Cubitt, A. B., Tsien, R. Y., et al. (1997) On/off blinking and switching behaviour of single molecules of green fluorescent protein, *Nature* 388, 3558–3358.

62. Lu, H. P., Xun, L., Xie, X. S. (1998) Single molecule enzymatic dynamics, *Science* 282, 1877–1882.

63. Boukobza, E., Sonnenfeld, A., Haran, G. (2001) Immobilization in surface-tethered lipid vesicles as a new tool for single biomolecule spectroscopy, *J Phys Chem B* 105, 12165–12170.

64. Harada, Y., Sakurada, K., Aoki, T., et al. (1990) Mechanochemical coupling in actomyosin energy transduction studied by in vitro movement assay, *J Mol Biol* 216, 49–68.

65. Englander, S. W., Calhoun, D. B., Englander, J. J. (1987) Biochemistry without oxygen, *Anal Biochem* 161, 300–306.

66. Schuler, B. (2007) Application of single molecule Förster resonance energy transfer to protein folding, *Methods Mol Biol* 350, 115–138.

67. Eggeling, C., Berger, S., Brand, L., et al. (2001) Data registration and selective single-molecule analysis using multi-parameter fluorescence detection, *J Biotechnol* 86, 163–180.

68. Friedel, M., Baumketner, A., Shea, J. E. (2006) Effects of surface tethering on protein folding mechanisms, *Proc Natl Acad Sci USA* 103, 8396–8401.

69. Yamasaki, K., Ogasahara, K., Yutani, K., et al. (1995) Folding pathway of Escherichia coli ribonuclease HI: A circular dichroism, fluorescence, and NMR study, *Biochemistry* 34, 16552–16562.

70. Parker, M. J., Marqusee, S. (1999) The cooperativity of burst phase reactions explored, *J Mol Biol* 293, 1195–1210.

71. Staniforth, R. A., Burston, S. G., Smith, C. J., et al. (1993) The energetics and cooperativity of protein folding: A simple experimental analysis based upon the solvation of internal residues, *Biochemistry* 32, 3842–3851.

72. Parker, M. J., Spencer, J., Clarke, A. R. (1995) An integrated kinetic analysis of intermediates and transition states in protein folding reactions, *J Mol Biol* 253, 771–786.

Chapter 14

Experimental Characterization of the Denatured State Ensemble of Proteins

Jae-Hyun Cho and Daniel P. Raleigh

Abstract

The traditional view of the denatured state ensemble of proteins is that it behaves as a classic random coil. This model has important implications for the analysis of protein stability, protein folding, and cooperativity; namely that the effects of mutations on the free energy of the denatured state ensemble can be ignored. This assumption, which is still routinely made, at least at the implicit level, greatly simplifies the analysis of such experiments. However it has long been recognized that the denatured state ensemble (DSE) of real proteins is often quite different from a random coil and can exhibit significant structural preferences. In some cases parts of the chain can even adopt relatively well-defined conformations, particularly under native conditions. Well-studied examples of DSE interactions include elements of hydrogen-bonded secondary structure, particularly helices or turns, as well hydrophobic clusters, hydrophobic aromatic clusters, and more recently interactions involving charged residues. Deviations from random-coil behavior are of practical importance if they influence protein folding, stability, or function, or if they compromise our analysis and interpretation of experiments. The existence of residual structure in the DSE naturally leads to the question of its role in protein folding and stability, and raises the possibility that some mutations could exert a significant part of their effect by altering the DSE. Much of our understanding of the interactions governing protein stability and the folding process have been generated by mutational studies; thus, a detailed understanding of the denatured state ensemble is critical.

Key words: Denatured state ensemble, unfolded state, protein stability, protein folding, protein engineering, NMR, protein design, thermodynamics, peptides, random coil.

1. Introduction

Early studies led to the view that the denatured state ensemble (DSE) of proteins could be treated as a classic random coil. The concept of a random coil has served as the standard model of the DSE of proteins for several decades and can be described as an ensemble of structures with nonbiased backbone conformations

in terms of their structure and energetics. Within this framework DSE interactions are considered to be limited to residues which are close in sequence. The random-coil model has important implications for the analysis of protein stability, protein folding, and cooperativity; namely that the effects of mutations on the free energy of the DSE can be ignored. This assumption, which is still routinely made, at least at the implicit level, greatly simplifies the analysis of such experiments. However it has long been recognized that the DSE of real proteins is often very different from a random coil, particularly under conditions which favor the native state, and the DSE can exhibit significance structural preferences. The existence of nonrandom structural propensities in the DSE leads to obvious questions about their role in folding and stability, and gives rise to the possibility that some mutations might exert part of their effect by altering the DSE. Our understanding of the interactions governing protein stability, cooperativity, and the protein-folding process have relied heavily upon mutational studies; thus, a deeper understanding of the role of the DSE and of the effects of mutations upon the energetics of the DSE is critical. Indeed, the characterization of the DSE has emerged as a major research area *(1–8)*. The vast majority of the work on protein stability and folding has focused on native-state effects and has ignored any potential complications caused by DSE effects. Disconcertingly, this assumption is sometimes even made for proteins that are known to have a compact DSE with significant residual structure.

A wide variety of methods have been applied to the study of the DSE and it is impossible to provide detailed protocols in single chapter, and in any case, such an exercise would probably not be particularly useful since experimental methods often have to be adapted to the particular protein and conditions of interest. Instead we seek to provide an overview of modern studies of the DSE and to provide selected references which the interested reader can consult for more details about experimental procedures. A key challenge in the field is to move beyond just characterizing the structural propensities of the DSE and to instead develop an understanding of how modulating the free energy of the DSE can influence protein stability and protein folding *(6–8)*. This requires an in depth understanding of the energetics of the DSE. This is generally extremely difficult to do and limited data is available on a few proteins.

It is worthwhile to take a moment to comment upon terminology and notation. The terms unfolded state, denatured state, and DSE are all found in the protein literature. Unfortunately there is no agreed upon convention for their use and one cannot assume that one set of terminology is universally used to refer to a state under a particular set of conditions, for example, high temperature, high concentrations of denaturant, or extremes of pH

etc. We use the terminology DSE as a generic term to avoid any implication that we are referring to fully unfolded proteins, such as might be populated at high temperature in the presence of high concentrations of denaturant. We prefer the terminology DSE to denatured state since the state is an interconverting ensemble of a large number of different conformations. The folded state and the native state are synonymous and we used the term folded state here.

2. Why Study the DSE?

A number of proteins fail to significantly populate a compact folded state in the absence of their interaction partners. The list of these so-called "intrinsically disordered" or "natively disordered" proteins is growing and there is increasing interest in defining the conformational preferences in the "intrinsically disordered" ensemble since it may be functionally significant *(9)*. The DSE of "normal" proteins is also of considerable interest since it plays an important role in folding and stability. The stability of a protein, defined as ΔG°_{u} of unfolding, is given by the difference between the Gibbs free energy of the DSE and the Gibbs free energy of the folded state; $\Delta G^{\circ}_{u} = G_{DSE} - G_{F}$. The existence of DSE interactions leads to the possibility that some mutations might exert part of their energetic effect by altering the free energy of the DSE. Formally it is impossible to tell from thermodynamic measurements if a mutation has altered the free energy of the DSE or the free energy of the folded state or both; only changes in ΔG° can be measured (**Fig. 14.1**). The stability of a protein represents a very small difference between two large numbers. Thus mutations or changes in solvent conditions which alter the energetics of the DSE even by just a Kcalmol^{-1} can have a significant effect upon protein stability.

Structure or the propensity to form structure in the DSE can also affect protein folding. The existence of non-native structure can slow the rate of folding since non-native interactions by definition have to be broken as the protein progresses towards the native state. However, it is important to bear in mind that non-native interactions do not have to exert a large effect upon the folding rate if they persist in the transition state and are broken on the downhill side of the free energy barrier *(10)*. Perhaps the most common physiologically relevant non-native interaction in the DSE is the population of non-native isomers of X-Pro peptide bonds. Cis-trans isomerism of the peptide bond is slow and the rate-limiting step in the folding of a protein that contains cis
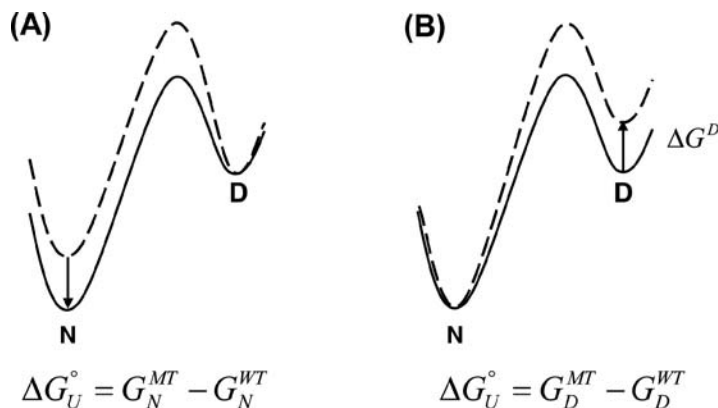
Fig. 14.1. Free energy diagrams showing that the same change in protein stability can arise from folded state effects or DSE effects. *The solid line* represents the wild-type and the *dashed line* the mutant. The superscript WT refers to the wild-type while the superscript MT refers to the mutant. In case-A the change in stability is due entirely to a decrease in the free energy of the folded state, while in case-B the change in stability is caused by an increase in the free energy of the DSE. In both cases the same change in stability, $\Delta\Delta G^\circ$ is observed. The example is for the case of a mutation which stabilizes a protein. The same principle holds for destabilizing mutations. In this case the mutation could increase the free energy of the folded state, decreases the free energy of the unfolded state or produce some combination of both DSE and folded state effects.

X-Pro peptide bonds in its folded state is often the requirement to isomerize to the correct isomer in the DSE before folding can begin. Native-like interactions in the DSE can speed up folding, but it is important to note that the mere presence of native-like interactions in the DSE does not necessarily mean that they lead to more rapid folding. The interaction in question may not take part in defining the rate-limiting step in folding. Only experiments which consider the kinetic consequences of disrupting DSE interactions can indicate if they speed up folding, slow it down, or have no effect. Examples of all of these types of behavior can be found in the literature.

There is another, more subtle, way in which DSE interactions can manifest themselves in studies of protein folding. Information on the role of each amino acid in the transition state for protein folding is most readily obtained by observing changes in the properties of the transition state upon site-specific mutation *(11–14)*. Undoubtedly, the most popular method for the analysis of side-chain interactions in the transition state for folding is the protein engineering approach known as Φ-value analysis. The effect of a conservative mutation upon the free energy of folding and the activation free energy are combined to yield the dimensionless ratio known as the Φ-value. In the absence of DSE effects, Φ-values have a simple structural interpretation. A Φ-value of zero means that the interaction being probed is no more developed in the transition state than it is in the DSE while a Φ-value of 1.0 is interpreted to indicate that the interaction is fully developed in the

$$\phi = \frac{\Delta\Delta G^{TS}}{\Delta\Delta G^{\circ}} = \frac{\Delta G^{TS}}{\Delta G^{N}} \qquad\qquad \phi = \frac{\Delta\Delta G^{TS}}{\Delta\Delta G^{\circ}} = \frac{\Delta G^{TS} - \Delta G^{D}}{\Delta G^{N} - \Delta G^{D}}$$
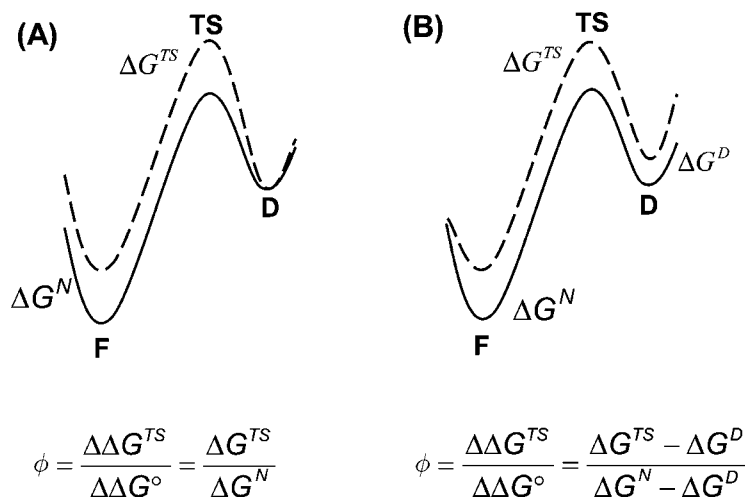
Fig. 14.2. Φ-values are dimensionless parameters defined as the ratio of the change in the activation free energy for folding, (or more exactly $-RT\Delta\ln K_{f}$), to the change in stability, $\Delta\Delta G^{\circ}$, caused by a conservative mutation. *The solid line* represents the wild-type and *the dashed line* the mutant. In the absence of denatured state effects, (**A**), the Φ-value is equal to the change in the free energy level of the transition state divided by the change in the free energy level of the folded state. In this case a simple structural interpretation can be made as described in the text. (**B**) The Φ-value value can still be defined if the mutation alters the free energy of the DSE but in this case it is no longer equal to the ratio of the change in the free energy level of the transition state to the change in the free energy of the folded state and the structural interpretation is less clear.

transition state. However, this simple structural interpretation breaks down if the mutation alters the free energy of the DSE (**Fig. 14.2**). For example, a Φ-value of 0.7 could mean that a native-like interaction was well developed in the transition state for folding; 70% developed if one assumes that Φ-values represent a linear scale; which they do not have to *(14)*. Conversely the same Φ-value could arise from the partial disruption of a non-native DSE interaction in the transition state for folding. Thus the analysis of protein folding transition states also requires an understanding of the effects of mutations on the DSE and interpretation of transition state parameters inevitably depends on knowledge of both folded state and DSE effects *(6, 15)*.

3. Which Denatured State to Study?

An important distinction should be made between the DSE populated under denaturing conditions such as elevated temperature or high concentrations of denaturants and the DSE populated under more native conditions. While both states are interesting, the

characterization of the DSE under native condition (i.e., under conditions in which the folded state is the most stable form of the protein) is the most relevant goal since it is the reference state for protein stability studies and is the starting state for protein folding. Unfortunately the DSE formed under native conditions is very difficult to study due both to its low population and because of the cooperativity of protein folding. In contrast, the DSE induced by high concentrations of chemical denaturants or at high temperature can be highly populated under equilibrium conditions and hence is much easier to study. However, the DSE populated under strongly denaturing conditions generally does not coincide with the DSE populated under more native conditions and can differ considerably *(5, 16–19)*.

4. Methods for Studying the DSE

It is impossible to provide a comprehensive review in one short chapter, thus we choose to consider selected illustrative examples rather than attempting to provide a detailed overview of the literature. Computational and theoretical studies have played an important role in our developing understanding of the DSE but here we restrict ourselves to experimental studies.

4.1. Global Parameters Cannot Always Distinguish Between a Random-Coil-Like DSE and a More Structured DSE

Many studies of the DSE have relied on analysis of global parameters such as *m*-values, the radius of gyration (R_g), or the radius of hydration (R_h) and this has lead to some confusion *(2, 3, 20, 21)*. Suggestions of significant residual structure in the DSE often appear to be at variance with the observation of random-coil behavior based on analysis of such global parameters *(3, 22)*. For example, the power law dependence of experimental R_g values with residue length is consistent with the classic random coil *(23)*. Recent simulations, however, have shown that random-coil statistics can be reproduced from a rigid-segment model in which 92% of native conformation is present *(4, 24)*. Experimental studies have confirmed that different DSEs of the same protein can have identical radii of hydration but differ significantly in their secondary structure content *(19)*. Consequently, more specific features need to be examined to distinguish between random-coil and structured DSE models. Of course the observation of an R_g or R_h value for a DSE which is significantly smaller than expected for a random coil provides direct evidence that the DSE is compact. Thus the methods are useful. R_g measurements are rather specialized since small angle scattering equipment is not widely available; however, R_h measurements are relatively straightforward using NMR-based diffusion measurements.

4.2. In Favorable Cases NMR Can Be Used to Obtained Residue-Specific Information About the DSE

In a few cases conditions have been found where the DSE is well populated and in equilibrium with the folded state under near-native conditions. If this is the case it may be possible to use NMR methods to obtain residue-specific information. This is most straightforward if the DSE and the folded state are in slow exchange on the NMR timescale since separate resonances from the two states can be detected and assignments made using standard triple resonance methods. One potential difficulty to bear in mind is that unfolded and partially unfolded proteins are often very prone to aggregate; thus, proper control experiments always need to be performed to ensure that self-association is not complicating the analysis of the DSE. There are numerous reviews on methods for the assignment of NMR spectra and is now relatively straightforward to assign the spectra of the DSE of small to moderately sized proteins, in part because the dispersion of the ^{13}C carbonyl and ^{15}N amide chemical shifts is largely preserved in unfolded states *(25, 26)*. The work of Forman-Kay and colleagues on the drkN SH3 domain is probably the most detailed. Both the folded state and DSE of the domain are populated in the absence of denaturant at pH 6 and the two states are in slow exchange on the NMR timescale *(5, 17, 27)*.

Normal NMR parameters, including nOe's and J-couplings can be used to characterize the DSE. The measured deviation of the chemical shifts from those expected for a fully random-coil ensemble of conformations, the so-called secondary chemical shifts, are widely used as indicators of secondary structure preferences in the DSE. Particular care needs to be taken with chemical shift referencing since the deviations from random-coil values are smaller than observed for folded states and small errors in referencing can lead to systematic errors. Often sequence-corrected random-coil chemical shifts are used for the analysis of ^{13}C carbonyl shifts because they are sensitive to sequence effects, but sequence corrections are less important for the other secondary shifts *(25)*. A variety of protocols have been proposed for analyzing chemical shift deviations and the SSP method of Forman-Kay appears to be particularly promising *(28)*. It is important to remember that secondary shifts are reporting on the local propensity to populate certain regions of the ϕ, ψ map, whereas CD requires that several consecutive residues adopt a helical conformation to generate a helical signal. Thus the results from NMR studies may not be directly comparable to more global spectroscopic probes. NMR relaxation studies have also proven useful as have paramagnetic relaxation enhancement experiments. In the latter method spin labels are attached to specific sites in a protein. The proximity of the spin-labeled site to other locations within the protein can be probed through the degree of broadening (relaxation enhancement) that is observed in the NMR signals of the rest of the protein *(29)*. The long-range effect of paramagnetic centers

allows transient long-range interactions to be probed. The analysis of residual dipolar coupling is widely used in NMR structure determination and the method has begun to be applied to unfolded systems too.

Relaxation dispersion measurements should extend the NMR approach to a much wider range of systems since they are applicable when the DSE has a low population. These experiments not only provide information about the rates of interconversion but they can also be used to estimate DSE chemical shifts *(9, 30, 31)*.

4.3. Indirect Approaches Normally Have to Be Used to Probe the DSE Under Native Conditions

Not all proteins can be tricked into significantly populating the DSE and native state simultaneously. Thus indirect methods normally need to be used to study the DSE under native conditions. A wide range of approaches have been used including, but not limited to, the study of peptide fragments, the analysis of destabilizing point mutants or truncation mutants, amide $^1H/^2H$ exchange experiments of the native state, changes in *m*-values upon mutation, and the analysis of the pH dependence of protein stability.

4.3.1. Peptide "Models" of Locally Stabilized Structure: A Useful but Necessarily Limited Approach

Studies of peptide fragments derived from the sequence of the protein of interest can provide useful information about the propensity to adopt locally stabilized structure, such as α-helices, turns, β-hairpins, or local clusters of aromatic and hydrophobic amino acids. The interference is that any observed structure, since it is populated in the absence of longer-range tertiary interactions, can be formed in the DSE. There are numerous examples of these types of studies. They have proven very useful for defining local propensities but one needs to bear in mind that observations made on small peptides may or may not translate into the DSE populated by the full chain. NMR is the method of choice for such studies since it is currently the only technique which can provide information about every residue, although isotope edited IR is beginning to make a contribution. One of the challenges is how to interpret structural parameters which are measured for an ensemble of rapidly interconverting conformation. The analysis of nOe intensities requires care since the $1/r^6$ averaging means a small population of a conformer which brings two protons into close proximity can give rise to an easily detectable nOe.

4.3.2. Truncation Mutants or Destabilizing Point Mutants Can be Useful Models of the DSE Populated Under Native Conditions

A potentially very powerful approach that can be used when one is not fortunate enough to have both the DSE and folded state populated under native conditions is to study mutations that destabilize the native state. Studies of truncation mutants have been employed, most notably the $\Delta 131$ mutant of *S. nuclease*, and single-point mutants have been studied too *(32, 33)*. Chemical modification of proteins can also be used to reduce the stability of the native state and drive the system into the DSE basin. The

advantage of these approaches is that equilibrium NMR methods can be used to characterize the protein; the potential disadvantage is that the mutation used to prevent folding might alter the properties of the DSE. For example mutation of a large hydrophobic core residue, a commonly used strategy, might impact the DSE by reducing the tendency to form hydrophobic clusters in the DSE. Nonetheless, the approach is very useful since it can be applied to a wide range of proteins.

4.3.3. The pH Dependence of Protein Stability Offers Another Indirect Probe of the DSE

Studies of the pH dependence of protein stability and folding kinetics can provide insight into the role of electrostatic interactions in protein stability and folding *(34)*. They also offer a relatively simple, albeit indirect, method for probing electrostatic interactions in the DSE *(1, 6, 35)*. The idea is to exploit the linkage relationship between pH-dependent changes in $\Delta G°$ and the difference in the number of protons bound to the native state and to the DSE *(35)*:

$$\partial \Delta G° / \partial pH = 2.303 RT \Delta Q. \qquad (14.1)$$

ΔQ is the difference in the number of protons bound to the native state (Q_N) and to the DSE (Q_{DSE}) and is a function of pH. $\Delta G°$ is the apparent free energy of unfolding. Q_N and Q_{DSE} can be determined using the pKa's of the various titratable groups in the folded state and in the DSE, provided that the titration behavior can be modeled as set of independently titrating sites. Q_N can often be directly measured by determining a set of native-state pKa's or from a potentiometric titration but Q_D under native conditions is normally not accessible. Thus ΔQ under native conditions cannot be determined, but information about the DSE can still be obtained. A model for the titration behavior of the DSE can be assumed and used to calculate the expected values of ΔQ. Comparison with the experimentally determined pH vs. stability curve rigorously tests if the model accounts for the data. A discrepancy proves that there must be interactions in the DSE that perturb Q_{DSE} from the values predicted by the model. Thus DSE electrostatic interactions can be probed and models tested. For example, the dependence of $\Delta G°$ on pH can be calculated using model compound values for DSE pK_as. The calculated result, $\Delta G°_{cal}$ vs. pH, has no simple direct physical meaning but a comparison of the $\Delta \Delta G°_{cal}$ vs pH curve with the experimental curve tests if the model DSE pK_as can reproduce the experimental result. If they cannot, then there must be interactions in the DSE that perturb the DSE pK_as away from the model values *(6)*. In contrast, agreement between the experimental and calculated plots does not prove that the chosen model pK_as provide an accurate description of the titration behavior of the DSE, because a positive deviation at one site can be masked by a negative deviation at another. The important point is that a discrepancy between

the calculated and experimental curves must be due to DSE effects if the titration behavior of the native state is known. The linkage relationship can be used even when individual native-state pK_a values cannot be measured. An alternative approach which can be employed in this case is to use a potentiometric titration to directly determine the number of protons bound to the folded state. The titration is then repeated in the presence of high concentrations of denaturant, which measures the number of protons bound to a fully unfolded state. Combination of the data yields a $\Delta\Delta G°$ vs. pH curve expected for an unstructured DSE. The plot can be compared to the one generated from experimentally determined $\Delta G°$ values. Any deviation between the two plots demonstrates the presence of electrostatic interactions in the DSE above and beyond those expected for a fully unfolded state *(1)*. In most of the cases examined there are clear deviations between the observed pH dependence of $\Delta G°$ and the behavior predicted based upon a fully unfolded DSE. For example, significant DSE electrostatic interactions have been detected in the N-terminal domain of L9, in RNase H, and in ribonuclease Sa as well as in a range of other proteins *(36)*. RNase H is very interesting because it provides an example of the functional consequences of DSE structure. The heat capacity change for the unfolding of thermophilic RNase H, $\Delta C_p°$, is smaller than the value for the mesophilic RNase H, which leads to a shallower $\Delta G°$ vs. pH curve for the thermophilic protein and a significantly higher midpoint temperature for unfolding. The smaller $\Delta C_p°$ for thermophilic RNase H is due to a pH-dependent hydrophobic cluster in the DSE *(36)*. The N-terminal domain of L9 and ribonuclease Sa provide well-documented examples of mutations which increase protein stability by modulating DSE interactions *(6, 21)*.

4.3.4. Amide Protection Factors Can be Used as a Probe of the DSE

Amide protection factors provide local probes of protein stability and can provide site-specific information about hydrogen-bonded structure in the DSE *(37–39)*. Apparent $\Delta G°_{ex}$ values for the exchange step can be calculated from the observed exchange rates and compared to the value of $\Delta G°$ for complete unfolding, provided exchange occurs in the EX2 limit. In the EX2 case, the observed rate of exchange is given by

$$k_{obs} = (k_{op}/k_{cl})k_{in}. \tag{14.2}$$

k_{op} is the rate of the opening reaction which leads to the exchange-competent state. k_{cl} is the rate of the reverse reaction from the exchange-competent state to the folded state. k_{in} is the rate expected for a residue in an unstructured polypeptide with the same sequence. The ratio k_{op}/k_{cl} equals the equilibrium constant for unfolding, K_u, for those sites which exchange by complete unfolding. Protection beyond that expected for global unfolding, "super-protection", offers evidence for hydrogen-bonded

structure in the DSE. Exchange of amide hydrogens is normally followed by recording a series of HSQC spectra after the protein is dissolved in D_2O. Of course, the studies are limited by the precision of the measurements and any uncertainty in k_{in} and, thus, are normally not able to detect sites whose protection factors are moderately increased over those expected for an unstructured peptide. It is important to stress that the failure to observe "super-protection" does not imply the complete absence of hydrogen bonding in the DSE and should not be interpreted to mean that the DSE state lacks any residual structure. For example, Shortle and coworkers pointed out that partially formed helical structure can lead to very low protection factors. Consider the case where a helix is fully formed 30% of the time and unstructured 70% of the time, the overall protection factor for exchange will still be very low (1.43), even if the H-bonded residues in the helical state have infinite protection factors *(39)*.

4.4. DSE Interactions as a Target for Protein Design

Attempts to rationally manipulate protein stability by targeting the DSE have a long, but not always successful, history. Early efforts attempted to increased stability by increasing the entropy of the DSE by the insertion of disulfides or the use of Gly-to-Ala and X-to-Pro substitution *(40–42)*. Difficulty arises if the mutations inadvertently stabilize a compact denatured state or if strain is introduced into the native state. Glycines have been the target of mutations designed to increase protein stability by reducing the entropy of the unfolded state. However glycine often adopts a conformation with positive ϕ-angles and substitution by an L-amino acid introduces strain into the folded state. An alternative strategy is to use D-amino acids and this has proven successful *(42)*. Targeting DSE electrostatic interactions provides another venue for manipulating protein stability *(6, 43)*.

References

1. Whitten, S. T., Garcia-Moreno, E. B. (2000) pH dependence of stability of staphylococcal nuclease: Evidence of substantial electrostatic interactions in the denatured state. *Biochemistry* 39, 14292–14304.
2. Shortle, D. (1996) The denatured state (the other half of the folding equation) and its role in protein stability. *FASEB J* 10, 27–34.
3. Millett, I. S., Doniach, S., Plaxco K. W. (2002) Toward a taxonomy of the denatured state: Small angle scattering studies of unfolded proteins. *Adv Protein Chem* 62, 241–262.
4. Baldwin, R. L. (2002) A new perspective on unfolded proteins. *Adv Protein Chem* 62, 361–367.
5. Choy, W. Y., Mulder, F. A. A., Crowhurst, K. A., et al. (2002) Distribution of molecular size within an unfolded state ensemble using small-angle X-ray scattering and pulse field gradient NMR techniques. *J Mol Biol* 316, 101–112.
6. Cho, J. H., Sato, S., Raleigh, D. P. (2004) Thermodynamics and kinetics of non-native interactions in protein folding: a single point mutant significantly stabilizes the N-terminal domain of L9 by modulating non-native interactions in the denatured state. *J Mol Biol* 338, 827–837.
7. Bowler, B. E. (2007) Thermodynamics of protein denatured states. *Mol Biosyst* 3, 88–99.

8. Dill, K. A., Shortle, D. (1991) Denatured states of proteins. *Annu Rev Biochem* 60, 795–825.

9. Sugase, K., Dyson, H. J., Wright, P. E. (2007) Mechanism of coupled folding and binding of an intrinsically disordered protein. *Nature* 447, 1021–1024.

10. Cho, J. H., Raleigh, D. P. (2005) Mutational analysis demonstrates that specific electrostatic interactions can play a key role in the denatured state ensemble of proteins. *J Mol Biol* 353, 174–185.

11. Matthews, C. R. (1987) Effect of point mutations on the folding of globular proteins. *Meth Enzymol* 154, 498–511.

12. Goldenberg, D. P., Frieden, R. W., Haack, J. A., et al. (1989) Mutational analysis of a protein folding pathway. *Nature* 338, 127–132.

13. Matouschek, A., Kellis, J. T., Serrano, L., et al. (1989) Mapping the transition state and pathway of protein folding by protein engineering. *Nature* 340, 122–126.

14. Fersht, A. R., Matouschek, A., Serrano, L. (1992) The folding of an enzyme: Theory of protein engineering analysis of stability and pathway of protein folding. *J Mol Biol* 224, 771–782.

15. Cho, J. H., Raleigh, D. P. (2006) Denatured state effects and the origin of non-classical phi-values in protein folding. *J Am Chem Soc* 128, 16492–16493.

16. Neri, D., Billeter, M., Wider, G., Wuthrich, K. (1992) NMR determination of residual structure in a urea-denatured protein, the 434-repressor. *Science* 257, 1559–1563.

17. Mok, Y. K., Kay, C. M., Kay, L. E., et al. (1999) NOE data demonstrating a compact unfolded state for an SH3 domain under non-denaturing conditions. *J Mol Biol* 289, 619–638.

18. Mohana-Borges, R., Goto, N. K., Kroon, G. J. A., et al. (2004) Structural characterization of unfolded states of apomyoglobin using residual dipolar couplings. *J Mol Biol* 340, 1131–1142.

19. Li, Y., Picart F., Raleigh, D. P. (2005) Direct characterization of the folded, unfolded and urea denatured states of the C-terminal domain of the ribosomal protein L9. *J Mol Biol* 349, 839–846.

20. Pace, C. N., Laurents, D. V., Erickson, R. E. (1992) Urea denaturation of barnase: pH dependence and characterization of the unfolded state. *Biochemistry* 31, 2728–2734.

21. Pace, C. N., Alston, R.W., Shaw, K.L. (2000) Charge–charge interactions influence the denatured state ensemble and contribute to protein stability. *Protein Sci* 9, 1395–1398.

22. Shortle, D., Ackerman, M. S. (2001) Persistence of native-like topology in a denatured protein in 8 M urea. *Science* 293, 487–489.

23. Kohn, J. E., Millett, I. S., Jacob, J., et al. (2004) Random-coil behavior and the dimensions of chemically unfolded proteins. *Proc Natl Acad Sci USA* 101, 12491–12496.

24. Fitzkee, N. C., Rose, G. D. (2004) Reassessing random-coil statistics in unfolded proteins. *Proc Natl Acad Sci USA* 101, 12497–12502.

25. Dyson, H. J., Wright, P. E. (2004) Unfolded proteins and protein folding studied by NMR. *Chem Rev* 104, 3607–3622.

26. Dyson, J. H., Wright, P. E. (2002) Insights into the structure and dynamics of unfolded proteins from nuclear magnetic resonance. *Advan Protein Chem* 62, 311–340.

27. Tollinger, M., Croehurst, K. A., Kay, L. E., et al. (2003) Site-specific contributions to the pH dependence of protein stability. *Proc Natl Acad Sci USA* 100, 4545–4550.

28. Marsh, J. A., Singh, V. K., Jia, Z., et al. (2006) Sensitivity of secondary structure propensities to sequence differences between alpha- and gamma-synuclein: Implications for fibrillation. *Protein Sci* 15, 2795–2804.

29. Gillespie, J. R., Shortle, D. (1997) Characterization of long-range structure in the denatured state of staphylococcal nuclease. 1. Paramagnetic relaxation enhancement by nitroxide spin labels. *J Mol Biol* 268, 158–169.

30. Grey, M. J., Tang, Y., Alexov, E., et al. (2006) Characterizing a partially folded intermediate of the villin headpiece domain under non-denaturing conditions: contribution of His41 to the pH-dependent stability of the N-terminal subdomain. *J Mol Biol* 355, 1078–1094.

31. Korzhnev, D. M., Religa, T. L., Lundstroem, P., et al. (2007) The folding pathway of an FF domain: Characterization of an on-pathway intermediate state under folding conditions by N-15, C-13(alpha) and C-13-methyl relaxation dispersion and $^1H/^2H$ H-exchange NMR spectroscopy. *J Mol Biol* 372, 497–512.

32. Zhang, O. W., Kay, L. E., Shortle, D., et al. (1997) Comprehensive NOE characterization

of a partially folded large fragment of staphy-locical nuclease Δ 131 Δ, using NMR meth-ods with improved resolution. *J Mol Biol* 272, 9–20.

33. Religa, T. L., Markson, J. S., Mayor, U., et al. (2005) Solution structure of a protein dena-tured state and folding intermediate. *Nature* 437, 1053–1056.

34. Yang, A. S., Honig, B. (1993) On the pH dependence of protein stability. *J Mol Biol* 231, 459–474.

35. Tanford, C. (1970) Potein denaturation. Part C. Theoretical models for the mechan-ism of denaturation. *Advan Protein Chem* 24, 1–95.

36. Guzman-Casado, M., Parody-Morreale, A., Robic, S., et al. (2003) Energetic evidence for formation of a pH dependent hydropho-bic cluster in the denatured state of *Thermus thermophilus* ribonuclease H. *J Mol Biol* 329, 731–743.

37. Rohl, C. A., Scholtz, J. M., York, E. J., et al.. (1992) Kinetics of amide proton exchange in helical peptides of varying chain length. Interpretation by the Lifson–Roig equation. *Biochemistry* 31, 1263–1269.

38. Marmorino, J. L., Auld, D., Betz, S. F., et al. (1993) Amide proton exchange rates of oxi-dized and reduced *Saccharomyces cerevisiae* iso-1-cytochrome c. *Protein Sci* 2, 1966–1974.

39. Mori, S., van Zijl, P. C., Shortle, D. (1997) Measurement of water-amide proton exchange rates in the denatured state of sta-phylococcal nuclease by a magnetization transfer technique. *Proteins* 28, 325–332.

40. Matsumura, M., Matthews, B.W. (1991) Stabilization of functional proteins by intro-duction of multiple disulfide bonds. *Meth Enzymol* 202, 336–356.

41. Betz, S. F. (1993) Disulfide bonds and the stability of globular proteins. *Protein Sci* 10, 1551–1558.

42. Anil, B., Song, B., Tang, Y., et al. (2004) Exploiting the right side of the Ramachan-dran plot: substitution of glycines by D-ala-nine can significantly increase protein stability. *J Am Chem Soc* 126, 13194–13195.

43. Anil, B., Craig-Schapiro, R., Raleigh, D. P. (2006) Design of a hyperstable protein by rational consideration of unfolded state inter-actions. *J Am Chem Soc* 128, 3144–3145.

INDEX